



HAL
open science

Studying the phenotypic and functional diversity of macrophages : characterization of brown adipose tissue and adrenal gland macrophages

Alexandre Gallerand

► **To cite this version:**

Alexandre Gallerand. Studying the phenotypic and functional diversity of macrophages : characterization of brown adipose tissue and adrenal gland macrophages. Human health and pathology. Université Côte d'Azur, 2022. English. NNT : 2022COAZ6014 . tel-04700057

HAL Id: tel-04700057

<https://theses.hal.science/tel-04700057v1>

Submitted on 17 Sep 2024

HAL is a multi-disciplinary open access archive for the deposit and dissemination of scientific research documents, whether they are published or not. The documents may come from teaching and research institutions in France or abroad, or from public or private research centers.

L'archive ouverte pluridisciplinaire **HAL**, est destinée au dépôt et à la diffusion de documents scientifiques de niveau recherche, publiés ou non, émanant des établissements d'enseignement et de recherche français ou étrangers, des laboratoires publics ou privés.

THÈSE DE DOCTORAT

Étude de la diversité phénotypique et fonctionnelle des macrophages :

Caractérisation des macrophages du tissu adipeux brun et des
glandes surrénales.

Alexandre GALLERAND

Laboratoire de Physiomédecine Moléculaire (LP2M)

**Présentée en vue de l'obtention
du grade de docteur en** Immunologie et
Microbiologie

d'Université Côte d'Azur

Dirigée par : Dr. Stoyan Ivanov

Soutenue le : 16 septembre 2022

Devant le jury, composé de :

Dr. Mireille Cormont, DR, C3M, Nice (présidente)

Dr. Marc Bajénoff, DR, CIML, Marseille

Dr. Joel Haas, CR, IPL, Lille

Dr. Elise Dalmas, CR, INEM, Paris

Dr. Florent Ginhoux, PR, A*STAR, Singapour

Dr. David Dombrowicz, DR, IPL, Lille

Dr. Stoyan Ivanov, CR, LP2M, Nice

Étude de la diversité phénotypique et fonctionnelle des macrophages :

Caractérisation des macrophages du tissu adipeux brun et des
glandes surrénales.

Jury :

Présidente du jury :

Dr. Mireille Cormont, DR, C3M, Nice

Rapporteurs :

Dr. Marc Bajénoff, DR, CIML, Marseille

Dr. Joel Haas, CR, IPL, Lille

Examineurs :

Dr. Elise Dalmas, CR, INEM, Paris

Dr. Florent Ginhoux, PR, A*STAR, Singapour

Invité :

Dr. David Dombrowicz, DR, IPL, Lille

Directeur de thèse :

Dr. Stoyan Ivanov, CR, LP2M, Nice

Étude de la diversité phénotypique et fonctionnelle des macrophages : caractérisation des macrophages du tissu adipeux brun et des glandes surrénales.

Résumé

Les macrophages sont des cellules myéloïdes faisant partie du système phagocytaire mononucléaire, reconnues notamment pour leur fonction d'élimination et de recyclage des cellules apoptotiques. Au cours de ces deux dernières décennies, l'étude de ces cellules a révélé une grande diversité phénotypique et fonctionnelle des macrophages. Dans les tissus, les macrophages exercent des fonctions spécifiques de chaque organe. Par exemple, les macrophages pulmonaires participeraient à la clairance du surfactant, tandis que les macrophages pancréatiques joueraient un rôle dans le recyclage de l'insuline. L'avènement des nouvelles technologies à résolution « single-cell » a cependant remis en cause la théorie selon laquelle la diversité des macrophages s'observerait uniquement à l'échelle des différents tissus, notamment en révélant une grande diversité de ces cellules à l'échelle sous-tissulaire. Divers facteurs tels que l'origine développementale ou la localisation de ces cellules au sein du tissu sont dorénavant reconnus comme facteurs clés dictant le phénotype et la fonction des macrophages. Par exemple, les macrophages cardiaques d'origine embryonnaire jouent des fonctions réparatrices tandis que les macrophages cardiaques dérivés des monocytes prônent l'inflammation et sont néfastes lors d'un infarctus du myocarde. D'autre part, la différenciation des monocytes en macrophages inflammatoires est accentuée au cours des maladies métaboliques telles que l'obésité et l'athérosclérose, et ce mécanisme est reconnu comme étant délétère. Ainsi, appréhender la diversité des macrophages au sein de chaque tissu et les mécanismes régulant leur maintenance semble être une étape majeure avant d'envisager des approches thérapeutiques centrées sur ces cellules.

Au cours de nos travaux, nous avons focalisé notre attention sur les macrophages du tissu adipeux brun et des glandes surrénales, deux populations peu – ou pas – caractérisées. Via une approche de séquençage ARN « single-cell », nous avons identifié diverses sous-populations de macrophages ayant chacune une signature transcriptionnelle propre suggérant des fonctions restreintes à chaque population. Nous avons pu expliquer cette diversité par l'origine et la localisation sous-tissulaire de ces cellules. De manière surprenante, nous avons également observé

des influences du sexe biologique sur la présence de certaines populations de macrophages. Nous avons pu déterminer que les monocytes jouent un rôle clé dans la maintenance des macrophages du tissu adipeux brun et des glandes surrénales, notamment en remplaçant les macrophages embryonnaires au fil du temps. D'un point de vue fonctionnel, au sein de ces deux tissus, la déplétion des macrophages induit une perturbation du métabolisme lipidique et une altération de l'homéostasie tissulaire, démontrant ainsi le rôle clé que jouent ces cellules.

Mots clé : Macrophage – Monocyte – Glandes surrénales – Tissu adipeux brun.

Studying the phenotypic and functional diversity of macrophages : characterization of brown adipose tissue and adrenal gland macrophages.

Abstract

Macrophages are myeloid immune cells and part of the mononuclear phagocyte system. They are known for their role in the clearance of apoptotic cells and phagocytosis of extracellular debris and pathogens. In the last two decades, several studies have brought to light the impressive phenotypic and functional heterogeneity of macrophages. In tissues, macrophages perform organ-specific functions. For example, lung macrophages clear surfactant while pancreatic islet macrophages participate in insulin recycling. However, recent single-cell based technologies have challenged the hypothesis that macrophage diversity is solely observed at the inter-organ scale, notably by revealing an underestimated macrophage diversity at the sub-tissular scale. Several parameters such as developmental origin and sub-tissular localization are now considered as key drivers of macrophage phenotype and function. For example, embryonic cardiac macrophages participate in tissue repair and resolution of inflammation while monocyte-derived cardiac macrophages support inflammation and are deleterious in myocardial infarction. Monocyte differentiation into macrophages with an inflammatory phenotype is enhanced in chronic metabolic diseases such as obesity and atherosclerosis, thus contributing to disease worsening. Understanding macrophage diversity and the mechanisms allowing the maintenance of these cells in each tissue therefore appear to be a critical step before therapeutic approaches can be designed to target these cells.

In this work, we focused on brown adipose tissue and adrenal gland macrophages, two poorly characterized macrophage populations. Using single-cell RNA sequencing, we identified macrophage sub-populations with a specific transcriptomic signature suggesting population-restricted functions. This phenotypic diversity could be explained by a different developmental origin and sub-tissular localization. Surprisingly, we observed the presence of sex-specific macrophage populations in adrenal glands that were tied to a specific sub-tissular niche. Monocytes played a key role in the renewal of both brown adipose tissue and adrenal gland macrophages, notably by replacing embryonically-seeded macrophage populations. On a functional standpoint, macrophage depletion induced a perturbation of lipid

homeostasis in both of these tissues, thus demonstrating the key role of macrophages in tissue homeostasis.

Key words : Macrophage – Monocyte – Adrenal glands – Brown adipose tissue.

Remerciements

Aux membres de mon jury,

Je tiens dans un premier lieu à remercier Dr. Mireille Cormont d'avoir accepté de présider mon jury de thèse. Je remercie mes rapporteurs Dr. Marc Bajénoff et Dr. Joel Haas, ainsi que mes examinateurs Dr. Élise Dalmas et Dr. Florent Ginhoux, d'avoir accepté de m'accorder un temps précieux afin d'évaluer mes travaux et d'en discuter lors de ma soutenance.

A mon comité de suivi de thèse,

Merci aux Drs. Abdelilah Wakkach et David Dombrowicz pour leur temps et leurs conseils bienveillants au cours de ma thèse. David, merci également pour vos multiples relectures très attentives de nos manuscrits ainsi que pour votre aide et votre accueil lors de notre venue à Lille.

Sto',

Je ne sais même pas par où commencer... Merci infiniment pour tout ! Au tout début, ça ne devait pas se passer comme ça et je suis bien heureux de la tournure des événements ! « L'important c'est qu'on s'éclate... ». Tu m'as clairement aidé à trouver ma vocation et j'ai beaucoup de chance d'avoir eu un mentor comme toi. Merci de t'être battu pour moi, merci pour ton soutien. Merci pour ton enseignement au travers de ton exigence mais aussi ta confiance et la liberté que tu m'as laissé. Je ne vais pas m'éterniser, pour rester bref tu es un directeur de thèse et maintenant un chef d'équipe parfait ! Et je peux dire avec beaucoup de confiance que ceci n'est pas la fin...

Rodolphe,

Tu as éveillé ma curiosité dès notre rencontre et je ne regrette pas d'avoir creusé. En plus de tes super goûts musicaux, j'ai découvert un scientifique hors pair, et j'ai beaucoup pu apprendre avec toi. Ton attention du moindre détail, ta débrouillardise et tes design de sioux font de toi une source d'inspiration. « En contrôle », je me demande souvent ce que tu dirais de mes manips ! Au-delà de ça, on a aussi traversé beaucoup de choses ensemble ces dernières années et je n'oublierai pas ça. Merci pour tout, je te souhaite beaucoup de belle science et surtout de bonheur.

Bastien,

Ton arrivée au sein du groupe était grandement attendue pour démarrer le projet, et surtout car tu serais mon premier acolyte de thèse, malheureusement tout ça fut un peu plombé par le covid ! Mais je dois dire qu'on s'est quand même pas mal débrouillés. Je suis heureux que tu aies choisi de rester avec nous pour ta thèse après ça, ce projet a été super fun à développer ensemble. Et je dois surtout dire que ton évolution a été fulgurante depuis ! Merci énormément pour ton aide au labo, et surtout d'avoir pris tant de choses en main au fil du temps. Merci aussi pour ton franc

parler et ton sens de l'humour bien aiguisé ! Et comme je sais à quel point tu aimes voyager, n'hésite pas si tu veux ajouter Saint Louis à ton palmarès...

Stephan,

Je n'oublierai jamais le jour où je t'ai vu débouler dans mon bureau pour te réfugier des cris du couloir... Une belle rencontre ! Bon, cette rencontre t'a coûté super cher en café... Mais quand même, une belle rencontre ! Merci énormément pour nos discussions (très) matinales quotidiennes et tes conseils. Et aussi, merci pour les cafés quand même ! Ce n'est qu'un aurevoir, keep in touch.

Johanna,

Tu es la première personne avec qui j'ai travaillé au labo, et je dois dire que tu m'as tout de suite impressionné par ton exigence et la quantité de boulot que tu abattais ! Merci énormément pour ton encadrement pendant mon stage de M1, tu as été une thésarde inspirante et j'aurais aimé que l'on puisse continuer à bosser ensemble par la suite ! Je te souhaite beaucoup de réussite en post-doc.

Adélie,

J'ai été super heureux de faire ta rencontre en début de thèse, c'était un plaisir de t'avoir comme voisine de bureau au quotidien. Faut dire qu'autant de savoir-vivre ça aide, surtout quand il s'agit de bière. Merci pour ton expertise et ton aide au labo, mais surtout pour ta bienveillance, tes conseils et ta sagacité dans les moments moins faciles ! A toi et au Kik', je vous souhaite beaucoup de bonheur ensemble ainsi que de la réussite dans vos carrières.

Nathalie,

Tu es l'incarnation de la bienveillance et la gentillesse, c'en est presque irréel. Merci pour ton aide très précieuse au labo et ta bonne humeur au quotidien ! Je te souhaite le meilleur.

Alexia / 647,

Je l'ai toujours dit : si un jour je lance mon labo, tu fais partie des premières personnes que je voudrais recruter ! Tu fais un boulot de qualité et si précieux, j'ai beaucoup de chance d'avoir eu ton aide pendant une partie de ma thèse. C'est dommage que nos chemins se soient séparés plus tôt que prévu (« ça me dégoûte » comme on dit). Merci aussi pour ta bonne humeur et ton humour ! Je te souhaite beaucoup de bonheur et de réussite.

Adeline,

Bien qu'on n'ait pas eu le temps de bosser ensemble très longtemps, je suis ravi d'avoir fait ta connaissance. Merci pour ton aide ces derniers mois ! Je suis très heureux que tu aies rejoint le labo et je suis convaincu que la suite du projet est entre de bonnes mains.

Zak',

Quel phénomène ! Merci beaucoup pour ces 6 mois passés ensemble à se marrer. Et pour le flux constant de M&M's. Bon, je dois dire aussi que tu as été un super stagiaire et que je suis impressionné par la vitesse à laquelle tu t'es approprié le projet ! Tu es un élément précieux au labo et je suis content que tu aies décidé de trainer encore un peu par ici !

Axelle,

Ce fut un plaisir de travailler avec toi ces 6 derniers mois ! Merci beaucoup pour ton aide sur le projet, tu as fait du super boulot. Je te souhaite de faire une super thèse, tu en as les capacités. Il faut juste s'en convaincre et s'énerver un peu plus ! Et n'oublie pas de lancer ta stim !

Fairouz,

Merci pour ta bonne humeur au quotidien, et les scènes surréalistes avec Bast' ! Je te souhaite de faire une super thèse et beaucoup de réussite. Je suis sûr que ça va rouler, Stoyan veille au grain.

Laurent,

Merci de m'avoir permis de rejoindre ton équipe il y a bientôt 5 ans et de m'y avoir laissé la liberté d'évoluer. Je n'oublie pas comment et avec qui tout cela a commencé.

A Laurent Boyer et Océane Dufies,

Merci énormément pour votre accueil lors de mon second stage, j'ai pris beaucoup de plaisir à travailler avec vous et toute l'équipe,

A tous ceux que j'ai eu le plaisir de rencontrer et côtoyer au cours de ces dernières années, merci beaucoup pour ces discussions (scientifiques ou pas) et parfois collaborations ! Je pense notamment à Jérôme Gilleron, Philippe Gual, Sandrine Marchetti, Véronique Corcelle, Claudine Blin, Julia Halper...

Et bien évidemment,

Je remercie ma famille et mes amis, et tout particulièrement ma femme et ma fille, sans qui rien ne serait possible et qui sont mes piliers au quotidien !

"It's not the Destination, it's the journey."
Ralph Waldo Emerson

Table of contents

RESUME	3
ABSTRACT	5
REMERCIEMENTS	7
TABLE OF CONTENTS	10
TABLE OF ILLUSTRATIONS	11
ABBREVIATIONS	12
INTRODUCTION	14
CHAPTER 1 – MONONUCLEAR PHAGOCYTES.	15
A. <i>Overview</i>	15
B. <i>Macrophages</i>	16
C. <i>Monocytes</i>	18
D. <i>Dendritic cells</i>	19
CHAPTER 2 – EMBRYONIC ORIGINS OF MACROPHAGES.	21
A. <i>Overview</i>	21
B. <i>Yolk-sac progenitors</i>	23
C. <i>Fetal liver hematopoiesis</i>	24
CHAPTER 3 – MYELOPOIESIS.	28
A. <i>Definitive hematopoiesis</i>	28
B. <i>Transcriptional control of myelopoiesis</i>	30
C. <i>Niche and HSC homeostasis</i>	33
CHAPTER 4 – BLOOD MONOCYTES	37
A. <i>Monocyte mobilization</i>	37
B. <i>Metabolic control of monocytes</i>	39
CHAPTER 5 – MONOCYTE-DERIVED MACROPHAGES.	41
A. <i>Overview</i>	41
B. <i>The macrophage niche</i>	41
C. <i>Homeostatic macrophage replenishment</i>	43
D. <i>Monocyte-derived macrophages in pathology : cardiovascular diseases.</i>	45
CHAPTER 6 – MACROPHAGE FUNCTIONS IN TISSUES	48
A. <i>Ovary macrophages</i>	48
B. <i>Testicular macrophages</i>	49
C. <i>Pancreatic macrophages</i>	50
D. <i>White adipose tissue macrophages</i>	52
RESULTS	55
PROJECT 1: DIVERSITY AND FUNCTIONS OF BROWN ADIPOSE TISSUE MACROPHAGES.	55
A. <i>Hypothesis and aims</i>	55
B. <i>Discussion and perspectives</i>	79
PROJECT 2: DIVERSITY AND FUNCTIONS OF ADRENAL GLAND MACROPHAGES.	89
A. <i>Hypothesis and aims</i>	89
B. <i>Discussion and perspectives</i>	128
LIMITATIONS OF THE STUDY	134
CONCLUSION	136
REFERENCES	138
OTHER ARTICLES AND REVIEWS	163

Table of illustrations

<i>Figure 1. Schematic representation of mononuclear phagocyte diversity</i>	15
<i>Figure 2. Schematic representation of macrophage seeding waves.</i>	27
<i>Figure 3. Current model for myelopoiesis.</i>	30
<i>Figure 4. Schematic representation of the bone marrow stem cell niche.</i>	34
<i>Figure 5. Schematic representation of Ly6C^{high} monocyte maturation into patrolling monocytes or monocyte-derived macrophages.</i>	38
<i>Figure 6. Schematic representation of the localization of the main adipose tissue depots in mice, and brown adipose tissue in humans.</i>	53
<i>Figure 7. Graphical summary of the findings on BAT monocytes and macrophages.</i>	79
<i>Figure 8. Diversity of brown adipose tissue macrophages.</i>	82
<i>Figure 9. Clues on potential BAT macrophage functions.</i>	86
<i>Figure 10. Schematic representation of adrenal gland organization and functions.</i>	89
<i>Figure 11. Development and evolution of the murine and human adrenal cortex.</i>	90
<i>Figure 12. Newly-recruited macrophages contribute to both MHC-II^{high} and MHC-II^{low} populations.</i>	131
<i>Table 1. Macrophage and monocyte fate mapping models.</i>	22

Abbreviations

AM : Alveolar macrophage
AMPK : Adenosine monophosphate-activated protein kinase
ATGL : Adipose triglyceride lipase
ATM : Adipose tissue macrophage
ATP : Adenosine triphosphate
BAT : Brown adipose tissue
BrdU : Bromodeoxyuridine
CAR cells : CXCL12- abundant reticular cells
CCL : C-C motif chemokine ligand
CCR : C-C motif chemokine receptor
CD : Cluster of differentiation
cKit : Proto-oncogene c-KIT
Clec : C-Type Lectin Domain Family
CLS : Crown-like structure
CNS : Central nervous system
cMoP : Common monocyte progenitor
CMP : Common myeloid progenitor
CSF1 : Colony stimulating factor 1
CSF2Rb : Colony stimulating factor 2 receptor subunit beta
CSF1R : Colony stimulating factor 1 receptor
CXCL12 : C-X-C motif chemokine 12
CXCR4 : C-X-C chemokine receptor type 4
CX3CR1 : CX3C chemokine receptor 1
DPE : Distal promoter element
DT(R) : Diphtheria toxin (receptor)
EGF : Epidermal growth factor
EMP : Erythro-myeloid progenitor
FAO : Fatty acid oxidation
FGF : Fibroblast growth factor
FIRE : Fms-intronic regulatory element
Flt3 : Fms-like tyrosine kinase 3
Flt3L : Fms-like tyrosine kinase 3 ligand
Glut1 : Glucose transporter 1
GMP : Granulocyte-monocyte progenitor
GM-CSF : Granulocyte-macrophage colony stimulating factor
GR : Glucocorticoid receptor
HIF-1 α : Hypoxia inducible factor 1 subunit alpha
HILPDA : Hypoxia inducible lipid droplet associated
HSC : Hematopoietic stem cell
IFN : Interferon
IL : Interleukin

IRF : Interferon regulatory factor
KC : Kupffer cell
Klf4 : Kruppel-like factor 4
LAM : Lipid-associated macrophage
LepR : Leptin receptor
Ly6C : Lymphocyte antigen 6 family member C
Lyve 1 : Lymphatic vessel endothelial hyaluronan receptor 1
LyzM : Lysosyme M
LXR α : Liver X receptor alpha
Mafk : MAF BZIP transcription factor B
MDP : Monocyte-dendritic cell progenitor
MEP : Megakaryocyte-erythrocyte progenitors
MerTK : Myeloid-epithelial-reproductive tyrosine kinase
MHC-II : Major histocompatibility complex class II
MPP : Multipotent progenitor
Ms4a3 : Membrane-spanning 4-domains subfamily A member 3
Mx1 : MX dynamin like GTPase 1
NASH : Non-alcoholic steatohepatitis
Nr4a1 : Nuclear receptor subfamily 4 group A member 1
PDGF : Platelet-derived growth factor
PPAR : Peroxisome proliferator-activated receptor
RNA : Ribonucleic Acid
Runx1 : RUNX family transcription factor 1
R26 : Rosa 26 locus
SAM : Sympathetic neuron-associated macrophage
Sca1 : Stem cell antigen 1
SCENITH : Single-cell energetic metabolism by profiling translation inhibition
Scf : Stem cell factor
TCA cycle : Tricarboxylic acid cycle
Timd4 : T-cell immunoglobulin and mucin domain containing 4
TNF α : Tumor necrosis factor alpha
Trem2 : Triggering receptor expressed on myeloid cells 2
Trem14 : Triggering receptor expressed on myeloid cells like 4
UCP1 : Uncoupling protein 1
VAM : Vasculature-associated macrophage
VEGF : Vascular endothelial growth factor
WAT : White adipose tissue
XCR1 : X-C motif chemokine receptor 1
Zbtb46 : Zinc finger and BTB Domain containing 46
Zeb2 : Zinc finger E-box binding homeobox 2

Introduction

Myeloid cells, together with lymphoid cells, represent the main cellular defense mechanism of the organism. The myeloid branch of the immune system is composed of macrophages, dendritic cells, monocytes, neutrophils and eosinophils. These effector cells can be rapidly mobilized upon infection to initiate the innate immune response, but they also play physiological roles at steady state, and can be activated in the presence of sterile inflammation. Dysfunctions of the immune system have been observed during pathologies such as auto-immune diseases and inflammatory diseases. Among myeloid cells, mononuclear phagocytes comprise macrophages, monocytes and dendritic cells¹. They are specialized in the detection, uptake and degradation of extracellular components such as pathogens, cellular debris or apoptotic cells. Resulting processed antigens may eventually be presented via major histocompatibility complexes to prime the adaptive immune system, therefore allowing to mount a full and effective immune response upon infection. Understanding the diversity and functions of mononuclear phagocytes in health and disease therefore appears crucial to envision new therapeutic approaches centered around those cells.

The results presented in this thesis focus on two poorly characterized macrophage populations, namely brown adipose tissue and adrenal gland macrophages, in order to characterize their diversity, ontogeny and functions.

Chapter 1 – Mononuclear phagocytes.

A. Overview

The developmental and functional interrelationship of mononuclear phagocytes have long been controversial, especially because these cells share many cell-surface markers confusing their identification¹. The emergence of new genetic tools has now allowed a better understanding of the diversity of these cells through fate-mapping experiments. It is now well-established that *bona fide* dendritic cells are seeded and maintain independently of the monocytic lineage, and monocyte-derived macrophages coexist with embryonic macrophages – which don't rely on monocyte recruitment for their maintenance – in most tissues. The first chapter of this manuscript will be dedicated to clearly defining the identity and general roles of mononuclear phagocytes, while the rest of the manuscript will focus on macrophage biology.

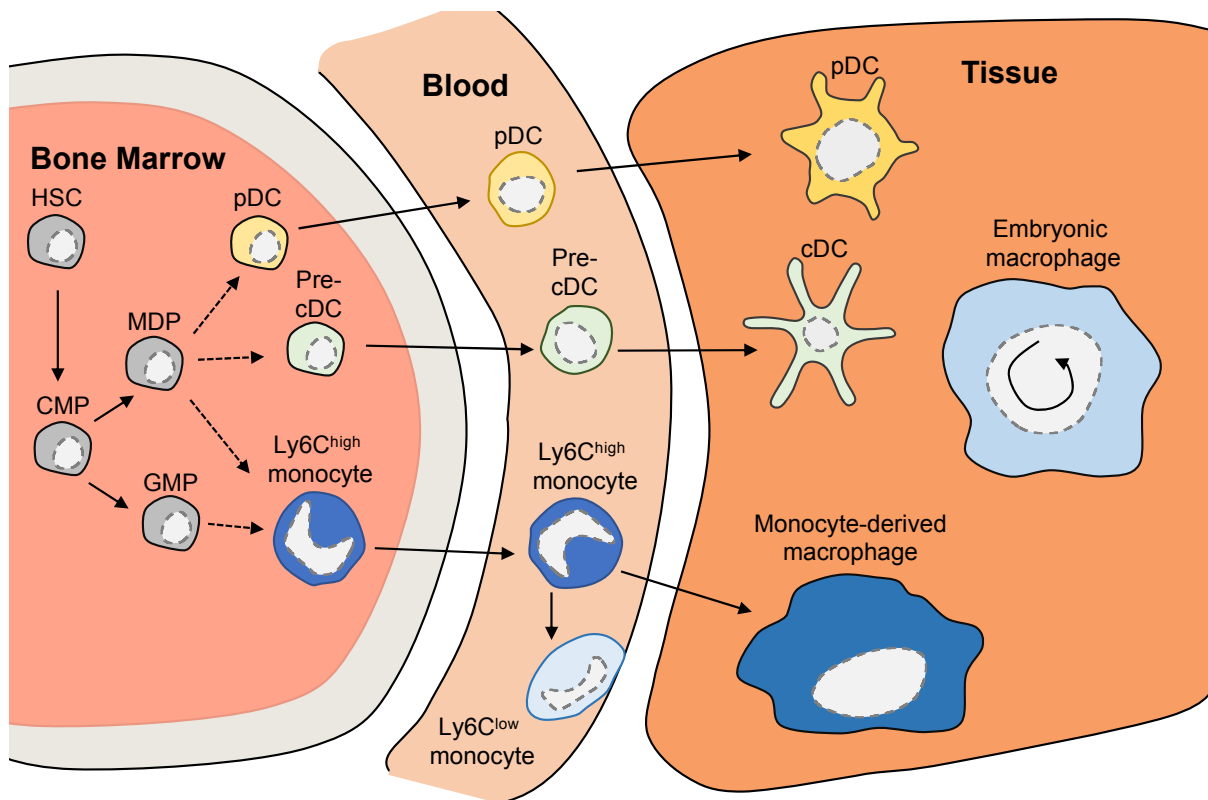


Figure 1. Schematic representation of mononuclear phagocyte diversity

B. Macrophages

Macrophages were first observed by Ilya Metchnikov in 1882 who gave the name “macrophage” to cells presenting the capacity to engulf and degrade extracellular material and foreign bodies. Metchnikov was later awarded the Nobel prize for his discovery of phagocytosis. Nowadays, macrophages are still mainly recognized for their capacity to engulf and recycle dead cells – a process called efferocytosis – and to clear foreign material such as pathogens. Historically, macrophages were identified *in vivo* by criteria such as morphology, size and intracellular composition. Later, identification of the F4/80 marker² facilitated the observation of macrophages in many tissues and allowed to define their particular sub-tissular localization, which suggested potential local functions³⁻⁷. Over the last four decades, extensive work has aimed at identifying the factors determining macrophage seeding, maintenance, activation and function, and how these parameters reflected through their phenotypic diversity. F4/80⁺ cells are decreased in most tissues of op/op mice which bear an inactivating mutation in the gene coding for the growth factor CSF1 (colony stimulating factor 1), indicating that CSF1 is necessary for macrophage survival^{8,9}. This phenotype was also observed in mice deficient for the CSF1 receptor (CSF1R, CD115)¹⁰, which is highly expressed among mononuclear phagocytes¹¹. Absence of macrophages was first attributed to the lack of blood monocytes in these mice, since previous work suggested that macrophages originated from bone marrow precursors¹²⁻¹⁴. However, although CSF1 administration rescued hematopoietic defects and monocyte production¹⁵, tissue macrophage restoration was mostly partial and restricted to certain tissues⁹. These results indicated that monocyte contribution to the tissue macrophage pool was not systematic, and supported other reports suggesting a dual origin of tissue macrophages^{16,17} and showing the existence of macrophage maintenance through self-proliferation¹⁸⁻²⁰. It is now well-established that CSF1R signaling – triggered by binding either CSF1 or IL-34²¹ – regulates seeding and survival of most tissue macrophages²², with the exception of lung alveolar macrophages which rely on GM-CSF²³. Analysis of CSF1-knockout mice showed persistence of microglia²⁴ while these cells were absent in CSF1R^{-/-} and IL-34^{-/-} mice²⁵, showing the dependence of microglia on IL-34^{25,26}. IL-34 is also necessary for maintenance of Langerhans cells²⁶ in the skin and peripheral nervous system macrophages²⁷.

More recent work established the current consensus that macrophages are identified as cells co-expressing CD64 (Fcgr1) and MerTK²⁸ in mice, while F4/80

expression was reported on other cell types (eosinophils and a subset of dendritic cells)^{29,30}. Phenotypic analysis of tissue resident macrophages using flow cytometry quickly revealed a heterogeneity of these cells across tissues. Furthermore, elaborate fate-mapping experiments established that macrophages are also heterogenous in development with either an embryonic origin, a monocytic origin, or a mixture of both³¹ (detailed in chapters 2 and 3). Comparative analysis of macrophage transcriptome and chromatin landscape from different tissues further brought to light the phenotypic diversity of these cells on the scale of the whole organism, and supported the idea of imprinting by the local environment^{28,32}. This also suggested that macrophages could play tissue-restricted functions on top of their canonical phagocytic properties^{28,32}. This complexity was further enhanced by recent single-cell RNA sequencing analysis, that revealed an unanticipated macrophage diversity at the sub-tissular level. It is now becoming clear that diverse macrophage subsets coexist across tissues, and these subsets are defined by their conserved origin, maintenance mechanisms, expression of specific surface markers and sub-tissular localization^{33,34}. Notably, across all tissues, Lyve1^{high} MHC-II^{low} macrophages are found to be mostly of embryonic origin and associated to blood vessels while Lyve1^{low} MHC-II^{high} CX3CR1⁺ macrophages are associated with neurons and are replenished by monocytes^{33,34}. Nevertheless, unbiased clustering of these macrophage subsets transcriptional signature across tissues still shows the dominance of tissue imprinting over developmental origin on macrophage phenotype³³.

Recent technologies have thus revealed an impressive macrophage diversity in almost every organ, raising many exciting questions about these cells. Our current understanding of macrophage biology suggests that subset-specific functions and phenotypes mainly depend on cell localization within the tissue, while contribution of monocytes to the macrophage pool may influence inflammatory potential. The functions of tissue resident macrophages have, for the most part, been addressed considering that macrophage populations were homogenous. Recent advances in the field have highlighted the heterogeneity of tissue resident macrophages and some of these past conclusions may need to be revisited thoroughly. Defining each subset's localization and the factors controlling their development, maintenance and functions will be the next step in the macrophage field.

C. Monocytes

Monocytes are short-lived circulating myeloid cells, generated in the bone marrow through hematopoiesis in a CSF1-dependent manner³⁵. *In vivo* use of ³H-thymidine allowed the identification of the hematopoietic origin of monocytes and their half-life in the blood circulation was estimated at around 20 hours both in mice^{36,37} and humans, although this observation did not take into account the diversity of monocytes³⁸. These early observations were recently revisited using genetic reporters³⁹. Pioneering studies described the phagocytic properties of monocytes^{40,41} and their capacity to differentiate to macrophages both *in vitro* and *in vivo*⁴²⁻⁴⁵. Monocytes have also been identified in tissues⁴⁶, where they can either differentiate into macrophages or uptake antigens and migrate to lymph nodes through lymphatic vessels^{46,47}.

Two major monocyte subsets are present in the blood, both in mice and humans : classical and patrolling monocytes^{48,49}. Although these monocyte subsets are developmentally interconnected, they differ in their phenotype and functions⁵⁰. Classical monocytes, also called inflammatory monocytes, are identified as CD14⁺ CD16⁻ cells in humans⁴⁸ and Ly6C^{high} in mice⁴⁹. Patrolling monocytes are identified as CD14^{low} CD16⁺ cells in humans⁴⁸ and Ly6C^{low} in mice⁴⁹, and they further express CD43⁵¹. As their name suggests, Ly6C^{low} monocytes have a patrolling behavior in the blood vasculature⁵². They are tightly associated to endothelial cells, which they survey in order to remove dying cells and maintain endothelium homeostasis⁵³. Patrolling monocytes have been shown to differentiate from classical monocytes both in mice and humans^{38,39,54,55}. The transition of Ly6C^{high} to Ly6C^{low} monocyte is characterized by down-regulation of Ly6C and CCR2 and up-regulation of Trem14 and CX3CR1⁵⁶, and the maintenance of patrolling monocytes depends on the transcription factor Nr4a1⁵⁷. Their half-life is longer than that of classical monocytes, and their survival is extended when classical monocytes are depleted due to increased circulating CSF1 availability^{38,39}. In humans, a third subset identified as CD14⁺ CD16⁺ is also found in significant proportions and these cells correspond to an intermediate differentiation stage of classical monocytes into patrolling monocytes³⁸.

Monocytes are important mediators of inflammation and their numbers in blood can be correlated to several pathologies. Understanding the factors influencing their generation, mobilization, survival and recruitment potential therefore appears crucial. Further insights about monocyte biology will be developed in chapter 4.

D. Dendritic cells

Dendritic cells are pivotal antigen presenting cells able to uptake antigens locally, migrate to lymph nodes through lymphatic vessels and activate both CD4⁺ and CD8⁺ T cells which can in turn spark the adaptative immune response. They were discovered in 1973 when Ralph Steinman and Zanvil Cohn isolated adherent cells from lymphoid organs with features different of macrophages⁵⁸. Unlike macrophages, these cells were motile and lowly phagocytic⁵⁸. The term “dendritic cell” was chosen due to their numerous protrusions, further defining the difference between these cells and macrophages⁵⁸. Distinguishing dendritic cells from macrophages and monocytes *in vivo* has always been challenging since expression of CD11c and MHC-II – two canonical DC markers – is shared among many mononuclear phagocytes¹. After their discovery, dendritic cells were quickly proposed to derive from circulating monocytes⁵⁹. Although this is possible *in vitro*⁶⁰, discovery of the Zbtb46 transcription factor which is expressed in conventional dendritic cells (cDCs) and their progenitors, but not in monocytes and macrophages^{60,61}, allowed a definitive separation of cDCs from the monocyte lineage⁶². Indeed, *Maifb^{cre} x R26^{YFP} x Zbtb46^{GFP}* mice allowing separate tracking of the monocyte and dendritic cell lineages lack YFP⁺ GFP⁺ cells in tissues even during inflammation, although Langherans cells stand out as the only cells with a dual origin and express both *Maifb* and *Zbtb46*⁶⁰. This result was further confirmed in *Ms4a3^{cre} x R26^{TdTomato}* mice, which allow tracking of the monocyte lineage and do not show labeling of dendritic cells⁶³.

Dendritic cells originate from bone marrow precursors and depend on Flt3-Flt3L signaling for their maturation and survival⁶⁴⁻⁶⁶. They comprise plasmacytoid dendritic cells (pDCs), and conventional dendritic cells (cDCs). pDCs are identified through their expression of the markers B220 and Siglec-H, and they are developmentally different from cDCs. Indeed, they do not arise from *Zbtb46*⁺ precursors and rely on the transcription factors E2-2 and IRF8 for their proper development and function^{67,68}. pDCs are mainly involved in antiviral responses through the production of type I interferon⁶⁹. cDCs can be further divided into two sub-types : cDC1s and cDC2s. All cDCs express high levels of the integrin CD11c and MHC class II but, in lymphoid tissues, cDC1s express CD8, CD24 and XCR1 while cDC2s are characterized by CD4 and *Sirpa* expression. In nonlymphoid tissues, cDC1s are described as CD103⁺ and XCR1⁺ and cDC2s as CD11b⁺ and *Sirpa*^{+70,71}. This phenotypic description correctly applies to the majority of tissues with few exceptions such as the small intestine, where

a population of CD103⁺ cDC2s was described⁷². A third cDC subset, named cDC3, was recently observed in studies using single-cell RNA sequencing⁷³. Upon activation, notably through pattern recognition receptors, dendritic cells migrate through lymphatic vessels to reach lymph nodes where they can initiate the adaptive immune response^{74,75}. Dendritic cell migration via the lymphatic system fully relies on their expression of the chemokine receptor CCR7^{76,77}, which depends on their activation status, and chemotactic gradients of the CCR7 ligands CCL19 and CCL21^{78,79}.

Chapter 2 – Embryonic origins of macrophages.

A. Overview

More than fifty years ago, a pioneering study reported the presence of yolk sac progenitors able to give rise to macrophages in mouse embryos⁸⁰. The formal presence of mature macrophages, identified via F4/80 immunostaining, was later reported in the yolk sac and liver as soon as embryonic day 10 (E10)⁸¹. It has since become clear that the establishment of these cells is preceded by successive waves of primitive hematopoiesis, which initiate in the yolk-sac. The first wave takes place around E7 and seeds predominantly microglia²⁵. The second wave initiates around E8.25 when erythro-myeloid progenitors (EMPs) arise in the yolk-sac and later colonize the fetal liver via the blood circulation in which they expand and participate to fetal liver hematopoiesis around E10⁸²⁻⁸⁵. Fetal liver hematopoiesis is completed by a third wave of HSCs that arise from the aorta-gonad-mesonephros and seed the fetal liver around E10.5. At birth, hematopoietic progenitors seed the bone marrow, which represents the major site of hematopoiesis throughout adult life (developed in chapter 3). Although they differ in development, macrophages seeded by yolk-sac precursors partly overlap phenotypically with macrophages arising from fetal liver hematopoiesis³⁴. By contrast, macrophages arising from definitive bone marrow hematopoiesis lack expression of these markers and they highly express MHC-II and CCR2³⁴. Embryonic and monocyte-derived macrophages co-exist in many tissues, and they perform different functions. Interestingly, some tissues rely entirely on one mechanism for macrophage maintenance. For instance, brain microglia is totally independent from monocytes at steady state while intestinal lamina propria macrophages are continuously replenished by monocytes⁸⁶. In this chapter, we will discuss the seeding of macrophages by yolk-sac and fetal liver progenitors.

Promoter	Model	Target cell	Conditional expression (inducible models)	Refs
Cx3cr1	cre	Monos & Mφ	Adults : Monocytes, CX3CR1 ⁺ Mφ E8.5 : YS Mφ & EMPs E13.5 onwards : FL HSPCs & monocytes	39,87-89
	creER			
Ccr2	GFP	Monos & Mφ	Adults : Ly6C ^{high} monocytes, CCR2 ⁺ Mφ	72,90-92
	cre			
	creER			
Ms4a3	GFP	GMP & progeny, partly MDP progeny	GMP & progeny, partly MDP progeny	63
	cre			
Csf1r	creER	Monos & Mφ	E8.5 : YS Mφ & EMPs Adults : Monocyte progenitors and lineage	85,93-98
	GFP			
	RFP			
Flt3	cre	FL MDPs, HSC & progeny	/	94,99,100
	creER			
Runx1	cre	HSCs, EMPs	E7.0-7.5 : YS Mφ E8.5 : YS Mφ & EMPs E9.5 onwards : HSCs	25,100,101
	merCREmer			
LysM	GFP	Myeloid cells	/	102,103
F4/80	cre	Macrophages	/	104
	cre			
Kit	cre	EMPs, HSPCs	E7.5 : YS Mφ E8.5 : YS Mφ, EMPs, AGM progenitors	105-108
	merCREmer			
Lyve1	cre	Lyve1 ⁺ Mφ	Lyve1 ⁺ Mφ	109-111
	creER			
Clec4f	cre	Kupffer cells	/	112
Mx1	cre	HSC & progeny	HSC-derived cells	94,113
Mafb	mCherry-cre	Monos & Mφ	/	62
Zbtb46	GFP	Conventional DCs	/	60,62

Table 1. Macrophage and monocyte fate mapping models.

Partly adapted from Xu Y *et al.*¹¹⁴. Only labelling in target cells is indicated. For instance, Ms4a3^{cre} is lowly expressed in sperm, Lyve1^{cre} labels lymphatic endothelial cells and dendritic cells express CX3CR1^{gfp}. *DPE : Distal promoter element. Csf1r-eCFP mice lack the DPE upstream of the Csf1r transcription start site, and only cells relying on the intronic FIRE enhancer are labeled in this mouse. Monos : monocytes. EMPs : erythromyeloid progenitors. HSPCs : hematopoietic stem and progenitor cells (includes cKit⁺ Sca1⁻ progenitors). HSCs : hematopoietic stem cells (Lin⁻ Sca1⁺ cKit⁺ cells). AGM : aorta-gonad-mesonephros. FL : fetal liver. YS : yolk sac. MDP : monocyte-dendritic cell progenitor. GMP : granulocyte-monocyte progenitor.

B. Yolk-sac progenitors

The emergence of genetic fate-mapping models allowed to robustly demonstrate the contribution of yolk-sac progenitors to hematopoiesis¹⁰¹. EMPs are characterized by their expression of cKit (CD117, the receptor for stem cell factor) and CSF1R. Their differentiation into pre-macrophages in the yolk-sac is characterized by loss of cKit expression and up-regulation of CX3CR1^{25,115}. Both EMPs and pre-macrophages start colonizing the embryo around E9, and the majority of this migration occurs before E12.5¹⁰⁶. This process necessitates the onset of the blood circulation, suggesting that seeding of tissue macrophages occurs through the vascular route^{25,84,106}. Trans-tissue migration of progenitors is another possibility that remains to be properly addressed. Optimal seeding of organs by pre-macrophages during embryogenesis depends on CX3CR1^{106,116}, and these cells start acquiring their tissue-specific signature as they differentiate¹¹⁶, highlighting the impact of microenvironmental imprinting even in the earliest stages of life. Mature macrophages start proliferating in tissues as soon as E10.5, and they maintain by self-proliferation throughout life⁹⁴.

Several genetic reporters have been used to track embryonic yolk-sac-derived macrophages¹¹⁴. These include inducible Runx1^{mer-CRE-mer 25} and CSF1R^{mer-CRE-mer 85,94} crossed to fluorescent reporters with cre induction at E8.5. This approach demonstrates that certain tissue-resident macrophage populations arise from Runx1⁺ or CD115⁺ cells present at this developmental stage, while cre induction at a later developmental stage fails to label them. The contribution of yolk-sac progenitors to macrophage seeding was further demonstrated by analyzing macrophage content in Myb-deficient embryos⁹⁴, which show major defects in hematopoietic stem cells (HSCs)¹¹⁷. Indeed, a population of F4/80^{bright} CD11b⁺ macrophages was maintained in Myb^{-/-} embryos, and inducible deletion of Myb in hematopoietic cells failed to deplete certain tissue-resident macrophages suggesting their independence from Myb and monocyte replenishment⁹⁴.

One classical example of yolk-sac-derived macrophages is that of microglia in the brain. The presence of microglial cells in brain rudiments, identified by F4/80 staining, was reported as soon as E8 and the yolk-sac was proposed as their origin¹¹⁸. These cells show strong proliferation *in situ* until they approach their maximal population size around two weeks post birth¹¹⁸. The seeding of microglia by yolk-sac-derived precursors was formally demonstrated in fate-mapping experiments with Runx1^{mer-CRE-mer} x R26^{eYFP} mice²⁵. Indeed, time-lapse induction of cre recombinase

activity showed a peak labelling efficiency around E7.25, before hematopoiesis takes place, and seeding of the brain by Runx1⁺ progenitors needed a functional vascular system²⁵. Development of microglia was altered in IRF8^{-/-} mice and absent in PU.1^{-/-} mice, and this was linked to impaired yolk-sac progenitor maturation further supporting the yolk-sac origin of microglia¹¹⁹. Microglia is maintained independently from monocyte recruitment throughout life at steady state. Indeed, parabiosis experiments showed that less than 5% of microglia were monocyte-derived even one year after parabiosis establishment²⁵, and no labeling of microglia was found using Ms4a3^{cre}-driven labeling of the monocyte lineage⁶³. However, monocytes can be recruited to the brain upon injury and give rise to microglial cells, often identified by their expression of Iba1^{120,121}. However, these monocyte-derived microglial cells are short-lived and do not maintain after resolution of inflammation¹²². Resident microglia plays key roles in the maintenance of brain homeostasis and function^{123,124}. However, the role of CNS (central nervous system)-infiltrating monocytes is not as straightforward. In experimental autoimmune encephalitis models, these cells play a detrimental role in the development of the disease¹²². However, they are beneficial in Alzheimer's disease models and contribute to alleviating amyloid plaque burden¹²⁵. Understanding the subset-restricted factors regulating the maintenance of resident and monocyte-derived microglia in disease conditions therefore appears crucial to envision new therapeutic strategies. The short lifespan of monocyte-derived microglial cells could perhaps be explained by the fact that maintenance of microglial identity relies on the transcription factor Sall1, which is not induced in monocyte-derived cells¹²⁶. Another factor that may explain this phenotype is their dependence on CSF1¹²⁷ while resident microglia depend on IL-34²⁵, the main CSF1R ligand produced in the brain¹²⁸. CSF1-producing and IL-34-producing neurons are situated in restricted regions of the brain¹²⁸, and whether monocyte-derived microglia competes with resident microglia to occupy specific niches during inflammation is an open question.

C. Fetal liver hematopoiesis

Fetal hematopoiesis is initiated when yolk-sac EMPs seed the fetal liver, proliferate *in situ* and give rise to blood myeloid cells and erythrocytes⁸⁵. The fetal liver is also seeded by HSCs that arise from the aorta-gonad-mesonephros region¹²⁹⁻¹³¹. Fetal liver-derived hematopoietic stem cells further disseminate through the blood

circulation and seed the definitive hematopoietic tissues¹³². The generation of fetal liver progenitors by EMPs depends on the transcription factor c-myb¹¹⁷, while myelopoiesis depends on the transcription factor PU.1^{133,134}. Both c-myb and PU.1 are induced in fetal liver EMPs during the establishment of hematopoiesis^{100,135}. Fetal liver monocytes arise either from c-myb-dependent EMPs, or from HSCs which engraft in the fetal liver after EMPs¹³⁶, and these monocytes start seeding tissues around E13.5¹⁰⁰. Importantly, fetal liver-derived monocytes start diluting or replacing tissue yolk-sac-derived macrophages at that stage¹⁰⁰, and fetal liver-derived macrophages are predominant in most adult tissues¹⁰⁷. These embryonic macrophages persist into adulthood and maintain independently from monocytes through self-proliferation, and they can be identified by their expression of the marker Timd4^{137,138}.

A well-characterized example of fetal liver-derived macrophage development is that of liver Kupffer cells (KCs). The first macrophages to be seeded in the fetal liver arise from CX3CR1⁺ yolk-sac pre-macrophages¹⁰⁶. Part of these cells persist through adult life^{94,106}, but they are greatly diluted by KCs arising from fetal liver hematopoiesis¹⁰⁰. Embryonic KCs down-regulate CX3CR1 and they are distinguishable from cells of adult hematopoietic origin³⁹. In adults, the contribution of monocytes to the KC pool is barely detectable at steady state, as demonstrated by analysis of reporter strains driven by Flt3^{cre} – which labels fetal liver MDPs and adult BM-derived cells¹⁰⁰ – or Ms4a3^{cre63}, and analysis of parabiotic mice¹³⁹. The KC-specific signature is imprinted on KCs by the liver microenvironment¹³⁷, which dictates their expression of markers such as Clec4F¹⁴⁰ and Clec2¹⁴¹. Clec4F expression is detected in fetal liver macrophages as soon as E12.5, and is a marker of *bona fide* KCs in adults (¹⁴² and RNA-seq data from¹¹⁶). As mentioned earlier, embryonic KCs further express Timd4 and they rely on the transcription factors Zeb2 and LXR α (coded by *Nr1h3*) for their maintenance^{112,137}. Interestingly, invalidation of Zeb2 using Clec4f^{cre} induces a 2.5 fold reduction in Timd4⁺ KC abundance, while the absence of this population is complemented by monocyte-derived Timd4⁻ KCs to keep the KC pool constant¹¹². Zeb2 expression is essential for myelopoiesis¹⁴³. Its expression is controlled by two key enhancers – one located 165kb upstream of the Zeb2 transcription start site (-165kb), and another located at +164kb¹⁴⁴. Mice with deletion of the -165kb enhancer show major hematopoietic defects and notably lack monocytes, while their KCs remain unaffected further supporting their independence from monocytes¹⁴⁴. However, the +164kb enhancer is specifically active in cells with an embryonic origin and it has been

proposed to control their development. This enhancer binds the transcription factor *Nr4a1*, and *Nr4a1*^{-/-} mice have abnormal fetal-liver hematopoiesis¹⁴⁴. Furthermore, it also binds the transcription factor LXR α (ChIP-seq from¹³⁷) which is essential for KC establishment, and transcriptomic signatures from *Zeb2*^{-/-} and *Nr1h3*^{-/-} KCs largely overlap¹¹². Both *Zeb2* and LXR α start being expressed in embryonic macrophages¹¹⁶. Together, these data strongly suggest that the loss of *Timd4*⁺ KCs observed in *Clec4f*^{cre} x *Zeb2*^{fl/fl} mice may be due to abnormal KC establishment, in a manner involving binding of the +164kb *Zeb2* enhancer by transcription factors such as *Nr4a1* and *Nr1h3* during embryonic development. The *Zeb2*-dependent development of KCs – and other macrophage populations deriving from fetal liver progenitors – could be thoroughly characterized by generating and analyzing mice lacking its +164kb enhancer.

Kupffer cells play key roles in both homeostasis and disease¹⁴⁵. Their roles include a participation in iron homeostasis^{146,147}, removal of damaged erythrocytes^{147,148}, bacterial clearing during infection¹⁴⁹, or detection of enterically-derived pathogenic signals that disseminate through the portal vein¹⁵⁰. A recent report revealed the existence of two distinct embryonic KC subsets – a predominant (80%) subset called KC1 and a minor (20%) subset called KC2¹⁵¹. While both subsets express canonical KC markers, KC2s are further characterized by high expression of CD206 and *Esam* and these cells were attributed metabolic functions. Upon challenge with high fat diet, KC2s accumulate and further upregulate CD36¹⁵¹, a scavenger receptor¹⁵² and receptor for lipids including long chain fatty acids and lipoproteins¹⁵³. KC2s display a transcriptomic signature reminiscent of lipid metabolism that is further enhanced upon high fat diet, and their depletion leads to alterations of hepatic metabolism. Upon challenge with western diet, embryonic KCs also accumulated intracellular lipids¹⁵⁴. These results suggest that KCs participate in the maintenance of liver homeostasis upon lipid overload. This was also suggested in a context of non-alcoholic steatohepatitis (NASH), a pathology associated with disappearance of embryonic KCs and CCR2-dependent replenishment of the KC pool by monocyte-derived cells^{141,154,155}. In particular, the lipid-associated macrophage markers *Trem2* and CD9¹⁵⁶ were strongly up-regulated in resident *Timd4*⁺ KCs during NASH, but also in newly-recruited monocyte-derived *Timd4*⁻ KCs^{141,154,155}. As indicated earlier, monocytes can give rise to *Timd4*⁻ KCs in conditions where homeostasis of embryonic KCs is perturbed. This notably occurs after irradiation¹⁵⁷ or diphtheria toxin-mediated KC depletion (in *Clec4f*^{cre} x R26^{DTR} mice)^{137,140}, which render hepatic niches available

for monocytes. These newly-recruited monocytes rapidly adopt the KC transcriptomic signature as they are exposed to tissue imprinting, and they notably upregulate the *bona fide* KC surface markers Clec4f^{137,140} and Clec2⁽¹⁴¹ and RNA-Seq data from¹³⁸). In NASH, KCs up-regulate CCL2 and favor the establishment of monocyte-derived KCs (moKCs) that gradually replace embryonic KCs, proliferate, and retain their KC profile in the long term after disease regression¹⁴¹. Although moKCs supported a reduction in liver triglyceride content, plasmatic alanine amino-transferase levels were increased during NASH in a model accelerating the replacement of embryonic KCs by moKCs¹⁴¹. Together with the clear inflammatory gene signature of moKCs¹⁴¹, these results suggest that replacement of specialized embryonic macrophages by monocyte-derived cells is deleterious in chronic metabolic diseases.

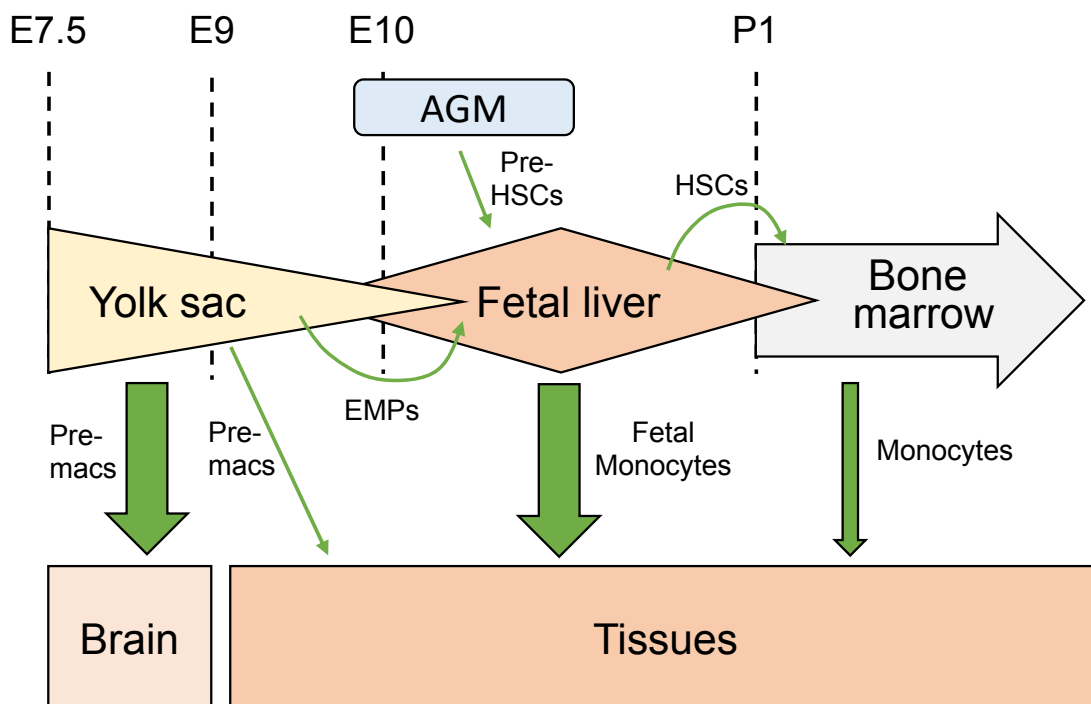


Figure 2. Schematic representation of macrophage seeding waves.

“Pre-macs” (pre-macrophages) represent the first wave of primitive hematopoiesis when yolk sac-derived cells seed the brain and give rise to microglia. Yolk sac-derived erythromyeloid progenitors (EMP) and macrophages later colonize the embryo to seed tissues and the fetal liver. Pre-HSCs originating from the aorta-gonad-mesonephros (AGM) region seed the fetal liver and, together with EMPs, allow fetal liver hematopoiesis to take place for the better part of embryogenesis. Fetal monocytes give rise to a great proportion of tissue-resident macrophages during this period and perinatally. HSCs seed the bone marrow at birth and allow adult hematopoiesis to take place.

Chapter 3 – Myelopoiesis.

A. Definitive hematopoiesis

Myelopoiesis is the hematopoietic differentiation program that gives rise to blood myeloid cells, including monocytes and granulocytes. This process takes place in the bone marrow at steady state, and is amplified in diverse pathogenic conditions¹⁵⁸⁻¹⁶¹. A complementary process called extramedullary hematopoiesis is activated in the spleen upon inflammatory conditions¹⁶². Beyond the transcription program that finely tunes myelopoiesis under physiological conditions, several factors have been shown to influence hematopoietic stem cells (HSCs) through modulations of their microenvironment or their metabolism. Changes in HSC homeostasis can directly impact leukocyte production including monocytes. Here we will discuss monocyte generation, diversity and cues that can influence their maintenance and functions.

Hematopoietic stem cells (HSCs) are identified through their co-expression of Sca1 (Stem cell antigen 1) and c-Kit, and their lack of mature cell markers such as CD11b or CD19 for example. The hematopoietic stem cell compartment (Sca1⁺ c-Kit⁺) contains both quiescent stem cells and proliferating multipotent progenitors (MPPs), that can be identified as CD150⁺ CD48⁻ and CD150⁻ CD48⁺ respectively^{163,164}. Maintenance of the HSC pool relies on balance between symmetrical and asymmetrical cellular divisions, which determine the number of stem cells and committed progenitors HSCs give rise to. Common myeloid progenitors (CMPs) derive from MPPs and they give rise to the myeloid lineage¹⁶⁵. CMPs differentiate either into granulocyte-monocyte progenitors (GMPs), monocyte-dendritic cell progenitors (MDPs) or megakaryocyte-erythrocyte progenitors (MEPs). Their commitment toward each lineage is tightly regulated by opposing effects of transcription factors – for example PU.1 governs differentiation towards GMPs while the PU.1 antagonists Id2 and Gata1 support differentiation towards MEPs^{166,167}. On top of their respective lineages (granulocytes and dendritic cells), both MDPs and GMPs also give rise to monocytes¹⁶⁸. A more mature monocyte-committed progenitor called the common monocyte progenitor (cMoP) was recently identified¹⁶⁹, and this progenitor give rise to CXCR4⁺ pre-monocytes that gradually lose CXCR4 expression and gain CD11b expression as they differentiate to fully mature monocytes⁵⁴.

Although *in vitro* work suggested that the cMoP could derive from MDPs¹⁶⁹, *in vivo* fate-mapping experiments refuted this hypothesis⁶³. Ms4a3 is a transcription factor specifically expressed by GMPs, and following the expression of Ms4a3^{cre}-driven reporters allowed a robust characterization of GMP contribution to the monocyte pool⁶³. It is now well-established that GMPs, and not MDPs, give rise to cMoPs that can in turn generate monocytes⁶³ that mature in the bone marrow before reaching the blood circulation⁵⁴. Transfer experiments showed that although MDPs do not express Ms4a3, its expression is induced in around 80% of MDP progeny compared to 100% of GMP progeny. Ms4a3^{cre} labeling reaches 95% and 90% in blood Ly6C^{high} and Ly6C^{low} monocytes respectively⁶³. This suggests that Ms4a3⁻ precursors deriving from MDPs may only have a small contribution to the monocyte pool. Ly6C^{high} monocytes are known to be precursors of Ly6C^{low} monocytes³⁹ and this notion is confirmed using Ms4a3^{cre}-driven reporters. Use of Ms4a3^{creERT2} mice allows the time-lapse tracking of GMP-derived cells, and Ly6C^{high} monocyte labelling reaches >90% around 3 days post tamoxifen injection. In comparison, labelling of Ly6C^{low} monocytes is delayed and reaches its peak at 60% around day 10 post-tamoxifen, suggesting a 60% replacement of these cells by Ly6C^{high}-derived cells over this time period. However, constitutive Ms4a3^{cre} labelling is slightly lower in Ly6C^{low} monocytes (around 90%) compared to Ly6C^{high} cells, and one would expect their labelling efficiency to be strictly identical to what is observed in Ly6C^{high} monocytes if these cells were their only precursors⁶³. This result either suggests that a small proportion of Ly6C^{low} monocytes may not derive from Ly6C^{high} monocytes, or that Ms4a3⁻ Ly6C^{high} cells are better at generating Ly6C^{low} monocytes. BrdU pulse-chase experiments previously allowed to demonstrate that labelling of bone marrow Ly6C^{low} monocytes occurs before labelling of blood Ly6C^{low} monocytes, suggesting tissue-restricted generation of these cells³⁹. Moreover, BrdU labeling of bone marrow Ly6C^{low} monocytes occurs 6hours after BrdU injection while the conversion of mature Ly6C^{high} monocytes to Ly6C^{low} monocytes takes 2 to 3 days³⁹. This suggests either that Ly6C^{low} monocytes proliferate in the bone marrow or that they can – in a small proportion – be generated in the bone marrow independently of Ly6C^{high} monocytes as previously proposed³⁹. Additional tools allowing to specifically track MDP-derived monocytes and thoroughly address this question and are currently lacking.

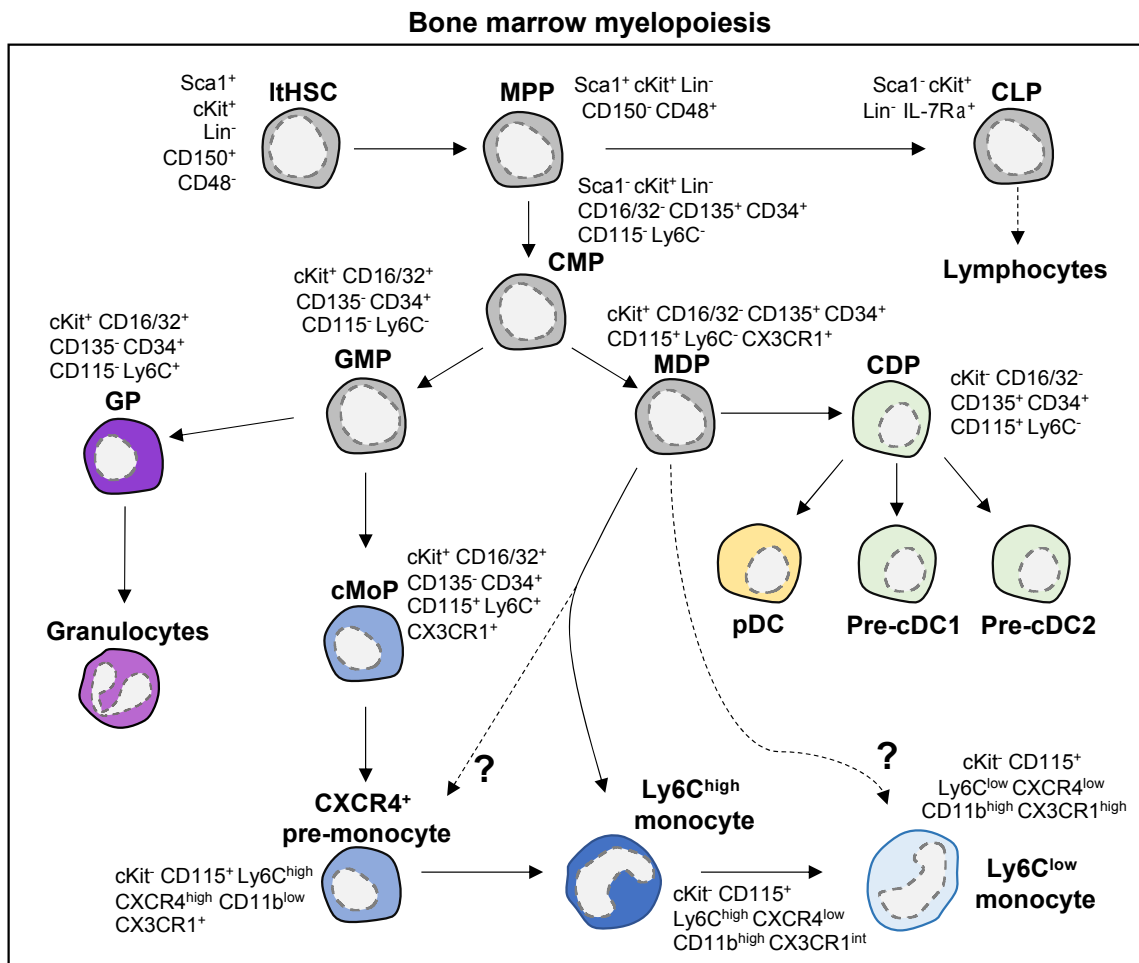


Figure 3. Current model for myelopoiesis.

B. Transcriptional control of myelopoiesis

The commitment of hematopoietic stem cells towards the monocytic lineage is tightly regulated, and notably involves transcription factors such as Myb⁹⁴, PU.1^{133,134}, MafB¹⁷⁰, Zeb2¹⁴³, IRF8¹⁷¹ and Klf4¹⁷² among others. As discussed earlier Myb is necessary for fetal liver hematopoiesis and its invalidation in adults (using Mx1^{cre}) completely abrogates myelopoiesis⁹⁴. The master regulator PU.1 is necessary for expression of CSF1R and a pro-myeloid signature in bone marrow and fetal liver monocyte progenitors^{133,134}. MafB is an inducer of monocyte differentiation¹⁷⁰. Its expression is found in long term HSCs, in which it inhibits PU.1 to maintain homeostatic commitment towards the myeloid lineage¹⁷³. MafB overexpression in human CD34⁺ cells induces monocyte differentiation and up-regulation of a strong monocyte/macrophage signature including CSF1R expression¹⁷⁴. Analysis of MafB reporter mice (MafB^{mCherry-Cre} x R26^{YFP}) confirmed low expression of MafB in early

progenitors, while its expression is strongly induced in blood monocytes and present in tissue macrophages^{28,62}. Monocytes and macrophages remain present in *MafB*^{-/-} mice, and they display increased proliferation capacity¹⁷⁵ that was attributed to inhibition of the transcription of self-renewal genes by *MafB*¹⁷⁶. The PU.1 target genes *Zeb2*¹⁴⁴ and *Klf4*¹⁷² are involved in expression of CSF1R in mature monocytes^{143,172}, and *Klf4* overexpression in *PU.1*^{-/-} fetal liver cells rescues CSF1R expression¹⁷². Transplantation of *Klf4*^{-/-} hematopoietic cells into wild-type recipients lead to a disappearance of Ly6C^{high} CD115⁺ blood monocytes, while bone marrow monocytes remained clearly detectable and peritoneal macrophage numbers were unchanged¹⁷⁷. *Klf4* is further regulated by IRF8, which is essential to induce *Klf4* expression in monocytes and their precursors^{171,178}. Monocytes – gated as CD11b⁺ CD115⁺ – were reported to be absent in IRF8-deficient mice^{171,178,179}. However, indefinite CD11b⁺ CD115^{low/-} cells accumulated in the spleen and blood of IRF8^{-/-} mice¹⁷¹. A more recent study showed accumulation of both neutrophils and monocytes – gated CD11b⁺ Ly6G⁺ Ly6C^{int} and CD11b⁺ Ly6G⁻ Ly6C⁺ respectively – in the spleen of IRF8^{-/-} mice, although Ly6C expression appeared lower in IRF8^{-/-} monocytes compared to wild-types¹⁸⁰. These data suggest that CSF1R and Ly6C down-regulation might have misled previous studies of *Klf4*^{-/-} and IRF8^{-/-} monocytes and confounded the identification of these cells. CD115⁺ Ly6C^{low} monocytes remain present in *Klf4*^{-/-} bone marrow chimeras and IRF8^{-/-} mice and their generation depends on Ly6C^{high} monocytes³⁹, supporting the idea that blood monocytes do not fully disappear in these models^{171,177}. Importantly, CSF1R expression was fully abolished in *Zeb2*^{-/-} bone marrow cells¹⁴³ – in a manner involving its -165kb enhancer^{144,181} – while it remained detectable in bone marrow cells from *Klf4*^{-/-} chimeras¹⁷⁷ and IRF8^{-/-} mice^{178,182}. These results suggest that CSF1R expression might be differentially regulated in the bone marrow and in the blood, and one could hypothesize that this would depend on tissue imprinting and niche-dependent induction of transcription factors. For example, whether interaction of Ly6C^{low} monocytes with the endothelium induces a specific transcription program allowing their subset-specific maintenance of CSF1R in IRF8^{-/-} mice remains to be established. *Klf4* is gradually upregulated along PU.1 during CMP to GMP transition¹⁷² while IRF8 is strongly induced in MDPs and cMoPs – which express CSF1R – but less expressed in GMPs¹⁸². IRF8^{-/-} mice show increased numbers of GMPs, MDPs and cMoPs^{178,179} and *Klf4*^{-/-} CMPs are biased towards granulocytes¹⁷². These results support the accumulation of CD11b⁺ myeloid cells in the periphery of IRF8^{-/-} mice and

emphasize the importance of time-restricted induction of transcriptional programs in hematopoiesis. This regulation is further complicated by the presence of multiple enhancers that can be bound by multiple – sometimes redundant – transcription factors¹⁸³.

The expression of CSF1R is tightly regulated notably by cell-specific and developmental stage-specific binding of transcription factors¹⁸⁴. CSF1R regulation by FIRE (*fms*-intronic regulatory element) has notably emerged as a major determinant of monocyte versus macrophage maintenance. FIRE is a highly conserved regulatory element in the second intron of the *Csf1r* gene that is bound by PU.1 and IRF8 among other transcription factors¹⁸⁴. Deletion of FIRE (FIRE^{ΔΔ}) leads to loss of specific macrophage populations including yolk-sac-derived macrophages and Langerhans cells¹⁸⁵. CSF1R has been shown to be dispensable for fetal liver hematopoiesis^{25,100}, and an early report of CSF1R blockade using a monoclonal antibody (AFS98) suggested a weak role of this receptor during myelopoiesis while c-Kit was dominant¹⁸⁶. FIRE is differentially regulated among tissue macrophages and blood monocytes, and its chromatin accessibility is high in macrophage populations that are missing in FIRE^{ΔΔ} mice. Hematopoiesis and Ly6C^{high} monocyte numbers appeared unaffected in FIRE^{ΔΔ} mice despite their loss of CSF1R expression and CSF1 binding¹⁸⁵. Interestingly CSF1R expression was maintained in Ly6C^{low} monocytes, a phenotype reminiscent of the dichotomy observed in IRF8^{-/-} mice (discussed above). Together, these results suggest that CSF1R expression might not be mandatory for myelopoiesis and monocyte maintenance at steady state. However, *in vivo* treatment with anti-CSF1R or anti-CSF1 monoclonal antibodies are well-known to reduce blood monocyte numbers^{187,188}. Using this approach, blood monocyte numbers are only halved while certain tissue-resident macrophages fully-disappear, suggesting that monocytes can still be generated during CSF1R blockade although less efficiently. *In vitro*, culture of FIRE^{ΔΔ} bone marrow cells with M-CSF still generated bone marrow-derived macrophages, although with a lesser yield¹⁸⁵. Hematopoietic defects in osteopetrotic mice can be linked to reduced osteoclast activity that is necessary to generate space for niche establishment^{189,190}. FIRE^{ΔΔ} mice do not display osteopetrosis or any bone defects associated with *op/op* and CSF1R^{-/-} mice¹⁸⁵, as osteoclasts in fact depend on a different transcription start site for CSF1R expression⁹⁷. A recent study using an inducible approach ubiquitously invalidated CSF1 in adults

after establishment of proper bone morphology¹⁸⁸. This resulted in partial (30 to 50%) diminution of bone marrow MDPs and cMoPs, and of bone marrow and blood monocytes while spleen monocytes remained unaffected¹⁸⁸. Although this result fully supports the notion that CSF1 is necessary for optimal myelopoiesis and monocyte maintenance, it also suggests that CSF1-independent mechanisms are involved in this process. Further work is required to fully comprehend the transcriptional mechanisms governing myelopoiesis and the complex roles of CSF1 and CSF1R in this context. Notably, whether the CD11b⁺ Ly6G⁻ Ly6C^{int} cells that accumulate in the spleen of IRF8^{-/-} mice¹⁸⁰ and monocytes from FIRE^{ΔΔ} mice are fully differentiated and functional monocytes remains to be properly addressed using genetic reporters that bypass CD115 and Ly6C staining. A fully detailed characterization of hematopoiesis in FIRE^{ΔΔ} mice is also lacking.

C. Niche and HSC homeostasis

Hematopoietic stem cells are located in specific trophic niches, in proximity to sinusoidal blood vessels both in the bone marrow¹⁹¹ and in the spleen¹⁹². These niches provide growth factors, influence HSC proliferation rate and potential skewing towards a certain lineage. Cells from the bone marrow niche include endothelial cells, CXCL12-abundant reticular cells (CAR cells), adipocytes, megakaryocytes and LepR⁺ mesenchymal stromal cells. They maintain hematopoietic stem cell homeostasis by producing SCF (stem cell factor) and CXCL12 (C-X-C motif chemokine 12) (among other factors) which regulate hematopoietic stem cell proliferation and homing¹⁹³. LepR⁺ mesenchymal stromal cells notably sense adipose tissue-derived leptin, which dampens SCF and CXCL12 expression, and leptin production is diminished during physical exercise conferring beneficial anti-inflammatory effects¹⁹⁴. Under homeostasis, HSCs are released from the bone marrow in a circadian manner, and this process directly relies on inhibition of CXCL12 production by niche cells in response to sympathetic stimuli¹⁹⁵ depending on β 2 and β 3 adrenergic receptors¹⁹⁶. Interestingly, pre-treatment with β -adrenergic agonists 24hours before bone marrow transplantation increases stem cell homing to the bone marrow and reconstitution efficiency¹⁹⁷. During chronic stress, elevated β -adrenergic stimulation of bone marrow cells by noradrenaline leads to extended reduction of CXCL12 production, which in turns promotes stem cell exhaustion and accelerated myelopoiesis¹⁶⁰. Myeloid

progenitors and monocytes also locate within specific niches, notably along CSF1-expressing endothelial cells^{188,198}. Regulation of myelopoietic progenitors is not restricted to stromal cells, and immune cells actively contribute to this process. CSF1 production was detected in skin¹⁹⁹ and bone marrow neutrophils and transplantation of CSF1^{-/-} bone marrow blunted the induction of myelopoiesis in a sleep fragmentation model²⁰⁰. Another example of the regulation of myelopoiesis by immune cells is that of bone marrow dendritic cells, which locate in proximity to myeloid progenitors¹⁹⁸. Upon infection, these dendritic cells can sense pathogens and stimulate hematopoiesis by secreting inflammatory cytokines such as IL-1 β ²⁰¹. B lymphocytes were reported to synthesize acetylcholine, which promotes CXCL12 production by LepR⁺ niche cells and dampens hematopoiesis²⁰². Bone-resorbing osteoclasts play a key role in the maintenance of the bone marrow niche. Osteopetrotic mice, which show major bone defects due to altered osteoclast function, also display hematopoietic alterations that can be rescued by restoring osteoclast activity^{189,190}.

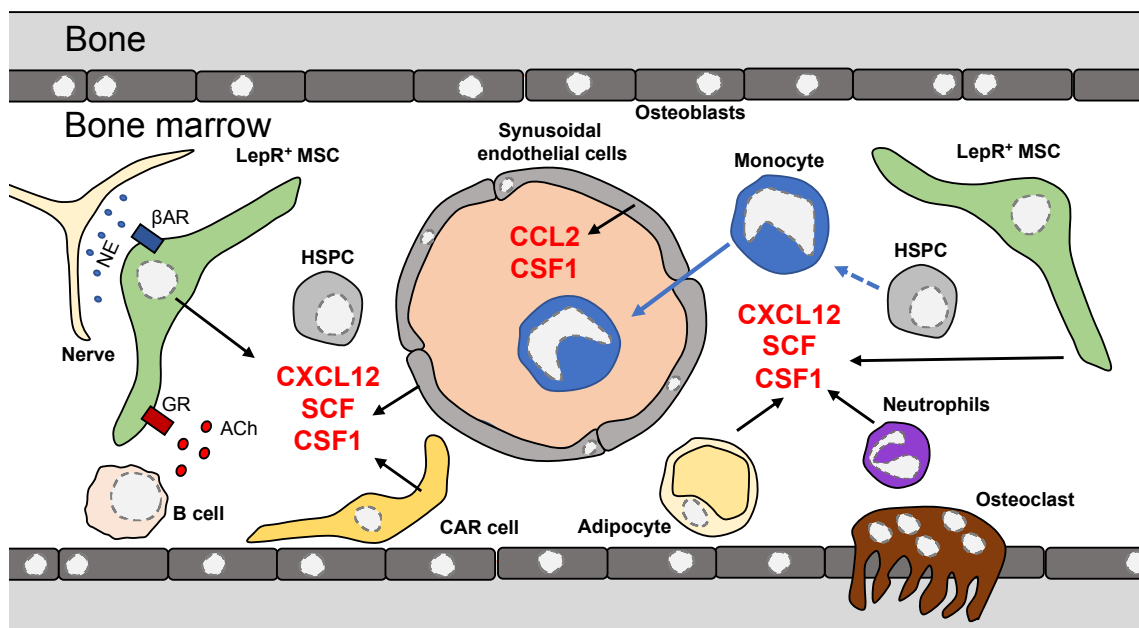


Figure 4. Schematic representation of the bone marrow stem cell niche.

Metabolism is another factor that impacts hematopoietic stem cell maintenance and proliferation. HSC biology has been shown to be impacted by metabolites such as glucose^{203,204}, fatty acids²⁰⁵, amino acids^{204,206}, cholesterol^{207,208} or vitamins²⁰⁹. In humans, metabolic pathologies are associated with increased bone marrow activity, measured by ¹⁸F-fluorodeoxyglucose uptake²¹⁰⁻²¹². The peri-sinusoidal niche in which HSCs locate is a hypoxic microenvironment that directly impacts HSC metabolism by

regulating access to oxygen and circulating metabolites²¹³⁻²¹⁵. HIF-1 α is expressed in HSCs, and its stabilization in hypoxic conditions – notably through niche-derived signals – promotes anaerobic glycolysis and maintenance of a quiescent state²¹⁶⁻²¹⁸. HIF-1 α ^{-/-} mice display increased myelopoiesis and lymphopoiesis, extramedullary hematopoiesis, and HIF-1 α ^{-/-} HSCs show a weak reconstitution potential suggesting stem cell exhaustion²¹⁶. HSCs display a low mitochondrial potential suggesting low mitochondrial activity, and glycolysis has been proposed to be essential to maintain the quiescent state of stem cells²¹⁷. Pyruvate, the end product of glycolysis, can either be converted into acetyl-CoA in the mitochondria via the enzyme pyruvate dehydrogenase (PDH) to fuel oxidative metabolism, or converted into lactate in the cytosol by the enzyme lactate dehydrogenase A (LDHA). This critical step of pyruvate conversion therefore appears pivotal, and it has been addressed in HSCs by invalidating Pdk proteins 2 and 4, which inhibit PDH to suppress pyruvate flux into mitochondria²¹⁹. Pdk2/4 are HIF-1 α targets that partially restore HSC maintenance and reconstitution potential when transduced in HIF-1 α ^{-/-} stem cells²¹⁹. Pdk2/4^{-/-} double knock-out HSCs show an increase in ROS generation, but also a decrease in LDH activity and pyruvate levels – although that could be due to increase flux towards mitochondrial metabolism rather than altered glycolysis. Importantly, loss of Pdk2/4 leads to stem cell exhaustion in the long term despite an unaltered initial capacity to generate every hematopoietic lineage²¹⁹. This result suggests that finely tuned balance between anaerobic glycolysis and mitochondrial metabolism is essential to HSC homeostasis. Overall cellular ATP production is higher in proliferating progenitors compared to HSCs, suggesting metabolic rewiring to accommodate differentiation^{219,220}. This idea is now supported by several studies of mitochondrial function in HSCs. For example, “mito-mice” which have severe mitochondrial dysfunctions due to deletions in mitochondrial genome, show an accumulation of HSCs and progenitors, reduced production of mature leukocytes and long term stem cell exhaustion²²⁰. Mice with Vav1^{cre}-driven hematopoietic deletion of the mitochondrial phosphatase PTPMT1 develop anemia resulting in perinatal death²²¹. Inducible PTPMT1 knock-out via Mx1^{cre} promoted glycolysis at the expense of mitochondrial metabolism, triggered HSC accumulation and loss of differentiation, and also results in 80% lethality within 3 weeks²²¹. Similarly, hematopoietic loss of Lkb1 – a tumor suppressor that interacts with AMPK – resulted in a drop of ATP levels in HSCs,

mitochondrial defects, loss of HSC quiescence, pan-leukopenia and subsequent death²²²⁻²²⁴. Importantly, loss of either PTPMT1 or Lkb1 in mature cells did not impact their peripheral numbers. These results suggest that although engagement of mitochondrial metabolism is necessary throughout stem cell differentiation, it also plays a crucial role in maintaining HSC homeostasis. As mentioned earlier, acetyl-CoA is essential in mitochondrial metabolism and it can be generated either from pyruvate – which seems to be a weak source in HSCs – or from mitochondrial fatty acid oxidation (FAO). In that regard, the role of FAO in HSCs was addressed by invalidating PPARb, a key regulator of FAO and the main member of the PPAR family expressed in HSCs²⁰⁵. Loss of hematopoietic PPARb blunted HSC reconstitution capacity and this was attributed to increased symmetric stem cell divisions leading to exhaustion²⁰⁵. PPAR-dependent induction of FAO notably relied on mitophagy²²⁵. FAO directly fuels the TCA cycle to generate ATP, and impairment of respiratory chain function in stem cells blunts their differentiation and maintenance, ultimately providing evidence that aerobic mitochondrial metabolism is crucial for HSC function²²⁶.

Chapter 4 – Blood monocytes

A. Monocyte mobilization

Once their maturation in the bone marrow is complete, monocytes can egress and be mobilized to the blood circulation before extravasating and being recruited to peripheral tissues. In tissues, newly-recruited monocytes can be identified as CD11b⁺ MerTK⁻ CD64⁺ Ly6C⁺ cells and they lose Ly6C expression and upregulate MHC-II during maturation⁴⁶. Monocyte mobilization is governed by the chemotactic axes CXCL12-CXCR4, responsible for monocyte retention in the bone marrow^{54,227,228}, and CCL2-CCR2 which regulates mobilization towards peripheral tissues²²⁹⁻²³². Both these mobilization and retention signals are regulated by the nervous system in a circadian manner and orchestrate monocyte oscillation between the bone marrow and the blood circulation^{195,197,233}. This mechanism depends on circadian control of sympathetic neural signals that stimulate β -adrenergic receptors on bone marrow cells to inhibit CXCL12 production^{195,197,233}. On the other hand, CCL2 is produced in a circadian manner by endothelial cells to regulate monocyte migration towards peripheral tissues¹⁹⁷. Sympathetic tone has also been shown to impact leukocyte migration via regulation of the vasculature²³⁴. Corticosterone is secreted in a circadian manner and it inhibits CXCL12 production in the bone marrow²³⁵. During acute stress, adrenal gland-derived corticosterone binds the glucocorticoid receptor (GR) on leukocytes including monocytes and leads to their disappearance from the blood circulation²³⁶. GR stimulation notably promotes expression of CXCR4 on leukocytes and their homing to the bone marrow²³⁶.

Comparative studies of murine and human monocytes have identified conserved features of both monocyte subsets, and that includes their respective expression of the chemokine receptors CX3CR1 and CCR2^{49,50}. Both human and murine monocytes express CX3CR1, although higher expression of this chemokine receptor is found on the patrolling subset while classical monocytes highly express CCR2^{49,50}. The Ly6C^{high} subset displays a high migratory capacity. It is at the origin of the majority of monocytes and monocyte-derived macrophages found in tissues, although Ly6C^{low} monocytes are also capable of migration and are notably recruited in the lung²³⁷. Several chemokine receptors were proposed to control monocyte recruitment²³⁸, and it is now widely accepted that CCR2 is the main chemokine receptor responsible for

monocyte recruitment to inflamed tissues²³⁹. Ly6C^{high} monocytes have historically been called “inflammatory” because of their enhanced production and recruitment to tissues during inflammation²⁴⁰. However, they also participate to the maintenance of macrophages and tissue homeostasis in several tissues at steady state^{31,46}.

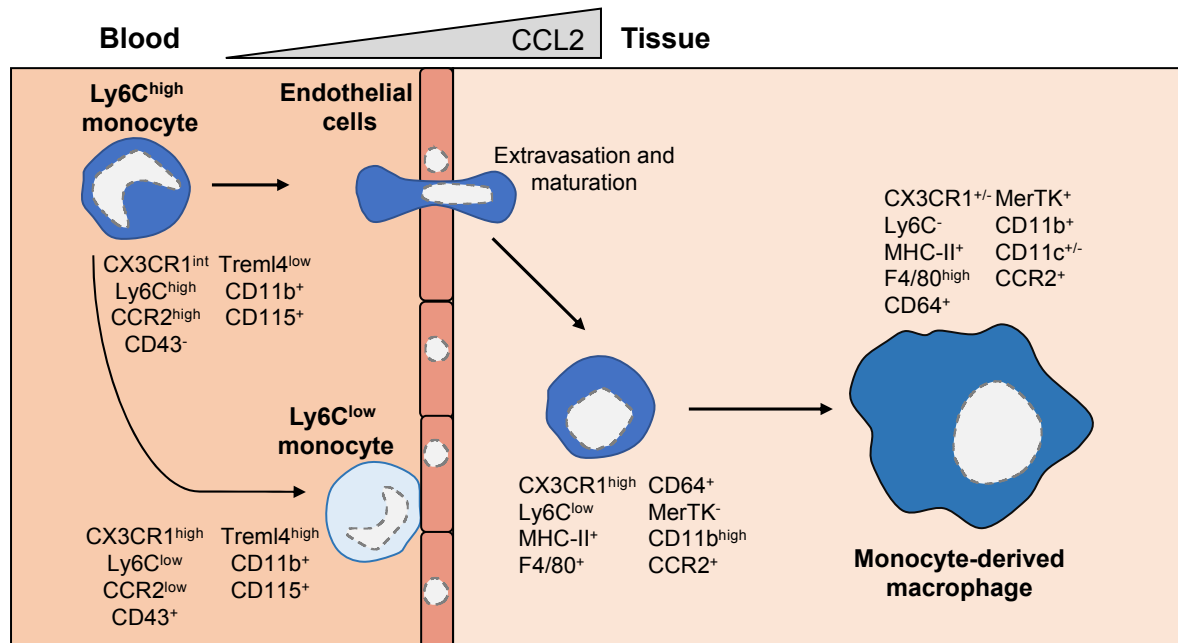


Figure 5. Schematic representation of Ly6C^{high} monocyte maturation into patrolling monocytes or monocyte-derived macrophages.

Trafficking and extravasation rely on adhesion molecules that regulate monocyte rolling on the endothelium, subsequent adhesion and transmigration. The role of different adhesion molecules has been addressed using genetic models, intravital microscopy and injection of neutralizing antibodies. An early report showed a role for the complement receptor 3 (CR3, consisting of CD11b and CD18) in monocyte adhesion²⁴¹. It is highly expressed in Ly6C^{low} monocytes which also express LFA-1 (consisting of CD11a and CD18)⁵². Injection of anti-CD11a or anti-CD18 antibodies results in a rapid release of monocytes crawling in the endothelial wall, while anti-CD11b injection did not produce such a striking result showing the essential role of CD11a, and CD18 in both CR3 and LFA-1⁵². A previous study using genetic invalidation of LFA-1 in a model of thioglycolate-induced peritonitis showed no reduction of Ly6C^{high} monocyte recruitment²⁴². L-selectin is also involved in monocyte recruitment in peritonitis models²⁴³. Moreover, optimal Ly6C^{high} monocyte recruitment to the liver upon bacterial infection required CD11b, CD44 and Icam-1 while CD11a

was not involved²⁴⁴. CD11b-deficient mice show reduced monocyte recruitment to the inflamed adipose tissue in obesity, resulting in reduced adipose tissue macrophage counts²⁴⁵. These results suggest the existence of recruitment mechanisms relying on subset-specific adhesion molecules. As discussed earlier, monocyte recruitment to tissues at steady state is circadian and endothelial expression of adhesion molecules that facilitate leukocyte migration is also circadian, adding further complexity in the regulation of monocyte recruitment¹⁹⁷.

B. Metabolic control of monocytes

In the past decade, the metabolic regulation of monocyte functions has started to be thoroughly investigated as monocytes have been identified as critical mediators of metabolic diseases. In these pathological conditions, they are known to support disease progression by producing cytokines and giving rise to pro-inflammatory macrophages in tissues. Monocyte numbers increase in the blood circulation in a context of obesity²⁴⁶ and they represent a risk factor for cardiovascular diseases such as atherosclerosis^{247,248}. Monocyte counts were further elevated in obese patients with type 2 diabetes and hyperglycemia²⁴⁶, and this was paralleled by increased CCL2 levels among other cytokines and chemokines²⁴⁹. The link between hyperglycemia and blood monocyte counts was also established in mice²⁵⁰. In this study, increased monocyte counts in diabetic mice were attributed to enhance myelopoiesis as discussed earlier²⁵⁰. The importance of glucose metabolism in monocytes was further brought to light by a recent study exploring the consequence of fasting on blood immune cells²⁵¹. Blood monocyte counts were significantly reduced in the fasted state both in mice and humans, and could be restored by glucose intake while lipid administration failed to do so²⁵¹. This monocyte mobilization was attributed to hepatic energy sensing and regulation of systemic CCL2 production²⁵¹. In conditions of chronic stress, increased monocyte production supports inflammation¹⁶⁰. Importantly, these cells undergo chromatin rewiring as a stress response to promote activation of inflammatory and glycolytic genes and repression of mitochondrial genes²⁵². This result suggests a pro-inflammatory role of monocyte glycolysis. A recent report showed that glucose injection induces a rapid increase in blood monocyte counts²⁵³. Importantly, this glucose-induced monocyte mobilization was blunted in LyzM^{cre} x Glut1^{fl/fl} mice. LdlR^{-/-} mice transplanted with LyzM^{cre} x Glut1^{fl/fl} bone marrow had fewer blood monocytes compared to controls²⁵³. These results further support previous

results showing that Glut1 is the main mediator of glucose intake in myeloid cells^{254,255}. How exactly this dynamic Glut1-dependent monocyte mobilization occurs following glucose intake remains to be established.

Studying monocytes *ex vivo* has always been challenging since limited amounts of these cells can be extracted, and their maintenance *in vitro* in an undifferentiated state is challenging. For this reason, studies profiling the metabolic needs of monocytes are scarce and extensive *in-vitro* work has instead been performed on bone marrow-derived macrophages. Metabolism quickly emerged as a major factor influencing macrophage phenotype, and this led to the creation of the M1/M2 macrophage activation paradigm. However, *in vivo* studies challenge this simplified view. Indeed, surface activation markers attributed to M1 (inflammatory) or M2 (anti-inflammatory) macrophages are actually co-expressed on many macrophages subsets *in vivo*, and this observation is also valid for cytokine production. Nevertheless, defining *in vivo* the metabolic needs of monocytes and macrophages and the influence of general metabolic state on their functions is an exciting challenge. The recently-described SCENITH approach has allowed to profile rare cell populations including blood monocytes²⁵⁶. In human healthy donors, both classical and patrolling monocytes were shown to have an important glucose dependence, and mitochondrial activity was found almost exclusively in the patrolling subset²⁵⁶. Glucose metabolism was also predominant in murine Ly6C^{high} monocytes, but mitochondrial activity was also detected at steady state²⁵⁶. These observations are in agreement with the results discussed above, pointing towards glucose as a major regulator of monocyte metabolism. How exactly glucose is used intracellularly downstream of Glut1-mediated uptake remains to be properly addressed. Short chain fatty acids generated by microbiota during fiber fermentation were also linked to the generation and function of patrolling Ly6C^{low} monocytes²⁵⁷. Whether monocytes subsets rely on other metabolic substrates such as amino acids or long chain fatty acids, both at steady states and during inflammation, is also an open question.

Chapter 5 – Monocyte-derived macrophages.

A. Overview

Monocytes participate to the maintenance of the macrophage pool in several tissues at steady state, and they can give rise to inflammatory macrophages during disease. Although mechanisms of monocyte recruitment to tissues are well established, what influences monocyte engraftment in tissues and their long-term survival as macrophages has only recently started to be addressed. Moreover, monocyte recruitment is accelerated in inflammatory conditions such as atherosclerosis, where monocytes give rise to macrophages in a rapidly-evolving microenvironment – the atheromatous plaque – devoid of resident macrophages. Here, we will develop on the contribution of monocytes to the tissue macrophage pool in health and disease.

B. The macrophage niche

Tissue macrophages are embedded within a complex micro-environment that comprises tissue-specific stromal cells – such as hepatocytes in the liver and adipocytes in adipose tissue –, blood and lymphatic²⁵⁸ endothelial cells, fibroblasts²⁵⁹, mesothelial cells²⁶⁰, neurons²⁶¹ or other immune cells for example. These cells constitute the tissue macrophage niche, that produces growth factors and other mediators responsible for imprinting of the tissue-specific and niche-specific macrophage signature^{32,262,263}. For example CSF1 produced by mesothelial cells maintains large peritoneal macrophages in the peritoneal cavity²⁶⁰, neurons maintain microglia via IL-34 production²⁶ and lung epithelial cells provide GM-CSF to alveolar macrophages²⁶⁴. Further complexity exists at the sub-tissular level as macrophage populations depending on different growth factors co-exist, suggesting the existence of different niche types within a given tissue. For example in the brain, CSF1 and IL-34 are produced in a non-overlapping pattern and are responsible for the zone-specific maintenance of microglial cells^{128,265}. In the liver, different anatomic niches co-exist and they are responsible for imprinting specific gene signatures on monocytes and macrophages in health and disease^{137,155,266}. Recently, macrophage subset distribution in specific hepatic niches was also extensively described using multi-omics approaches and the findings fully support this concept²⁶⁷. Across tissues,

macrophages display conserved niche-associated phenotypes. Well described examples include neuron-associated macrophages which express CX3CR1 and MHC-II^{33,268} and have been linked to tissue innervation²⁶⁸, and blood vasculature-associated macrophages which express CD206 and Lyve1³³ and maintain blood vessel tone²⁶⁹. These findings and the niche theory provide an explanation for the macrophage heterogeneity that is observed both at the pan-tissue scale, and at the sub-tissular scale.

Macrophage replacement by monocyte-derived cells occurs at steady state and is enhanced in inflammation. According to the niche theory, long-term maintenance of these monocyte-derived cells necessitates their occupation of a niche that includes growth factor-producing cells. Niche availability depends on either the creation of a new niche that will accommodate newly-recruited cells, for example when a tissue expands, the death of a previous macrophage in the niche, or out-competition of the previous occupant. Early studies addressing the replacement of tissue macrophages by monocytes used bone marrow transplantation, however this approach has been shown to cause tissue damage due to irradiation and induce an overestimation of monocyte recruitment. For example, up to 20% of microglial cells were of donor origin using this approach while parabiosis showed less than 5% monocyte contribution²⁵. More refined approaches are now used such as depletion models using DT-DTR, parabiosis or fate-mapping of monocytes using specific cre reporters. As discussed earlier, liberating hepatic niches via depletion of Kupffer cells in *Clec4f^{cre} x R26^{DTR}* mice allows reconstitution of the KC pool by monocyte-derived KCs that almost fully acquire the KC signature^{137,140}. This was also explored with lung alveolar macrophages (AMs). *Csf2rb^{-/-}* mice lack alveolar macrophages – suggesting the presence of open niches – and the alveolar macrophage pool can be restored by transfer of either yolk-sac macrophages, fetal liver monocytes or bone marrow monocytes²⁷⁰. Interestingly, upon mixed competitive transfer of these three precursors, fetal liver monocytes quickly became predominant, showing their competitive advantage²⁷⁰. Alveolar macrophages originate from fetal hematopoiesis and seed the lung perinatally at a time when bone marrow monocytes are being generated²³. The advantage of fetal liver monocytes over bone marrow monocytes was attributed to a better responsiveness to GM-CSF stimulation, rather than a selection of specific progenitors by the niche. Retrieving and sequencing donor-derived AMs revealed that they had adopted a signature similar to wild-type AMs, further demonstrating the impact of tissue imprinting. Similarly to what

we discussed with Kupffer cells during NASH, AMs are replaced by inflammatory monocyte-derived macrophages following influenza infection, further suggesting that establishment of monocyte-derived macrophages is facilitated during inflammation²⁷¹.

C. Homeostatic macrophage replenishment

Although the studies mentioned above provide inciteful evidence for the validity of the niche theory, the capacity of bone marrow monocytes to occupy a tissue niche that was not previously actively depleted of macrophages may be different in a steady state context. During development, yolk-sac macrophages seed tissues and they are quickly replaced by fetal liver monocytes, suggesting competition between different progenitors even in the earliest stages of life^{23,100,107}. Moreover, kinetic labeling of fetal liver progenitors between E11.5 and E17.5 showed that certain niches open during a limited time-window to allow tissue seeding by monocytic progenitors¹⁰⁷. For example, labeling Kit⁺ progenitors at E15.5 results in >20% labelling of peritoneal macrophages while labeling at E11.5 or E17.5 results in 7% labelling¹⁰⁷. Similarly to what was demonstrated for GM-CSF responsiveness during niche seeding, capacity to detect M-CSF and trigger CSF1R signaling might be a limiting factor for monocytes entering tissues. CSF1R expression is tightly regulated and depends on the binding of transcription factors on tissue or subset-restricted enhancers¹⁸⁴. For example CSF1R expression by microglia and peritoneal macrophages relies on the enhancer FIRE¹⁸⁵ (discussed previously) while its expression by Kupffer cells and spleen macrophages depends on a distal promoter element (DPE) upstream of the transcription start site²⁷². Blood monocytes rely on FIRE for CSF1R expression¹⁸⁵ and their expression of CSF1R is maintained in tissues independently of the DPE⁹⁸. Tissue-resident macrophages show higher consumption of CSF1 compared to monocytes⁹⁸. Whether upregulating CSF1R expression – possibly through chromatin modifications – expression is necessary for monocytes to gain competitive advantage after being recruited to tissues remains to be defined. Other cytokines such as GM-CSF and IFN γ have been proposed to play a role in monocyte differentiation in inflammatory conditions²⁷³, and whether they may offer monocytes a competitive advantage to gain niche occupancy is ill-defined.

The gut is a tissue that displays an important homeostatic macrophage turnover from blood monocytes. This observation has been linked to chronic exposure to microbial products from the microbiota that generate a low grade inflammation and

favor macrophage turnover^{274,275}. Intestinal macrophages maintain gut homeostasis notably through their bactericidal activity²⁷⁶, their production of IL-10²⁷⁷ and inherent anti-inflammatory phenotype^{278,279}. They were also shown to interact with the local blood vasculature, as well as neurons that directly impact macrophage phenotype through β 2-adrenergic receptor-mediated stimulation^{261,280-282}. Ms4a3^{cre}-driven labeling reaches 70% in this tissue⁶³, and this result is consistent with the fact that CCR2^{-/-} mice show a two thirds reduction of gut macrophage abundance²⁷⁵. Embryonic macrophages are predominant in the gut at birth. Although the majority are quickly replaced by macrophages deriving from Ly6C^{high} monocytes recruited in a CCR2-dependent manner²⁷⁵. Part of these embryonic macrophages persist through life and they can be identified by their Timd4 expression^{274,282}, while some monocyte-derived cells also maintain for a long period in the tissue and are identified by their expression of CD4^{274,282}. Importantly, the contribution of monocytes to the macrophage pool is subset-specific with a high, low and null contribution to the Timd4⁻ CD4⁻, Timd4⁻ CD4⁺ and Timd4⁺ CD4⁺ populations respectively²⁷⁴. Because of its high monocyte recruitment rate at steady state and macrophage diversity, the intestinal microenvironment offers opportunities to study mechanisms of macrophage replacement by monocyte-derived cells that take over the niche.

While monocyte recruitment rarely mainly appears tissue-specific, recent studies have also brought to light the sex-specificity of this mechanism in the peritoneum. Peritoneal macrophages consist of two populations : F4/80^{high} large peritoneal macrophages (LPMs) and F4/80^{low} small peritoneal macrophages (SPMs). LPMs are also identified by their expression of Icam2 and they rely on the transcription factor Gata6 for their survival²⁸³. SPMs express CD226 and necessitate replenishment from blood monocytes that mature into SPMs in a IRF4-dependant manner²⁸⁴. LPMs have an embryonic origin and they are maintained by both self-proliferation and differentiation of SPMs that adopt the LPM signature and notably Gata6 expression²⁸⁵. Importantly, the replenishment rate of male LPMs is higher compared to females, and that notably depends on contribution of monocyte-derived cells to the LPM pool^{285,286}. This sex-specific monocyte-replenishment rate was imposed on LPMs by the microenvironment – the niche – in a sex chromosome-independent manner involving the ovaries (i.e. female gonads act against monocyte recruitment in the peritoneal cavity), although estradiol was not involved²⁸⁶. Interestingly, sex-specific monocyte recruitment rate was also reported in the kidney although the specific mechanism

remains unexplored in this tissue²⁸⁵. Analysis of Ms4a3^{cre}-driven labeling fully supports these observations⁶³, and so far sex-specific macrophage turnover from monocytes has only been reported to be dominant in male peritoneum and kidneys. These results bring further evidence for macrophage plasticity and heterogeneity, and emphasize the need to address sex-specificity when studying macrophage phenotype and functions.

D. Monocyte-derived macrophages in pathology : cardiovascular diseases.

The role of monocyte-derived macrophages in driving inflammation is now well-established. Although this can be beneficial during pathogenic infections, it is largely detrimental during sterile inflammation that notably occurs in chronic metabolic diseases such as atherosclerosis. Atherosclerosis is characterized by an accumulation of immune cells – mainly macrophages – in the intima of blood vessels that is triggered by cholesterol-dominated dyslipidemia. The presence of atherosclerotic plaques is a risk factor and poor prognosis for the development of cardiovascular complications such as myocardial infarctions and strokes that represent the world-leading cause of death. Atherosclerotic plaques represent a complex microenvironment in which few resident macrophages cohabit with an overwhelming majority of monocyte-derived cells that fuel disease progression. Hypercholesterolemia promotes monocyte production²⁸⁷, and increased blood monocyte counts represent a risk factor for cardiovascular diseases in humans²⁴⁷. In murine atherosclerosis models, invalidation of the CCL2-CCR2 axis ablates monocyte recruitment and severely blunts plaque progression, highlighting the key role played by these cells in the disease^{288,289}. For this reason, atherosclerosis models offer the opportunity to dissect the fundamental mechanisms governing monocyte recruitment and their fate *in situ*. Plaque formation is initiated by intima resident macrophages which, during hypercholesterolemia, initiate monocyte recruitment towards the intimal wall²⁹⁰. These resident macrophages turn into foam cells as they uptake and accumulate lipids²⁹⁰. Foam cells display a specific transcriptomic program related to lipid handling²⁹¹ which could perhaps play a role in the resolution of arterial inflammation. On the other hand, monocyte-derived macrophages adopt a pro-inflammatory phenotype notably associated with *il1β*, *tnfa* and *cc12* expression, further amplifying monocyte recruitment and disease progression²⁹¹. Blood monocytes are recruited to the plaque from the luminal side, and they quickly lose motility as they differentiate into macrophages in the plaque²⁹².

Immotile macrophages that were previously present in the plaque become embedded in an inflammatory, hypoxic and possibly metabolically-stale microenvironment that promotes macrophage dysfunction and death. The inability of newly-recruited macrophages to reach deeper plaque areas leads to an accumulation of debris and apoptotic cells that form necrotic cores, which are hallmarks of unstable plaques. The overall capacity of plaque macrophages to perform efferocytosis is a strong determinant of atherosclerosis progression^{293,294} and development into further cardiovascular complications such as myocardial infarctions in humans.

Several macrophage populations are present in both murine and human heart, and these comprise both embryonic and monocyte-derived cells that can notably be identified through differential CCR2 expression^{95,295,296}. CCR2⁻ embryonic cardiac macrophages originate in small part from the yolk-sac, but the majority of these cells are seeded during fetal liver hematopoiesis^{89,95}. They are long lived tissue-resident macrophages and two-thirds of CCR2⁻ macrophages express the embryonic macrophage marker Timd4²⁹⁷. Embryonic heart macrophages are maintained through self-proliferation at steady state, and this mechanism fades with age and is compensated by monocyte recruitment to maintain the cardiac macrophage pool⁸⁹. The CCR2⁺ subset represents around 10-15% of heart macrophages in adult mice at steady state and these cells are constantly replenished by recruited monocytes²⁹⁷. The heart represents a good example of a tissue where macrophages with distinct origin play different functions, as CCR2⁻ and CCR2⁺ macrophages play differential roles during and following myocardial infarction. The tissue-resident CCR2⁻ subset notably participates in heart homeostasis by supporting coronary angiogenesis both in development and in heart failure models, and promote tissue healing following myocardial infarction²⁹⁷⁻²⁹⁹. Myocardial infarction rapidly leads to a major loss of CCR2⁻ Timd4⁺ heart macrophages²⁹⁷. In this setting, CCR2⁺ macrophages trigger inflammation by releasing cytokines and chemokines that promote monocyte and neutrophil recruitment, while CCR2⁻ macrophages suppress this inflammation²⁹⁵. Remaining tissue-resident macrophages increase their proliferation rate to partly recover their initial numbers as the tissue heals, while monocytes contribute to transitory macrophage expansion by generating CCR2⁺ macrophages. Importantly, the proportion of monocyte-derived CCR2⁺ cells remains increased in the long run and the initial balance of embryonic and monocyte-derived macrophages is lost^{297,300}. Efferocytosis of apoptotic cardiomyocytes is essential to cardiac healing³⁰¹, and Timd4

is involved in macrophage efferocytosis mechanisms³⁰². How this change in cardiac macrophage content may affect the outcome of successive myocardial infarctions remains to be addressed. Whether the disappearance of Timd4⁺ macrophages following myocardial infarction is due to excess local damage signals and apoptosis, or the death of niche cells and loss of niche-derived trophic factors remains to be established.

Chapter 6 – Macrophage functions in tissues

A. Ovary macrophages

Ovary macrophages were traditionally identified by their expression of the lysosome-associated glycoprotein CD68, but they also express MHC-II, CD11b and F4/80²⁸. Like in other organs, embryonic and monocyte-derived macrophage coexist in ovaries³⁰³. These cells acquire their typical MHC-II expression as they mature after birth³⁰³. The counts and distribution of ovary macrophages correlate with the reproductive cycle. When follicles grow before ovulation, macrophages are found outside granulosa layers³⁰⁴. Op/op mice suffer from low pregnancy rate and have reduced numbers of ovarian macrophages, suggesting that these cells require CSF1 for their survival³⁰⁵. The cellular source of CSF1 in ovaries is still under debate. For instance, granulosa cells have been demonstrated to secrete CSF-1 during follicular growth and its concentration in follicular fluid is higher than in the serum³⁰⁶. Consequently, during follicular growth, ovary macrophage numbers increase³⁰⁴. Ovary macrophages were attributed a trophic role to support follicular growth by secreting soluble factors such as TNF α ³⁰⁷. Ovary macrophages are closely associated to blood vessels and secrete cytokines and enzymes such as metalloproteinases (MMP-1, 2, 7 and 9)³⁰⁸. They also produce ROS (reactive oxygen species which cause oxidative stress) which degrade the follicular wall before the ovulation. Finally, after ovulation during the luteal phase, MHC-II positive macrophages are the most abundant immune cells. They can promote angiogenesis through secretion of factors such as VEGF, EGF (Epidermal Growth Factor), and FGF (Fibroblast Growth Factor), and angiogenesis is impaired when macrophages are absent. Ovary macrophages participate in the clearance of debris, and several studies found that those macrophages play a role in the production of progesterone by luteal cells³⁰⁹. Taken together, these data suggest multiple roles for macrophages in ovaries : a trophic function to support hormonal production and matrix remodeling, and a hypothetic role in efferocytosis of apoptotic cells. However, one limitation of this set of literature is the markers used to define ovary macrophages. The aforementioned studies used CD11b-DTR or CD11c-DTR mice to deplete ovary macrophages. This approach could also trigger DCs and monocyte depletion, suggesting that the results cannot be definitely attributed solely to macrophage depletion²⁸. A recent report showed, using mass cytometry, that only a

part of CD64⁺ F4/80⁺ cells in ovaries express MerTK³⁰³. Most studies of ovary immune cells did not assess MerTK expression and functions attributed to macrophages may actually be performed by other immune cells. Therefore, ovary macrophages still need to be more thoroughly characterized. One intriguing question is whether some populations of ovary macrophages could be involved in the establishment of ovary deficiency and premature ovarian failure.

B. Testicular macrophages

Two tissue-resident macrophage populations are found in testis : CD64^{high} MHC-II^{low} macrophages tightly associated to testosterone-producing Leydig cells in the seminiferous tubules interstitium, and CD64^{low} MHC-II^{high} peritubular macrophages that are closely associated to seminiferous tubules where spermatogonial stem cells are located³¹⁰. Similar macrophage populations were recently identified in epididymis³¹¹. Testicular macrophages are also heterogenous in origin. Genetic E9.0 fate mapping with CX3CR1^{CreERT2} x R26^{YFP} mice show that around 5.5% of testes macrophages have an embryonic origin in adults, and these embryonic macrophages are only part of the interstitial CD64^{high} MHC-II^{low} population^{310,312}. At birth, monocytes arising from definitive hematopoiesis dilute or replace embryonic interstitial macrophages and seed peritubular macrophages^{310 311}. Testicular macrophages express highly CD115 and Leydig cells were found to secrete CSF1. Importantly, op/op mice have low numbers of macrophages in testes. CSF1 supplementation in these mice restores testicular macrophage density³¹³. Interestingly, interstitial macrophages are MHC-II⁻ in contrast to MHC-II⁺ peritubular macrophages. Peritubular macrophages have high MHC-II expression, which might predispose to antigen-presentation to T-cells. Both macrophage populations have an anti-inflammatory profile supported by high expression levels of IL-10, and TGFβ and low IL-12, IL-1β and TNFα levels³¹⁴. In op/op mice, sperm counts are 60% lower than in control mice with a two times higher dead sperm rate³¹³. In addition, testosterone concentration is 86% lower in these mice. This observation is supported by a study using CD11b^{DTR} and reporting 50% lower testosterone levels³¹⁵. Interstitial macrophages associated to Leydig cells produce 25-hydroxicholesterol from cholesterol conversion by the cholesterol 25-hydroxylase enzyme. Subsequently, 25-hydroxicholesterol is converted to testosterone by Leydig cells. This might explain the lower testosterone blood concentration in op/op mice. Additionally, macrophages play a trophic role and stimulate Leydig cells proliferation.

Op/op mice have a lower renewal rate of spermatogonial stem cells that could be either a direct consequence of the peritubular macrophages lack, enhancing spermatogonia proliferation by retinoic acid production³¹⁵, or, an indirect consequence of insufficient Leydig cells testosterone secretion. Macrophages were thus initially proposed to play an essential role in spermatogenesis. A recent report showed that depletion of macrophages in utero, but not postnatally, impacted spermatogenesis³¹². This result suggests that testis macrophages are rather involved in proper development of the organ. Although testes macrophages and functions characterization are more advanced than in the ovaries, understanding the precise function of testicular macrophages still needs further proteomic and functional analyses.

C. Pancreatic macrophages

The pancreas is composed of two different areas: the exocrine area secreting digestive enzymes, and the endocrine area composed of islets of Langerhans, secreting insulin and glucagon. A pioneer study⁶ established the presence of F4/80⁺ cells, likely macrophages, in the islets. Macrophages in non-diabetic mice account for nearly 98% of immune cells in the islets. These cells were further characterized by a high expression of CD11c, MHC-II, F4/80, CD11b, CD64, MerTK, lysozyme M, CX3CR1, and CD68³¹⁶. Due to the absence of Zbtb46⁺ cells, a *bona fide* DC marker²⁸, the authors excluded the possibility of a DC enrichment. A genetic fate-mapping analysis established that islet macrophages are derived from definitive hematopoiesis while stromal macrophages derive from yolk-sac precursors³¹⁶. In addition, pancreatic macrophages are localized nearby blood vessels and have projections within the islets interacting with beta cells, the main insulin producers. This proximity suggests an involvement of pancreatic macrophages in immune regulations. Interestingly, islet macrophage depletion reduces VEGF-A (Vascular endothelial growth factor-A) secretion, leading to altered vascular density and islet remodeling³¹⁷.

Considering the pancreatic macrophage localization, one can expect them to also play a role in the physiology and architecture of the gland. Indeed, op/op mice show decreased macrophage numbers in the pancreas³¹⁸. Beta cell mass was 30% lower in op/op mice compared to control mice³¹⁸ (large islets are less numerous, leading to a decreased insulin volume). Moreover, it was demonstrated that in context of obesity, resident islet macrophages expand locally without monocyte recruitment. A parabiosis experiment using CD45.1 and CD45.2 congenic mice showed that despite their bone

marrow origins, the replenishment of islet macrophages by bone marrow monocytes was low, and their renewal was dependent on in-situ proliferation³¹⁶. Islet macrophages induce beta cells proliferation by the engagement of the PDGF/PDGFR pathway³¹⁹. Taken together, these data suggest an important role of tissue resident macrophages in pancreatic beta cells homeostasis.

Interestingly, it was demonstrated that pancreatic beta cells transfer insulin-containing granules or insulin catabolites to neighboring macrophages³²⁰. However, the relevance of this observation in the gland physiology is not yet understood. One can hypothesize that macrophages protect beta cells from auto-immune destruction by T cells during diabetes. Indeed, Unanue and colleagues also showed that insulin degradation is a crucial part of tissue homeostasis maintenance. Macrophages play a key protective role in this process by capturing and digesting the insulin β chain, therefore preventing its uptake by DCs. The degradation of reactive β chain-derivatives by islet macrophages prevents T-cells activation and inhibits an eventual deleterious auto-immune response³²⁰. In contrast, macrophage-depleted NOD mice, which spontaneously develop auto-immune diabetes, were protected against the disease development, indicating a role in the initiation of autoimmune process³²¹. This might be a consequence of the macrophage pro-inflammatory cytokines release, such as IFN β , in the very early stages of diabetes initiation preceding DC and T cell recruitment to the pancreas.

The existence of at least two populations of macrophages was suggested in the pancreas: the stromal macrophages, derived from embryonic precursors and expressing the CD206/CD301 anti-inflammatory markers, and the islet macrophages with a pro-inflammatory signature expressing TNF α (tumor necrosis factor- α) and IL-1 β . More recently, single-cell RNA sequencing of murine islets revealed that 5 macrophage subsets co-exist in the pancreas. These cells possess a unique transcriptional signature and functional markers, including inflammatory activation markers, regulatory and efferocytosis functions or cell-cycle genes³²². These data highlight the diversity of pancreatic macrophage subsets that likely supports the endocrine functions of the tissue and modulate the induction and development of autoimmune disorders.

D. White adipose tissue macrophages

White adipose tissue is the main lipid storage organ where triglycerides accumulate in adipocytes inside lipid droplets, and localizes essentially in the visceral region in mice (figure 6). White adipose tissue also comprises subcutaneous depots, that contains “beige” adipocytes with thermogenic activity. On the opposite, mitochondria-rich brown adipose tissue does not play a lipid storage role at steady state and instead consumes metabolites such as lipids and glucose to fuel thermogenesis.

White adipose tissue is rich with macrophages that represent the main immune population in this organ. The accumulation of macrophages in adipose tissue during obesity initially led to the idea that these cells originate from the bone marrow compartment^{323,324}. However, more recent reports showed that the majority of these cells have an embryonic origin (and associated *Timd4* expression) and sustain independently of monocyte input^{325,326}. The adipose tissue macrophage (ATM) pool was initially considered to contain two populations : anti-inflammatory M2 macrophages that express CD206 and are present at steady state, and inflammatory M1 macrophages identified by CD11c expression and that infiltrate the tissue during obesity³²⁷. However, recent studies using more resolutive approaches like single cell RNA sequencing or multiparametric cytometry revealed a more complex diversity of ATMs^{156,326,328-330}. Several subpopulations of ATMs with restricted transcriptomic signature and sub-tissular localization are indeed found at steady state, and ATM phenotype evolves during disease (notably obesity). These include lipid-associated macrophages (LAM) characterized by *Trem2* expression¹⁵⁶, vasculature-associated macrophages (VAM) with high CD206 expression^{330,331}, and CX3CR1⁺ sympathetic neuron associated macrophages (SAM) proposed to recycle norepinephrine³³².

The adipose tissue is exposed to daily fluctuations in activation state. Periods of feeding lead to energy storage in the form of triglycerides and thus promote adipose tissue expansion. On the contrary, periods of fasting promote lipolysis, the process of triglyceride degradation to release free fatty acids in the blood circulation. ATMs thus constantly readapt to their fluctuating microenvironment. For instance, fasting induces a rapid disappearance of vasculature-associated macrophages and re-feeding allows the replenishment of this population³³⁰. Treatment with the β 3-agonist CL 316,243 to induce lipolysis reproduces VAM disappearance but also induces a strong monocyte recruitment³³⁰.

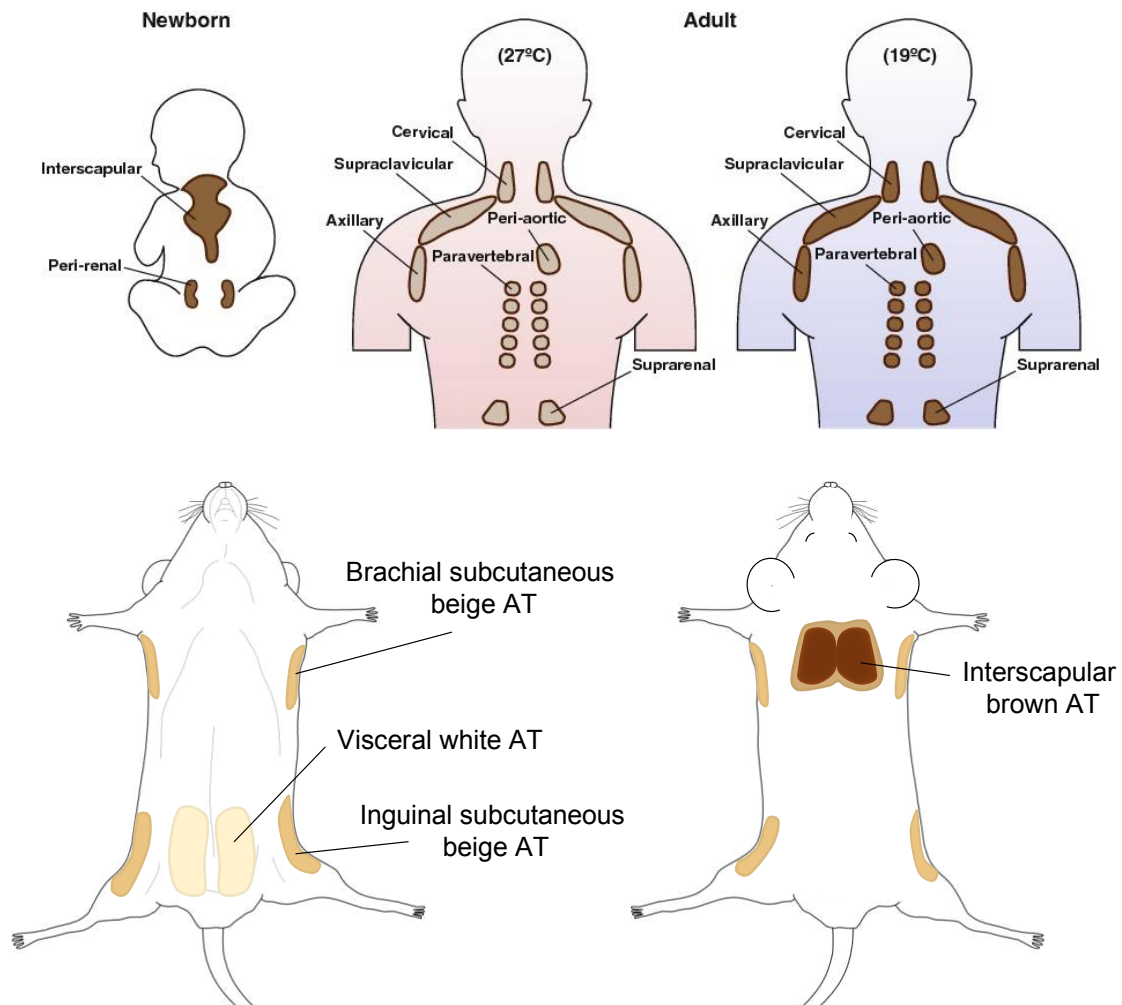


Figure 6. Schematic representation of the localization of the main adipose tissue depots in mice, and brown adipose tissue in humans.

Adapted in part from Jung SM *et al.*³³³.

Similarly to what is observed in other tissues, ATM maintain tissue homeostasis through their canonical function of efferocytosis. Upon metabolic challenge and notably obesity-related hypertrophy, adipocytes may undergo apoptosis. This leads to the formation of crown-like structures (CLS), thought to represent macrophages surrounding a dying adipocyte to orchestrate its removal and recycling³³⁴. Genetically triggering adipocyte death leads to recruitment of macrophages with an anti-inflammatory phenotype that clear the tissue of apoptotic cells and promote return to homeostasis³³⁵. Although this is poorly characterized, neutrophils have also been observed inside CLSs³³⁰. ATMs further display a vast array of functions involved in white adipose tissue homeostasis, such as promoting tissue innervation³³⁶ through

PDGF production³³⁷, recycling damaged mitochondria³³⁸, and influence adipocyte lipid storage^{156,339}.

Macrophages themselves contain lipid droplets at steady state, and they express the enzyme ATGL allowing triglyceride degradation. Lipid storage by macrophages was proposed to play a role in obesity-related insulin resistance³⁴⁰ and its key regulator is the protein HILPDA (hypoxia inducible lipid droplet associated)³⁴¹. HILPDA promotes lipid storage in macrophages by inhibiting ATGL³⁴¹ and its expression can be induced by adrenergic stimuli³⁴², lipids³⁴² or LPS³⁴³. This suggests that macrophage lipid storage could be induced both during fasting, when β -adrenergic stimulation is induced and lipolysis-derived lipids are abundant, and during obesity with abundance of both circulating fatty acids and lipids deriving from dying adipocytes. Although HILPDA/ATGL-mediated lipid accumulation and breakdown has been shown to impact macrophage activation and inflammatory cytokine secretion, no impact on adipose tissue inflammation was observed^{341,343}. Other ATGL-independent lysosomal lipolysis plays a role in macrophage activation³⁴⁴ and influences adipose tissue homeostasis³⁴⁵. Macrophages preferentially uptake lipids via the scavenger receptor CD36³⁴⁴, but a “lipidic” crosstalk also exists between adipocytes and macrophages. Indeed, adipocytes were shown to release lipidic vesicles (independently of lipolysis) that can readily be taken up by surrounding macrophages, and this process is accentuated during obesity³⁴⁶. In this obesity context, a population of lipid-associated macrophages expressing TREM2 accumulates in adipose tissue¹⁵⁶. These cells promote homeostatic lipid storage by adipocytes, and loss of TREM2 worsens obesity-related metabolic syndrome¹⁵⁶. Macrophages were recently showed to promote adipocyte lipid storage via production of platelet-derived growth factor cc (PDGFcc)³³⁹. Long-term macrophage depletion using either a α -CSF1R monoclonal antibody or PLX5622 prevents obesity in mice fed a high fat diet and mice with invalidation of PDGFcc in macrophages showed the same phenotype. These results thus demonstrate that specialized macrophage sub-populations are important regulators of tissue lipid homeostasis. Lipid storage can happen in other tissues such as the liver, heart, muscle or brown adipose tissue under specific conditions and whether macrophages drive lipid content locally in these tissues or instead buffer circulating lipids needs further investigation.

Results


Project 1: Diversity and functions of brown adipose tissue macrophages.

A. Hypothesis and aims

In placental mammals, two different adipose tissues have been identified³⁴⁷. White adipose tissue (WAT) is the most studied. WAT stores energy in the form of triglycerides³⁴⁷. Depending on the nutritional state, white adipocytes accumulate lipids (lipogenesis) or mobilize them (lipolysis) to supply the organism' energetic and structural needs. Brown adipose tissue (BAT) plays a key role in thermogenesis³⁴⁷. The mitochondrial protein Ucp1 (Uncoupling Protein 1) is essential for heat generation and is a hallmark of brown adipocytes³⁴⁸. More recently, beige adipocytes have been identified³⁴⁹. These cells reside within WAT and express low Ucp1 levels at steady state, but increase its expression, in particular during cold exposure, thus contributing to adaptative thermogenesis³⁴⁹. Importantly, white, brown and beige adipocytes have a specific developmental origin and possess a well-defined transcriptomic signature^{347,350}. The presence of distinct immune cell types has been documented in all adipose tissues and their content vary according to metabolic status and environmental conditions. The most abundant immune cells in these depots are macrophages . While the diversity and developmental origin of WAT macrophages is well documented, little is known about the diversity and functions of BAT macrophages^{326,330,339}.

A pioneering work suggested that CX3CR1⁺ BAT macrophages are involved in thermogenesis²⁶⁸. More recently, it was shown that a subset of CD169⁺ BAT macrophages was involved in damaged mitochondria uptake and recycling, thus favouring optimal BAT physiological activity and thermogenesis³⁵¹. However, the interconnections between these two BAT macrophage populations remains to be established and the diversity of BAT macrophages is ill-defined. Thus, we decided to investigate the diversity and functions of BAT myeloid cells. The data that we obtained are presented below.

Brown adipose tissue monocytes support tissue expansion

Alexandre Gallerand^{1,10}, Marion I. Stunault ^{1,10}, Johanna Merlin¹, Hannah P. Luehmann ², Deborah H. Sultan², Maria M. Firulyova³, Virginie Magnone⁴, Narges Khedher¹, Antoine Jalil⁵, Bastien Dolfi¹, Alexia Castiglione¹, Adeline Dumont¹, Marion Ayrault¹, Nathalie Vaillant¹, Jérôme Gilleron¹, Pascal Barbry ⁴, David Dombrowicz ⁶, Matthias Mack ⁷, David Masson ⁵, Thomas Bertero ⁴, Burkhard Becher ⁸, Jesse W. Williams ⁹, Konstantin Zaitsev ³, Yongjian Liu ², Rodolphe R. Guinamard¹, Laurent Yvan-Charvet¹ & Stoyan Ivanov ¹✉

Monocytes are part of the mononuclear phagocytic system. Monocytes play a central role during inflammatory conditions and a better understanding of their dynamics might open therapeutic opportunities. In the present study, we focused on the characterization and impact of monocytes on brown adipose tissue (BAT) functions during tissue remodeling. Single-cell RNA sequencing analysis of BAT immune cells uncovered a large diversity in monocyte and macrophage populations. Fate-mapping experiments demonstrated that the BAT macrophage pool requires constant replenishment from monocytes. Using a genetic model of BAT expansion, we found that brown fat monocyte numbers were selectively increased in this scenario. This observation was confirmed using a CCR2-binding radiotracer and positron emission tomography. Importantly, in line with their tissue recruitment, blood monocyte counts were decreased while bone marrow hematopoiesis was not affected. Monocyte depletion prevented brown adipose tissue expansion and altered its architecture. Podoplanin engagement is strictly required for BAT expansion. Together, these data redefine the diversity of immune cells in the BAT and emphasize the role of monocyte recruitment for tissue remodeling.

¹ Université Côte d'Azur, INSERM, C3M, Nice, France. ² Department of Radiology, Washington University School of Medicine, Saint Louis, MO, USA. ³ Computer Technologies Department, ITMO University, Saint Petersburg, Russia. ⁴ Université Côte d'Azur, CNRS, IPMC, Valbonne, France. ⁵ Université Bourgogne Franche-Comté, LNC UMR1231, Dijon, France. ⁶ Univ.Lille, Inserm, CHU Lille, Institut Pasteur de Lille, U1011-EGID, Lille, France. ⁷ Department of Internal Medicine - Nephrology, University Hospital Regensburg, Regensburg, Germany. ⁸ Institute of Experimental Immunology, University of Zürich, Zürich, Switzerland. ⁹ Department of Integrative Biology and Physiology, Center for Immunology, University of Minnesota Medical School, Minneapolis, MN, USA. ¹⁰ These authors contributed equally: Alexandre Gallerand, Marion I. Stunault. ✉email: Stoyan.ivanov@unice.fr

Monocytes are part of the mononuclear phagocytic system together with macrophages and dendritic cells (DCs)¹. These cells are generated in the bone marrow compartment where they originate from hematopoietic stem cells (HSC) through myelopoiesis, a tightly regulated process². The growth factor colony-stimulating factor 1 (CSF1), binds to its receptor CSF1R (CD115) expressed on monocytes and macrophages to promote their survival³. Bone marrow-derived monocytes egress to the blood circulation and this process is under the control of chemokine–chemokine receptor interactions. For instance, stromal cell-derived CXCL12 (SDF-1) binds to monocyte CXCR4 and this interaction is required for monocyte retention within the bone marrow compartment⁴. By contrast, CCL2-CCR2 interactions control monocyte egress from bone marrow to blood and their peripheral tissue recruitment from the blood circulation^{5,6}. Two major subsets of blood monocytes have been described according to the expression of the cell surface marker Ly6C. Ly6C^{high} monocytes, also called “classical monocytes”, are recruited to peripheral tissues and can give rise to macrophages during infection, acute or chronic inflammation, or cancer and contribute to the control and the resolution of tissue inflammation^{7,8}. Ly6C^{low} “non-classical” monocytes patrol the blood vasculature, cleaning debris and promote healing of the injured endothelium⁹. During infection and excessive or chronic inflammation, monocytes are recruited to peripheral tissues where they differentiate into macrophages. In every organ, macrophages have been demonstrated to play a tissue-specific function. For example, splenic red pulp macrophages control iron content while testis macrophages have been implicated into spermatogenesis^{10–12}.

The adipose tissue has long been considered as a simple triglyceride storage organ. Various types of adipose tissue have been documented including white adipose tissue (WAT), beige adipose tissue, and brown adipose tissue (BAT). In mice, WAT is typically localized in the peritoneal cavity and subcutaneously, with its most studied depot, the perigonadal (epididymal) adipose tissue (EAT). BAT is located in the interscapular region and its main function is thermogenesis orchestrated by the mitochondrial uncoupling protein 1 (*Ucp1*). Beige adipose tissue is located subcutaneously (SCAT) and comprises among others the brachial and inguinal depots. Adipose tissue depot size is regulated through variations in adipocyte size and numbers. Triglycerides (TGs) are stored in lipid droplets inside adipocytes and their mobilization relies on a process named lipolysis. The first step of lipolysis is under control of the rate-limiting enzyme ATGL (adipose triglyceride lipase)^{13–15} leading to TG degradation into diacylglycerol (DAG) and a fatty acid. Macrophages have been identified in BAT where they have been proposed to control neuron network density and BAT thermogenesis¹⁶. Nevertheless, the diversity of BAT macrophages and the mechanism responsible for their maintenance remain underappreciated. In this work, we found several populations of macrophages in BAT of wild-type mice. Additionally, we observed the existence of tissue-resident monocytes that contributed to BAT macrophage homeostasis. We used an established mouse model of adipocyte-selective Atgl-deficiency leading to BAT expansion and evaluated monocyte numbers in bone marrow and blood, and monocyte and macrophage numbers and diversity in adipose tissues. Thus, our data show that monocytes contribute to BAT expansion in a Podoplanin-dependent mechanism and favor matrix remodeling, uncovering a new function for this cell type.

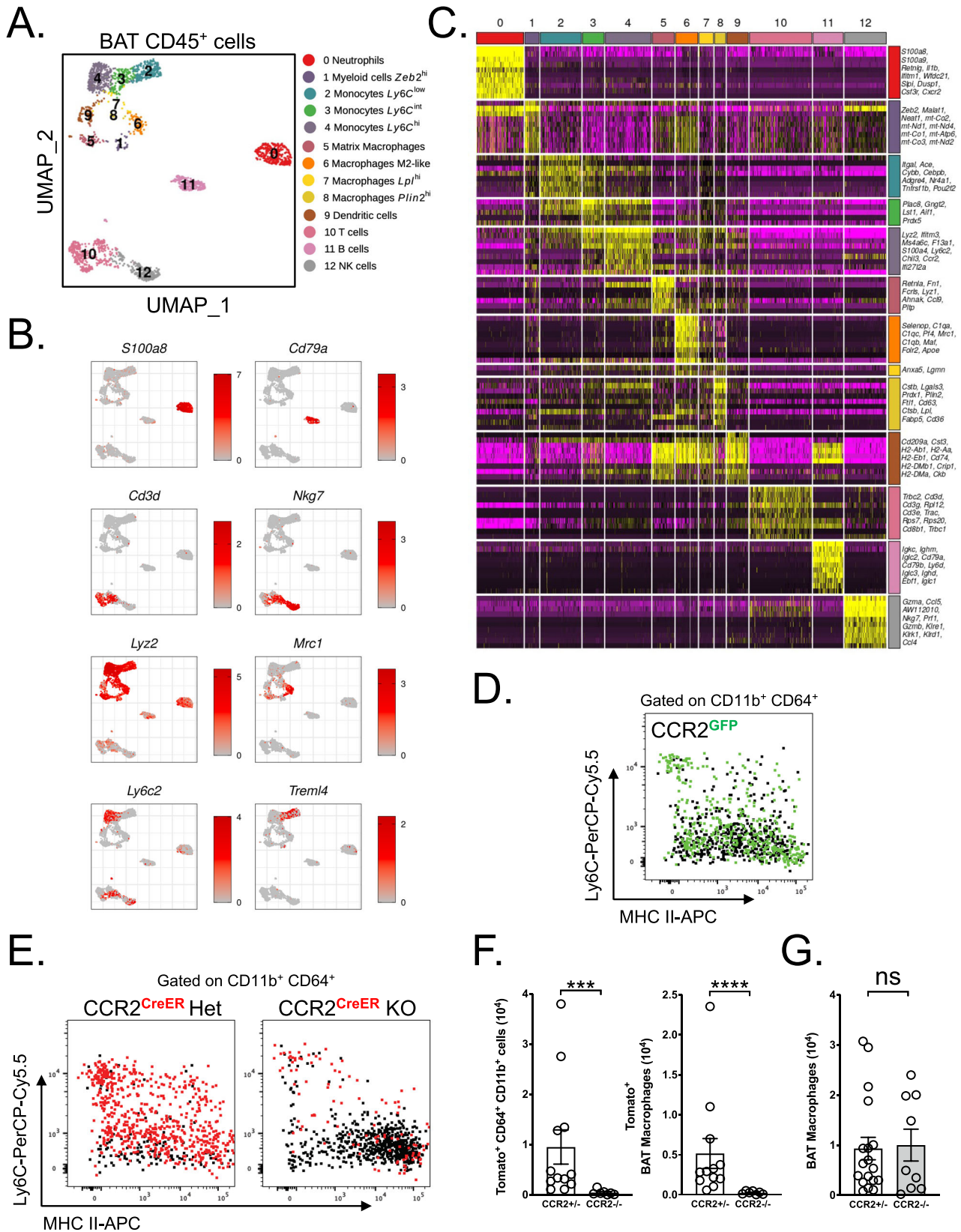
Results

BAT macrophage diversity and monocyte contribution to their maintenance. To investigate the diversity of BAT myeloid cell

populations, we performed single-cell RNA sequencing (scRNA-seq) analysis of cell-sorted CD45⁺ cells (Fig. S1A) from C57BL/6 mice housed at room temperature and fed on a normal chow diet. These data revealed an unprecedented diversity of leukocytes residing in BAT (Fig. 1A), which can be represented by 13 unique clusters (Fig. 1A). We detected populations of T cells, B cells, and NK cells (clusters 10, 11, and 12 respectively) (Fig. 1B, C). Furthermore, among myeloid cells, we identified a population of neutrophils (cluster 0) and three separate populations of monocytes (clusters 2, 3, and 4). These subsets reflected Ly6C^{low}, Ly6C^{int}, and Ly6C^{high} monocytes respectively (Fig. 1C). Of interest, we were able to identify four different macrophage populations (clusters 5, 6, 7, and 8) (Fig. 1C). These cells expressed a specific set of genes, which are represented by gene set enrichment analysis across all 13 clusters (Fig. 1C). Cluster 6 expressed many canonical alternative macrophage polarization markers including *Mrc1* (CD206) and *Clec10a* (CD301). Additionally, this cluster was enriched in genes (*C1qa*, *C1qb*, *C1qc*) encoding for proteins involved in the complement pathway. Clusters 7 and 8 highly expressed genes involved in lipid metabolisms such as *CD36*, *Lpl*, and *Lipa*. Finally, cluster 5 was enriched in genes involved in tissue remodeling (*Ecm1*, *MMP12*, *MMP19*, *Fn1*). This BAT macrophage subset diversity might reflect their involvement in various functions from lipid handling (Clusters 6, 7, and 8) to tissue remodeling (Cluster 5). Since we detected many monocytes in our single-cell RNA sequencing data (Fig. 1A, C), we validated this observation in the BAT using *CCR2*^{GFP/+} mice. In agreement with the transcriptomic data, we found many GFP⁺ cell in BAT that were distributed among monocyte and macrophage populations (Fig. 1D). These data suggested that monocytes may contribute to BAT macrophage pool maintenance. To study this hypothesis, we used a pulse-chase model allowing to label monocytes and follow their differentiation into macrophages over a short period of time. *CCR2*^{creERT2} mice were crossed with TdTomato reporter. To induce *CCR2*-driven TdTomato expression, mice were administered with tamoxifen by oral gavage and analyzed 48 h later. We observed a large fraction of TdTomato⁺ cells among BAT monocytes and macrophages (Fig. 1E). Moreover, BAT Tomato⁺ monocyte and macrophage counts were decreased in *CCR2*-deficient mice, demonstrating the relevance of this axis in BAT macrophage pool size maintenance (Fig. 1E, F). However, macrophage counts remained similar in *CCR2*^{+/-} and *CCR2*^{-/-} mice, suggesting that even though monocyte recruitment plays a critical role to maintain BAT macrophage pool, a compensatory mechanism, likely proliferation, could occur in the absence of monocyte recruitment to sustain constant BAT macrophage numbers (Fig. 1G).

BAT expansion is supported by monocyte recruitment and local macrophage differentiation.

To address how BAT monocyte and macrophage populations are affected during tissue remodeling, we generated a mouse model selectively lacking ATGL in mature adipocytes (*Adipo*^{Δ/Δ}). For this purpose, *Pnpla2*^{f/f} mice were crossed with *AdipoQ*^{creERT2} mice in order to ablate ATGL protein production specifically in mature adipocytes (Fig. S1B). To validate the efficiency of our system, those mice were crossed with *TdTomato*^{f/f} reporter mice, in which the TdTomato expression reflects Cre recombinase activity (Fig. S1B). Additionally, we crossed these mice with *CX3CR1*^{gfp} mice to facilitate analysis of monocyte distribution in tissues by flow cytometry and microscopy (Fig. S1B). Indeed, fluorescence microscopy analysis of EAT and BAT tissue sections revealed that almost all adipocytes expressed the TdTomato protein 3 weeks following tamoxifen treatment, further validating the efficiency of



our experimental system (Fig. S1C). Western blotting analysis of BAT protein extracts showed an almost complete absence of ATGL protein in *Adipo*^{Δ/Δ} mice, in comparison to littermate control animals, further confirming the deletion efficiency (Fig. S1D). The low remaining ATGL protein levels in *Adipo*^{Δ/Δ} mice could originate from adipose tissue immune cells such as

macrophages or neutrophils, previously shown to express this protein¹⁷ but in which the adiponectin promoter is not active. As expected, serum glycerol concentrations were decreased in *Adipo*^{Δ/Δ} mice compared to control animals (Fig. S1E). Serum lipidomic analysis further revealed decreased concentrations of palmitic acid (C16:0), the most abundant non-esterified fatty

Fig. 1 Monocytes contribute to BAT macrophage pool at a steady state. **A** Single-cell RNA-Seq analysis of BAT CD45⁺ cells from 7–8-week-old male mice. **B** UMAP representations of genes used to identify cell types among BAT CD45⁺ cells. **C** Heatmap showing normalized expression levels of marker genes helping to identify cell types present in the data. **D** Flow cytometry plot showing CCR2^{GFP} expression among BAT Ly6C⁺/MHCII⁺ cells (gated on CD45⁺ CD11b⁺ CD64⁺ cells). **E** Flow cytometry plot showing TdTomato expression among BAT Ly6C⁺/MHCII⁺ cells (gated on CD45⁺ CD11b⁺ CD64⁺ cells) from CCR2^{creERT2/+} and CCR2^{creERT2/GFP} mice 48 h after tamoxifen gavage. **F** Quantification of TdTomato⁺ cells among CD45⁺ CD64⁺ CD11b⁺ cells ($p = 0.0002$) and macrophages (CD45⁺ CD64⁺ CD11b⁺ Ly6C⁻) ($p < 0.0001$) in the BAT of CCR2^{creERT2/+} (CCR2^{+/-}, $n = 12$) and CCR2^{creERT2/GFP} (CCR2^{-/-}, $n = 7$) mice 48 h after tamoxifen gavage. **G** Quantification of macrophages in the BAT of CCR2^{+/-} ($n = 18$) and CCR2^{-/-} ($n = 9$) mice, $p = 0.8997$. Panels **D**, **E**, **F**, and **G** represent pooled data from two independent experiments. All data are represented in means \pm SEM. Two-tailed Mann–Whitney tests were used to determine statistical significance. ns $p > 0.05$; * $p < 0.05$; ** $p < 0.01$. Source data are provided as a Source Data file.

acids (NEFA) (approximately 33% of total NEFAs). Myristic (C14:0), and α -linolenic (C18:3 n-3) acids were also decreased (Fig. S1F). Interestingly, other types of fatty acids were not modulated in Adipo ^{Δ/Δ} mice when compared to littermate control animals (Fig. S1G).

In agreement with previous reports using constitutive *Atgl* deletion^{18,19}, we found a strikingly increased BAT weight ($\times 2.5$ fold) in Adipo ^{Δ/Δ} mice in comparison to co-housed littermate controls after 3 weeks of Cre induction (Fig. 2A). Nevertheless, EAT had a similar weight in both genotypes (Fig. 2A). Tissue histology analysis revealed widespread changes in brown adipocyte morphology with the appearance of larger lipid droplets, a process named “whitening” of the brown adipose depot (Fig. 2B)²⁰. We also observed the appearance of CD11b⁺ cells in the BAT of Adipo ^{Δ/Δ} mice, in patterns similar to “crown-like structures” reported in EAT during obesity (Fig. 2C)²⁰. These cells were rarely detected in control mice (Fig. 2C).

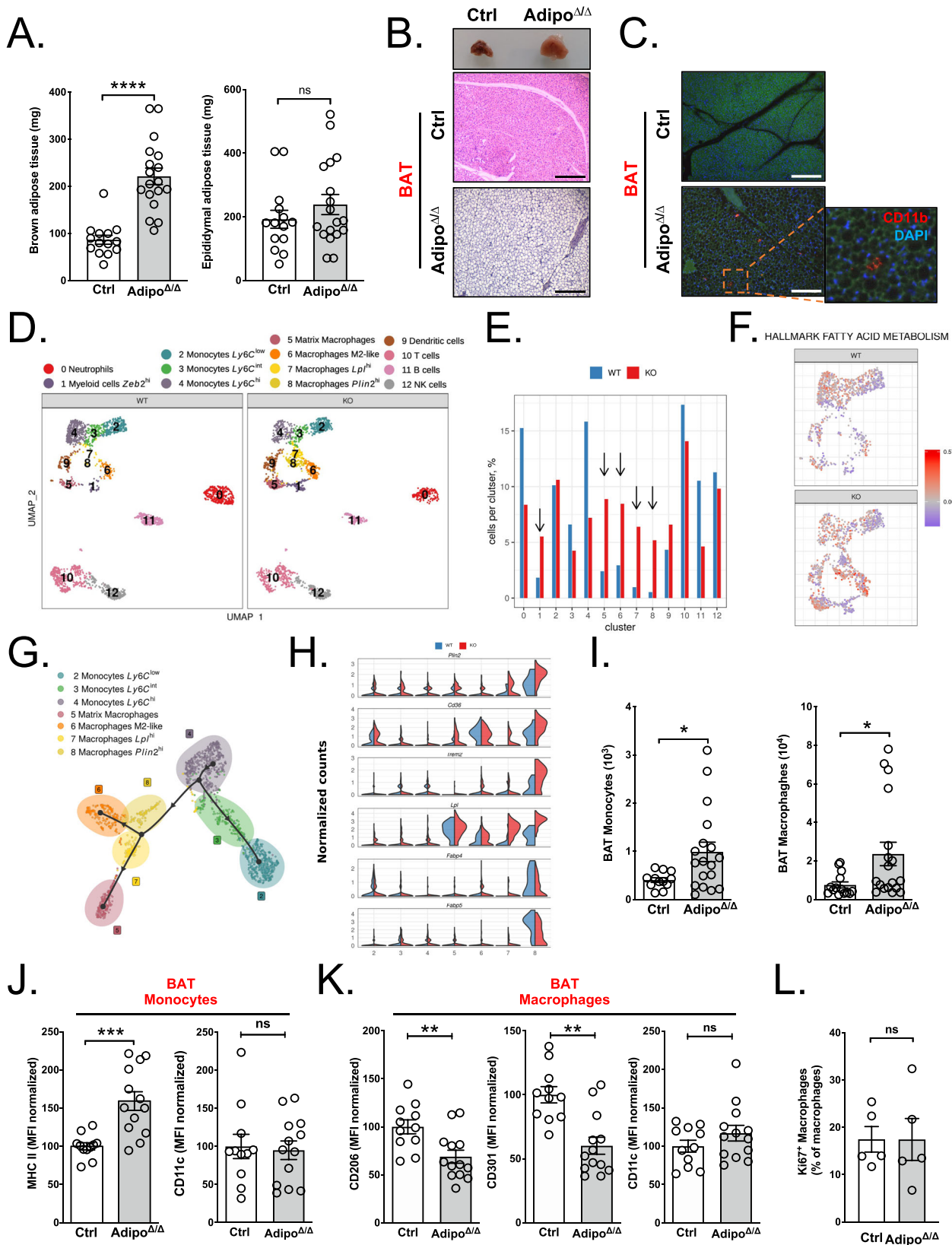
To further define whether specific immune cell subsets were enriched in Adipo ^{Δ/Δ} mice, we performed a comparative single-cell RNA-seq analysis between cell-sorted CD45⁺ cells from control and adipocyte-*Atgl*-deficient mice. We noticed a major and specific enrichment in all macrophage clusters in Adipo ^{Δ/Δ} animals without affecting the populations of B cells, T cells, and NK cells (Fig. 2D, E). This observation indicated that BAT expansion induced a macrophage-specific enrichment in the organ. Moreover, a distinctive fatty acid-centered metabolic signature was detected in these macrophage subsets (Figs. 2F and S2A). Using the Slingshot tool, we established a predictive differentiation model linking monocytes to macrophage clusters (Fig. 2G). This model suggested that Ly6C^{high} monocytes give rise to two intermediate macrophage populations (clusters 7 and 8). Two terminally differentiated macrophage clusters (clusters 5 and 6) were identified and corresponded to clusters involved in lipid metabolism and matrix remodeling (Fig. 2G). In line with our pathway enrichment analysis, these cells displayed higher expression of genes involved in lipid handling including *Plin2*, *CD36*, *Trem2*, and *Lpl* in Adipo ^{Δ/Δ} mice compared to controls (Fig. 2H). Although *Mrc1* expression was found on all macrophage subsets, higher expression of this marker was observed on cluster 6 (Fig. S2B). On the other hand, cluster 5 macrophages were found to specifically express *CD226* (Fig. S2B).

To phenotypically confirm the data from our scRNAseq analysis, we performed a flow cytometry analysis of adipose tissues obtained from control and Adipo ^{Δ/Δ} mice. Since tissue expansion did not occur in the EAT of Adipo ^{Δ/Δ} mice, we investigated macrophage and monocyte phenotypes in both the BAT and EAT of control and Adipo ^{Δ/Δ} mice. We applied an established gating strategy to separately analyze macrophages and monocytes (Fig. S2C)^{21,22}. Previous reports demonstrated the presence, at a low frequency, of monocytes residing in tissues²². In our study, we identified monocytes as CD45⁺CD64⁺MerTK⁻CD11b⁺ cells and macrophages as CD45⁺CD64⁺MerTK⁺ (Fig. S2C). Furthermore, we developed a gating strategy for the in-vivo identification of cluster 5 and cluster 6 cells, namely CD226^{high} and CD206^{high} macrophages (Fig. S2D).

The proportion of CD206^{high} macrophages was equivalent in BAT and EAT from Adipo ^{Δ/Δ} mice. However, we found that the population of CD226^{high} macrophages was markedly enriched in BAT compared to EAT (Fig. S2D). Increased monocyte and macrophage counts were observed in the BAT of Adipo ^{Δ/Δ} mice (Fig. 2I), but not in their EAT (Fig. S2E). To apprehend whether this accumulation was triggered solely by the loss of BAT lipolysis or could be linked to ATGL deficiency in other adipose depots, we analyzed BAT myeloid cells in *Ucp1*^{cre} \times *Prnpla2*^{fl/fl} (BAT ^{Δ/Δ}) mice. *Ucp1* is highly expressed in brown adipocytes and lacking in white adipocytes. BAT monocytes and macrophages were more numerous in BAT ^{Δ/Δ} mice in comparison to controls, suggesting that the Adipo ^{Δ/Δ} BAT phenotype was driven by BAT-mediated cues (Fig. S2F). Moreover, BAT monocytes in Adipo ^{Δ/Δ} mice expressed higher levels of MHC II, a marker that is upregulated in monocytes that recently egressed the blood vasculature and entered an organ (Fig. 2J)²². However, their CD11c expression remained similar between both genotypes (Fig. 2J). Importantly, MHC II expression was comparable between EAT monocytes obtained from control and Adipo ^{Δ/Δ} mice (Fig. S2G). As a whole, BAT macrophages from Adipo ^{Δ/Δ} mice, but not EAT macrophages, also displayed altered expression of the canonical alternative polarization markers CD206 and CD301 (Figs. 2K and S2H). This may be representative of the increased presence of CD206^{low} CD301^{low} macrophages (mainly in clusters 7 and 8), as *Mrc1* and *Clec10a* expression did not appear to be diminished in M2-like macrophages (cluster 6) (Fig. S2I). The expression of CD11c, a classical M1 activation marker, was not altered (Fig. 2K). Taken together, this demonstrated that ATGL-deletion in adipocytes triggers monocyte BAT recruitment and leads to increased numbers of BAT macrophages with a specific phenotype.

Local proliferation of tissue-resident macrophages is involved in their pool maintenance²³. To investigate macrophage proliferation rate, we performed Ki67 staining and found a similar level of proliferation in BAT macrophages from control and Adipo ^{Δ/Δ} mice (Fig. 2L). This observation was also supported by the analysis of our single-cell RNA sequencing data that revealed that few BAT macrophages show expression of proliferation-related genes including *Mki67*, *Ccna2*, and *Top2a* (Fig. S2J).

BAT-selective monocyte recruitment leads to diminished blood monocyte counts without affecting bone marrow hematopoiesis. We next asked whether increased monocyte counts in Adipo ^{Δ/Δ} mice are specific to BAT or could also be observed in other peripheral tissues. To monitor monocyte distribution across tissues we took advantage of a CCR2-targeting radiotracer ⁶⁴Cu-DOTA-ECL1i for non-invasive positron emission tomography (PET)/computed tomography (CT) imaging of CCR2⁺ cells distribution across multiple tissues without the biases of tissue digestion. This provides the opportunity to simultaneously investigate numerous organs, thus limiting the risk to miss an unexpected tracer accumulation in a specific location^{24,25}. Representative PET/CT images revealed significantly increased signal, indicative of CCR2 accumulation, in the BAT of Adipo ^{Δ/Δ}



mice at 16 days, but not at 2 days, post-tamoxifen administration (Cre⁺TAM⁺) (Fig. 3A, B). These data confirm the progressive monocyte infiltration in BAT after *Atgl*-deletion. Of note, we observed a comparable level of BAT CCR2 signal in both Adipo^{Cre+} animals treated with vehicle (oil) (Cre⁺TAM⁻) and Adipo^{+/+} mice treated with tamoxifen (Cre⁻TAM⁺) (Fig. 3A, B).

To analyze monocyte density, the biodistribution of the tracer was measured across tissues and we observed that CCR2 signal was selectively increased in the BAT of Adipo $\Delta\Delta$ mice (Fig. 3C). Despite a detectable signal in several organs, we did not observe a differential CCR2 distribution in any other tissue (Fig. 3C). Of

Fig. 2 Monocytes and macrophages accumulate in the BAT during tissue expansion. **A** BAT and EAT weight in control ($n = 14$) and Adipo $^{\Delta/\Delta}$ ($n = 18$) mice. $p < 0.0001$ (left) and $p = 0.4582$ (right). **B** Representative images of BAT morphology and analysis using H&E staining in Adipo $^{\Delta/\Delta}$ mice and controls. **C** CD11b staining (red) in the BAT of Adipo $^{\Delta/\Delta}$ and control mice. The presence of CLS is highlighted in the magnified box. **D** Single-cell RNA-Seq analysis of BAT CD45 $^+$ cells from 7–8-week-old control and Adipo $^{\Delta/\Delta}$ male mice. **E** Proportion of each cluster identified in scRNA-Seq analysis. **F** Single-cell RNA-Seq analysis of the “fatty acid metabolism” Hallmark gene set expression. **G** Differentiation model of BAT myeloid cells generated using the Slingshot tool. **H** Violin plots showing RNA-Seq analysis of *Plin2*, *CD36*, *Trem2*, *Lpl*, *Fabp4*, and *Fabp5* expression by BAT macrophages and monocytes from Adipo $^{\Delta/\Delta}$ and control mice. **I** Quantification of BAT monocyte and macrophage numbers in control ($n = 12$) and Adipo $^{\Delta/\Delta}$ ($n = 18$) mice using flow cytometry. $p = 0.0346$ (left) and $p = 0.0143$ (right). **J** Quantification of surface MHC II and CD11c expression by BAT monocytes in control ($n = 11$) and Adipo $^{\Delta/\Delta}$ ($n = 13$) mice using flow cytometry. $p = 0.0004$ (left) and $p = 0.8646$ (right). **K** Quantification of surface CD206, CD301, and CD11c expression by BAT macrophages in control ($n = 11$) and Adipo $^{\Delta/\Delta}$ ($n = 13$) mice using flow cytometry. $p = 0.0031$ (left), $p = 0.0012$ (middle), $p = 0.3607$ (right). **L** Proportion of Ki-67-expressing macrophages in the BAT of control ($n = 5$) and Adipo $^{\Delta/\Delta}$ ($n = 5$) mice analyzed by flow cytometry. $p = 0.6905$. Panels **A**, **I**, **J**, and **K** represent pooled data from four independent experiments. Panels **B**, **C** are representative of two independent experiments. Panel **L** represents data from one experiment. All data are represented in means \pm SEM. Two-tailed Mann–Whitney tests were used to determine statistical significance. ns $p > 0.05$; * $p < 0.05$; ** $p < 0.01$; *** $p < 0.001$; **** $p < 0.0001$. Source data are provided as a Source Data file.

interest, blood CCR2 signal was reduced, even though the difference was not significant, in Adipo $^{\Delta/\Delta}$ animals (Fig. 3C). Ex vivo tissue collections showed an enlarged mass of BAT in Adipo $^{\Delta/\Delta}$ animals compared to the other two groups. Moreover, autoradiography showed specific tracer uptake in the BAT and not in the surrounding white adipose tissue, thus supporting PET data (Fig. S3A). Taken together, this suggests that adipocyte-specific Atgl deletion leads to BAT-selective monocyte recruitment. Thus, disruption of BAT homeostasis leads to a very specific monocyte recruitment without affecting any other peripheral organ.

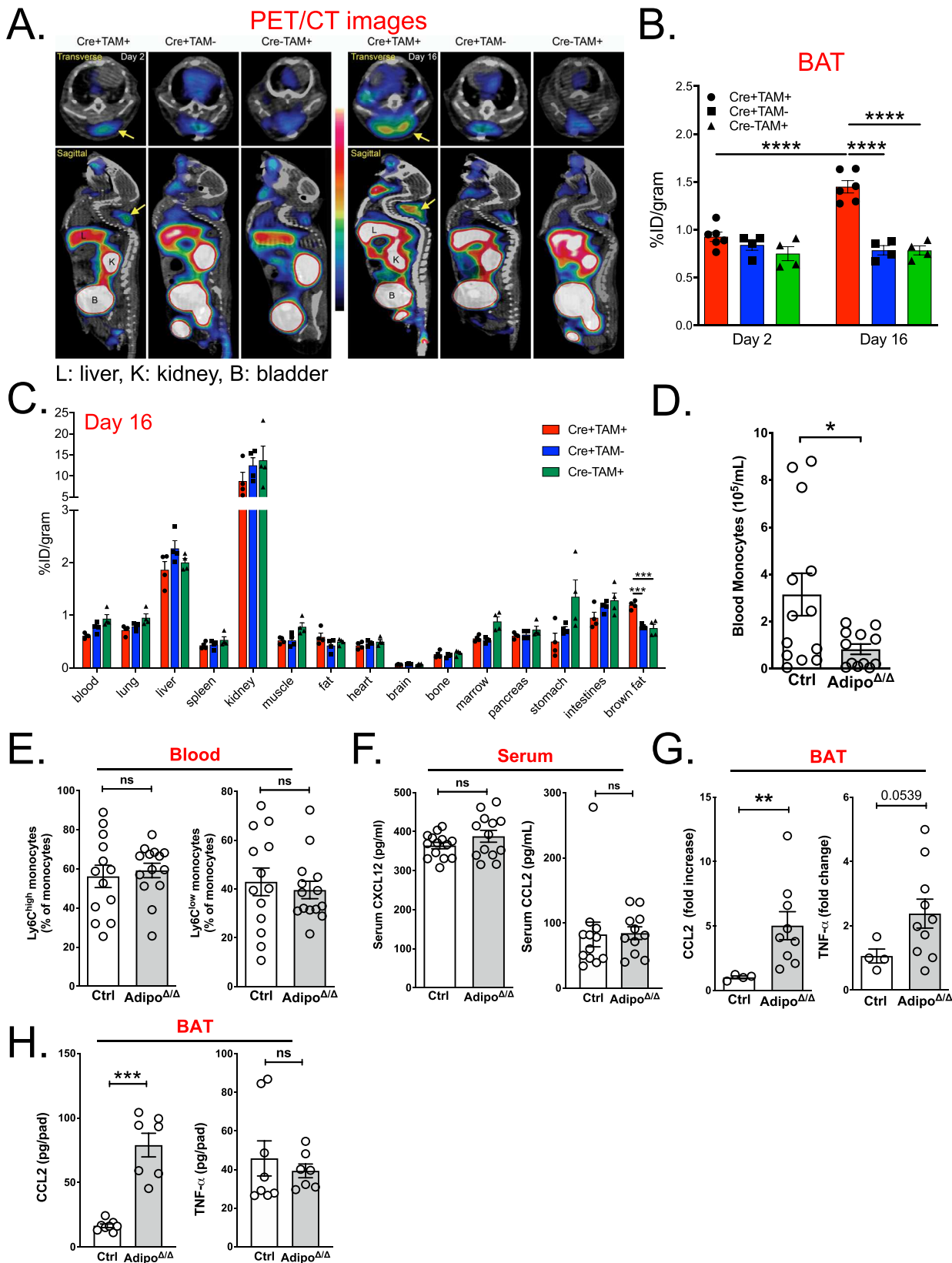
Because we observed a tendency to decreased CCR2 signal in blood (Fig. 3C), we next wondered whether BAT monocyte recruitment could affect the pool of circulating blood monocytes. Using flow cytometry analysis, we detected a marked decrease in the numbers of blood monocytes (CD45 $^+$ CD115 $^+$ CD11b $^+$ cells) (Fig. 3D and Fig. S3B). This observation was valid for both Ly6C $^{\text{hi}}$ and Ly6C $^{\text{lo}}$ monocyte subsets (Fig. 3E). However, neutrophil (CD45 $^+$ Gr1 $^+$ CD11b $^+$ CD115 $^{\text{low}}$), B cell (CD45 $^+$ CD19 $^+$) and T cell (CD45 $^+$ TCR β^+) numbers were similar in ATGL-sufficient and deficient mice (Fig. S3C). Likewise, CCL2 and CXCL12 serum levels were not modulated by the loss of adipose tissue lipolysis, excluding systemic inflammation as a cause for the decrease in blood monocyte numbers (Fig. 3F). We thus hypothesized that reduced blood monocyte numbers in ATGL-deficient mice result from either an altered hematopoiesis or mature monocyte export from bone marrow to blood. Flow cytometry analysis revealed no substantial difference in the number of monocyte precursor cells including LSK (Lin $^-$ Sca1 $^+$ cKit $^+$) (Fig. S3D). Bone marrow monocyte counts were also very similar in control and adipocyte ATGL-deficient mice (Fig. S3D). Thus, blood monocyte number reduction is unlikely to result from defects in bone marrow hematopoiesis or stromal niche alteration. Since the pool of bone marrow monocytes results from the dynamic interaction between monocyte proliferation, death, and export to peripheral blood, we analyzed these parameters. Monocyte proliferation was comparable in Adipo $^{\Delta/\Delta}$ and littermate control mice (Fig. S3E). Annexin V staining on bone marrow monocytes suggested a similar level of apoptosis in both genotypes, ruling out a role for cell death (Fig. S3E). To analyze monocyte export from bone marrow to blood, we i.v. injected mice with BrdU and analyzed the percentage of BrdU positive monocytes in blood 16 h post-injection. We found that approximately 70% of blood monocytes had undergone proliferation by incorporating BrdU (Fig. S3F) in both control and Adipo $^{\Delta/\Delta}$ mice. Therefore, we concluded that the monocyte export rate is not modified during BAT expansion and could not account for diminished blood monocyte numbers. To apprehend the mechanisms that could account for increased brown adipose tissue monocyte numbers, we performed real-time PCR analysis. We found an increased expression of the

pro-inflammatory gene *tnfa* and the chemokine *ccl2* in the BAT of Adipo $^{\Delta/\Delta}$ mice (Fig. 3G). The latest is responsible for monocyte recruitment to tissues and could explain increased numbers of BAT monocytes and macrophages. Although ELISA analysis of BAT homogenates failed to confirm an increase in TNF α levels, CCL2 protein levels were markedly augmented in the BAT of Adipo $^{\Delta/\Delta}$ mice (Fig. 3H). Together, these data suggest the onset of a very low-grade tissue inflammation with specific CCL2-mediated monocyte recruitment to the BAT of Adipo $^{\Delta/\Delta}$ mice.

Monocyte depletion prevents BAT expansion and sustains tissue browning.

To address whether BAT monocyte recruitment is involved in tissue remodeling and growth, we depleted blood monocytes via administration of anti-CCR2 antibody (MC-21) 26 (Fig. 4A). Mice received tamoxifen treatment and were then allowed to rest for one week during which BAT started expanding. MC-21 or vehicle treatment were then administered daily for 5 days. Blood and tissues were analyzed 16 h after the last MC-21 injection (Fig. 4A). This procedure led to the complete depletion of blood monocytes as previously described 26 (Fig. S4A). The spleen monocyte population was also completely depleted in MC-21-treated mice (Fig. S4A). Flow cytometry analysis demonstrated a major monocyte depletion in the BAT of MC-21-treated Adipo $^{\Delta/\Delta}$ animals in comparison to vehicle-administered controls (Fig. 4B). BAT macrophage numbers were slightly, but not significantly decreased in MC-21-treated Adipo $^{\Delta/\Delta}$ mice (Fig. 4C). Importantly, BAT weight was significantly decreased, by approximately 40%, in Adipo $^{\Delta/\Delta}$ mice treated with anti-CCR2 Ab in comparison to vehicle administered Adipo $^{\Delta/\Delta}$ animals (Fig. 4D). We observed that in control mice, in which BAT is not expanding, CCR2 depletion had no effect on tissue weight (Fig. 4D). EAT weight remained similar among MC-21-treated and vehicle-treated animals (Fig. S4B). Tissue histology analysis revealed that EAT adipocyte size was similar in control and Adipo $^{\Delta/\Delta}$ mice (Fig. S4B). BAT histology analysis revealed that MC-21 administration exacerbated the appearance of CLS (Fig. S4C). MC-21 treatment had no impact on serum glycerol, TG and NEFA levels (Fig. S4D). However, we detected numerous multilocular zones in MC-21-treated animals in comparison to vehicle-treated Adipo $^{\Delta/\Delta}$ mice (Fig. 4E), suggesting that monocyte recruitment to BAT modulates tissue morphology and favors BAT “whitening”. Whether this mechanism is solely responsible for BAT weight decrease in MC-21-treated mice remains to be established.

Monocytes regulate BAT expansion via Podoplanin engagement. Previous data demonstrated that myeloid cells could modulate tissue expansion by interacting with stromal fibroblastic



reticular cells (FRCs)²⁷. Thus, we sought to determine whether monocytes in BAT might interact with fibroblasts to favor tissue expansion. Using α -SMA staining, we identified the presence of α -SMA⁺ cells with a fibroblastic morphology in the BAT of Adipo^{Δ/Δ} mice, suggesting the existence of activated fibroblasts in expanding BAT (Fig. S5A). To test whether monocytes could

interact with fibroblasts, we co-cultured mouse embryonic fibroblasts (MEFs) with primary blood monocytes. Monocyte addition induced an increase in fibroblast cellular area (Fig. 5A, B). Importantly, we observed increased numbers of cell protrusions in MEFs cultured in the presence of blood monocytes (Fig. 5A, B). We next investigated whether this interaction

Fig. 3 Adipocyte ATGL deletion induces a specific recruitment of blood monocytes to the BAT. **A** ^{64}Cu -DOTA-ECL1i PET/CT images analyzing tracer uptake in control and $\text{Adipo}^{\Delta/\Delta}$ mice 2 days (left panel) and 16 days (right panel) post-tamoxifen administration ($n = 4\text{--}6/\text{group}$). L: liver; B: bladder; K: kidney. **B** Quantification of tracer uptake in the BAT of Cre^- tamoxifen-treated ($\text{Cre}^- \text{ Tam}^+$, $n = 4$) and Cre^+ vehicle-treated ($\text{Cre}^+ \text{ Tam}^-$, $n = 4$) controls and $\text{Adipo}^{\Delta/\Delta}$ animals ($\text{Cre}^+ \text{ Tam}^+$, $n = 6$) 2- and 16-days post-tamoxifen administration. $p < 0.0001$ for each comparison. **C** Biodistribution of ^{64}Cu -DOTA-ECL1i in $\text{Cre}^- \text{ Tam}^+$ and $\text{Cre}^+ \text{ Tam}^-$ controls and $\text{Adipo}^{\Delta/\Delta}$ animals 16 days post-tamoxifen administration ($n = 4/\text{group}$). $p < 0.001$ for each comparison in BAT. **D** Quantification of blood monocyte counts in control ($n = 13$) and $\text{Adipo}^{\Delta/\Delta}$ ($n = 12$) mice using flow cytometry. $p = 0.0384$. **E** Proportions of $\text{Ly6C}^{\text{high}}$ and Ly6C^{low} monocytes among total blood monocytes in control ($n = 13$) and $\text{Adipo}^{\Delta/\Delta}$ ($n = 14$) mice using flow cytometry. $p = 0.6940$ (left) and $p = 0.6160$ (right). **F** Analysis of serum CCL2 and CXCL12 in control ($n = 14$) and $\text{Adipo}^{\Delta/\Delta}$ ($n = 13$) mice by ELISA. $p = 0.2388$ (left) and $p = 0.3793$ (right). **G** Analysis of BAT CCL2 and $\text{TNF}\alpha$ expression in control ($n = 4$) and $\text{Adipo}^{\Delta/\Delta}$ ($n = 9$ and 10 respectively) mice by qPCR. $p = 0.0028$ (left) and $p = 0.0539$ (right). **H** Quantification of CCL2 and $\text{TNF}\alpha$ protein levels in BAT homogenates from control ($n = 8$) and $\text{Adipo}^{\Delta/\Delta}$ ($n = 7$) mice by ELISA. $p = 0.0003$ (left) and $p = 0.6126$ (right). Panels **D**, **E** represent pooled data from four independent experiments. Panels **F**, **G** represent pooled data from two independent experiments. Panel **H** represents data from one experiment. All data are represented in means \pm SEM. Ordinary one-way ANOVA with Bonferroni post-test were used to determine statistical significance in panels **B**, **C**. Two-tailed Mann–Whitney tests were used to determine statistical significance in panels **D–H**. ns $p > 0.05$; * $p < 0.05$; ** $p < 0.01$; *** $p < 0.001$; **** $p < 0.0001$. Source data are provided as a Source Data file.

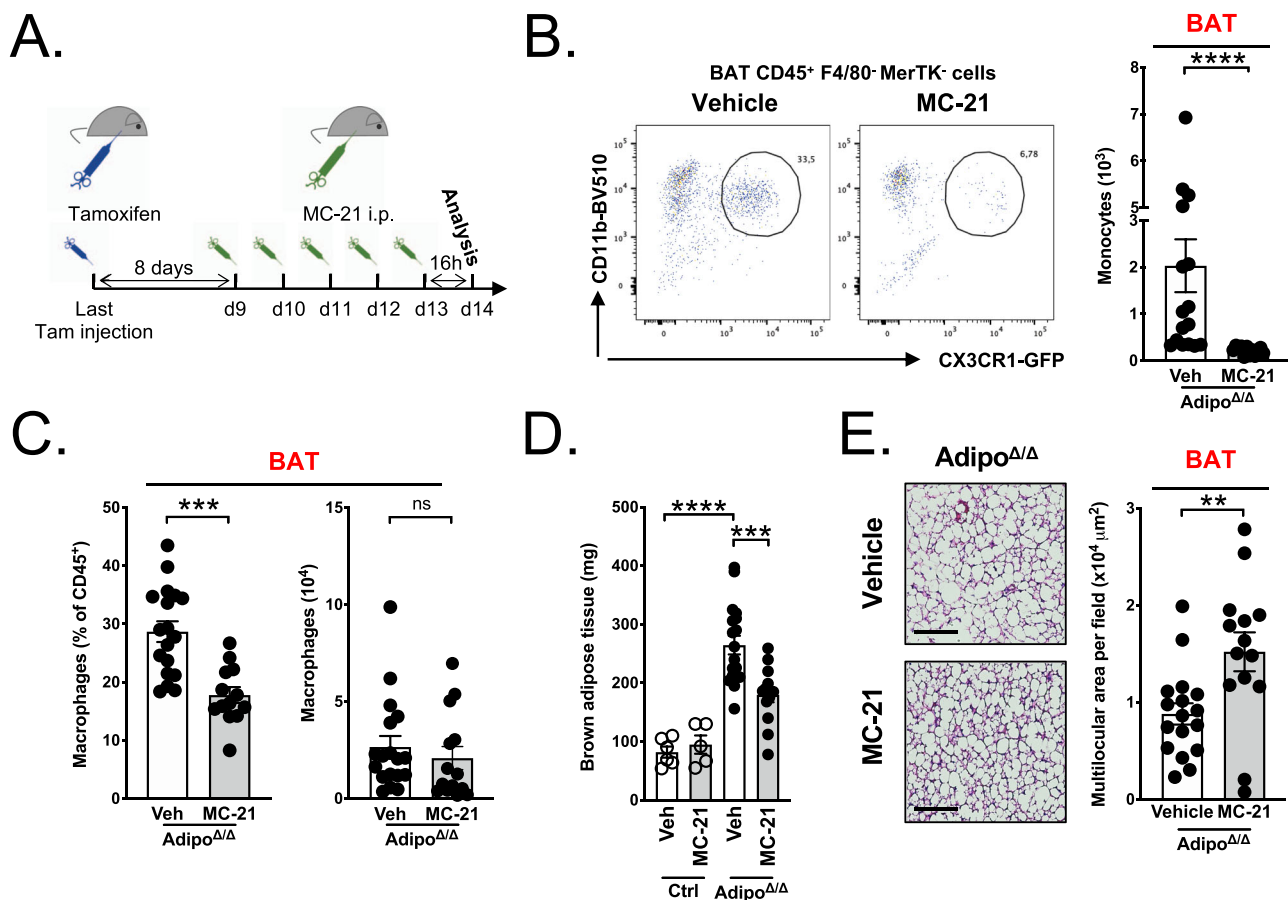


Fig. 4 Monocyte depletion prevents the expansion of lipolysis-deficient BAT. **A** Schematic representation of the experimental procedure used for MC-21-mediated monocyte depletion. **B** Representative dot plots (left) and quantification (right) of BAT monocytes in MC-21 ($n = 12$) or vehicle-treated ($n = 16$) $\text{Adipo}^{\Delta/\Delta}$ mice. $p < 0.0001$. **C** Frequency and numbers of BAT macrophages in MC-21 ($n = 13$) or vehicle-treated ($n = 18$) $\text{Adipo}^{\Delta/\Delta}$ mice. $p = 0.0001$ (left) and $p = 0.3189$ (right). **D** Brown adipose tissue weight in MC-21 ($n = 5$) or vehicle-treated ($n = 6$) control mice, and MC-21 ($n = 14$) or vehicle-treated ($n = 18$) $\text{Adipo}^{\Delta/\Delta}$ mice. $p < 0.0001$ (vehicle-treated control and $\text{Adipo}^{\Delta/\Delta}$ mice) and $p = 0.0002$ (vehicle-treated and MC-21-treated $\text{Adipo}^{\Delta/\Delta}$ mice). **E** Representative images of H&E-stained BAT and quantification of multilocular areas in MC-21 ($n = 14$) or vehicle-treated ($n = 17$) $\text{Adipo}^{\Delta/\Delta}$ mice. Scale bar = $100 \mu\text{m}$. $p = 0.0053$. Data were derived from three pooled independent experiments. All data are represented in means \pm SEM. Two-tailed Mann–Whitney tests were used to determine statistical significance. ns $p > 0.05$; * $p < 0.05$; ** $p < 0.01$; *** $p < 0.001$. Source data are provided as a Source Data file.

required a cell-to-cell contact, or alternatively was mediated by soluble mediators. In a transwell experiment, allowing for physical separation between fibroblasts and monocytes, we observed that fibroblast spreading occurred even in the absence of direct contact with monocytes (Fig. 5A, B). These results indicated that

monocyte interaction with fibroblasts induced changes in their morphology. Therefore, we investigated whether these morphological changes were paralleled by modulations of fibroblast mechanical properties. Using a traction force microscopy approach, we observed that fibroblasts co-cultured with

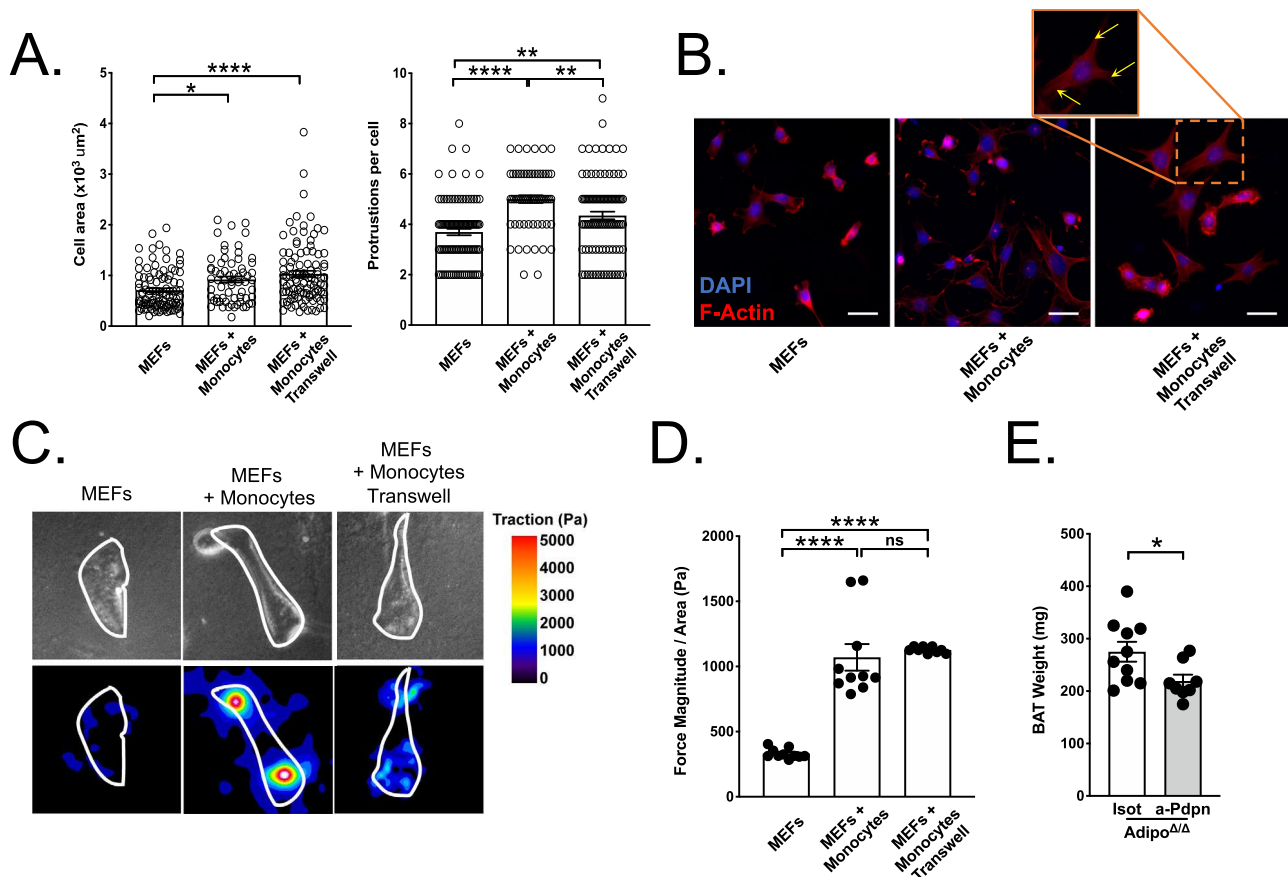


Fig. 5 Monocyte interaction with fibroblasts through the Podoplanin axis is required for BAT expansion. **A** Quantification of MEF morphological features after a 18 h co-culture experiment with monocytes placed in the same well or in a transwell insert with 0.4 μm pores. Each dot represents a cell. $n = 101$ (MEFs), 64 (MEFs + Monocytes) and 103 (MEFs + Monocytes Transwell) cells representative of three independent experiments. *: $p = 0.0257$, ****: $p < 0.0001$ (left). **: $p < 0.01$, ****: $p < 0.0001$ (right). **B** Representative images of MEF morphology after a 18 h co-culture experiment with monocytes placed in the same well or in a transwell insert with 0.4 μm pores. F-actin was revealed using phalloidin staining. Yellow arrows indicate protrusions. Scale bar = 20 μm . Representative heat map **(C)** and quantification **(D)** showing contractile forces generate by MEFs plated on 8 kPa hydrogel after a 18 h co-culture experiment with monocytes placed in the same well or in a transwell insert with 0.4 μm pores. Mean of $n = 10$ wells per condition. ****: $p < 0.0001$. **E** Brown adipose tissue weight in anti-Podoplanin ($n = 8$) or isotretinoin control-treated ($n = 10$) $\text{Adipo}^{\Delta/\Delta}$ mice. $p = 0.0363$. Panels **A**, **B** are representative of three independent experiments. Panel **D** is representative of two independent experiments. Panel **E** represents pooled data from two independent experiments. All data are represented in means \pm SEM. Ordinary one-way ANOVA with Bonferroni post-test were used to determine statistical significance in panels **(A, D)**. A two-tailed Mann–Whitney test was used to determine statistical significance in panel **(E)**. ns $p > 0.05$; * $p < 0.05$; ** $p < 0.01$; *** $p < 0.001$. Source data are provided as a Source Data file.

monocytes exerted increased traction forces on their substrate (Fig. 5C, D). This observation was also repeated when using a transwell system, confirming that cell-contact between MEFs and monocytes was not required for modulations of fibroblast activation (Fig. 5C, D).

Myeloid cells were previously shown to favor tissue expansion through the CLEC-2-Podoplanin (Pdpn) axis²⁷. CLEC-2 expression was documented on immune cells, including dendritic cells^{28,29}. We aimed to investigate whether BAT immune cells express CLEC-2. Flow cytometry analysis revealed that BAT macrophages, and to a lesser degree BAT monocytes, express detectable CLEC-2 levels on their cell-surface (Fig. S5B). We next decided to inquire whether Pdpn engagement is involved in BAT expansion. When we included a Pdpn-blocking antibody to our in vitro co-culture system, we observed that fibroblast spreading was prevented, demonstrating the role of these factors in our system (Fig. S5C). In vivo, Pdpn blocking blunted BAT expansion in $\text{Adipo}^{\Delta/\Delta}$ mice, similarly to MC-21 treatment (Fig. 5E). Flow cytometry analysis demonstrated that administration of Pdpn blocking Ab had no effect on monocyte and macrophage

numbers in BAT (Fig. S5D). This observation was not surprising since Pdpn engagement occurs downstream of monocyte BAT recruitment. Furthermore, we analyzed serum NEFA, glycerol, and TG levels in $\text{Adipo}^{\Delta/\Delta}$ animals following Pdpn blockade or control treatment. We detected a similar concentration of these metabolites suggesting that blocking Pdpn engagement prevents BAT expansion without affecting systemic NEFA, glycerol, and TG levels (Fig. S5F). Taken together, this set of data identified the Pdpn axis as a central regulator of BAT expansion.

Discussion

Although macrophages were detected in previous single-nuclei RNA-seq analyses of murine and human whole BAT^{30,31}, their proportions among total BAT cells were too small to gain detailed insights into their diversity. Using scRNA-seq analysis of BAT CD45⁺ cells, the present study uncovered the co-existence of several macrophage and monocyte subsets in healthy BAT. We found that monocytes intensely contribute to BAT macrophage maintenance. In a genetic model of BAT expansion, we observed

a massive monocyte and macrophage recruitment that sustained changes in tissue morphology. This myeloid cell recruitment was BAT-specific and did not affect other adipose tissue depots (EAT) or peripheral tissues. Tissue inflammation remained low as TNF α levels were unchanged in the expanding BAT. However, CCL2 accumulation was paralleled by increased CCR2 signal, suggesting a key role for the CCL2-CCR2 axis in BAT monocyte recruitment. CX3CR1–CX3CL1 interactions have been proposed to be involved in WAT homeostasis. Whether this axis plays a role in BAT macrophage homeostasis remains to be defined. We did not observe a systemic inflammation but found a surprising decrease in blood monocyte counts. Importantly, in this scenario medullary hematopoiesis was not affected. Monocyte depletion compromised BAT expansion and modulated BAT architecture, thus suggesting a key role of monocytes or monocyte-derived macrophages during BAT expansion. Whether a specific population of BAT monocytes or macrophages is responsible for BAT expansion remains to be defined.

Monocytes play a key role, beneficial or detrimental, during many pathological conditions, and controlling their numbers and functions could improve disease outcome. For example, during cardiovascular disease development, monocyte counts are an independent risk factor^{32,33}. Mice living at thermoneutrality (30 °C) have lower peripheral blood monocytes²⁵. Interestingly, in this scenario monocytes accumulated inside the bone marrow. This was paralleled by a lower CCR2 signal in brown fat, suggesting altered monocyte recruitment in this organ²⁵. Importantly, the recruitment of CCR2⁺ cells to subcutaneous adipose tissue, but not to BAT contributes to adaptive thermogenesis during cold exposure³⁴. Whether monocyte recruitment to BAT favors thermogenesis and heat dissipation remains to be established. In our study, we revealed that monocyte depletion favors a multilocular phenotype in BAT adipocytes. This parameter might reflect local thermogenesis. In a mouse model of burn injury, CCR2⁺ cells were also shown to contribute to adipose tissue thermogenesis³⁵. On the other hand, during cold exposure blood monocyte counts are increased in both mice and humans and this is mirrored by augmented adipose tissue lipolysis²⁵. Mice with constitutive *AdipoQ*-driven ATGL deficiency display reduced BAT *Ucp1* expression³⁶, paralleled by increased CCL2 and TNF α expression³⁷. We did not detect significant BAT inflammation in our short-term tamoxifen-induced setup, but rather a very specific CCL2-mediated monocyte recruitment. The precise cellular source of BAT-produced CCL2, and its contribution to tissue architecture remain to be established. Brown fat lipolysis is dispensable for thermogenesis, and *Ucp1* levels remain stable in mice specifically lacking BAT lipolysis^{18,19}. Importantly, accumulation of BAT macrophages and monocytes still occurred in BAT Δ/Δ animals, suggesting that local, rather than systemic ATGL-deletion, leads to monocyte recruitment.

Monocyte recruitment to BAT allows optimal tissue expendability. Previous work established the involvement of myeloid cells in the control of tissue contractility and the ability to expand^{27,38}. The engagement of the Podoplanin-CLEC-2 axis modulates lymph node fibroblastic reticular cells stiffness and favors lymph node relaxation. Whether this mechanism occurs in other tissues, and in BAT, in particular, remains to be defined. We were able to detect CLEC-2 expression on BAT macrophages and monocytes. Moreover, we observed that blocking podoplanin prevented BAT expansion in vivo. Extracellular matrix modulations during diabetes modulate key adipocyte metabolic functions including lipolysis and glucose handling³⁹. One could expect that macrophages, and notably CD226^{high} macrophages from cluster 5, are involved in this process and could regulate BAT function. Establishing genetic or pharmacological models allowing for the

selective depletion of these cells will provide a unique opportunity to define their precise function.

BAT expansion and whitening are characterized by CLS appearance and collagen accumulation²⁰. Whether monocytes participate to BAT CLS formation or, alternatively, locally resident BAT macrophages are solely involved in this mechanism, remains to be completely established. Our data show that depletion of CCR2⁺ cells, likely monocytes, leads to increased frequency of CLS in the BAT of *Adipo* Δ/Δ mice. This might be due to the accumulation of dead or dying adipocytes in the absence of monocyte BAT recruitment, suggesting that monocytes play a key role in maintaining BAT homeostasis. Limited BAT expansion in CCR2-depleted mice could also be due to affected adipocyte lineage generation. Whether adipocyte generation is altered in monocyte-depleted animals is an intriguing question that is beyond the scope of interest of the current manuscript.

Thus, controlling macrophage numbers in healthy and inflamed tissues seems critical. Previous work demonstrated the existence of brown adipose tissue-resident macrophages. These cells have been shown to control local neuron network density and the subsequent norepinephrine production and thermogenesis¹⁶. We found here that healthy and inflamed BAT contains four different macrophage subsets. Further work is required to establish the precise function of each population through the generation of specific genetic models or pharmacological inhibitors.

Methods

Mice

Generation of *Adipo* Δ/Δ and *BAT* Δ/Δ mice. *Pnpla2*^{fl/fl} [B6N.129S-Pnpla2^{tm1Eek}/J], *CX3CR1*^{sgP} [B6.129P-Cx3cr1^{tm1Litt}/J], and *TdTomato*^{fl/fl} [B6.Cg-Gt(ROSA)26Sor^{tm9(CAG-tdTomato)Hze}/J] mice were crossed together and then crossed to *AdipoQ*^{creERT2} [C57BL/6-Tg(Adipoq-cre/ERT2)1Soff/J] or *Ucp1*^{Cre} [B6.FVB-Tg(Ucp1-cre)1Evdrr/J] mice (all mice were purchased from The Jackson Laboratory; Ucp1^{Cre} mice were kindly provided by Dr. Jean-François Tanti). *CCR2*^{creERT2} [C57BL/6NTac-Ccr2^{tm2982}(T2A-Cre7ESR1-T2A-mKate2)] mice were kindly provided by Dr. Burkhard Becher and crossed to *TdTomato*^{fl/fl} and *CCR2*^{GFP} [B6(C)-Ccr2^{tm1.1Cln}/J] provided by Dr. Marco Colonna^{40,41}. For each experiment, co-housed littermate controls were used. Animal protocols were approved by the Institutional Animal Care and Use Committee of the French Ministry of Higher Education and Research and the Mediterranean Center of Molecular Medicine (INSERM U1065) and were undertaken in accordance with the European Guidelines for Care and Use of Experimental Animals. Animals had free access to food and water and were housed in a controlled environment with a 12 h light–dark cycle and constant temperature (20–23 °C).

Induction of the Cre recombinase. At 21 days-old (P21) mice were weaned and co-housed under a 12 h light/dark cycle. One week later, at P28, *Adipo* Δ/Δ mice were injected every two days intra-peritoneally with either 10 mg/ml Tamoxifen (200 μ L per mouse in 10% EtoH and sunflower oil) or vehicle, for 1 week. Mice were then allowed to rest for 2 weeks. Mice were then sacrificed, and tissues were harvested for further investigations. *BAT* Δ/Δ mice were analyzed when 6–8-week-old.

Conditional labeling of CCR2⁺ monocytes. *CCR2*^{creERT2} *TdTomato* reporter mice were treated with tamoxifen dissolved in corn oil (20 mg/mL) by a single oral gavage (250 μ L/mouse). Forty-eight hours later, animals were sacrificed and assessed for labeling efficiency in blood and BAT by flow cytometry.

Monocyte depletion protocol. Mice were injected every two days intra-peritoneally with 10 mg/ml Tamoxifen (200 μ L per mouse in 10% EtoH and sunflower oil) for 1 week and were then allowed to rest for 1 week. Mice were then injected intra-peritoneally once a day for 5 days with 20 μ g MC-21 (anti-CCR2) antibody or vehicle (PBS), and were sacrificed 16 h after the last injection for further investigations.

In vivo Podoplanin blockade. Mice were injected every two days intra-peritoneally with 10 mg/ml Tamoxifen (200 μ L per mouse in 10% EtoH and sunflower oil) for 1 week and were then allowed to rest for 1 week. Mice were then injected intra-peritoneally with 100 μ g anti-Podoplanin or isotype control once every two days for

6 days (three injections), and were sacrificed 16 h after the last injection for further investigations.

Genotyping. All primer sequences used for genotyping in this study are indicated in Supplementary Table 1.

DNA was extracted from tail biopsies by incubation with 50 mM NaOH for 30 min at 95 °C. DNA was amplified by PCR using DreamTaq Green PCR Master Mix (2X) (Thermo Scientific) and the following primers recognizing the sequences of the *AdipoQ*, *Pnpla2* (coding for ATGL), *TdTomato*, or *CX3CR1* gene.

PCR products were visualized on a 2% agarose gel.

Control mice present a single band 235 bp for *Pnpla2*, 410 bp for *CX3CR1*, 297 bp for *TdTomato*, and 514 bp for *CCR2*. Homozygotes mutant mice present a single band of 390 bp for *Pnpla2*, 500 bp for *CX3CR1*, 196 bp for *TdTomato*, 150 bp for *CCR2(GFP)*, 341 bp for *CCR2(creERT2)*. Heterozygote mice present each band of control and mutant genotype for these genes. The presence of the *AdipoQ^{creERT2}* allele is indicated by a 272 bp band, with an internal control 175 bp band. Control mice only present the internal control band.

Metabolite analyses

Glycerol, TG, and NEFA analysis. Glycerol, TG, and NEFA contents were measured from serum. Free glycerol reagent and standard were used according to the manufacturer's protocol. NEFA-HR2 R1 + R2 FUJIFILM were used according to the manufacturer's protocol.

Free fatty acids quantitation by NCI-GCMS. Deuterated fatty acids were from Cayman (Bertin Pharma, Montigny le Bretonneux, France). Chemicals of the highest grade available were purchased from Sigma Aldrich (Saint-Quentin Fallavier, France). LCMSMS quality grade solvents were purchased from Fischer Scientific (Illkirch, France). Plasma was spiked with 5 μ L of free fatty acids internal mix containing 635, 326, 95 ng, of linoleic acid d4, arachidonic acid-d8, DHA-d5, respectively. Plasma was mixed with 1.2 ml of Dole's reagent (Isopropanol/Hexane/Phosphoric acid 2 M 40/10/1 v/v/v). Free fatty acids were further extracted with 1 ml of Hexane and 1.5 ml of distilled water. Organic phase was collected and evaporated under vacuum. Fatty acids were analyzed as pentafluorobenzyl esters (PFB-FAs esters) by GCMS in negative chemical ionization mode. Calibration curves were obtained using linoleic acid (0.5–18 ng) arachidonic acid (0.3–11 ng) docosahexaenoic acid (0.1–3.5 ng) and docosapentaenoic acid (0.1–3.5 ng) extracted by the same method used for plasma. Linear regression was applied for calculations.

Western blotting. Tissues were harvested with a precellys (Bertin Instruments) in RIPA buffer. Tissues homogenate was then agitated for 1 h at 4 °C before being centrifuged at 14000 \times g for 10 min at 4 °C. Supernatants were used for SDS-PAGE. Protein samples were resolved on 10% SDS-PAGE gels and were then transferred onto polyvinylidene difluoride (PVDF) membrane using a wet transfer system. Membranes were blocked in 5% (w/v) BSA in Tris-buffered saline-Tween (TBST) for one hour at room temperature. Membranes were incubated with primary antibody (HSP90 diluted in 4% BSA or ATGL diluted in 10% nonfat dry milk) overnight at 4 °C followed by the appropriate horseradish peroxidase-conjugated secondary antibody for 2 h at room temperature. Proteins were detected by ECL chemiluminescence (Pierce).

Flow cytometry analysis. All antibodies, supplier names, clones, and catalog numbers used in this study are provided in Supplementary Table 2. All antibodies were diluted according to the manufacturer's instructions.

Blood analysis. Just before the animal sacrifice, few drops of blood were collected by submandibular bleeding. Lysing buffer was used for red blood cells lysis. Cells were then centrifuged (400 \times g, 5 min at 4 °C) and stained for 25 min protected from light in FACS buffer (RPMI medium, 0.3 mM EDTA, and 0.06% BSA). Cells were then washed, centrifuged and data were acquired on BD FACS Canto flow cytometer. Analysis was performed using FlowJo software (Tree Star).

Tissue analysis. Adipose tissues were harvested, shredded with scissors, and then incubated for 30 min with PBS containing 1.5 mg/ml collagenase A at 37 °C. Digested adipose tissue was homogenized using a 1 mL syringe with a 20G needle and passed through a 100 μ m sieve. Spleens were crushed with a piston in PBS through a 100 μ m sieve. The resulting suspension was lysed and processed as described in the previous paragraph.

Femurs and tibias were harvested and flushed with FACS buffer. Cells were then centrifuged (400 \times g, 5 min at 4 °C), lysed, and stained as previously described.

BrdU protocol. Mice were injected with BrdU 16 h prior experiments. Blood and tissues were then processed and analyzed by flow cytometry as previously described.

Histology. Tissues were harvested and fixed in PFA-sucrose 30% 2 h at room temperature, then overnight at 4 °C. First, a paraffin infiltration was performed to dehydrated tissues (Myr Spin Tissue Processor STP 120). Then, tissues were embedded in paraffin (Center d'inclusion EC350-B&PMP). 7 μ m sections were performed using a HM340E microtome (Microm Microtech, Francheville France) and immuno-stained as follow.

Immunostaining. Paraffin sections were de-paraffinized and H&E stained or rehydrated by washes in 100% xylene, 100% ethanol, 95% ethanol, 70% ethanol, and then washed in phosphate-buffered saline (PBS). Heat-induced antigen retrieval of sections was carried out using IHC Antigen retrieval solution (eBiosciences) and then washed in PBS. Sections were then blocked for 1 h in buffer (1% BSA, 1% Tween, in PBS), then incubated with primary antibodies overnight at 4 °C. Slides were then stained with DAPI (1 μ g/mL) and secondary antibodies for 1 h at room temperature, and then washed thoroughly. Coverslips were mounted with ImmunoHistoMount. Following co-culture experiments, cells were fixed and incubated with PBS containing 1% BSA 1% Tween for 1 h. Cells were stained with DAPI and Texas Red Phalloidin for 1 h at room temperature, and then washed thoroughly. Coverslips were then mounted with ImmunoHistoMount. Immunostaining and histology data were analyzed using the Fiji-2 software⁴².

Co-culture experiments. MEFs were cultured in DMEM medium containing 10% FBS, 4.5 g/L Glucose, 2 mM L-Glutamine, 1 mM Sodium Pyruvate, 50 U/mL Penicillin, 50 μ g/mL Streptomycin. Monocytes were purified from the blood of C57BL/6 wild-type mice. Blood was collected by submandibular bleeding just before the animal sacrifice. Lysing buffer was used for red blood cells lysis. White blood cells were resuspended in FACS Buffer and stained with a depletion cocktail containing biotin-conjugated anti-CD3, anti-B220, anti-NK1.1, anti-Ly6G, anti-Ter119, and anti-SiglecF. Cells were then incubated with anti-biotin microbeads (Miltenyi Biotec) and passed through Miltenyi columns following the supplier's instructions. The flowthrough was collected and passed a total of four times on Miltenyi columns for optimal monocyte enrichment.

3×10^4 MEFs were plated on glass coverslips in 24 well plates and left to adhere for 8 h before the addition of monocytes and/or anti-podoplanin. 1.5×10^4 monocytes were directly put in contact with MEFs or placed in cell culture inserts with 0.4 μ m pores. Additionally, the podoplanin blockade was realized when indicated by adding 2 μ g/mL anti-podoplanin (8.1.1 clone). Eighteen hours after addition of monocytes and/or anti-podoplanin, medium was removed, cells were washed once with PBS and fixed in 4% PFA for 20 min.

Traction force microscopy. Contractile forces exerted by MEF on 8 kPa hydrogels were assessed by traction force microscopy essentially as described (Liu et al. 2016). Briefly, polyacrylamide substrates with shear moduli of 8 kPa conjugated with fluorescent latex microspheres (0.5 μ m, 505/515 ex/em) were purchased from Matrigel. MEF were plated on fluorescent bead-conjugated discrete stiffness gels and grown for 24 h, at which time they were treated with the indicated treatments for 18 h before traction force measurements. Images of gel surface-conjugated fluorescent beads were acquired for each cell before and after cell removal using a Axiovert 200 M motorized microscope stand (Zeiss) and a $\times 32$ magnification objective. Traction forces exerted by MEF were estimated by measuring bead displacement fields, computing corresponding traction fields using Fourier transform traction microscopy, and calculating root-mean-square traction using the PIV (particle image velocity) and TFM (Traction force microscopy) package on ImageJ (Tseng et al. 2012). To measure baseline noise, the same procedure was performed on a cell-free region.

Positron emission tomographic imaging/computed tomography (PET/CT) and post-PET biodistribution of ⁶⁴Cu-DOTA-ECL1i. For PET/CT, 45–60 min dynamic scan was performed after the injection of ⁶⁴Cu-DOTA-ECL1i (3.7 MBq in 100 μ L saline) via tail vein with Inveon PET/CT system (Siemens, Malvern, PA). The PET images were reconstructed with the maximum a posteriori algorithm and analyzed by Inveon Research Workplace. The organ uptake was calculated as the percent injected dose per gram of tissue in three-dimensional regions of interest without the correction for partial volume effect. Right after PET/CT, the mice were euthanized by cervical dislocation. Organs of interest were collected, weighed, and counted in a Beckman 8000 gamma counter (Beckman, Fullerton, CA). Standards were prepared and measured along with the samples to calculate the percentage of the injected dose per gram of tissue.

Autoradiography. After the collection of BATs, the radio activities in the tissues were detected by autoradiography using a Storm 840 Phosphorimager (GE, Marlborough, MA).

Single-cell RNA-seq data analysis

Cell preparation. Adipose tissues were harvested, shredded with scissors, and then incubated for 30 min with PBS containing 1.5 mg/ml collagenase A at 37 °C.

Digested adipose tissues were homogenized using a 1 mL syringe with a 20G needle and passed through a 100 μ m sieve. The resulting suspensions were centrifuged (400 \times g, 5 min, 4 °C) and stained with anti-CD45-APC-Cy7 antibody. Cells were washed and passed again through a 100 μ m sieve. Unstained cells were acquired to measure autofluorescence. Dapi was added to the cell preparation before the acquisition, and CD45⁺ Dapi⁻ cells were purified using a BD FACS Aria III cell sorter.

Sequencing. Cells were loaded on a Chromium Controller (10x Genomics) with a target output of 5000 cells per sample. Reverse transcription, cDNA synthesis/amplification, and library preparation were performed according to the 10x Genomics protocol (Chromium™ Single Cell 3' Reagent Kit, v3.1 Chemistry). scRNA libraries were sequenced on an Illumina NextSeq 500/550 High Output flowcell: the forward read had a length of 28 bases that included the cell barcode and the UMI; the reverse read had a length of 55 bases that contained the cDNA insert.

Alignment, barcode assignment, and UMI counting with Cell Ranger v4.0.0 were used to perform sample demultiplexing, barcode processing, and single-cell 3' counting. Cell Ranger's mkfastq function was used to demultiplex raw base call files from the HiSeq4000 sequencer into sample-specific FASTQ files.

Barcodes in both samples that were considered to represent noise and low-quality cells were filtered out using knee-inflection strategy available in DropletUtils⁴³ package (version 1.4.3). For analysis, Seurat package (version 3.1.0)⁴⁴ was used, genes which express in less than two cells and cells which have non-zero counts in less than 200 genes were additionally filtered from both barcode expression matrices, and the result matrices were used as analysis inputs. The fraction of mitochondrial genes was calculated for every cell, and cells with a mitochondrial fraction >2% were filtered out. After all filtering procedures, 2,242 cells were left in the scRNA-seq data of control sample, and 2,139 cells were left in scRNA-seq of Adipo^{ΔΔ} sample.

Both samples were normalized using SCTransform function with mitochondrial percentage as a variable to regress out in a second non-regularized linear regression. For integration purpose, variable features across the samples were selected by SelectIntegrationFeatures function with the number of features equal to 2000. Then the object was prepared for integration (PrepSCTIntegration function), the anchors were found (FindIntegrationAnchors function) and the samples were integrated into the whole object (IntegrateData function). The dimensionality of the object was reduced by principal component analysis, and the first 20 principal components (PCs) were used further to generate uniform manifold approximation and projection (UMAP) dimensionality reduction by RunUMAP function. Graph-based clustering was run using FindNeighbors and FindClusters with a resolution of 1.0 and the first 20 PCs as input, and the 17 clusters were identified. In order to exclude the technical bias across the samples, both the counts slot from SCTransform assay and the data slot from integrated assay were used as input for trajectory inference.

For visualization purposes, the custom labels were assigned to several clusters by merging multiple clusters for simplification (e.g., clusters 5, 6, and 14 were merged as T cells, clusters 4, 16 were merged as B cells and clusters 3, 15 were merged as NK cells). Violin plots were drawn using the data slot of SCT assay. To generate pathway enrichment plots we took the expression of genes from the pathway from the data slot of SCT counts assay, used standard normalization (z-score) for these vectors, and then calculated the average vector. The gene signature heatmap was drawn using the scaled data slot of the integrated assay.

For trajectory analysis, clusters assigned as monocytes and macrophages were used, and infer_trajectory function from the dyno package (version 0.1.2) was used with the available slingshot⁴⁵ singularity container (version 1.0.3). Trajectory visualization was implemented after dimensionality reduction by UMAP using dimred_umap function.

Real-time qPCR. All primer sequences used for RT-qPCR are indicated in Supplementary Table 1.

Total RNA was isolated using the RNeasy Plus Mini Kit and quantified using a Nanodrop. cDNA was prepared using 2,77 ng/ μ l total RNA by a RT-PCR using a high-capacity cDNA reverse transcription kit according to the manufacturer's instructions. Real-time qPCR was performed on cDNA using SYBR Green and GAPDH, β -Actin, CXCL12, CCL2, or TNF- α forward and reverse primers (Invitrogen). qPCRs were performed on the StepOne device (Applied Biosystem). Results were normalized on GAPDH or β -Actin gene expression. All conditions were performed in triplicates. All fold changes are expressed normalized to the untreated control.

ELISA assays. BATs were harvested and flash-frozen in liquid nitrogen. At the time of the experiment, tissues were homogenized in 500 μ l sodium acetate solution (0.2 M, pH 4.5) using Precellys tissue homogenizer and centrifuged at 800 \times g for 10 min at room temperature to pellet debris.

Mouse CXCL12 or CCL2 assays were performed on mice serum or tissue homogenates according to the recommended manufacturer instructions.

Statistical analysis. All the data of this paper are expressed in mean \pm SEM. Mann–Whitney test was performed with GraphPad Prism 8 software to test the samples significance (* p < 0.05; ** p < 0.01; *** p < 0.001; **** p < 0.0001).

Reporting summary. Further information on research design is available in the Nature Research Reporting Summary linked to this article.

Data availability

Gene expression data (scRNA-seq) used in this study have been uploaded to the Gene Expression Omnibus (GEO) repository for public availability under the accession code GSE177635 and can be explored here <https://artiyomovlab.wustl.edu/scn/?token=GSE177635>. All other data supporting the findings of this study are available from the corresponding author upon reasonable request. Source data are provided with this paper.

Received: 28 January 2021; Accepted: 12 August 2021;

Published online: 06 September 2021

References

- Guilliams, M. et al. Dendritic cells, monocytes, and macrophages: a unified nomenclature based on ontogeny. *Nat. Rev. Immunol.* **14**, 571–578 (2014).
- Hettinger, J. et al. Origin of monocytes and macrophages in a committed progenitor. *Nat. Immunol.* **14**, 821–830 (2013).
- Yona, S. et al. Fate mapping reveals origins and dynamics of monocytes and tissue macrophages under homeostasis. *Immunity* **38**, 79–91 (2013).
- Chong, S. Z. et al. CXCR4 identifies transitional bone marrow premonocytes that replenish the mature monocyte pool for peripheral responses. *J. Exp. Med.* **213**, 2293–2314 (2016).
- Tsou, C. L. et al. Critical roles for CCR2 and MCP-3 in monocyte mobilization from bone marrow and recruitment to inflammatory sites. *J. Clin. Invest.* **117**, 902–909 (2007).
- Serbina, N. V. & Pamer, E. G. Monocyte emigration from bone marrow during bacterial infection requires signals mediated by chemokine receptor CCR2. *Nat. Immunol.* **7**, 311–317 (2006).
- Jakubzick, C. V., Randolph, G. J. & Henson, P. M. Monocyte differentiation and antigen-presenting functions. *Nat. Rev. Immunol.* **17**, 349–362 (2017).
- Shi, C. & Pamer, E. G. Monocyte recruitment during infection and inflammation. *Nat. Rev. Immunol.* **11**, 762–774 (2011).
- Carlin, L. M. et al. Nr4a1-dependent Ly6C(low) monocytes monitor endothelial cells and orchestrate their disposal. *Cell* **153**, 362–375 (2013).
- Kohyama, M. et al. Role for Spi-C in the development of red pulp macrophages and splenic iron homeostasis. *Nature* **457**, 318–321 (2009).
- Lokka, E. et al. Generation, localization and functions of macrophages during the development of testis. *Nat. Commun.* **11**, 4375 (2020).
- Mossadegh-Keller, N. et al. Developmental origin and maintenance of distinct testicular macrophage populations. *J. Exp. Med.* **214**, 2829–2841 (2017).
- Jenkins, C. M. et al. Identification, cloning, expression, and purification of three novel human calcium-independent phospholipase A2 family members possessing triacylglycerol lipase and acylglycerol transacylase activities. *J. Biol. Chem.* **279**, 48968–48975 (2004).
- Villena, J. A., Roy, S., Sarkadi-Nagy, E., Kim, K. H. & Sul, H. S. Desnutrin, an adipocyte gene encoding a novel patatin domain-containing protein, is induced by fasting and glucocorticoids: ectopic expression of desnutrin increases triglyceride hydrolysis. *J. Biol. Chem.* **279**, 47066–47075 (2004).
- Zimmermann, R. et al. Fat mobilization in adipose tissue is promoted by adipose triglyceride lipase. *Science* **306**, 1383–1386 (2004).
- Wolf, Y. et al. Brown-adipose-tissue macrophages control tissue innervation and homeostatic energy expenditure. *Nat. Immunol.* **18**, 665–674 (2017).
- Lammers, B. et al. Macrophage adipose triglyceride lipase deficiency attenuates atherosclerotic lesion development in low-density lipoprotein receptor knockout mice. *Arterioscler. Thromb. Vasc. Biol.* **31**, 67–73 (2011).
- Schreiber, R. et al. Cold-induced thermogenesis depends on ATGL-mediated lipolysis in cardiac muscle, but not brown adipose tissue. *Cell Metab.* **26**, 753–763.e757 (2017).
- Shin, H. et al. Lipolysis in brown adipocytes is not essential for cold-induced thermogenesis in mice. *Cell Metab.* **26**, 764–777 (2017). e765.
- Kotzbeck, P. et al. Brown adipose tissue whitening leads to brown adipocyte death and adipose tissue inflammation. *J. Lipid Res.* **59**, 784–794 (2018).
- Gautier, E. L. et al. Gene-expression profiles and transcriptional regulatory pathways that underlie the identity and diversity of mouse tissue macrophages. *Nat. Immunol.* **13**, 1118–1128 (2012).
- Jakubzick, C. et al. Minimal differentiation of classical monocytes as they survey steady-state tissues and transport antigen to lymph nodes. *Immunity* **39**, 599–610 (2013).

23. Amano, S. U. et al. Local proliferation of macrophages contributes to obesity-associated adipose tissue inflammation. *Cell Metab.* **19**, 162–171 (2014).
24. Liu, Y. et al. Noninvasive imaging of CCR2(+) cells in ischemia-reperfusion injury after lung transplantation. *Am. J. Transpl.* **16**, 3016–3023 (2016).
25. Williams, J. W. et al. Thermoneutrality but not UCP1 deficiency suppresses monocyte mobilization into blood. *Circ. Res.* **121**, 662–676 (2017).
26. Mack, M. et al. Expression and characterization of the chemokine receptors CCR2 and CCR5 in mice. *J. Immunol.* **166**, 4697–4704 (2001).
27. Acton, S. E. et al. Dendritic cells control fibroblastic reticular network tension and lymph node expansion. *Nature* **514**, 498–502 (2014).
28. Colonna, M., Samaridis, J. & Angman, L. Molecular characterization of two novel C-type lectin-like receptors, one of which is selectively expressed in human dendritic cells. *Eur. J. Immunol.* **30**, 697–704 (2000).
29. Acton, S. E. et al. Podoplanin-rich stromal networks induce dendritic cell motility via activation of the C-type lectin receptor CLEC-2. *Immunity* **37**, 276–289 (2012).
30. Benitez, G. J. & Shinoda, K. Isolation of adipose tissue nuclei for single-cell genomic applications. *J. Vis. Exp.* <https://doi.org/10.3791/61230> (2020).
31. Sun, W. et al. snRNA-seq reveals a subpopulation of adipocytes that regulates thermogenesis. *Nature* **587**, 98–102 (2020).
32. Collier, B. S. Leukocytosis and ischemic vascular disease morbidity and mortality: is it time to intervene? *Arterioscler. Thromb. Vasc. Biol.* **25**, 658–670 (2005).
33. Olivares, R., Ducimetiere, P. & Claude, J. R. Monocyte count: a risk factor for coronary heart disease? *Am. J. Epidemiol.* **137**, 49–53 (1993).
34. Qiu, Y. et al. Eosinophils and type 2 cytokine signaling in macrophages orchestrate development of functional beige fat. *Cell* **157**, 1292–1308 (2014).
35. Abdullahi, A. et al. Alternatively activated macrophages drive browning of white adipose tissue in burns. *Ann. Surg.* **269**, 554–563 (2019).
36. Ahmadian, M. et al. Desnutrin/ATGL is regulated by AMPK and is required for a brown adipose phenotype. *Cell Metab.* **13**, 739–748 (2011).
37. Schoiswohl, G. et al. Impact of reduced ATGL-mediated adipocyte lipolysis on obesity-associated insulin resistance and inflammation in male mice. *Endocrinology* **156**, 3610–3624 (2015).
38. Astarita, J. L. et al. The CLEC-2-podoplanin axis controls the contractility of fibroblastic reticular cells and lymph node microarchitecture. *Nat. Immunol.* **16**, 75–84 (2015).
39. Baker, N. A. et al. Diabetes-specific regulation of adipocyte metabolism by the adipose tissue extracellular matrix. *J. Clin. Endocrinol. Metab.* **102**, 1032–1043 (2017).
40. Croxford, A. L. et al. The cytokine GM-CSF drives the inflammatory signature of CCR2+ monocytes and licenses autoimmunity. *Immunity* **43**, 502–514 (2015).
41. Satpathy, A. T. et al. Notch2-dependent classical dendritic cells orchestrate intestinal immunity to attaching-and-effacing bacterial pathogens. *Nat. Immunol.* **14**, 937–948 (2013).
42. Schindelin, J. et al. Fiji: an open-source platform for biological-image analysis. *Nat. Methods* **9**, 676–682 (2012).
43. Lun, A. T. L. et al. EmptyDrops: distinguishing cells from empty droplets in droplet-based single-cell RNA sequencing data. *Genome Biol.* **20**, 63 (2019).
44. Stuart, T. et al. Comprehensive integration of single-cell data. *Cell* **177**, 1888–1902.e1821 (2019).
45. Street, K. et al. Slingshot: cell lineage and pseudotime inference for single-cell transcriptomics. *BMC Genomics* **19**, 477 (2018).

Acknowledgements

We would like to thank Dr Pierre Leclère for the helpful discussions. We would like to thank Jean-Paul Pais de Barros from the Lipidomic Analytic platform (LAP) of the University of Burgundy for technical support. We thank the C3M Animal facility for technical support and the GIS-IBISA multi-sites platform Microscopie Imagerie Côte d'Azur (MICA), and particularly the imaging site of C3M (INSERM U1065) supported by Conseil Régional, Conseil Départemental, and IBISA. We sincerely thank Maéva Gesson and Marie Irondele for their help. We acknowledge the flow cytometry facility from the «Institut de Pharmacologie Moléculaire et Cellulaire», part of the MICA GIS

IBISA labeled platform, and we thank Julie Cazareth for her help. We thank Dr. Jean-François Tanti for sharing Ucp1^{Cre} mice and Dr. Stephan Clavel for sharing MEFs. A.G. is supported by the French government, through the UCAJedi Investments in the Future projects managed by the National Research Agency (ANR) (ANR-15-IDEX-01). T.B. is supported by Agence Nationale de la Recherche (ANR-18-CE14-0025 and ANR-20-CE14-0006-02). M.F. and K.Z. were supported by the Government of Russian Federation (Grant 08-08). R.R.G. is supported by Center National de la Recherche Scientifique (CNRS). D.D. was supported by grants from the ANR and the European Union: EGID ANR-10-LABX-46. J.W.W. was supported by the National Institutes of Health (NIH) grant HL138163. L.Y.C. is supported by Institut National de la Santé et de la Recherche Médicale (INSERM), Fondation de France (00066474), and the European Research Council (ERC) consolidator program (ERC2016COG724838). S.I. is supported by Institut National de la Santé et de la Recherche Médicale (INSERM) and Agence Nationale de la Recherche (ANR-17-CE14-0017-01 and ANR-19-ECVD-0005-01).

Author contributions

A.G., M.I.S., R.R.G., L.Y.C., and S.I. designed and performed experiments, and wrote the paper. A.G., M.I.S., J.M., N.K., N.V., J.G., and S.I. analyzed experiments. J.M., N.K., V.M., B.D., M.A., A.C., J.G., P.B., A.D., and N.V. helped performing experiments. A.J. and D.M. performed and analyzed the lipidomic analysis and edited the paper. H.P.L., D.S., and Y.L. performed and analyzed CCR2 PET/CT, biodistribution, and autoradiography experiments and edited the paper. M.M.F. and K.Z. analyzed scRNA-Seq data and edited the paper. T.B. performed and analyzed traction force microscopy experiments and edited the paper. B.B. provided CCR2^{cre/ERT2} tdTomato mice and expertise on data analysis. J.W.W. performed monocyte fate-mapping experiments and edited the paper. M.M. provided MC-21 Ab, expertise on data analysis, and edited the paper. D.D. provided expertise on data analysis, wrote and edited the paper. A.G., M.I.S., S.I., M.M.F., K.Z., T.B., and Y.L. created figures. L.Y.C., R.R.G., and S.I. conceived the study. S.I. obtained funding for the project.

Competing interests

The authors declare no competing interests.

Additional information

Supplementary information The online version contains supplementary material available at <https://doi.org/10.1038/s41467-021-25616-1>.

Correspondence and requests for materials should be addressed to S.I.

Peer review information *Nature Communications* thanks Rasheed Ahmad and Kosaku Shinoda for their contribution to the peer review of this work. Peer reviewer reports are available.

Reprints and permission information is available at <http://www.nature.com/reprints>

Publisher's note Springer Nature remains neutral with regard to jurisdictional claims in published maps and institutional affiliations.



Open Access This article is licensed under a Creative Commons Attribution 4.0 International License, which permits use, sharing, adaptation, distribution and reproduction in any medium or format, as long as you give appropriate credit to the original author(s) and the source, provide a link to the Creative Commons license, and indicate if changes were made. The images or other third party material in this article are included in the article's Creative Commons license, unless indicated otherwise in a credit line to the material. If material is not included in the article's Creative Commons license and your intended use is not permitted by statutory regulation or exceeds the permitted use, you will need to obtain permission directly from the copyright holder. To view a copy of this license, visit <http://creativecommons.org/licenses/by/4.0/>.

© The Author(s) 2021

Supplementary information for :

Brown adipose tissue monocytes support tissue expansion.

Authors

Alexandre Gallerand^{1£}, Marion I. Stunault^{1£}, Johanna Merlin¹, Hannah P. Luehmann², Deborah H. Sultan², Maria M. Firulyova³, Virginie Magnone⁴, Narges Khedher¹, Antoine Jalil⁵, Bastien Dolfi¹, Alexia Castiglione¹, Adélie Dumont¹, Marion Ayrault¹, Nathalie Vaillant¹, Jérôme Gilleron¹, Pascal Barbry⁴, David Dombrowicz⁶, Matthias Mack⁷, David Masson⁵, Thomas Bertero⁴, Burkhard Becher⁸, Jesse W. Williams⁹, Konstantin Zaitsev³, Yongjian Liu², Rodolphe R. Guinamard¹, Laurent Yvan-Charvet¹ and Stoyan Ivanov^{1*}

Affiliations

¹ Université Côte d'Azur, INSERM, C3M, Nice, France.

² Department of Radiology, Washington University School of Medicine, Saint Louis, Missouri 63110 United States.

³ Computer Technologies Department, ITMO University, Saint Petersburg, Russia.

⁴ Université Côte d'Azur, CNRS, IPMC, Valbonne, France.

⁵ Université Bourgogne Franche-Comté, LNC UMR1231, F-21000 Dijon, France.

⁶ Univ.Lille, Inserm, CHU Lille, Institut Pasteur de Lille, U1011-EGID, 59000 Lille, France.

⁷ Department of Internal Medicine - Nephrology, University Hospital Regensburg, Regensburg, Germany.

⁸ Institute of Experimental Immunology, University of Zürich, Switzerland.

⁹ Department of Integrative Biology and Physiology, Center for Immunology, University of Minnesota Medical School, Minneapolis, MN, USA.

£Equal contribution

*Corresponding author

Correspondence to:

Stoyan.ivanov@unice.fr

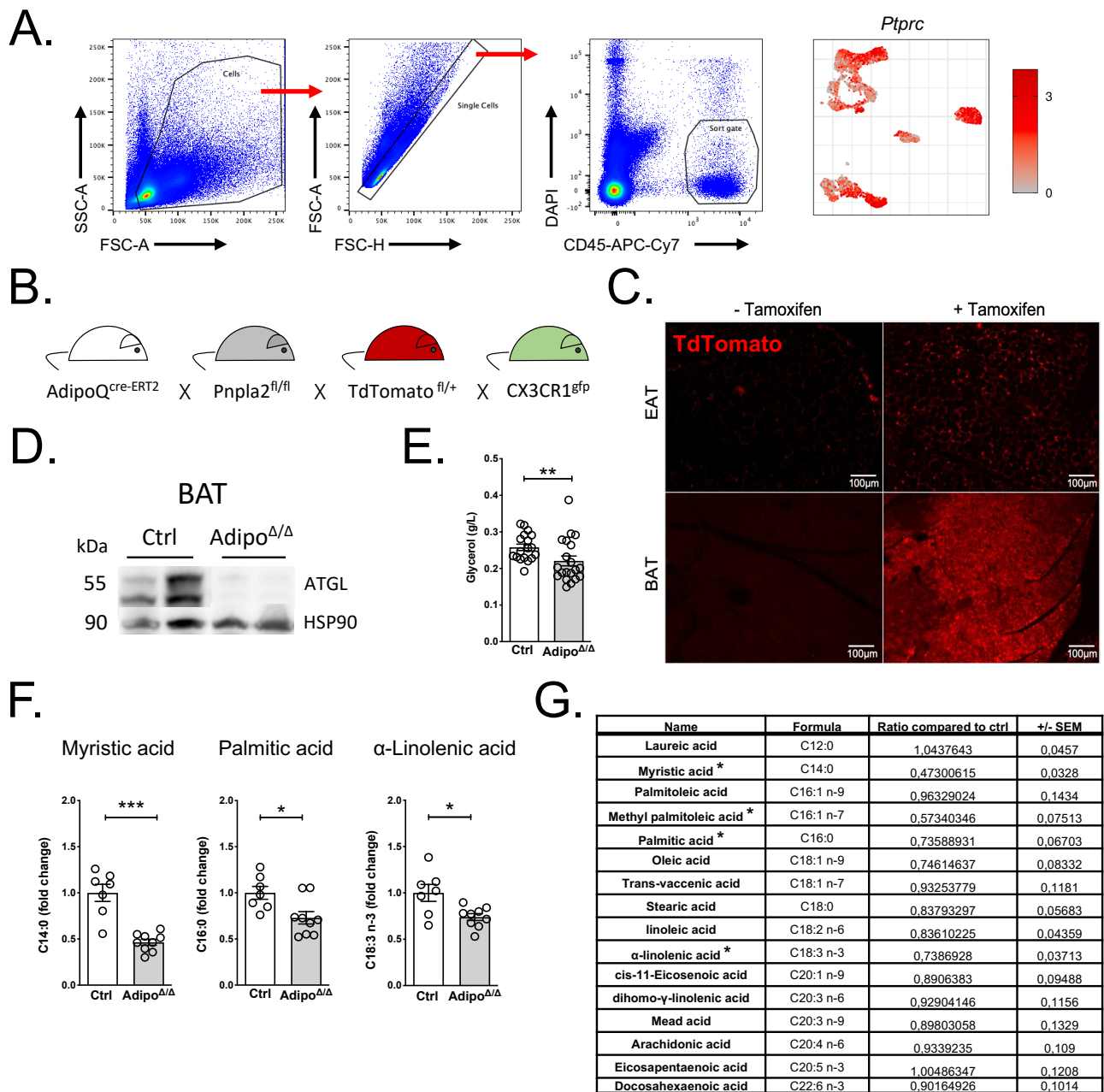


Figure S1. This figure is related to Figure 1.

(A) (Left) Cell-sorting strategy used for isolation of BAT CD45⁺ cells before scRNA-Seq and (right) Single Cell RNA-Seq analysis of *Ptpcr* expression among BAT CD45⁺ cells (B) Breeding scheme for generating Adipo Δ/Δ mice. (C) TdTomato reporter expression (red) in epididymal (EAT) and brown (BAT) adipose tissues by fluorescence microscopy. (D) ATGL protein expression in Adipo Δ/Δ mice brown adipose tissue (BAT) compared to controls (Ctrl) by Western Blot analysis; HSP90 was used as loading control for protein expression. (E) Glycerol levels in control (n=18) and Adipo Δ/Δ (n=20) mice sera. $p=0,0096$. (F) Myristic acid (C14:0), palmitic acid (C16:0) and α -linoleic acid (C18:3 n-3) levels in control (n=7) and Adipo Δ/Δ (n=9) mice sera. $p=0,0003$ (left), $p=0,0115$ (middle), $p=0,0418$ (right). (G) Lipidomic analysis of serum from control and Adipo Δ/Δ mice. Data are represented in ratio compared to Ctrl condition \pm SEM. Stars indicate a statistically significant difference between controls and Adipo Δ/Δ mice ($p < 0,05$).

Panel C is representative of 3 experiments. Panel D represents one experiment. Panel E represents pooled data from 5 independent experiments. Panels F and G represent pooled data from 2 independent experiments. All data are represented in means \pm SEM. Two-tailed Mann Whitney tests were used to determine statistical significance in panels E and F. ns $p > 0,05$; * $p < 0,05$; ** $p < 0,01$; *** $p < 0,001$; **** $p < 0,0001$. Source data, and notably uncropped blots for panel S1D, are provided as a Source Data file.

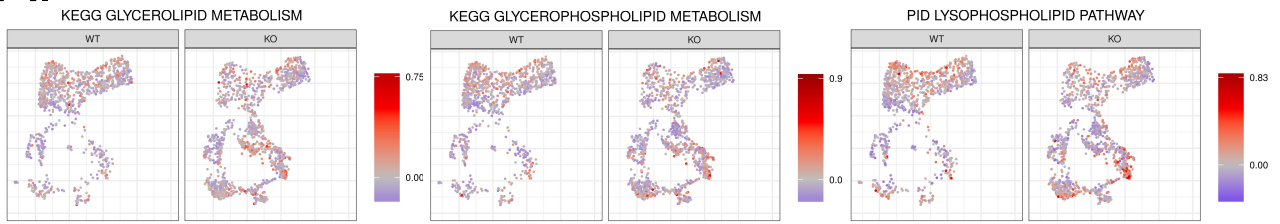
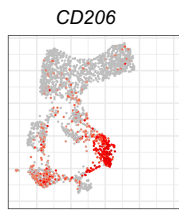
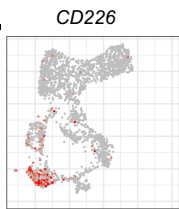
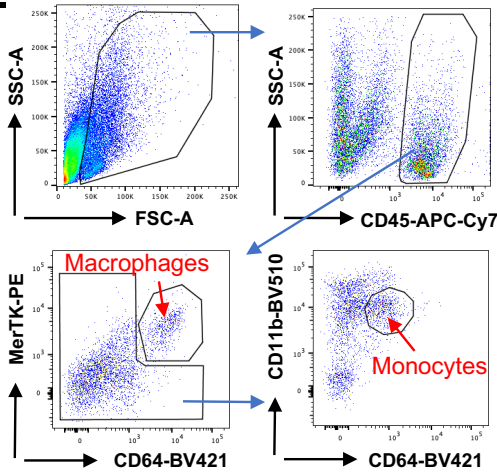
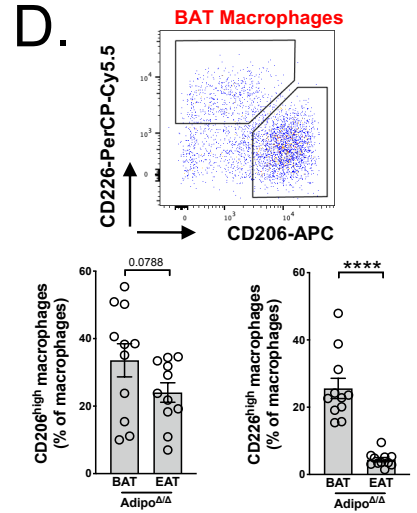
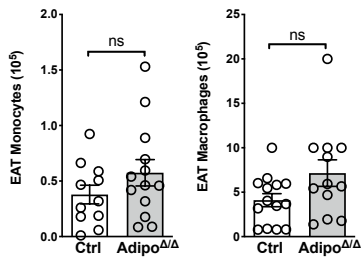
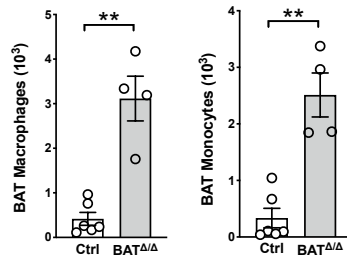
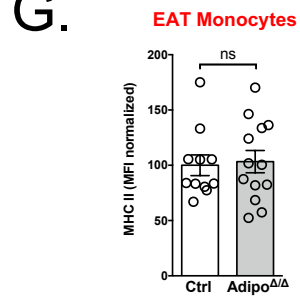
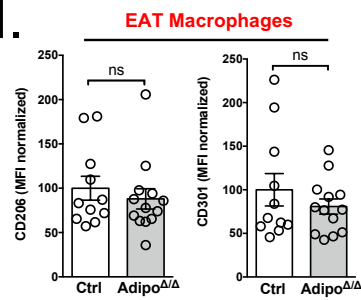
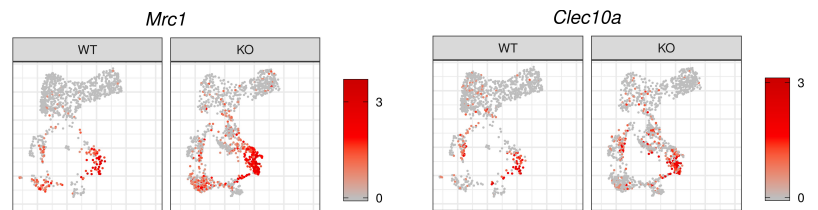
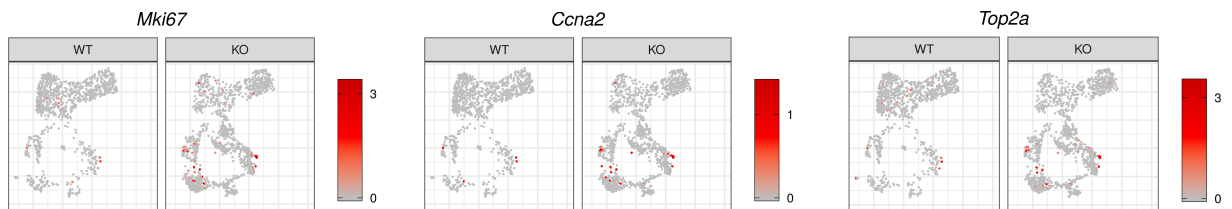
A.**B.****C.****D.****E.****F.****G.****H.****I.****J.**

Figure S2. This figure is related to Figure 2.

(A) Single Cell RNA-Seq analysis of the PID “lysophospholipid metabolism” pathway, the KEGG “glycerolipid metabolism” gene set and the KEGG “glycerophospholipid metabolism” gene set expression. (B) Single Cell RNA-Seq analysis of *Mrc1* and *CD226* expression among BAT monocytes and macrophages. (C) Gating strategy used for identification of tissue macrophages, and tissue monocytes in mice lacking the *CX3CR1^{gfp}* reporter. (D) Representative dot plots (left) and proportions (right) of BAT and EAT CD206^{high} and CD226^{high} macrophages in Adipo^{ΔΔ} mice (n=11). $p=0,0788$ (left), $p<0,0001$ (right). (E) Quantification of EAT macrophage and monocyte counts in control (n=11) and Adipo^{ΔΔ} (n=16) mice using flow cytometry. $p=0,3607$ (left), $p=0,1207$ (right). (F) Quantification of BAT monocyte and macrophage numbers in control (n=6) and BAT^{ΔΔ} (n=4) mice using flow cytometry. $p= 0,0095$ (left and right). (G) Quantification of surface MHCII expression on EAT monocytes in control (n=14) and Adipo^{ΔΔ} mice (n=15) using flow cytometry. $p=0,9095$. (H) Quantification of surface CD206 and CD301 expression by EAT macrophages in control (n=11) and Adipo^{ΔΔ} (n=16) mice using flow cytometry. $p=0,6905$ (left and right). (I) Single Cell RNA-Seq analysis of *Mrc1* (CD206) and *Clec10a* (CD301) expression among BAT myeloid cells. (J) Single Cell RNA-Seq analysis of genes involved in cell proliferation.

Panel D represents pooled data from 2 independent experiments. Panels E, G and H represent pooled data from 4 independent experiments. Panel F is representative from 2 independent experiments. All data are represented in means \pm SEM. Two-tailed Mann Whitney tests were used to determine statistical significance. ns $p>0,05$; * $p<0,05$; ** $<0,01$; *** $p<0,001$; **** $p<0,0001$. Source data are provided as a Source Data file.

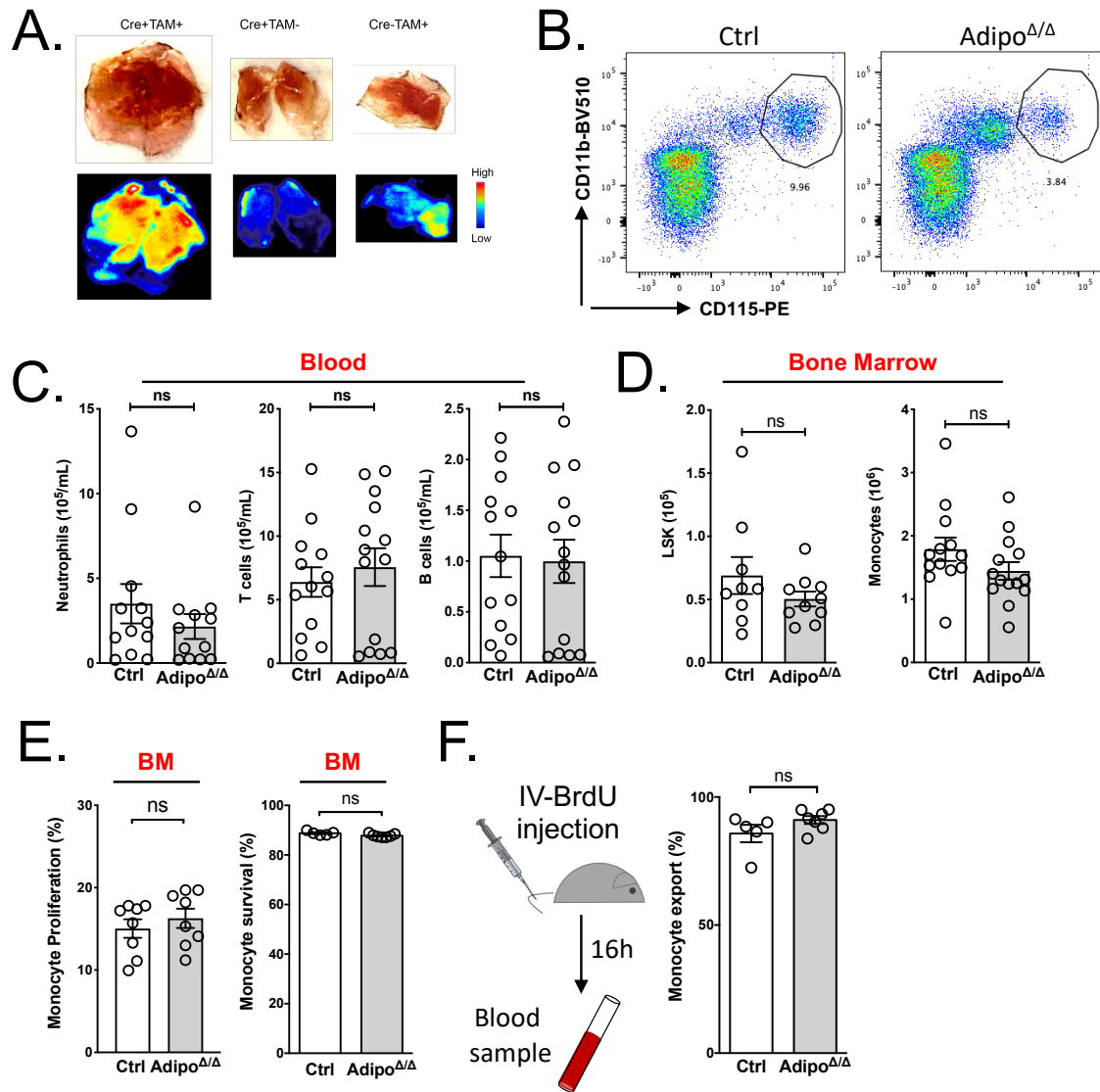


Figure S3. This figure is related to Figure 3.

(A) (Top panel) Representative photos showing the enlarged BAT in Adipo $\Delta\Delta$ mice compared to control groups 16 days post-tamoxifen administration. (Bottom panel) Representative autoradiography images showing the increased ^{64}Cu -DOTA-ECL1i signals in the BAT of Adipo $\Delta\Delta$ mice compared to control groups 16 days post-tamoxifen administration. (B) Representative dot plots of blood monocytes in control and Adipo $\Delta\Delta$ mice. (C) Quantification of blood neutrophil, T cell and B cell counts in control (n=12) and Adipo $\Delta\Delta$ (n=14) mice using flow cytometry. $p=0,4428$ (left), $p=0,5826$ (middle), $p=0,6848$ (right). (D) Quantification of bone marrow LSK (Lin $^-$ Scal $^+$ cKit $^+$) and monocytes in control (n=9 and 13 respectively) and Adipo $\Delta\Delta$ (n=10 and 14 respectively) mice using flow cytometry. $p=0,4002$ (left) and $p=0,0850$ (right). (E) Bone marrow monocyte proliferation rate and survival in control (n=4 and n=5 respectively) and Adipo $\Delta\Delta$ (n=8 and n=7 respectively) mice by flow cytometry. $p=0,3144$ (left), $p=0,0657$ (right). (F) Schematic representation of BrdU injection protocol to visualize monocyte export from bone marrow to blood (left) and its quantification by flow cytometry in control (n=5) and Adipo $\Delta\Delta$ mice (n=7). $p=0,1490$.

Panels C and D represent pooled data from 4 independent experiments. Panel E (left) represents pooled data from 2 independent experiments. Panels E (right) and F are representative of one experiment. All data are represented in means \pm SEM. Two-tailed Mann Whitney tests were used to determine statistical significance. ns $p>0,05$; * $p<0,05$; ** $p<0,01$; *** $p<0,001$; **** $p<0,0001$. Source data are provided as a Source Data file.

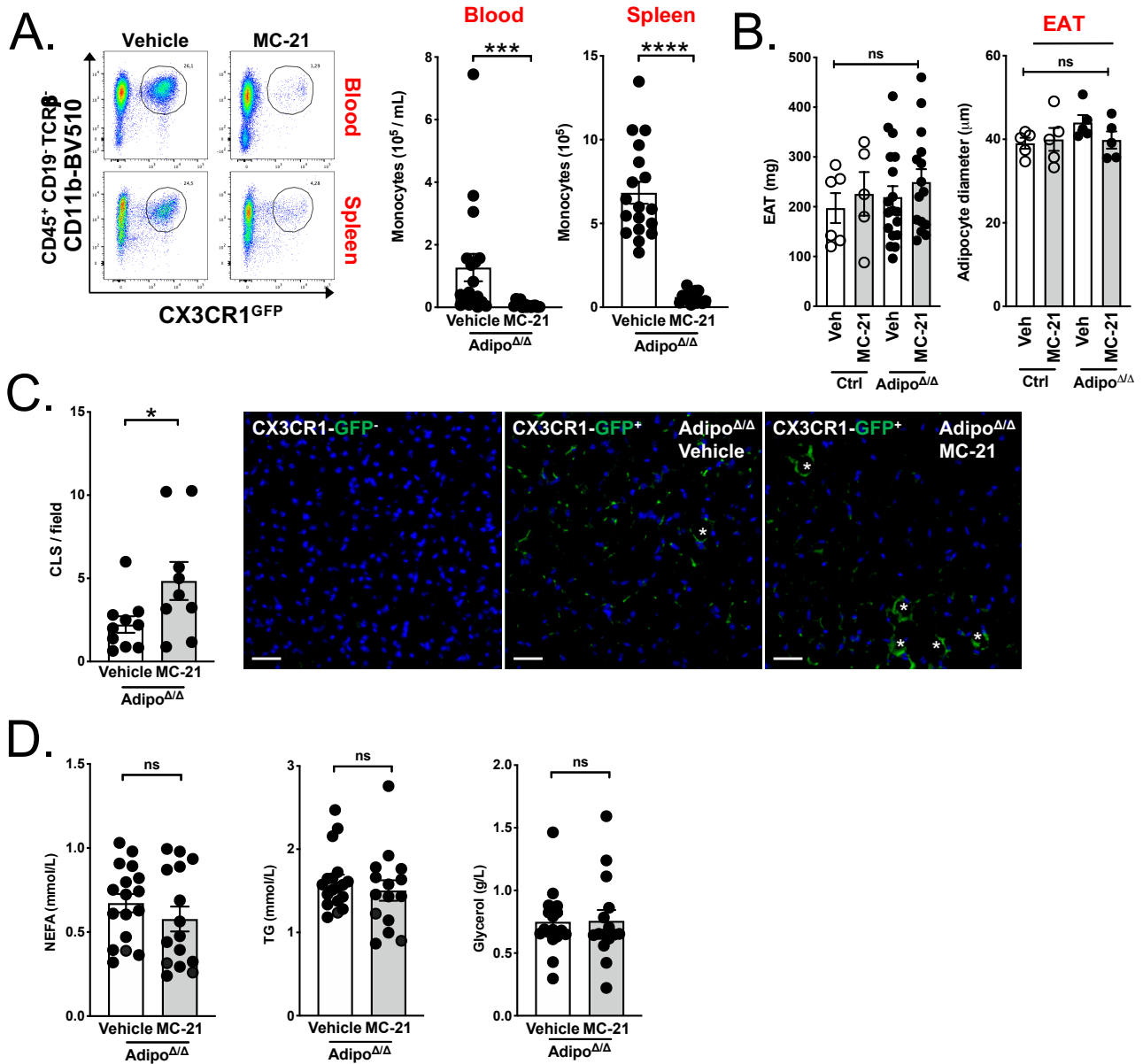


Figure S4. This figure is related to Figure 4.

(A) Representative dot plots (left) and quantification (right) of blood and spleen monocytes in MC-21 (n=13 and 15 respectively) or vehicle-treated (n=15 and 18 respectively) *Adipo^{ΔΔ}* mice. $p = 0,0002$ (left) and $p < 0,0001$ (right). (B) (Left panel) EAT weight of MC-21 or vehicle-treated control (n=5 and 6 respectively) and *Adipo^{ΔΔ}* (n=15 and 18 respectively) mice and (right panel) EAT adipocyte diameter measurement. $p > 0,05$ (all comparisons). (C) Quantification of crown-like structures (CLS) (left) and immunofluorescence microscopy analysis in BAT of control (n=10) and MC-21-treated (n=9) *Adipo^{ΔΔ}* mice. *CX3CR1^{+/+}* samples were used to determine background signal. White stars indicate crown-like structures. Scale bar = 100um. $p = 0,0364$. (D) Glycerol, TG and NEFA levels in the serum of control (n=17) and MC-21-treated (n=15) *Adipo^{ΔΔ}* mice. $p = 0,2948$ (left), $p = 0,5800$ (middle) and $p = 0,4474$ (right).

Data were obtained from 3 pooled independent experiments. All data are represented in means \pm SEM. Two-tailed Mann Whitney tests were used to determine statistical significance. ns $p > 0,05$; * $p < 0,05$; ** $p < 0,01$; *** $p < 0,001$; **** $p < 0,0001$. Source data are provided as a Source Data file.

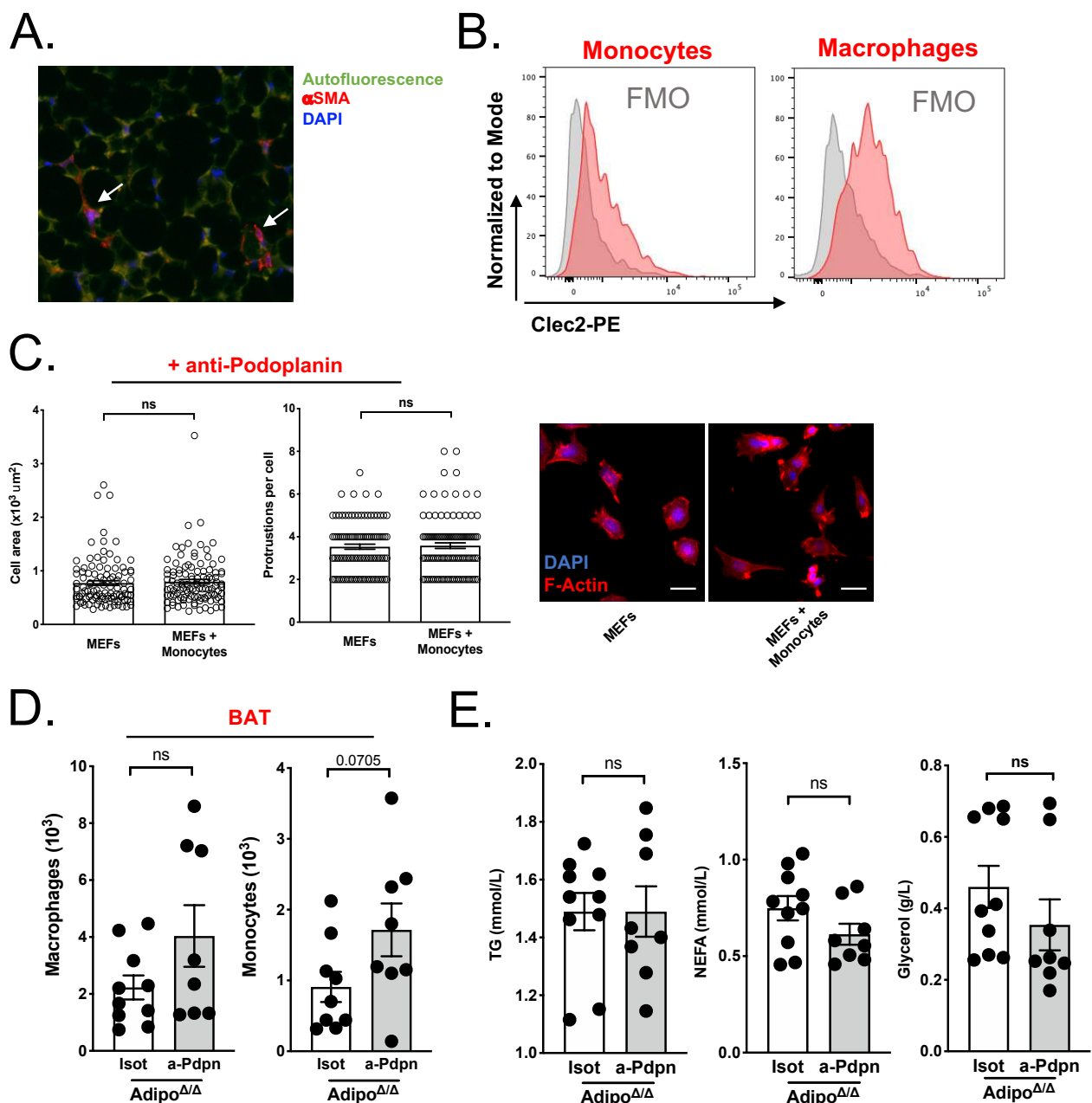


Figure S5. This figure is related to Figure 5.

(A) α -SMA staining (red) in the BAT of $\text{Adipo}^{\Delta/\Delta}$ mice. Autofluorescence signal (green) is used to show tissue architecture. Data representative of 2 independent experiments. (B) Histograms showing CLEC-2 and FMO stainings among BAT monocytes and macrophages from $\text{Adipo}^{\Delta/\Delta}$ mice. Data representative of 2 independent experiments. (C) (Left) Quantification of MEF morphological features after a 18hour co-culture experiment with monocytes in the presence of anti-Podoplanin blocking antibody. (Right) Representative images of MEF morphology at the end of the co-culture experiment. Scale bar = $20\mu\text{m}$. $p=0,3784$ (left) and $p=0,9203$ (right). Data representative of 2 independent experiments. (D) Quantification of BAT macrophage and monocyte numbers in anti-Podoplanin ($n=8$) and isotype control-treated ($n=10$) $\text{Adipo}^{\Delta/\Delta}$ mice using flow cytometry. (E) Glycerol, TG and NEFA levels in the serum of isotype control ($n=10$) and anti-Podoplanin-treated ($n=8$) $\text{Adipo}^{\Delta/\Delta}$ mice. Data were obtained from 2 pooled independent experiments.

Panel C is representative of 2 independent experiments. Panels D and E represent pooled data from 2 pooled independent experiments. All data are represented in means \pm SEM. Two-tailed Mann Whitney tests were used to determine statistical significance. ns $p>0,05$; * $p<0,05$; ** $p<0,01$; *** $p<0,001$; **** $p<0,0001$. Source data are provided as a Source Data file.

Supplementary Table 1

Primers used for genotyping and RT-qPCR.

Mouse	Genotyping Primer sequences	
Gene name	Primer Forward (Left)	Primer Reverse (Right)
GAPDH	ACCACAGTCCATGCCATCACTGCCA	GGCCATCCACAGTCTTCTGC
β -Actin	GAGACCTTCAACACCCC	GTGGTGGTGAAGCTGTAGGC
CXCL12	CCAAACTCTCCCCTTCAGAT	ATTTGCGGTCAATGCACACT
CCL2	CATCCACGTGTTGGCTCA	GATCATCTTGCTGGTGAATGAGT
TNF- α	CACAAGATGCTGGGACAGTGA	TCCTTGATGGTGGTGCATGA

Mouse	RT-qPCR Primer sequences	
Gene name	Primer Forward (Left)	Primer Reverse (Right)
GAPDH	ACCACAGTCCATGCCATCACTGCCA	GGCCATCCACAGTCTTCTGC
β -Actin	GAGACCTTCAACACCCC	GTGGTGGTGAAGCTGTAGGC
CXCL12	CCAAACTCTCCCCTTCAGAT	ATTTGCGGTCAATGCACACT
CCL2	CATCCACGTGTTGGCTCA	GATCATCTTGCTGGTGAATGAGT
TNF- α	CACAAGATGCTGGGACAGTGA	TCCTTGATGGTGGTGCATGA

Supplementary Table 2

List of reagents, materials, models and software used.

Reagent or resource	Source	Identifier
---------------------	--------	------------

Antibodies

CD115 PE (clone AFS98)	eBioscience	Cat# 12-1152-82
CD11b Brilliant Violet 510 (cloneM1/70)	Biolegend	Cat# 101263
Gr1 PerCP-Cy5.5 (clone RB6-8C5)	BD Biosciences	Cat# 552093
Ly6C PerCP-Cy5.5 (clone HK1.4)	Biolegend	Cat# 128011
F4/80 PE-Cy7 (clone BM8)	Biolegend	Cat# 123114
CD45 APC-Cy7 (clone 30-F11)	BD Biosciences	Cat# 557659
CD64 Brilliant Violet 421 (clone X54-5/7.1)	Biolegend	Cat# 139309
CD19 FITC (clone 6D5)	Biolegend	Cat# 115506
CD301 FITC (clone ER-MP23)	Bio-Rad	Cat# MCA2392
MerTK PE (clone 2B10C42)	Biolegend	Cat# 151506
CD11c PE-Cy7 (clone HL3)	BD Biosciences	Cat# 558079
MHC II IA/IE APC (clone M5/114.15.2)	Biolegend	Cat# 107618
CD206 PerCp-Cy5.5 (clone C068C2)	Biolegend	Cat# 141715
CD206 AF647 (clone C068C2)	Biolegend	Cat# 141712
CD226 PerCp-Cy5.5 (clone10E5)	Biolegend	Cat# 128813
Clec2 PE (clone 17D9/CLEC-2)	Biolegend	Cat# 146103
TCR β PB (clone H57-597)	Biolegend	Cat# 109226
CD3 APC (clone 17A2)	Biolegend	Cat# 100236
NK1.1 APC (clone PK136)	Biolegend	Cat# 108720
Ter119 APC (clone TER-119)	Biolegend	Cat# 116212
B220 APC (clone RA3-6B2)	BD Biosciences	Cat# 561226
CD19 APC (clone REA749)	Miltenyi Biotec	Cat# 130-111-884
CD150 PE-Cy7 (clone TC15-12F12.2)	Biolegend	Cat# 115914
Sca1 PB (clone D7)	Biolegend	Cat# 108120
c-Kit APC-Cy7 (clone ACK2)	eBioscience	Cat# 47-1172-82
CD48 AF488 (clone HM48-1)	Biolegend	Cat# 103414

CXCR4 APC (clone 2B11)	eBioscience	Cat# 51-9991-80
CD11b APC (clone M1/70)	Biologend	Cat# 101218
MC-21	Dr Mack M.	
Podoplanin (clone 8.1.1)	BioXCell	Cat# BE0236
<i>InVivo</i> MAb polyclonal Syrian hamster IgG	BioXCell	Cat# BE0087
Ly6G Biotin (clone REA526)	Miltenyi biotec	Cat# 130-116-512
CD3 Biotin (clone REA641)	Miltenyi biotec	Cat# 130-123-861
B220 Biotin (clone REA755)	Miltenyi biotec	Cat# 130-110-844
NK1.1 Biotin (clone REA1162)	Miltenyi biotec	Cat# 130-120-513
Ter-119 Biotin (clone Ter-119)	Miltenyi biotec	Cat# 130-120-828
SiglecF Biotin (clone REA798)	Miltenyi biotec	Cat# 130-112-329
α -SMA	Abcam	Cat# ab5694
Goat anti Rabbit Cy3	Jackson ImmunoResearch	Cat# 111-165-003

Chemicals

DAPI	Sigma	Cat# D9542
Phalloidin Texas Red	Invitrogen	Cat# T7471
PFA 4%	VWR International	Cat# 9713.1000
Bovine serum Albumin (BSA)	Sigma	Cat# A7030
Tamoxifen	Sigma	Cat# T5648
RPMI medium	Life Technologies	Cat# 21875091
DMEM medium	Life Technologies	Cat# 11960044
Collagenase A	Sigma	Cat# 11088793001
IHC Antigen retrieval solution	eBiosciences	Cat# 00-4955-58
ImmunoHistoMount	Sigma	Cat# I1161
Thiazolyl blue tetrazolium bromide	Sigma	Cat# M2128
Fetal bovine serum	Fisher Scientific	Cat# 12350273
Lysing buffer	BD Biosciences	Cat# 555899
L-Glutamine	Life Technologies	Cat# 25030024
Penicillin Streptomycin	Life Technologies	Cat# 15070063
Sodium Pyruvate	Life Technologies	Cat# 11360039
Free glycerol reagent	Sigma	Cat# F6428
<i>Power</i> SYBR™ green PCR Master Mix	Applied Biosystems	Cat# 4367659
RIPA buffer	Cell signaling	Cat# 9806
Anti-Biotin MicroBeads	Miltenyi Biotec	Cat# 130-090-858

Critical commercial Assays

High-Capacity cDNA reverse transcription kit	Applied Biosystems	Cat# 4368814
CCL2 DuoSet ELISA	R&D Systems	Cat# DY479-05
TNF-alpha DuoSet ELISA	R&D Systems	Cat# DY410-05
RNeasy Plus Mini Kit (250)	QIAGEN	Cat# 74136
Mouse CXCL12/SDF-1 DuoSet ELISA	R&D Systems	Cat# DY460
(Stromal Cell Derived Factor 1), Human, Elisa Kit	EUROMEDEX	Cat# EH3755
NEFA-HR2 R1 + R2 FUJIFILM	WAKO	Cat# W1W270-77000
Glucose dosage Kit	BioSentec	Cat# 075
Triglyceride dosage Kit	DiaSys	Cat# 157109910021
BrdU APC Staining Kit	ThermoFisher	Cat# 8817-6600-42
0.4 μ m Cell culture Inserts 24 well format	Falcon	Cat# 353095

Experimental models: Organisms/Strains

Mouse: C57BL/6-Tg(Adipoq-cre/ERT2)1Soff/J	The Jackson laboratory	JaxStock# 025124
Mouse: B6.FVB-Tg(Ucp1-cre)1Evdr/J	The Jackson laboratory	JaxStock# 024670
Mouse: B6N.129S-Pnpla2 ^{tm1Eek} /J	The Jackson laboratory	JaxStock# 024278
Mouse: B6.129P-Cx3cr1 ^{tm1Litt} /J	The Jackson laboratory	JaxStock# 008451
Mouse: B6.Cg-Gt(ROSA)26Sor ^{tm9(CAG-tdTomato)Hze} /J	The Jackson laboratory	JaxStock# 007909
Mouse: C57BL/6NTac-Ccr2 ^{tm2982} (T2A-Cre7ESR1-T2A-mKate2]	Dr. Burkhard Becher	N/A
Mouse: CCR2 ^{GFP}	Dr. Marco Colonna	N/A
Cell line : Mouse Embryonic Fibroblasts (MEFs)	ATCC	CRL-2907

Accessories

StepOne	Applied Biosystem	N/A
Thermo Cycler SimpliAmp	Applied Biosystem	N/A
Nanodrop	OZYME	
MACS Multistand	Miltenyi Biotec	Cat# 130-042-303
MACS LS Columns	Miltenyi Biotec	Cat# 130-042-401

Softwares

Prism6	GraphPad	N/A
FlowJo	Tree Star	N/A
Fuji	Fiji	N/A
GENESys	Syngene	N/A
StepOne Software v.2.2.2	Applied Biosystem	N/A
Fiji	https://imagej.net/software/fiji/	N/A

B. Discussion and perspectives

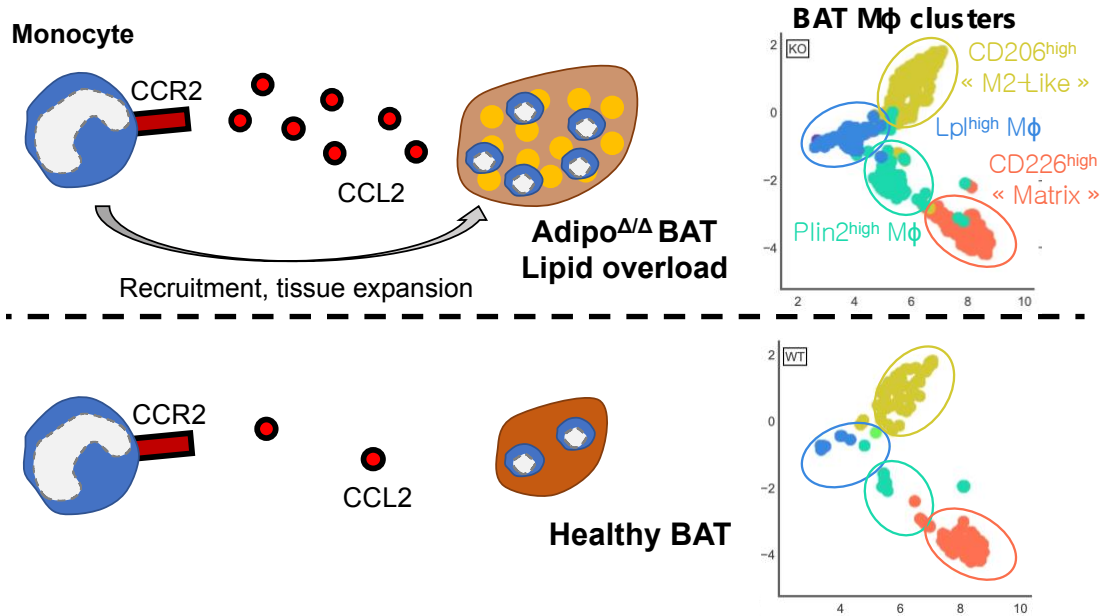


Figure 7. Graphical summary of the findings on BAT monocytes and macrophages.

a. Diversity of BAT myeloid cells

We discovered the co-existence of several myeloid cell populations in healthy BAT. These included neutrophils, dendritic cells, monocytes and macrophages. Macrophages were the most abundant immune cells in this organ and their population comprised four separate and well-defined subsets. Importantly, slingshot analysis predicted two possible differentiation trajectories of monocytes into macrophages : “M2-like” macrophages (M2M ϕ) identified by high CD206 expression, or “Matrix” macrophages (MaM ϕ) which highly express CD226.

Since neither of these markers were previously used to identify BAT macrophage subsets, we asked how the subsets we identified might relate to previously-reported CX3CR1⁺²⁶⁸ and CD169⁺³⁵¹ macrophages. *Siglec1* (CD169) expression appeared restricted to a part of the M2-like cluster (Figure 8A). Although *Cx3cr1* mRNA was weakly detected, *Cx3cr1*⁺ cells appeared in all four macrophage clusters, likely reflecting the monocyte flux that contributes to macrophage maintenance (Figure 8A). No macrophage clusters were clearly defined based on *Siglec1* and *Cx3cr1* expression, although this could be due to the low detection of *Siglec1* and *Cx3cr1* mRNA in BAT macrophages in our scRNA-seq data. Thus, we further used flow cytometry to analyzed BAT from CX3CR1^{GFP} mice and define how the CX3CR1⁺ and CD169⁺ subsets might overlap with the terminally-differentiated macrophage clusters

we identified (CD226⁺ MaM ϕ and CD206⁺ M2M ϕ). We used UMAP for dimension reduction of our flow cytometry data and first visualized our manually-gated CD206⁺, CD226⁺ and CD206⁻ CD226⁻ populations on the plot (Figure 8B). CX3CR1^{GFP} expression was mostly observed on the CD206⁻ CD226⁻ population, though it also partly overlapped with CD206⁺ and CD226⁺ subsets (Figure 8C). On the other hand, CD169 expression was found almost exclusively among CD206⁺ macrophages. CD169 and CX3CR1 expression appeared exclusive (Figure 8C and 8D). We found that CD226⁺ macrophages did not overlap with CD169⁺ cells, and were predominantly found among the CX3CR1⁻ CD169⁻ population (Figure 8E). On the other hand, nearly 90% of CD169⁺ cells were CD206^{high} suggesting a strong overlap between these populations. Nevertheless, CD206^{high} cells were also found in significant proportions among the CX3CR1⁻ CD169⁻ and CX3CR1⁺ CD169⁻ populations (Figure 8E). These results suggest that CX3CR1 and CD226 expression can identify two clear subsets while the CD206⁺ population is more heterogenous. We found that the CD206⁺ subset contains macrophages expressing CD163, a marker associated with long tissue residency, as well as Lyve1⁺ Timd4⁺ MHC-II⁻ macrophages reminiscent of the resident populations described by Chakarov *et al.*³³ and Dick *et al.*³⁴ (Figure 8F). Still in agreement with these reports, CCR2 expression was mostly found on CD206⁻ cells which belong to both the CD226⁺ and CX3CR1⁺ subsets. CCR2 expression also overlapped with MHC-II and CD11c expression, further supporting the idea that CX3CR1⁺ and CD226⁺ macrophages might be monocyte-derived cells. Interestingly, the CX3CR1⁺ macrophage population contains both CD11c^{high} CCR2^{low} and CD11c^{low} CCR2^{high} cells, resembling clusters 8 and 7 respectively. Additional markers are still required to properly identify these “non-terminal” clusters. Using other approaches such as CITE-seq analysis could provide further insights about BAT macrophage diversity.

Because we used single-cell RNA-sequencing, we were able to define BAT macrophage diversity with a resolution that goes beyond previous observations of CX3CR1⁺²⁶⁸ and CD169⁺³⁵¹ macrophages. This allowed the identification of the subset-specific markers CD226 (MaM ϕ) and CD206 (M2M ϕ). Markers allowing the clear identification of clusters 7 and 8 are still ill-defined, although our flow cytometry analysis suggests these are contained within the CX3CR1⁺ population. As illustrated in Figure 8, more than 4 macrophage populations could be identified using solely surface markers. Indeed, only the CD226⁺ population appears homogenous while the

CX3CR1⁺ and CD206⁺ populations could be further sub-divided using our flow cytometry panel. Although our results clearly reveal an impressive macrophage diversity in BAT, they also raise the question of whether sub-dividing them into 4 clusters gives a good-enough representation of reality, or if we are still under-estimating their diversity. This is still an open question that should perhaps be addressed on a functional point of view.

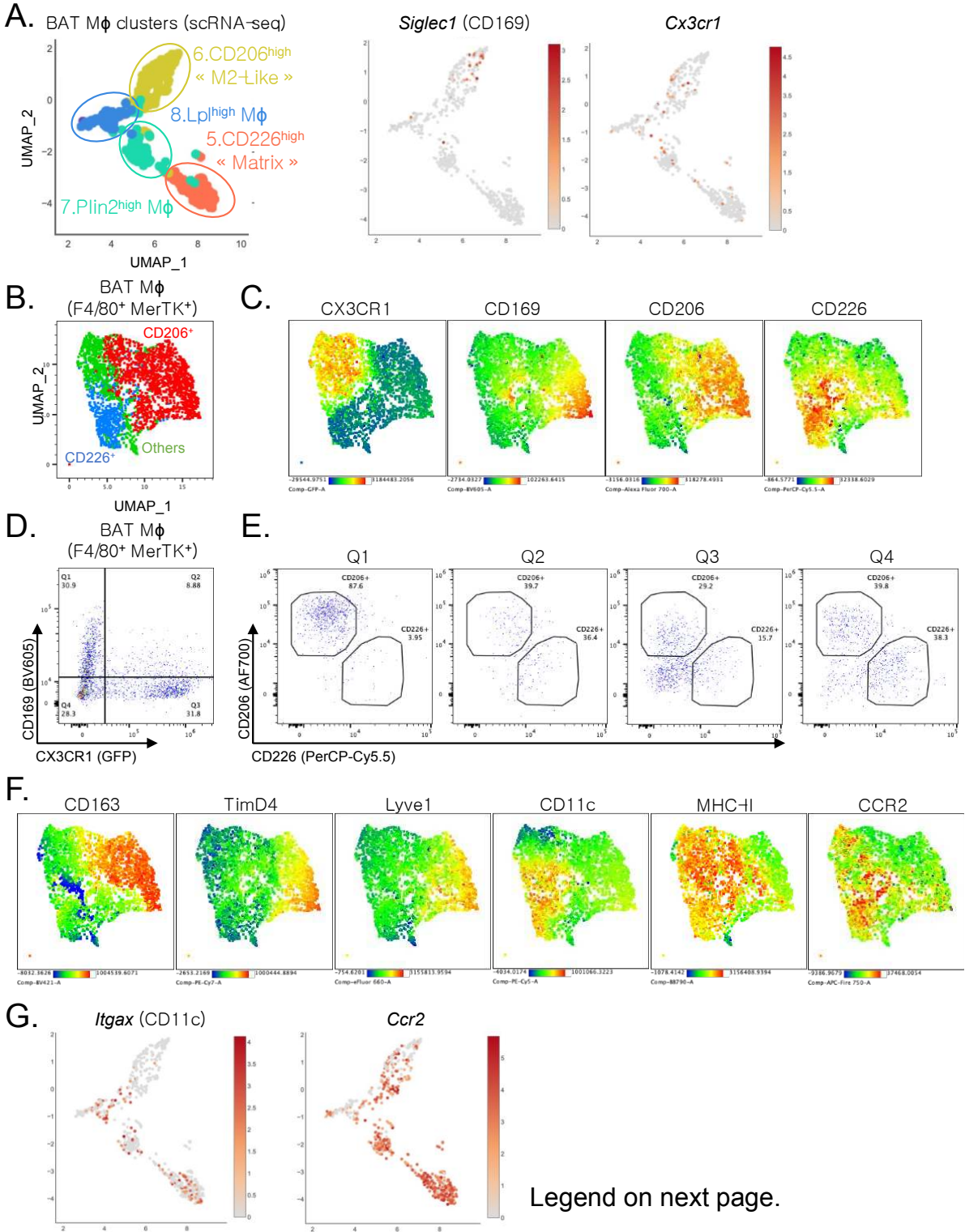


Figure 8. Diversity of brown adipose tissue macrophages.

(A) UMAP representation of the four macrophage clusters from our scRNA-seq sequencing of BAT immune cells, and their expression of *Siglec1* and *Cx3cr1*. (B) UMAP representation of BAT macrophages analyzed by flow cytometry. CD206⁺, CD226⁺ and CD206⁻ CD226⁻ cells were manually gated and overlaid on the UMAP plot. (C) Representation of CX3CR1, CD169, CD206 and CD226 expression by BAT macrophages. (D,E) Supervised flow cytometry analysis of BAT macrophage subsets. (F) Representation of CD163, TimD4, Lyve1, CD11c, MHC-II and CCR2 expression by BAT macrophages. (G) scRNA-seq analysis of *Itgax* and *Ccr2* expression by BAT macrophages.

b. Functions of BAT monocytes and macrophages

The functions of BAT myeloid cells have only recently started to be addressed, and they remain poorly explored. A previous study suggested that CX3CR1⁺ macrophages interact with BAT neurons and control the sympathetic neuronal network density to regulate thermogenesis²⁶⁸. The interaction of CX3CR1⁺ macrophages with neurons appears to be a conserved feature across organs³³. This particular distribution likely reflects on a specific set of proteins allowing residence in a specialized niche. For example, CX3CR1 expression could be imprinted on macrophages by neurons on a microenvironmental scale, and thus reflect tissue localization. Whether BAT neurons express the CX3CR1 ligand CX3CL1 is undetermined. However, in CX3CR1^{GFP/GFP} mice macrophages remain still in close proximity to neurons, suggesting that this chemokine receptor might not be solely responsible for their particular localization.

BAT macrophages were proposed to interact with nearby neurons in a PlexinA4-dependent manner²⁶⁸. Curiously, *Plxna4* mRNA could only be detected in M2M ϕ and MaM ϕ in our scRNA-seq data (Figure 9A), and these subsets contain few CX3CR1⁺ cells. Our data suggest that the CX3CR1⁺ macrophage population might be heterogenous and contain cells identified as clusters 7 and 8 in our scRNA-seq. It is possible that macrophages from clusters 7 and 8 express *Plxna4* at a level below the detection threshold of our scRNA-seq. Indeed, bulk RNA-seq of BAT macrophages identified a higher expression of *Plxna4* in CX3CR1⁺ macrophages compared to their CX3CR1⁻ counterpart²⁶⁸. However, the fact that we clearly detect *Plxna4* mRNA in M2M ϕ and MaM ϕ suggests that attributing the role of regulating tissue innervation selectively to CX3CR1⁺ macrophages might have been an oversimplification by *Wolf et al.*. Moreover, this study relies on the use of CX3CR1^{cre} mice which, as they

demonstrate, labels 90% of BAT macrophages. This is in full adequation with our observation that monocytes actively contribute to the BAT macrophage pool. Using CX3CR1^{creERT2/GFP} x R26^{TdTomato} double reporter mice, we have also observed the presence of GFP⁻ TdTomato⁺ macrophages after one week of tamoxifen treatment (Figure 9B). This result demonstrates that CX3CR1⁺ macrophages can give rise to CX3CR1⁻ macrophages, as was suggested by our slingshot analysis. The use of *Cx3cr1*-driven cre models therefore appears inappropriate for the study of BAT macrophage subsets. Thus, although BAT macrophages seemingly regulate tissue innervation, the fact that this function could be strictly restricted to a subset of macrophages defined by CX3CR1 expression appears unsure.

The intra-organ distribution of the BAT macrophage subsets we identified is yet to be established. Our preliminary data suggest that CD226⁺ MaM ϕ are localized near cells from the nervous system at steady state (data not shown). The observation that MaM ϕ are intimately associated with neurons is rather puzzling since only a small proportion of CD226⁺ cells express CX3CR1. As mentioned before, *Plxna4* mRNA is detectable in CD226⁺ macrophages. This result suggests that several macrophage subsets might interact with BAT neurons in the very same microenvironment. Whether selective BAT macrophage subsets preferentially interact with specific neurons remains to be defined. One might hypothesize that interaction of CX3CR1⁺ M ϕ and MaM ϕ with neurons could trigger different effects on tissue physiology, and the functional consequences of this observation remain to be established. Interestingly, macrophages from clusters 7 and 8 greatly accumulate in our BAT expansion model and we observed CX3CR1⁺ macrophages forming crown-like structures in this condition. On a transcriptomic level, these cells (and especially cluster 8) display a phenotype similar to recently-described lipid-associated macrophages¹⁵⁶, characterized by expression of CD9, CD63 and Trem2 (Figure 9C). Together, these results suggest that macrophages that accumulate during lipid overload may be specialized in lipid detoxification and removal of damaged adipocytes (especially because lipid storage is not the *bona fide* function of brown adipocytes). Moreover, they demonstrate that CX3CR1⁺ macrophages do not only interact with neurons.

A more recent study using CD169^{DTR} mice linked CD169⁺ BAT macrophages to recycling of damages mitochondria, a mechanism essential for optimal thermogenesis³⁵¹. Our data demonstrated that CD169⁺ macrophages are a part of our

M2M ϕ cluster and thus suggest that CD169^{DTR} mice represent a good model to specifically study this macrophage population (i.e. depletion of CD169⁺ macrophages does not affect other clusters). Interestingly, CD169⁺ macrophages are scarce in BAT at thermoneutrality and they accumulate upon cold exposure³⁵¹. Whether these cells arise from monocytes or represent a maturation state of CD206⁺ macrophages is unknown. Our flow cytometry data show a co-expression of CD169 and Timd4 by a subset of M2M ϕ at 22°C. Although this result supports the maturation hypothesis (because monocytes do not give rise to Timd4⁺ macrophages), this remains to be addressed using proper fate-mapping tools such as the Mrc1^{creERT2} mouse¹⁵¹. Our preliminary data show a close association of CD206⁺ cells with blood endothelial cells, though the molecular mechanism regulating this interaction remains to be identified. A subset of M2M ϕ in BAT expresses Lyve1 which was previously implicated in governing macrophage interaction with endothelial cells²⁶⁹. Moreover, CD206⁺ macrophages are able to uptake blood-borne material, while MaM ϕ barely do so (data not shown). Whether all CD206⁺ macrophages or solely the Lyve1⁺ CD206⁺ subset survey the blood circulation remains to be tested. Our scRNA-seq data suggest that the population of BAT M2M ϕ actively metabolizes lipids. Moreover, the lipid content of these cells is higher than that of MaM ϕ suggesting a specialized lipid-associated function (data not shown). A recent report showed that depletion of macrophages altered lipid storage in white adipose tissue and the liver during obesity, and this was linked to production of PDGF α by macrophages³³⁹. We also observed this phenotype in BAT using the same approach (data not shown) and PDGF α is selectively expressed by M2M ϕ (Figure 9D), suggesting that the same mechanism might be at play in brown adipose tissue. Whether BAT M2M ϕ affect adipocyte lipid storage by other mechanisms remains to be tested.

Using genetic reporters, we observed a robust contribution of monocytes to the BAT macrophage pool. This mechanism was CCR2-dependent and we consequently observed numerous CCR2-GFP⁺ BAT macrophages. Importantly, triggering BAT expansion by invalidating adipose triglyceride lipase (ATGL) in adipocytes led to accelerated monocyte recruitment through the CCL2-CCR2 axis and increased macrophage counts. Depleting monocytes chronically using the anti-CCR2 monoclonal antibody MC-21 after induction of ATGL deletion reduced BAT expansion, suggesting that monocytes play a role in tissue remodeling. As a consequence, brown

adipocyte lipid droplets retained a multilocular structure, a feature of steady state BAT. However, monocyte depletion also led to an increase in CLS, suggesting increased adipocyte death. It therefore appears that recruitment of CCR2⁺ cells is necessary for BAT expansion, adaptation to lipid overload and maintenance of homeostasis. Interestingly, this mechanism was not necessary for adaptation of white adipose tissue during obesity, suggesting the existence of BAT-specific mechanisms³³⁹. Although we did not observe increased collagen content in monocyte-depleted BAT (data not shown), we found increased numbers of α -SMA⁺ cells that were not located near blood vessels, suggesting the presence of activated fibroblasts. We therefore explored the hypothesis that monocytes might interact with fibroblasts to affect tissue remodeling. Monocytes were able to affect the shape and contractility of mouse embryonic fibroblasts (MEFs) *ex vivo*. Dendritic cells were previously reported to affect the expansion of lymph nodes through the Clec2-Podoplanin axis following immunization^{352,353}. We therefore tested whether the same mechanisms might be at play in our conditions. Adding an anti-Podoplanin (α -Pdpn) monoclonal antibody to our co-culture experiments blunted fibroblast activation, and Podoplanin blockade *in vivo* reduced BAT expansion. Curiously, monocyte counts tended to be augmented in α -Pdpn treated mice, possibly reflecting the induction of monocyte recruitment in absence of proper BAT expansion. As an example supporting this concept, *Ccl2* expression was increased in the BAT of MC-21 treated mice (bulk RNA seq data, not shown). This also suggests the existence of a dialogue between monocytes and niche cells, which in this case would sense the absence of monocytes and react via increased CCL2 production to compensate it. Although we were able to detect surface Clec2 expression on BAT monocytes and macrophages, we lack evidence that this Podoplanin ligand is involved in our experimental setup. Indeed, BAT myeloid cells express other Podoplanin ligands such as CD44 and CD9, and further work is required to determine the precise mechanisms governing monocyte-fibroblast interactions.

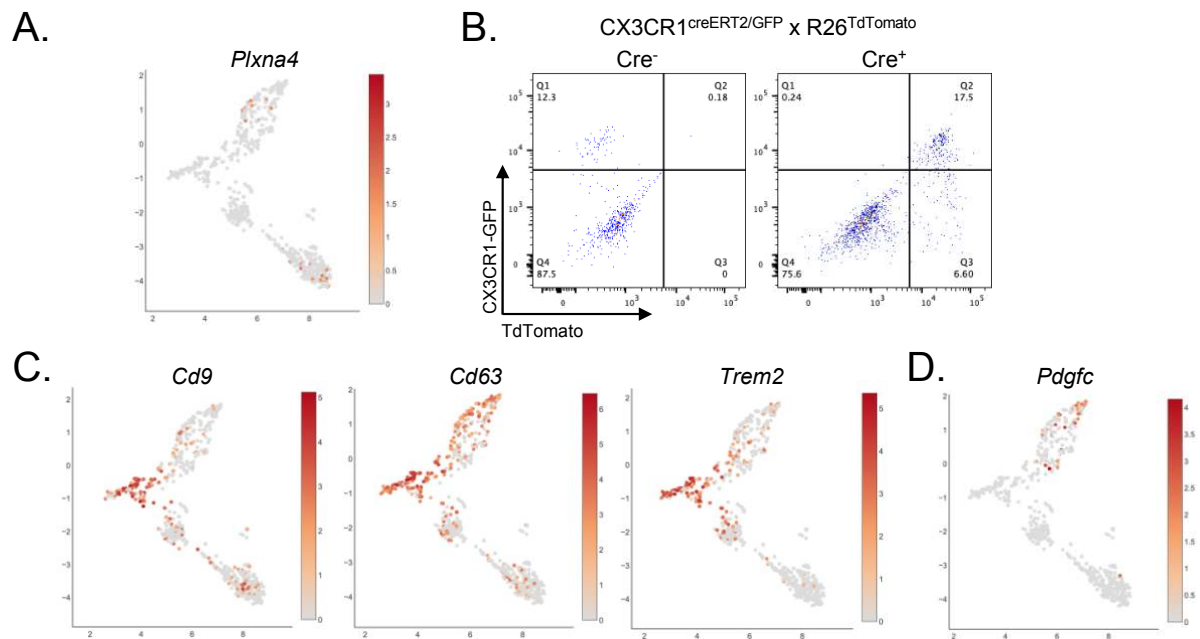


Figure 9. Clues on potential BAT macrophage functions.

(A) scRNA-seq analysis of *Plxna4* expression by BAT macrophages. (B) Flow cytometry analysis of GFP and TdTomato expression by BAT macrophages from *CX3CR1^{creERT2/GFP} × R26^{TdTomato}* mice which we treated with tamoxifen daily for 5 days, and analyzed 48hours after the last injection. (C) scRNA-seq analysis of *Cd9*, *Cd63*, *Trem2* and *Pdgfc* expression by BAT macrophages. (D) scRNA-seq analysis of *Pdgfc* expression by BAT macrophages.

c. Perspectives

Brown adipose tissue plays a key role during cold and stress exposure by generating heat which dissipates to sustain body temperature. To fulfil efficient thermogenesis, BAT burns glucose and triglycerides and stimulating BAT activation is emerging as a new treatment strategy in metabolic diseases. In rodents, prolonged BAT activation exerts a beneficial effect on the host metabolic status³⁵⁴. Chronic cold exposure triggers BAT remodelling and its expansion. The precise regulation of the different BAT subsets that we identified during acute and chronic cold exposure remains to be defined. Aging induces BAT remodelling characterized by increased number of larger lipid droplets and diminished thermogenic capacity. Whether this is correlated with a modulation of BAT macrophage subsets abundance and distribution is yet to be investigated. Given the key role of BAT macrophages in tissue innervation and the maintenance of the thermogenic program, this could an important direction to pursue.

During the past decade the presence of active BAT in adult humans was documented. BAT mass decreases with aging and following exposure to warm ambient temperature, thus limiting BAT contribution to the organism's energy balance^{355,356}. BAT presence in Humans was associated with lower blood glucose and triglyceride levels³⁵⁷. Furthermore, in Humans, BAT activity was correlated with lower body mass index (BMI)³⁵⁸. Stimulating BAT expansion and activity represents an interesting strategy to consider for the prevention of metabolic diseases. Therefore, should we identify BAT macrophages as *bona fide* regulators of tissue activity in preclinical models, we will investigate the translational potential of our observations. To obtain fresh BAT biopsies is challenging and represents a considerable hurdle to overcome in order to investigate BAT immune cell content in healthy and obese Humans.

In our study, we explored the diversity of brown adipose tissue immune cells at steady state and in a model of tissue expansion caused by invalidation of adipose lipolysis. Although we provided novel evidence on the diversity and maintenance of brown adipose tissue macrophages and monocytes, the canonical function of BAT – thermogenesis – is unaltered in our model. It is therefore of great interest to use our newly-acquired knowledge on the fundamental identity of BAT-resident myeloid cells to develop subset-specific tools and inquire about the precise function of each macrophage population in this tissue during thermogenesis. Such models are yet to be established but would provide an exciting new direction of research that we would like to embrace. A more in-depth analysis of each macrophage subset's transcriptome might provide insights about their precise functions and metabolic requirements. Our single-cell RNA-seq data did not reveal the existence of transcription factors specific for one macrophage cluster that may allow to selectively deplete a population when targeted. Still, we were able to identify some cluster-specific transcripts that may help to serve this goal. Future directions for the project include :

- Targeting MaM ϕ at steady-state and upon BAT activation (i.e. cold exposure) using Retnla^{cre} x R26^{TdTomato/DTR} mice. Transcripts specific for MaM ϕ (cluster 5) include CD226 and Retnla. Surface expression of CD226 greatly facilitated our identification of MaM ϕ by flow cytometry, but genetic tools using the *Cd226* promoter are lacking. However, Retnla^{cre} mice were recently generated and would allow specific tracking and targeting of this population³⁵⁹.

- Targeting M2M ϕ at steady-state and upon BAT activation using Mrc1^{creERT2} x R26^{TdTomato/DTR} mice. Although M2M ϕ (cluster 6) comprise several sub-populations that could be identified by their expression of CD163, Timd4 or Lyve1 (as discussed before), one could argue that these sub-populations are unified by a common transcriptome consisting of the “M2 macrophage” signature, therefore suggesting the existence of a common function for these cells. The use of a “broad” system such as the recently-published Mrc1^{creERT2} mouse¹⁵¹ could therefore be ideal to target M2M ϕ as a whole. It is tempting to speculate that other markers may rather reflect macrophage origin (Timd4 for embryonic macrophages, CD163 for long-term resident macrophages) or localization (Lyve1 for vessel-associated macrophages). However, as discussed above, targeting only CD169⁺ M2M ϕ yielded interesting results suggesting that sub-populations of M2M ϕ might also play restricted functions. For this reason, we could also envision using Lyve1^{cre 109-111} or CD163^{cre 360} mice to target specific macrophage populations.

- Targeting lipid-associated macrophages during lipid overload. We identified the accumulation of cluster 8 macrophages during brown adipose tissue expansion. This population is characterized by its expression of the “lipid-associated macrophage” signature which includes CD9, CD63 and Trem2. Recent evidence suggests that these cells might exert their function through Trem2¹⁵⁶. It would therefore be interesting to invalidate Trem2 in macrophages using LyzM^{cre} x Trem2^{fllox} mice (available within our network) in contexts of obesity, ageing or thermogenesis to study the function of this population.

- Exploring the function of other BAT myeloid cells. We robustly detected the presence of neutrophils and dendritic cells in BAT, and the function of these cells remains unknown. Whether BAT contains an abundant lymphatic vasculature is also unknown. It is tempting to speculate that thermogenic stress might increase the generation of immunogenic peptides (deriving from damaged mitochondria for example) that could trigger an immune response if taken up by DCs. Exploring BAT lymphatic drainage and T cell activation by BAT DCs in a context of thermogenesis or obesity could be an exciting perspective.

Project 2: Diversity and functions of adrenal gland macrophages.

A. Hypothesis and aims

The endocrine system is a central rheostat of the mammalian body that allows, through the production of different hormones, a systemic coordination of various physiological mechanisms. The adrenal glands are located on top of each kidney and adopt a zonated organization with a medulla in the center (producing catecholamines) and a surrounding cortex (producing predominantly glucocorticoids and mineralocorticoids) (figure 8). These hormones trigger behavioral changes, increase supply of metabolic fuels and impact cardiovascular performance. A pioneering study reported the presence of F4/80⁺ cells in both the adrenal cortex and medulla⁶. F4/80 expression is not restricted to macrophages and the precise diversity and function of macrophages in adrenal glands were unknown when we initiated the present study.

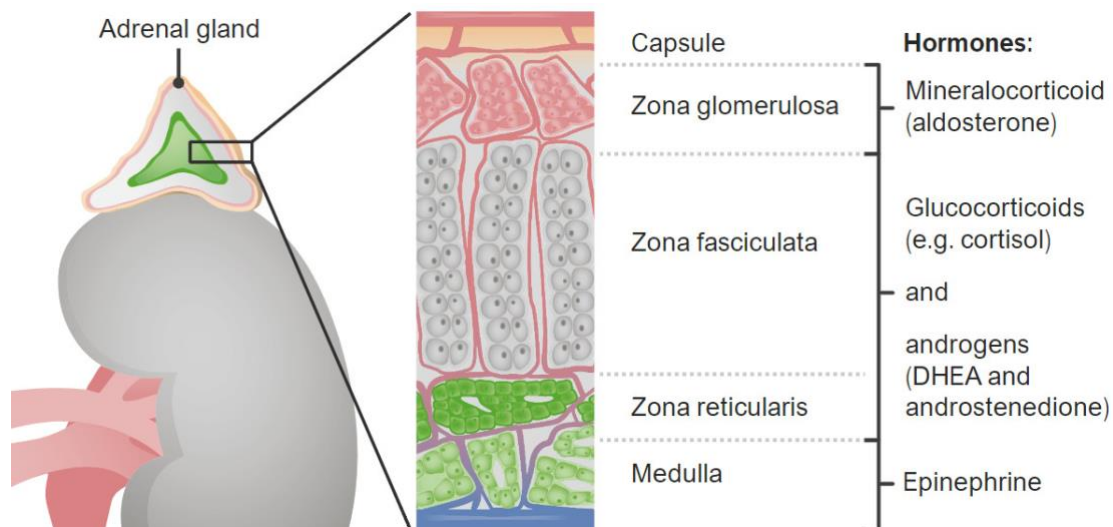


Figure 10. Schematic representation of adrenal gland organization and functions.

The adrenal gland is “two in one” organ composed of a cortex that originates from the mesoderm and encapsulates the medulla, which originates from the neuroectoderm. The cortex is further subdivided into three zones with restricted functions as depicted above. In mice, the zona reticularis is absent and a fetal remnant called the “X-zone” is found in its place. Image from lecturio.com.

In mice, the adrenal gland is a sexually-dimorphic organ³⁶¹ (figure 9). Recent reports showed sex-specific regulations of macrophage turnover and maintenance^{63,285,286}. We therefore hypothesized that the adrenal gland microenvironment might also contain elements – possibly specific niches – that would drive sex-specific macrophage diversity, providing the opportunity to further characterize tissue-resident macrophages in their specific microenvironment. In adipose tissue, macrophages are involved in neuron-derived norepinephrine clearance³³² and, because synthesis of specific hormones (such as aldosterone) are restricted to adrenal glands, we hypothesized that adrenal gland macrophages may also modulate local and systemic hormone levels.

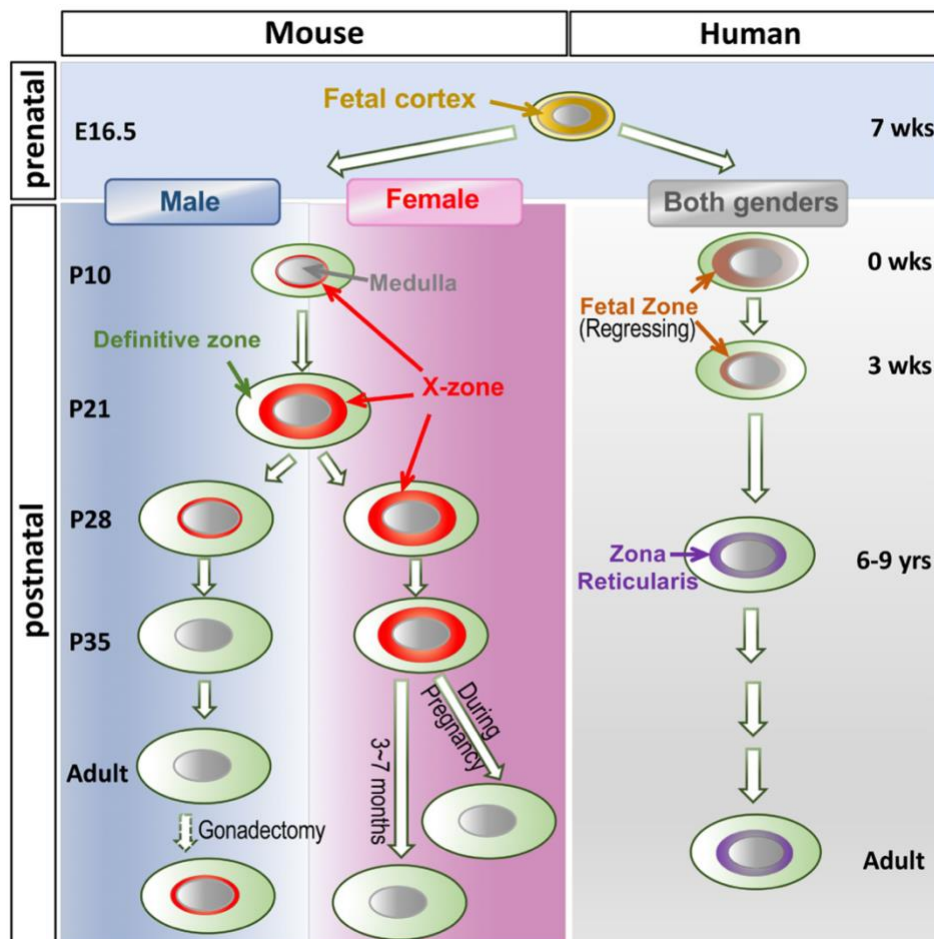
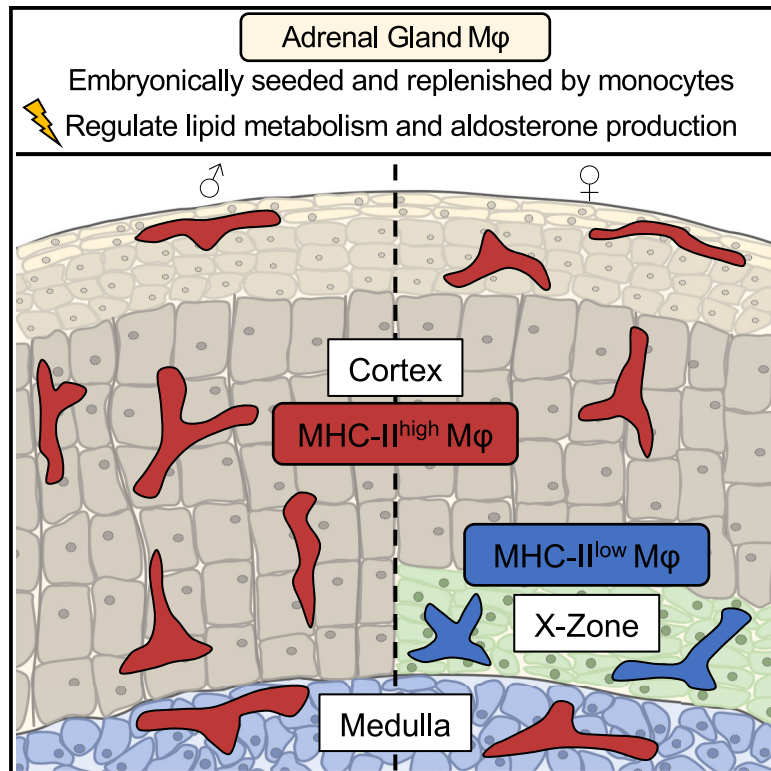


Figure 11. Development and evolution of the murine and human adrenal cortex.

Although X-zone presence easily allows identification of sex dimorphism in murine adrenal glands, the cortical structure is similar between both genders in humans. The murine X-zone is highly similar to the human fetal zone, although its regression only appears under the influence of androgens at puberty in males or during pregnancy in females. Figure from C-C Huang and Y Kang³⁶².

Unravelling the sex-specific diversity and functions of adrenal gland macrophages

Graphical abstract



Authors

Bastien Dolfi, Alexandre Gallerand, Maria M. Firulyova, ..., Rodolphe R. Guinamard, Jesse W. Williams, Stoyan Ivanov

Correspondence

jww@umn.edu (J.W.W.), stoyan.ivanov@unice.fr (S.I.)

In brief

Dolfi et al. uncover the sex-specific heterogeneity of adrenal gland macrophages and their ontogeny, maintenance, tissue distribution, and role in local lipid homeostasis.

Highlights

- Adrenal glands contain multiple macrophage populations
- Macrophage sex dimorphism depends on the presence of the cortical X zone
- Embryonic and monocyte-derived macrophages co-exist in adrenal glands
- Adrenal gland macrophage depletion alters tissue lipid metabolism



Article

Unravelling the sex-specific diversity and functions of adrenal gland macrophages

Bastien Dolfi,^{1,9,17} Alexandre Gallerand,^{1,9,17} Maria M. Firulyova,² Yingzheng Xu,³ Johanna Merlin,¹ Adélie Dumont,¹ Alexia Castiglione,¹ Nathalie Vaillant,¹ Sandrine Quemener,⁴ Heidi Gerke,^{5,6} Marion I. Stunault,¹ Patricia R. Schrank,³ Seung-Hyeon Kim,⁷ Alisha Zhu,³ Jie Ding,⁷ Jerome Gilleron,¹ Virginie Magnone,⁸ Pascal Barbry,⁸ David Dombrowicz,⁴ Christophe Duranton,⁹ Abdelilah Wakkach,⁹ Claudine Blin-Wakkach,⁹ Burkhard Becher,¹⁰ Sophie Pagnotta,¹¹ Rafael J. Argüello,¹² Pia Rantakari,^{5,6} Svetoslav Chakarov,¹³ Florent Ginhoux,^{13,14,15,16} Konstantin Zaitsev,² Ki-Wook Kim,⁷ Laurent Yvan-Charvet,¹ Rodolphe R. Guinamard,^{1,9} Jesse W. Williams,^{3,*} and Stoyan Ivanov^{1,9,18,*}

¹Université Côte d'Azur, INSERM, C3M, Nice, France

²Computer Technologies Department, ITMO University, Saint Petersburg, Russia

³Center for Immunology, Department of Integrative Biology and Physiology, University of Minnesota Medical School, Minneapolis, MN, USA

⁴Univ.Lille, INSERM, CHU Lille, Institut Pasteur de Lille, U1011-EGID, 59000 Lille, France

⁵Turku Bioscience Centre, University of Turku and Åbo Akademi University, Turku, Finland

⁶InFLAMES Research Flagship Center, University of Turku, Turku, Finland

⁷Department of Pharmacology and Regenerative Medicine, University of Illinois College of Medicine, Chicago, IL, USA

⁸Université Côte d'Azur, CNRS, IPMC, Valbonne, France

⁹Université Côte d'Azur, CNRS, LP2M, Nice, France

¹⁰Institute of Experimental Immunology, University of Zürich, Switzerland

¹¹Université Côte d'Azur, Centre Commun de Microscopie Appliquée (CCMA), Parc Valrose, 06108 Nice, France

¹²Aix Marseille Université, CNRS, INSERM, CIML, Centre d'Immunologie de Marseille-Luminy, Marseille, France

¹³Shanghai Institute of Immunology, Shanghai Jiao Tong University School of Medicine, Shanghai 200025, China

¹⁴Singapore Immunology Network (SigN), Agency for Science, Technology and Research (A*)STAR, Singapore 138648, Singapore

¹⁵Department of Microbiology and Immunology, Immunology Translational Research Program, Yong Loo Lin School of Medicine, Immunology Program, Life Sciences Institute, National University of Singapore, Singapore 117543, Singapore

¹⁶Translational Immunology Institute, SingHealth Duke-NUS Academic Medical Centre, Singapore 169856, Singapore

¹⁷These authors contributed equally

¹⁸Lead contact

*Correspondence: jww@umn.edu (J.W.W.), stoyan.ivanov@unice.fr (S.I.)

<https://doi.org/10.1016/j.celrep.2022.110949>

SUMMARY

Despite the ubiquitous function of macrophages across the body, the diversity, origin, and function of adrenal gland macrophages remain largely unknown. We define the heterogeneity of adrenal gland immune cells using single-cell RNA sequencing and use genetic models to explore the developmental mechanisms yielding macrophage diversity. We define populations of monocyte-derived and embryonically seeded adrenal gland macrophages and identify a female-specific subset with low major histocompatibility complex (MHC) class II expression. In adulthood, monocyte recruitment dominates adrenal gland macrophage maintenance in female mice. Adrenal gland macrophage sub-tissular distribution follows a sex-dimorphic pattern, with MHC class II^{low} macrophages located at the cortico-medullary junction. Macrophage sex dimorphism depends on the presence of the cortical X-zone. Adrenal gland macrophage depletion results in altered tissue homeostasis, modulated lipid metabolism, and decreased local aldosterone production during stress exposure. Overall, these data reveal the heterogeneity of adrenal gland macrophages and point toward sex-restricted distribution and functions of these cells.

INTRODUCTION

Tissue resident macrophages play a key role in health and disease (Cox et al., 2021). Macrophages are present at diverse frequencies in all tissues, and they are identified by the expression of the surface receptors CD64 and MerTK (Gautier et al., 2012). Their functions can be organ specific and are dictated by the local microenvironment. For example, brown adipose tissue (BAT) macrophages regulate adipocyte heat production, and

spleen macrophages capture iron (Kohyama et al., 2009; Wolf et al., 2017). Tissue-resident macrophages originate from embryonic or bone marrow precursors (Epelman et al., 2014). For instance, microglia at steady state are strictly derived from yolk sac progenitors, while intestinal lamina propria macrophages are entirely monocyte derived (Bain et al., 2014; Ginhoux et al., 2010; Gomez Perdiguero et al., 2015; Schulz et al., 2012). In general, populations of embryonically and bone-marrow-derived cells co-exist in adult peripheral tissues (Ensan et al., 2016). A



seminal work in heart established that a self-renewing tissue-resident macrophage subset possesses tissue-remodeling functions during inflammatory events, whereas monocyte-derived cells have a pro-inflammatory phenotype (Dick et al., 2019). During aging, monocyte-derived macrophages progressively replace embryonically derived macrophages (Ginhoux and Guilleliams, 2016; Molawi et al., 2014). Sex-specific differences in macrophage maintenance have been documented, suggesting that macrophage populations might display a sex-dependent diversity and function (Bain et al., 2016, 2020). Among other tissues, macrophages have been described in endocrine organs including pancreas, testis, and ovaries (Calderon et al., 2015; Ferris et al., 2017; Jokela et al., 2020; Lokka et al., 2020; Mossa-degh-Keller et al., 2017). Yet, the diversity, phenotype, and functions of endocrine organ macrophages remain to be completely elucidated.

The adrenal gland is composed of a medulla and a cortex. In humans, the cortex can be further divided into three zones: zona glomerulosa, zona fasciculata, and zona reticularis. In mice, the zona reticularis is called the X zone and displays sex-dependent regulation. Mouse adrenal glands present sexually dimorphic organization, size, and functions (Lyraki and Schedl, 2021). Female adrenal glands are heavier than their male counterparts, which are characterized by a slower growth rate (Biellohuby et al., 2007). Importantly, adrenal gland pathologies occur earlier in life and with higher incidence in women than in men (Audenet et al., 2013; Lacroix et al., 2015). The presence of F4/80⁺ cells, likely macrophages, was demonstrated in adrenal glands by a pioneering work (Hume et al., 1984). However, recent reports established that F4/80 expression was shared among several myeloid cell types, including macrophages, monocytes, dendritic cells (DCs), and eosinophils (Ginhoux et al., 2009). Whether the sex-specific regulation of adrenal gland tissue homeostasis is paralleled by sex dimorphism in macrophage diversity and function is not yet documented. Furthermore, adrenal gland immune cell sex dimorphism could also contribute to adrenal pathologies initiation and progression.

RESULTS

Adrenal gland macrophage identification and topology

To evaluate immune cell diversity in adrenal glands, we performed a flow-cytometry analysis of adrenal gland CD45⁺ cells from 7-week-old C57BL/6 mice, with a particular focus on macrophage and monocyte subsets. Macrophages were identified as CD64⁺MerTK⁺ cells and monocytes as CD64⁺MerTK⁻ cells (Figure S1A) (Jakubzick et al., 2013). Neutrophils were scarce in this tissue, suggesting low blood contamination in our analysis (Figure S1A, bottom panel). The adrenal gland is composed of a cortex and a medulla responsible for selective hormone production. Because adrenal glands display a sex-specific organization in adult mice, we analyzed both female and male animals. Although macrophage numbers were similar in both sexes, higher monocyte counts tended to be detected in females (Figure 1A). DCs, identified as CD64⁺MerTK⁻MHC-II⁺CD11c⁺ cells, were also present in low numbers in adrenal glands without sex-specific differences (Figures 1A and S1A). Neutrophil, B cell, and T cell counts were similar between female

and male mice (Figure S1B). To further characterize the phenotype of adrenal gland immune cells in female and male mice, we performed spectral flow cytometry (Figure S1C). Unsupervised analysis confirmed the presence of diverse immune cell clusters in adrenal glands (Figure S1D). These clusters corresponding to populations of macrophages, monocytes, DCs, neutrophils, B cells, and CD4⁺ and CD8⁺ T cells expressed characteristic markers (Figure S1E). Notably, adrenal gland macrophages (AGMs) uniformly expressed F4/80 and the integrins CD11b and CD11c (Figures 1B and S1E).

Next, we investigated macrophage topologic distribution. F4/80⁺ cells were observed both in the adrenal gland cortex and medulla (Figure S1F). To further validate that these cells were macrophages, we used macrophage reporter strains, including Lyz2^{cre} x R26^{TdTomato} and CD115^{creERT2} x R26^{TdTomato} mice. Virtually 100% of macrophages were labeled in Lyz2^{cre} x R26^{TdTomato} mice (Figure S1G). In those models, we found that R26^{TdTomato} macrophages were present in both the adrenal cortex and the medulla (Figures 1C and 1D). Using CX3CR1^{GFP/+} reporter mice, we found that CX3CR1 was expressed by most AGMs in both female and male mice (Figures 1E and S1F). The number of CX3CR1⁺ macrophages was similar in female and male mice (Figure 1E). The distribution of CX3CR1^{GFP+} cells in adrenal glands followed a sex-specific pattern, with a quasi-uniform distribution in both cortex and medulla in male mice (Figure 1F). By contrast, in females, CX3CR1^{GFP+} cells were preferentially located under the adrenal capsule and at the border between the cortex and the medulla (Figure 1F). These data revealed a sex-specific pattern of AGM distribution.

AGM diversity and mechanisms controlling their homeostatic maintenance

To obtain further insights on the sex-specific myeloid cell diversity in adrenal glands and their specific functions, we performed single-cell RNA sequencing (scRNA-seq) analysis on cell-sorted CD45⁺ cells isolated from 7-week-old C57BL/6 female and male mice (Figure 2A). Doublet contamination was identified and removed from the analysis (Figure S2A). Data from female and male mice were integrated with Seurat and projection maps made using uniform manifold approximation and projection (UMAP). Our data revealed a diversity in immune cell populations residing within the adrenal glands of both sexes (Figures 2A and S2B). In line with our flow-cytometry data, monocytes, DCs, neutrophils, B cells, and T cells were present in adrenal glands (Figure 2A). Natural killer (NK) cells and a population of innate lymphoid cells (ILCs) were also identified (Figure 2A). Flow-cytometry analysis confirmed the presence of NK cells and Klrp1⁺NK1.1⁻CD3⁻ ILCs in adrenal glands (Figure S2C). Importantly, and in agreement with our flow-cytometry observations, macrophages were the most abundant immune cell type (Figures 2A and 2B). We observed the presence of 4 separate and well-defined macrophage clusters (clusters 2–5) in both female and male mice (Figure 2A). All macrophage clusters expressed Mertk mRNA (Figure S2D). Our scRNA-seq data revealed that all four macrophage populations also expressed the canonical macrophage markers *Lyz2*, *CD68*, *CD11b* (*Itgam*), *CD64* (*Fcgr1*), and *F4/80* (*Adgre1*) in both sexes (Figures S2B and S2E). *CD11c* (*Itgax*) was also expressed on AGMs

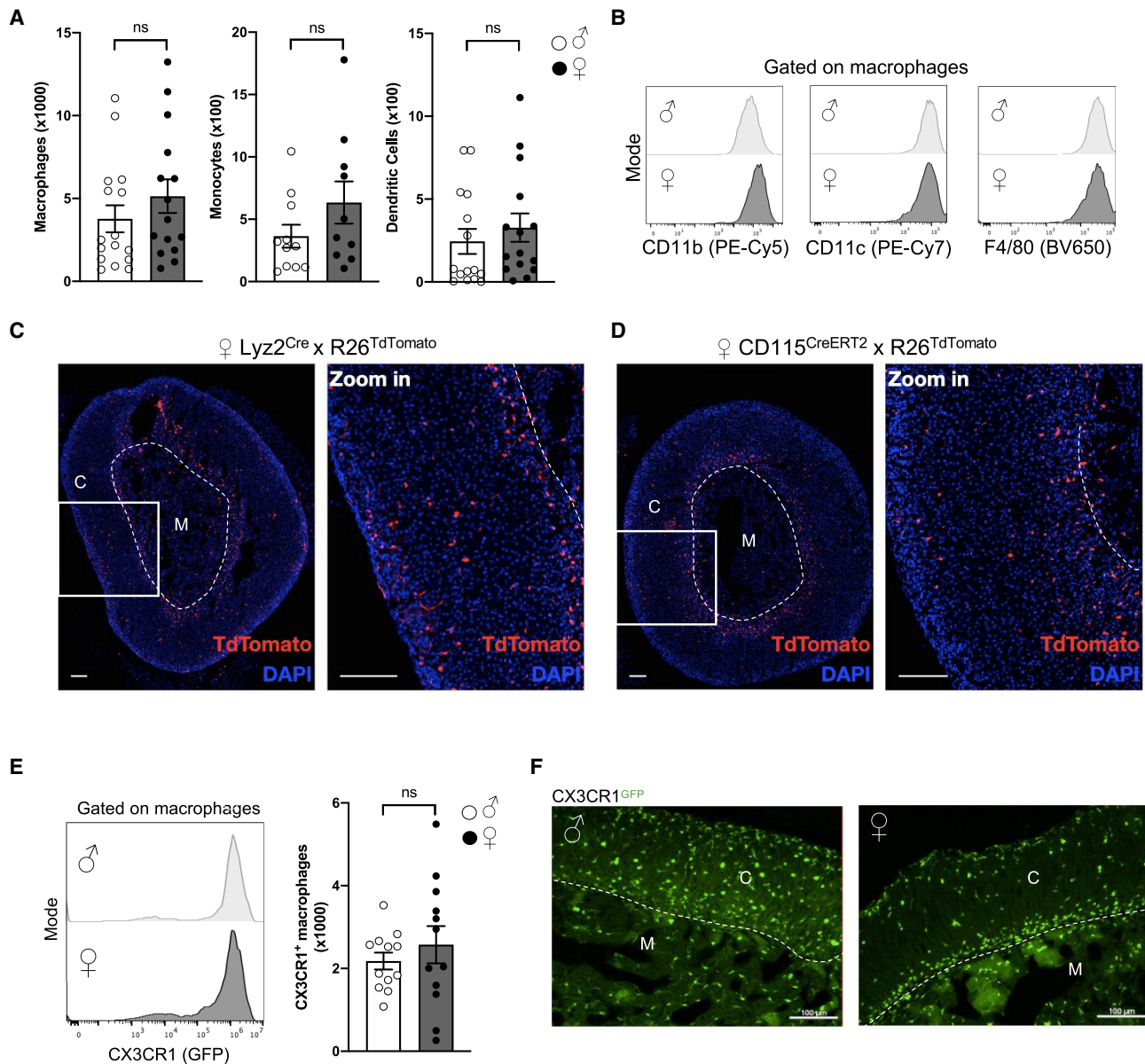
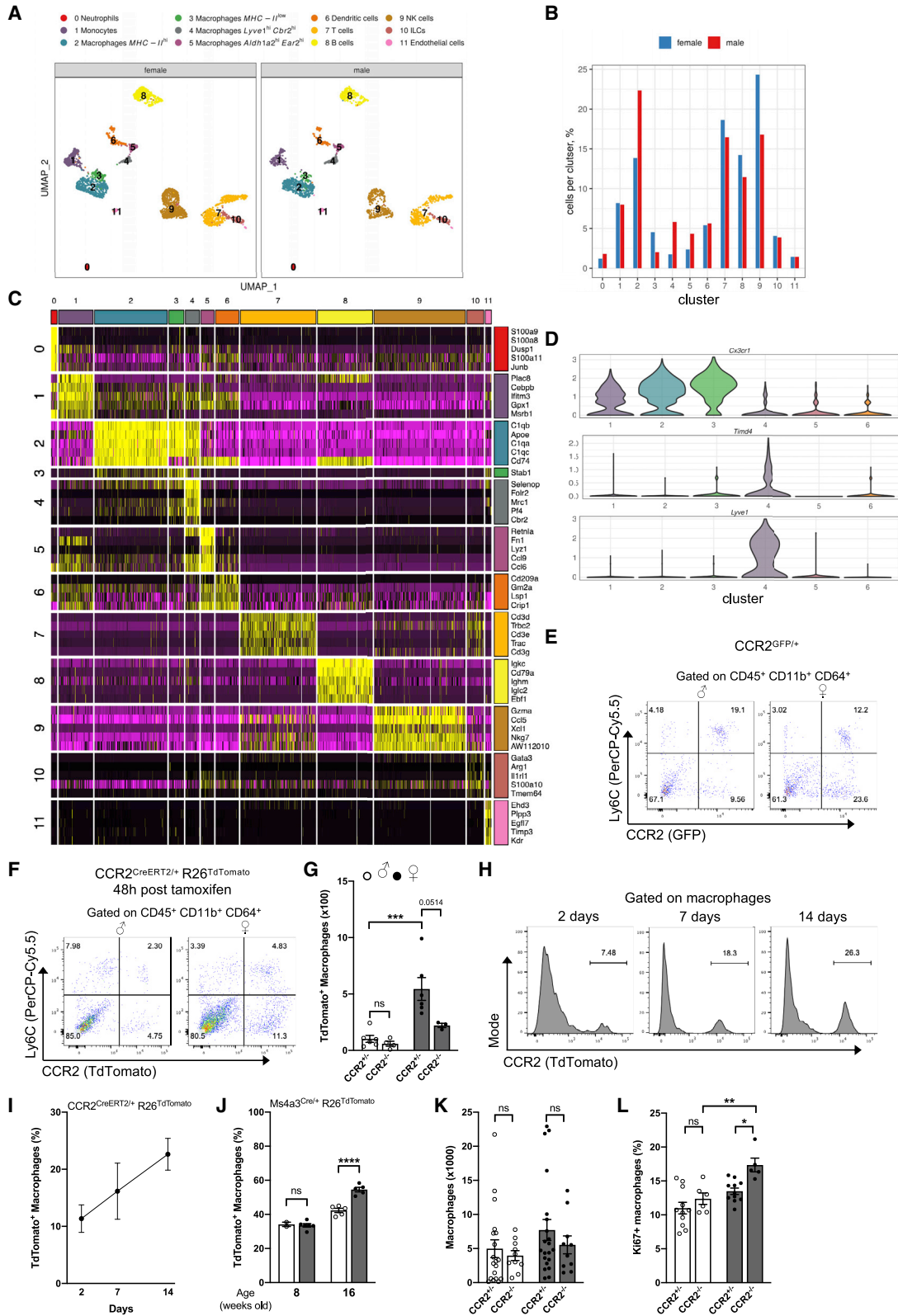


Figure 1. Macrophages are the main adrenal gland immune subset and possess a sex-specific localization

(A) Quantification of macrophages, monocytes, and DCs in the adrenal glands of 7-week-old male and female wild-type mice. Macrophages: ♂ n = 16 and ♀ n = 15. Monocytes: ♂ n = 11 and ♀ n = 10. DCs: ♂ and ♀ n = 15. Data pooled from 2 (monocytes) or 3 (macrophages and DCs) independent experiments. (B) Histograms representing CD11b, CD11c, and F4/80 expression on male and female AGMs. Data are representative of at least 4 independent experiments. (C and D) Representative images of R26^{TdTomato} expression in adrenal glands from 10- to 12-week-old female Lyz2^{Cre} (C) and CD115^{CreERT2} (D) mice 24 h after TAM administration. Scale bars: 100 μm. Data are from one experiment. (E) Flow-cytometry analysis of CX3CR1^{GFP} expression in male and female AGMs. ♂ n = 12 and ♀ n = 12. Data are pooled from 3 independent experiments. (F) Microscopy analysis of CX3CR1⁺ cells localization in 8-week-old male and female (nulliparous) CX3CR1^{GFP/+} mice. Scale bar: 100 μm. Data are representative of at least 4 independent experiments. Two-tailed Mann-Whitney tests were used for statistical analysis. See also Figure S1 and Table S1.

(Figure S2E). We identified two major macrophage clusters that were characterized by high or low MHC class II expression (clusters 2 and 3, respectively). Importantly, the proportion of macrophage subsets was different between female and male mice, with a specific enrichment of MHC class II^{low} macrophages in females, while MHC class II^{high} macrophages were more

abundant in males (Figure 2B). Two additional macrophage populations expressing Lyve1 (cluster 4) or Aldh1a2 (cluster 5) were present in both female and male mice (Figure 2A). We observed that myeloid cells presented a highly conserved signature between females and males, with only a few genes being differentially expressed between sexes (Table S1). Among those,



(legend on next page)

Ly6A (Sca1) and ApoC2 mRNAs were highly expressed in female macrophages compared with their male counterparts (Figure S2F). Flow-cytometry analysis of surface Sca1 protein distribution confirmed a higher expression on AGMs isolated from female mice when compared with males (Figure S2G). Among the four macrophage clusters, we found a transcriptional diversity, suggesting a particular developmental origin, localization, or function for each cluster (Figure 2C; Data S1 and S2). The macrophage clusters 2 and 3 expressed *Cx3cr1* mRNA, while clusters 4 and 5 appeared to have lower *Cx3cr1* expression (Figure 2D). Of interest, *Lyve1* and *Timd4* mRNA expression were restricted to macrophage cluster 4 (Figure 2D).

Tissue-resident macrophage numbers are regulated by monocyte recruitment from the blood circulation or local self-proliferation (Ginhoux and Guillemins, 2016). Thus, we next sought to determine the contribution of monocytes to AGM pool size. For this purpose, we took advantage of *CCR2^{GFP}*-reporter mice. *CCR2* is a chemokine receptor highly expressed on monocytes and involved both in their export from bone marrow to blood and in their recruitment to tissues. We found that the population of adrenal gland CD11b⁺CD64⁺ cells, containing both monocytes and macrophages, comprised numerous *CCR2⁺* cells in both sexes (Figure 2E). These cells were detected both in the monocyte (Ly6C^{high}) and the macrophage (Ly6C^{low}) populations (Figure 2E). This observation was further supported by our scRNA-seq data, where *Ccr2* mRNA expression was detected both in monocyte and macrophage clusters (Figure S2H). This result suggested that monocytes might be constantly recruited into adrenal glands, in which they differentiate into macrophages. To evaluate monocyte contribution to the AGM pool size, we performed a short-term fate-mapping experiment. For this purpose, *CCR2^{creERT2}* × *R26^{TdTomato}* mice were administered with tamoxifen (TAM), and we analyzed adrenal glands 48 h later. We detected a large fraction of *R26^{TdTomato}*⁺ cells in adrenal glands, demonstrating that monocyte recruitment plays a central role to maintain macrophage pool homeostasis

(Figure 2F). Importantly, monocyte recruitment was decreased in *CCR2*-deficient female mice (Figure 2G). Furthermore, we found that monocyte recruitment to adrenal glands was more robust in females when compared with age-matched males (Figures 2F and 2G). To determine monocyte fate in adrenal glands, we next performed time course pulse-chase experiments where *CCR2^{creERT2}* × *R26^{TdTomato}* mice were administered with TAM and analyzed 2, 7, and 14 days later. Two days post TAM injection, around 10% of AGMs were *R26^{TdTomato}*⁺ (Figures 2H and 2I). At days 7 and 14, the percentage of *R26^{TdTomato}*⁺ macrophages slowly and progressively increased to nearly 20% of the total macrophage population (Figures 2H and 2I). To confirm the contribution of monocytes to AGM pool size, we took advantage of *Ms4a3^{cre}* × *R26^{TdTomato}* mice (Liu et al., 2019). *Ms4a3* is specifically and transiently expressed by monocyte precursors in the bone marrow and absent from tissue macrophages. It therefore could cope with potential direct labeling of tissue macrophages in *CCR2* fate mapping. In this genetic model, monocyte-derived cells are labeled, and their numbers can be estimated in tissues. The relative abundance of TdTomato⁺ macrophages was similar in 8-week-old male and female mice (Figure 2J). However, in older 16-week-old animals, the percentage of TdTomato⁺ macrophages was significantly increased in female mice compared with in males (Figure 2J). This result further supports our observation that monocyte recruitment to adrenal glands is more robust in females than males. Finally, in order to determine whether monocyte recruitment is mandatory to sustain AGM populations, we quantified macrophages in *CCR2*-deficient mice, which have severely reduced blood monocyte counts (Serbina and Pamer, 2006). We observed that macrophage counts remained similar in *CCR2*-sufficient and -deficient mice (Figure 2K). This suggests that a compensatory mechanism occurs to ensure the maintenance of tissue macrophage density in the absence of optimal monocyte recruitment. These data suggest that monocyte recruitment plays an important role in the maintenance of AGM

Figure 2. scRNA-seq analysis reveals adrenal gland leukocyte diversity and monocyte contribution to the macrophage pool

- (A) scRNA-seq analysis of adrenal gland CD45⁺ cells from 7-week-old male and female wild-type mice.
- (B) Proportion of each cluster identified in scRNA-seq analysis.
- (C) Heatmap showing normalized expression levels of cluster-specific genes.
- (D) Violin plots showing *Cx3cr1*, *Timd4*, and *Lyve1* expression by cells from clusters 1–6.
- (E) Flow-cytometry plot showing Ly6C and *CCR2^{GFP}* expression among adrenal gland CD45⁺CD11b⁺CD64⁺ cells in male and female *CCR2^{GFP/+}* mice. Data are representative of three independent experiments.
- (F) Flow-cytometry plot showing Ly6C and TdTomato expression among adrenal gland CD45⁺CD11b⁺CD64⁺ cells from male and female *CCR2^{creERT2}* × *R26^{TdTomato}* mice 48 h after TAM gavage. Data are representative of two independent experiments.
- (G) Quantification of TdTomato⁺ macrophages in 16- to 20-week-old male and female heterozygous (*CCR2^{+/-}*, ♂ n = 6 and ♀ n = 6) or double knockin (*CCR2^{-/-}*, ♂ n = 4 and ♀ n = 3) *CCR2^{creERT2}* × *R26^{TdTomato}* mice 48 h after TAM gavage. Data are pooled from two independent experiments.
- (H) Histograms representing *R26^{TdTomato}* expression in AGMs from 10-week-old female *CCR2^{creERT2/+}* × *R26^{TdTomato}* mice 2, 7, and 14 days after TAM gavage. Data are representative of one (days 7 and 14) or two (day 2) experiments.
- (I) Proportions of TdTomato⁺ macrophages from 10-week-old female *CCR2^{creERT2/+}* × *R26^{TdTomato}* mice 2 (n = 8), 7 (n = 4), and 14 (n = 3) days after TAM gavage. Data from one (days 7 and 14) or two (day 2) experiments.
- (J) Proportions of TdTomato⁺ macrophages from 8 (♂ n = 2, ♀ n = 6) or 16 (♂ n = 5, ♀ n = 5)-week-old male and female *Ms4a3^{cre/+}* × *R26^{TdTomato}* mice. Data are from one experiment.
- (K) Quantification of AGMs in male and female *CCR2^{+/-}* (♂ n = 18, ♀ n = 21) and *CCR2^{-/-}* (♂ n = 10, ♀ n = 10) mice. Data are pooled from four independent experiments.
- (L) Proportions of Ki67⁺ AGMs in male and female *CCR2^{+/-}* (♂ n = 11, ♀ n = 11) and *CCR2^{-/-}* (♂ n = 6, ♀ n = 5) mice. Data are pooled from two independent experiments.

Statistical analysis was performed using two-way ANOVA with Bonferroni's post-test.

See also Figure S2.

pool size but also sheds light on the existence of alternative mechanism(s) that actively contribute to this process. Embryonically seeded macrophages are renewing through self-proliferation in adults. Our scRNA-seq data indicated that few macrophages were proliferating in adrenal glands as reflected by low *Mki67*, *Ccna2*, and *Top2a* mRNA expression (Figure S21; data not shown). A recent study reported that peritoneal macrophages show a sex-specific proliferation rate (Bain et al., 2020). Therefore, we assessed the macrophage proliferating rate in male and female CCR2-sufficient and -deficient mice using intracellular Ki67 staining. Flow-cytometry analysis revealed a similar proliferation rate between male and female CCR2-sufficient mice (Figure 2L). However, loss of CCR2 led to increased macrophage proliferation in female mice, while this was not the case in CCR2-deficient males (Figure 2L). Together, these results show that both monocyte recruitment and self-proliferation contribute to the maintenance of AGM pool size in a sex-specific manner.

Embryonic and monocyte-derived AGMs co-exist at homeostasis

Our flow-cytometry data demonstrated that most (around 90%) of AGMs expressed CX3CR1 (Figure 1E). Macrophage *Cx3cr1* expression appeared restricted to clusters 2 and 3 in our scRNA-seq data (Figure 2D). To address the mechanisms governing AGM maintenance, we analyzed CCR2^{creERT2} x R26^{TdTomato} x CX3CR1^{GFP} mice 48 h post TAM administration. CCR2⁺ cells were found to preferentially give rise to CX3CR1⁺ macrophages upon their entry into adrenal glands (Figure 3A). Indeed, 48 h post TAM injection, 80% of R26^{TdTomato+} macrophages were CX3CR1^{GFP} positive (Figure 3A). To determine whether CX3CR1⁺ monocyte-derived macrophages could give rise to CX3CR1⁻ macrophages, we took advantage of double reporter CX3CR1^{creERT2/GFP}R26^{TdTomato} mice, allowing us to assess present and past CX3CR1 expression. We found that more than 80% of AGMs were TdTomato⁺GFP⁺ 2 days after TAM administration (Figure 3B). GFP⁺R26^{TdTomato-} and GFP⁻R26^{TdTomato+} cells were virtually absent at this time point (Figure 3B). This set of data indicated that 48 h after TAM administration, CX3CR1⁺ cells were not giving rise to CX3CR1^{low} macrophages (Figure 3B). Furthermore, even 7 days after TAM injection, we still detected approximately 80% of R26^{TdTomato+} GFP⁺ macrophages (Figure 3C). Yet, a population of newly recruited monocyte-derived cells (GFP⁺ R26^{TdTomato-}) was observed (Figure 3C). However, we did not observe the appearance and accumulation of GFP⁻R26^{TdTomato+} cells (Figure 3C). We therefore concluded that CX3CR1⁺ cells are not precursors of CX3CR1⁻ macrophages in adults. We next characterized the phenotype and origin of CX3CR1⁻ AGMs. Our scRNA-seq data pointed out that cells from cluster 4, which are a part of CX3CR1⁻ macrophages, expressed *Timd4* and *Lyve1* mRNA (Figure 2D). We confirmed the presence of Lyve1⁺Timd4⁺ macrophages in female and male mice using flow cytometry, even though these cells represented a minor subpopulation (Figure S3A). Timd4 expression was higher on Lyve1⁺ macrophages compared with Lyve1⁻ cells in both female and male mice (Figure S3B). Moreover, we confirmed that Timd4⁺ macrophages were CX3CR1⁻ (Figure 3D). Lyve1 and Timd4 are markers associated with an embryonic macrophage origin (Dick et al., 2019). We therefore hypothesized that

embryonic and monocyte-derived macrophages could co-exist in adrenal glands.

A previous report showed that populations of embryonically seeded macrophages express CX3CR1 during development but lose this expression in adulthood (Yona et al., 2013). To investigate the developmental origin of AGMs, we performed embryonic pulse-chase experiments. Pregnant CX3CR1^{creERT2} x R26^{TdTomato} mice were injected with TAM at embryonic day 14.5, and their progeny was analyzed at the adult stage (8 weeks old) (Figure 3E). Approximately 15% of AGMs were labeled, suggesting an embryonic seeding for these cells (Figure 3E). The percentage of R26^{TdTomato+} cells was similar in male and female mice, suggesting that embryonic seeding was not following a sex-specific pattern (Figure 3E). In a similar set of experiments, we observed by fluorescence microscopy R26^{TdTomato+} cells in adult adrenal glands, further demonstrating the presence of embryonically seeded macrophages (Figure 3F). Flow-cytometry analysis identified the presence of macrophages in embryos, and many of these cells were Timd4⁺ (Figure 3G). These data are consistent with recent reports demonstrating that Timd4 is a marker of embryonically derived macrophages (Bain et al., 2020; Dick et al., 2019; Sakai et al., 2019). Interestingly, Lyve1⁺ macrophages from cluster 4 showed high expression of Mrc1 (CD206), a marker associated with macrophage alternative polarization (Figure S3C). Consistent with our observations using Timd4 staining, Lyve1⁺CD206⁺ cells represented the major macrophage subset in juvenile animals but only a minor population in adults (Figure S3C). We next performed a separate embryonic labeling experiment where mice were sacrificed at postnatal day 7 (P7) following embryonic labeling at embryonic day 14.5 (E14.5) to determine whether embryonic TdTomato⁺ macrophages expressed Lyve1 and Timd4. We observed that >80% of TdTomato⁺ cells expressed both Lyve1 and Timd4, confirming the embryonic origin of cells from cluster 4 (Figure 3H). Importantly, at this early stage, more than 60% of macrophages were TdTomato⁺ (Figure 3H) compared with 15% in 7-week-old mice, suggesting that embryonically seeded AGMs may be replaced by monocyte-derived cells over time.

Low MHC class II expression defines a female-specific AGM subset with restricted sub-tissular distribution

A major difference in macrophage subsets was related to their expression of genes related to the MHC class II. This allowed the identification of MHC class II^{high} and class II^{low} macrophages (clusters 2 and 3, respectively) (Figure 2A). MHC class II^{low} macrophages were characterized by low expression of *H2-Aa*, *CD74*, and *Ciita* mRNA (Figure 4A). Expression of the KEGG “Antigen processing and presentation” pathway appeared higher on MHC class II^{high} macrophages (Figure 4A). The cluster of MHC class II^{low} macrophages was enriched in females when compared with males (Figure 2A). Flow-cytometry analysis confirmed that MHC class II expression on AGMs displayed a well-defined sex-specific pattern. We observed that the MHC class II^{high} population represented about 90% of AGMs in adult males but only 70% of macrophages in females (Figure 4B). While the number of MHC class II^{high} macrophages was comparable between male and female mice, the number of MHC class II^{low} macrophages was about 5-fold higher in females when

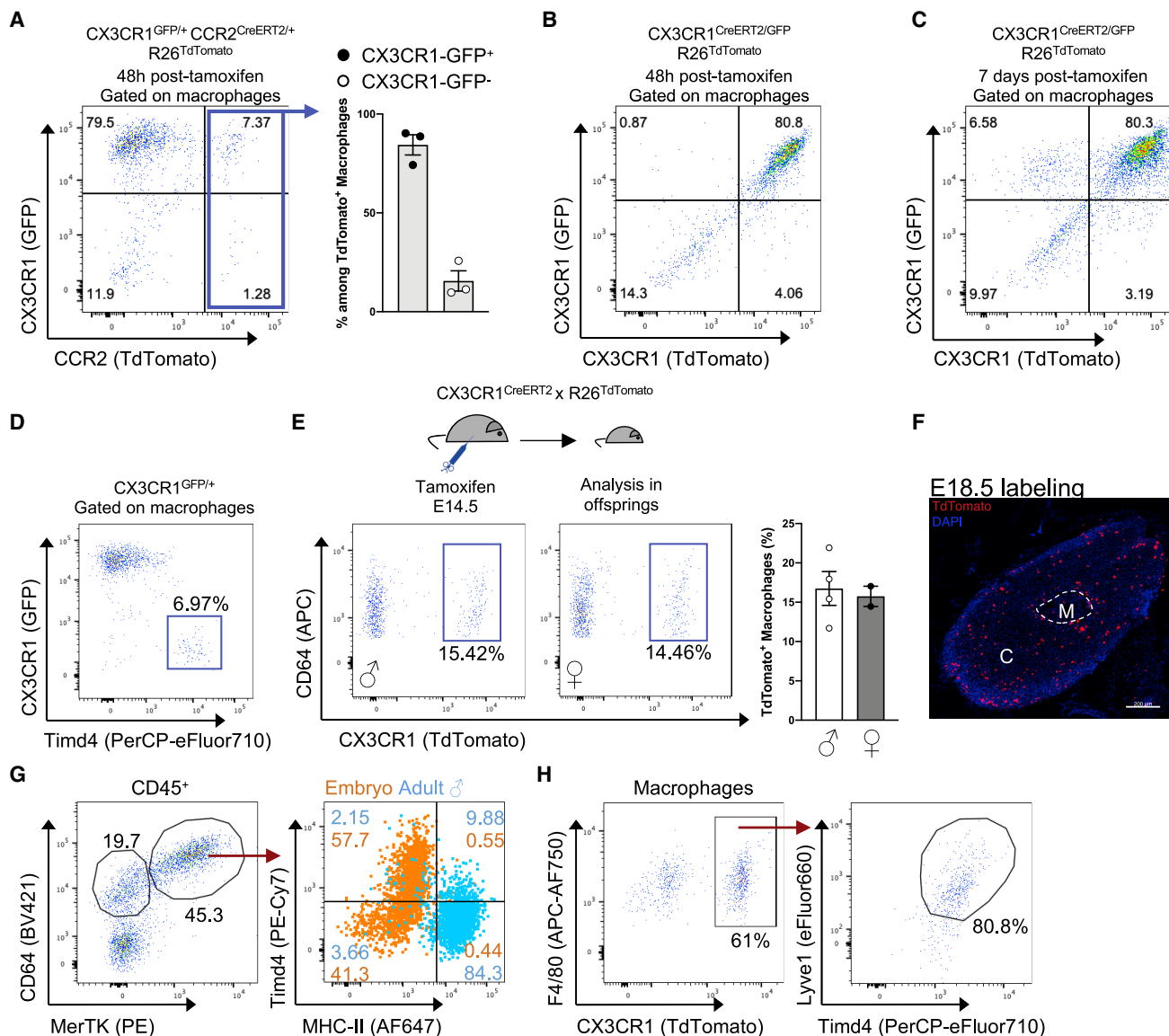


Figure 3. Embryonic and monocyte-derived adrenal gland macrophages are distinct subsets identified through CX3CR1 expression

(A) (Left) Representative plot of macrophage CX3CR1-GFP and R26^{TdTomato} expression and (right) proportions of CX3CR1-GFP⁺ and CX3CR1-GFP⁻ cells among R26^{TdTomato}+ AGMs from (n = 3) female CX3CR1^{GFP/+} CCR2^{CreERT2/+} R26^{TdTomato} mice 48 h post TAM gavage. Data are from one experiment.

(B) Representative plot of macrophage CX3CR1 and R26^{TdTomato} expression in double reporter CX3CR1^{CreERT2/GFP} R26^{TdTomato} mice 48 h post TAM administration. Data are from one experiment.

(C) Representative plot of macrophage CX3CR1 and R26^{TdTomato} expression in double reporter CX3CR1^{CreERT2/GFP} R26^{TdTomato} mice 7 days post tamoxifen administration. Data are from one experiment.

(D) Flow-cytometry plot showing Timd4 and CX3CR1 expression by AGMs. Data are representative of at least 4 independent experiments.

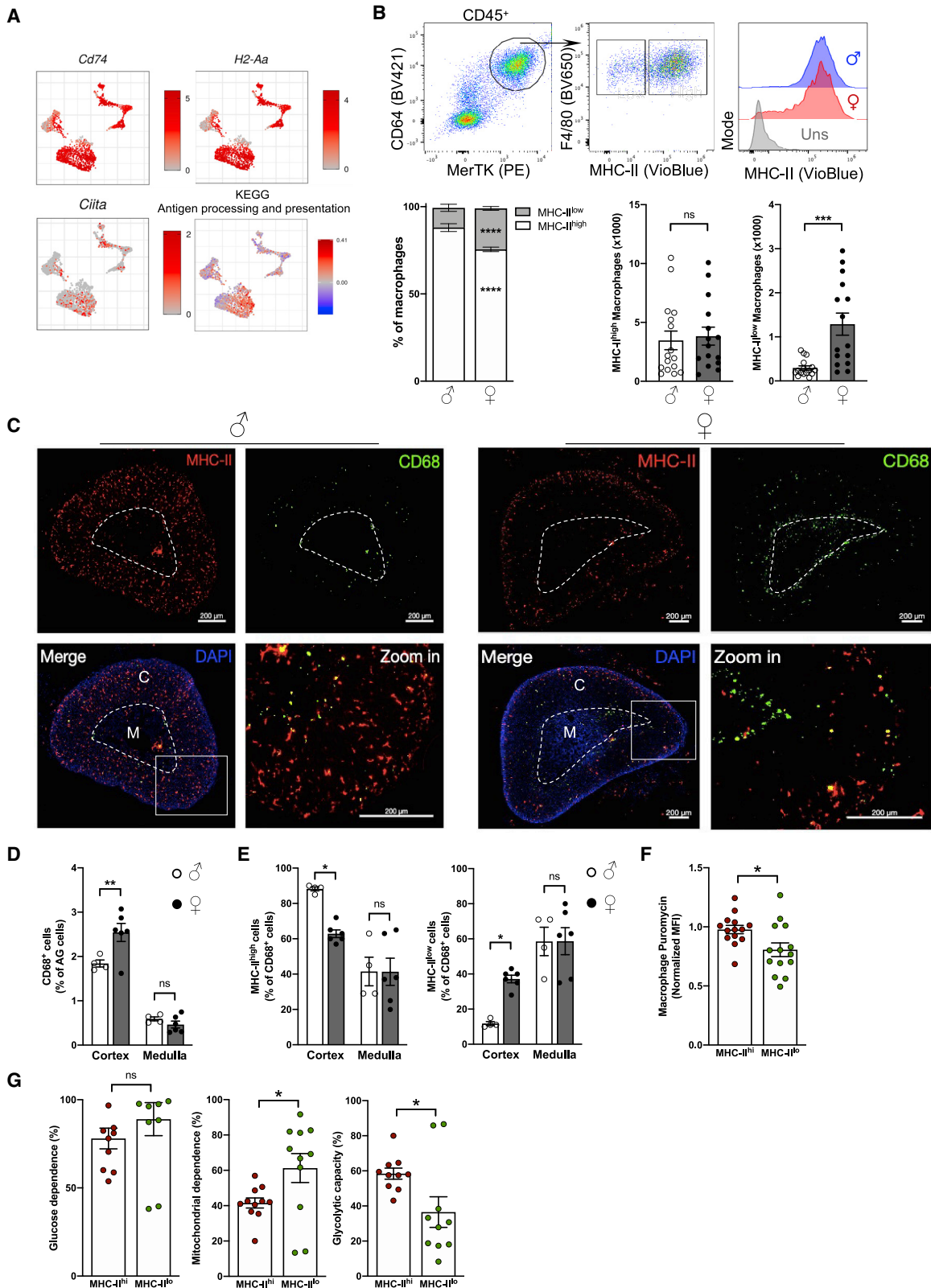
(E) Embryonic labeling of CX3CR1^{CreERT2} R26^{TdTomato} mice was performed at E14.5. R26^{TdTomato}+ cells were identified in 8-week-old male (n = 4) and female (n = 2) offspring. Data are representative of 2 independent experiments.

(F) Embryonic labeling of CX3CR1^{CreERT2} R26^{TdTomato} mice was performed at E18.5. R26^{TdTomato}+ cells were identified in 10-week-old female offspring. Scale bar: 200 μ m. Data are representative of 2 independent experiments.

(G) Flow-cytometry analysis of Timd4 and MHC class II expression in AGMs from E18–E20 embryos and male adult (9-week-old) mice. Data are from one experiment.

(H) Embryonic labeling of CX3CR1^{CreERT2} R26^{TdTomato} mice was performed at E14.5. R26^{TdTomato}+ cells were identified in 1-week-old male offspring (left panel), which comprised mainly Timd4⁺ Lyve1⁺ cells (right panel). Data are representative of n = 2 mice. Data are from one experiment. Two-tailed Mann-Whitney tests were used for statistical analysis.

See also Figure S3.



(legend on next page)

compared with age-matched males (Figure 4B). Thus, we next investigated how MHC class II^{high} and class II^{low} macrophages were related to the CX3CR1⁺ and CX3CR1⁻ macrophage subsets. CX3CR1⁺ macrophages were enriched among MHC class II^{high} macrophages compared with the MHC class II^{low} subset (Figure S3D). Moreover, CX3CR1⁺ cells were more frequent among female MHC class II^{low} macrophages compared with their male counterparts (Figure S3D). Timd4 and Lyve1 expressions were higher on MHC class II^{low} macrophages, suggesting that this subset may be enriched in embryonically derived macrophages (Figure S3E). However, MHC class II^{low} macrophages were more numerous in females compared with males, and this was independently of their Timd4 and Lyve1 expression (Figure S3F). Flow-cytometry analysis revealed that CD11c expression was higher in MHC class II^{high} macrophages compared with the MHC class II^{low} subset in both males and females (Figure S3G). Similar to CX3CR1, CD11c expression was higher in female MHC class II^{low} macrophages compared with their male counterparts, further supporting the sex-dimorphic nature of the MHC class II^{low} subset (Figure S3G). Unsupervised spectral flow-cytometry analysis confirmed that AGMs display a sex-specific expression of MHC class II and CX3CR1 (Figures S3H and S3I). Because we observed that the pathway “Antigen processing and presentation” appeared specific for MHC class II^{high} macrophages (Figure 4A), we measured the expression of proteins involved in antigen presentation. CD86 expression was higher on MHC class II^{high} macrophages compared with their MHC class II^{low} counterparts, and CD40 expression tended to follow the same pattern (Figure S3J). However, the markers CD80 and ICOSL appeared highly expressed in female MHC class II^{low} macrophages (Figure S3J). These results suggest that AGM subsets may have a singular antigen presentation potential. Importantly, sexually dimorphic features appear restrained to MHC class II^{low} macrophages, which stand out as a female-enriched population.

To determine whether macrophage subsets displayed a sex-specific distribution across the cortex and medulla, we performed fluorescence microscopy analysis. Pan-macrophage CD68 staining revealed that most macrophages are nested in the cortex rather than the medulla both in female and male mice (Figure 4C). Additionally, we found an enrichment of CD68⁺ cells in the cortex of females compared with in males (Figure 4D). MHC class II staining demonstrated that most cortical

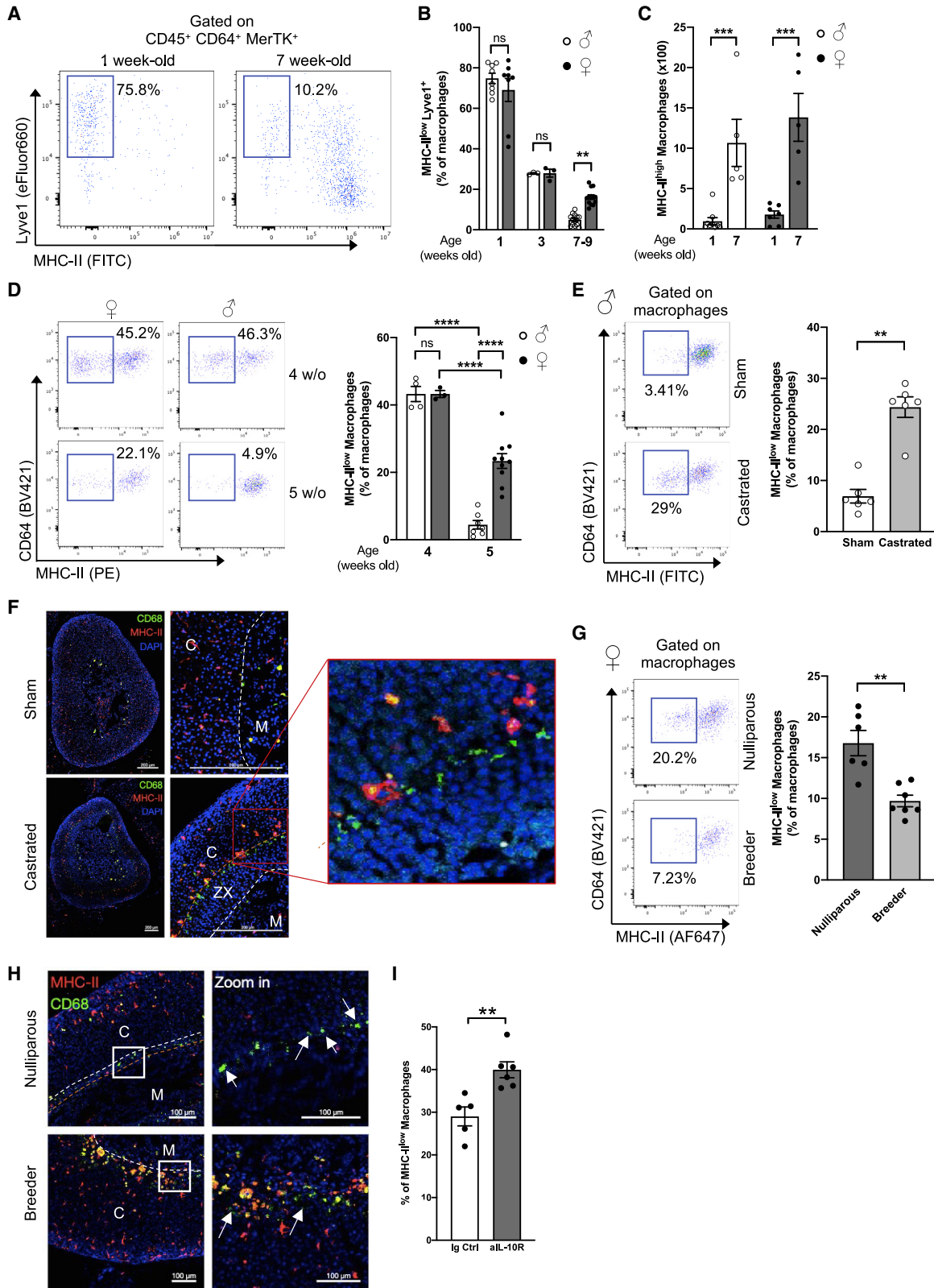
macrophages are MHC class II^{high} in male animals (Figure 4E). This percentage was significantly lower in female mice, which had increased proportion of MHC class II^{low} cells in their adrenal gland cortex (Figure 4E). Interestingly, MHC class II^{low} CD68⁺ cells were enriched at the border between the cortex and the medulla in female mice (Figure 4C). This phenotype was also observed using F4/80 staining, further indicating that these cells are macrophages (Figure S3K). Our data did not reveal a sexual dimorphism in the distribution of MHC class II^{high} and class II^{low} macrophages in the adrenal gland medulla (Figure 4E). Thus, the sex dimorphism in macrophage MHC class II expression identified by flow cytometry and fluorescence microscopy appears restricted to the adrenal gland cortex and, in particular, to a zone between the cortex and the medulla. Finally, we assessed the metabolic configuration of adrenal gland MHC class II^{high} and class II^{low} macrophages using the recently described SCENITH method (Arguello et al., 2020). MHC class II^{high} macrophages appeared to have more active metabolism as illustrated by increased puromycin integration when compared with MHC class II^{low} macrophages (Figure 4F). The glucose dependence was similar between both macrophage subsets (Figure 4G). However, MHC class II^{low} macrophages displayed higher mitochondrial dependence, while MHC class II^{high} macrophages were characterized by increased glycolytic capacity (Figure 4G). Thus, MHC class II^{high} and class II^{low} AGMs relied on different metabolic pathways at steady state.

MHC class II^{low} macrophages locate within the X-zone and are tied to its maintenance

Since MHC class II^{low} macrophages appeared to be specifically located at the border between the cortex and the medulla, we asked whether this population may be associated with the X-zone, a cortical zone that regresses along organ maturation in males (Gannon et al., 2019). To address this question, we compared young mice, in which the X-zone is intact, and adults in which the sex-specific organ structure is already established. Flow-cytometry analysis demonstrated that the majority (around 75%) of AGMs in juvenile 1-week-old mice stained positive for Lyve1 but not for MHC class II (Figure 5A). MHC class II^{high} macrophages became the predominant subset in adulthood (Figure 5A). Importantly, we did not observe sex dimorphism in 1- and 3-week-old animals, while it was clearly established in 7-week-old mice (Figure 5B). These results suggested that sex

Figure 4. MHC class II^{low} macrophages are a female-specific subset with restricted localization

- (A) scRNA-seq analysis of *CD74*, *H2-Aa*, *Ciita*, and the KEGG pathway “Antigen processing and presentation” expression among myeloid cells.
- (B) (Top) Flow-cytometry plots showing F4/80 and MHC class II expression among AGMs from 7-week-old male and female mice. (Bottom) Proportions and numbers of MHC class II^{high} and class II^{low} AGMs from 7-week-old male and female wild-type mice. δ n = 16 and η n = 15. Data are pooled from 3 independent experiments.
- (C) Fluorescence-microscopy analysis of CD68 and MHC class II expression in adrenal glands from 7-week-old male and female mice. Scale bar: 200 μ m. M, medulla; C, cortex. Data are representative of at least 3 independent experiments.
- (D) Distribution of CD68⁺ cells between cortex and medulla from adrenal glands of 7-week-old male and female mice. Data are represented as proportion of CD68⁺ cells from each zone among total cells. δ n = 4 and η n = 6. Quantification from one experiment.
- (E) Proportion of MHC-II^{high} and MHC-II^{low} CD68⁺ cells in the cortex and medulla of adrenal glands from 7-week-old male and female mice. δ n = 4 and η n = 6. Quantification from one experiment.
- (F) Analysis of macrophage metabolic activity using SCENITH, represented by Puromycin MFI (n = 14). Data pooled from 4 independent experiments.
- (G) Measure of glycolytic and mitochondrial metabolism in macrophages using SCENITH (n = 10–11). Data pooled from 3 independent experiments.
- Statistical analysis was performed using two-tailed Mann-Whitney tests (panel B, quantifications), two-way ANOVA with Bonferroni's post-test (proportions in panel B, panel D and panel E), or paired Wilcoxon t-tests (panels F and G). See also Figure S4.



(legend on next page)

dimorphism appears before 7 weeks of age, likely together with puberty onset and X-zone disappearance in males. The high proportions of MHC class II^{low} macrophages in juvenile mice was mirrored by very low numbers of MHC class II^{high} macrophages, while this subset was enriched in 7-week-old mice (Figure 5C). Concomitantly, we measured lower CCL2 levels in adrenal gland homogenates from 3-week-old mice compared with 6- to 7-week-old mice, while their serum CCL2 levels remained similar (Figure S4A). This suggests that adrenal gland maturation is mirrored by increased local CCL2 production, which could trigger accelerated monocyte recruitment.

A recent report demonstrated that sexual hormones, and particularly estrogens, affected the phenotype and functions of peritoneal macrophages (Bain et al., 2020). To determine whether estrogens were responsible for the accumulation of MHC class II^{low} macrophages, 6-week-old female mice were ovariectomized or received a control surgery (sham). As expected, uteri weights were decreased in ovariectomized (OVX) mice compared with sham-operated animals (Figure S4B). We analyzed their adrenal glands 6 weeks post-surgery and found no differences in the numbers of adrenal gland monocytes or macrophages between sham-operated and OVX mice (Figure S4C). The numbers of MHC class II^{high} and class II^{low} macrophages were also unchanged between sham-operated and OVX animals (Figure S4D). Taken together, these data demonstrated that ovaries-derived hormones are unlikely regulators of AGM sex dimorphism.

X-zone regression occurs between P28 and P35 in male mice (Huang and Kang, 2019). Microscopy analysis revealed that the X-zone was present in 4-week-old females but absent in males in our experimental conditions (Figure S4E). We observed that the percentage of MHC class II^{low} macrophages was similar in 4-week-old females and males (Figure 5D). Strikingly, in 5-week-old males, the percentage of MHC class II^{low} macrophages decreased to 5%, while it remained around 20% in females (Figure 5D). These data suggest that X-zone disappearance precedes macrophage sex-dimorphism establishment and correlated with the loss of MHC class II^{low} macrophages in

males. To further establish a causal link between X-zone presence and AGM sex dimorphism, males were castrated at 3 weeks of age to prevent X-zone degradation. We analyzed their adrenal glands when the mice were 7-week-old. MHC class II staining demonstrated an increase in the population of MHC class II^{low} macrophages in castrated mice when compared with sham-operated animals (Figure 5E). Interestingly, when we analyzed the localization of AGM, we found that MHC class II^{high} macrophages had a very particular distribution at the border with the X-zone in castrated mice (Figure 5F). In this same location, we found an increased number of MHC class II^{low} macrophages in castrated mice compared with sham-operated controls (Figure 5F). These data demonstrated that X-zone maintenance is sufficient to maintain MHC class II^{low} macrophages in castrated males.

Next, we analyzed adrenal glands from female retired breeders, in which the X-zone was degraded during pregnancy, and age-matched nulliparous controls. MHC class II^{low} macrophage proportions dropped to 10% in retired breeders, similar to what we observed in males, while it was close to 20% in age-matched nulliparous mice (Figure 5G). The distribution pattern of MHC class II⁺ cells in female retired breeders resembled the pattern observed in males (Figure 5H). No sex dimorphism was observed between male and female retired breeders (Figure S4F). Thus, we concluded that X-zone disappearance drives the establishment of sex dimorphism in AGM phenotype and tissue distribution.

We then analyzed the molecular mechanisms controlling MHC class II expression in AGMs. While MHC class II regulation in DCs is well established, relatively little is known about the mechanisms occurring in monocytes and macrophages (Unanue et al., 2016). Interleukin-10 (IL-10) signaling was previously shown to modulate MHC class II expression in monocyte-derived cells (Koppelman et al., 1997). Thus, we injected IL-10R-blocking antibodies (Abs) and analyzed macrophage MHC class II expression 72 h later. Preventing IL-10 receptor signaling in females led to increased proportions of MHC class II^{low} macrophages (Figure 5I). This result suggests that local IL-10

Figure 5. Adrenal gland macrophage sex-dimorphism is established with organ maturation and depends on X-zone presence

- (A) Representative plots showing AGM MHC-II and Lyve1 expression in male 1- or 7-week-old mice. Data representative of 2 independent experiments.
- (B) Proportions of MHC-II^{low} Lyve1⁺ macrophages in male and female 1-(δ n = 8, η n = 8), 3-(δ n = 3, η n = 3) or 7 to 9-week-old (δ n = 13, η n = 13) mice. Data pooled from 2 independent experiments.
- (C) Quantification of MHC-II^{high} AGMs in male and female 1- (δ n = 9, η n = 7) or 7-week-old (δ n = 5, η n = 5) mice. Data are pooled from 2 independent experiments.
- (D) (Left) Representative plots showing MHC class II expression and (right) proportions of MHC class II^{low} macrophages in male and female 4- (δ n = 4, η n = 3) and 5-week-old (δ n = 7, η n = 10) wild-type mice. Data are pooled from 2 independent experiments.
- (E) (Left) Representative plots showing MHC class II expression and (right) proportions of MHC class II^{low} AGMs in 7-week-old castrated (n = 6) and sham-operated (n = 6) wild-type male mice. Data are pooled from 2 independent experiments.
- (F) Confocal-microscopy analysis of MHC class II and CD68 expression in 7-week-old castrated and sham-operated wild-type mice. The X-zone is comprised between white and orange dots. Scale bar: 200 μ m. M, medulla; C, cortex; ZX, X- zone. Data are representative of 2 independent experiments.
- (G) (Left) Representative plots showing MHC class II expression and (right) proportions of MHC class II^{low} AGMs in female retired breeders (n = 7) and age-matched nulliparous (n = 6) mice. Data are pooled from 2 independent experiments.
- (H) Fluorescence-microscopy analysis of CD68 and MHC class II expression in adrenal glands from 12-week-old female retired breeders and age-matched nulliparous mice. The X zone is comprised between white and orange dots. Scale bar: 100 μ m. M, medulla; C, cortex. Data are representative of 2 independent experiments.
- (I) Proportions of MHC class II^{low} macrophages in female mice treated with anti-IL-10R-blocking antibody or isotype control. Data are pooled from 3 independent experiments.

Statistical analysis was performed using two-way ANOVA with Bonferroni's post-test (B–D) or two-tailed Mann-Whitney tests (E, G, and I).

See also Figure S5.

production may drive the zone-restricted macrophage phenotype observed on MHC class II expression. Further investigation is required to define the precise mechanisms involved in this process and whether IL-10 controls MHC class II export, recycling, or degradation in AGMs.

AGMs impact local lipid homeostasis

Finally, we decided to inquire about the functions of AGMs. We investigated whether AGMs could sample blood-borne particulate material, a function reported in adipose tissue, intestinal, and lung macrophages (Silva et al., 2019). We injected intravenous (i.v.) tetramethylrhodamine (TRITC)-conjugated dextran (65–85 kDa) and compared perigonadal white adipose tissue (WAT) macrophages, used as a positive control, and AGMs 20 min post-injection. As expected, WAT macrophages stained positive for dextran, confirming their access to blood-derived particles (Figure S5A). However, AGMs remained negative for TRITC-dextran, suggesting that these cells did not access blood-borne particles rapidly (Figure S5A). This was the case both in female and male mice (Figure S5A). Our data does not exclude the possibility that AGMs might access blood material with a slower rate when compared with WAT macrophages. To gain further insight into AGM morphology in their native environment, we performed electron-microscopy analysis of adrenal glands. Macrophage presence in adrenal glands was sparse. Cells with a macrophage morphology were observed, and their surrounding cells contained lipid droplets (Figure S5B). Electron-microscopy analysis of purified macrophages showed that, compared with peritoneal macrophages, AGMs were enriched in structures resembling lipid droplets (Figure S5C, red arrows). This suggests that AGMs might uptake material, likely lipid derivatives, produced and released by neighboring cells and possibly dead cells and thus contribute to tissue lipid homeostasis. We next investigated whether AGMs might be involved in the control of norepinephrine (NE) release, a hormone produced by the adrenal gland medulla. Our scRNA-seq data indicated that AGMs express enzymes involved in NE degradation, namely monoamine oxidase (*Maoa*) and *Comt* (Figure S5D). *Maoa* expression was low in adrenal gland immune cells with only few macrophages possessing detectable *Maoa* mRNA (Figure S5D). *Comt* expression was detected in several populations of adrenal gland immune cells (Figure S5D). In our dataset, we did not detect the expression of enzymes involved in NE synthesis in immune cells (*Th*, *Ddc*, and *Dbh*) (data not shown). To investigate whether AGMs can degrade NE, we sorted CD64⁺MerTK⁺ cells and incubated them overnight in the presence of NE and clorgyline, a selective *Maoa* pharmacological inhibitor. Clorgyline addition did not impact on the concentration of NE detected in our experimental setup (Figure S5D). Thus, we concluded that AGMs, at least *ex vivo*, have a limited ability to degrade NE through *Maoa* (Figure S5D). This might be due to the sorting of the whole population of AGMs, thus diluting the population of medulla-resident macrophages for which a specific marker is yet to be identified and validated.

Next, we decided to investigate the growth-factor dependence of AGMs. Macrophages rely on macrophage colony-stimulating factor (M-CSF) and/or granulocyte M-CSF (GM-CSF) for their survival in peripheral tissues (Cecchini et al., 1994; Dai et al.,

2002; Williams et al., 2013; Nishinakamura et al., 1996; Pridans et al., 2018). CSF1 is produced by several cell types including fibroblasts and mesothelial cells (Bellomo et al., 2020; Ivanov et al., 2019). In adrenal glands, CSF1 is thought to derive from the zona reticularis (Bellomo et al., 2020; Ryan et al., 2001). To decipher AGM dependence on growth factors, we injected a CD115 (CSF1R)-blocking Ab. Compared with isotype control-treated mice, anti-CD115 Ab administration completely depleted AGMs (Figure 6A). Fluorescence-microscopy analysis in CX3CR1^{GFP+} mice, administered with anti-CD115 Ab, confirmed the complete disappearance of AGMs (Figure 6B). These data demonstrated that AGMs depend on CSF1R for their survival. Tissue analysis did not show a major alteration of adrenal gland morphology in macrophage-depleted mice (Figure S5E). Serum aldosterone and corticosterone levels remained similar between macrophage-depleted and control mice, suggesting that macrophages are not involved in the systemic control of these hormone levels at steady state (Figure S5F). Additionally, serum potassium concentration, a surrogate readout for aldosterone pathway activation, remained similar in control and macrophage-depleted mice (Figure S5G).

To further investigate the contribution of AGMs to tissue homeostasis, we performed RNA-seq analysis of adrenal glands extracted from female and male mice treated with isotype control or with anti-CD115 Ab. We identified a well-defined transcriptomic signature associated with macrophage depletion in both sexes (Figure S6A). Among the top differentially regulated genes, we observed multiple macrophage-associated genes (CX3CR1, CSF1R, *Lyz2*, *Adgre1*), confirming the depletion efficiency in this experiment (Figure S6B). In agreement with our observations that AGMs express MHC class II, and in particular in adult males, macrophage depletion was correlated with decreased expression of transcripts encoding for proteins involved in MHC class II synthesis and regulation (Figure S6C). Macrophage depletion was associated with decreased lipid-associated metabolism in adrenal glands (Figure S6D). To determine how this prediction reflected on adrenal gland morphology and lipid-content distribution, we performed Bodipy staining. Microscopy analysis found that the number of small-size (up to 5 μm²) Bodipy⁺ particles was increased in macrophage-depleted mice compared with isotype-injected controls (Figures 6C and 6D). The distribution of larger Bodipy⁺ particles was not affected by macrophage removal (Figures 6C and 6D). The precise nature of lipids modulated in macrophage-depleted mice remains to be established.

One of the most regulated genes associated with macrophage depletion in female and male mice was *Cybb* (Figure S6E). *Cybb* encodes for a subunit of Nox2 and subsequently impacts reactive oxygen species (ROS) generation. Nox2 was implicated in macrophage ROS generation and microbial killing (Bedard and Krause, 2007). Furthermore, Nox2 is also involved in Cyp11b2-dependent aldosterone generation by adrenal gland cortical cells (Rajamohan et al., 2012). Our data revealed that AGM subsets express high *Cybb* mRNA levels when compared with other adrenal gland immune cells (Figure S6F). Since macrophage depletion was correlated with a loss of adrenal *Cybb* mRNA expression, we decided to investigate whether local aldosterone levels were affected in macrophage-depleted adrenal glands.

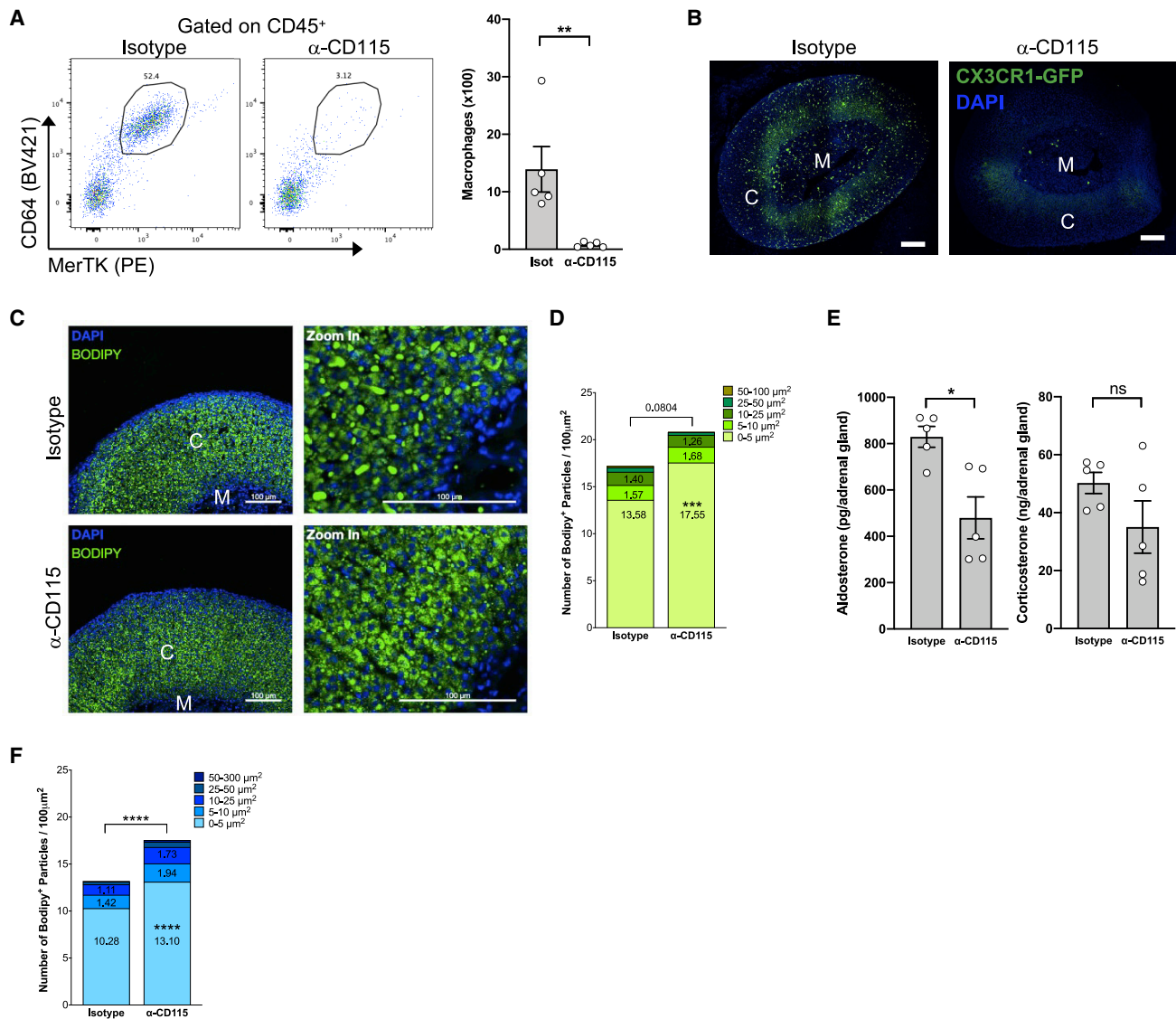


Figure 6. Adrenal gland macrophages control tissue lipid metabolism

(A) (Left) Representative plots and (right) quantification of AGMs in 7- to 8-week-old CX3CR1^{GFP/+} mice after macrophage depletion using α -CD115 (n = 5) or isotype control (n = 5).

(B) Microscopy analysis of adrenal glands from α -CD115- or isotype-control-treated CX3CR1^{GFP/+} mice. One microscopy experiment was performed to confirm depletion efficiency.

(C) Microscopy analysis of adrenal glands from α -CD115- or isotype-control-treated male mice using Bodipy staining. Data are from one experiment.

(D) Quantification of Bodipy⁺ particles of different sizes in adrenal glands from α -CD115- (n = 3) or isotype-control- (n = 3) treated male mice. Data are from one experiment.

(E) Aldosterone and corticosterone levels in adrenal gland homogenates from 8-week-old α -CD115- (n = 5) or isotype-control- (n = 5) treated female mice submitted to a 12 h cold challenge. Data are from one experiment.

(F) Quantification of Bodipy⁺ particles of different sizes in adrenal glands from 8-week-old α -CD115- (n = 5) or isotype-control- (n = 5) treated female mice submitted to a 12 h cold challenge.

Statistical analysis was performed using two-way ANOVA with Bonferroni's post-test (D and F) or two-tailed Mann-Whitney tests (A and E).

See also Figure S6.

For this purpose, we housed mice at 4°C for 12 h. Indeed, cold exposure has been shown to trigger a stress response and increased systemic corticosterone concentration (Williams et al., 2017). To assess whether hormone production was modulated by macrophages in cold-challenged mice, we injected

isotype control or anti-CD115-blocking Ab, and we evaluated local production and systemic levels of corticosterone and aldosterone. Our data revealed that while corticosterone levels were not altered in the adrenal glands of macrophage-depleted mice, aldosterone concentration was lessened in the absence of

macrophages (Figure 6E). However, this did not translate into decreased systemic aldosterone levels (Figure S6G). Corticosterone serum concentration was also comparable in both experimental groups (Figure S6G). Importantly, *Cyp11b2* mRNA expression, a key enzyme in the aldosterone synthesis pathway, was decreased in adrenal glands following macrophage depletion (Figure S6E), further demonstrating macrophage involvement in aldosterone production. Cold challenge further amplified the difference in lipid-particle content between control and macrophage-depleted mice (Figure 6F). Mice treated with anti-CD115 Ab had increased number of Bodipy⁺ lipid particles compared with isotype-injected animals (Figure 6F). As observed at steady state, the small-size particles were the most affected (Figure 6F). Whether a specific cortical macrophage subset is involved in this mechanism remains to be defined.

DISCUSSION

In the present study, we observed that monocyte recruitment was more important in female mice compared with age-matched male animals. The molecular mechanisms governing this differential monocyte recruitment are yet to be defined. We observed that CCL2 adrenal gland concentration is similar between females and males. Nevertheless, whether additional CCR2 ligands, such as CCL7, are expressed in a sex- and age-dependent manner in adrenal glands and could account for the differential monocyte recruitment remains to be established. Another important question that the current study rose is whether monocyte recruitment occurs in specific adrenal cortex sites and whether these sites differ depending on the sex.

We identified a cluster of embryonically seeded macrophages co-expressing *Timd4* and *Lyve1*. The presence of *Lyve1*-expressing macrophages was previously documented around large blood vessels (Lim et al., 2018). Perivascular *Lyve1*⁺ macrophages contribute to vessel function by interacting with the extracellular matrix (Lim et al., 2018). *Lyve1*⁺*MHC-II*^{low} macrophages have also been identified in lung, adipose tissue, heart, and dermis (Chakarov et al., 2019). Importantly, *Lyve1*⁺*Timd4*⁺ macrophages across different tissues have been associated with an embryonic origin, similar to our conclusions in adrenal glands (Dick et al., 2022). These cells were frequently located in close proximity to blood vessels (Chakarov et al., 2019). The tissue localization and precise function of *Lyve1*⁺ macrophages in adrenal glands require further investigation. These cells were previously shown to decrease fibrosis development in lung and heart (Chakarov et al., 2019). Whether they modulate fibrosis progression during chronic inflammation or tumor development in adrenal glands is an exciting question that needs to be addressed.

The presence of *MHC class II*^{low} macrophages was observed in female mice. These cells depended on X-zone maintenance, and its disappearance led to the loss of *MHC class II*^{low} macrophages. One could speculate that adrenal gland X-zone removal is associated with the generation of peptides that could be loaded and presented on macrophage *MHC class II*. This could trigger an auto-immune response and generate exacerbated and deleterious inflammation. Thus, a major role of adrenal gland *MHC class II*^{low} macrophages could be to uptake and

degrade antigens avoiding unnecessary local and systemic T cell activation.

AGM depletion was characterized by a dysregulation of tissue lipid metabolism. During stress induction, macrophage depletion resulted in lower aldosterone local production. The very same trend was also observed for corticosterone. Increased aldosterone production leads to hypertension. Thus, controlling adrenal gland aldosterone production and release are critical to prevent hypertension. Our data suggest a role for macrophages in adrenal gland aldosterone generation. However, the administration of anti-CD115 Ab leads to macrophage depletion in multiple tissues (Carrero et al., 2017). Therefore, decreased aldosterone production in adrenal glands might not be a direct consequence of AGM depletion. To test the causal role of AGMs in the control of aldosterone production upon stress, one would need to selectively deplete adrenal macrophages without affecting macrophage populations in other organs. Such models have been established for liver and brain macrophages following extensive analysis of their transcriptome (Buttgereit et al., 2016; Scott et al., 2016). Nevertheless, genetic or pharmacological approaches for selective AGM depletion are yet to be developed and validated. Aldosterone is produced by a specialized layer in the adrenal gland cortex: zona glomerulosa (Zennaro et al., 2020). Among the macrophage subsets present in the adrenal gland cortex, the population involved in aldosterone generation remains to be defined.

Together, our observations define the development and heterogeneity of AGMs in male and female mice. These results lay the foundation for future studies to address the interplay between macrophages and endocrine cells in the adrenal gland and their potential homeostatic or pathological contributions during disease responses and stress-hormone production.

Limitations of the study

The main limitation of the current study is the lack of genetic models allowing to selectively target AGMs for depletion or conditional expression studies. Generating such tools will provide the opportunity to dissect the precise function of AGMs in tissue homeostasis and during stress exposure. Additionally, and due to the very low number of AGM subsets, the analysis of their metabolic configuration in their native microenvironment is challenging.

STAR★METHODS

Detailed methods are provided in the online version of this paper and include the following:

- KEY RESOURCES TABLE
- RESOURCE AVAILABILITY
 - Lead contact
 - Materials availability
 - Data and code availability
- EXPERIMENTAL MODEL AND SUBJECT DETAILS
- METHOD DETAILS
 - Tamoxifen treatments
 - Surgery procedures
 - *In vivo* macrophage depletion
 - *In vivo* IL-10R blockade

- Flow cytometry analysis
- SCENITH
- Dextran uptake assay
- Norepinephrine degradation assay
- ELISA assays
- Bulk RNA-seq
- Quantification of serum cation concentration
- Single-cell RNA-seq data analysis
- Tissue histology
- Immunostaining
- Immunofluorescence quantification method
- Fluorescence microscopy
- Electron microscopy

● **QUANTIFICATION AND STATISTICAL ANALYSIS**

SUPPLEMENTAL INFORMATION

Supplemental information can be found online at <https://doi.org/10.1016/j.celrep.2022.110949>.

ACKNOWLEDGMENTS

We would like to thank the C3M animal facility for technical support and the GIS-IBISA multi-sites platform Microscopie Imagerie Côte d'Azur (MICA), and particularly the imaging site of C3M supported by Conseil Régional, Conseil Départemental, and IBISA. We sincerely thank Narges Khedher and Marie Iron-delle for their help. We would like to thank Fabien Labbal and Kevin Lebrigand and the UCA Genomix Platform. We acknowledge the flow cytometry facility from the "Institut de Pharmacologie Moléculaire et Cellulaire" part of the MICA GIS IBISA labeled platform and the UMN flow cytometry core facility. A.G. was supported by the French government through the UCAJedi Investments in the Future projects managed by the National Research Agency (ANR) (ANR-15-IDEX-01). M.M.F. and K.Z. were supported by Government of Russian Federation (grant 08-08). K.-W.K. is supported by NIH (DK126753). R.R.G. is supported by Centre National de la Recherche Scientifique (CNRS). L.Y.-C. is supported by Institut National de la Santé et de la Recherche Médicale (INSERM), Fondation de France (00066474), and the European Research Council (ERC) consolidator program (ERC2016COG724838). J.W.W. was supported by National Institutes of Health (HL138163) and American Heart Association (CDA 855022). S.I. was supported by INSERM and Agence Nationale de la Recherche (ANR-17-CE14-0017-01 and ANR-19-ECVD-0005-01). D.D. was supported by grants from the ANR and the European Union: EGID ANR-10-LABX-46. R.J.A. was supported by ANR-20-CE-CE14-0028-01 and CoPoC MAT-PI-17493-A-04.

AUTHOR CONTRIBUTIONS

S.I., J.W.W., and R.R.G. conceptualized the study. B.D., A.G., Y.X., J.M., A.D., A.C., N.V., S.Q., H.G., M.I.S., P.R.S., S.-H.K., A.Z., J.D., J.G., V.M., P.B., C.D., A.W., C.B.-W., S.P., S.C., K.-W.K., L.Y.-C., R.R.G., J.W.W., and S.I. performed experiments, analyzed the data, and edited the manuscript. B.D., A.G., R.R.G., J.W.W., and S.I. wrote the manuscript. M.M.F. and K.Z. performed the analysis of the scRNA-seq data and bulk RNA-seq data and wrote and edited the manuscript. D.D., B.B., R.J.A., P.R., and F.G. provided tools and expertise and edited the manuscript.

DECLARATION OF INTERESTS

The authors declare no competing interests.

Received: November 9, 2021

Revised: March 10, 2022

Accepted: May 23, 2022

Published: June 14, 2022

REFERENCES

- Arguello, R.J., Combes, A.J., Char, R., Gigan, J.P., Baaziz, A.I., Bousiquot, E., Camosseto, V., Samad, B., Tsui, J., Yan, P., et al. (2020). SCENITH: a flow cytometry-based method to functionally profile energy metabolism with single-cell resolution. *Cell Metabol.* 32, 1063–1075.e7. <https://doi.org/10.1016/j.cmet.2020.11.007>.
- Audenet, F., Mejean, A., Chartier-Kastler, E., and Roupert, M. (2013). Adrenal tumours are more predominant in females regardless of their histological subtype: a review. *World J. Urol.* 31, 1037–1043. <https://doi.org/10.1007/s00345-012-1011-1>.
- Bain, C.C., Bravo-Blas, A., Scott, C.L., Gomez Perdiguer, E., Geissmann, F., Henri, S., Malissen, B., Osborne, L.C., Artis, D., and Mowat, A.M. (2014). Constant replenishment from circulating monocytes maintains the macrophage pool in the intestine of adult mice. *Nat. Immunol.* 15, 929–937. <https://doi.org/10.1038/ni.2967>.
- Bain, C.C., Gibson, D.A., Steers, N.J., Boufea, K., Louwe, P.A., Doherty, C., Gonzalez-Huici, V., Gentek, R., Magalhaes-Pinto, M., Shaw, T., et al. (2020). Rate of replenishment and microenvironment contribute to the sexually dimorphic phenotype and function of peritoneal macrophages. *Sci. Immunol.* 5, eabc4466. <https://doi.org/10.1126/sciimmunol.abc4466>.
- Bain, C.C., Hawley, C.A., Garner, H., Scott, C.L., Schridde, A., Steers, N.J., Mack, M., Joshi, A., Williams, M., Mowat, A.M.I., et al. (2016). Long-lived self-renewing bone marrow-derived macrophages displace embryo-derived cells to inhabit adult serous cavities. *Nat. Commun.* 7, ncomms11852. <https://doi.org/10.1038/ncomms11852>.
- Bedard, K., and Krause, K.H. (2007). The NOX family of ROS-generating NADPH oxidases: physiology and pathophysiology. *Physiol. Rev.* 87, 245–313. <https://doi.org/10.1152/physrev.00044.2005>.
- Bellomo, A., Mondor, I., Spinelli, L., Laguerie, M., Stewart, B.J., Brouilly, N., Malissen, B., Clatworthy, M.R., and Bajenoff, M. (2020). Reticular fibroblasts expressing the transcription factor WT1 define a stromal niche that maintains and replenishes splenic red pulp macrophages. *Immunity* 53, 127–142.e7. <https://doi.org/10.1016/j.immuni.2020.06.008>.
- Bielohuby, M., Herbach, N., Wanke, R., Maser-Gluth, C., Beuschlein, F., Wolf, E., and Hoefflich, A. (2007). Growth analysis of the mouse adrenal gland from weaning to adulthood: time- and gender-dependent alterations of cell size and number in the cortical compartment. *Am. J. Physiol. Endocrinol. Metab.* 293, E139–E146. <https://doi.org/10.1152/ajpendo.00705.2006>.
- Butler, A., Hoffman, P., Smibert, P., Papalex, E., and Satija, R. (2018). Integrating single-cell transcriptomic data across different conditions, technologies, and species. *Nat. Biotechnol.* 36, 411–420. <https://doi.org/10.1038/nbt.4096>.
- Buttgereit, A., Lelios, I., Yu, X., Vrohings, M., Krakoski, N.R., Gautier, E.L., Nishinakamura, R., Becher, B., and Greter, M. (2016). Sall1 is a transcriptional regulator defining microglia identity and function. *Nat. Immunol.* 17, 1397–1406. <https://doi.org/10.1038/ni.3585>.
- Calderon, B., Carrero, J.A., Ferris, S.T., Sojka, D.K., Moore, L., Epelman, S., Murphy, K.M., Yokoyama, W.M., Randolph, G.J., and Unanue, E.R. (2015). The pancreas anatomy conditions the origin and properties of resident macrophages. *J. Exp. Med.* 212, 1497–1512. <https://doi.org/10.1084/jem.20150496>.
- Carrero, J.A., McCarthy, D.P., Ferris, S.T., Wan, X., Hu, H., Zinselmeyer, B.H., Vomund, A.N., and Unanue, E.R. (2017). Resident macrophages of pancreatic islets have a seminal role in the initiation of autoimmune diabetes of NOD mice. *Proc. Natl. Acad. Sci. U S A* 114, E10418–E10427. <https://doi.org/10.1073/pnas.1713543114>.
- Cecchini, M.G., Dominguez, M.G., Mocci, S., Wetterwald, A., Felix, R., Fleisch, H., Chisholm, O., Hofstetter, W., Pollard, J.W., and Stanley, E.R. (1994). Role of colony stimulating factor-1 in the establishment and regulation of tissue macrophages during postnatal development of the mouse. *Development* 120, 1357–1372. <https://doi.org/10.1242/dev.120.6.1357>.
- Chakarov, S., Lim, H.Y., Tan, L., Lim, S.Y., See, P., Lum, J., Zhang, X.M., Foo, S., Nakamizo, S., Duan, K., et al. (2019). Two distinct interstitial macrophage

- populations coexist across tissues in specific subtissular niches. *Science* 363, eaau0964. <https://doi.org/10.1126/science.aau0964>.
- Cox, N., Pokrovskii, M., Vicario, R., and Geissmann, F. (2021). Origins, biology, and diseases of tissue macrophages. *Annu. Rev. Immunol.* 39, 313–344. <https://doi.org/10.1146/annurev-immunol-093019-111748>.
- Croxford, A.L., Lanzinger, M., Hartmann, F.J., Schreiner, B., Mair, F., Pelczar, P., Clausen, B.E., Jung, S., Greter, M., and Becher, B. (2015). The cytokine GM-CSF drives the inflammatory signature of CCR2+ monocytes and licenses autoimmunity. *Immunity* 43, 502–514. <https://doi.org/10.1016/j.immuni.2015.08.010>.
- Dai, X.M., Ryan, G.R., Hapel, A.J., Dominguez, M.G., Russell, R.G., Kapp, S., Sylvestre, V., and Stanley, E.R. (2002). Targeted disruption of the mouse colony-stimulating factor 1 receptor gene results in osteopetrosis, mononuclear phagocyte deficiency, increased primitive progenitor cell frequencies, and reproductive defects. *Blood* 99, 111–120. <https://doi.org/10.1182/blood.v99.1.111>.
- Dick, S.A., Macklin, J.A., Nejat, S., Momen, A., Clemente-Casares, X., Althagafi, M.G., Chen, J., Kantores, C., Hosseinzadeh, S., Aronoff, L., et al. (2019). Self-renewing resident cardiac macrophages limit adverse remodeling following myocardial infarction. *Nat. Immunol.* 20, 29–39. <https://doi.org/10.1038/s41590-018-0272-2>.
- Dick, S.A., Wong, A., Hamidzadeh, H., Nejat, S., Nechanitzky, R., Vohra, S., Mueller, B., Zaman, R., Kantores, C., Aronoff, L., et al. (2022). Three tissue resident macrophage subsets coexist across organs with conserved origins and life cycles. *Sci. Immunol.* 7, eabf7777. <https://doi.org/10.1126/sciimmunol.abf7777>.
- Ensan, S., Li, A., Besla, R., Degousee, N., Cosme, J., Roufaiel, M., Shikatani, E.A., El-Maklizi, M., Williams, J.W., Robins, L., et al. (2016). Self-renewing resident arterial macrophages arise from embryonic CX3CR1(+) precursors and circulating monocytes immediately after birth. *Nat. Immunol.* 17, 159–168. <https://doi.org/10.1038/ni.3343>.
- Epelman, S., Lavine, K.J., and Randolph, G.J. (2014). Origin and functions of tissue macrophages. *Immunity* 41, 21–35. <https://doi.org/10.1016/j.immuni.2014.06.013>.
- Ferris, S.T., Zakharov, P.N., Wan, X., Calderon, B., Artyomov, M.N., Unanue, E.R., and Carrero, J.A. (2017). The islet-resident macrophage is in an inflammatory state and senses microbial products in blood. *J. Exp. Med.* 214, 2369–2385. <https://doi.org/10.1084/jem.20170074>.
- Gannon, A.L., O'Hara, L., Mason, J.I., Jorgensen, A., Frederiksen, H., Milne, L., Smith, S., Mitchell, R.T., and Smith, L.B. (2019). Androgen receptor signalling in the male adrenal facilitates X-zone regression, cell turnover and protects against adrenal degeneration during ageing. *Sci. Rep.* 9, 10457. <https://doi.org/10.1038/s41598-019-46049-3>.
- Gautier, E.L., Shay, T., Miller, J., Greter, M., Jakubzick, C., Ivanov, S., Helft, J., Chow, A., Elpek, K.G., Gordonov, S., et al. (2012). Gene-expression profiles and transcriptional regulatory pathways that underlie the identity and diversity of mouse tissue macrophages. *Nat. Immunol.* 13, 1118–1128. <https://doi.org/10.1038/ni.2419>.
- Ginhoux, F., and Williams, M. (2016). Tissue-resident macrophage ontogeny and homeostasis. *Immunity* 44, 439–449. <https://doi.org/10.1016/j.immuni.2016.02.024>.
- Ginhoux, F., Greter, M., Leboeuf, M., Nandi, S., See, P., Gokhan, S., Mehler, M.F., Conway, S.J., Ng, L.G., Stanley, E.R., et al. (2010). Fate mapping analysis reveals that adult microglia derive from primitive macrophages. *Science* 330, 841–845. <https://doi.org/10.1126/science.1194637>.
- Ginhoux, F., Liu, K., Helft, J., Bogunovic, M., Greter, M., Hashimoto, D., Price, J., Yin, N., Bromberg, J., Lira, S.A., et al. (2009). The origin and development of nonlymphoid tissue CD103+ DCs. *J. Exp. Med.* 206, 3115–3130. <https://doi.org/10.1084/jem.20091756>.
- Perdiguer, E.G., Klapproth, K., Schulz, C., Busch, K., Azzoni, E., Crozet, L., Garner, H., Trouillet, C., de Bruijn, M.F., Geissmann, F., and Rodewald, H.R. (2015). Tissue-resident macrophages originate from yolk-sac-derived erythro-myeloid progenitors. *Nature* 433, S64–S551. <https://doi.org/10.1016/j.exphem.2015.06.130>.
- Guilliams, M., De Kleer, I., Henri, S., Post, S., Vanhoutte, L., De Prijck, S., Deswarte, K., Malissen, B., Hammad, H., and Lambrecht, B.N. (2013). Alveolar macrophages develop from fetal monocytes that differentiate into long-lived cells in the first week of life via GM-CSF. *J. Exp. Med.* 210, 1977–1992. <https://doi.org/10.1084/jem.20131199>.
- Hafemeister, C., and Satija, R. (2019). Normalization and variance stabilization of single-cell RNA-seq data using regularized negative binomial regression. *Genome Biol.* 20, 296. <https://doi.org/10.1186/s13059-019-1874-1>.
- Huang, C.C.J., and Kang, Y. (2019). The transient cortical zone in the adrenal gland: the mystery of the adrenal X-zone. *J. Endocrinol.* 241, R51–R63. <https://doi.org/10.1530/joe-18-0632>.
- Hume, D.A., Halpin, D., Charlton, H., and Gordon, S. (1984). The mononuclear phagocyte system of the mouse defined by immunohistochemical localization of antigen F4/80: macrophages of endocrine organs. *Proc. Natl. Acad. Sci. U S A* 81, 4174–4177. <https://doi.org/10.1073/pnas.81.13.4174>.
- Ivanov, S., Gallerand, A., Gros, M., Stunault, M.I., Merlin, J., Vaillant, N., Yvan-Charvet, L., and Guinamard, R.R. (2019). Mesothelial cell CSF1 sustains peritoneal macrophage proliferation. *Eur. J. Immunol.* 49, 2012–2018. <https://doi.org/10.1002/eji.201948164>.
- Jakubzick, C., Gautier, E.L., Gibbings, S.L., Sojka, D.K., Schlitzer, A., Johnson, T.E., Ivanov, S., Duan, Q., Bala, S., Condon, T., et al. (2013). Minimal differentiation of classical monocytes as they survey steady-state tissues and transport antigen to lymph nodes. *Immunity* 39, 599–610. <https://doi.org/10.1016/j.immuni.2013.08.007>.
- Jokela, H., Lokka, E., Kiviranta, M., Tyystjarvi, S., Gerke, H., Elima, K., Salmi, M., and Rantakari, P. (2020). Fetal-derived macrophages persist and sequentially mature in ovaries after birth in mice. *Eur. J. Immunol.* 50, 1500–1514. <https://doi.org/10.1002/eji.202048531>.
- Kim, D., Paggi, J.M., Park, C., Bennett, C., and Salzberg, S.L. (2019). Graph-based genome alignment and genotyping with HISAT2 and HISAT-genotype. *Nat. Biotechnol.* 37, 907–915. <https://doi.org/10.1038/s41587-019-0201-4>.
- Kohyama, M., Ise, W., Edelson, B.T., Wilker, P.R., Hildner, K., Mejia, C., Frazier, W.A., Murphy, T.L., and Murphy, K.M. (2009). Role for Spi-C in the development of red pulp macrophages and splenic iron homeostasis. *Nature* 457, 318–321. <https://doi.org/10.1038/nature07472>.
- Koppelman, B., Neefjes, J.J., de Vries, J.E., and de Waal Malefyt, R. (1997). Interleukin-10 down-regulates MHC class II $\alpha\beta$ peptide complexes at the plasma membrane of monocytes by affecting arrival and recycling. *Immunity* 7, 861–871. [https://doi.org/10.1016/s1074-7613\(00\)80404-5](https://doi.org/10.1016/s1074-7613(00)80404-5).
- Lacroix, A., Feelders, R.A., Stratakis, C.A., and Nieman, L.K. (2015). Cushing's syndrome. *Lancet* 386, 913–927. [https://doi.org/10.1016/s0140-6736\(14\)61375-1](https://doi.org/10.1016/s0140-6736(14)61375-1).
- Liao, Y., Smyth, G.K., and Shi, W. (2014). featureCounts: an efficient general purpose program for assigning sequence reads to genomic features. *Bioinformatics* 30, 923–930. <https://doi.org/10.1093/bioinformatics/btt656>.
- Lim, H.Y., Lim, S.Y., Tan, C.K., Thiam, C.H., Goh, C.C., Carbajo, D., Chew, S.H.S., See, P., Chakarov, S., Wang, X.N., et al. (2018). Hyaluronan receptor LYVE-1-expressing macrophages maintain arterial tone through hyaluronan-mediated regulation of smooth muscle cell collagen. *Immunity* 49, 326–341.e7. <https://doi.org/10.1016/j.immuni.2018.06.008>.
- Liu, Z., Gu, Y., Chakarov, S., Blieriot, C., Kwok, I., Chen, X., Shin, A., Huang, W., Dress, R.J., Dutertre, C.A., et al. (2019). Fate mapping via ms4a3-expression history traces monocyte-derived cells. *Cell* 178, 1509–1525.e19. <https://doi.org/10.1016/j.cell.2019.08.009>.
- Lokka, E., Lintukorpi, L., Cisneros-Montalvo, S., Makela, J.A., Tyystjarvi, S., Ojasalo, V., Gerke, H., Toppari, J., Rantakari, P., and Salmi, M. (2020). Generation, localization and functions of macrophages during the development of testis. *Nat. Commun.* 11, 4375. <https://doi.org/10.1038/s41467-020-18206-0>.
- Love, M.I., Huber, W., and Anders, S. (2014). Moderated estimation of fold change and dispersion for RNA-seq data with DESeq2. *Genome Biol.* 15, 550. <https://doi.org/10.1186/s13059-014-0550-8>.

- Lyra, R., and Schedl, A. (2021). Adrenal cortex renewal in health and disease. *Nat. Rev. Endocrinol.* *17*, 421–434. <https://doi.org/10.1038/s41574-021-00491-4>.
- McGinnis, C.S., Murrow, L.M., and Gartner, Z.J. (2019). DoubletFinder: doublet detection in single-cell RNA sequencing data using artificial nearest neighbors. *Cell Syst.* *8*, 329–337.e4. <https://doi.org/10.1016/j.cels.2019.03.003>.
- Molawi, K., Wolf, Y., Kandalla, P.K., Favret, J., Hagemeyer, N., Frenzel, K., Pinto, A.R., Klapproth, K., Henri, S., Malissen, B., et al. (2014). Progressive replacement of embryo-derived cardiac macrophages with age. *J. Exp. Med.* *211*, 2151–2158. <https://doi.org/10.1084/jem.20140639>.
- Mossadegh-Keller, N., Gentek, R., Gimenez, G., Bigot, S., Mailfert, S., and Sieweke, M.H. (2017). Developmental origin and maintenance of distinct testicular macrophage populations. *J. Exp. Med.* *214*, 2829–2841. <https://doi.org/10.1084/jem.20170829>.
- Nishinakamura, R., Wiler, R., Dirksen, U., Morikawa, Y., Arai, K., Miyajima, A., Burdach, S., and Murray, R. (1996). The pulmonary alveolar proteinosis in granulocyte macrophage colony-stimulating factor/interleukins 3/5 beta c receptor-deficient mice is reversed by bone marrow transplantation. *J. Exp. Med.* *183*, 2657–2662. <https://doi.org/10.1084/jem.183.6.2657>.
- Pridans, C., Raper, A., Davis, G.M., Alves, J., Sauter, K.A., Lefevre, L., Regan, T., Meek, S., Sutherland, L., Thomson, A.J., et al. (2018). Pleiotropic impacts of macrophage and microglial deficiency on development in rats with targeted mutation of the *Csf1r* locus. *J. Immunol.* *201*, 2683–2699. <https://doi.org/10.4049/jimmunol.1701783>.
- Rajamohan, S.B., Raghuraman, G., Prabhakar, N.R., and Kumar, G.K. (2012). NADPH oxidase-derived H₂O₂ contributes to angiotensin II-induced aldosterone synthesis in human and rat adrenal cortical cells. *Antioxidants Redox Signal.* *17*, 445–459. <https://doi.org/10.1089/ars.2011.4176>.
- Ryan, G.R., Dai, X.M., Dominguez, M.G., Tong, W., Chuan, F., Chisholm, O., Russell, R.G., Pollard, J.W., and Stanley, E.R. (2001). Rescue of the colony-stimulating factor 1 (CSF-1)-nullizygous mouse (*Csf1*(op)/*Csf1*(op)) phenotype with a CSF-1 transgene and identification of sites of local CSF-1 synthesis. *Blood* *98*, 74–84. <https://doi.org/10.1182/blood.v98.1.74>.
- Saelens, W., Cannoodt, R., Todorov, H., and Saeys, Y. (2019). A comparison of single-cell trajectory inference methods. *Nat. Biotechnol.* *37*, 547–554. <https://doi.org/10.1038/s41587-019-0071-9>.
- Sakai, M., Troutman, T.D., Seidman, J.S., Ouyang, Z., Spann, N.J., Abe, Y., Ego, K.M., Bruni, C.M., Deng, Z., Schlachetzki, J.C.M., et al. (2019). Liver-derived signals sequentially reprogram myeloid enhancers to initiate and maintain kupffer cell identity. *Immunity* *51*, 655–670.e8. <https://doi.org/10.1016/j.immuni.2019.09.002>.
- Satpathy, A.T., Briseno, C.G., Lee, J.S., Ng, D., Manieri, N.A., Kc, W., Wu, X., Thomas, S.R., Lee, W.L., Turkoz, M., et al. (2013). Notch2-dependent classical dendritic cells orchestrate intestinal immunity to attaching-and-effacing bacterial pathogens. *Nat. Immunol.* *14*, 937–948. <https://doi.org/10.1038/ni.2679>.
- Schulz, C., Gomez Perdiguero, E., Chorro, L., Szabo-Rogers, H., Cagnard, N., Kierdorf, K., Prinz, M., Wu, B., Jacobsen, S.E.W., Pollard, J.W., et al. (2012). A lineage of myeloid cells independent of Myb and hematopoietic stem cells. *Science* *336*, 86–90. <https://doi.org/10.1126/science.1219179>.
- Scott, C.L., Zheng, F., De Baetselier, P., Martens, L., Saeys, Y., De Prijck, S., Lippens, S., Abels, C., Schoonooghe, S., Raes, G., et al. (2016). Bone marrow-derived monocytes give rise to self-renewing and fully differentiated Kupffer cells. *Nat. Commun.* *7*, 10321. <https://doi.org/10.1038/ncomms10321>.
- Serbina, N.V., and Pamer, E.G. (2006). Monocyte emigration from bone marrow during bacterial infection requires signals mediated by chemokine receptor CCR2. *Nat. Immunol.* *7*, 311–317. <https://doi.org/10.1038/ni1309>.
- Sergushichev, A.A., Loboda, A.A., Jha, A.K., Vincent, E.E., Driggers, E.M., Jones, R.G., Pearce, E.J., and Artyomov, M.N. (2016). GAM: a web-service for integrated transcriptional and metabolic network analysis. *Nucleic Acids Res.* *44*, W194–W200. <https://doi.org/10.1093/nar/gkw266>.
- Silva, H.M., Bafica, A., Rodrigues-Luiz, G.F., Chi, J., Santos, P.D.A., Reis, B.S., Hoytema van Konijnenburg, D.P., Crane, A., Arifa, R.D.N., Martin, P., et al. (2019). Vasculature-associated fat macrophages readily adapt to inflammatory and metabolic challenges. *J. Exp. Med.* *216*, 786–806. <https://doi.org/10.1084/jem.20181049>.
- Street, K., Rizzo, D., Fletcher, R.B., Das, D., Ngai, J., Yosef, N., Purdom, E., and Dudoit, S. (2018). Slingshot: cell lineage and pseudotime inference for single-cell transcriptomics. *BMC Genom.* *19*, 477. <https://doi.org/10.1186/s12864-018-4772-0>.
- Stuart, T., Butler, A., Hoffman, P., Hafemeister, C., Papalexi, E., Mauck, W.M., 3rd, Hao, Y., Stoekius, M., Smibert, P., and Satija, R. (2019). Comprehensive integration of single-cell data. *Cell* *177*, 1888–1902.e21. <https://doi.org/10.1016/j.cell.2019.05.031>.
- Unanue, E.R., Turk, V., and Neefjes, J. (2016). Variations in MHC class II antigen processing and presentation in health and disease. *Annu. Rev. Immunol.* *34*, 265–297. <https://doi.org/10.1146/annurev-immunol-041015-055420>.
- Williams, J.W., Elvington, A., Ivanov, S., Kessler, S., Luehmann, H., Baba, O., Saunders, B.T., Kim, K.W., Johnson, M.W., Craft, C.S., et al. (2017). Thermoneutrality but not UCP1 deficiency suppresses monocyte mobilization into blood. *Circ. Res.* *121*, 662–676. <https://doi.org/10.1161/circresaha.117.311519>.
- Wolf, Y., Boura-Halfon, S., Cortese, N., Haimon, Z., Sar Shalom, H., Kuperman, Y., Kalchenko, V., Brandis, A., David, E., Segal-Hayoun, Y., et al. (2017). Brown-adipose-tissue macrophages control tissue innervation and homeostatic energy expenditure. *Nat. Immunol.* *18*, 665–674. <https://doi.org/10.1038/ni.3746>.
- Yona, S., Kim, K.W., Wolf, Y., Mildner, A., Varol, D., Breker, M., Strauss-Ayali, D., Viukov, S., Guilliams, M., Misharin, A., et al. (2013). Fate mapping reveals origins and dynamics of monocytes and tissue macrophages under homeostasis. *Immunity* *38*, 79–91. <https://doi.org/10.1016/j.immuni.2012.12.001>.
- Zennaro, M.C., Boulkroun, S., and Fernandes-Rosa, F.L. (2020). Pathogenesis and treatment of primary aldosteronism. *Nat. Rev. Endocrinol.* *16*, 578–589. <https://doi.org/10.1038/s41574-020-0382-4>.

STAR★METHODS

KEY RESOURCES TABLE

REAGENT or RESOURCE	SOURCE	IDENTIFIER
Antibodies		
CD11b PE-Cy5 (Clone M1/70)	Biolegend	Cat# 101209, RRID:AB_312792
CD11b Brilliant Violet 510 (Clone M1/70)	Biolegend	Cat# 101263, RRID:AB_2629529
CD11b APC-Cy7 (Clone M1/70)	Biolegend	Cat# 101226, RRID:AB_830642
F4/80 PE-Cy7 (Clone BM8)	Biolegend	Cat# 123114, RRID:AB_893478
F4/80 Alexa Fluor 488 (Clone BM8)	Biolegend	Cat# 123120, RRID:AB_893479
F4/80 Brilliant Violet 650 (Clone BM8)	Biolegend	Cat# 123149, RRID:AB_2564589
F4/80 APC (Clone REA126)	Miltenyi	Cat# 130-116-525 RRID:AB_2733417
CD45 APC-Cy7 (Clone 30-F11)	BD Biosciences	Cat# 557659, RRID:AB_396774
CD45 Pacific Blue (Clone 30-F11)	Biolegend	Cat# 103126, RRID:AB_493535
CD45 VioGreen (Clone REA737)	Miltenyi	Cat# 130-110-803, RRID: AB_2658224
CD45 Brilliant Violet 570 (Clone 30-F11)	Biolegend	Cat# 103136, RRID:AB_10898325
CD45 APC-Vio 770 (Clone REA737)	Miltenyi	Cat# 130-110-662, RRID:AB_2658231
CD64 Brilliant Violet 421 (Clone x54-5/7.1)	Biolegend	Cat# 139309, RRID: AB_2562694
CD64 Brilliant Violet 711 (Clone x54-5/7.1)	Biolegend	Cat# 139311, RRID: AB_2563846
CD64 PE/Dazzle 594 (Clone x54-5/7.1)	Biolegend	Cat# 139320, RRID:AB_2566559
Ly6C APC (Clone HK1.4)	Biolegend	Cat# 128015, RRID:AB_1732087
Ly6C PerCP-Cy5.5 (Clone HK1.4)	Biolegend	Cat# 128012, RRID: AB_1659241
Ly6G PerCP-Cy5.5 (Clone 1A8)	Biolegend	Cat# 127615, RRID:AB_1877272
Ly6G Brilliant Violet 510 (Clone 1A8)	Biolegend	Cat#127633, RRID: AB_2562937
Ly6G Brilliant Violet 785 (Clone 1A8)	Biolegend	Cat# 127645, RRID:AB_2566317
Klrg1 PE-Cy7 (Clone 2F1/KLRG1)	Biolegend	Cat# 138416, RRID:AB_2561736
CD115 PE-Cy7 (AFS98)	Biolegend	Cat# 135524, RRID: AB_2566460
CD115 PE (Clone AFS98)	Biolegend	Cat# 135506, RRID:AB_1937253
CD115 PE (Clone REA827)	Miltenyi	Cat# 130-112-639, RRID:AB_2654553
Gr-1 PerCP-Cy5.5 (Clone RB6-8C5)	Biolegend	Cat# 108426, RRID:AB_893557
NK1.1 FITC (Clone PK136)	Biolegend	Cat# 108706, RRID:AB_313393
Sca1 Pacific Blue (Clone D7)	Biolegend	Cat# 108120, RRID:AB_493273
CD19 PE (Clone REA749)	Miltenyi	Cat# 130-112-035, RRID:AB_2655822
CD19 BUV737 (Clone 1D3)	BD Biosciences	Cat# 612782, RRID:AB_2870111
CD3 APC (Clone 17A2)	Biolegend	Cat# 100236, RRID:AB_2561456
CD8a Brilliant Violet 510 (Clone 53-6.7)	Biolegend	Cat# 100752, RRID:AB_2563057
CD4 Alexa Fluor 700 (Clone RM4-5)	Biolegend	Cat# 100536, RRID:AB_493701
MHC-II IA/IE PE (Clone 2G9)	BD Biosciences	Cat# 558593, RRID:AB_647221
MHC-II IA/IE FITC (Clone 2G9)	BD Biosciences	Cat# 553623, RRID:AB_394958
MHC-II IA/IE Brilliant Violet 510 (Clone M5/114.15.2)	Biolegend	Cat# 107636, RRID : AB_2734168
MHC-II IA/IE Alexa Fluor 647 (Clone M5/114.15.2)	Biolegend	Cat# 107618, RRID:AB_493525
MHC-II VioBlue (Clone REA813)	Miltenyi	Cat# 130-112-394, RRID:AB_2652908
Timd4 PE-Cy7 (Clone RMT4-54)	Biolegend	Cat# 130010, RRID:AB_2565719
Timd4 PerCP-eFluor710 (Clone RMT4-54)	Invitrogen	Cat# 46-5866-80, RRID:AB_2573780
Lyve1 eFluor660 (Clone ALY7)	Invitrogen	Cat# 50-0443-80, RRID:AB_10598060
CD206 PerCP-Cy5.5 (Clone C068C2)	Biolegend	Cat# 141716, RRID:AB_2561992

(Continued on next page)

Continued

REAGENT or RESOURCE	SOURCE	IDENTIFIER
MerTK PE (Clone 2B10C42)	Biolegend	Cat# 151506, RRID:AB_2617037
MerTK APC (Clone 2B10C42)	Biolegend	Cat# 151508, RRID: AB_2650739
CD11c PE-Cy7 (Clone HL3)	BD Biosciences	Cat# 558079, RRID:AB_647251
CD24 BUV496 (Clone M1/69)	BD Biosciences	Cat# 612953, RRID:AB_2870229
NKp46 Brilliant Violet 421 (Clone 29A1.4)	Biolegend	Cat# 137611, RRID:AB_10915472
CCR2 APC-Fire750 (Clone SA203T11)	Biolegend	Cat# 150629, RRID :AB_2810416
CD40 BUV395 (Clone 3/23)	BD Biosciences	Cat# 745697, RRID: AB_2743179
CD40 APC-Vio770 (Clone REA965)	Miltenyi	Cat# 130-116-113, RRID:AB_2727355
CD80 BUV615 (Clone 16-10A1)	BD Biosciences	Cat# 751328, RRID:AB_2875337
CD80 PerCP-Vio770 (Clone REA983)	Miltenyi	Cat# 130-116-464, RRID:AB_2727561
CD86 BUV805 (Clone GL1)	BD Biosciences	Cat# 741946, RRID:AB_2871258
CD86 PE (Clone REA1190)	Miltenyi	Cat# 130-122-129, RRID:AB_2819412
ICOSL (CD275) PE-Vio770 (Clone REA990)	Miltenyi	Cat# 130-116-448, RRID:AB_2727549
CD68 Alexa Fluor 647 (Clone FA-11)	Biolegend	Cat# 137004, RRID:AB_2044002
<i>InVivo</i> MAB anti-mouse CSF1R (Clone AFS98)	BioXCell	Cat# BE0213, RRID:AB_2687699
<i>InVivo</i> MAB rat IgG2a isotype control, anti-trinitrophenol (Clone 2A3)	BioXCell	Cat# BE0089, RRID:AB_1107769
<i>InVivo</i> MAB anti-mouse IL10R (Clone BE0050)	BioXCell	Cat# BE0050, RRID:AB_1107611
<i>InVivo</i> MAB anti-mouse CD16/CD32 (Clone 2.4G2)	BioXCell	Cat# BE0307, RRID:AB_2736987

Chemicals, peptides, and recombinant Proteins

DAPI	Sigma	Cat# D9542
LIVE/DEAD™ Fixable Violet Dead Cell Stain Kit	ThermoFisher	Cat# L34955
PFA 4%	VWR International	Cat# 9713.1000
Bovine serum Albumin (BSA)	Sigma	Cat# A7030
Tamoxifen	Sigma	Cat# T5648
Collagenase A	Sigma	Cat# 11088793001
IHC Antigen retrieval solution	eBiosciences	Cat# 00-4955-58
Antifade mounting medium with DAPI	Vectashield	Cat# H-1500
Fetal bovine serum	Fisher Scientific	Cat# 12350273
Lysing buffer	BD Biosciences	Cat# 555899
Liberase	Roche	Cat# 05401054001
DNase I	Roche	Cat# 10104159001
Penicillin Streptomycin	Life Technologies	Cat# 15070063
L-Glutamine	Life Technologies	Cat# 25030024
Mouse M-CSF	Miltenyi Biotec	Cat# 130-094-129
RPMI medium	Life Technologies	Cat# 21875091
Clorgyline	Abcam	Cat# ab145646
Norepinephrine	Sigma	Cat# A7257
TRITC-Dextran 65–85 kDa	Sigma	Cat# T1162
Bodipy	Thermofisher	Cat# D3922

Critical commercial assays

Mouse CCL2 DuoSet ELISA	R&D Systems	Cat# DY479-05
Norepinephrine ELISA Kit	Tebu-bio	Cat# 157KA1891
Aldosterone Parameter Assay Kit	R&D Systems	Cat# KGE016
Corticosterone Parameter Assay Kit	R&D Systems	Cat# KGE009

(Continued on next page)

Continued

REAGENT or RESOURCE	SOURCE	IDENTIFIER
Ki67 Staining Kit PE	BD Biosciences	Cat# 51-36525x
FoxP3 Staining Buffer Set	Miltenyi	Cat# 130-093-142
RNA extraction kit	QIAGEN	Cat# 74136
Software and algorithms		
Prism 8	GraphPad	N/A
Chromeleon software	Thermo Scientific	N/A
FlowJo	Tree Star	N/A
Seurat package version 3.1.0	https://satijalab.org/seurat/	N/A
BD FACSDiva	BD Biosciences	N/A
ImageJ	NIH	N/A
SpectroFlo	Cytek	N/A
Phantasus	Artyomov Lab	N/A

RESOURCE AVAILABILITY

Lead contact

Further information and requests for resources and reagents should be directed to and will be fulfilled by the lead contact Dr. Stoyan Ivanov (Stoyan.ivanov@unice.fr).

Materials availability

This study did not generate new unique reagents.

Data and code availability

All sequencing datasets in this article are deposited in an international public repository, Gene Expression Omnibus (GEO), under accession ID GSE203096 for bulk RNA sequencing and GSE203095 for single cell RNA sequencing data. This paper does not report original code. Any additional information required to reanalyze the data reported in this paper is available from the [lead contact](#) upon request.

EXPERIMENTAL MODEL AND SUBJECT DETAILS

Wild-type C57BL/6J mice were purchased from Janvier Labs. CX3CR1^{9fp} (B6.Cg-Ptprca Cx3cr1^{tm1Litt/LittJ}), Lyz2^{cre} (B6.129P2-Lyz2^{tm1(cre)lfo/J}), CD115^{creERT2} (FVB-Tg(Csf1r-cre/Esr1*)1Jwp/J), R26^{TdTomato} (B6.Cg-Gt(ROSA)26Sor^{tm9(CAG-tdTomato)Hze/J}) and CX3CR1^{creERT2} (B6.129P2(C)-Cx3cr1^{tm2.1(cre/ERT2)Jung/J}) were on B6 background. CCR2^{cre/ERT2} (C57BL/6NTac-Ccr2^{tm2982(T2A-Cre7ESR1-T2A-mKate2)}) (Croxford et al., 2015) mice were kindly provided by Dr. Burkhard Becher and crossed with R26^{TdTomato} and CCR2^{GFP} mice (B6(C)-Ccr2^{tm1.1Cln/J}) provided by Dr. Marco Colonna (Satpathy et al., 2013). Ms4a3^{cre} (C57BL/6J-Ms4a3^{em2(cre)Fgnx/J}) mice, initially described in (Liu et al., 2019), were kindly provided by Dr. Florent Ginhoux. When possible, co-housed littermate controls were used. Because age appeared as a relevant parameter, mice of different ages were used as indicated in each figure legend. Age-matched animals were used for male and female comparisons. All mice were bred and housed in specific pathogen-free conditions maintained by animal facilities in either the Mediterranean Center of Molecular Medicine (INSERM U1065, Université Côte d'Azur), the University of Minnesota Medical School Research Animal Resources, the University of Illinois at Chicago, or the EOPS2 facility, Lille University Hospital Campus. Facilities were maintained at ambient temperature of ~20–23°C, with 12/12-h light/dark cycle and food available ad libitum. Animal protocols were authorized by the French Ministry of Higher Education and Research upon approval of the local ethical committees, by the Institutional Animal Care and Use Committee (IACUC) at University of Minnesota Medical School, by the IACUC at University of Illinois College of Medicine.

METHOD DETAILS

Tamoxifen treatments

CD115^{creERT2} × R26^{TdTomato} reporter mice were treated with tamoxifen dissolved in corn oil (20 mg/mL) by oral gavage (200 μL/mouse) on three consecutive days and were sacrificed 24 h after the last dose was administered.

CCR2^{creERT2} x R26^{TdTomato} reporter mice were treated with tamoxifen dissolved in corn oil (20 mg/mL) by a single oral gavage (250 μ L/mouse). Animals were sacrificed 2, 7, or 14 days later and assessed for labeling efficiency in blood and adrenal glands by flow cytometry.

Pregnant CX3CR1^{creERT2} x R26^{TdTomato} mice were given 4 mg of TAM dissolved in corn oil. Mice were treated by oral gavage at the indicated embryonic day. Pups were obtained by cesarean delivery at E19.5 and taken care of by foster mothers until weaning periods. Brain microglia labeling was >97% and blood monocytes labeling was below 0.3% in all mice that received embryonic labeling. For pulse-chase experiments in adults, CX3CR1^{creERT2} x R26^{TdTomato} mice were injected intra-peritoneally with 10 mg/mL TAM (200 μ L per mouse in 10% EtOH and sunflower oil) daily for 5 days. Labelling efficiency was assessed in brain, blood and adrenal glands for each experiment involving this strain.

Surgery procedures

Castration or control procedure (Sham) were performed on 3-week-old C57BL/6 male mice, which were sacrificed 4 weeks later for analysis of adrenal glands. Ovariectomy (OVX) and sham surgery were performed on 6-week-old C57BL/6 female mice, in accordance with the Institutional Ethics Committee on Laboratory Animals (CIEPAL-Azur, Nice Sophia-Antipolis, France). Mice were sacrificed 6 weeks after surgery.

In vivo macrophage depletion

C57BL/6 mice received an intraperitoneal injection of 500 μ g *InVivo*MAb anti-mouse CSF1R (CD115) antibody (Clone AFS98, BioXCell cat No. BE0213) or isotype control (Clone 2A3, BioXCell cat No. BE0089). The injection was repeated 2 days later. Mice were sacrificed 16 h after the second injection. For cold exposure, macrophage depleted, and control mice were housed for 12 h at 4°C. Mice were single housed with identical light/dark cycle and food available ad libitum.

In vivo IL-10R blockade

5- to 12-week-old C57BL/6 mice received an intraperitoneal injection of 250 μ g *InVivo*MAb anti-mouse IL-10R antibody (clone 1B1.3A, BioXCell cat no. BE0050) or PBS. The injection was repeated 2 days later. Mice were sacrificed 16 h after the second injection.

Flow cytometry analysis

Tissues were harvested and washed in PBS. Adipose depots surrounding the adrenal glands were carefully removed before shredding the tissue with scissors. Then the samples were incubated for 30 min at 37°C in PBS containing 300 μ g/mL Liberase and 100 μ g/mL DNase I. The resulting suspension was homogenized using a syringe and a 20G needle, passed through a 100 μ m sieve and centrifuged at 400g for 5 min. Cells were then resuspended in FACS buffer (PBS containing 0.3 mM EDTA and 0.06% BSA), stained for 30 min at 4°C in the dark and then washed. A viability stain (DAPI or Live/Dead fixable viability dye) was used whenever possible. Conventional cytometry data were acquired on a BD FACS Canto II or BD LSRFortessa X-20. Spectral cytometry data were acquired on a Cytex Aurora cytometer. All analysis, including unsupervised t-SNE analysis, was performed using FlowJo software (Tree Star).

SCENITH

The method was performed as described in (Arguello et al., 2020). SCENITH reagents kit (inhibitors, puromycin and antibodies) were obtained from www.scenith.com/try-it and used according to the provided protocol for ex-vivo analysis of myeloid cells. Briefly, adrenal glands were harvested, added to 50 μ L DMEM (4.5g/L glucose) containing either Control, 2-Deoxy-D-Glucose (100mM), Oligomycin (1 μ M), 2-Deoxy-D-Glucose + Oligomycin or Harringtonine (2 μ g/mL), minced and incubated at 37°C for 30 min. Puromycin (10 μ g/mL), Liberase (300 μ g/mL) and DNase I (100 μ g/mL) were then added to each tube. Adrenal glands were further incubated at 37°C for 30 min, and were then washed with 1mL cold PBS and put on ice. The suspension was homogenized using a syringe and a 20G needle, passed through a 100 μ m sieve and centrifuged at 400g for 5 min. Cells were first stained with Live/Dead fixable viability dye, washed, and incubated with Fc Block (2.4G2, BioXcell) before surface staining. Cells were fixed and permeabilized using Foxp3 fixation/permeabilization buffer (Miltenyi) and then stained with anti-Puromycin (Alexa Fluor 647). Cells that were not incubated with Puromycin were used as a negative control for anti-Puromycin signal. Cells that received surface staining but no anti-Puromycin staining (full minus one) were used to measure subset-specific autofluorescence in the AF647 channel, and this background signal was subtracted. Glucose dependence, Mitochondrial dependence and Glycolytic capacity were calculated as previously described (Arguello et al., 2020).

Dextran uptake assay

Mice were injected intravenously with 100 μ L TRITC-Dextran solution (65–85 kDa, 10 mg/mL diluted in PBS) and sacrificed twenty minutes later. Adrenal glands and epididymal adipose tissue were then processed and analyzed by flow cytometry. PBS-injected mice were used as controls to determine autofluorescence.

Norepinephrine degradation assay

Adrenal glands were processed as previously described. CD45⁺CD64⁺MerTK⁺ cells were sorted using a BD FACSAria II Cell Sorter. Macrophages were cultured overnight in RPMI medium (10% SVF, 2 mM L-Glutamine, 50 U/mL Penicillin, 50 μg/mL Streptomycin) containing 50 ng/mL recombinant M-CSF, as well as norepinephrine (NE) (5 μM) and/or clorgyline (100 μM). Supernatants were collected at the end of the incubation period and macrophage viability was assessed using Live/Dead staining.

ELISA assays

Blood was collected by submandibular bleeding. One adrenal gland was crushed in 200 μL PBS using 0.1 mm glass beads and a precellys homogenizer (Biospec cat No. 11079101). Corticosterone and aldosterone levels were measured in serum and adrenal gland homogenates as instructed (R&D Systems catalog No.KGE009 and No.KGE016 respectively). Norepinephrine was measured in AGM culture supernatant using Norepinephrine ELISA Kit (Abnova cat No.KA1891).

Bulk RNA-seq

RNA was extracted from adrenal glands using RNA extraction kit (QIAGEN cat No. 7413). Both adrenals were crushed using 0.1 mm glass beads in a precellys homogenizer (Biospec cat No. 11079101) containing RLT buffer from the RNA extraction kit. Total RNAs were extracted in RNase-free water from adrenals and were analyzed in DNBseqTM sequencing platform using DNBSEQ stranded mRNA library. Paired RNA-seq reads were aligned to the Ensembl 84 *Mus musculus* reference genome with hisat2 (version 2.2.1) (Kim et al., 2019). Count matrixes for each sample were obtained by featureCounts (version 2.0.1) in reversely stranded mode (Liao et al., 2014). Differential expression analysis was implemented by DESeq2 (version 1.30.1) (Love et al., 2014). Principal component analysis (PCA) was performed based on variance stabilized transformation output, and the heatmaps were drawn by Phantasus based on raw counts under the regularized log transformation (<https://genome.ifmo.ru/phantasus>, <https://artyomovlab.wustl.edu/phantasus>). Analysis of metabolic pathways was performed with Shiny GAM (Sergushichev et al., 2016).

Quantification of serum cation concentration

K⁺ concentrations in serum was evaluated by ion chromatography analysis. Serum samples and ion standard solutions were previously diluted (1/100), deproteinized by addition of acetonitrile (dilution 1:1 volume) mixed and centrifuged at 12,000g (10 min at 4°C). Ion concentrations of the supernatants were determined using an ion chromatography Dionex ICS-5000 plus system (Thermo Scientific). The system included an autosampler, pumps, eluent generator and conductivity detectors. The system is equipped with an eluent generator cartridge (Dionex EGC500MSA) and a cation column (IonPac AS-11 HC, 2 mm). Ion concentrations were determined using Chromeleon software (Thermo Scientific) by measuring surface area of the peaks and were compared to the corresponding ion standard profiles.

Single-cell RNA-seq data analysis

Cells were loaded on a Chromium Controller (10× Genomics) with a target output of 5000 cells per sample. Reverse transcription, cDNA synthesis/amplification and library preparation were performed according to the 10× Genomics protocol (ChromiumTM Single Cell 3' Reagent Kit, v3.1 Chemistry). scRNA libraries were sequenced on an Illumina NextSeq 500/550 High Output flowcell: the forward read had a length of 28 bases that included the cell barcode and the UMI; the reverse read had a length of 55 bases that contained the cDNA insert.

Alignment, barcode assignment and UMI counting with Cell Ranger v4.0.0 was used to perform sample demultiplexing, barcode processing and single-cell 3' counting. Cell Ranger's mkfastq function was used to demultiplex raw base call files from the HiSeq4000 sequencer into sample specific FASTQ files.

Barcodes in both samples that were considered to represent noise and low-quality cells were filtered out using knee-inflection approach available in DropletUtils package (version 1.4.3). For analysis, Seurat package (version 3.1.0) was used, genes which express in less than 2 cells and cells which have non-zero counts in less than 200 genes were additionally filtered from both barcode expression matrices, and the result matrices were used as analysis inputs (Butler et al., 2018). The fraction of mitochondrial genes was calculated for every cell, and cells with a mitochondrial fraction >1.2% were filtered out. After all filtering procedures, 3,636 cells were left in the scRNA-seq data of the female sample, and 2,240 cells were left in scRNA-seq of the male sample.

Both samples were normalized using SCTransform function with mitochondrial content as variable to regress out in a second non-regularized linear regression (Hafemeister and Satija, 2019). For integration purpose, variable features across the samples were selected by SelectIntegrationFeatures function with the number of features equal to 2000. Then the object was prepared for integration (PrepSCTIntegration function), the anchors were found (FindIntegrationAnchors function) and the samples were merged into the whole object (IntegrateData function) (Stuart et al., 2019). The dimensionality of the object was reduced by principal component analysis (PCA), and the first 20 principal components (PCs) were used further to obtain uniform manifold approximation and projection (UMAP) dimensionality reduction by RunUMAP function. Graph-based clustering was run using FindNeighbors and FindClusters with a resolution of 1.0 and the first 20 PCs as input, and the 21 clusters were identified. Differential expression analysis was implemented using MAST package.

During manual cluster annotation using canonical gene markers, a cluster corresponding to doublets of NK cells and macrophages was identified and excluded from the main figures. We provide this suggestion using DoubletFinder package (version 2.0.3) using

doubletFinder_v3 function (with parameters PCs = 10, pN = 0.25, pK = 0.005) for each sample separately (Figure S2A) (McGinnis et al., 2019).

For visualization purposes, the custom labels were assigned to several clusters by merging several clusters for simplification (e.g., clusters 1, 6, 20 were merged as T cells, clusters 2, 12 were merged as B cells and clusters 0, 3, 19 were merged as NK cells). The gene signature heatmap was drawn using the scaled data slot of the integrated assay.

For trajectory analysis, clusters assigned as monocytes and macrophages were used, and infer_trajectory function from the dyno package (version 0.1.2) was used with the available slingshot singularity container (version 1.0.3) (Saelens et al., 2019; Street et al., 2018). In order to exclude the technical bias across the samples, the data slot from the integrated assay was used as an input expression for trajectory inference. Monocytes cluster was used as a root cluster in terms of given priors to slingshot algorithm. Trajectory visualization was implemented after dimensionality reduction by UMAP using dimred_umap function.

Tissue histology

Adrenal glands were fixed in 4% paraformaldehyde containing 30% sucrose for a minimum of 24 h, and then embedded in OCT. Sections of 16 μ m were cut using cryostat CM350 between -20°C and -26°C . Sections were mounted on histological slides (Thermo, Superfrost Plus) and preserved at -20°C until further analysis. For paraffin histology analysis, adrenal glands were fixed as aforementioned. Samples were then dehydrated in ethanol using STP120 tissue processor and included in paraffin. Sections of 8 μ m were cut using Microtome Microme HM340E. Sections were mounted on histological slides and preserved at 4°C until further analysis.

Immunostaining

Sections were blocked for 1 h with 3% BSA and 0.1% Tween 20. Antibodies were diluted in PBS with 3% BSA, 0.1% Tween 20. The next day, sections were washed 3 times for 10 min with PBS and mounted in Antifade mounting medium with DAPI. For Bodipy staining, slides were incubated for 15 min with 400 μM of Bodipy and then washed 3 times for 10 min and mounted in Antifade mounting medium with DAPI.

Immunofluorescence quantification method

IHC analyses and quantifications were performed manually using ImageJ. For counting of DAPI-positive cells, nuclei were automatically counted after setting a threshold and counted using the plugin “analyze particles” with a range of 1–20 μm . Bodipy analysis was performed by cropping multiple areas in the sample and then setting a threshold. Bodipy-positive cells were counted using the plugin “analyze particles” with a range located between 0 and 300 μm .

Fluorescence microscopy

The widefield microscope was a DM5500B upright stand (Leica, Germany). Acquisitions were performed using an Orca-ER camera (Hamamatsu, Japan). Mosaics were realized using a widefield/TIRF DMI6000 inverted stand microscope (Leica, Germany). Acquisitions were obtained using a DFC360 FX camera (Leica, Germany). The confocal microscope was a Nikon A1R confocal. Image acquisition was done with Leica AF suite software and analysed with image J.

Electron microscopy

The adrenal glands were fixed in 2.5% glutaraldehyde in 0.1 M cacodylate buffer (pH 7.4), rinsed with the same buffer and then post-fixed in osmium tetroxide (1% in cacodylate buffer). After rinsing with water, the specimens were dehydrated with acetone and embedded in Epon resin. The 80-nm ultrathin sections were contrasted with uranyl acetate and lead citrate for observation on a JEM 1400 JEOL Transmission Electron Microscope operating at 100 kV and equipped with an SIS Morada camera.

QUANTIFICATION AND STATISTICAL ANALYSIS

All data are represented in means \pm SEM. Statistical analysis was performed with GraphPad Prism 8 as indicated in each figure legend. Details of the specific statistical test used are described in figure legends. The number of replicates used in the experiments are noted in figures, figure legends, or by graphs represented as dot plots, where n represents number of biological replicates. ns $p > 0.05$; * $p < 0.05$; ** $p < 0.01$; *** $p < 0.001$; **** $p < 0.0001$.

Supplemental information

Unravelling the sex-specific diversity and functions of adrenal gland macrophages

Bastien Dolfi, Alexandre Gallerand, Maria M. Firulyova, Yingzheng Xu, Johanna Merlin, Adélie Dumont, Alexia Castiglione, Nathalie Vaillant, Sandrine Quemener, Heidi Gerke, Marion I. Stunault, Patricia R. Schrank, Seung-Hyeon Kim, Alisha Zhu, Jie Ding, Jerome Gilleron, Virginie Magnone, Pascal Barbry, David Dombrowicz, Christophe Duranton, Abdelilah Wakkach, Claudine Blin-Wakkach, Burkhard Becher, Sophie Pagnotta, Rafael J. Argüello, Pia Rantakari, Svetoslav Chakarov, Florent Ginhoux, Konstantin Zaitsev, Ki-Wook Kim, Laurent Yvan-Charvet, Rodolphe R. Guinamard, Jesse W. Williams, and Stoyan Ivanov

Sup. Table 1

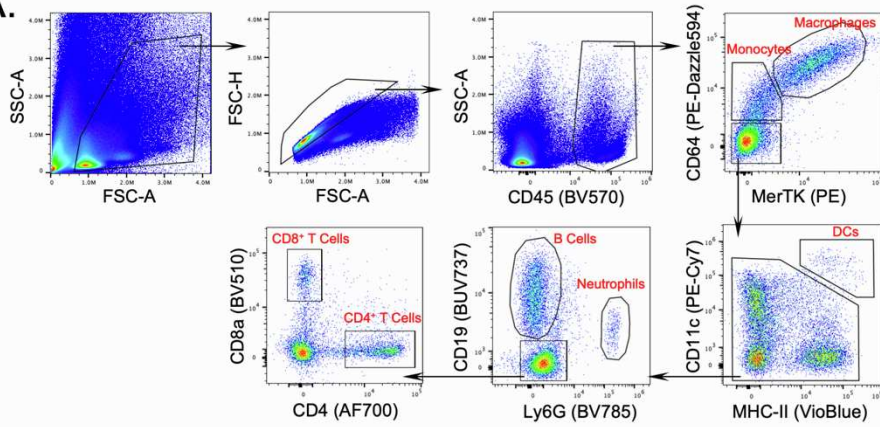
gene	p_val	avg_logFC (female over male)	pct.1	pct.2	p_val_adj
Xist	0	1.54951258733711	0.828	0	0
Rpl35	7.62774369759271e-40	0.3327951311151709	0.975	0.916	1.1416443992187e-35
Apoc2	3.69158130258448e-26	0.332692544859788	0.379	0.167	5.52518973557819e-22
AA467197	6.22673290146039e-23	0.369648525877762	0.16	0.037	9.31955113361576e-19
Lyz2	2.17567047442043e-22	0.386902156024932	0.999	0.999	3.25632599906506e-18
Tsc22d3	6.49050153643698e-22	0.329842436397367	0.611	0.429	9.71433364958522e-18
Fxyd5	8.32816037140203e-22	0.27680960279782	0.944	0.892	1.24647576278774e-17
Ap1s2	1.73034399696515e-21	0.294384138791506	0.516	0.367	2.58980586025774e-17
Sla	3.91862476256913e-20	0.266959924479275	0.497	0.332	5.86500568213722e-16
Ly6a	1.0545988034916e-15	0.366701350118315	0.206	0.097	1.57841802918587e-11
Cebpb	8.00698976030681e-15	0.250943124974004	0.712	0.549	1.19840615742512e-10
Msrb1	5.40275053801241e-14	0.275219903461956	0.558	0.398	8.08629673024318e-10
Tmsb10	4.60848480745743e-12	0.380808925495099	0.801	0.725	6.89751921132154e-08
Ms4a4c	8.66898423345473e-11	0.25134064025716	0.4	0.286	1.29748687022117e-06
Chil3	4.8237747978503e-10	0.394563532638321	0.186	0.087	7.21974373994254e-06
Ifitm3	3.73254227181447e-08	0.266876571843615	0.88	0.835	0.000558649601822472
Ly6c2	3.5363257330096e-07	0.29637517528339	0.18	0.097	0.00529281872459546
Plac8	4.98692265535371e-07	0.460921076326878	0.294	0.193	0.0074639271382679
Apoe	7.50291402455461e-07	0.48830922785863	0.969	0.955	0.0112296114205509
S100a6	1.08763499763158e-06	0.276562829675311	0.591	0.514	0.0162786330095518

Table S1.

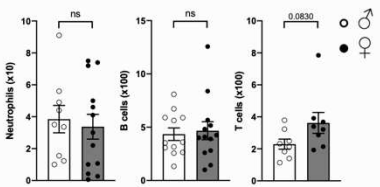
List of genes differentially expressed among myeloid cells in female and male mice. This table is related to figure 2.

Sup. Fig. 1

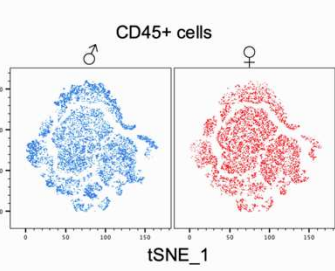
A.



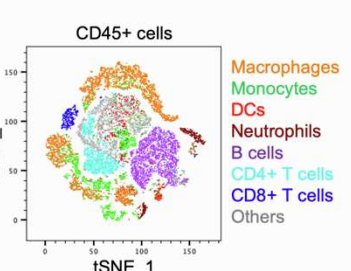
B.



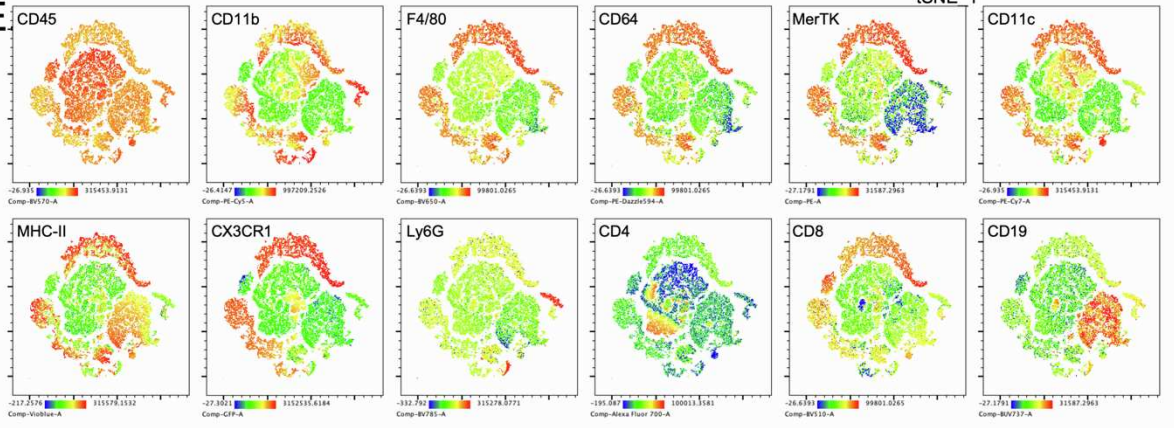
C.



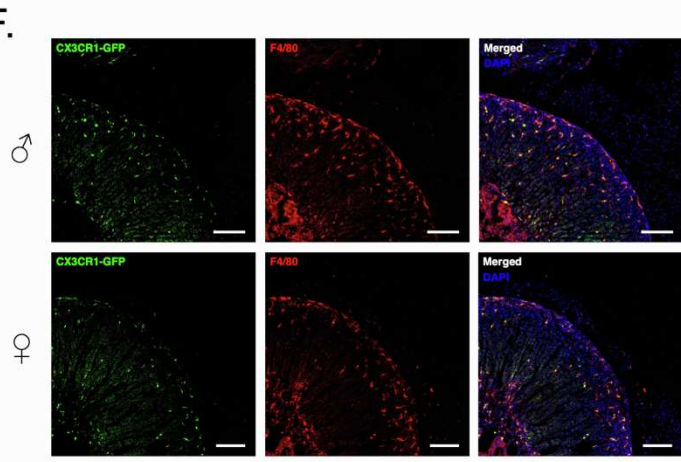
D.



E.



F.



G.

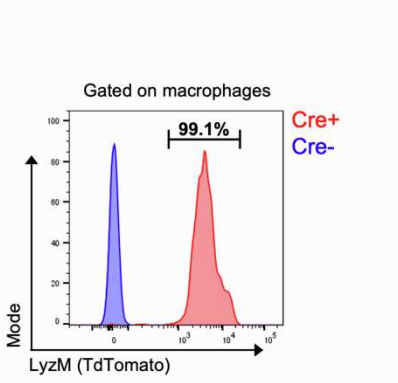


Figure S1. Flow cytometry analysis of immune cell diversity in male and female adrenal glands. This figure is complementary to figure 1.

(A) Gating strategy used to identify adrenal gland immune cells. Concatenated data from 8 7-week-old female mice. (B) Quantification of neutrophils (♂ n=9 and ♀ n=13), B cells (♂ n=12 and ♀ n=13) and T cells (♂ n=8 and ♀ n=8) in male and female adrenal glands. Data pooled from one (T cells) or two (neutrophils and B cells) independent experiments. (C) Clustering of CD45⁺ adrenal gland cells from male and female CX3CR1^{GFP} mice using unsupervised t-distributed stochastic neighbor embedding (tSNE) analysis of flow cytometry data. Panel : CD40 (BUV395) ; CD24 (BUV496) ; CD80 (BUV615) ; CD19 (BUV737) ; F4/80 (BV650) ; Ly6G (BV785) ; CX3CR1 (GFP reporter) ; MerTK (PE) ; CD64 (PE-Dazzle594) ; CD11b (PE-Cy5) ; CD206 (PerCP-Cy5.5) ; Timd4 (PerCP-eFluor710) ; CD11c (PE-Cy7) ; Lyve1 (eFluor660) ; CD4 (AF700) ; CCR2 (APC-Fire750). (D) Identification of adrenal gland immune subsets. Cells were gated manually and overlaid on tSNE plot to identify clusters. Macrophages : CD45⁺ CD64⁺ MerTK⁺. Monocytes : CD45⁺ MerTK⁻ CD11b⁺ CX3CR1⁺. Dendritic Cells (DCs) : CD45⁺ MerTK⁻ CD11c⁺ MHC-II⁺. Neutrophils : CD45⁺ CD11b⁺ Ly6G⁺. B cells : CD45⁺ MerTK⁻ CD11c⁻ MHC-II⁺ CD19⁺. CD4⁺ T cells : CD45⁺ MerTK⁻ MHC-II⁻ CD4⁺. CD8⁺ T cells : CD45⁺ MerTK⁻ MHC-II⁻ CD8⁺. (E) tSNE representation of the expression levels of CD45, CD11b, F4/80, CD64, MerTK, CD11c, MHC-II, CX3CR1, Ly6G, CD4, CD8 and CD19 among adrenal gland CD45⁺ cells. (F) Microscopy analysis of F4/80 staining in adrenal glands of CX3CR1^{GFP/+} mice. Scale bar : 100µm. (G) Flow cytometry analysis of TdTomato expression in adrenal gland macrophages from 8-week-old male Lyz2^{cre} x R26^{TdTomato} mice. Data from one experiment. All data are represented in means ± SEM. Statistical analysis was performed using two-tailed Mann-Whitney tests. ns p>0.05 ; * p<0.05 ; ** p<0.01 ; *** p<0.001 ; **** p<0.0001.

Sup. Fig. 2

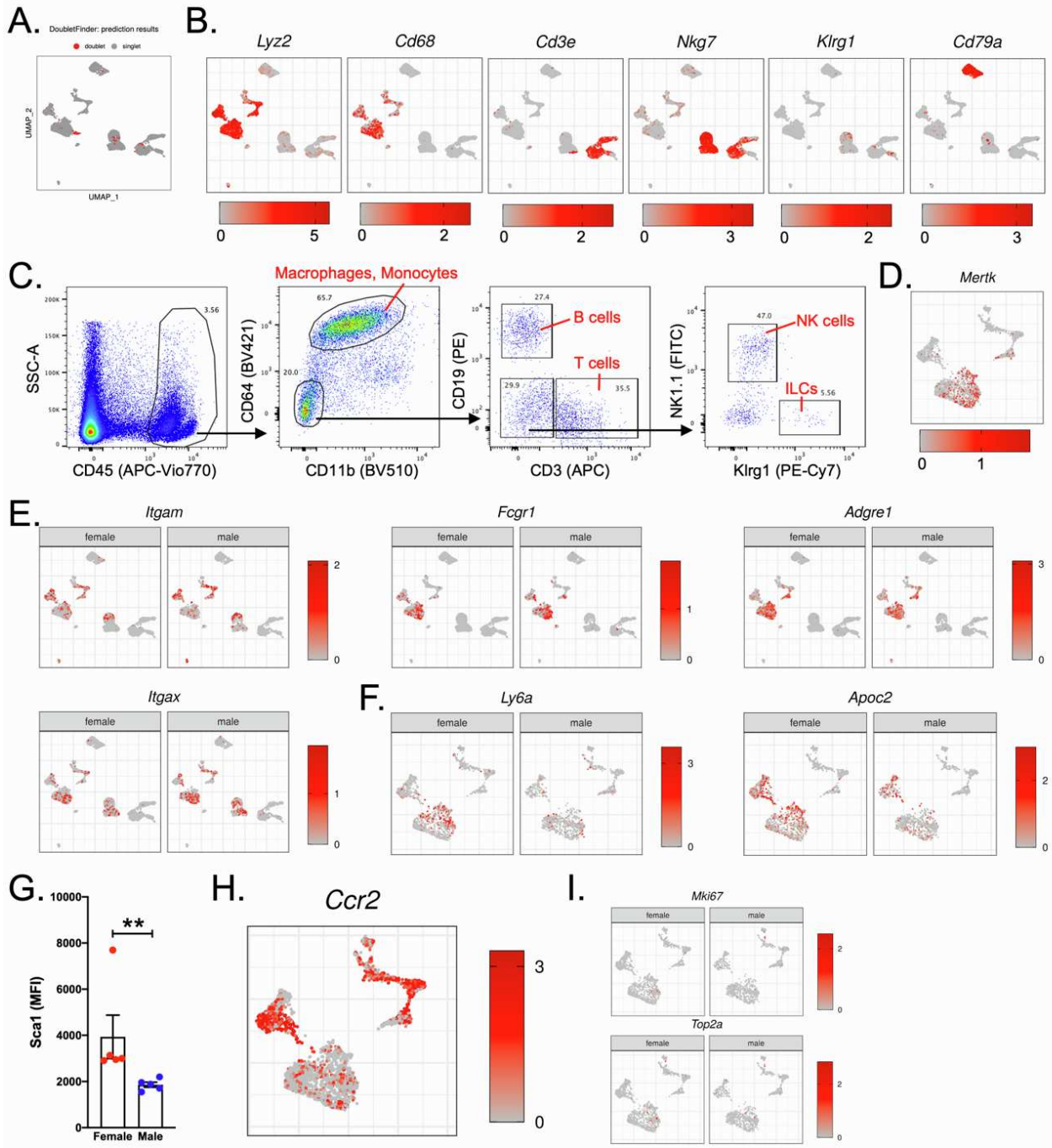


Figure S2. Single cell RNA-seq analysis of adrenal gland immune cell diversity. This figure is complementary to figure 2.

(A) Identification of doublets in scRNA-seq data using the DoubletFinder package. Doublets were removed from analysis. (B) scRNA-seq analysis of genes used to identify cell types (*Lyz2*, *CD68*, *CD3e*, *Nkg7*, *Klrg1* and *CD79a*). (C) Flow cytometry plots validating the presence of immune cell types corresponding to clusters identified in the scRNA-seq analysis. (D) scRNA-seq analysis of *Mertk* expression among adrenal gland myeloid cells. (E) scRNA-seq analysis of myeloid cell canonical markers by adrenal gland CD45⁺ cells from 7-week-old male and female mice. (F) scRNA-seq analysis of sex-enriched genes in adrenal gland myeloid cells. (G) Flow cytometry analysis of Sca1 expression in female and male mice (n=5 mice per group). Data pooled from two independent experiments. (H) scRNA-seq analysis of *CCR2* expression among adrenal gland myeloid cells. (I) scRNA-seq analysis of *Mki67* and *Top2a* mRNA expression. All data are represented in means \pm SEM. Statistical analysis was performed using two-tailed Mann-Whitney tests. ns p>0.05 ; * p<0.05 ; ** p<0.01 ; *** p<0.001 ; **** p<0.0001.

Sup. Fig. 3

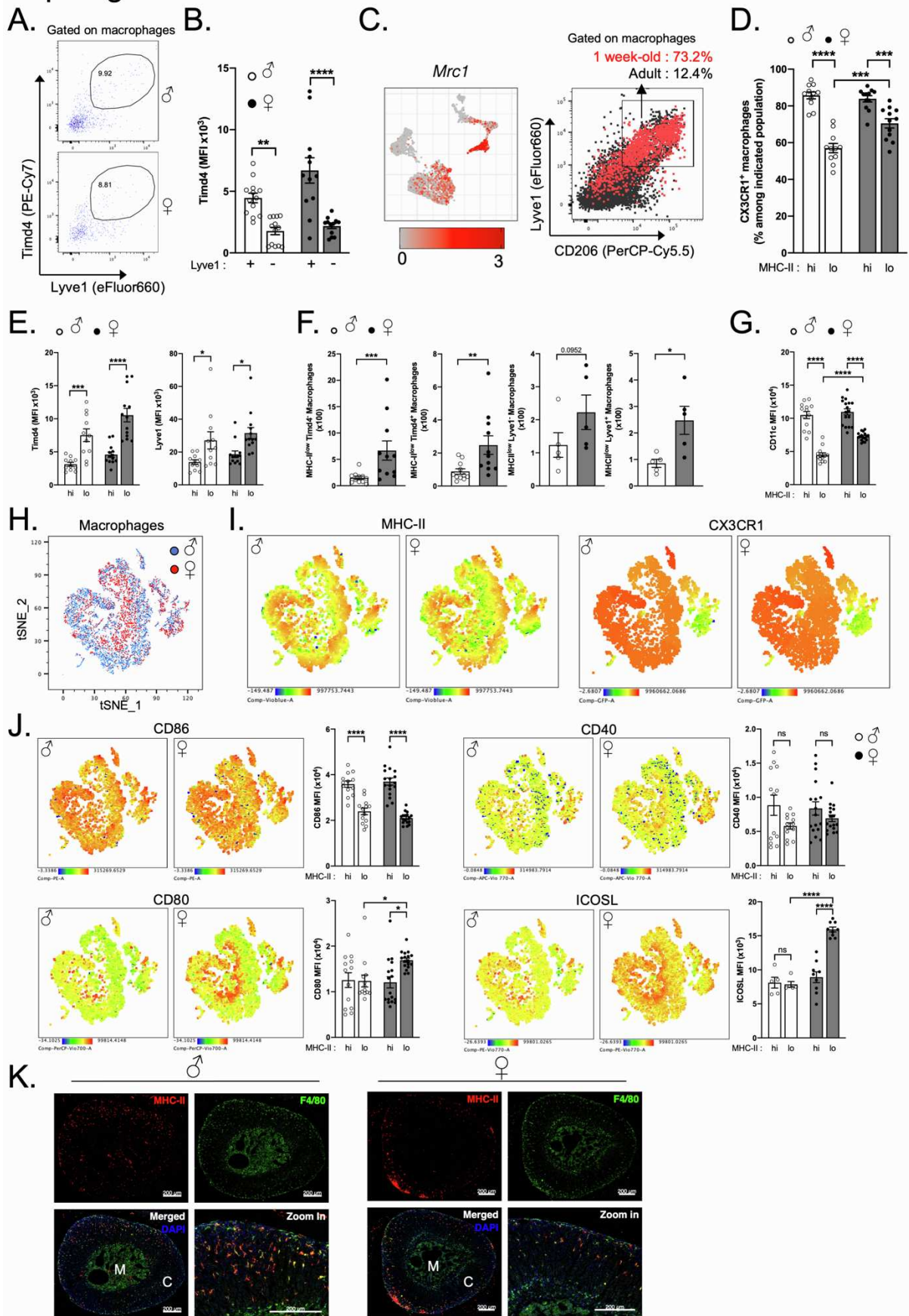


Figure S3. MHC-II expression identifies two macrophage populations with sex-specific abundance and distribution. This figure is complementary to figures 3 and 4.

(A) Representative plots showing adrenal gland macrophage Timd4 and Lyve1 expression in male and female mice. Data representative of at least 3 independent experiments. (B) Mean Timd4 fluorescence intensity among Lyve1⁺ and Lyve1⁻ macrophage subsets in male and female mice. ♂ n=13 and ♀ n=12. Data pooled from 2 independent experiments. (C) (Left) scRNA-seq analysis of *Mrc1* mRNA expression and (Right) representative plot showing adrenal gland macrophage Lyve1 and CD206 expression in 1- and 9-week-old male mice. Data from one experiment. (D) Proportions of CX3CR1⁺ cells among MHC-II^{high} and MHC-II^{low} adrenal gland macrophages from male and female CX3CR1^{GFP} mice. ♂ n=11 and ♀ n=12. Data pooled from 2 independent experiments. (E) Mean Timd4 and Lyve1 fluorescence intensity among MHC-II^{high} and MHC-II^{low} adrenal gland macrophages from male and female mice. ♂ n=12 and ♀ n=13. Data pooled from 2 independent experiments. (F) Quantification of MHC-II^{low} adrenal gland macrophage subsets according to Lyve1 and Timd4 expression in 7-week-old male and female mice. Timd4 subsets : ♂ n=11 and ♀ n=11. Data pooled from 2 independent experiments. Lyve1 subsets : ♂ n=5 and ♀ n=5. Data from one experiment. (G) Mean CD11c fluorescence intensity among MHC-II^{high} and MHC-II^{low} adrenal gland macrophages from male and female mice. ♂ n=13 and ♀ n=17. Data pooled from 3 independent experiments. (H) Clustering of adrenal gland macrophages from male and female CX3CR1^{GFP} mice using unsupervised t-distributed stochastic neighbor embedding (tSNE) analysis of flow cytometry data. Panel : CD24 (BUV496) ; CD19 (BUV737) ; MHC-II (VioBlue) ; CD11b (BV510) ; CD45 (BV570) ; F4/80 (BV650) ; CX3CR1 (GFP reporter) ; CD86 (PE) ; CD64 (PE-Dazzle594) ; CD11c (PE-Cy5) ; CD80 (PerCP-Vio700) ; ICOSL (PE-Vio770) ; Ly6C (APC) ; CD40 (APC-Vio770). Data representative of 3 independent experiments. (I) tSNE representation of MHC-II and CX3CR1 expression levels in adrenal gland macrophages from male and female CX3CR1^{GFP} mice. Data representative of 3 independent experiments. (J) tSNE representation and quantification of CD86, CD80, CD40 and ICOSL expression levels in adrenal gland macrophages from male and female CX3CR1^{GFP} mice. ♂ n=13 and ♀ n=17. Pooled data from 2 (ICOSL) or 3 (CD86, CD80, CD40) independent experiments. (K) Fluorescence microscopy analysis of F4/80 and MHC-II expression in adrenal glands from 7-week-old male and female wild-type mice. Scale bar : 200μm. M (medulla); C (cortex). Data representative of at least 3 independent experiments. All data are represented in means ± SEM. Statistical analysis was performed using two-way ANOVA with Bonferroni's post-test (panels B, D, E, F, G and J) or two-tailed Mann-Whitney tests (panel G). ns p>0.05 ; * p<0.05 ; ** p<0.01 ; *** p<0.001 ; **** p<0.0001.

Sup. Fig. 4

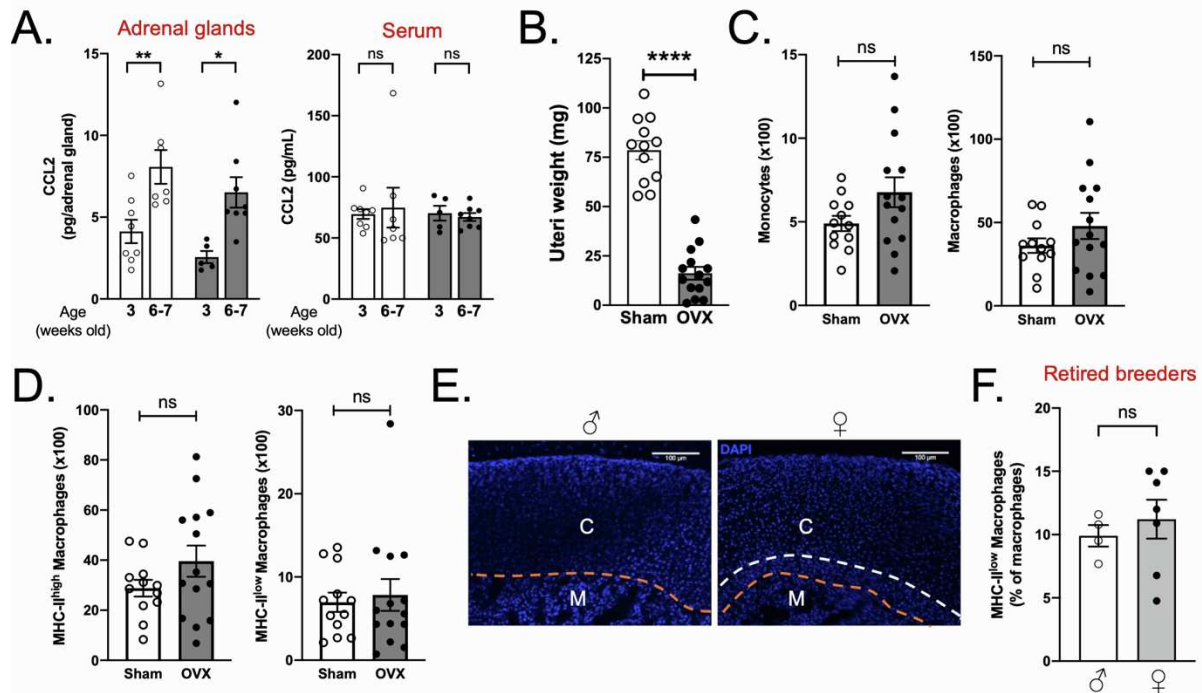


Figure S4. Ovariectomy does not affect adrenal gland macrophage content. This figure is complementary to figure 5.

(A) CCL2 levels in adrenal gland homogenates and serum from 3 (♂ n=8 and ♀ n=5) or 6 to 7 (♂ n=7 and ♀ n=8) week-old male and female wild-type mice. Data pooled from 4 independent experiments. (B) Weight of uteri from sham-operated (n=12) and OVX (n=14) mice. Data pooled from 2 independent experiments. (C) Quantification of adrenal gland monocytes and macrophages in ovariectomized (n=14) and sham-operated (n=12) wild-type mice. Data pooled from 2 independent experiments. (D) Quantification of adrenal gland MHC-II^{low} and MHC-II^{high} macrophages in ovariectomized (n=14) and sham-operated (n=12) wild-type mice. Data pooled from 2 independent experiments. (E) Confocal microscopy analysis of adrenal glands from male and female 4-week-old wild-type mice. Orange dots indicate the border between the cortex (C) and the medulla (M). The X-Zone is comprised between white and orange dots. Scale bar : 100um. (F) Proportions of MHC-II^{low} adrenal gland macrophages in male and female retired breeders (♂ n=4 and ♀ n=7). Data pooled from 2 independent experiments. All data are represented in means ± SEM. Statistical analysis was performed using two-way ANOVA with Bonferroni's post-test (panel A) or two-tailed Mann-Whitney tests (panels B, C, D and F). ns p>0.05 ; * p<0.05 ; ** p<0.01 ; *** p<0.001 ; **** p<0.0001.

Sup. Fig. 5

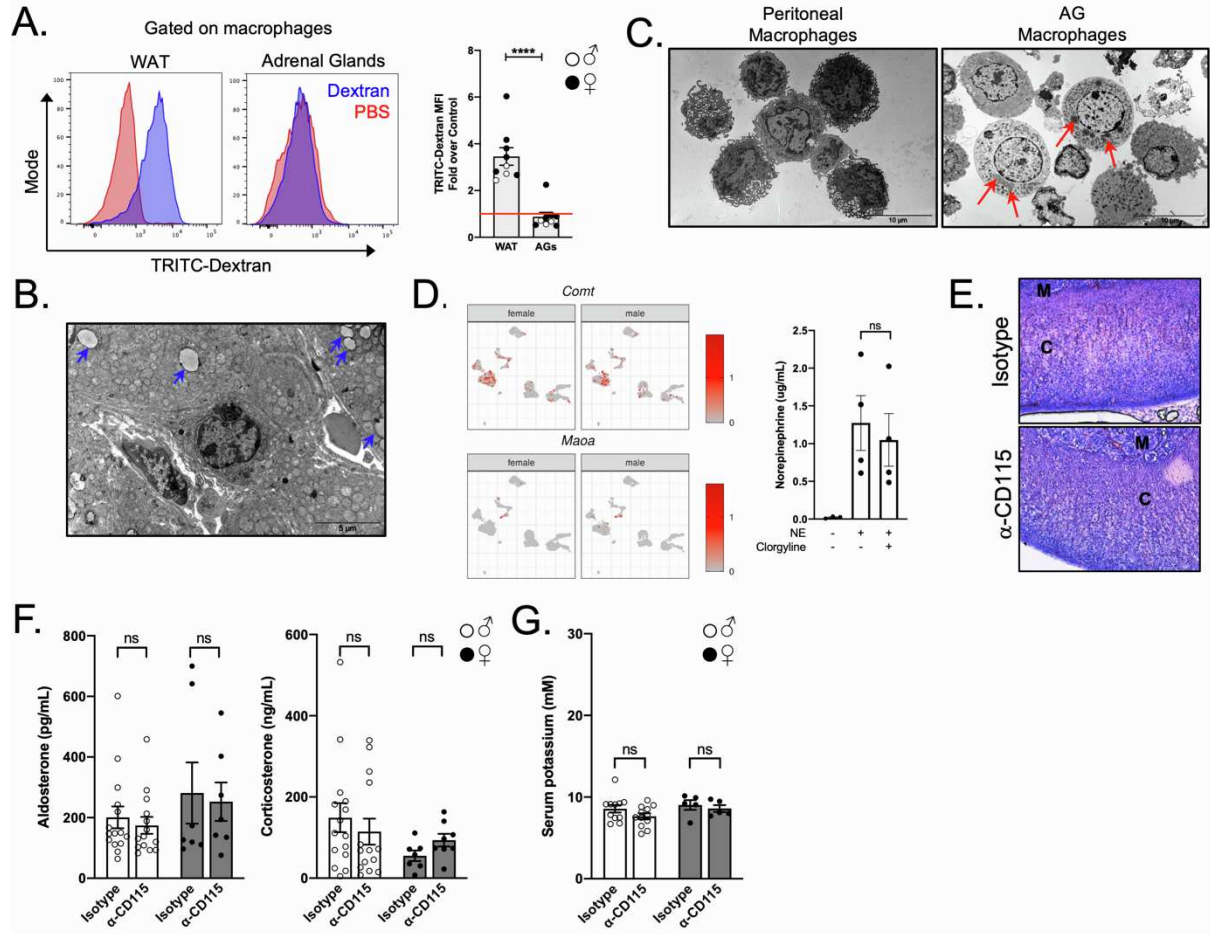
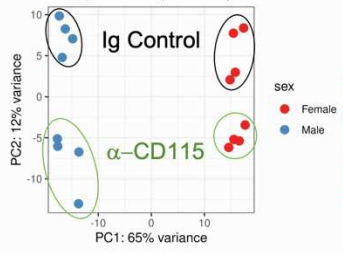


Figure S5. Macrophage depletion does not alter adrenal gland architecture and hormone production at steady state. This figure is complementary to figure 6.

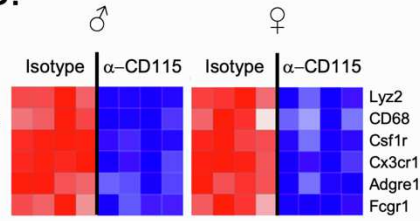
(A) Representative flow cytometry plots (left) and quantification (right) of TRITC-Dextran uptake by adipose tissue and adrenal gland macrophages 20 minutes after intravenous injection of 1mg 65-85kDa TRITC-Dextran. (♂ n=3 and ♀ n=6). Data from one experiment. (B) Electron microscopy analysis of adrenal gland macrophages. Blue arrows indicate the presence of lipid droplets in stroma. Scale bar : 5 μ m. (C) Electron microscopy analysis of purified peritoneal and adrenal gland macrophages. Red arrows indicate the presence of lipid droplets in macrophages. Scale bar : 10 μ m. Data from one experiment. (D) (Left) scRNA-seq analysis of *Maoa* and *Comt* mRNA expression and (Right) norepinephrine levels after overnight culture of cell-sorted adrenal gland macrophages in the presence/absence of norepinephrine and/or clorgyline. n=3 (baseline) or 4 (+NE) biological replicates. Data from 3 pooled experiments. (E) Microscopy analysis of adrenal gland morphology in isotype control-treated and α -CD115-treated wild-type mice using H&E staining. Data from one experiment. (F) Serum aldosterone and corticosterone levels in isotype control-treated (♂ n=15 and ♀ n=7) and α -CD115-treated (♂ n=14 and ♀ n=7-8) male and female wild-type mice. (G) Serum K⁺ levels in isotype control-treated (♂ n=11 and ♀ n=5) and α -CD115-treated (♂ n=12 and ♀ n=5) male and female wild-type mice. Pooled data from 3 independent experiments. Statistical analysis was performed using two-way ANOVA with Bonferroni's post-test (panels F and G), one-way ANOVA with Bonferroni's post-test (panel D) or two-tailed Mann-Whitney tests (panel A). ns p>0.05 ; * p<0.05 ; ** p<0.01 ; *** p<0.001 ; **** p<0.0001.

Sup. Fig. 6

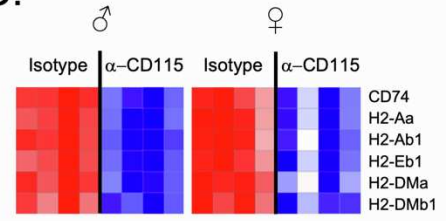
A. PCA (vsd-based): all samples



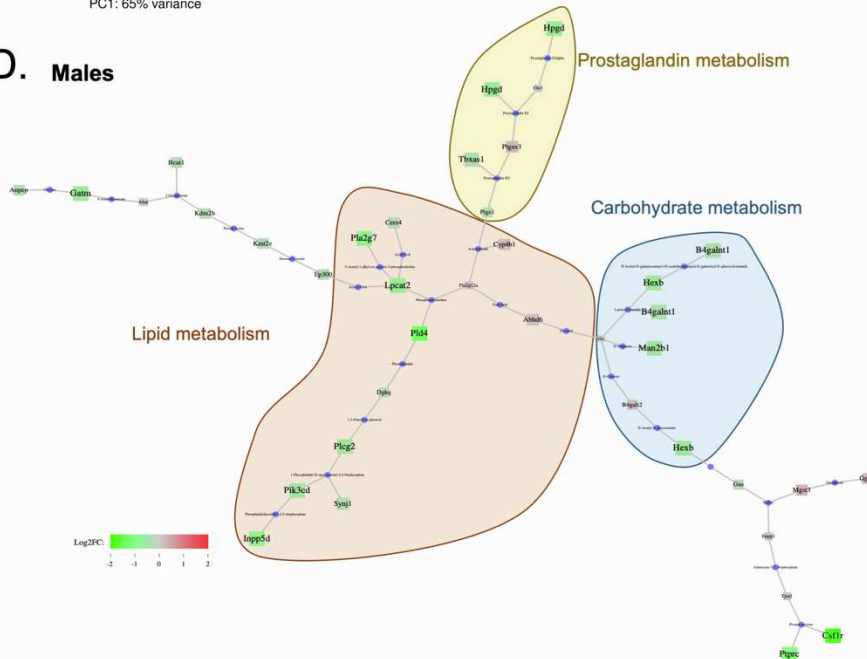
B.



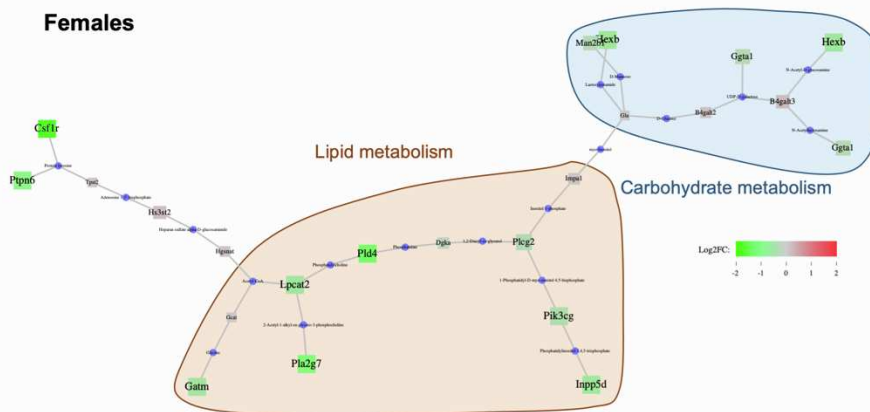
C.



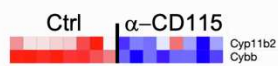
D. Males



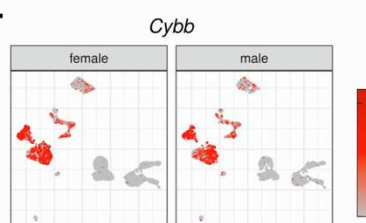
Females



E.



F.



G.

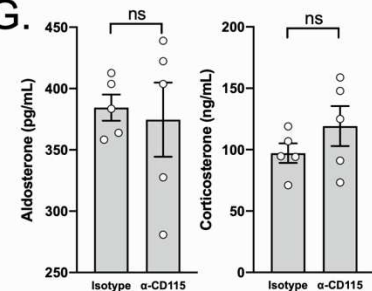


Figure S6. Macrophage depletion affects adrenal gland lipid metabolism. This figure is complementary to figure 6.

(A) Principal Component Analysis (PCA) of adrenal gland bulk RNA-seq from isotype control-treated and α -CD115-treated male and female wild-type mice. (B) RNA-seq analysis of myeloid cell-related genes in adrenal glands from isotype control-treated and α -CD115-treated male and female wild-type mice. (C) RNA-seq analysis of MHC-II-related genes in adrenal glands from isotype control-treated and α -CD115-treated male and female wild-type mice. (D) Transcriptional analysis of metabolic pathways in adrenal glands from α -CD115 or isotype control treated male and female mice. The size of nodes represent the significance of changes in gene expression : bigger size of nodes means lower p-values. A high resolution version of this panel is supplied as supplementary item 3. (E) RNA-seq analysis of *Cyp11b2* and *Cybb* expression in adrenal glands from isotype control-treated and α -CD115-treated wild-type mice. (F) scRNA-seq analysis of *Cybb* mRNA expression. (G) Serum aldosterone and corticosterone levels in α -CD115 (n=5) or isotype control-treated (n=5) female wild-type mice submitted to a 12-hour cold challenge. Data from one experiment. Statistical analysis was performed using two-tailed Mann-Whitney tests (panel G). ns p>0.05.

B. Discussion and perspectives

a. Diversity of adrenal gland macrophages

In this work, we first aimed at providing a detailed characterization of adrenal gland macrophages. Indeed, these cells had been observed using F4/80 staining but no in-depth analysis had been conducted to define their diversity and gain insights about their potential functions. We paid particular attention to potential sex-specific phenotypes, since adrenal glands present a sex-specific architecture and turnover rate. We observed the presence of four macrophage clusters in adrenal glands from female and male mice. These included a cluster of embryonic macrophages, commonly found across organs and recently dubbed “TLF” macrophages³⁴ (Timd4⁺ Lyve1⁺ Folr2⁺). On the opposite, the most abundant cluster consisted of MHC-II^{high} CX3CR1^{high} macrophages. The presence of these two macrophage populations is in full adequation with recent reports of their conserved presence across organs^{33,34}. Very interestingly, a third cluster consisted of CD226⁺ *Retnla*⁺ macrophages that very strongly resembled the MaM ϕ cluster we described in BAT. Finally, a MHC-II^{low} macrophage stood out as a female-specific macrophage population. Whether such a diversity in immune cell, and particularly macrophage content exists in human adrenal glands is yet to be explored. Studies on adrenal gland immune cells in humans are scarce and the samples studied often were obtained from patients with tumors, further raising the question of adrenal gland immune cell pattern in healthy individuals. Importantly, the incidence of adrenal gland pathology prevails in women in comparison to men^{363,364}. Whether a heterogenous immune cell component is at the origin or related to this phenomenon is currently unknown. Immune cell heterogeneity could be a consequence of sex hormones action, or a partial X chromosome inactivation due to local factors. Those two complementary hypotheses require further investigation.

Using genetic fate mapping tools, we observed that monocyte recruitment contributed to adrenal gland macrophage pool size maintenance. Using CCR2^{creERT2} reporter mice, we observed a robust monocyte recruitment in adrenal glands, and this necessitated functional CCR2. We confirmed this observation using Ms4a3^{cre} reporter mice which notably indicated a steady rise in monocyte-derived macrophage proportions across time. Importantly, both of these models brought forward the higher monocyte recruitment rate in female mice compared to their male counterparts. CCL2 levels in adrenal gland homogenates were comparable between male and female

mice, suggesting that CCL2 production was not the leading cause for this phenotype. The turnover rate of the adrenal gland cortex is higher in females compared to males³⁶¹. This implies a higher proliferation rate of stem cells, located under the adrenal capsule, and higher apoptosis of cortical cells which occurs around the X-zone³⁶¹. A consequence of this fast turnover of the adrenal cortex would be the frequent opening of new short-lived niches that accommodate newly-recruited monocytes, while closing of older niches would trigger the death of associated macrophages. α -CD115 treatment fully depleted adrenal gland macrophages and a CSF-1 transgene was reported to rescue adrenal gland macrophage numbers in op/op mice³⁶⁵. Whether IL-34 is also involved in the maintenance of adrenal gland macrophages remains unknown. Loss of CCR2 blunted monocyte recruitment but also led to an increase in macrophage proliferation rate specifically in female mice, thus highlighting the higher turnover rate of female adrenal gland macrophages. Importantly, macrophage proliferation was not statistically different between male and female CCR2-sufficient mice, suggesting that monocyte recruitment is the dominant macrophage maintenance mechanism in adrenal gland. Monocytes might thus have a higher tropism towards newly-opened niches compared to proliferating cells. Alternatively, monocytes could have a competitive advantage for growth factors compared to tissue-resident macrophage, although this hypothesis is discredited by reports showing higher CSF1 consumption by tissue-resident macrophages⁹⁸. The fact that loss of CCR2 triggers higher macrophage proliferation rather than longer macrophage lifespan supports the idea that adrenal gland niches are short-lived and frequently renewed. Adrenal cortical cells are not immotile. Indeed, steroidogenic cells follow a centripetal migration pattern starting in the outer cortex and ending near the medulla. One would thus expect adrenal gland macrophages to follow the same migration pattern to maintain contact with niche cells that are providing growth factors. To test such a hypothesis, optogenetic models could be used to selectively label subcapsular macrophages and follow their localization in a time-course experiment.

Whether monocyte recruitment occurs in specific sub-tissular zones is an interesting issue to solve. Indeed, this might help to elaborate strategies to efficiently control the rate of monocyte entry in tissues and limit or increase the proportion of monocyte-derived cells during a selective time lapse. The interconnection between MHC-II^{high} and MHC-II^{low} adrenal gland macrophages requires further investigation. Our data suggested that monocytes can give rise to both populations. The precise

kinetics of monocyte MHC-II regulation following their tissue entry and engagement into differentiation program are not known in adrenal glands. One might expect that following tissue entry, monocytes progressively increase their MHC-II expression as usually accepted⁴⁶. This scenario is not supported by our observations. In our short-term pulse-chase experiments, we observed a similar rate of monocyte contribution to both MHC-II^{low} and MHC-II^{high} adrenal gland macrophages subsets. Indeed, the proportions of MHC-II^{high} macrophages were similar among newly-recruited cells compared to tissue-resident macrophages, suggesting the absence of a preferential differentiation pattern (Figure 12A). This result supports the hypothesis that microenvironmental cues drive monocyte maturation following entry in the tissue. Further analysis is required to determine whether TdTomato⁺ MHC-II^{low} macrophages effectively locate within the X-zone, while TdTomato⁺ MHC-II^{high} macrophages would rather locate in other zones of the cortex. Despite a large amount of data addressing MHC-II regulation in DCs³⁶⁶, little is known about the mechanisms controlling its expression on monocytes. IL-10 signaling was previously shown to impact MHC-II recycling and surface expression by monocytes³⁶⁷. We therefore hypothesized that locally-produced IL-10 might drive the phenotype we observed on MHC-II^{low} macrophages. To our surprise, treatment with an anti-IL-10R monoclonal antibody did not induce an upregulation of MHC-II as we expected, but rather produced the opposite effect. Whether α -IL-10R treatment effectively affected macrophage interactions with their niche or regulated MHC-II expression independently of microenvironmental cues remains to be determined.

The MHC-II^{low} macrophage population particularly caught our attention since it was specifically enriched in female mice. Co-staining for MHC-II and F4/80 or CD68 showed a distinct localization of MHC-II^{low} macrophages that was restricted to the X-zone, at the border between the medulla and the cortex. We were able to establish a link between X-zone presence and maintenance of the MHC-II^{low} macrophage subset. Indeed, this particular structure disappears in females during pregnancy, and this was associated with disappearance of MHC-II^{low} macrophages. As an alternative approach, we castrated males before puberty to prevent the androgen-induced degradation of the X-zone and its forced maintenance allowed the persistence of MHC-II^{low} macrophages. These results highlight the impact of microenvironment on MHC-II expression and the imprinting of a niche-specific macrophage phenotype. Castration of adult males was reported to cause the re-appearance of a pseudo X-zone. Although

we did not use this approach, it would be interesting to test whether newly-recruited macrophages that locate in this zone would adopt the MHC-II^{low} phenotype. We also observed a different metabolic configuration of MHC-II^{low} and MHC-II^{high} macrophages. Since these subsets do not locate close to each-other, this result also suggests that microenvironment can directly impact macrophage metabolism. Whether metabolite availability differs in the X-zone compared to the outer cortex remains to be tested.

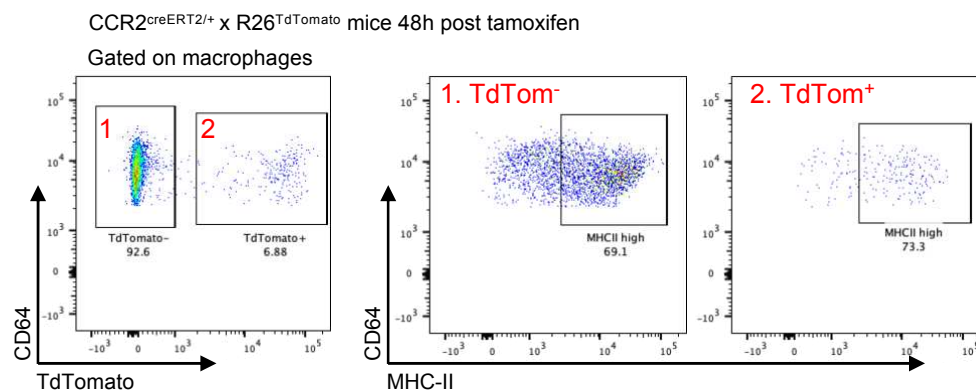


Figure 12. Newly-recruited macrophages contribute to both MHC-II^{high} and MHC-II^{low} populations.

CCR2^{creERT2/+} x R26^{TdTomato} mice received oral gavage with tamoxifen and their adrenal glands were analyzed 48h later. Macrophages were gated as CD64⁺ MerTK⁺ and further gated as resident (1) or newly-recruited (2) based on TdTomato expression.

b. Functions of adrenal gland macrophages

The subset-specific localization of adrenal gland macrophages in this well-structured organ strongly suggests the existence of specialized functions. For example, we hypothesize that the low expression of MHC-II by macrophages in the X-zone, near the apoptotic front of migrating cortex cells, would serve an immunoprotective function. Indeed, one could expect an abundance of damage-associated molecular patterns in this zone, along with numerous cellular debris that could serve to generate potentially immunogenic peptides. Absence of MHC-II-mediated peptide presentation could be protective in this context.

Interestingly, our observations suggested a key role of adrenal gland macrophages in the handling of lipid content. In-depth analysis is still required to determine whether a singular macrophage subset is responsible for lipid handling. Indeed, we observed in our single-cell RNA-seq data, and by flow cytometry, the presence of a macrophage cluster that highly express Trem2 and CD63, closely resembling the phenotype of foam cells in atherosclerotic plaques and Trem2^{high} lipid-

associated macrophages^{156,291}. The localization of these cells in the adrenal gland cortex or medulla remains to be established. One might wonder whether Trem2^{high} adrenal gland macrophages are specialized in handling cholesterol derivatives locally and to contribute to the metabolism of aldosterone and corticosterone. To tackle this question, one needs to develop and validate tools targeting selectively this subset without affecting the other adrenal gland macrophages.

To define the role of adrenal gland macrophages during chronic or acute environmental stress seems an important task to accomplish. The role of physiological stress on the immune response and on hematopoiesis is well-established^{160,236}. Although adrenal glands play a role in this process, the contribution of adrenal gland macrophages to this mechanism is still not defined. We would like to assess how acute and chronic stress modulate adrenal gland macrophage subsets density and phenotype. Genetic or pharmacological depletion of adrenal gland macrophages, or if possible of particular macrophage subsets using genetic approaches, will shed light on the role of these cells during stress. Future directions for the project include :

- Targeting adrenal gland macrophages during chronic stress. Similarly to the experiments we previously conducted, we could deplete macrophages by injecting α -CD115 antibodies chronically while mice are subjected to chronic stress. Although we could analyse adrenal glands in this model and infer potential roles played by adrenal gland macrophages locally, this approach retains the disadvantage of systemically depleting macrophages. Another approach could be crossing Sf1^{cre} mice to Csf1^{fllox} mice to test whether a more restricted depletion of macrophages occurs. However, Sf1 is expressed in the hypothalamus and the pituitary, which are involved in the stress response. The complementary use of hypothalamus or pituitary-specific genetic models could help dissect any phenotype observed during chronic stress.

- Targeting CD226⁺ adrenal gland macrophages at steady-state and during chronic stress using Retnla^{cre} x R26^{TdTomato/DTR} mice. Similarly to what we proposed for analysis of BAT MaM ϕ , Retnla^{cre} mice would allow tracking and targeting of this population. Nevertheless, the frequent observation of Retnla⁺ macrophages across tissues would require a thorough analysis to determine whether any phenotype observed is linked to adrenal gland macrophage function.

- Targeting lipid-associated macrophages during lipid overload. We identified the accumulation of cluster 8 macrophages during brown adipose tissue expansion. This population is characterized by its expression of the “lipid-associated macrophage”

signature which includes CD9, CD63 and Trem2. Recent evidence suggests that these cells might exert their function through Trem2¹⁵⁶. It would therefore be interesting to invalidate Trem2 in macrophages using LyzM^{cre} x Trem2^{flox} mice (available within our network) in contexts of obesity, ageing or thermogenesis to study the function of this population.

- Determining the role of Trem2 in adrenal gland macrophages during hypercholesterolemia. Our data suggest a link between macrophages, cholesterol, and adrenal hormone homeostasis. As mentioned before, Trem2 expression is strongly detected among adrenal gland macrophages. It would therefore be interesting to invalidate Trem2 in macrophages using LyzM^{cre} x Trem2^{flox} mice in a context of hypercholesterolemia, for example in atherosclerosis models, to study the function of this population.

- To define the diversity of human adrenal gland immune cells in healthy and pathological scenarios. We aim to investigate the diversity of adrenal gland immune cells by scRNAseq and spectral flow cytometry. Whether immune cell diversity could be related to biological sex is an intriguing question.

Limitations of the study

In this work, we used several approaches to dissect adrenal gland a brown adipose tissue macrophage diversity and functions, including single-cell RNA sequencing, genetic fate mapping and antibody-mediated depletion strategies. The two studies presented here share several models and therefore present similar limitations.

For our scRNA-seq experiments, we chose to analyze cell-sorted CD45⁺ cells in order to improve our resolution of immune cell subsets. This approach revealed an important macrophage diversity, while these cells only represent a minor homogenous population in most scRNA-seq studies of whole tissues. As discussed previously, the question of whether our macrophage clustering is close-enough to reality still remains. Additional complementary approaches are needed to determine whether the subsets we identified are indeed different sub-populations with specialized functions.

Our data suggests that monocytes are continuously recruited to both BAT and adrenals to contribute to macrophage turnover. This was brought forward by our use of CCR2^{creERT2} x R26^{TdTomato} mice. CCR2^{GFP} mice also showed the presence of CCR2⁺ macrophages in those tissues. Thus, it is sound to expect a labeling of both CCR2⁺ monocytes and CCR2⁺ tissue-resident macrophages follow tamoxifen administration, and in this case labeling would not reflect solely monocyte recruitment. To resolve this problem, we compared labeling in CCR2^{creERT2/+} heterozygous mice which maintain a functional CCR2 allele, to CCR2^{creERT2/GFP} double knock-in mice which lack functional CCR2. This approach revealed that a significant proportion of labeling depended on the presence of functional CCR2, suggesting that we were effectively measuring monocyte recruitment. However, whether macrophage diversity is altered (despite maintained macrophage numbers) in CCR2-deficient mice remains unclear. Indeed, the diminished labeling we observed in CCR2^{creERT2/GFP} mice could also reflect a loss of the CCR2⁺ tissue-resident macrophage subset that would be compensated in numbers by CCR2⁻ macrophages. The use of Ms4a3^{cre} x R26^{TdTomato} mice puts a definitive answer on this problem, and effectively showed that monocytes were continuously recruited to adrenal glands. We did not have access to this model at the time of our BAT analysis, and these mice would allow a clear definition of how many BAT macrophages effectively derive from monocytes.

A similar issue can be raised in relation to our use of the MC-21 antibody. Indeed, MC-21 treatment effectively depletes blood and tissue monocytes, but whether tissue-resident CCR2⁺ macrophages are affected is untested. Total BAT macrophage numbers remained unchanged in MC-21-treated mice after 5 days of treatment. The same observation was made for adrenal glands (data not shown). However, we observed the disappearance of CX3CR1⁺ macrophages in BAT after a 5-day MC-21 treatment. This was not the case after a single MC-21 injection, while peripheral and tissue monocytes were effectively depleted at this early timepoint. Although this result suggests that altered monocyte flux is responsible for alterations in BAT macrophage diversity, and that monocytes rapidly give rise to CX3CR1⁺ macrophages, further analysis is required to effectively track monocytes in BAT over time.

We used CSF1R blockade to address the function of adrenal gland macrophages. As discussed before, this treatment induces a systemic macrophage depletion which might affect our analysis of adrenal glands. Other strategies allowing to specifically target adrenal gland or brown adipose tissue macrophages need to be identified and generated to avoid this problem.

One important limitation of our study is the difficult access to human BAT and adrenal gland samples. As discussed above one of our main objectives is to further apply our observation to human tissues and try to develop strategies to specifically target these cells in a safe manner.

Conclusion

This thesis focuses mainly on the heterogeneity of macrophages across organs and inside organs, and on the role of monocytes in maintaining tissue homeostasis notably by generating specific macrophage subpopulations. We sought to unravel macrophage ontogeny and diversity in two organs that were poorly characterized on an immune standpoint : the brown adipose tissue and adrenal glands.

By dissecting macrophage diversity in brown adipose tissue, we uncovered two terminally-differentiated macrophage populations resembling in part populations observed in other organs. Indeed, “M2M ϕ ” highly resemble white adipose tissue vasculature-associated macrophages. Surprisingly, the “Matrix M ϕ ” population that we uncovered does not recall any population previously observed in adipose depots and is absent from white adipose tissue. Rather, it resembles small peritoneal and pleural cavity macrophages characterized by high expression of CD226. Although it seems easy to speculate on the function of the M2M ϕ population, clues on the potential function of the MaM ϕ population are scarce and restricted to expression of a cluster of genes linked to extracellular matrix remodelling. Importantly, expression of CX3CR1 is low in both of these populations suggesting that they are distinct from the previously observed nerve-associated CX3CR1⁺ BAT macrophages. Upon genetically-induced BAT lipid overload and expansion, we observed the accumulation of two additional monocyte-derived populations characterized by a strong “lipid handling” signature and resembling in part foam cells and lipid-associated macrophages. Depletion of monocytes during BAT expansion prevented lipid accumulation and reduced BAT weight, showing the importance of monocyte recruitment in tissue remodelling. Moreover, *in vitro* experiments showed that monocytes could influence fibroblast activation and *in vivo* blockade of podoplanin resulted in reduced BAT weight. However, depletion of CCR2⁺ cells also led to accumulation of crown-like structures suggesting increased adipocyte apoptosis. Monocytes and/or monocyte-derived cells generated over this short (5 days) period therefore participate to homeostatic lipid storage.

We found that although adrenal gland macrophages were seeded by fetal liver progenitors, embryonic macrophages were quickly replaced after birth and monocyte recruitment instead became the norm to maintain a homeostatic macrophage pool. A

small proportion of embryonic Timd4^+ Lyve1^+ macrophages was maintained independently of monocyte input. Importantly, organ maturation was associated with the disappearance of the $\text{MHC-II}^{\text{low}}$ macrophage subset. These cells locate in the X-zone which is degraded during puberty in males and maintained in females, and we identified X-zone maintenance to be necessary for $\text{MHC-II}^{\text{low}}$ macrophage maintenance. This result suggests that closure of the niche rather than senescence or proliferative exhaustion is responsible for the loss of this population. Importantly, monocytes also contributed to the $\text{MHC-II}^{\text{low}}$ macrophage pool suggesting that microenvironmental niche-derived factors dictate their phenotype and MHC-II expression. The fate of the X-zone is inevitably to be degraded either at puberty or during pregnancy. The maintenance of an $\text{MHC-II}^{\text{low}}$ macrophage population in this specific localization might therefore prevent presentation of self-antigens derived from apoptotic X-zone cells in a context where damage-associated molecular patterns are also abundant. $\text{MHC-II}^{\text{low}}$ macrophages are robustly found in endocrine organs and might serve a similar purpose on an auto-immune standpoint. The adrenal gland is an organ with a fast renewal, which might explain the constant closing and opening of niches thus promoting macrophage turnover. Similarly to what we observed in BAT, adrenal gland macrophage numbers were unchanged in $\text{CCR2}^{-/-}$ mice. Instead, proliferation compensated for the lack of monocyte recruitment in a sex-specific manner, with females needing a higher macrophage turnover than males. Interestingly, CCR2 deficiency does not lead to increased proliferation among large peritoneal macrophages despite their important turnover rate²⁸⁶. This existence of this compensation mechanism highlights the fact that tissue homeostasis is linked to the presence of an optimal macrophage pool which needs to be maintained. We observed that adrenal gland macrophages were required for optimal local aldosterone production during acute stress. Macrophage depletion led to altered lipid homeostasis which may limit availability of molecular precursors necessary for the synthesis of hormones. Thus, maintaining a constant and robust adrenal gland macrophage pool during lifespan appears necessary to be able to mount a quick and efficient stress response.

References

- 1 Geissmann, F., Gordon, S., Hume, D. A., Mowat, A. M. & Randolph, G. J. Unravelling mononuclear phagocyte heterogeneity. *Nat. Rev. Immunol.* **10**, 453-460, doi:10.1038/nri2784 (2010).
- 2 Austyn, J. M. & Gordon, S. F4/80, a monoclonal antibody directed specifically against the mouse macrophage. *Eur. J. Immunol.* **11**, 805-815, doi:10.1002/eji.1830111013 (1981).
- 3 Hume, D. A. & Gordon, S. Mononuclear phagocyte system of the mouse defined by immunohistochemical localization of antigen F4/80. Identification of resident macrophages in renal medullary and cortical interstitium and the juxtaglomerular complex. *J. Exp. Med.* **157**, 1704-1709, doi:10.1084/jem.157.5.1704 (1983).
- 4 Hume, D. A., Robinson, A. P., MacPherson, G. G. & Gordon, S. The mononuclear phagocyte system of the mouse defined by immunohistochemical localization of antigen F4/80. Relationship between macrophages, Langerhans cells, reticular cells, and dendritic cells in lymphoid and hematopoietic organs. *J. Exp. Med.* **158**, 1522-1536, doi:10.1084/jem.158.5.1522 (1983).
- 5 Hume, D. A., Loutit, J. F. & Gordon, S. The mononuclear phagocyte system of the mouse defined by immunohistochemical localization of antigen F4/80: macrophages of bone and associated connective tissue. *J. Cell Sci.* **66**, 189-194, doi:10.1242/jcs.66.1.189 (1984).
- 6 Hume, D. A., Halpin, D., Charlton, H. & Gordon, S. The mononuclear phagocyte system of the mouse defined by immunohistochemical localization of antigen F4/80: macrophages of endocrine organs. *Proc Natl Acad Sci U S A* **81**, 4174-4177, doi:10.1073/pnas.81.13.4174 (1984).
- 7 Hume, D. A., Perry, V. H. & Gordon, S. The mononuclear phagocyte system of the mouse defined by immunohistochemical localisation of antigen F4/80: macrophages associated with epithelia. *Anat. Rec.* **210**, 503-512, doi:10.1002/ar.1092100311 (1984).
- 8 Naito, M. *et al.* Abnormal differentiation of tissue macrophage populations in 'osteopetrosis' (op) mice defective in the production of macrophage colony-stimulating factor. *Am. J. Pathol.* **139**, 657-667 (1991).
- 9 Cecchini, M. G. *et al.* Role of colony stimulating factor-1 in the establishment and regulation of tissue macrophages during postnatal development of the mouse. *Development* **120**, 1357-1372, doi:10.1242/dev.120.6.1357 (1994).
- 10 Dai, X. M. *et al.* Targeted disruption of the mouse colony-stimulating factor 1 receptor gene results in osteopetrosis, mononuclear phagocyte deficiency, increased primitive progenitor cell frequencies, and reproductive defects. *Blood* **99**, 111-120, doi:10.1182/blood.v99.1.111 (2002).
- 11 Sasmono, R. T. *et al.* A macrophage colony-stimulating factor receptor-green fluorescent protein transgene is expressed throughout the mononuclear phagocyte system of the mouse. *Blood* **101**, 1155-1163, doi:10.1182/blood-2002-02-0569 (2003).
- 12 Volkman, A. & Gowans, J. L. The Origin of Macrophages from Bone Marrow

- in the Rat. *Br. J. Exp. Pathol.* **46**, 62-70 (1965).
- 13 Volkman, A. & Gowans, J. L. The Production of Macrophages in the Rat. *Br. J. Exp. Pathol.* **46**, 50-61 (1965).
- 14 Cohn, Z. A. & Benson, B. The Differentiation of Mononuclear Phagocytes. Morphology, Cytochemistry, and Biochemistry. *J. Exp. Med.* **121**, 153-170, doi:10.1084/jem.121.1.153 (1965).
- 15 Kodama, H. *et al.* Congenital osteoclast deficiency in osteopetrotic (op/op) mice is cured by injections of macrophage colony-stimulating factor. *J. Exp. Med.* **173**, 269-272, doi:10.1084/jem.173.1.269 (1991).
- 16 van Furth, R. & Diesselhoff-den Dulk, M. M. Dual origin of mouse spleen macrophages. *J. Exp. Med.* **160**, 1273-1283, doi:10.1084/jem.160.5.1273 (1984).
- 17 Lawson, L. J., Perry, V. H. & Gordon, S. Turnover of resident microglia in the normal adult mouse brain. *Neuroscience* **48**, 405-415, doi:10.1016/0306-4522(92)90500-2 (1992).
- 18 Wijffels, J. F., de Rover, Z., Beelen, R. H., Kraal, G. & van Rooijen, N. Macrophage subpopulations in the mouse spleen renewed by local proliferation. *Immunobiology* **191**, 52-64, doi:10.1016/s0171-2985(11)80267-6 (1994).
- 19 North, R. J. The mitotic potential of fixed phagocytes in the liver as revealed during the development of cellular immunity. *J. Exp. Med.* **130**, 315-326, doi:10.1084/jem.130.2.315 (1969).
- 20 Hashimoto, D. *et al.* Tissue-resident macrophages self-maintain locally throughout adult life with minimal contribution from circulating monocytes. *Immunity* **38**, 792-804, doi:10.1016/j.immuni.2013.04.004 (2013).
- 21 Lin, H. *et al.* Discovery of a cytokine and its receptor by functional screening of the extracellular proteome. *Science* **320**, 807-811, doi:10.1126/science.1154370 (2008).
- 22 MacDonald, K. P. *et al.* An antibody against the colony-stimulating factor 1 receptor depletes the resident subset of monocytes and tissue- and tumor-associated macrophages but does not inhibit inflammation. *Blood* **116**, 3955-3963, doi:10.1182/blood-2010-02-266296 (2010).
- 23 Guilliams, M. *et al.* Alveolar macrophages develop from fetal monocytes that differentiate into long-lived cells in the first week of life via GM-CSF. *J. Exp. Med.* **210**, 1977-1992, doi:10.1084/jem.20131199 (2013).
- 24 Blevins, G. & Fedoroff, S. Microglia in colony-stimulating factor 1-deficient op/op mice. *J. Neurosci. Res.* **40**, 535-544, doi:10.1002/jnr.490400412 (1995).
- 25 Ginhoux, F. *et al.* Fate mapping analysis reveals that adult microglia derive from primitive macrophages. *Science* **330**, 841-845, doi:10.1126/science.1194637 (2010).
- 26 Greter, M. *et al.* Stroma-derived interleukin-34 controls the development and maintenance of langerhans cells and the maintenance of microglia. *Immunity* **37**, 1050-1060, doi:10.1016/j.immuni.2012.11.001 (2012).
- 27 Wang, P. L. *et al.* Peripheral nerve resident macrophages share tissue-specific programming and features of activated microglia. *Nat Commun* **11**, 2552, doi:10.1038/s41467-020-16355-w (2020).
- 28 Gautier, E. L. *et al.* Gene-expression profiles and transcriptional regulatory

- pathways that underlie the identity and diversity of mouse tissue macrophages. *Nat Immunol* **13**, 1118-1128, doi:10.1038/ni.2419 (2012).
- 29 Bogunovic, M. *et al.* Origin of the lamina propria dendritic cell network. *Immunity* **31**, 513-525, doi:10.1016/j.immuni.2009.08.010 (2009).
- 30 Ginhoux, F. *et al.* The origin and development of nonlymphoid tissue CD103+ DCs. *J. Exp. Med.* **206**, 3115-3130, doi:10.1084/jem.20091756 (2009).
- 31 Epelman, S., Lavine, K. J. & Randolph, G. J. Origin and functions of tissue macrophages. *Immunity* **41**, 21-35, doi:10.1016/j.immuni.2014.06.013 (2014).
- 32 Lavin, Y. *et al.* Tissue-resident macrophage enhancer landscapes are shaped by the local microenvironment. *Cell* **159**, 1312-1326, doi:10.1016/j.cell.2014.11.018 (2014).
- 33 Chakarov, S. *et al.* Two distinct interstitial macrophage populations coexist across tissues in specific subtissular niches. *Science* **363**, doi:10.1126/science.aau0964 (2019).
- 34 Dick, S. A. *et al.* Three tissue resident macrophage subsets coexist across organs with conserved origins and life cycles. *Sci Immunol* **7**, eabf7777, doi:10.1126/sciimmunol.abf7777 (2022).
- 35 Auffray, C., Sieweke, M. H. & Geissmann, F. Blood monocytes: development, heterogeneity, and relationship with dendritic cells. *Annu. Rev. Immunol.* **27**, 669-692, doi:10.1146/annurev.immunol.021908.132557 (2009).
- 36 van Furth, R. & Cohn, Z. A. The origin and kinetics of mononuclear phagocytes. *J. Exp. Med.* **128**, 415-435, doi:10.1084/jem.128.3.415 (1968).
- 37 van Furth, R. & Diesselhoff-Den Dulk, M. M. The kinetics of promonocytes and monocytes in the bone marrow. *J. Exp. Med.* **132**, 813-828, doi:10.1084/jem.132.4.813 (1970).
- 38 Patel, A. A. *et al.* The fate and lifespan of human monocyte subsets in steady state and systemic inflammation. *J. Exp. Med.* **214**, 1913-1923, doi:10.1084/jem.20170355 (2017).
- 39 Yona, S. *et al.* Fate mapping reveals origins and dynamics of monocytes and tissue macrophages under homeostasis. *Immunity* **38**, 79-91, doi:10.1016/j.immuni.2012.12.001 (2013).
- 40 Lewis, M. R. The Formation of Macrophages, Epithelioid Cells and Giant Cells from Leucocytes in Incubated Blood. *Am. J. Pathol.* **1**, 91-100 101 (1925).
- 41 Bennett, W. E. & Cohn, Z. A. The isolation and selected properties of blood monocytes. *J. Exp. Med.* **123**, 145-160, doi:10.1084/jem.123.1.145 (1966).
- 42 Ebert, R. H. & Florey, H. W. The Extravascular Development of the Monocyte Observed In vivo. *Br. J. Exp. Pathol.* **20**, 342-356 (1939).
- 43 Crofton, R. W., Diesselhoff-den Dulk, M. M. & van Furth, R. The origin, kinetics, and characteristics of the Kupffer cells in the normal steady state. *J. Exp. Med.* **148**, 1-17, doi:10.1084/jem.148.1.1 (1978).
- 44 Thomas, E. D., Ramberg, R. E., Sale, G. E., Sparkes, R. S. & Golde, D. W. Direct evidence for a bone marrow origin of the alveolar macrophage in man. *Science* **192**, 1016-1018, doi:10.1126/science.775638 (1976).
- 45 Yamamoto, T. *et al.* Repopulation of murine Kupffer cells after intravenous administration of liposome-

- encapsulated dichloromethylene diphosphonate. *Am. J. Pathol.* **149**, 1271-1286 (1996).
- 46 Jakubzick, C. *et al.* Minimal differentiation of classical monocytes as they survey steady-state tissues and transport antigen to lymph nodes. *Immunity* **39**, 599-610, doi:10.1016/j.immuni.2013.08.007 (2013).
- 47 Palframan, R. T. *et al.* Inflammatory chemokine transport and presentation in HEV: a remote control mechanism for monocyte recruitment to lymph nodes in inflamed tissues. *J. Exp. Med.* **194**, 1361-1373, doi:10.1084/jem.194.9.1361 (2001).
- 48 Passlick, B., Flieger, D. & Ziegler-Heitbrock, H. W. Identification and characterization of a novel monocyte subpopulation in human peripheral blood. *Blood* **74**, 2527-2534 (1989).
- 49 Geissmann, F., Jung, S. & Littman, D. R. Blood monocytes consist of two principal subsets with distinct migratory properties. *Immunity* **19**, 71-82, doi:10.1016/s1074-7613(03)00174-2 (2003).
- 50 Ingersoll, M. A. *et al.* Comparison of gene expression profiles between human and mouse monocyte subsets. *Blood* **115**, e10-19, doi:10.1182/blood-2009-07-235028 (2010).
- 51 Ahuja, V., Miller, S. E. & Howell, D. N. Identification of two subpopulations of rat monocytes expressing disparate molecular forms and quantities of CD43. *Cell. Immunol.* **163**, 59-69, doi:10.1006/cimm.1995.1099 (1995).
- 52 Auffray, C. *et al.* Monitoring of blood vessels and tissues by a population of monocytes with patrolling behavior. *Science* **317**, 666-670, doi:10.1126/science.1142883 (2007).
- 53 Carlin, L. M. *et al.* Nr4a1-dependent Ly6C(low) monocytes monitor endothelial cells and orchestrate their disposal. *Cell* **153**, 362-375, doi:10.1016/j.cell.2013.03.010 (2013).
- 54 Chong, S. Z. *et al.* CXCR4 identifies transitional bone marrow premonocytes that replenish the mature monocyte pool for peripheral responses. *J. Exp. Med.* **213**, 2293-2314, doi:10.1084/jem.20160800 (2016).
- 55 Sunderkotter, C. *et al.* Subpopulations of mouse blood monocytes differ in maturation stage and inflammatory response. *J. Immunol.* **172**, 4410-4417, doi:10.4049/jimmunol.172.7.4410 (2004).
- 56 Briseno, C. G. *et al.* Distinct Transcriptional Programs Control Cross-Priming in Classical and Monocyte-Derived Dendritic Cells. *Cell Rep.* **15**, 2462-2474, doi:10.1016/j.celrep.2016.05.025 (2016).
- 57 Hanna, R. N. *et al.* The transcription factor NR4A1 (Nur77) controls bone marrow differentiation and the survival of Ly6C- monocytes. *Nat. Immunol.* **12**, 778-785, doi:10.1038/ni.2063 (2011).
- 58 Steinman, R. M. & Cohn, Z. A. Identification of a novel cell type in peripheral lymphoid organs of mice. I. Morphology, quantitation, tissue distribution. *J. Exp. Med.* **137**, 1142-1162, doi:10.1084/jem.137.5.1142 (1973).
- 59 Randolph, G. J., Beaulieu, S., Lebecque, S., Steinman, R. M. & Muller, W. A. Differentiation of monocytes into dendritic cells in a model of transendothelial trafficking. *Science* **282**, 480-483,

- doi:10.1126/science.282.5388.480 (1998).
- 60 Satpathy, A. T. *et al.* Zbtb46 expression distinguishes classical dendritic cells and their committed progenitors from other immune lineages. *J. Exp. Med.* **209**, 1135-1152, doi:10.1084/jem.20120030 (2012).
- 61 Meredith, M. M. *et al.* Expression of the zinc finger transcription factor zDC (Zbtb46, Btbd4) defines the classical dendritic cell lineage. *J. Exp. Med.* **209**, 1153-1165, doi:10.1084/jem.20112675 (2012).
- 62 Wu, X. *et al.* Mafb lineage tracing to distinguish macrophages from other immune lineages reveals dual identity of Langerhans cells. *J. Exp. Med.* **213**, 2553-2565, doi:10.1084/jem.20160600 (2016).
- 63 Liu, Z. *et al.* Fate Mapping via Ms4a3-Expression History Traces Monocyte-Derived Cells. *Cell* **178**, 1509-1525 e1519, doi:10.1016/j.cell.2019.08.009 (2019).
- 64 Karsunky, H., Merad, M., Cozzio, A., Weissman, I. L. & Manz, M. G. Flt3 ligand regulates dendritic cell development from Flt3+ lymphoid and myeloid-committed progenitors to Flt3+ dendritic cells in vivo. *J. Exp. Med.* **198**, 305-313, doi:10.1084/jem.20030323 (2003).
- 65 Waskow, C. *et al.* The receptor tyrosine kinase Flt3 is required for dendritic cell development in peripheral lymphoid tissues. *Nat. Immunol.* **9**, 676-683, doi:10.1038/ni.1615 (2008).
- 66 Schlitzer, A. *et al.* Identification of cDC1- and cDC2-committed DC progenitors reveals early lineage priming at the common DC progenitor stage in the bone marrow. *Nat. Immunol.* **16**, 718-728, doi:10.1038/ni.3200 (2015).
- 67 Ghosh, H. S., Cisse, B., Bunin, A., Lewis, K. L. & Reizis, B. Continuous expression of the transcription factor e2-2 maintains the cell fate of mature plasmacytoid dendritic cells. *Immunity* **33**, 905-916, doi:10.1016/j.immuni.2010.11.023 (2010).
- 68 Sichien, D. *et al.* IRF8 Transcription Factor Controls Survival and Function of Terminally Differentiated Conventional and Plasmacytoid Dendritic Cells, Respectively. *Immunity* **45**, 626-640, doi:10.1016/j.immuni.2016.08.013 (2016).
- 69 Swiecki, M. & Colonna, M. The multifaceted biology of plasmacytoid dendritic cells. *Nat. Rev. Immunol.* **15**, 471-485, doi:10.1038/nri3865 (2015).
- 70 Murphy, T. L. *et al.* Transcriptional Control of Dendritic Cell Development. *Annu. Rev. Immunol.* **34**, 93-119, doi:10.1146/annurev-immunol-032713-120204 (2016).
- 71 Mildner, A. & Jung, S. Development and function of dendritic cell subsets. *Immunity* **40**, 642-656, doi:10.1016/j.immuni.2014.04.016 (2014).
- 72 Satpathy, A. T. *et al.* Notch2-dependent classical dendritic cells orchestrate intestinal immunity to attaching-and-effacing bacterial pathogens. *Nat. Immunol.* **14**, 937-948, doi:10.1038/ni.2679 (2013).
- 73 Ginhoux, F., Williams, M. & Merad, M. Expanding dendritic cell nomenclature in the single-cell era. *Nat. Rev. Immunol.* **22**, 67-68, doi:10.1038/s41577-022-00675-7 (2022).
- 74 Dalod, M., Chelbi, R., Malissen, B. & Lawrence, T. Dendritic cell maturation: functional specialization through signaling specificity and transcriptional programming. *EMBO*

- J. **33**, 1104-1116, doi:10.1002/embj.201488027 (2014).
- 75 Randolph, G. J., Ivanov, S., Zinselmeyer, B. H. & Scallan, J. P. The Lymphatic System: Integral Roles in Immunity. *Annu. Rev. Immunol.* **35**, 31-52, doi:10.1146/annurev-immunol-041015-055354 (2017).
- 76 Forster, R. *et al.* CCR7 coordinates the primary immune response by establishing functional microenvironments in secondary lymphoid organs. *Cell* **99**, 23-33, doi:10.1016/s0092-8674(00)80059-8 (1999).
- 77 Ohl, L. *et al.* CCR7 governs skin dendritic cell migration under inflammatory and steady-state conditions. *Immunity* **21**, 279-288, doi:10.1016/j.immuni.2004.06.014 (2004).
- 78 Weber, M. *et al.* Interstitial dendritic cell guidance by haptotactic chemokine gradients. *Science* **339**, 328-332, doi:10.1126/science.1228456 (2013).
- 79 Forster, R., Davalos-Misslitz, A. C. & Rot, A. CCR7 and its ligands: balancing immunity and tolerance. *Nat. Rev. Immunol.* **8**, 362-371, doi:10.1038/nri2297 (2008).
- 80 Moore, M. A. & Metcalf, D. Ontogeny of the haemopoietic system: yolk sac origin of in vivo and in vitro colony forming cells in the developing mouse embryo. *Br. J. Haematol.* **18**, 279-296, doi:10.1111/j.1365-2141.1970.tb01443.x (1970).
- 81 Morris, L., Graham, C. F. & Gordon, S. Macrophages in haemopoietic and other tissues of the developing mouse detected by the monoclonal antibody F4/80. *Development* **112**, 517-526, doi:10.1242/dev.112.2.517 (1991).
- 82 Palis, J., Robertson, S., Kennedy, M., Wall, C. & Keller, G. Development of erythroid and myeloid progenitors in the yolk sac and embryo proper of the mouse. *Development* **126**, 5073-5084, doi:10.1242/dev.126.22.5073 (1999).
- 83 Lin, Y., Yoder, M. C. & Yoshimoto, M. Lymphoid progenitor emergence in the murine embryo and yolk sac precedes stem cell detection. *Stem Cells Dev.* **23**, 1168-1177, doi:10.1089/scd.2013.0536 (2014).
- 84 Lux, C. T. *et al.* All primitive and definitive hematopoietic progenitor cells emerging before E10 in the mouse embryo are products of the yolk sac. *Blood* **111**, 3435-3438, doi:10.1182/blood-2007-08-107086 (2008).
- 85 Gomez Perdiguero, E. *et al.* Tissue-resident macrophages originate from yolk-sac-derived erythro-myeloid progenitors. *Nature* **518**, 547-551, doi:10.1038/nature13989 (2015).
- 86 Ginhoux, F. & Guilliams, M. Tissue-Resident Macrophage Ontogeny and Homeostasis. *Immunity* **44**, 439-449, doi:10.1016/j.immuni.2016.02.024 (2016).
- 87 Jung, S. *et al.* Analysis of fractalkine receptor CX3CR1 function by targeted deletion and green fluorescent protein reporter gene insertion. *Mol Cell Biol* **20**, 4106-4114, doi:10.1128/MCB.20.11.4106-4114.2000 (2000).
- 88 Ensan, S. *et al.* Self-renewing resident arterial macrophages arise from embryonic CX3CR1(+) precursors and circulating monocytes immediately after birth. *Nat. Immunol.* **17**, 159-168, doi:10.1038/ni.3343 (2016).
- 89 Molawi, K. *et al.* Progressive replacement of embryo-derived cardiac macrophages with age. *J. Exp. Med.* **211**, 2151-2158, doi:10.1084/jem.20140639 (2014).
- 90 Heung, L. J. & Hohl, T. M. Inflammatory monocytes are detrimental to the host immune

- response during acute infection with *Cryptococcus neoformans*. *PLoS Pathog.* **15**, e1007627, doi:10.1371/journal.ppat.1007627 (2019).
- 91 Croxford, A. L. *et al.* The Cytokine GM-CSF Drives the Inflammatory Signature of CCR2+ Monocytes and Licenses Autoimmunity. *Immunity* **43**, 502-514, doi:10.1016/j.immuni.2015.08.010 (2015).
- 92 Saederup, N. *et al.* Selective chemokine receptor usage by central nervous system myeloid cells in CCR2-red fluorescent protein knock-in mice. *PLoS One* **5**, e13693, doi:10.1371/journal.pone.0013693 (2010).
- 93 Deng, L. *et al.* A novel mouse model of inflammatory bowel disease links mammalian target of rapamycin-dependent hyperproliferation of colonic epithelium to inflammation-associated tumorigenesis. *Am. J. Pathol.* **176**, 952-967, doi:10.2353/ajpath.2010.090622 (2010).
- 94 Schulz, C. *et al.* A lineage of myeloid cells independent of Myb and hematopoietic stem cells. *Science* **336**, 86-90, doi:10.1126/science.1219179 (2012).
- 95 Epelman, S. *et al.* Embryonic and adult-derived resident cardiac macrophages are maintained through distinct mechanisms at steady state and during inflammation. *Immunity* **40**, 91-104, doi:10.1016/j.immuni.2013.11.019 (2014).
- 96 Qian, B. Z. *et al.* CCL2 recruits inflammatory monocytes to facilitate breast-tumour metastasis. *Nature* **475**, 222-225, doi:10.1038/nature10138 (2011).
- 97 Ovchinnikov, D. A., DeBats, C. E., Sester, D. P., Sweet, M. J. & Hume, D. A. A conserved distal segment of the mouse CSF-1 receptor promoter is required for maximal expression of a reporter gene in macrophages and osteoclasts of transgenic mice. *J. Leukoc. Biol.* **87**, 815-822, doi:10.1189/jlb.0809557 (2010).
- 98 Hawley, C. A. *et al.* Csf1r-mApple Transgene Expression and Ligand Binding In Vivo Reveal Dynamics of CSF1R Expression within the Mononuclear Phagocyte System. *J. Immunol.* **200**, 2209-2223, doi:10.4049/jimmunol.1701488 (2018).
- 99 Boyer, S. W., Schroeder, A. V., Smith-Berdan, S. & Forsberg, E. C. All hematopoietic cells develop from hematopoietic stem cells through Flk2/Flt3-positive progenitor cells. *Cell Stem Cell* **9**, 64-73, doi:10.1016/j.stem.2011.04.021 (2011).
- 100 Hoeffel, G. *et al.* C-Myb(+) erythromyeloid progenitor-derived fetal monocytes give rise to adult tissue-resident macrophages. *Immunity* **42**, 665-678, doi:10.1016/j.immuni.2015.03.011 (2015).
- 101 Samokhvalov, I. M., Samokhvalova, N. I. & Nishikawa, S. Cell tracing shows the contribution of the yolk sac to adult haematopoiesis. *Nature* **446**, 1056-1061, doi:10.1038/nature05725 (2007).
- 102 Faust, N., Varas, F., Kelly, L. M., Heck, S. & Graf, T. Insertion of enhanced green fluorescent protein into the lysozyme gene creates mice with green fluorescent granulocytes and macrophages. *Blood* **96**, 719-726 (2000).
- 103 Clausen, B. E., Burkhardt, C., Reith, W., Renkawitz, R. & Forster, I.

- Conditional gene targeting in macrophages and granulocytes using LysMcre mice. *Transgenic Res.* **8**, 265-277, doi:10.1023/a:1008942828960 (1999).
- 104 Schaller, E. *et al.* Inactivation of the F4/80 glycoprotein in the mouse germ line. *Mol Cell Biol* **22**, 8035-8043, doi:10.1128/MCB.22.22.8035-8043.2002 (2002).
- 105 van Berlo, J. H. *et al.* c-kit⁺ cells minimally contribute cardiomyocytes to the heart. *Nature* **509**, 337-341, doi:10.1038/nature13309 (2014).
- 106 Stremmel, C. *et al.* Yolk sac macrophage progenitors traffic to the embryo during defined stages of development. *Nat Commun* **9**, 75, doi:10.1038/s41467-017-02492-2 (2018).
- 107 Sheng, J., Ruedl, C. & Karjalainen, K. Most Tissue-Resident Macrophages Except Microglia Are Derived from Fetal Hematopoietic Stem Cells. *Immunity* **43**, 382-393, doi:10.1016/j.immuni.2015.07.016 (2015).
- 108 Hatzistergos, K. E. *et al.* cKit⁺ cardiac progenitors of neural crest origin. *Proc. Natl. Acad. Sci. U. S. A.* **112**, 13051-13056, doi:10.1073/pnas.1517201112 (2015).
- 109 Pham, T. H. *et al.* Lymphatic endothelial cell sphingosine kinase activity is required for lymphocyte egress and lymphatic patterning. *J. Exp. Med.* **207**, 17-27, doi:10.1084/jem.20091619 (2010).
- 110 Zhang, N. *et al.* LYVE1⁺ macrophages of murine peritoneal mesothelium promote omentum-independent ovarian tumor growth. *J. Exp. Med.* **218**, doi:10.1084/jem.20210924 (2021).
- 111 Connor, A. L., Kelley, P. M. & Tempero, R. M. Lymphatic endothelial lineage assemblage during corneal lymphangiogenesis. *Lab. Invest.* **96**, 270-282, doi:10.1038/labinvest.2015.147 (2016).
- 112 Scott, C. L. *et al.* The Transcription Factor ZEB2 Is Required to Maintain the Tissue-Specific Identities of Macrophages. *Immunity* **49**, 312-325 e315, doi:10.1016/j.immuni.2018.07.004 (2018).
- 113 Kuhn, R., Schwenk, F., Aguet, M. & Rajewsky, K. Inducible gene targeting in mice. *Science* **269**, 1427-1429, doi:10.1126/science.7660125 (1995).
- 114 Xu, Y., Schrank, P. R. & Williams, J. W. Macrophage Fate Mapping. *Curr Protoc* **2**, e456, doi:10.1002/cpz1.456 (2022).
- 115 Bertrand, J. Y. *et al.* Three pathways to mature macrophages in the early mouse yolk sac. *Blood* **106**, 3004-3011, doi:10.1182/blood-2005-02-0461 (2005).
- 116 Mass, E. *et al.* Specification of tissue-resident macrophages during organogenesis. *Science* **353**, doi:10.1126/science.aaf4238 (2016).
- 117 Mucenski, M. L. *et al.* A functional c-myb gene is required for normal murine fetal hepatic hematopoiesis. *Cell* **65**, 677-689, doi:10.1016/0092-8674(91)90099-k (1991).
- 118 Alliot, F., Godin, I. & Pessac, B. Microglia derive from progenitors, originating from the yolk sac, and which proliferate in the brain. *Brain Res. Dev. Brain Res.* **117**, 145-152, doi:10.1016/s0165-3806(99)00113-3 (1999).
- 119 Kierdorf, K. *et al.* Microglia emerge from erythromyeloid precursors via Pu.1- and Irf8-dependent pathways. *Nat. Neurosci.* **16**, 273-280, doi:10.1038/nn.3318 (2013).

- 120 Mildner, A. *et al.* Microglia in the adult brain arise from Ly-6ChiCCR2+ monocytes only under defined host conditions. *Nat. Neurosci.* **10**, 1544-1553, doi:10.1038/nn2015 (2007).
- 121 Ydens, E. *et al.* Profiling peripheral nerve macrophages reveals two macrophage subsets with distinct localization, transcriptome and response to injury. *Nat. Neurosci.* **23**, 676-689, doi:10.1038/s41593-020-0618-6 (2020).
- 122 Ajami, B., Bennett, J. L., Krieger, C., McNagny, K. M. & Rossi, F. M. Infiltrating monocytes trigger EAE progression, but do not contribute to the resident microglia pool. *Nat. Neurosci.* **14**, 1142-1149, doi:10.1038/nn.2887 (2011).
- 123 Parkhurst, C. N. *et al.* Microglia promote learning-dependent synapse formation through brain-derived neurotrophic factor. *Cell* **155**, 1596-1609, doi:10.1016/j.cell.2013.11.030 (2013).
- 124 Wu, Y., Dissing-Olesen, L., MacVicar, B. A. & Stevens, B. Microglia: Dynamic Mediators of Synapse Development and Plasticity. *Trends Immunol.* **36**, 605-613, doi:10.1016/j.it.2015.08.008 (2015).
- 125 Yan, P. *et al.* Peripheral monocyte-derived cells counter amyloid plaque pathogenesis in a mouse model of Alzheimer's disease. *J. Clin. Invest.* **132**, doi:10.1172/JCI152565 (2022).
- 126 Buttgereit, A. *et al.* Sall1 is a transcriptional regulator defining microglia identity and function. *Nat. Immunol.* **17**, 1397-1406, doi:10.1038/ni.3585 (2016).
- 127 Hwang, D. *et al.* CSF-1 maintains pathogenic but not homeostatic myeloid cells in the central nervous system during autoimmune neuroinflammation. *Proc. Natl. Acad. Sci. U. S. A.* **119**, e2111804119, doi:10.1073/pnas.2111804119 (2022).
- 128 Chitu, V., Gokhan, S., Nandi, S., Mehler, M. F. & Stanley, E. R. Emerging Roles for CSF-1 Receptor and its Ligands in the Nervous System. *Trends Neurosci.* **39**, 378-393, doi:10.1016/j.tins.2016.03.005 (2016).
- 129 Bertrand, J. Y. *et al.* Haematopoietic stem cells derive directly from aortic endothelium during development. *Nature* **464**, 108-111, doi:10.1038/nature08738 (2010).
- 130 Boisset, J. C. *et al.* In vivo imaging of haematopoietic cells emerging from the mouse aortic endothelium. *Nature* **464**, 116-120, doi:10.1038/nature08764 (2010).
- 131 Kissa, K. & Herbomel, P. Blood stem cells emerge from aortic endothelium by a novel type of cell transition. *Nature* **464**, 112-115, doi:10.1038/nature08761 (2010).
- 132 Christensen, J. L., Wright, D. E., Wagers, A. J. & Weissman, I. L. Circulation and chemotaxis of fetal hematopoietic stem cells. *PLoS Biol.* **2**, E75, doi:10.1371/journal.pbio.0020075 (2004).
- 133 DeKoter, R. P., Walsh, J. C. & Singh, H. PU.1 regulates both cytokine-dependent proliferation and differentiation of granulocyte/macrophage progenitors. *EMBO J.* **17**, 4456-4468, doi:10.1093/emboj/17.15.4456 (1998).
- 134 Dakic, A. *et al.* PU.1 regulates the commitment of adult hematopoietic progenitors and restricts granulopoiesis. *J. Exp. Med.* **201**, 1487-1502, doi:10.1084/jem.20050075 (2005).
- 135 Lichanska, A. M. *et al.* Differentiation of the mononuclear phagocyte

- system during mouse embryogenesis: the role of transcription factor PU.1. *Blood* **94**, 127-138 (1999).
- 136 Kiousseian, A., Brunet de la Grange, P., Burlen-Defranoux, O., Godin, I. & Cumano, A. Immature hematopoietic stem cells undergo maturation in the fetal liver. *Development* **139**, 3521-3530, doi:10.1242/dev.079210 (2012).
- 137 Sakai, M. *et al.* Liver-Derived Signals Sequentially Reprogram Myeloid Enhancers to Initiate and Maintain Kupffer Cell Identity. *Immunity* **51**, 655-670 e658, doi:10.1016/j.immuni.2019.09.002 (2019).
- 138 Zigmond, E. *et al.* Infiltrating monocyte-derived macrophages and resident kupffer cells display different ontogeny and functions in acute liver injury. *J. Immunol.* **193**, 344-353, doi:10.4049/jimmunol.1400574 (2014).
- 139 Sierro, F. *et al.* A Liver Capsular Network of Monocyte-Derived Macrophages Restricts Hepatic Dissemination of Intraperitoneal Bacteria by Neutrophil Recruitment. *Immunity* **47**, 374-388 e376, doi:10.1016/j.immuni.2017.07.018 (2017).
- 140 Scott, C. L. *et al.* Bone marrow-derived monocytes give rise to self-renewing and fully differentiated Kupffer cells. *Nat Commun* **7**, 10321, doi:10.1038/ncomms10321 (2016).
- 141 Tran, S. *et al.* Impaired Kupffer Cell Self-Renewal Alters the Liver Response to Lipid Overload during Non-alcoholic Steatohepatitis. *Immunity* **53**, 627-640 e625, doi:10.1016/j.immuni.2020.06.003 (2020).
- 142 Yang, C. Y. *et al.* CLEC4F is an inducible C-type lectin in F4/80-positive cells and is involved in alpha-galactosylceramide presentation in liver. *PLoS One* **8**, e65070, doi:10.1371/journal.pone.0065070 (2013).
- 143 Wu, X. *et al.* Transcription factor Zeb2 regulates commitment to plasmacytoid dendritic cell and monocyte fate. *Proc. Natl. Acad. Sci. U. S. A.* **113**, 14775-14780, doi:10.1073/pnas.1611408114 (2016).
- 144 Huang, X. *et al.* Differential usage of transcriptional repressor Zeb2 enhancers distinguishes adult and embryonic hematopoiesis. *Immunity* **54**, 1417-1432 e1417, doi:10.1016/j.immuni.2021.04.015 (2021).
- 145 Krenkel, O. & Tacke, F. Liver macrophages in tissue homeostasis and disease. *Nat. Rev. Immunol.* **17**, 306-321, doi:10.1038/nri.2017.11 (2017).
- 146 Theurl, M. *et al.* Kupffer cells modulate iron homeostasis in mice via regulation of hepcidin expression. *J. Mol. Med. (Berl.)* **86**, 825-835, doi:10.1007/s00109-008-0346-y (2008).
- 147 Theurl, I. *et al.* On-demand erythrocyte disposal and iron recycling requires transient macrophages in the liver. *Nat. Med.* **22**, 945-951, doi:10.1038/nm.4146 (2016).
- 148 Willekens, F. L. *et al.* Liver Kupffer cells rapidly remove red blood cell-derived vesicles from the circulation by scavenger receptors. *Blood* **105**, 2141-2145, doi:10.1182/blood-2004-04-1578 (2005).
- 149 Bleriot, C. *et al.* Liver-resident macrophage necroptosis orchestrates type 1 microbicidal inflammation and type-2-mediated tissue repair during bacterial infection. *Immunity* **42**, 145-158,

- doi:10.1016/j.immuni.2014.12.020 (2015).
- 150 Han, Y. H. *et al.* Enterically derived high-density lipoprotein restrains liver injury through the portal vein. *Science* **373**, doi:10.1126/science.abe6729 (2021).
- 151 Bleriot, C. *et al.* A subset of Kupffer cells regulates metabolism through the expression of CD36. *Immunity* **54**, 2101-2116 e2106, doi:10.1016/j.immuni.2021.08.006 (2021).
- 152 Silverstein, R. L. & Febbraio, M. CD36, a scavenger receptor involved in immunity, metabolism, angiogenesis, and behavior. *Sci Signal* **2**, re3, doi:10.1126/scisignal.272re3 (2009).
- 153 Pepino, M. Y., Kuda, O., Samovski, D. & Abumrad, N. A. Structure-function of CD36 and importance of fatty acid signal transduction in fat metabolism. *Annu. Rev. Nutr.* **34**, 281-303, doi:10.1146/annurev-nutr-071812-161220 (2014).
- 154 Remmerie, A. *et al.* Osteopontin Expression Identifies a Subset of Recruited Macrophages Distinct from Kupffer Cells in the Fatty Liver. *Immunity* **53**, 641-657 e614, doi:10.1016/j.immuni.2020.08.004 (2020).
- 155 Seidman, J. S. *et al.* Niche-Specific Reprogramming of Epigenetic Landscapes Drives Myeloid Cell Diversity in Nonalcoholic Steatohepatitis. *Immunity* **52**, 1057-1074 e1057, doi:10.1016/j.immuni.2020.04.001 (2020).
- 156 Jaitin, D. A. *et al.* Lipid-Associated Macrophages Control Metabolic Homeostasis in a Trem2-Dependent Manner. *Cell* **178**, 686-698 e614, doi:10.1016/j.cell.2019.05.054 (2019).
- 157 Beattie, L. *et al.* Bone marrow-derived and resident liver macrophages display unique transcriptomic signatures but similar biological functions. *J. Hepatol.* **65**, 758-768, doi:10.1016/j.jhep.2016.05.037 (2016).
- 158 Dutta, P. *et al.* Myocardial Infarction Activates CCR2(+) Hematopoietic Stem and Progenitor Cells. *Cell Stem Cell* **16**, 477-487, doi:10.1016/j.stem.2015.04.008 (2015).
- 159 Courties, G. *et al.* Ischemic stroke activates hematopoietic bone marrow stem cells. *Circ. Res.* **116**, 407-417, doi:10.1161/CIRCRESAHA.116.305207 (2015).
- 160 Heidt, T. *et al.* Chronic variable stress activates hematopoietic stem cells. *Nat. Med.* **20**, 754-758, doi:10.1038/nm.3589 (2014).
- 161 Poller, W. C., Nahrendorf, M. & Swirski, F. K. Hematopoiesis and Cardiovascular Disease. *Circ. Res.* **126**, 1061-1085, doi:10.1161/CIRCRESAHA.120.315895 (2020).
- 162 Robbins, C. S. *et al.* Extramedullary hematopoiesis generates Ly-6C(high) monocytes that infiltrate atherosclerotic lesions. *Circulation* **125**, 364-374, doi:10.1161/CIRCULATIONAHA.111.061986 (2012).
- 163 Wilson, A. *et al.* Hematopoietic stem cells reversibly switch from dormancy to self-renewal during homeostasis and repair. *Cell* **135**, 1118-1129, doi:10.1016/j.cell.2008.10.048 (2008).
- 164 Cabezas-Wallscheid, N. *et al.* Identification of regulatory networks in HSCs and their immediate progeny via integrated proteome, transcriptome, and DNA methylome

- analysis. *Cell Stem Cell* **15**, 507-522, doi:10.1016/j.stem.2014.07.005 (2014).
- 165 Akashi, K., Traver, D., Miyamoto, T. & Weissman, I. L. A clonogenic common myeloid progenitor that gives rise to all myeloid lineages. *Nature* **404**, 193-197, doi:10.1038/35004599 (2000).
- 166 Ji, M. *et al.* Id2 intrinsically regulates lymphoid and erythroid development via interaction with different target proteins. *Blood* **112**, 1068-1077, doi:10.1182/blood-2008-01-133504 (2008).
- 167 Nerlov, C. & Graf, T. PU.1 induces myeloid lineage commitment in multipotent hematopoietic progenitors. *Genes Dev* **12**, 2403-2412, doi:10.1101/gad.12.15.2403 (1998).
- 168 Yanez, A. *et al.* Granulocyte-Monocyte Progenitors and Monocyte-Dendritic Cell Progenitors Independently Produce Functionally Distinct Monocytes. *Immunity* **47**, 890-902 e894, doi:10.1016/j.immuni.2017.10.021 (2017).
- 169 Hettinger, J. *et al.* Origin of monocytes and macrophages in a committed progenitor. *Nat. Immunol.* **14**, 821-830, doi:10.1038/ni.2638 (2013).
- 170 Kelly, L. M., Englmeier, U., Lafon, I., Sieweke, M. H. & Graf, T. MafB is an inducer of monocytic differentiation. *EMBO J.* **19**, 1987-1997, doi:10.1093/emboj/19.9.1987 (2000).
- 171 Kurotaki, D. *et al.* Essential role of the IRF8-KLF4 transcription factor cascade in murine monocyte differentiation. *Blood* **121**, 1839-1849, doi:10.1182/blood-2012-06-437863 (2013).
- 172 Feinberg, M. W. *et al.* The Kruppel-like factor KLF4 is a critical regulator of monocyte differentiation. *EMBO J.* **26**, 4138-4148, doi:10.1038/sj.emboj.7601824 (2007).
- 173 Sarrazin, S. *et al.* MafB restricts M-CSF-dependent myeloid commitment divisions of hematopoietic stem cells. *Cell* **138**, 300-313, doi:10.1016/j.cell.2009.04.057 (2009).
- 174 Gemelli, C. *et al.* Virally mediated MafB transduction induces the monocyte commitment of human CD34+ hematopoietic stem/progenitor cells. *Cell Death Differ* **13**, 1686-1696, doi:10.1038/sj.cdd.4401860 (2006).
- 175 Aziz, A., Soucie, E., Sarrazin, S. & Sieweke, M. H. MafB/c-Maf deficiency enables self-renewal of differentiated functional macrophages. *Science* **326**, 867-871, doi:10.1126/science.1176056 (2009).
- 176 Soucie, E. L. *et al.* Lineage-specific enhancers activate self-renewal genes in macrophages and embryonic stem cells. *Science* **351**, aad5510, doi:10.1126/science.aad5510 (2016).
- 177 Alder, J. K. *et al.* Kruppel-like factor 4 is essential for inflammatory monocyte differentiation in vivo. *J. Immunol.* **180**, 5645-5652, doi:10.4049/jimmunol.180.8.5645 (2008).
- 178 Murakami, K. *et al.* A RUNX-CBFbeta-driven enhancer directs the Irf8 dose-dependent lineage choice between DCs and monocytes. *Nat. Immunol.* **22**, 301-311, doi:10.1038/s41590-021-00871-y (2021).
- 179 Yanez, A., Ng, M. Y., Hassanzadeh-Kiabi, N. & Goodridge, H. S. IRF8 acts in lineage-committed rather than oligopotent progenitors to control neutrophil vs monocyte production. *Blood* **125**, 1452-1459, doi:10.1182/blood-2014-09-600833 (2015).

- 180 Durai, V. *et al.* Cryptic activation of an lrf8 enhancer governs cDC1 fate specification. *Nat. Immunol.* **20**, 1161-1173, doi:10.1038/s41590-019-0450-x (2019).
- 181 Liu, T. T. *et al.* Ablation of cDC2 development by triple mutations within the Zeb2 enhancer. *Nature*, doi:10.1038/s41586-022-04866-z (2022).
- 182 Kurotaki, D. *et al.* Transcription Factor IRF8 Governs Enhancer Landscape Dynamics in Mononuclear Phagocyte Progenitors. *Cell Rep.* **22**, 2628-2641, doi:10.1016/j.celrep.2018.02.048 (2018).
- 183 Osterwalder, M. *et al.* Enhancer redundancy provides phenotypic robustness in mammalian development. *Nature* **554**, 239-243, doi:10.1038/nature25461 (2018).
- 184 Rojo, R., Pridans, C., Langlais, D. & Hume, D. A. Transcriptional mechanisms that control expression of the macrophage colony-stimulating factor receptor locus. *Clin. Sci. (Lond.)* **131**, 2161-2182, doi:10.1042/CS20170238 (2017).
- 185 Rojo, R. *et al.* Deletion of a Csf1r enhancer selectively impacts CSF1R expression and development of tissue macrophage populations. *Nat Commun* **10**, 3215, doi:10.1038/s41467-019-11053-8 (2019).
- 186 Sudo, T. *et al.* Functional hierarchy of c-kit and c-fms in intramarrow production of CFU-M. *Oncogene* **11**, 2469-2476 (1995).
- 187 Hashimoto, D. *et al.* Pretransplant CSF-1 therapy expands recipient macrophages and ameliorates GVHD after allogeneic hematopoietic cell transplantation. *J. Exp. Med.* **208**, 1069-1082, doi:10.1084/jem.20101709 (2011).
- 188 Emoto, T. *et al.* Colony stimulating factor-1 producing endothelial cells and mesenchymal stromal cells maintain monocytes within a perivascular bone marrow niche. *Immunity* **55**, 862-878 e868, doi:10.1016/j.immuni.2022.04.005 (2022).
- 189 Mansour, A. *et al.* Osteoclasts promote the formation of hematopoietic stem cell niches in the bone marrow. *J. Exp. Med.* **209**, 537-549, doi:10.1084/jem.20110994 (2012).
- 190 Begg, S. K. *et al.* Delayed hematopoietic development in osteopetrotic (op/op) mice. *J. Exp. Med.* **177**, 237-242, doi:10.1084/jem.177.1.237 (1993).
- 191 Acar, M. *et al.* Deep imaging of bone marrow shows non-dividing stem cells are mainly perisinusoidal. *Nature* **526**, 126-130, doi:10.1038/nature15250 (2015).
- 192 Inra, C. N. *et al.* A perisinusoidal niche for extramedullary haematopoiesis in the spleen. *Nature* **527**, 466-471, doi:10.1038/nature15530 (2015).
- 193 Comazzetto, S., Shen, B. & Morrison, S. J. Niches that regulate stem cells and hematopoiesis in adult bone marrow. *Dev. Cell* **56**, 1848-1860, doi:10.1016/j.devcel.2021.05.018 (2021).
- 194 Frodermann, V. *et al.* Exercise reduces inflammatory cell production and cardiovascular inflammation via instruction of hematopoietic progenitor cells. *Nat. Med.* **25**, 1761-1771, doi:10.1038/s41591-019-0633-x (2019).
- 195 Mendez-Ferrer, S., Lucas, D., Battista, M. & Frenette, P. S. Haematopoietic stem cell release is regulated by circadian oscillations. *Nature* **452**, 442-447, doi:10.1038/nature06685 (2008).

- 196 Mendez-Ferrer, S., Battista, M. & Frenette, P. S. Cooperation of beta(2)- and beta(3)-adrenergic receptors in hematopoietic progenitor cell mobilization. *Ann. N. Y. Acad. Sci.* **1192**, 139-144, doi:10.1111/j.1749-6632.2010.05390.x (2010).
- 197 Scheiermann, C. *et al.* Adrenergic nerves govern circadian leukocyte recruitment to tissues. *Immunity* **37**, 290-301, doi:10.1016/j.immuni.2012.05.021 (2012).
- 198 Zhang, J. *et al.* In situ mapping identifies distinct vascular niches for myelopoiesis. *Nature* **590**, 457-462, doi:10.1038/s41586-021-03201-2 (2021).
- 199 Wang, Y. *et al.* Nonredundant roles of keratinocyte-derived IL-34 and neutrophil-derived CSF1 in Langerhans cell renewal in the steady state and during inflammation. *Eur. J. Immunol.* **46**, 552-559, doi:10.1002/eji.201545917 (2016).
- 200 McAlpine, C. S. *et al.* Sleep modulates haematopoiesis and protects against atherosclerosis. *Nature* **566**, 383-387, doi:10.1038/s41586-019-0948-2 (2019).
- 201 Li, S. *et al.* IL-1b expression in bone marrow dendritic cells is induced by TLR2 agonists and regulates HSC function. *Blood*, doi:10.1182/blood.2022016084 (2022).
- 202 Schloss, M. J. *et al.* B lymphocyte-derived acetylcholine limits steady-state and emergency hematopoiesis. *Nat. Immunol.* **23**, 605-618, doi:10.1038/s41590-022-01165-7 (2022).
- 203 Sarrazy, V. *et al.* Disruption of Glut1 in Hematopoietic Stem Cells Prevents Myelopoiesis and Enhanced Glucose Flux in Atheromatous Plaques of ApoE(-/-) Mice. *Circ. Res.* **118**, 1062-1077, doi:10.1161/CIRCRESAHA.115.307599 (2016).
- 204 Oburoglu, L. *et al.* Glucose and glutamine metabolism regulate human hematopoietic stem cell lineage specification. *Cell Stem Cell* **15**, 169-184, doi:10.1016/j.stem.2014.06.002 (2014).
- 205 Ito, K. *et al.* A PML-PPAR-delta pathway for fatty acid oxidation regulates hematopoietic stem cell maintenance. *Nat. Med.* **18**, 1350-1358, doi:10.1038/nm.2882 (2012).
- 206 Qi, L. *et al.* Aspartate availability limits hematopoietic stem cell function during hematopoietic regeneration. *Cell Stem Cell* **28**, 1982-1999 e1988, doi:10.1016/j.stem.2021.07.011 (2021).
- 207 Westerterp, M. *et al.* Regulation of hematopoietic stem and progenitor cell mobilization by cholesterol efflux pathways. *Cell Stem Cell* **11**, 195-206, doi:10.1016/j.stem.2012.04.024 (2012).
- 208 Yvan-Charvet, L. *et al.* ATP-binding cassette transporters and HDL suppress hematopoietic stem cell proliferation. *Science* **328**, 1689-1693, doi:10.1126/science.1189731 (2010).
- 209 Agathocleous, M. *et al.* Ascorbate regulates haematopoietic stem cell function and leukaemogenesis. *Nature* **549**, 476-481, doi:10.1038/nature23876 (2017).
- 210 Devesa, A. *et al.* Bone marrow activation in response to metabolic syndrome and early atherosclerosis. *Eur. Heart J.* **43**, 1809-1828, doi:10.1093/eurheartj/ehac102 (2022).
- 211 van der Valk, F. M. *et al.* Increased haematopoietic activity in patients with atherosclerosis. *Eur. Heart J.* **38**, 425-432,

- doi:10.1093/eurheartj/ehw246 (2017).
- 212 Emami, H. *et al.* Splenic metabolic activity predicts risk of future cardiovascular events: demonstration of a cardioplemic axis in humans. *JACC Cardiovasc. Imaging* **8**, 121-130, doi:10.1016/j.jcmg.2014.10.009 (2015).
- 213 Parmar, K., Mauch, P., Vergilio, J. A., Sackstein, R. & Down, J. D. Distribution of hematopoietic stem cells in the bone marrow according to regional hypoxia. *Proc. Natl. Acad. Sci. U. S. A.* **104**, 5431-5436, doi:10.1073/pnas.0701152104 (2007).
- 214 Nombela-Arrieta, C. *et al.* Quantitative imaging of haematopoietic stem and progenitor cell localization and hypoxic status in the bone marrow microenvironment. *Nat. Cell Biol.* **15**, 533-543, doi:10.1038/ncb2730 (2013).
- 215 Spencer, J. A. *et al.* Direct measurement of local oxygen concentration in the bone marrow of live animals. *Nature* **508**, 269-273, doi:10.1038/nature13034 (2014).
- 216 Takubo, K. *et al.* Regulation of the HIF-1alpha level is essential for hematopoietic stem cells. *Cell Stem Cell* **7**, 391-402, doi:10.1016/j.stem.2010.06.020 (2010).
- 217 Simsek, T. *et al.* The distinct metabolic profile of hematopoietic stem cells reflects their location in a hypoxic niche. *Cell Stem Cell* **7**, 380-390, doi:10.1016/j.stem.2010.07.011 (2010).
- 218 Miharada, K. *et al.* Cripto regulates hematopoietic stem cells as a hypoxic-niche-related factor through cell surface receptor GRP78. *Cell Stem Cell* **9**, 330-344, doi:10.1016/j.stem.2011.07.016 (2011).
- 219 Takubo, K. *et al.* Regulation of glycolysis by Pdk functions as a metabolic checkpoint for cell cycle quiescence in hematopoietic stem cells. *Cell Stem Cell* **12**, 49-61, doi:10.1016/j.stem.2012.10.011 (2013).
- 220 Inoue, S. *et al.* Mitochondrial respiration defects modulate differentiation but not proliferation of hematopoietic stem and progenitor cells. *FEBS Lett.* **584**, 3402-3409, doi:10.1016/j.febslet.2010.06.036 (2010).
- 221 Yu, W. M. *et al.* Metabolic regulation by the mitochondrial phosphatase PTPMT1 is required for hematopoietic stem cell differentiation. *Cell Stem Cell* **12**, 62-74, doi:10.1016/j.stem.2012.11.022 (2013).
- 222 Gan, B. *et al.* Lkb1 regulates quiescence and metabolic homeostasis of haematopoietic stem cells. *Nature* **468**, 701-704, doi:10.1038/nature09595 (2010).
- 223 Gurumurthy, S. *et al.* The Lkb1 metabolic sensor maintains haematopoietic stem cell survival. *Nature* **468**, 659-663, doi:10.1038/nature09572 (2010).
- 224 Nakada, D., Saunders, T. L. & Morrison, S. J. Lkb1 regulates cell cycle and energy metabolism in haematopoietic stem cells. *Nature* **468**, 653-658, doi:10.1038/nature09571 (2010).
- 225 Ito, K. *et al.* Self-renewal of a purified Tie2+ hematopoietic stem cell population relies on mitochondrial clearance. *Science* **354**, 1156-1160, doi:10.1126/science.aaf5530 (2016).
- 226 Anso, E. *et al.* The mitochondrial respiratory chain is essential for haematopoietic stem cell function.

- Nat. Cell Biol.* **19**, 614-625, doi:10.1038/ncb3529 (2017).
- 227 Liles, W. C. *et al.* Mobilization of hematopoietic progenitor cells in healthy volunteers by AMD3100, a CXCR4 antagonist. *Blood* **102**, 2728-2730, doi:10.1182/blood-2003-02-0663 (2003).
- 228 Jung, H., Mithal, D. S., Park, J. E. & Miller, R. J. Localized CCR2 Activation in the Bone Marrow Niche Mobilizes Monocytes by Desensitizing CXCR4. *PLoS One* **10**, e0128387, doi:10.1371/journal.pone.0128387 (2015).
- 229 Lu, B. *et al.* Abnormalities in monocyte recruitment and cytokine expression in monocyte chemoattractant protein 1-deficient mice. *J. Exp. Med.* **187**, 601-608, doi:10.1084/jem.187.4.601 (1998).
- 230 Kurihara, T., Warr, G., Loy, J. & Bravo, R. Defects in macrophage recruitment and host defense in mice lacking the CCR2 chemokine receptor. *J. Exp. Med.* **186**, 1757-1762, doi:10.1084/jem.186.10.1757 (1997).
- 231 Boring, L. *et al.* Impaired monocyte migration and reduced type 1 (Th1) cytokine responses in C-C chemokine receptor 2 knockout mice. *J. Clin. Invest.* **100**, 2552-2561, doi:10.1172/JCI119798 (1997).
- 232 Tsou, C. L. *et al.* Critical roles for CCR2 and MCP-3 in monocyte mobilization from bone marrow and recruitment to inflammatory sites. *J. Clin. Invest.* **117**, 902-909, doi:10.1172/JCI29919 (2007).
- 233 Nguyen, K. D. *et al.* Circadian gene *Bmal1* regulates diurnal oscillations of Ly6C(hi) inflammatory monocytes. *Science* **341**, 1483-1488, doi:10.1126/science.1240636 (2013).
- 234 Devi, S. *et al.* Adrenergic regulation of the vasculature impairs leukocyte interstitial migration and suppresses immune responses. *Immunity* **54**, 1219-1230 e1217, doi:10.1016/j.immuni.2021.03.025 (2021).
- 235 Kollet, O. *et al.* Physiologic corticosterone oscillations regulate murine hematopoietic stem/progenitor cell proliferation and CXCL12 expression by bone marrow stromal progenitors. *Leukemia* **27**, 2006-2015, doi:10.1038/leu.2013.154 (2013).
- 236 Poller, W. C. *et al.* Brain motor and fear circuits regulate leukocytes during acute stress. *Nature*, doi:10.1038/s41586-022-04890-z (2022).
- 237 Schyns, J. *et al.* Non-classical tissue monocytes and two functionally distinct populations of interstitial macrophages populate the mouse lung. *Nat Commun* **10**, 3964, doi:10.1038/s41467-019-11843-0 (2019).
- 238 Tacke, F. *et al.* Monocyte subsets differentially employ CCR2, CCR5, and CX3CR1 to accumulate within atherosclerotic plaques. *J. Clin. Invest.* **117**, 185-194, doi:10.1172/JCI28549 (2007).
- 239 Dyer, D. P. *et al.* Chemokine Receptor Redundancy and Specificity Are Context Dependent. *Immunity* **50**, 378-389 e375, doi:10.1016/j.immuni.2019.01.009 (2019).
- 240 Swirski, F. K. *et al.* Ly-6Chi monocytes dominate hypercholesterolemia-associated monocytes and give rise to macrophages in atheromata. *J. Clin. Invest.* **117**, 195-205, doi:10.1172/JCI29950 (2007).
- 241 Rosen, H. & Gordon, S. Monoclonal antibody to the murine type 3 complement receptor inhibits adhesion of myelomonocytic cells in vitro and inflammatory cell

- recruitment in vivo. *J. Exp. Med.* **166**, 1685-1701, doi:10.1084/jem.166.6.1685 (1987).
- 242 Henderson, R. B., Hobbs, J. A., Mathies, M. & Hogg, N. Rapid recruitment of inflammatory monocytes is independent of neutrophil migration. *Blood* **102**, 328-335, doi:10.1182/blood-2002-10-3228 (2003).
- 243 Tedder, T. F., Steeber, D. A. & Pizcueta, P. L-selectin-deficient mice have impaired leukocyte recruitment into inflammatory sites. *J. Exp. Med.* **181**, 2259-2264, doi:10.1084/jem.181.6.2259 (1995).
- 244 Shi, C. *et al.* Monocyte trafficking to hepatic sites of bacterial infection is chemokine independent and directed by focal intercellular adhesion molecule-1 expression. *J. Immunol.* **184**, 6266-6274, doi:10.4049/jimmunol.0904160 (2010).
- 245 Zheng, C. *et al.* CD11b regulates obesity-induced insulin resistance via limiting alternative activation and proliferation of adipose tissue macrophages. *Proc. Natl. Acad. Sci. U. S. A.* **112**, E7239-7248, doi:10.1073/pnas.1500396113 (2015).
- 246 Poitou, C. *et al.* CD14^{dim}CD16⁺ and CD14⁺CD16⁺ monocytes in obesity and during weight loss: relationships with fat mass and subclinical atherosclerosis. *Arterioscler. Thromb. Vasc. Biol.* **31**, 2322-2330, doi:10.1161/ATVBAHA.111.230979 (2011).
- 247 Chapman, C. M., Beilby, J. P., McQuillan, B. M., Thompson, P. L. & Hung, J. Monocyte count, but not C-reactive protein or interleukin-6, is an independent risk marker for subclinical carotid atherosclerosis. *Stroke* **35**, 1619-1624, doi:10.1161/01.STR.0000130857.19423.ad (2004).
- 248 Waterhouse, D. F., Cahill, R. A., Sheehan, F. & McCreery, C. Prediction of calculated future cardiovascular disease by monocyte count in an asymptomatic population. *Vasc Health Risk Manag* **4**, 177-187, doi:10.2147/vhrm.2008.04.01.177 (2008).
- 249 Dalmas, E. *et al.* Variations in circulating inflammatory factors are related to changes in calorie and carbohydrate intakes early in the course of surgery-induced weight reduction. *Am. J. Clin. Nutr.* **94**, 450-458, doi:10.3945/ajcn.111.013771 (2011).
- 250 Nagareddy, P. R. *et al.* Hyperglycemia promotes myelopoiesis and impairs the resolution of atherosclerosis. *Cell Metab.* **17**, 695-708, doi:10.1016/j.cmet.2013.04.001 (2013).
- 251 Jordan, S. *et al.* Dietary Intake Regulates the Circulating Inflammatory Monocyte Pool. *Cell* **178**, 1102-1114 e1117, doi:10.1016/j.cell.2019.07.050 (2019).
- 252 Barrett, T. J. *et al.* Chronic stress primes innate immune responses in mice and humans. *Cell Rep.* **36**, 109595, doi:10.1016/j.celrep.2021.109595 (2021).
- 253 Flynn, M. C. *et al.* Transient Intermittent Hyperglycemia Accelerates Atherosclerosis by Promoting Myelopoiesis. *Circ. Res.* **127**, 877-892, doi:10.1161/CIRCRESAHA.120.316653 (2020).
- 254 Freemerman, A. J. *et al.* Metabolic reprogramming of macrophages: glucose transporter 1 (GLUT1)-mediated glucose metabolism drives

- a proinflammatory phenotype. *J. Biol. Chem.* **289**, 7884-7896, doi:10.1074/jbc.M113.522037 (2014).
- 255 Freerman, A. J. *et al.* Myeloid Slc2a1-Deficient Murine Model Revealed Macrophage Activation and Metabolic Phenotype Are Fueled by GLUT1. *J. Immunol.* **202**, 1265-1286, doi:10.4049/jimmunol.1800002 (2019).
- 256 Arguello, R. J. *et al.* SCENITH: A Flow Cytometry-Based Method to Functionally Profile Energy Metabolism with Single-Cell Resolution. *Cell Metab.* **32**, 1063-1075 e1067, doi:10.1016/j.cmet.2020.11.007 (2020).
- 257 Trompette, A. *et al.* Dietary Fiber Confers Protection against Flu by Shaping Ly6c(-) Patrolling Monocyte Hematopoiesis and CD8(+) T Cell Metabolism. *Immunity* **48**, 992-1005 e1008, doi:10.1016/j.immuni.2018.04.022 (2018).
- 258 Mondor, I. *et al.* Lymphatic Endothelial Cells Are Essential Components of the Subcapsular Sinus Macrophage Niche. *Immunity* **50**, 1453-1466 e1454, doi:10.1016/j.immuni.2019.04.002 (2019).
- 259 Bellomo, A. *et al.* Reticular Fibroblasts Expressing the Transcription Factor WT1 Define a Stromal Niche that Maintains and Replenishes Splenic Red Pulp Macrophages. *Immunity* **53**, 127-142 e127, doi:10.1016/j.immuni.2020.06.008 (2020).
- 260 Ivanov, S. *et al.* Mesothelial cell CSF1 sustains peritoneal macrophage proliferation. *Eur. J. Immunol.* **49**, 2012-2018, doi:10.1002/eji.201948164 (2019).
- 261 Gabanyi, I. *et al.* Neuro-immune Interactions Drive Tissue Programming in Intestinal Macrophages. *Cell* **164**, 378-391, doi:10.1016/j.cell.2015.12.023 (2016).
- 262 Guilliams, M., Thierry, G. R., Bonnardel, J. & Bajenoff, M. Establishment and Maintenance of the Macrophage Niche. *Immunity* **52**, 434-451, doi:10.1016/j.immuni.2020.02.015 (2020).
- 263 T'Jonck, W., Guilliams, M. & Bonnardel, J. Niche signals and transcription factors involved in tissue-resident macrophage development. *Cell. Immunol.* **330**, 43-53, doi:10.1016/j.cellimm.2018.02.005 (2018).
- 264 Sheih, A., Parks, W. C. & Ziegler, S. F. GM-CSF produced by the airway epithelium is required for sensitization to cockroach allergen. *Mucosal Immunol.* **10**, 705-715, doi:10.1038/mi.2016.90 (2017).
- 265 Kana, V. *et al.* CSF-1 controls cerebellar microglia and is required for motor function and social interaction. *J. Exp. Med.* **216**, 2265-2281, doi:10.1084/jem.20182037 (2019).
- 266 Bonnardel, J. *et al.* Stellate Cells, Hepatocytes, and Endothelial Cells Imprint the Kupffer Cell Identity on Monocytes Colonizing the Liver Macrophage Niche. *Immunity* **51**, 638-654 e639, doi:10.1016/j.immuni.2019.08.017 (2019).
- 267 Guilliams, M. *et al.* Spatial proteogenomics reveals distinct and evolutionarily conserved hepatic macrophage niches. *Cell* **185**, 379-396 e338, doi:10.1016/j.cell.2021.12.018 (2022).

- 268 Wolf, Y. *et al.* Brown-adipose-tissue macrophages control tissue innervation and homeostatic energy expenditure. *Nat Immunol* **18**, 665-674, doi:10.1038/ni.3746 (2017).
- 269 Lim, H. Y. *et al.* Hyaluronan Receptor LYVE-1-Expressing Macrophages Maintain Arterial Tone through Hyaluronan-Mediated Regulation of Smooth Muscle Cell Collagen. *Immunity* **49**, 326-341 e327, doi:10.1016/j.immuni.2018.06.008 (2018).
- 270 van de Laar, L. *et al.* Yolk Sac Macrophages, Fetal Liver, and Adult Monocytes Can Colonize an Empty Niche and Develop into Functional Tissue-Resident Macrophages. *Immunity* **44**, 755-768, doi:10.1016/j.immuni.2016.02.017 (2016).
- 271 Li, F. *et al.* Monocyte-derived alveolar macrophages autonomously determine severe outcome of respiratory viral infection. *Sci Immunol* **7**, eabj5761, doi:10.1126/sciimmunol.abj5761 (2022).
- 272 Sauter, K. A. *et al.* The MacBlue binary transgene (csf1r-gal4VP16/UAS-ECFP) provides a novel marker for visualisation of subsets of monocytes, macrophages and dendritic cells and responsiveness to CSF1 administration. *PLoS One* **9**, e105429, doi:10.1371/journal.pone.0105429 (2014).
- 273 Amorim, A. *et al.* IFN γ and GM-CSF control complementary differentiation programs in the monocyte-to-phagocyte transition during neuroinflammation. *Nat. Immunol.* **23**, 217-228, doi:10.1038/s41590-021-01117-7 (2022).
- 274 Shaw, T. N. *et al.* Tissue-resident macrophages in the intestine are long lived and defined by Tim-4 and CD4 expression. *J. Exp. Med.* **215**, 1507-1518, doi:10.1084/jem.20180019 (2018).
- 275 Bain, C. C. *et al.* Constant replenishment from circulating monocytes maintains the macrophage pool in the intestine of adult mice. *Nat. Immunol.* **15**, 929-937, doi:10.1038/ni.2967 (2014).
- 276 Smythies, L. E. *et al.* Human intestinal macrophages display profound inflammatory anergy despite avid phagocytic and bacteriocidal activity. *J. Clin. Invest.* **115**, 66-75, doi:10.1172/JCI19229 (2005).
- 277 Bain, C. C. *et al.* Resident and pro-inflammatory macrophages in the colon represent alternative context-dependent fates of the same Ly6Chi monocyte precursors. *Mucosal Immunol.* **6**, 498-510, doi:10.1038/mi.2012.89 (2013).
- 278 Smythies, L. E. *et al.* Inflammation anergy in human intestinal macrophages is due to Smad-induced I κ B α expression and NF- κ B inactivation. *J. Biol. Chem.* **285**, 19593-19604, doi:10.1074/jbc.M109.069955 (2010).
- 279 Schridde, A. *et al.* Tissue-specific differentiation of colonic macrophages requires TGF β receptor-mediated signaling. *Mucosal Immunol.* **10**, 1387-1399, doi:10.1038/mi.2016.142 (2017).
- 280 Matheis, F. *et al.* Adrenergic Signaling in Muscularis Macrophages Limits Infection-Induced Neuronal Loss. *Cell* **180**, 64-78 e16, doi:10.1016/j.cell.2019.12.002 (2020).
- 281 Muller, P. A. *et al.* Crosstalk between muscularis macrophages and enteric neurons regulates gastrointestinal motility. *Cell* **158**, 300-313,

- doi:10.1016/j.cell.2014.04.050
(2014).
- 282 De Schepper, S. *et al.* Self-Maintaining Gut Macrophages Are Essential for Intestinal Homeostasis. *Cell* **175**, 400-415 e413, doi:10.1016/j.cell.2018.07.048 (2018).
- 283 Gautier, E. L. *et al.* Gata6 regulates aspartoacylase expression in resident peritoneal macrophages and controls their survival. *J. Exp. Med.* **211**, 1525-1531, doi:10.1084/jem.20140570 (2014).
- 284 Kim, K. W. *et al.* MHC II+ resident peritoneal and pleural macrophages rely on IRF4 for development from circulating monocytes. *J. Exp. Med.* **213**, 1951-1959, doi:10.1084/jem.20160486 (2016).
- 285 Bain, C. C. *et al.* Long-lived self-renewing bone marrow-derived macrophages displace embryo-derived cells to inhabit adult serous cavities. *Nat Commun* **7**, ncomms11852, doi:10.1038/ncomms11852 (2016).
- 286 Bain, C. C. *et al.* Rate of replenishment and microenvironment contribute to the sexually dimorphic phenotype and function of peritoneal macrophages. *Sci Immunol* **5**, doi:10.1126/sciimmunol.abc4466 (2020).
- 287 Stiekema, L. C. A. *et al.* Impact of cholesterol on proinflammatory monocyte production by the bone marrow. *Eur. Heart J.* **42**, 4309-4320, doi:10.1093/eurheartj/ehab465 (2021).
- 288 Boring, L., Gosling, J., Cleary, M. & Charo, I. F. Decreased lesion formation in CCR2^{-/-} mice reveals a role for chemokines in the initiation of atherosclerosis. *Nature* **394**, 894-897, doi:10.1038/29788 (1998).
- 289 Gu, L. *et al.* Absence of monocyte chemoattractant protein-1 reduces atherosclerosis in low density lipoprotein receptor-deficient mice. *Mol. Cell* **2**, 275-281, doi:10.1016/s1097-2765(00)80139-2 (1998).
- 290 Williams, J. W. *et al.* Limited proliferation capacity of aortic intima resident macrophages requires monocyte recruitment for atherosclerotic plaque progression. *Nat. Immunol.* **21**, 1194-1204, doi:10.1038/s41590-020-0768-4 (2020).
- 291 Kim, K. *et al.* Transcriptome Analysis Reveals Nonfoamy Rather Than Foamy Plaque Macrophages Are Proinflammatory in Atherosclerotic Murine Models. *Circ. Res.* **123**, 1127-1142, doi:10.1161/CIRCRESAHA.118.312804 (2018).
- 292 Williams, J. W. *et al.* Limited Macrophage Positional Dynamics in Progressing or Regressing Murine Atherosclerotic Plaques-Brief Report. *Arterioscler. Thromb. Vasc. Biol.* **38**, 1702-1710, doi:10.1161/ATVBAHA.118.311319 (2018).
- 293 Doran, A. C., Yurdagul, A., Jr. & Tabas, I. Efferocytosis in health and disease. *Nat. Rev. Immunol.* **20**, 254-267, doi:10.1038/s41577-019-0240-6 (2020).
- 294 Tabas, I. & Bornfeldt, K. E. Intracellular and Intercellular Aspects of Macrophage Immunometabolism in Atherosclerosis. *Circ. Res.* **126**, 1209-1227, doi:10.1161/CIRCRESAHA.119.315939 (2020).
- 295 Bajpai, G. *et al.* Tissue Resident CCR2⁻ and CCR2⁺ Cardiac Macrophages Differentially Orchestrate Monocyte Recruitment and Fate Specification

- Following Myocardial Injury. *Circ. Res.* **124**, 263-278, doi:10.1161/CIRCRESAHA.118.314028 (2019). 303
- 296 Bajpai, G. *et al.* The human heart contains distinct macrophage subsets with divergent origins and functions. *Nat. Med.* **24**, 1234-1245, doi:10.1038/s41591-018-0059-x (2018). 304
- 297 Dick, S. A. *et al.* Self-renewing resident cardiac macrophages limit adverse remodeling following myocardial infarction. *Nat. Immunol.* **20**, 29-39, doi:10.1038/s41590-018-0272-2 (2019). 305
- 298 Wong, N. R. *et al.* Resident cardiac macrophages mediate adaptive myocardial remodeling. *Immunity* **54**, 2072-2088 e2077, doi:10.1016/j.immuni.2021.07.003 (2021). 306
- 299 Leid, J. *et al.* Primitive Embryonic Macrophages are Required for Coronary Development and Maturation. *Circ. Res.* **118**, 1498-1511, doi:10.1161/CIRCRESAHA.115.308270 (2016). 307
- 300 Sager, H. B. *et al.* Proliferation and Recruitment Contribute to Myocardial Macrophage Expansion in Chronic Heart Failure. *Circ. Res.* **119**, 853-864, doi:10.1161/CIRCRESAHA.116.309001 (2016). 308
- 301 Wan, E. *et al.* Enhanced efferocytosis of apoptotic cardiomyocytes through tyrosine kinase links acute inflammation resolution to cardiac repair after infarction. *Circ. Res.* **113**, 1004-1012, doi:10.1161/CIRCRESAHA.113.301198 (2013). 309
- 302 Miyanishi, M. *et al.* Identification of Tim4 as a phosphatidylserine receptor. *Nature* **450**, 435-439, doi:10.1038/nature06307 (2007).
- Jokela, H. *et al.* Fetal-derived macrophages persist and sequentially mature in ovaries after birth in mice. *Eur. J. Immunol.* **50**, 1500-1514, doi:10.1002/eji.202048531 (2020).
- Van der Hoek, K. H. *et al.* Intrabursal injection of clodronate liposomes causes macrophage depletion and inhibits ovulation in the mouse ovary. *Biol. Reprod.* **62**, 1059-1066, doi:10.1095/biolreprod62.4.1059 (2000).
- Cohen, P. E., Zhu, L. & Pollard, J. W. Absence of colony stimulating factor-1 in osteopetrotic (csfmop/csfp) mice disrupts estrous cycles and ovulation. *Biol. Reprod.* **56**, 110-118, doi:10.1095/biolreprod56.1.110 (1997).
- Cohen, P. E., Nishimura, K., Zhu, L. & Pollard, J. W. Macrophages: important accessory cells for reproductive function. *J. Leukoc. Biol.* **66**, 765-772, doi:10.1002/jlb.66.5.765 (1999).
- Brannstrom, M., Bonello, N., Wang, L. J. & Norman, R. J. Effects of tumour necrosis factor alpha (TNF alpha) on ovulation in the rat ovary. *Reprod. Fertil. Dev.* **7**, 67-73, doi:10.1071/rd9950067 (1995).
- Hagglund, A. C., Ny, A., Leonardsson, G. & Ny, T. Regulation and localization of matrix metalloproteinases and tissue inhibitors of metalloproteinases in the mouse ovary during gonadotropin-induced ovulation. *Endocrinology* **140**, 4351-4358, doi:10.1210/endo.140.9.7002 (1999).
- Wu, R., Van der Hoek, K. H., Ryan, N. K., Norman, R. J. & Robker, R. L. Macrophage contributions to ovarian function. *Hum. Reprod. Update* **10**, 119-133,

- doi:10.1093/humupd/dmh011 (2004).
- 310 Mossadegh-Keller, N. *et al.* Developmental origin and maintenance of distinct testicular macrophage populations. *J. Exp. Med.* **214**, 2829-2841, doi:10.1084/jem.20170829 (2017).
- 311 Wang, M. *et al.* Two populations of self-maintaining monocyte-independent macrophages exist in adult epididymis and testis. *Proc. Natl. Acad. Sci. U. S. A.* **118**, doi:10.1073/pnas.2013686117 (2021).
- 312 Lokka, E. *et al.* Generation, localization and functions of macrophages during the development of testis. *Nat Commun* **11**, 4375, doi:10.1038/s41467-020-18206-0 (2020).
- 313 Pollard, J. W., Dominguez, M. G., Mocci, S., Cohen, P. E. & Stanley, E. R. Effect of the colony-stimulating factor-1 null mutation, osteopetrotic (*csfm(op)*), on the distribution of macrophages in the male mouse reproductive tract. *Biol Reprod* **56**, 1290-1300, doi:10.1095/biolreprod56.5.1290 (1997).
- 314 Shechter, R., London, A. & Schwartz, M. Orchestrated leukocyte recruitment to immune-privileged sites: absolute barriers versus educational gates. *Nat Rev Immunol* **13**, 206-218, doi:10.1038/nri3391 (2013).
- 315 DeFalco, T. *et al.* Macrophages Contribute to the Spermatogonial Niche in the Adult Testis. *Cell Rep.* **12**, 1107-1119, doi:10.1016/j.celrep.2015.07.015 (2015).
- 316 Calderon, B. *et al.* The pancreas anatomy conditions the origin and properties of resident macrophages. *J Exp Med* **212**, 1497-1512, doi:10.1084/jem.20150496 (2015).
- 317 Chittezhath, M. *et al.* Islet macrophages are associated with islet vascular remodeling and compensatory hyperinsulinemia during diabetes. *Am J Physiol Endocrinol Metab* **317**, E1108-E1120, doi:10.1152/ajpendo.00248.2019 (2019).
- 318 Banaei-Bouchareb, L. *et al.* Insulin cell mass is altered in *Csf1op/Csf1op* macrophage-deficient mice. *J Leukoc Biol* **76**, 359-367, doi:10.1189/jlb.1103591 (2004).
- 319 Ying, W. *et al.* Expansion of Islet-Resident Macrophages Leads to Inflammation Affecting beta Cell Proliferation and Function in Obesity. *Cell Metab* **29**, 457-474 e455, doi:10.1016/j.cmet.2018.12.003 (2019).
- 320 Vomund, A. N. *et al.* Beta cells transfer vesicles containing insulin to phagocytes for presentation to T cells. *Proc Natl Acad Sci U S A* **112**, E5496-5502, doi:10.1073/pnas.1515954112 (2015).
- 321 Carrero, J. A. *et al.* Resident macrophages of pancreatic islets have a seminal role in the initiation of autoimmune diabetes of NOD mice. *Proc Natl Acad Sci U S A* **114**, E10418-E10427, doi:10.1073/pnas.1713543114 (2017).
- 322 Zakharov, P. N., Hu, H., Wan, X. & Unanue, E. R. Single-cell RNA sequencing of murine islets shows high cellular complexity at all stages of autoimmune diabetes. *J Exp Med* **217**, doi:10.1084/jem.20192362 (2020).
- 323 Weisberg, S. P. *et al.* Obesity is associated with macrophage accumulation in adipose tissue. *J. Clin.*

- Invest.* **112**, 1796-1808, doi:10.1172/JCI19246 (2003).
- 324 Xu, H. *et al.* Chronic inflammation in fat plays a crucial role in the development of obesity-related insulin resistance. *J. Clin. Invest.* **112**, 1821-1830, doi:10.1172/JCI19451 (2003).
- 325 Hassnain Waqas, S. F. *et al.* Adipose tissue macrophages develop from bone marrow-independent progenitors in *Xenopus laevis* and mouse. *J. Leukoc. Biol.* **102**, 845-855, doi:10.1189/jlb.1A0317-082RR (2017).
- 326 Felix, I. *et al.* Single-Cell Proteomics Reveals the Defined Heterogeneity of Resident Macrophages in White Adipose Tissue. *Front. Immunol.* **12**, 719979, doi:10.3389/fimmu.2021.719979 (2021).
- 327 Ivanov, S., Merlin, J., Lee, M. K. S., Murphy, A. J. & Guinamard, R. R. Biology and function of adipose tissue macrophages, dendritic cells and B cells. *Atherosclerosis* **271**, 102-110, doi:10.1016/j.atherosclerosis.2018.01.018 (2018).
- 328 Chakarov, S., Bleriot, C. & Ginhoux, F. Role of adipose tissue macrophages in obesity-related disorders. *J. Exp. Med.* **219**, doi:10.1084/jem.20211948 (2022).
- 329 Weinstock, A. *et al.* Single-Cell RNA Sequencing of Visceral Adipose Tissue Leukocytes Reveals that Caloric Restriction Following Obesity Promotes the Accumulation of a Distinct Macrophage Population with Features of Phagocytic Cells. *Immunometabolism* **1**, doi:10.20900/immunometab20190008 (2019).
- 330 Silva, H. M. *et al.* Vasculature-associated fat macrophages readily adapt to inflammatory and metabolic challenges. *J. Exp. Med.* **216**, 786-806, doi:10.1084/jem.20181049 (2019).
- 331 Moura Silva, H. *et al.* c-MAF-dependent perivascular macrophages regulate diet-induced metabolic syndrome. *Sci Immunol* **6**, eabg7506, doi:10.1126/sciimmunol.abg7506 (2021).
- 332 Pirzgalska, R. M. *et al.* Sympathetic neuron-associated macrophages contribute to obesity by importing and metabolizing norepinephrine. *Nat. Med.* **23**, 1309-1318, doi:10.1038/nm.4422 (2017).
- 333 Jung, S. M., Sanchez-Gurmaches, J. & Guertin, D. A. Brown Adipose Tissue Development and Metabolism. *Handb. Exp. Pharmacol.* **251**, 3-36, doi:10.1007/164_2018_168 (2019).
- 334 Lindhorst, A. *et al.* Adipocyte death triggers a pro-inflammatory response and induces metabolic activation of resident macrophages. *Cell Death Dis.* **12**, 579, doi:10.1038/s41419-021-03872-9 (2021).
- 335 Fischer-Posovszky, P., Wang, Q. A., Asterholm, I. W., Rutkowski, J. M. & Scherer, P. E. Targeted deletion of adipocytes by apoptosis leads to adipose tissue recruitment of alternatively activated M2 macrophages. *Endocrinology* **152**, 3074-3081, doi:10.1210/en.2011-1031 (2011).
- 336 Cho, C. H. *et al.* Angiogenic role of LYVE-1-positive macrophages in adipose tissue. *Circ. Res.* **100**, e47-57, doi:10.1161/01.RES.0000259564.92792.93 (2007).
- 337 Pang, C. *et al.* Macrophage infiltration into adipose tissue may promote angiogenesis for adipose tissue remodeling in obesity. *Am. J. Physiol. Endocrinol. Metab.* **295**, E313-322, doi:10.1152/ajpendo.90296.2008 (2008).

- 338 Brestoff, J. R. *et al.* Intercellular Mitochondria Transfer to Macrophages Regulates White Adipose Tissue Homeostasis and Is Impaired in Obesity. *Cell Metab.* **33**, 270-282 e278, doi:10.1016/j.cmet.2020.11.008 (2021).
- 339 Cox, N. *et al.* Diet-regulated production of PDGF α by macrophages controls energy storage. *Science* **373**, doi:10.1126/science.abe9383 (2021).
- 340 Aouadi, M. *et al.* Lipid storage by adipose tissue macrophages regulates systemic glucose tolerance. *Am. J. Physiol. Endocrinol. Metab.* **307**, E374-383, doi:10.1152/ajpendo.00187.2014 (2014).
- 341 van Dierendonck, X. *et al.* HILPDA Uncouples Lipid Droplet Accumulation in Adipose Tissue Macrophages from Inflammation and Metabolic Dysregulation. *Cell Rep.* **30**, 1811-1822 e1816, doi:10.1016/j.celrep.2020.01.046 (2020).
- 342 Petkevicius, K. *et al.* Norepinephrine promotes triglyceride storage in macrophages via beta2-adrenergic receptor activation. *FASEB J.* **35**, e21266, doi:10.1096/fj.202001101R (2021).
- 343 van Dierendonck, X. *et al.* Triglyceride breakdown from lipid droplets regulates the inflammatory response in macrophages. *Proc. Natl. Acad. Sci. U. S. A.* **119**, e2114739119, doi:10.1073/pnas.2114739119 (2022).
- 344 Huang, S. C. *et al.* Cell-intrinsic lysosomal lipolysis is essential for alternative activation of macrophages. *Nat. Immunol.* **15**, 846-855, doi:10.1038/ni.2956 (2014).
- 345 Xu, X. *et al.* Obesity activates a program of lysosomal-dependent lipid metabolism in adipose tissue macrophages independently of classic activation. *Cell Metab.* **18**, 816-830, doi:10.1016/j.cmet.2013.11.001 (2013).
- 346 Flaherty, S. E., 3rd *et al.* A lipase-independent pathway of lipid release and immune modulation by adipocytes. *Science* **363**, 989-993, doi:10.1126/science.aaw2586 (2019).
- 347 Rosen, E. D. & Spiegelman, B. M. What we talk about when we talk about fat. *Cell* **156**, 20-44, doi:10.1016/j.cell.2013.12.012 (2014).
- 348 Nicholls, D. G. The hunt for the molecular mechanism of brown fat thermogenesis. *Biochimie* **134**, 9-18, doi:10.1016/j.biochi.2016.09.003 (2017).
- 349 Wu, J. *et al.* Beige adipocytes are a distinct type of thermogenic fat cell in mouse and human. *Cell* **150**, 366-376 (2012).
- 350 Shapira, S. N. & Seale, P. Transcriptional Control of Brown and Beige Fat Development and Function. *Obesity (Silver Spring)* **27**, 13-21, doi:10.1002/oby.22334 (2019).
- 351 Rosina, M. *et al.* Ejection of damaged mitochondria and their removal by macrophages ensure efficient thermogenesis in brown adipose tissue. *Cell Metab* **34**, 533-548 e512, doi:10.1016/j.cmet.2022.02.016 (2022).
- 352 Astarita, J. L. *et al.* The CLEC-2-podoplanin axis controls the contractility of fibroblastic reticular cells and lymph node microarchitecture. *Nat. Immunol.* **16**, 75-84, doi:10.1038/ni.3035 (2015).
- 353 Acton, S. E. *et al.* Podoplanin-rich stromal networks induce dendritic cell motility via activation of the C-

- type lectin receptor CLEC-2. *Immunity* **37**, 276-289, doi:10.1016/j.immuni.2012.05.022 (2012).
- 354 Cannon, B. & Nedergaard, J. Brown adipose tissue: function and physiological significance. *Physiol Rev* **84**, 277-359, doi:10.1152/physrev.00015.2003 (2004).
- 355 Lee, P. *et al.* Temperature-acclimated brown adipose tissue modulates insulin sensitivity in humans. *Diabetes* **63**, 3686-3698, doi:10.2337/db14-0513 (2014).
- 356 Cypess, A. M. *et al.* Identification and importance of brown adipose tissue in adult humans. *N Engl J Med* **360**, 1509-1517, doi:10.1056/NEJMoa0810780 (2009).
- 357 Becher, T. *et al.* Brown adipose tissue is associated with cardiometabolic health. *Nat Med* **27**, 58-65, doi:10.1038/s41591-020-1126-7 (2021).
- 358 Betz, M. J. & Enerback, S. Human Brown Adipose Tissue: What We Have Learned So Far. *Diabetes* **64**, 2352-2360, doi:10.2337/db15-0146 (2015).
- 359 Krljanac, B. *et al.* RELM α -expressing macrophages protect against fatal lung damage and reduce parasite burden during helminth infection. *Sci Immunol* **4**, doi:10.1126/sciimmunol.aau3814 (2019).
- 360 Etzerodt, A. *et al.* Specific targeting of CD163(+) TAMs mobilizes inflammatory monocytes and promotes T cell-mediated tumor regression. *J. Exp. Med.* **216**, 2394-2411, doi:10.1084/jem.20182124 (2019).
- 361 Grabek, A. *et al.* The Adult Adrenal Cortex Undergoes Rapid Tissue Renewal in a Sex-Specific Manner. *Cell Stem Cell* **25**, 290-296 e292, doi:10.1016/j.stem.2019.04.012 (2019).
- 362 Huang, C. C. & Kang, Y. The transient cortical zone in the adrenal gland: the mystery of the adrenal X-zone. *J. Endocrinol.* **241**, R51-R63, doi:10.1530/JOE-18-0632 (2019).
- 363 Steffensen, C., Bak, A. M., Rubeck, K. Z. & Jorgensen, J. O. Epidemiology of Cushing's syndrome. *Neuroendocrinology* **92 Suppl 1**, 1-5, doi:10.1159/000314297 (2010).
- 364 Ten, S., New, M. & Maclaren, N. Clinical review 130: Addison's disease 2001. *J Clin Endocrinol Metab* **86**, 2909-2922, doi:10.1210/jcem.86.7.7636 (2001).
- 365 Ryan, G. R. *et al.* Rescue of the colony-stimulating factor 1 (CSF-1)-nullizygous mouse (Csf1(op)/Csf1(op)) phenotype with a CSF-1 transgene and identification of sites of local CSF-1 synthesis. *Blood* **98**, 74-84, doi:10.1182/blood.v98.1.74 (2001).
- 366 Unanue, E. R., Turk, V. & Neefjes, J. Variations in MHC Class II Antigen Processing and Presentation in Health and Disease. *Annu. Rev. Immunol.* **34**, 265-297, doi:10.1146/annurev-immunol-041015-055420 (2016).
- 367 Koppelman, B., Neefjes, J. J., de Vries, J. E. & de Waal Malefyt, R. Interleukin-10 down-regulates MHC class II α peptide complexes at the plasma membrane of monocytes by affecting arrival and recycling. *Immunity* **7**, 861-871, doi:10.1016/s1074-7613(00)80404-5 (1997).

Other articles and reviews

Ivanov S, Gallerand A, Gros M, *et al.* Mesothelial cell CSF1 sustains peritoneal macrophage proliferation. *Eur J Immunol.* 2019 Nov;49(11):2012-2018. doi: 10.1002/eji.201948164.

Gallerand A, Stunault MI, Merlin J, *et al.* Myeloid Cell Diversity and Impact of Metabolic Cues during Atherosclerosis. *Immunometabolism.* 2020;2(4):e200028. doi: 10.20900/immunometab20200028.

Czepielewski R, Gallerand A, *et al.* Lymphatic and blood network analysis during obesity. *J Vis Exp.* 2020 Nov 19;(165). doi: 10.3791/61814.

Dufies O, *et al.* Escherichia coli Rho GTPase-activating toxin CNF1 mediates NLRP3 inflammasome activation via p21-activated kinases-1/2 during bacteraemia in mice. 2021 Mar;6(3):401-412. doi: 10.1038/s41564-020-00832-5.


Sencio V, *et al.* Influenza Virus Infection Impairs the Gut's Barrier Properties and Favors Secondary Enteric Bacterial Infection through Reduced Production of Short-Chain Fatty Acids. 2021 Aug 16;89(9):e0073420. doi: 10.1128/IAI.00734-20.

Dolfi B, Gallerand A, *et al.* Macrophage metabolic regulation in atherosclerotic plaque. *Atherosclerosis.* 2021 Aug 17;334:1-8. doi: 10.1016/j.atherosclerosis.2021.08.010.

Merlin J, Ivanov S, Dumont A, *et al.* Non-canonical glutamine transamination sustains efferocytosis by coupling redox buffering to oxidative phosphorylation. 2021 Oct;3(10):1313-1326. doi: 10.1038/s42255-021-00471-y.

Short Communication

Mesothelial cell CSF1 sustains peritoneal macrophage proliferation

Stoyan Ivanov*¹ , Alexandre Gallerand*¹, Marilyn Gros*²,
Marion I. Stunault¹, Johanna Merlin¹, Nathalie Vaillant¹,
Laurent Yvan-Charvet¹ and Rodolphe R. Guinamard¹

¹ Centre méditerranéen de médecine moléculaire, Université Côte d'Azur - INSERM, U1065, Team 13, Nice, France

² Muscle & ALS Department, Centre Hospitalier Universitaire de Nice, Université Côte d'Azur, Peripheral Nervous System, Pasteur 2 Hospital, Nice, France

Macrophages play a central role during infection, inflammation and tissue homeostasis maintenance. Macrophages have been identified in all organs and their core transcriptomic signature and functions differ from one tissue to another. Interestingly, macrophages have also been identified in the peritoneal cavity and these cells have been extensively used as a model for phagocytosis, efferocytosis and polarization. Peritoneal macrophages are involved in B-cell IgA production, control of inflammation and wound healing following thermal-induced liver surface injury. These cells presumably require and interact with the omentum, where milky spot stromal cells have been proposed to secrete CSF1 (colony stimulating factor 1). Peritoneal macrophages depend on CSF1 for their generation and survival, but the identity of CSF1 producing cells inside the large peritoneal cavity remains unknown. Here we investigated peritoneal macrophage localization and their interaction with mesothelial cells, the major cell type predicted to secrete CSF1. Our data revealed that mesothelial cells produce membrane bound and secreted CSF1 that both sustain peritoneal macrophage growth.

Keywords: CSF1 · mesothelial cell · peritoneal macrophage



Additional supporting information may be found online in the Supporting Information section at the end of the article.

Introduction

The peritoneal cavity hosts several myeloid cell populations including large peritoneal macrophages (LPMs) and small peritoneal macrophages (SPMs). These two populations express the markers CD64 (the high affinity IgG receptor) and MerTK that are conserved in all tissue resident macrophages [1]. Nevertheless, LPMs are characterized by a high CD102 (ICAM-2) and F4/80

expression that distinguish them from SPMs [2]. Large peritoneal macrophages are arguably the most studied population of tissue resident macrophages. The transcription factor Gata6 controls their development in a vitamin A-dependent manner [3–5]. However, little is known about LPMs localization inside the peritoneal cavity and whether a tissue specific tropism exists. The peritoneal cavity has an estimated surface area equivalent to skin and represents the largest serous membrane in the body [6]. A single layer

Correspondence: Dr. Stoyan Ivanov and Rodolphe R. Guinamard
e-mail: stoyan.ivanov@unice.fr; rodolphe.guinamard@unice.fr

*These authors equally contributed to this work.

of mesothelial cells (MCs) covers the stratum of connective tissue inside the peritoneal cavity and constantly secretes fluid acting as lubricate and facilitating inter-organ frictions [6]. LPMs depend on the growth factor CSF1 for their survival and express high levels of its receptor CSF1R (CD115) on their cell surface [2, 7]. CSF1 is crucial for both monocyte survival and tissue resident macrophage maintenance [8, 9]. Peritoneal macrophages are completely absent in osteopetrotic op/op mice, presenting a spontaneous mutation in the CSF1 gene and lacking functional protein [10–12]. Nevertheless, the cellular source of CSF1 inside the peritoneal cavity remains currently unknown. Our data revealed that mesothelial cells produce CSF1 and induce peritoneal macrophage proliferation likely contributing to their homeostatic maintenance.

Results and discussion

Recently generated publicly available single cell transcriptional analysis data [13] (Tabula Muris Consortium) revealed that adipose tissue mesenchymal precursor cells, mammary gland epithelial cells, bladder cells, non-myeloid brain cells and blood endothelial cells selectively express CSF1 mRNA in comparison to other stromal and immune cells (Fig. 1A and B). Since adipose tissue blood endothelial cells are not directly connected with the peritoneal cavity, this suggests that adipose tissue mesenchymal cells, including cells with mesothelial markers such as mesothelin and WT1, are likely the major cell type producing CSF1 inside the peritoneal cavity. Another candidate is neutrophil-derived CSF1 as those cells were shown to stimulate macrophage proliferation [14]. This is rather unlikely to occur inside the peritoneal cavity since neutrophils are barely present at steady state in this location (65% LPMs against 0.4% neutrophils among CD45⁺ cells in our colony, data not shown). We analyzed whether LPMs are present at the outer surface of an intraperitoneal organ, the epididymal adipose tissue (eAT). To document cell topology, we injected i.p. labelled antibodies directed against hematopoietic cells (anti-CD45) and mesothelial cells (anti-podoplanin (Pdpn)) and analyzed mice 5 min post-antibody administration. eAT was excised and submitted to a brief surface trypsin digestion, a process known to liberate mesothelial cells, and then fully digested with collagenase A (Fig. 1C). Trypsin digestion resulted in a large fraction of CD45⁻CD31⁻CD90⁺ cells that was accessible to the i.p. injected anti-Pdpn, and its surface location and phenotype is reminiscent of mesothelial cells. Trypsin failed to digest endothelial cells as revealed by the small CD45⁻CD31⁺CD90⁻ fraction (Fig. 1D). By contrast, collagenase A liberated a large endothelial cell fraction that were not stained by the i.p. injected anti-Pdpn. Among CD45⁺ cells, surface trypsin digestion liberated preferentially a population of CD45⁺CD11b^{bright}F4/80^{bright} cells that stained positive for ICAM-2 and was accessible to the i.p. injected anti-CD45 and very few to none CD45⁺CD11b^{hi}F4/80^{int} cells (Fig. 1D). The latter population was recovered preferentially after a full enzymatic digestion and stained negative for ICAM-2 and the injected anti-CD45. Altogether, this suggests that the ICAM-2⁺ population resides inside the peritoneal cavity and

represents a fraction of the LPM pool (Fig. 1D). We sought to determine whether those LPMs are tightly associated to adipose tissue mesothelial cells. We collected both eAT pads, washed one and compared it to the non-washed control pad. Flow cytometry analysis revealed that the peritoneal macrophage population (CD64⁺F4/80⁺ICAM-2⁺) at the outer surface of eAT was lost following PBS wash, suggesting that the interaction, if any, between LPMs and mesothelial cells was rather loose (Fig. 1E and F). By contrast, omentum residing LPMs were not removed following the washing procedure (Fig. 1E and F). The population of adipose tissue macrophages (non-LPMs in eAT) was not affected by the lavage confirming that these cells reside inside the organ (Fig. 1F).

To better apprehend the mesothelial cells-LPMs dialogue, we developed a co-culture system between these two cell types. Mesothelial cell identity was confirmed using microscopy that revealed the typical pavementous morphology of these cells and Pdpn staining (Fig. 2A and not shown). Total cells were extracted from the peritoneal cavity of Lyz2^{cre} × TdTomato^{fl/fl} mice and macrophages were followed by counting Tomato⁺ cells using Incucyte live imaging system. Over a period of 8 days, LPMs exponentially increased in the presence of mesothelial cells while they were lost when grown among their co-inhabitants of the peritoneal cavity (Fig. 2A and B). We confirmed cell identities in the co-culture using CD90/Pdpn staining for mesothelial cells and Lyz2 reporter together with CD11b, F4/80, CD64 and MerTK for LPMs (Fig. 2C and not shown). These data confirmed LPM expansion (100% Tomato⁺ are F4/80⁺CD64⁺CD11b⁺ MerTK⁺ cells, Fig. 2C and 2H) in the presence of mesothelial cells that likely produced a growth factor supporting their proliferation. Such dynamic interaction between two cell types was recently reported between fibroblasts and macrophages [15]. CSF1 protein was secreted by mesothelial cells as revealed by ELISA test (Fig. 2D). Both adipose tissue and liver-derived mesothelial cells produced CSF1 and its concentration strongly decreased when LPMs were added to the culture, suggesting that the latter ones are consuming large amounts of CSF1 (Fig. 2D). Of interest, the addition of CSF1R-neutralizing antibody completely prevented LPMs proliferation, demonstrating the dominance of the CSF1-CSF1R axis in our system (Fig. 2E). This was paralleled by increased CSF1 concentration in the co-culture supernatants when CSF1R-neutralizing antibody was added (Fig. 2F). Bone marrow contains a large monocyte fraction expressing CSF1R and known to respond to CSF1 stimulation [9]. To test the prediction that mesothelial cell would promote their expansion, we added bone marrow cells (BMs) on top of adipose tissue mesothelial cells and we observed an impressive expansion of Tomato⁺ BM cell (Fig. 2G). This dataset suggests that mesothelial cells can, by mean of CSF1 production, stimulate the proliferation of any CSF1R-expressing cells with no particular specificity for LPMs. Further analysis of mesothelial cell/peritoneal cell co-cultures revealed that all TdTomato⁺ cells stained positive for F4/80 and CD11b but were CX3CR1^{low}, suggesting that after 8 days of co-culture LPMs kept their typical phenotypic markers (Fig. 2H). Interestingly, when BM cells were co-cultured with mesothelial cells, all TdTomato⁺ cells were F4/80⁺ and CD11b⁺

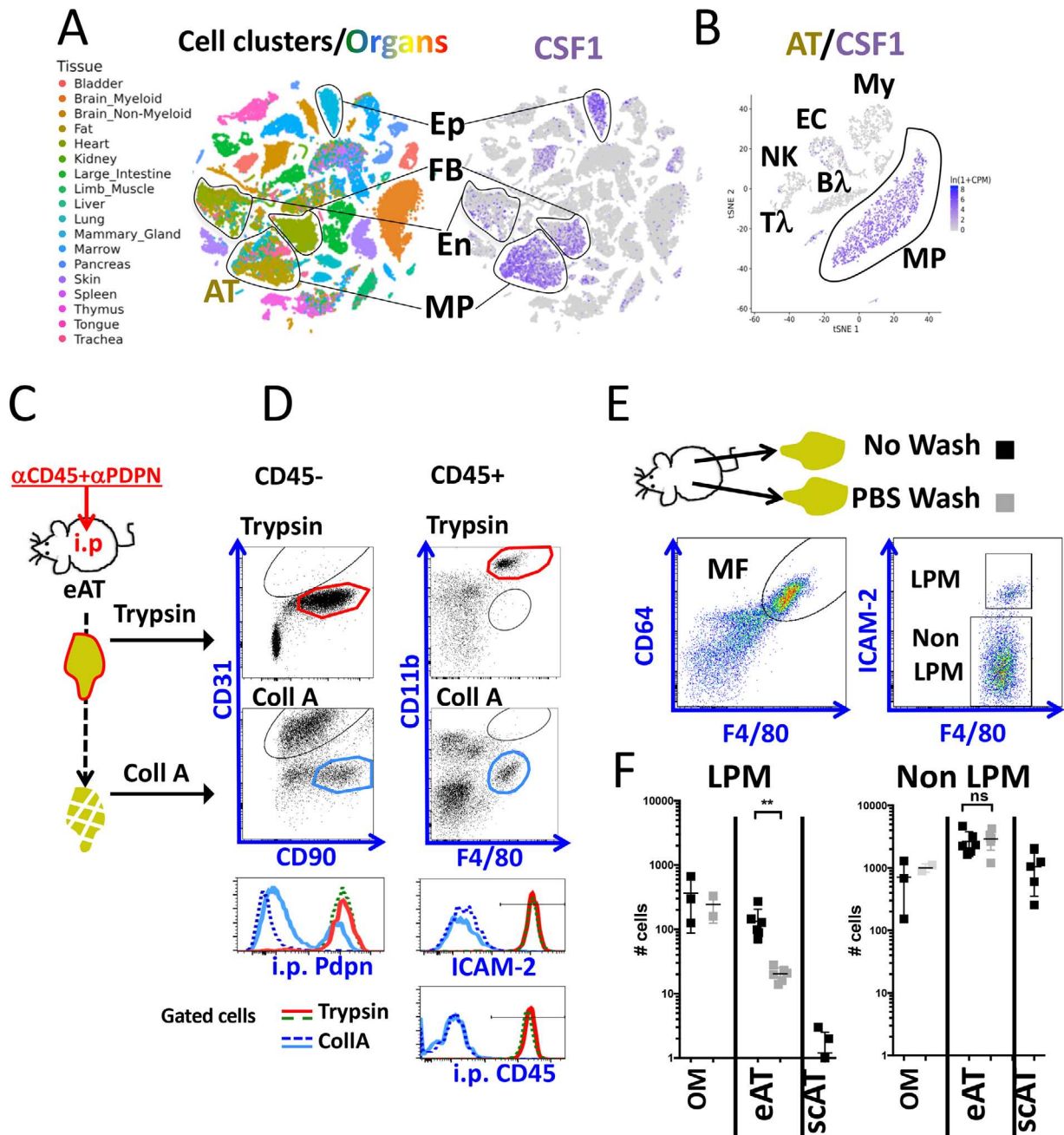


Figure 1. Transcriptional analysis of CSF1 mRNA across tissues and potential role for LPMs maintenance. (A) Clusters corresponding to major cell types expressing CSF1 are boxed as Ep (Epithelial cells), FB (Fibroblast), EC (Endothelial cell) and MP (Mesenchymal Precursor cells). Color code refers to organ of origin according to the presented list (left panel). (B) Focus on adipose tissue, with major cell type clusters highlighted. My: myeloid cell; EC: Natural Killer cell; B: B cell; T: T cell and MP. (C) Experimental design includes 5-min intra-peritoneal injection of 1 μ g of PE-(Phycoerythrin) labelled anti-CD45 antibody together with 1 μ g of APC-Cy7 labelled anti-Pdpn, surface tryptic digestion of full tissue (surface digestion) followed by mincing and collagenase A digestion (2nd digestion). (D) Dot plot representing CD90 versus CD31 staining of CD45⁻ cells and staining by the i.p. injected anti-Pdpn of the CD45⁻CD90⁺CD31⁻ gated populations and dot plot of F4/80 and CD11b staining of CD45⁺ cells with further staining for ICAM-2 and injected i.p. anti-CD45 of the gated populations. (red boxed F4/80^{bright}CD11b^{bright} cells from tryptic digestion and blue boxed F4/80^{int}CD11b^{hi} cells from collagenase A digestion), the experiment presented compares two injected mice and is one representative experiment of three (2–6 mice per experiment with similar results). (E) Experimental design and gating strategies. Epididymal adipose tissue (eAT), omentum (OM) and subcutaneous adipose tissue (scAT) were either digested in collagenase A directly or after 4 PBS washes. Dot plot representing gating strategy that includes CD64⁺F4/80⁺ macrophages and further ICAM-2 staining, allowing the separation of LPMs (ICAM-2⁺) and (non-LPM) (ICAM-2⁻). (F) LPM and non-LPM quantification per organ is presented, each symbol representing one organ (black symbols = not washed, grey symbols = washed) (F was performed using 5 mice and repeated once with 6 mice and similar results; ns = non-significant, ** = $p < 0.005$ with two tailed non-parametric t-test followed by Mann–Whitney test).

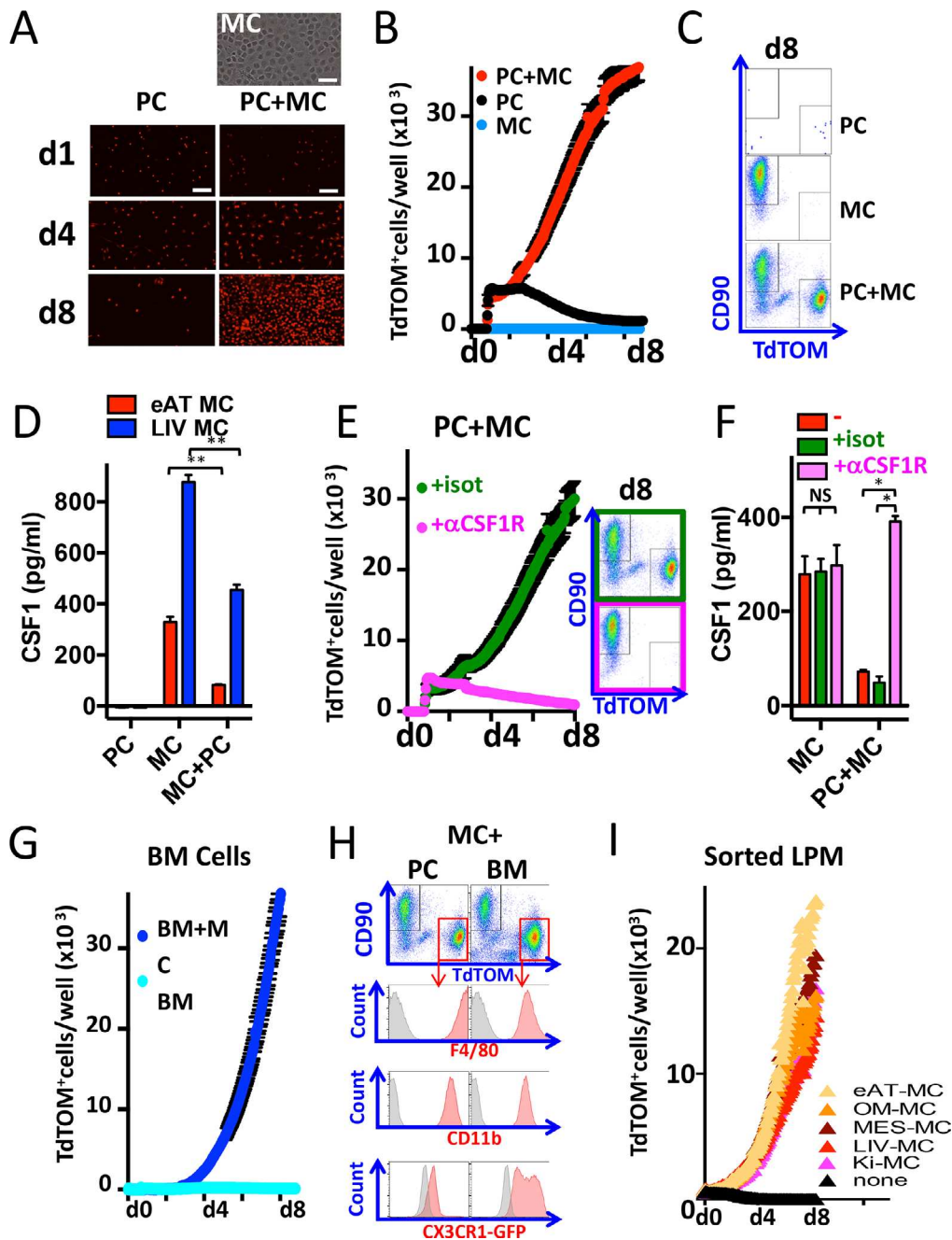


Figure 2. Mesothelial cells promote CSF1 dependent myeloid cell proliferation. 200 000 mesothelial cells (MC) were plated at day 0 and overlaid with 100 000 peritoneal cells (PCs) isolated from *Lyz2^{cre} × TdTomato^{fl/fl} / CX3CR1^{GFP}* mice. Macrophage growth with or without MC was documented in real time by counting Tomato⁺ fluorescent cells; (A) Representative pictures of red fluorescence (TdTomato⁺ cells) at indicated times; top panel, exemplifies MC morphology. (Scale bar = 100 μm) (B) Real time quantification of macrophage growth (TdTomato⁺ cells per well of a 24-well plate); (C) Dot plot showing CD90 versus TdTomato staining of live cells at the end of the co-culture (Day 8). (D) CSF1 quantification by ELISA test during 96 h of PCs, MCs and PCs+MCs co-cultures. (E) As described in 2A/B/C with the addition of blocking anti-CSF1R monoclonal antibody (10 μg/mL) or isotype control at day 1 of culture. (F) PCs + MCs co-cultures were first established for 4 days before medium was exchanged and replaced by medium with or without anti-CSF1R or isotype control, and supernatants were taken 3 days later and analyzed for CSF1 by ELISA. (G) As described in 2B, except that total bone marrow was used. (H) Staining of day 8 MCs + PCs or BMs co-cultures, CD90 vs TdTomato dot plot of live cells is presented as well as F4/80, CD11b and CX3CR1^{GFP} staining of the CD90⁺ TdTomato⁺ population. (I) MCs were generated by organ surface trypsin digestion from epididymal adipose tissue (eAT), omentum (OM), mesenteric adipose tissue (MES), liver (LIV) and kidney (Ki). Cell-sorted LPMs obtained from *Lyz2^{cre} × TdTomato^{fl/fl}* mice (1×10^4 cells) were then added. One representative experiment is presented out of four for LPM growth and out of two for ELISA tests and blocking anti-CSF1R assay. All experiments were done at least three times except for 2I that was done twice. Two tailed non-parametric t-test followed by Mann-Whitney test was performed with GraphPad Prism 6 software to test the samples statistical significance (**p* < 0.05; ***p* < 0.01).

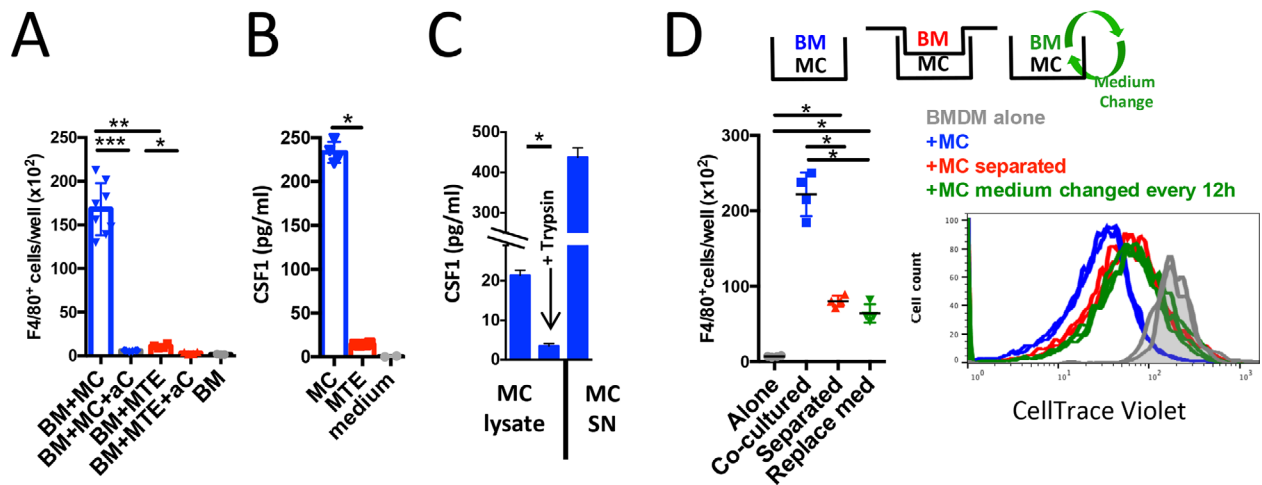


Figure 3. Cell-contact and secretion control CSF1 dependent myeloid cell proliferation. (A) 10 000 mesothelial cells (MC) or MTE4.14 (MTE) thymic stromal cells were plated at day 0 and overlaid 24 h later with 5000 BMDMs. At day 7, cells were stained for F4/80 and CD45 and the number of CD45⁺F4/80⁺ cells was counted. (B) CSF1 was measured in the supernatant of eAT MC and MTE cells cultured for 3 days. (C) eAT MC co-culture supernatant (MC SN) was collected, cells washed 3x with PBS and either lysed directly in RIPA buffer (MC lysate) or following a 5-min surface trypsin digestion. Data shown are from quadruplicates of one representative of two experiments. (D) 400 000 eAT MCs were plated at day 0 in 6-well plates. 48 h later, 100 000 violet proliferation dye stained BM cells were either co-cultured in the same well or placed on 0.4 μ M transwell inserts (Greiner). In half of the co-culture wells culture supernatant was removed completely and replaced with fresh medium every 12 h. After 6 days, the number of live F4/80⁺ was counted and violet staining of F4/80⁺ cells in different conditions was plotted (values are of triplicates, with 2 experiments performed). Two tailed non-parametric t-test followed by Mann–Whitney test was performed with GraphPad Prism 6 software to test the samples statistical significance (* $p < 0.05$; ** $p < 0.01$; *** $p < 0.001$).

but a fraction was CX3CR1^{sp+} as well, suggesting a diversity in these cells (Fig. 2H). Given that both liver and adipose tissue mesothelial cells were able to sustain CSF1 dependent growth, we hypothesized that this might represent a conserved function of all peritoneal organ mesothelial cells. We found that all peritoneal mesothelial cells that we tested were capable of sustaining LPMs growth. This ubiquitous ability to grow myeloid cells was not shared by a thymic stromal cell line or by culturing large amount of bone marrow, blood or peritoneal cells that contains numerous diverse cell types (Fig. 3A and not shown). Thymic stromal cells produced few CSF1 in comparison to mesothelial cells (Fig. 3B). CSF1 is produced in 3 different biologically active isoforms including a membrane-spanning glycoprotein, a secreted proteoglycan and a secreted glycoprotein [16]. We tested for the presence of a membrane bound isoform by dosing CSF1 in mesothelial cell lysates. We detected a trypsin sensitive cell-associated CSF1 in lysates (~20 pg/mL), even though the amount was lower in comparison to the secreted form found in cell-culture supernatants (~450 pg/mL) (Fig. 3C). Finally, we tested whether LPM proliferation requires cell–contact interaction or, alternatively, is mediated by secreted CSF1. We performed Transwell assay in which mesothelial cells were seeded in the bottom and BM cells added to the upper well (Fig. 3D). Surprisingly, and despite the large amount of CSF1 detected in the culture supernatant, BM cell proliferation was largely blunted when physically separated from mesothelial cells (Fig. 3D). Also, to test for the importance of the soluble form, culture supernatant was replaced every 12 h with fresh medium, a similar strong decrease in myeloid cell proliferation was measured. Our data suggest that both membrane and secreted factors including CSF1 are present and secreted by

mesothelial cells that can induce macrophage proliferation (Fig. 3C and D). Mice expressing only one CSF1 isoform have been previously generated [17, 18] but how this affects LPMs proliferation remains currently unknown.

Taken together, we defined peritoneal mesothelial cells as a major source of CSF1 and critical contributor to peritoneal macrophage homeostasis. Currently, there is an urgent need to generate mouse genetic model to validate our finding that mesothelial cells-derived CSF1 contributes to peritoneal macrophage survival. Indeed, we are not aware of mesothelial cell specific Cre mouse model that can be crossed to CSF1 floxed mice [19] and validate our findings in vivo. Mesothelin-driven Cre expression in mice is not exclusively restricted to mesothelial cells but also affects, among others, hepatic portal fibroblasts [20, 21]. Nevertheless, we believe that our study reveals a new role for mesothelial cells. By CSF1 production, these cells potentially contribute to peritoneal macrophage pool maintenance.

Concluding remarks

In the present study we described an unprecedentedly attributed function of peritoneal mesothelial cells. By secreting CSF1 they sustain peritoneal macrophage proliferation. This interaction is completely CSF1R dependent as illustrated by the addition of neutralizing antibody. Both cell contact between mesothelial cells and LPMs and CSF1 secretion are required for optimal macrophage proliferation. This might explain differential myeloid cell turn-over upon steady versus injury conditions that promote adhesion [22].

Materials and methods

Lyz2^{Cre} mice (B6.129P2-Lyz2tm1(cre)Ifo/J, The Jackson Laboratory) have been crossed to TdTomato reporter mice (B6.Cg-Gt(ROSA)26Sortm9(CAG-tdTomato)Hze/J, The Jackson Laboratory) and CX3CR1^{8fp} mice (B6.129P-Cx3cr1^{tm1Litt}/J, The Jackson Laboratory). Animal protocols were approved by the Institutional Animal Care and Use Committee of the French Ministry of Higher Education and Research and the Mediterranean Center of Molecular Medicine (Inserm U1065) and were undertaken in accordance with the European Guidelines for Care and Use of Experimental Animals. Animals had free access to food and water and were housed in a controlled environment with a 12-h light–dark cycle and constant room temperature (22°C).

Flow cytometry

Tissues were collected, and surface digested or not with Trypsin before shredding and then incubating for 30 min at 37°C with RPMI medium containing 2 mg/mL collagenase A (Roche Diagnostics). Following red blood cells were lysed (BD Pharmlyse), cells were centrifuged (400 g, 5 min at 4°C) and stained for 25 min on ice. Stained cells were acquired on a BD FACSCanto flow cytometer. Analysis was performed using FlowJo software (Tree Star). The authors adhered and followed the guidelines described in ‘Guidelines for the use of flow cytometry and cell sorting in immunological studies’.

Antibodies and reagents

The following list of reagents and antibodies was used: rCSF1 (Miltenyi); ICAM-2-APC conjugated (clone 3C4(mIC2/4), BioLegend); CD11b-APC-Cy7 conjugated (clone M1/70, BioLegend); F4/80-Pe-Cy7 conjugated (clone BM8, BioLegend); Podoplanin-FITC or APC-Cy7 -conjugated (clone 8.1.1, BioLegend); CD90.2-BrilliantViolet510 conjugated (clone 53-2.1, BioLegend); CD31-PerCP-Cy5.5 conjugated (clone 390, BioLegend); CD45-PE conjugated (clone 30-F11, BioLegend); CD64-BrilliantViolet421 conjugated (clone X54-5/7.1, BioLegend); CSF1R-neutralizing antibody (BioXcell); rat IgG2b isotype control (BioXcell); Mouse M-CSF Quantikine ELISA Kit (R&D Systems). LIVE/DEAD[®] Fixable Aqua Dead Cell Stain Kit and CellTrace Violet Cell Proliferation Kit were purchased from ThermoScientific and used according to the manufacturer’s instruction.

Peritoneal macrophage generation

Peritoneal lavage was performed with 5 mL of FACS Buffer (RPMI medium, 0.3 mM EDTA and 0.06% BSA). Cells were centrifuged for 5 min at 1500 rpm at 4°C, counted and used in various experiments.

Incucyte

Adipose tissue and liver were collected, washed in PBS 1x and the surface was digested with Trypsin-EDTA 0,05% (Gibco) for 10 min at 37°C. Cells were cultured as previously described [23]. Cells were counted and plated at 2*10⁵ cells per well in 24-well tissue culture plates for 24 h. Macrophages and BM cells (1*10⁵ cells) were then added. Photomicrographs were taken every hour using an Incucyte live cell imager (Essen Biosciences) for 8 days and tomato positive cells number were counted using Incucyte software (Essen Biosciences).

Statistical analyses

Statistical analyses were generated with GraphPad Prism software using statistical tests indicated for each experiment.

Acknowledgements: We would like to thank Julie Gall, Marion Ayrault, Emma Guilbaud and Gaël Bories for their technical assistance and helpful discussions and Philippe Gual for sharing CD44^{-/-} mice. SI is supported by Institut National de la Sante et de la Recherche Medicale (INSERM) and Agence Nationale de la Recherche (ANR-17-CE14-0017-01). LYC is supported by Institut National de la Sante et de la Recherche Medicale (INSERM), Fondation de France (00066474) and the European Research Council (ERC) consolidator program (ERC2016COG724838). RRG is supported by Centre National de la Recherche Scientifique (CNRS).

Authorship contributions: SI and RG designed and performed experiments, analyzed the data and wrote the manuscript. AG, MJG, MIS, JM and NV performed experiments, analyzed data and edited the manuscript. LYC supervised the project and edited the manuscript.

Conflicts of interest: The authors have no disclosures or conflicts of interest to declare.

References

- Gautier, E. L., Shay, T., Miller, J., Greter, M., Jakubzick, C., Ivanov, S., Helft, J. et al., Gene-expression profiles and transcriptional regulatory pathways that underlie the identity and diversity of mouse tissue macrophages. *Nat. Immunol.* 2012. 13: 1118–1128.
- Kim, K. W., Williams, J. W., Wang, Y. T., Ivanov, S., Gilfillan, S., Colonna, M., Virgin, H. W. et al., MHC II+ resident peritoneal and pleural macrophages rely on IRF4 for development from circulating monocytes. *J. Exp. Med.* 2016. 213: 1951–1959.

- 3 Rosas, M., Davies, L. C., Giles, P. J., Liao, C. T., Kharfan, B., Stone, T. C., O'Donnell, V. B. et al., The transcription factor Gata6 links tissue macrophage phenotype and proliferative renewal. *Science* 2014. **344**: 645–648.
- 4 Gautier, E. L., Ivanov, S., Williams, J. W., Huang, S. C., Marcelin, G., Fairfax, K., Wang, P. L. et al., Gata6 regulates aspartoacylase expression in resident peritoneal macrophages and controls their survival. *J. Exp. Med.* 2014. **211**: 1525–1531.
- 5 Okabe, Y. and Medzhitov, R., Tissue-specific signals control reversible program of localization and functional polarization of macrophages. *Cell* 2014. **157**: 832–844.
- 6 van Baal, J. O., Van de Vijver, K. K., Nieuwland, R., van Noorden, C. J., van Driel, W. J., Sturk, A., Kenter, G. G. et al., The histophysiology and pathophysiology of the peritoneum. *Tissue. Cell* 2017. **49**: 95–105.
- 7 Gautier, E. L., Ivanov, S., Lesnik, P. and Randolph, G. J., Local apoptosis mediates clearance of macrophages from resolving inflammation in mice. *Blood* 2013. **122**: 2714–2722.
- 8 Louis, C., Cook, A. D., Lacey, D., Fleetwood, A. J., Vlahos, R., Anderson, G. P. and Hamilton, J. A., Specific contributions of CSF-1 and GM-CSF to the dynamics of the mononuclear phagocyte system. *J. Immunol.* 2015. **195**: 134–144.
- 9 Yona, S., Kim, K. W., Wolf, Y., Mildner, A., Varol, D., Breker, M., Strauss-Ayali, D. et al., Fate mapping reveals origins and dynamics of monocytes and tissue macrophages under homeostasis. *Immunity* 2013. **38**: 79–91.
- 10 Yoshida, H., Hayashi, S., Kunisada, T., Ogawa, M., Nishikawa, S., Okamura, H., Sudo, T. et al., The murine mutation osteopetrosis is in the coding region of the macrophage colony stimulating factor gene. *Nature* 1990. **345**: 442–444.
- 11 Naito, M., Kodama, T., Matsumoto, A., Doi, T. and Takahashi, K., Tissue distribution, intracellular localization, and in vitro expression of bovine macrophage scavenger receptors. *Am. J. Pathol.* 1991. **139**: 1411–1423.
- 12 Wiktor-Jedrzejczak, W. W., Ahmed, A., Szczylik, C. and Skelly, R. R., Hematological characterization of congenital osteopetrosis in op/op mouse. Possible mechanism for abnormal macrophage differentiation. *J. Exp. Med.* 1982. **156**: 1516–1527.
- 13 The Tabula Muris Consortium, Single-cell transcriptomics of 20 mouse organs creates a Tabula Muris. *Nature* 2018. **562**: 367–372.
- 14 Braza, M. S., Conde, P., Garcia, M., Cortegano, I., Brahmachary, M., Pothula, V., Fay, F. et al., Neutrophil derived CSF1 induces macrophage polarization and promotes transplantation tolerance. *Am. J. Transplant.* 2018. **18**: 1247–1255.
- 15 Zhou, X., Franklin, R. A., Adler, M., Jacox, J. B., Bailis, W., Shyer, J. A., Flavell, R. A. et al., Circuit design features of a stable two-cell system. *Cell* 2018. **172**: 744–757 e717.
- 16 Pixley, F. J. and Stanley, E. R., CSF-1 regulation of the wandering macrophage: complexity in action. *Trends. Cell. Biol.* 2004. **14**: 628–638.
- 17 Dai, X. M., Zong, X. H., Sylvestre, V. and Stanley, E. R., Incomplete restoration of colony-stimulating factor 1 (CSF-1) function in CSF-1-deficient Csf1op/Csf1op mice by transgenic expression of cell surface CSF-1. *Blood* 2004. **103**: 1114–1123.
- 18 Ryan, G. R., Dai, X. M., Dominguez, M. G., Tong, W., Chuan, F., Chisholm, O., Russell, R. G. et al., Rescue of the colony-stimulating factor 1 (CSF-1)-nullizygous mouse (Csf1(op)/Csf1(op)) phenotype with a CSF-1 transgene and identification of sites of local CSF-1 synthesis. *Blood* 2001. **98**: 74–84.
- 19 Harris, S. E., MacDougall, M., Horn, D., Woodruff, K., Zimmer, S. N., Rebel, V. I., Fajardo, R. et al., Meox2Cre-mediated disruption of CSF-1 leads to osteopetrosis and osteocyte defects. *Bone* 2012. **50**: 42–53.
- 20 Koyama, Y., Wang, P., Liang, S., Iwaisako, K., Liu, X., Xu, J., Zhang, M. et al., Mesothelin/mucin 16 signaling in activated portal fibroblasts regulates cholestatic liver fibrosis. *J. Clin. Invest.* 2017. **127**: 1254–1270.
- 21 Rinkevich, Y., Mori, T., Sahoo, D., Xu, P. X., Bermingham, J. R., Jr. and Weissman, I. L., Identification and prospective isolation of a mesothelial precursor lineage giving rise to smooth muscle cells and fibroblasts for mammalian internal organs, and their vasculature. *Nat. Cell. Biol.* 2012. **14**: 1251–1260.
- 22 Zhang, N., Czepielewski, R. S., Jarjour, N. N., Erlich, E. C., Esaulova, E., Saunders, B. T., Grover, S. P. et al., Expression of factor V by resident macrophages boosts host defense in the peritoneal cavity. *J. Exp. Med.* 2019.
- 23 Bot, J., Whitaker, D., Vivian, J., Lake, R., Yao, V. and McCauley, R., Culturing mouse peritoneal mesothelial cells. *Pathol. Res. Pract.* 2003. **199**: 341–344.

Abbreviations: BMs: bone marrow cells · LPMs: large peritoneal macrophages · MCs: mesothelial cells · SPMs: small peritoneal macrophages

Full correspondence: Dr. Stoyan Ivanov, Centre méditerranéen de médecine moléculaire - Université Côte d'Azur - INSERM U1065, Team 13, Nice, France
e-mail: stoyan.ivanov@unice.fr

Additional correspondence: Dr. Rodolphe Guinamard, Centre méditerranéen de médecine moléculaire - Université Côte d'Azur - INSERM U1065, Team 13, Nice, France
e-mail: rodolphe.guinamard@unice.fr

The peer review history for this article is available at <https://publons.com/publon/10.1002/eji.201948164>

Received: 22/2/2019

Revised: 7/5/2019

Accepted: 26/6/2019

Accepted article online: 28/6/2019

Review

Myeloid Cell Diversity and Impact of Metabolic Cues during Atherosclerosis

Alexandre Gallerand †, Marion I. Stunault †, Johanna Merlin †,
Rodolphe R. Guinamard, Laurent Yvan-Charvet, Stoyan Ivanov *

Mediterranean center of molecular medicine (C3M)–Université Côte d’Azur–
INSERM U1065, Team 13, Nice, 06200, France

† These authors contributed equally to this work.

* Correspondence: Stoyan Ivanov, Email: Stoyan.ivanov@unice.fr.

ABSTRACT

Myeloid cells are key contributors to tissue, immune and metabolic homeostasis and their alteration fuels inflammation and associated disorders such as atherosclerosis. Conversely, in a classical chicken-and-egg situation, systemic and local metabolism, together with receptor-mediated activation, regulate intracellular metabolism and reprogram myeloid cell functions. Those regulatory loops are notable during the development of atherosclerotic lesions. Therefore, understanding the intricate metabolic mechanisms regulating myeloid cell biology could lead to innovative approaches to prevent and treat cardiovascular diseases. In this review, we will attempt to summarize the different metabolic factors regulating myeloid cell homeostasis and contribution to atherosclerosis, the most frequent cardiovascular disease.

KEYWORDS: macrophage; monocyte; dendritic cell; metabolism; atherosclerosis

INTRODUCTION

Atherosclerosis is a major vascular disease that continuously spreads worldwide. Atherosclerosis contributes to cardiovascular disease (CVD)-related deaths, estimated to account for more than 17 million deaths per year worldwide, making this pathology a major public health issue. Atherosclerosis is described as a metabolic disease associated with a chronic low-grade inflammation linked to lipid accumulation in the intima of large and medium-sized arteries, which favors plaque formation [1,2]. Since the 1950’s, mounting evidence linked cholesterol metabolism to atherosclerosis development. Atherosclerotic patients not only showed increased serum cholesterol levels, and more specifically cholesterol present in the low-density lipoproteins fraction (LDL), but also accumulation of cholesterol in macrophage foam cells pointing out to cholesterol as a culprit of immunometabolic perturbations in the establishment and development of atherosclerosis. LDL-cholesterol levels are now considered as an independent risk factor for CVDs [3,4].

Open Access

Received: 29 June 2020

Accepted: 10 August 2020

Published: 17 August 2020

Copyright © 2020 by the author(s). Licensee Hapres, London, United Kingdom. This is an open access article distributed under the terms and conditions of [Creative Commons Attribution 4.0 International License](https://creativecommons.org/licenses/by/4.0/).

Interestingly, LDL accumulation into the arterial wall is associated with inflammatory signals which trigger the attraction of myeloid cells such as dendritic cells (DC), neutrophils, macrophages and monocytes [5]. Advanced atherosclerotic plaques are complex structures containing lipids, necrotic cores, calcification zones and immune cells [6]. Plaque growth increases arterial stiffness and could be responsible for disturbed blood flow, while their rupture can lead to ischaemic strokes and transient cerebral ischaemic attacks [7].

During the past two decades, tremendous progress has been made highlighting the involvement of immune cells at all stages of the disease including plaque initiation, development and rupture. Particularly, the accumulation of myeloid cells in human atheromatous plaques is a strong marker of plaque instability and predictor of negative outcome [8,9]. The respective role of the different myeloid cell types in the establishment and progression of the disease has since been thoroughly investigated using pre-clinical mouse models. Monocytes, which enter atheromatous plaques from the blood circulation and differentiate into macrophages, are the main culprits of atherosclerosis development. Further mechanistic complexity came later with the realization of the involvement of neutrophils and DCs in the disease, the latter driving and bringing adaptative immunity in the picture.

Myeloid cell precursors have diverse origins: some emerge from hematopoiesis in the bone marrow, while others arise from primitive embryonic structures [10]. Their functional diversity is thought to be acquired via the action of tissue-specific cues but little is known on how this local developmental imprinting of myeloid cells takes place [11]. This observation particularly stands regarding myeloid cell immunometabolism, as microenvironmental signals can trigger rapid metabolic adaptations to adjust the immune response. In atherosclerosis, myeloid cell metabolism influences plaque development [12]. For example, under inflammatory conditions, macrophages display increased glycolytic metabolism and Glut1 expression, the main myeloid cell glucose transporter [13]. Monocytes and macrophages from atherosclerotic patients show increased mitochondrial oxygen consumption rate (OCR). Together these findings suggest a global change in metabolic activation state [14].

A metabolomics-based analysis of human carotid plaques revealed a correlation between plaque metabolic signatures, namely elevated glycolysis and low fatty-acid oxidation, and the presence of plaque instability features [15]. This observation strongly suggests that intra-plaque metabolic cues may determine the outcome of the disease. A better understanding of how metabolites affect in situ myeloid cell activation would help for the design of new therapeutic approaches to prevent and treat atherosclerosis. In this review, we will address how metabolic signals impact on myeloid cell diversity and function in the context of atherosclerosis.

IMMUNE CELL DIVERSITY IN PLAQUES

Pioneering studies revealed that human plaques contain a variety of immune cells. These observations were repeated in mouse pre-clinical models of atherosclerosis development, namely *Ldlr*^{-/-} and *ApoE*^{-/-} mice. Although wild-type mice are protected against the disease, high cholesterol diet feeding of *Ldlr*^{-/-} and *ApoE*^{-/-} mice promotes hypercholesterolemia and atherosclerosis development. Descriptions of plaque immune cells were initially based on immunohistochemistry and demonstrated the presence of macrophages, B and T cells in plaque lesions [16]. Nevertheless, the limited number of parameters available was not adapted to grasp the full spectrum of immune cells residing in advanced plaques. With the improvement of flow cytometry, the number of parameters simultaneously analyzed progressively increased and a further complexity in plaque immune cell populations emerged [17,18]. Single-cell RNA-Seq and Cytometry by Time of Flight (CyTOF) technologies further extended our ability to discover and characterize new tissue-resident immune populations and their activation states. This technological leap offered a new perspective to decipher in greater depth immune cell diversity in atherosclerotic plaques [19]. In the past two years, multiple studies applied single-cell RNA-Seq techniques to human plaque samples from endarterectomy patients [20], and to aortic cells extracted from wild-type and atherosclerotic mice [18,21–25]. This generated an extensive characterization of the blood vessel-residing immune landscape in health and disease (**Tables 1 and 2**). Interestingly, only a small number of myeloid cells (of which around 70% were monocytes) were observed at steady state in the aortic wall of wild-type mice [25]. It seems reasonable that monocytes crawling on endothelial cells were the main population of immune cells detected in those studies. Leukocyte diversity was shown to greatly increase in the aorta during atherosclerosis development, as neutrophils, T cells, B cells and NK cells were also identified in *Ldlr*^{-/-} and *ApoE*^{-/-} mice fed a chow or a high fat diet [21,22,24]. This diversity was also observed in human samples [20,22].

Table 1. Recent single-cell based studies assessing plaque composition.

References	Samples
Kim K et al., 2018 [23]	<i>Ldlr</i> ^{-/-} mice; 12 weeks HFD; aortic CD45 ⁺ cells
Cochain C et al., 2018 [21]	<i>Ldlr</i> ^{-/-} mice; 12 weeks HFD; aortic CD45 ⁺ cells
Winkels H et al., 2018 [22]	<i>Ldlr</i> ^{-/-} mice; 12 weeks CD or HFD; aortic CD45 ⁺ cells Transcriptomic data; 126 samples from the biobank of Karolinska Endarterectomies
Fernandez DM et al., 2019 [20]	Endarterectomy plaque samples
Cole JE et al., 2018 [24]	<i>ApoE</i> ^{-/-} mice; CD or HFD 12 weeks; aortic CD45 ⁺ cells
Kalluri AS et al., 2019 [25]	WT digested aorta

Table 2. Summary of the reported plaque leukocyte proportions across the reports mentioned in Table 1.

Refs	Samples	Method	Macrophages	Monocytes	Dendritic cells			Neutrophils	T cells		B cells	NK cells
					pDC	cDC1	cDC2		CD4 ⁺	CD8 ⁺		
[23]	Male LdlR ^{-/-} HFD 12 weeks	Single cell RNA-Seq	83.9%*	ND	ND	2.2%*	6.9%*	ND	3%*		ND	ND
[21]	Male LdlR ^{-/-} HFD 11 weeks	Single cell RNA-Seq	28.9%	12.3%	14.9%			2%	8.7%	19.6%	2%	4%
	Male LdlR ^{-/-} HFD 20 weeks		49.6%	ND	14.2%			ND	8.5%	16.8%	2.1%*	2.4%*
[22]	Male LdlR ^{-/-} CD	Single cell RNA-Seq	13.6%	Myeloid cells: 6.2%				54.1%		24.4%	1.7%	
	Male LdlR ^{-/-} HFD 12 weeks		27%	Myeloid cells: 21.1%				45.8%		4%	2.1%	
	Female ApoE ^{-/-} CD		4.9%	Myeloid cells: 10.3%				60.6%		21.9%	2.4%	
	Female ApoE ^{-/-} HFD 12 weeks		9.6%	Myeloid cells: 12.6%				49%		27.2%	1.6%	
	Human	Bulk RNA-Seq deconvolution	50%*	12%	ND			ND	20%*		10%*	5%
[20]	Human	CytoF	10.6%	2.5%	0.4%	0.1%	ND	0.1%	31.6%	31.1%	2.6%	4.1%
	Human	CITE-Seq	16%	ND	6%*	1.5%*	ND	ND	20%*	26%*	8%*	11%*
[24]	ApoE ^{-/-} sex unspecified CD	CyTOF	60%	2.5%	0.25%	1.6%	8.5%	2.5%	3%	3%	8%	1%
	ApoE ^{-/-} sex unspecified HFD 12 weeks		57%	7%	1%	1.8%	6.5%	4%	3%	3%	5%	0.75%
[25]	Female WT CD	Single cell RNA-Seq	23%*	73.4%*	3.3%*			ND	ND		ND	ND

When possible, we reported the proportion of each cell type among total leukocytes as indicated by the authors. Stars (*) indicate missing information that was estimated and completed using the Single-Cell Explorer software (Artyomov Lab, Washington University St Louis). WT = Wild-Type. CD = Chow Diet. HFD = High Fat Diet. ND = Not Determined.

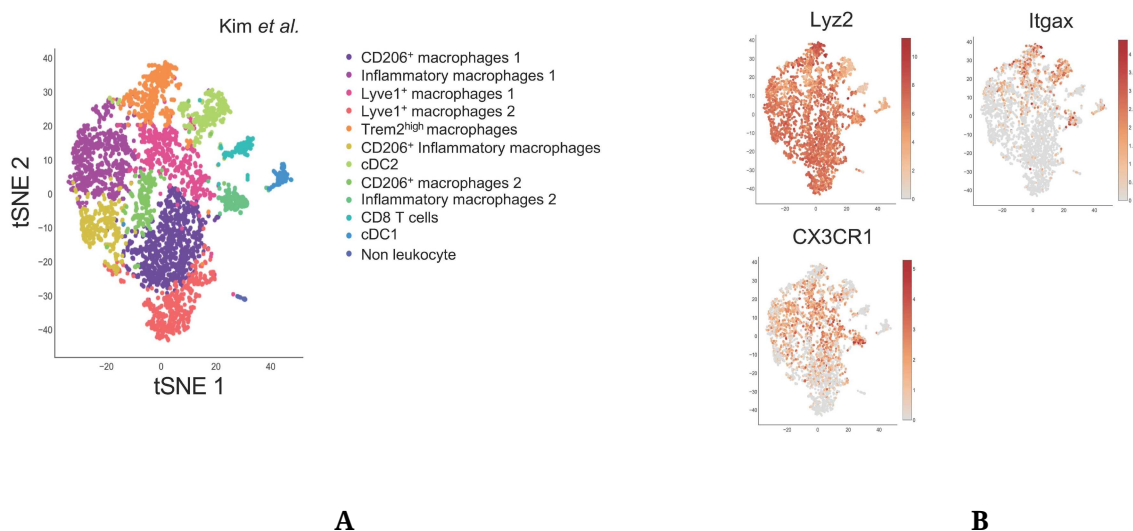


Figure 1. Single-Cell approaches highlight plaque immune cell diversity. (A) Single-Cell RNA-Seq of aortic CD45⁺ cells from *Ldlr*^{-/-} mice fed a HFD for 12 weeks. Data from Kim et al. [23] (GSM3215435) were analyzed using the Single-Cell Explorer software. **List of markers used:** CD206⁺ Macrophages: *Fcgr1*, *Itgam*, *Mafb*, *Mrc1*. Inflammatory macrophages: *Fcgr1*, *Itgam*, *Mafb*, *NLRP3*, *IL1b*, *Nfkbia*. Lyve1⁺ macrophages: *Fcgr1*, *Itgam*, *Mafb*, *Lyve1*. TREM2^{high} macrophages: *Fcgr1*, *Itgam*, *Mafb*, *TREM2*, *ABCG1*, *Lpl*, *Lipa*. CD206⁺ Inflammatory macrophages: *Fcgr1*, *Itgam*, *Mafb*, *Mrc1*, *NLRP3*, *IL1b* (low), *Nfkbia*, *TNF*. CD8 T cells: *Lck*, *CD3*, *CD8*. cDC2: *Zbtb46*, *Itgax*, *Flt3*, *Itgam* (+), *Itgae* (-). cDC1: *Zbtb46*, *Itgax*, *Flt3*, *Itgam* (-), *Itgae*, *IRF8*. Non leukocyte: *Ptprpc* (-). (B) Expression pattern of genes used for targeted Cre expression in myeloid cells.

However, the relative proportion of each cell type reported by different single-cell studies shows significant fluctuations. In mice, macrophages were reported to represent from 9 to 80% of the aortic leukocyte pool and, inversely, T cells represented from 3 to 60% of leukocytes. The same variations were observed in human samples (Table 2). These differences could be explained by multiple factors, and notably differences in tissue digestion technique, leukocyte purification method, and the markers and transcripts used for cell type identification. The entry of atherosclerosis research in the single cell RNA-Seq era could therefore benefit from a universal experimental pipeline that would facilitate comparison between studies. A first step toward this direction could consist in generating a meta-analysis of the data from the studies summarized in Table 1 to characterize plaque composition. A meta-analysis study was recently published and evidenced the immune cell diversity in plaque and the markers allowing to define each population [26].

These studies illustrate that single-cell approaches are amongst the most powerful tools to precisely identify cell subsets as well as their respective metabolic demands. Myeloid cells were broadly shown to represent a significant part (up to 90%) of immune cells in atherosclerotic lesions [23]. Here, we will briefly discuss the identity and origin of plaque resident myeloid cells.

Monocytes

Monocytes are short-lived mononuclear phagocytes that are generated in the bone marrow (BM) during hematopoiesis [27,28]. They rely on CSF1R (Colony Stimulating Factor 1 Receptor) signaling for their development and survival [29,30]. Among leukocytes, which have been positively correlated with cardiovascular events in humans [31–33], monocytes play a pivotal role in atherosclerosis development. Hypercholesterolemia, a key component of atherosclerosis, has been associated with increased circulating monocyte numbers (monocytosis) in mice, rabbits, swines and humans [34–36].

Circulating monocytes are identified as CD11b⁺ CD115⁺ cells, and exist as two functionally distinct subsets in both mice and humans: classical monocytes, identified as Ly6C^{high} in mice and CD14^{high} CD16^{low} in humans, and non-classical monocytes, identified as Ly6C^{low} and CD14^{low} CD16^{high} [37]. An additional human population of CD14⁺CD16⁺ monocytes has also been documented. Developmentally, Ly6C^{low} monocytes were proposed to arise from Ly6C^{high} monocytes [38,39]. Ly6C^{low} monocytes require the transcription factor Nr4a1 (Nur77) for their maturation [40], they are commonly referred to as “patrolling monocytes”, as they are closely associated to the endothelium which they survey in order to remove dead endothelial cells [41,42].

Ly6C^{high} monocytes are also called “inflammatory” monocytes, as they accumulate during infections and are preferentially recruited to inflamed tissues [38]. They display a high expression of CCR2 [43,44], the main chemokine receptor governing monocyte recruitment to inflammatory sites [45] as well as into atherosclerotic plaques. Plaque initiation is driven by Ly6C^{high} monocyte recruitment to the intima of the endothelial wall [46–50]. Their inflammatory nature seems to be supported by the fact that osteopetrotic mice, which lack functional CSF1 (Colony Stimulating Factor 1) and therefore monocytes [51], are protected against hypercholesterolemia-induced atherosclerosis [52–54]. In 1998, two independent studies documented the key role played by monocyte recruitment to atheromatous lesions through the CCL2-CCR2 chemotactic axis, as mice deficient for CCR2 [55] or its ligand CCL2 [56] also displayed reduced atherosclerotic lesions. Monocyte chemotaxis in atherosclerosis was further characterized in 2007, as Tacke and colleagues provided evidence of the relative contribution of CCR2, CCR5 and CX3CR1 for monocyte recruitment into plaques [47]. CX3CR1 is highly expressed on Ly6C^{low} monocytes and remains detectable on Ly6C^{high} monocyte subset [57]. In contrast, CCR2 is predominantly expressed by the Ly6C^{high} population [57].

Understanding the roles played by metabolism in monocyte biology is of key importance considering the limitations of current therapies. Indeed, limiting monocyte recruitment to the plaque seems to be a reasonable strategy for reducing the development of atherosclerotic lesions. Complementarily, new anti-inflammatory approaches have recently

gained great interest. Indeed, lowering the inflammatory response has emerged as a novel therapeutic target to decrease CVDs related death and comorbidities. Interleukine-6 (IL-6) and IL-1 β are two well-established pro-inflammatory mediators and their levels are increased during atherosclerosis progression [58]. Among those two, the pro-inflammatory cytokine IL-1 β emerged as a major mediator of atherosclerosis development [59–61]. Surprisingly, IL-1 β signaling was also shown to be an important component of plaque remodeling and stability [62]. The Canakinumab Anti-inflammatory Thrombosis Outcome Study (CANTOS) trial showed that patients treated with the IL-1 β -targeting monoclonal antibody Canakinumab had a lowered cardiovascular-event-related mortality rate. However, Canakinumab treatment induced various side effects and increased susceptibility to infections, resulting in no overall survival benefits and underlining the urgent need for other therapeutic approaches [63,64].

Macrophages

Macrophages are highly phagocytic cells that can be identified through their co-expression of CD64 and MerTK [11]. Macrophages are ubiquitously present across organs and play key roles both in health and disease [11]. A key function of tissue-resident macrophage is the removal of dead cells, a process named efferocytosis [65]. Every day around 0.4% of the total estimated number of 3.7×10^{13} cells die in the adult human body [66]. Although all macrophage populations perform efferocytosis, they also display tissue-specific functions such as heme detoxification and iron handling in the spleen, surfactant clearing in the lungs or thermogenesis regulation in brown adipose tissue [67,68]. This functional heterogeneity can partly be explained by the developmental origin of macrophages. Microglia, the population of brain resident macrophages, arise from yolk sac precursors present at early developmental stages [69,70]. Alveolar pulmonary macrophages originate from foetal liver progenitors [71] while the population of gut macrophages derives from bone marrow precursors [72]. Consequently, embryonically-derived macrophages and monocyte-derived macrophages often coexist in adult tissues [73,74]. Like monocytes, tissue-resident macrophages rely on CSF1R signalling, which can bind either IL-34 or CSF1, for their maintenance. Interestingly, a tissue specificity for either ligand has been observed among tissue-resident macrophages, as microglia rely on IL-34 while large peritoneal macrophages rely exclusively on CSF1 [75,76]. Furthermore, macrophage heterogeneity can be attributed to local environmental features, even between subsets that share a common developmental origin [11].

Atheromatous plaque macrophages are monocyte-derived macrophages with the ability to proliferate in situ following their recruitment and differentiation. The understanding of macrophage diversity in metabolic disorders and inflammatory diseases is of particular

interest during atherosclerosis, as multiple macrophage subsets with specific immune profiles and functions have been observed within the plaque [18,21–23] (Figure 1A). Our knowledge on plaque macrophage diversity was previously restricted to pro-inflammatory “M1” macrophages, anti-inflammatory “M2” macrophages, and foam cells which were considered inflammatory cells [5]. The in situ identification of these subsets was based on immunohistochemistry approaches, while their functions were explored using in vitro models. However, new single cell methods have now revealed more layers of complexity in plaque macrophage subsets [18,21–23]. Notably, the single-cell RNA-Seq dataset from Kim and colleagues [23], which displays the greater myeloid cell enrichment, shows the existence of several distinct populations of inflammatory and anti-inflammatory subsets. Surprisingly, expression of the archetypical anti-inflammatory macrophage marker CD206 also appears on populations expressing inflammatory markers (Figure 1A). Two macrophage populations expressed high levels of Lyve1, a marker associated with tissue-resident macrophages [77] which were also identified by Cochain et al. [21] (Figure 1A). This new technology also allowed a detailed in vivo characterization of foam cells, identified as Trem2^{high} macrophages [23,78,79].

Single cell studies now pave the way to understanding plaque macrophage biology. Further investigation is needed to determine how these different subsets participate to inflammation or its resolution via efferocytosis and plaque remodelling [19]. To establish the developmental connection between plaque macrophage populations and their particular localization and metabolic demands is of crucial significance to understand the pathological mechanisms occurring during atherosclerosis progression.

Dendritic Cells

DCs are professional antigen presenting cells (APC). Two major DCs populations have been identified in mice and humans: the conventional (cDCs) and the plasmacytoid dendritic cells (pDCs). Both human and mouse cDCs highly and selectively express the transcription factor Zbtb46 (Zinc finger and BTB domain containing 46) [80,81]. Zbtb46 is not expressed by other myeloid cells such as macrophages, monocytes or neutrophils. In mice, cDCs populations highly express CD11c and MHC II and two main subsets have been identified in lymphoid and non-lymphoid tissues. In lymphoid tissues, cDC1s express CD8, CD24 and XCR1 while cDC2s are characterized by CD4 and Sirpa expression [82]. In the majority of nonlymphoid tissues, cDC1s are described as CD103⁺ XCR1⁺ and cDC2s as CD11b⁺ Sirpa⁺. cDC1 and cDC2 require specific transcription factors for their development. cDC1 depend on BATF3 (Basic Leucine Zipper activating transcription factor–like transcription factor 3) and IRF8 (IFN regulatory factor 8) while cDC2 rely on IRF4 and Notch2 for their development and maintenance [82]. A key feature of cDCs is their high

capacity to capture antigens in peripheral tissues and subsequently migrate to local draining lymph nodes to initiate the adaptive immune response. Another major function of cDCs is the production of pro-inflammatory cytokine such as IL-6, TNF α and IL-1 following activation of innate immunity receptors. This cytokine production leads to immune cell recruitment and mobilization and allows for specific and efficient immune responses. On the other hand, pDCs essentially release type 1 interferons (IFN-I), both IFN α and IFN β , in response to virus infections [83]. Their potential implication in atherosclerosis is suggested by the fact that IFN-I decreases macrophage phagocytic abilities [84] and that IFNAR-deficient animals have decreased plaque area and macrophage content [85].

In the context of atherosclerosis, cDCs contribute to chronic inflammation by attracting and activating T cells [86]. The production of CCL17 by mature cDCs contributes to CD4⁺ T cells and regulatory T cells (Tregs) migration and recruitment to plaques. CCL17 deletion leads to a slower atherosclerosis progression and a decreased number of macrophages and T cells in plaques [87]. The presence of CD4⁺ T cells with a phenotype of antigen activated (CD44⁺) cells was documented in mouse atherosclerotic models [17]. CD4⁺ T cells stimulation requires a peptide loading on major histocompatibility complex (MHC II), selectively expressed by antigen presenting cells. The cDC antigen presentation function seems to play a pivotal role in the progression of atherosclerosis. Nevertheless, and despite recent progress in the field, the nature of the antigen (peptide or lipid) remains to be fully understood. For instance, ApoB (the core protein in LDL) reactive CD4⁺ T cells were identified in pre-clinical atherosclerotic models [17] and humans [88]. Immunization strategies were developed using ApoB epitopes and those demonstrated atheroprotective effect, illustrated by reduced plaque area, when conjugated to appropriate adjuvants [89,90]. This protection was associated with increased IL-10 production, an anti-inflammatory cytokine mainly secreted by regulatory T cells (Tregs). In atherosclerotic patients, an oligoclonal T cell repertoire was observed in comparison to healthy patients [91,92]. This observation further supports the relevance of antigen presentation during disease development. Recently, the generation of MHC II tetramers loaded with ApoB-derived peptide revealed that the majority of ApoB-recognizing T cells are T regs [88]. Moreover, the deletion of two important costimulatory molecules: CD80 and CD86 in mice DCs decreased T-cell activation/infiltration in plaques [93] demonstrating that cDCs play a crucial role during disease development.

In advanced plaques, apoptotic cell accumulation due to defective efferocytosis leads to DNGR-1 activation (dendritic cell NK lectin group receptor-1) on CD8a⁺ cDC1s, which blunts IL-10 production, therefore contributing to atherosclerosis aggravation [94]. However, the mechanisms underlying the defective efferocytosis in DCs are still unknown and need to be deciphered. In conclusion, DCs, as pivotal players

linking innate and adaptive immunity, offer new insights that may lead to new therapeutic targets and notably vaccination strategies.

Neutrophils

Neutrophils are associated with the early inflammatory response [95]. Neutrophils have been shown to either be able to directly affect atherogenesis [96], or contribute to pathology onset by driving immune cell entry in atherosclerotic lesions [97] and by promoting plaque rupture [98] respectively. This suggests an important crosstalk between neutrophils and other immune and stromal cells.

Growing evidence suggests that neutrophils play a pivotal role in the initiation of atherosclerosis. Neutrophil adhesion to the endothelial wall through CCL3 and CCL5 binding on CCR1, CCR3 or CCR5 triggers neutrophils extravasation and their entry into plaques [99]. There, activated neutrophils release granule proteins containing chemotactic “alarmins”, such as cathelicidin/LL-37 in Human (CRAMP in mice), Human α -defensins (human neutrophil peptides, HNPs), azurocidin (HBP, CAP37) and serprocidins (elastase, cathepsin G, proteinase-3), inducing leukocytes attraction and recruitment to the site of inflammation (for review see [100]). In addition, S100A8/A9, a cytoplasmic protein, reduces neutrophils rolling on the endothelial wall and activates β 2 integrin to facilitate leukocyte extravasation and entry to the site of inflammation [101]. Interestingly, alarmins have also been reported to contribute to the activation of inflammasomes such as NLRP3 [102]. NLRP3 activation leads to IL-1 β and IL-18 production and to the HMGB1 alarmin (High-mobility group box 1 protein) release, creating a loop that amplifies innate immune responses [103]. NLRP3 inflammasome activation then increases neutrophil recruitment to inflammatory sites leading to the activation of neutrophil extracellular traps (NETs) [104]. NETs are web-like fiber structures released by neutrophils and made of extracellular chromatin, nuclear proteins, and serine proteases. NETs are known to increase monocyte recruitment to inflamed sites and trigger reactive oxygen species (ROS) and proinflammatory cytokines release by macrophages [105,106]. In this context, NETs may promote type I interferon (IFN-I) release from pDCs contributing therefore to atherosclerosis progression and suggesting an essential crosstalk between neutrophils and pDCs [107].

Neutrophils have been found at sites of plaque rupture in patients with acute coronary syndrome [108]. Interestingly, neutrophils are essentially located in the unstable layers of human atherosclerotic lesions with a high inflammatory activity and also correlated to the elevated numbers of monocytes found in these regions [99]. In addition, NETs are thought to be involved in plaque destabilization through the induction of endothelial cell wall cytotoxicity in humans [109,110]. Neutrophils are the main producer of myeloperoxidase (MPO) [111]. MPO is a heme-containing peroxidase that catalyzes the formation of reactive oxygen species intermediates [112] that induce macrophage cholesterylester

accumulation and foam cell formation, leading to atherosclerosis aggravation [113]. Recent studies have highlighted that neutrophils undergo transcriptional regulations under inflammatory conditions and NETosis [114,115]. The significance of NETs during atherosclerosis was extensively described in a recent manuscript [115].

Mouse Models

Mouse Cre-Lox systems have extensively been used to explore the role of myeloid cell functions in atherosclerosis. *Lyz2^{Cre}*, *CX3CR1^{Cre}* and *CD11c^{Cre}* mice were the most commonly used to study macrophages and neutrophils, monocytes, and dendritic cells respectively. Although these genes are dominantly expressed by the aforementioned cell types, some well-documented overlaps in their expression exist between myeloid cell types. Single-cell sequencing approaches have now brought to light the subset-specific expression pattern of these genes within the plaque (Figure 1B), which may allow more specific targeting of myeloid subsets within plaques and reinterpretation of previously generated data.

As expected, *Lyz2^{Cre}* appears to be virtually ubiquitously expressed across plaque resident myeloid cells. Although *CX3CR1* expression is only restricted to certain myeloid subsets within the plaque, most macrophages are monocyte-derived cells which therefore expressed *CX3CR1*-driven Cre at an earlier differentiation stage. However, the use of inducible *CX3CR1^{CreERT2}* models gives more flexibility to the model. As an example, Lin and colleagues recently used *Cx3cr1^{CreERT2-IRES-YFP/+}Rosa26^{fl-tdTomato/+}* mice in a fate-mapping and single-cell approach [18]. The authors induced Cre expression when plaques were established, immediately prior to plaque regression induction in order to differentially characterize *CX3CR1⁺* plaque cells and cells derived from *CX3CR1⁺* precursors [18]. *CD11c^{Cre}* mice were extensively used to characterize DCs functions in health and disease. However, *CD11c* was also shown to be expressed by *Ly6C^{low}* monocytes [57] which can, to a lower extent than *Ly6C^{high}* monocytes, infiltrate atheromatous lesions [47]. As shown in Figure 1B, plaque expression of *CD11c* is not restricted to DCs, but also concerns certain macrophage subsets including the now well identified *TREM2^{high}* foam cells [23,78,79]. *CD11c^{Cre}* mice could therefore be a valuable model to study foam cell metabolism during atherosclerosis.

METABOLIC PHENOTYPE OF PLAQUE IMMUNE CELLS

Atherosclerosis progression is accompanied by a modulation of systemic and plaque metabolites. Recently, non-invasive imaging techniques, commonly used in oncology, were deployed to predict rupture-prone plaques. Positron emission tomography (PET) is traditionally employed to investigate myocardial reperfusion. PET/CT studies revealed an accumulation of the glucose analog 18F-fluoro-2-deoxy-d-glucose (18F-FDG) in atherosclerotic lesions in humans [116]. This suggested increased glucose avidity and potentially metabolization in

plaque residing cells. A metabolomic analysis performed on iliac-femoral arteries extracted from control and atherogenic rabbits revealed an increased abundance of glycolysis and pentose phosphate pathway (PPP) metabolites in plaque-enriched vessels [117]. Whether these metabolites accumulate in specific immune or stromal cell-type remains to be established. In the following section we will discuss the impact of myeloid cell glucose metabolism on plaque development.

Lipid Handling

Monocytes

Hypercholesterolemia, the predominant metabolic feature of cardiovascular diseases, is known to influence hematopoiesis and induce a differentiation bias of hematopoietic stem cells (HSCs) towards the myeloid lineage. Indeed, HSCs obtained from ABCA1^{-/-} ABCG1^{-/-} mice, lacking transporters involved in cholesterol efflux, display increased proliferation and myelopoiesis switch [118]. This phenomenon is amplified in ApoE^{-/-} mice, one of the most commonly used murine models of hypercholesterolemia-induced atherosclerosis [119]. Taken together, recent data on cholesterol-related myelopoiesis exacerbation suggest that an increase in cellular cholesterol content promotes membrane lipid raft formation in HSCs, thus promoting the stabilization of chemokine and cytokine receptors at the cell surface and signal HSCs to quit quiescence [118,120–122].

Emerging immunometabolism-centered studies have mainly focused on macrophages, while only a few studies investigated monocyte metabolic requirements. This may partly be explained by technical difficulty of using undifferentiated monocytes in *in vitro* cultures. Recent studies pointed towards lipid metabolism as an important factor of monocyte homeostasis. Using a BM transplant approach, Babaev and colleagues reported a decreased CCR2 expression on blood monocytes from Ldlr^{-/-} mice with FABP5^{-/-} (Fatty-acid binding protein) hematopoietic compartment, suggesting a chemotaxis-dependent proatherogenic role of myeloid FABP5 expression [123]. FABPs regulate intracellular lipid traffic and control their access to specific organelles. By contrast, FABP4 deletion in immune cells had no impact on plaque development [123]. ApoE^{-/-} mice with myeloid-specific deletion of lipoprotein lipase (Lpl) displayed decreased plaque development [124]. Lpl hydrolyzes circulating TGs and control their levels. Impaired monocyte generation and differentiation to macrophages were observed in a mouse model of Lpl deficiency and were attributed to Lpl-dependent regulation of CSF1R signaling [125]. Interestingly, FABP5 and Lpl mRNA were highly and selectively expressed in Trem2⁺ foam cells (Figure 2A,B). This could suggest that the atheroprotective effects of myeloid-specific deletion of Lpl might not be caused solely by monocytes but could additionally be the consequence of foam cell dysfunction.

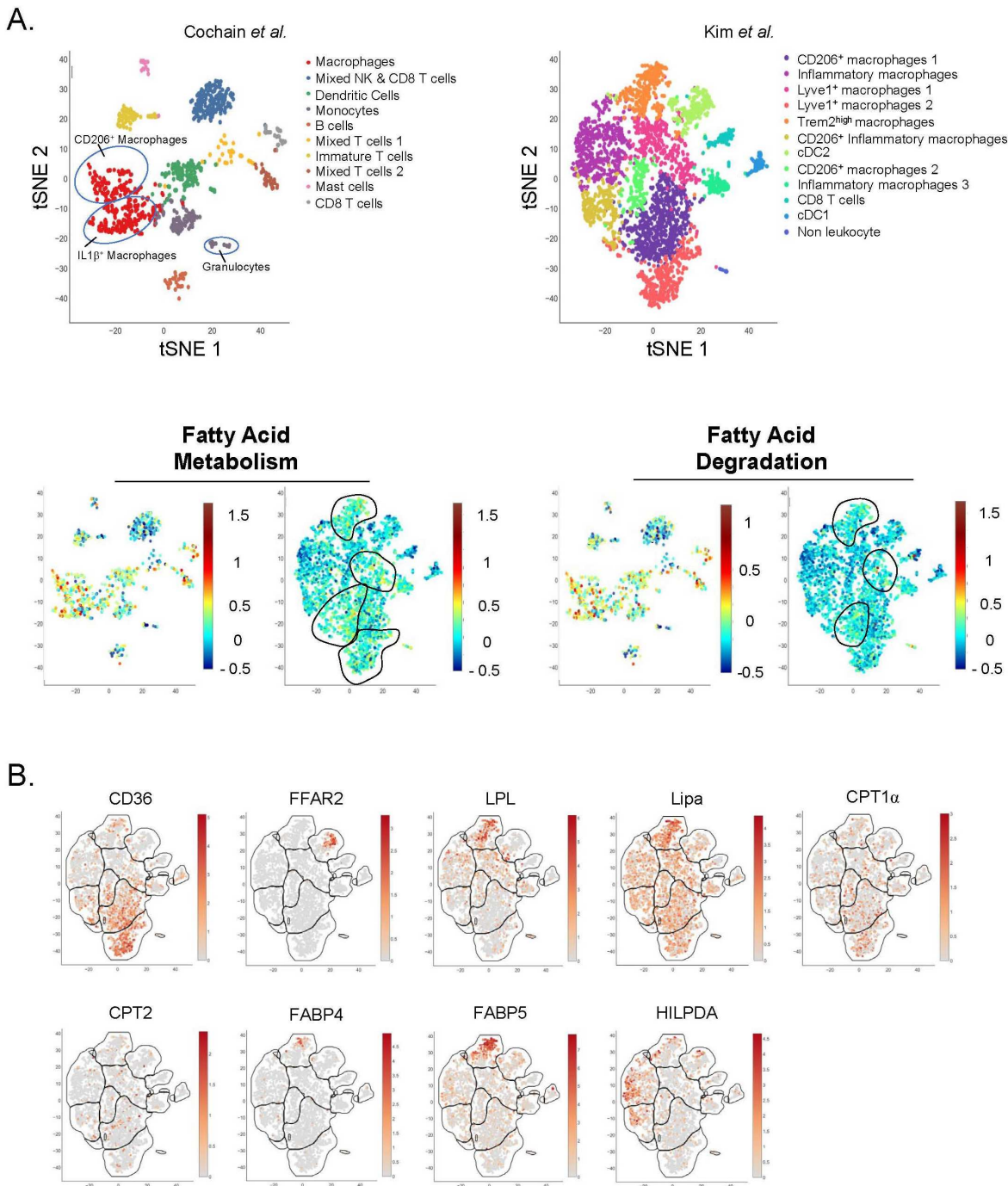


Figure 2. Single-Cell analysis of plaque immune cell lipid metabolism. (A,B) Single-Cell RNA-Seq of aortic CD45⁺ cells from *Ldlr*^{-/-} mice fed a HFD for (left) 11 weeks or (right) 12 weeks. Data from (left) Cochain et al. [21] (GSE97310) and (right) Kim et al. [23] (GSM3215435) were analyzed using the Single-Cell Explorer software (Artyomov lab). (A) Leukocyte clusters and corresponding KEGG Metabolic Pathway analysis. Fatty-Acid metabolism: KEGG mmu01212. Fatty-Acid degradation: KEGG mmu00071. **List of markers used in Cochain et al.:** Macrophages (mixed subsets): *Itgam*, *Fcgr1*, *MerTK*. Mixed NK and CD8 T cells: *CD3*, *CD8*, *Klrb1c*, *Ncr1*, *Gzmb*. Dendritic Cells (mixed subsets): *Itgax*, *Ciita*, *Zbtb46*. Monocytes: *Itgam*, *Fcgr1*, *Ly6C*, *CCR2*. B cells: *Ciita*, *CD19*, *CD79 α/β* . Mixed T cells: *Lck*, *CD3*, *CD4*, *CD8*, *Rag1*. Immature T cells: *Lck* (-), *CD3*(+), *Rag1* (-), *CD4* (-), *CD8* (-). Mast cells: *Furin*, *Il1r1l*. CD8 T cells: *Lck*, *CD3*, *CD8*. **Markers used in Kim et al. are in the legend for Figure 1A.** (B) Expression pattern of genes involved in lipid metabolism (Kim et al. [23] (GSM3215435)).

The importance of monocyte lipid metabolism was challenged by recent data. Jordan and colleagues observed a decrease in blood monocyte numbers during fasting in humans. This effect could not be reverted by fat supplementation in mice, while carbohydrate and protein supplementation both restored blood monocyte counts [126]. However, this modulation of monocyte counts was attributed to modulations of CCL2 production through a liver-BM axis, and not to monocyte cell-intrinsic mechanisms. Nevertheless, monocytes from fasted mice were in a pronounced quiescent metabolic state in comparison to controls, as extracellular flux analysis of these cells showed reduction in both oxygen consumption rate and extracellular acidification rate. This was associated with up-regulation of inositol triphosphate metabolism and suppression of serine and glutathione metabolism. Overall, this metabolic adaptation of monocytes to fasting was associated with improved outcomes in models of chronic inflammatory diseases [126].

As atherosclerosis is associated with numerous systemic metabolic alterations, these exciting results support the urgent need to identify the dietary-related metabolic mechanisms controlling monocyte inflammatory and migratory potentials in this disease. Indeed, both qualitative and quantitative diet modulations could then be envisioned as non-invasive prophylactic therapies for patients presenting monocytosis and metabolic syndrome.

Macrophages

Lipid-laden macrophages were first described inside of atherosclerotic lesions in the late 1970s [127]. These macrophages, called foam cells, take up excessive cholesterol and oxidized LDL (oxLDL) particles via their scavenger receptors, which leads to the intracellular formation of lipid droplets [128–131]. The presence of these cells is considered as a hallmark of atherosclerosis, and foamy macrophages have historically been held culprit for plaque progression.

Intracellular accumulation of cholesterol has been linked to foam cell formation, cytokine production and atherosclerosis progression in a mouse model of defective cholesterol efflux [132]. Atherosclerosis progression has been associated with the formation of cholesterol crystals, which results from reduced esterification of free cholesterol [133]. These crystals can trigger inflammation through the activation of the NLRP3 inflammasome and subsequent IL-1 β maturation, which have lately been a major focus of atherosclerosis research [134]. These results support a beneficial role for cholesterol efflux, which is mediated through the liver X receptor (LXR)-regulated transcriptional control of among others the cholesterol transporters ABCA1 and ABCG1. Mice deficient for LXR α and LXR β display the formation of atheromatous lesions containing foam cells even in the absence of diet-induced hypercholesterolemia [135]. Subsequently, attempts have been made to decrease intracellular cholesterol accumulation and foam cell formation by the use of synthetic

LXR agonists which have proven to be beneficial in pre-clinical models of atherosclerosis [136–138]. Consistently, myeloid-specific deletion of the LXR-regulated ABCA1/G1 cholesterol transporters was shown to exacerbate atherosclerosis development [139]. Alternatively activated (M2) human monocytes and macrophages were reported to be less responsive to LXR agonists [140]. Interestingly, they also displayed less foam cell traits despite decreased ABCA1 expression. This was countered by an improved cholesterol esterification capacity (an anti-inflammatory mechanism) [141], suggesting that efficient cholesterol handling may be more valuable than cholesterol efflux [140]. PPAR α stimulation positively regulates ABCA1 expression [142]. Additionally, PPAR γ activation also increases ABCA1 expression via LXR [143]. PPAR α prevents foam cell formation and decreases plaque development [144,145]. PPAR γ agonist also decreased foam cell formation [144]. The role of PPARs in macrophage biology and atherosclerosis is extensively reviewed in [146,147]. However, whether and how precisely PPARs affect specifically different myeloid cell populations in plaque remains to be defined. We recently reported that lysosomal acid lipase (LIPA)-dependent cholesterol hydrolysis promotes macrophage efferocytic capacity [148]. LIPA is expressed by all plaque macrophage subsets and is particularly enriched in foam cells (Figure 2B). The relevance of our observations linking LIPA activity and efferocytosis to atherosclerosis needs to be further investigated, as multiple studies reported a correlation between LIPA variants and coronary artery disease [149,150].

Macrophage foam cell formation is regulated by natural antibodies recognizing modified LDL particles and apolipoproteins. Indeed, the inhibition of oxLDL uptake by oxLDL-specific natural IgMs, which mask oxidized epitopes, decreases foam cell formation, inflammation and atherosclerosis development [151–153]. The production of oxLDL-specific antibodies, both of the IgM and IgG isotype, occurs during the development of atherosclerosis [154]. IgG-containing immune complexes are recognized by Fc γ R receptors, and ApoE^{-/-} mice deficient for Fc γ RIIb/CD32b, a low affinity inhibitory receptor, showed reduced plaque lipid content suggesting lower foam cell formation [155]. This was associated with an overall increase in plaque stability, as well as in circulating levels of oxLDL and IgG-ApoB immune complexes, suggesting a lower uptake of these particles by macrophages [155]. Foam cell formation was also reported to be induced by ApoA1-specific IgG in vitro [156]. Although atherosclerosis-associated IgMs and IgGs display different roles in foam cell formation, only the former are robustly associated with a (protective) role in the development of the disease [157].

In macrophages, a consequence of foam cell formation could be lipid overload-induced toxicity, which may hypothetically be a determinant of plaque necrosis. Both fatty acid metabolism and degradation pathways are enriched in plaque macrophages (Figure 2A). The hypoxia-inducible lipid-droplet-associated (Hilpda) protein has emerged as a key player in lipid

droplet handling. Its role as a lipid-sensor and inhibitor of ATGL (the rate limiting enzyme of adipose tissue lipolysis) promotes lipid accumulation into lipid droplets and foam cell formation [158]. In plaques, Hilpda mRNA was preferentially expressed in inflammatory macrophages (Figure 2B). This Hilpda-mediated lipid storage was reported to be necessary for the maintenance of macrophage viability upon lipid overload, suggesting a beneficial role for lipid storage in terms of survival [159]. Nevertheless, Hilpda deficiency was shown to decrease atherosclerosis development and plaque lipid content, without affecting plaque macrophage apoptosis [159]. The authors attributed this phenotype to the Hilpda-dependent macrophage lipid accumulation and production of prostaglandin E₂, which promotes vascular inflammation [160].

Overall, previous reports point towards a proatherogenic role for foam cells. However, the emergence of omics approaches led recent studies to challenge this view. Foamy peritoneal macrophages extracted from *Ldlr*^{-/-} mice fed a high cholesterol diet surprisingly showed a LXR-mediated down-regulation of genes associated with inflammatory responses and chemotaxis [161]. A turning point in foam cell research was reached by Kim and colleagues, who developed a strategy to isolate and characterize plaque foam cells using a lipid probe-based strategy [23]. Surprisingly, their results showed that foam cells only represent around 10% of aortic macrophages in atherosclerotic mice, although this proportion may vary depending on isolation efficiency. Moreover, both bulk and single cell RNA-Seq approaches showed that foamy macrophages are rather anti-inflammatory in comparison to non-foamy plaque macrophages. As discussed earlier, this is of particular interest in the context of the recent CANTOS trial, as NLRP3 and IL-1 β expression were clearly a feature of non-foamy macrophages [23]. While previous studies relied greatly on *in vitro* models to analyze macrophage lipid metabolism and foam cell formation, this innovative approach may have supplied the methodology to further characterize foam cells *in vivo*. As discussed earlier, studying macrophages in the context of their micro-environment has repeatedly proven to be the key to understanding their biology.

In vitro studies revealed that IL-4 induces a specific metabolic profile in macrophages. These cells are named alternatively activated (M2) macrophages and rely on fatty acid oxidation for their metabolic needs [162]. Seminal studies demonstrated that fatty acid oxidation inhibition in macrophages prevents their M2 phenotype. This concept was recently challenged by the demonstration that etomoxir, a specific Cpt1a inhibitor, has “off-target” effects even at fairly low concentrations [163,164]. Genetic Cpt2-deletion failed to affect macrophage alternative polarization, further challenging the previously established dogma [165]. Cpt1 and Cpt2 mRNA were detected in plaque-resident myeloid cells without a subset-specific signature (Figure 2B). Whether plaque resident macrophages rely on fatty acid oxidation and Cpt1 remains currently unknown. Importantly, macrophage alternative activation depends on CD36, a membrane receptor for long

chain fatty acids [162]. Single-cell RNA-Seq analysis revealed that CD36 is highly expressed in Lyve1⁺ plaque resident macrophages (Figure 2B). Of interest, Lyve1 is a canonical M2 activation marker which, together with CD36 expression, might help identifying the real *in vivo* alternatively activated macrophage relying on fatty acid oxidation (at least in the context of the plaque). CD36 is involved in non-classical monocyte patrolling during atherosclerosis induction [166]. Previous reports demonstrated that CD36 plays a crucial role during atherosclerosis development but it remains unclear how CD36 governs plaque myeloid cell metabolism [167–170]. For instance, CD36 signaling is involved in ROS generation and controls macrophage cytoskeleton organization [171].

Dendritic cells

One of the major proofs of DCs implication in atherosclerosis development is their impact on cholesterol homeostasis. Indeed, DC depletion in hyperlipidemic CD11c-DTR ApoE^{-/-} mice leads to increased hypercholesterolemia but no change in atherosclerosis due to lower DC-driven T-cell activation, suggesting that there is a close relationship between DCs and cholesterol homeostasis. CD11c expression in plaque is not restricted to DCs, and this function might be shared with CD11c-expressing macrophages (Figure 1B). Increasing DC survival by overexpressing Bcl2 leads to decreased cholesterol plasma levels [172]. However, long term DC depletion led to a progressive myeloproliferative syndrome, highlighting an indirect impact on the hematopoietic system [173]. Additionally, in Ldlr-deficient mice, DCs in atherosclerotic lesions have been shown to capture oxLDL contributing to foam cell formation and therefore to atherosclerosis progression [174].

Despite the fact that pDCs are present in a relatively low frequency in human and mouse atherosclerotic plaques, this cell type also plays a role in atherosclerosis development. pDCs numbers are increased in aortas of ApoE^{-/-} and Ldlr^{-/-} mice fed a high-fat diet [24,175]. Intriguingly, ApoE^{-/-} mice depleted in pDCs display decreased lipid-containing area, lower T cell activation and lower macrophage accumulation in the plaque [176]. In addition, when treated with oxLDL, pDCs show increased phagocytic capacity as well as a stimulated antigen-specific T cell response [177]. Genetic pDC depletion, following diphtheria toxin administration in BDCA2-DTR atherogenic mice, led to increased lesion area [175]. Moreover, TLR-induced IFN-I production by pDCs is triggered by neutrophils NETs in human atherosclerotic plaque [178]. All together, these data suggest that pDCs might be interesting targets in controlling the evolution of atherosclerosis. However, pDCs role in atherosclerosis is still under debate due to the opposite effects the antibody used against pDC bone marrow stromal cell antigen-2/PDCA1 has on Ldlr^{-/-} and ApoE^{-/-} mouse [176,177,179].

Neutrophils

Cholesterol metabolism appears to play a key role in neutrophil biology, as both *Ldlr*^{-/-} and *ApoE*^{-/-} mice fed a high fat diet display increased blood neutrophil numbers [119]. Cholesterol efflux receptors such as ABCA1/ABCG1 notably regulate neutrophil adhesion and activation [180]. Moreover, neutrophil accumulation and NETosis have also been found in the context of defective cholesterol efflux induced by ABCA1 and ABCG1 deficiency [181] (for review see [182]). Additionally, inhibition of cholesterol efflux in myeloid progenitors led to increased neutrophil production while a disruption in the chemotactic axis CXCL12-CXCR4 in the BM led to neutrophilia and therefore amplified lesion formation [97]. Moreover, mice fed a high-fat diet show significant increase in circulating neutrophil numbers [183]. However, surprisingly, epidemiological studies in humans have shown a positive correlation between elevated numbers of circulating neutrophils and cardiovascular events, independently from serum cholesterol levels [184]. In addition, fatty acids have also been proposed to be involved in neutrophils metabolic demands. Indeed, fatty acid receptors including free fatty acid receptor-1 (FFAR1/GPR40), free fatty acid receptor 2 (FFAR2/GPR43), and GPR84 are expressed on neutrophils [185]. However, short term fasting in humans had no effect on circulating neutrophil levels [126]. Cell-autonomous effects of lipids on neutrophils and their relevance in atherosclerosis require further investigations.

Glucose Metabolism in Myeloid Cells

Monocytes

Unlike tissue-resident immune cells, monocytes need to quickly adapt to their new environment after blood vessel extravasation and entry into peripheral tissues. This seems critical in atherogenic conditions, as recent evidence suggests that monocytes might contribute to the onset of the disease due to their sensitivity to the plaque micro-environment, rather than to a preexisting inflammatory phenotype. Notably, Williams and colleagues showed that newly-recruited monocytes lose motility as they differentiate into macrophages within the plaque, thus reducing their capacity to reach apoptotic cells located deeper within the plaque and perform efferocytosis [186]. This rapid adaptation probably requires an adjustment of metabolic pathways to the locally available substrates.

In humans, glucose metabolism disorders such as *diabetes mellitus* have been associated with cardiovascular diseases, though the underlying cellular mechanisms remain unclear [187,188]. The use of the glucose analog 18F-FDG in PET-CT imaging has brought to light a correlation between acute coronary syndrome and 18F-FDG accumulation (representative of glucose avidity) in the bone marrow and the spleen (the later probably reflecting extramedullary hematopoiesis) in at least two independent cohorts [189]. Interestingly, Oburoglu and colleagues showed

that in vitro (human CD34⁺ cells) and in vivo (newborn mice), administration of 2-deoxyglucose, a partially non metabolizable glucose analog used to inhibit glycolysis, restricted myeloid differentiation while promoting erythroid differentiation of HSCs [190]. Consistently, using chimeric pre-clinical models of atherosclerosis, our group previously reported a decrease in myelopoiesis and plaque development in mice with partial deficiency for Glut1, the main glucose transporter in the hematopoietic compartment [191]. Increased glucose levels in diabetic mice drive myelopoiesis, further supporting the evidence that glucose metabolism favors myeloid cells generation [192]. Interestingly, Jordan and colleagues reported a direct relation between food intake and systemic CCL2 levels, which allows for monocyte egress from the bone marrow compartment to the blood circulation [126]. This effect was mainly attributed to glucose metabolism, as the authors observed a positive correlation between blood monocyte counts and the quantity of gavage-administered glucose. Furthermore, monocyte mobilization could be inhibited by gavage with 2-deoxyglucose [126]. As discussed earlier, the CCL2-CCR2 chemotactic axis governs monocyte recruitment to atherosclerotic plaques and progression of the diseases [47]. Importantly, monocyte CCR2 expression strongly associates with vascular wall inflammation in patients with CVD risk [193]. However, whether glucose affects chemokine receptor expression on monocytes and facilitates their entry into inflamed plaques remains to be explored. In a pre-clinical plaque regression model, it was demonstrated that lowering plasma glucose concentration prevents monocyte entry into the inflamed plaque and improves pathology resolution [192]. Nevertheless, whether glucose lowering therapies affect monocyte CCR2 expression and their ability to enter into plaques and differentiate into macrophages also requires further investigations.

Macrophages

Macrophages rely on the membrane transporter Glut1, encoded by Slc2a1, for glucose entry. Slc2a1 is ubiquitously expressed among plaque myeloid cells (Figure 3A,B). However, transcriptomic analysis revealed an enrichment in transcripts related to glycolysis and PPP pathways in macrophages and DCs (Figure 3A,B). Glut1 is solely responsible for glucose entry into macrophages, as its ablation using genetic models demonstrated that other members of this family of transporters cannot substitute its absence [194]. Thus, $Lyz2^{cre} \times Slc2a1^{fl/fl}$ animals have minimal glucose entry associated with decreased levels of many glycolysis and PPP-related metabolites [194]. Compensatory mechanisms led to increased tricarboxylic acid cycle (TCA) metabolites in Glut1-deficient macrophages in comparison to controls [194]. Interestingly, when crossed to atherogenic $Ldlr^{-/-}$ mice, $Lyz2^{cre} \times Slc2a1^{fl/fl} \times Ldlr^{-/-}$ animals had similar plaque size as control mice [194]. Macrophage content, quantified by MOMA2 staining, remained similar as well. However, mice with Glut1-deficient myeloid

cells had an elevated frequency of necrotic core per plaque that paired with a partial deficiency in efferocytosis [194]. This observation was confirmed in another study using the same genetic model [195]. Indeed, efferocytosis triggers a specific metabolic reprogramming of macrophages that relies mainly on glycolysis [195] and lowering glucose concentration, or pharmacological or genetic Glut1-inhibition all efficiently alter macrophage efferocytosis [195]. Glut1 expression is increased following macrophage TLR4 stimulation with LPS to facilitate glucose entry [196], though the relevance of this observation for plaque formation or maintenance requires further investigation. LPS also leads to accelerated glucose flux and increased glycolysis and PPP activation. This is supported by the transcriptional regulation of key enzymes involved in the aforementioned pathways. Thus, LPS increases the expression of two critical enzymes (HK3 and PFKFB3) involved in glycolysis, and this is paralleled by increased pro-inflammatory cytokine production [13]. In plaques, HK3 is found mainly in a population of Trem2⁺ macrophages, while PFKFB3 expression is higher in inflammatory macrophages (Figure 3B). Four HK (hexokinase) isoforms have been identified. Interestingly, HK1 was not enriched in a specific plaque immune subset, while HK2 is highly expressed in inflammatory macrophages (Figure 3B). Again, the biological significance of this observation needs further work. However, macrophage-specific Glut1 overexpression, despite increasing glucose entry and metabolization, failed to generate an increased pro-inflammatory cytokine production [13]. Plaque size, macrophage content and necrotic core area were similar between control and macrophage-Glut1 overexpressing animals [13]. This observation is surprising since increased glucose levels in mice have been associated with a macrophage pro-inflammatory phenotype and disease severity. Taken together, these observations suggest that glucose flux through Glut1 contributes to myeloid cells activation during atherosclerosis, but this is not sufficient to fully explain the pro-inflammatory phenotype of plaque macrophages. Macrophage alternative polarization also requires efficient glucose metabolism [197]. Blocking pyruvate mitochondrial entry and subsequent TCA incorporation leads to decreased ATP production [197]. This is consistent with the role of glucose in TCA cycle activation and ATP generation. Inhibition of the enzyme Acly, playing a key role in Acetyl-CoA generation, prevents macrophage alternative polarization in murine macrophages [198]. The human relevance of this observation was challenged in a recent report using pharmacological inhibitors and genetic approaches [199]. However, whether those pathways affect particularly the metabolic rewiring of a specific subset of plaque resident myeloid cells remains to be defined.

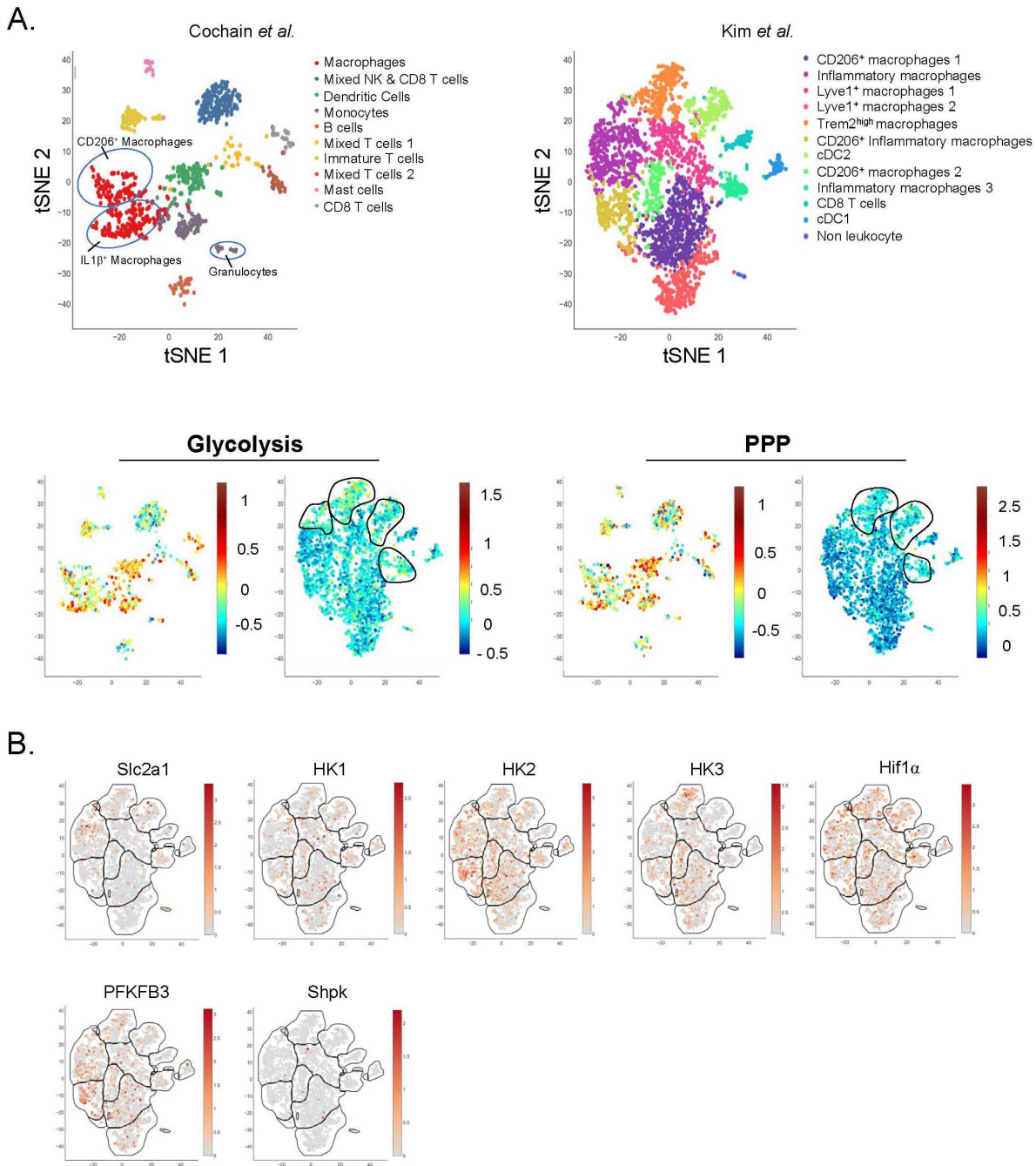


Figure 3. Single-Cell analysis of plaque immune cell glucose metabolism. (A,B) Single-Cell RNA-Seq of aortic CD45⁺ cells from Ldlr^{-/-} mice fed a HFD for (left) 11 weeks or (right) 12 weeks. Data from (left) Cochain et al. [21] (GSE97310) and (right) Kim et al. [23] (GSM3215435) were analyzed using the Single-Cell Explorer software (Artyomov lab). (A) Leukocyte clusters and corresponding KEGG Metabolic Pathway analysis. Glycolysis: KEGG mmu00010. Pentose Phosphate Pathway: KEGG mmu00030. The lists of markers used to identify subsets are in the legend of Figures 1 and 2. (B) Expression pattern of genes involved in glucose metabolism (Kim et al. [23] (GSM3215435)).

Interestingly, Folco and colleagues reported no modulations in glucose uptake when stimulating human primary macrophages with pro-inflammatory cytokines [200]. However, glucose uptake was increased in hypoxic conditions, along with increased HK2 expression, while HK1

expression remained unchanged. Immuno-histochemical analysis of human atherosclerotic lesions showed a colocalization of HK2 with the transcription factor HIF-1 α (Hypoxia-inducible factor-1), a well-established regulator of glycolysis [200]. Hif-1 α mRNA is ubiquitously expressed among plaque resident immune cells, most of which also express HK2 but not HK1, thus supporting these observations (Figure 3B). Advanced plaques contain hypoxic regions due to restricted blood supply and Hif-1 α expression was detected in mouse and human plaques [201–204]. Conditional deletion of Hif-1 α in myeloid cells (Lyz2^{cre} \times Hif-1 α ^{fl/fl} mice) didn't impact plaque size [205]. However, when Hif-1 α was deleted in CD11c-expressing cells, an increased plaque area was documented, suggesting that this transcription factor mainly operates in CD11c-positive cells that could be DCs or a subset of macrophages (Figure 1B) [205]. CD11c^{cre} \times Hif-1 α ^{fl/fl} mice displayed increased necrotic core area that might result from defective glucose-driven efferocytosis [205]. However, a recent report demonstrated that Lyz2^{cre} \times Hif-1 α ^{fl/fl} mice have less plaque lesions when compared to control mice [206]. Surprisingly, Hif-1 α deficient mice displayed less apoptotic cells and blunted glucose uptake [206].

LPS also regulates glucose flux into the PPP. LPS decreased the expression of the enzyme Shpk (CARKL) involved in the non-oxidative branch of the PPP [207]. Conversely, IL-4 induced CARKL expression is required for optimal macrophage alternative polarization. CARKL genetic deficiency forces glucose flux into the glycolysis pathway at a level similar to the one seen upon LPS challenge [207]. Shpk expression is not restricted to a selective myeloid cell population in plaques (Figure 3B). In advanced plaque, macrophage local proliferation contributes to plaque growth [208] and one would expect that the PPP pathway, involved in nucleotide generation, is highly activated. This was not yet documented to our knowledge. Interestingly, a recent report demonstrated that hypercholesterolemia suppressed the PPP in macrophages [209]. Whether this mechanism occurs in plaque during atherosclerosis development remains to be tested.

Dendritic cells

Several populations of DCs have been identified in plaques, both in mice and humans (**Table 2 and Figure 1**). However, little is known about the metabolic configuration of plaque resident DCs. Following TLR4 activation with LPS, DCs rapidly undergo a metabolic switch towards glycolysis [210,211]. LPS exposure increases glucose consumption rate and increases Glut1 expression in DCs [210]. This is paralleled by augmented nitric oxide (NO) production that subsequently decreases oxidative phosphorylation (OXPHOS) activity, ATP levels and mitochondrial activity. Consistently, activated DCs show less oxygen consumption rate than resting DCs [210]. Thus, NO seems to play a pivotal role in metabolic regulation [211]. In DCs, endogenous nitric oxide production inhibits OXPHOS and commit those cells to glucose metabolism and aerobic

glycolysis similar to the Warburg effect described in tumor cells [211]. Additionally, LPS-induced NO production contributes to DCs induced death following activation [211]. This glycolytic reprogramming that happens within minutes after TLR stimulation is called the “glycolytic burst” and leads to *de novo* fatty acid synthesis needed for inflammatory cytokine production [212]. In addition, glucose restriction decreases activated-DC maturation, life span and cytokine secretion.

As compared to the rapid increase in glucose flux, Glut1 upregulation in DCs takes hours to build up following TLR stimulation. Therefore, exogenous glucose internalization seems unlikely to be the source required during early DC activation. This lag was recently solved by Thwe and colleagues who showed that intracellular glycogen reserves fuel DCs metabolic demands during early DC activation and that glycogen metabolism is required by these cells to initiate proper immune effector responses [213]. Of note, high glucose concentration increased the oxLDL-uptake capacity of DCs and augmented their IL-6 and IL-12 secretion while decreasing their IL-10 production [214].

Neutrophils

Unlike macrophages and monocytes, little is known about neutrophil metabolic configuration in health and disease. This might be explained by the difficulty to analyze these cells *ex vivo*. Moreover, single-cell RNA-Seq analysis on neutrophils is rather difficult because these cells typically possess lower number of transcripts when compared to T cells and macrophages. Neutrophils have long been thought to mainly rely on glycolytic metabolism [215], but neutrophils are able to switch from glycolysis to different metabolic pathways such as OXPHOS [216,217]. Increased glycemia favors granulopoiesis and neutrophil release in the blood circulation [191,192]. How modulation of plasma glucose levels impacts on neutrophil chemotaxis, especially their recruitment, retention and survival in the atherosclerotic plaque, is another exciting question.

Amino Acids

In addition to glucose and lipids, amino acids are a source of energy for immune cells. Amino acids are essential metabolites for protein synthesis that act as intermediates in metabolic pathways. Amino acids modulate immune cell functions such as activation, differentiation, proliferation, gene expression, redox status or cytokine production. However, the role of amino acids on immune cell functions during atherosclerosis remains poorly understood.

In vitro studies have demonstrated the impact of glutamine metabolism on macrophage polarization [218,219]. More recently, Tavakoli et al. highlighted increased glutamine accumulation in aortas obtained from *Ldlr*^{-/-} mice. In this study, the autoradiography shows a non-homogenous glutamine accumulation that diverges according to macrophage activation profile. The combination of 2-deoxyglucose and glutamine accumulation

within the aorta could predict the dominant macrophage polarization profile within the plaque. Indeed, a greater accumulation of glutamine than 2-deoxyglucose supposes a dominant anti-inflammatory population while the opposite indicates a higher content of pro-inflammatory macrophages. This study is one of the first to suggest a role for glutamine on plaque macrophage functions [220].

Besides glutamine, arginine is a key metabolite in vascular function and tone due to its role in the production of nitric oxide (NO). Indeed, arginine is metabolized both by arginase 1 (Arg1) and inducible nitric oxide synthase (iNOS) to produce ornithine and urea or NO respectively. As those two enzymes compete for the same substrate, the use of arginine by Arg1 limits NO production, a macrophage pro-atherogenic factor [221]. In *Ldlr*^{-/-} mice, microarray analysis showed an increase Arg1 expression in carotid artery during early atherosclerotic lesions. Moreover, Arg1 deficiency promoted NO synthesis upon lipid loading. Hematopoietic Arg1 deletion induced increase foam cell formation in the peritoneum. However, after 10 weeks of western diet, Arg1 deficiency in *Ldlr*^{-/-} mice had no effect on the plaque size nor on the plaque composition [222]. Similarly, in *Ldlr*^{-/-} mice deficient for Arg1 specifically in myeloid cells, Yurdagul et al. did not observe any phenotypic difference within the plaque. However, in a regression model, the authors demonstrated defective efferocytosis within the plaque leading to impaired regression, increased necrotic core area and decreased cap thickness. In addition, ornithine produced by Arg1 can be subsequently metabolized to putrescine by ODC (ornithine decarboxylase) [223,224]. Putrescine supplementation improves plaque macrophage efferocytosis leading to reduced lesion and necrotic core size, as well as cap thickness [225]. Conversely, *ApoE*^{-/-} mice deficient for iNOS in the bone marrow compartment have reduced atheromatous lesions showing that leukocyte mediates the pro-atherogenic effect of iNOS in mice [226].

CONCLUSIONS AND FUTURE DIRECTIONS

The field of immunometabolism is a rapidly expanding one that provides new insights on the role of specific metabolites in immune cells during health and disease. Atherosclerosis is characterized by increased plasma glucose and cholesterol concentrations, and we only recently started to appreciate how precisely these two metabolites impact on plaque resident myeloid cell functions and on their generation from bone marrow-derived precursors. The precise circuits incorporating glucose in macrophages, monocytes, DCs and neutrophils remain to be fully understood. Eventually this might help to apprehend how metabolism supports key functions specific for each population. For example, understanding how metabolism guides monocyte recruitment to plaques as well as their retention or eventual egress will be of significant importance for the field. Regarding macrophages, we recently learned that glucose metabolism sustains one of their key functions: the removal of

apoptotic cells [194,195]. Whether glucose modulates macrophage motility in plaque or their interaction with the extracellular matrix remains to be elucidated. Recent reports demonstrated that DCs cytokine production is tightly regulated by their metabolic configuration [227]. Glucose metabolism regulates DCs migration via regulation of the key chemokine receptor CCR7 [228,229]. Of note, the role of CCR7 during atherosclerosis remains debated with studies reporting that CCR7-deficient mice display smaller [230], similar [231] and increased [232] plaque area. One might wonder whether this mechanism occurs during atherosclerosis as well. Specific metabolic configuration might be required for efficient peptide presentation to conventional T cells via MHC II or lipids to NKT (Natural Killer T) cells via CD1d. Another crucial question is whether the way of metabolite incorporation in myeloid cells affects their intracellular distribution. Apoptotic cell ingestion by myeloid cells leads to internalization of metabolites contained in the dying cell [225]. Thus, the efferocytes need to either incorporate these metabolites into their circuits, store them in specialized compartments or expulse them in the interstitial space where they could be used by neighbor cells.

Single-Cell RNA-Seq moved the field forward toward a better understanding of the immune diversity and functions in atherosclerotic plaque. Nevertheless, the predictions generated via this technique need in detail in situ validation. Recently, an elegant approach was validated to investigate single-cell metabolism in local environment [233]. This new technical advance will be helpful to investigate whether different myeloid cell populations residing in plaque possess a unique enzymatic profile. These analyses could also reveal a zonation in plaque enzyme and metabolite distribution. The field will benefit from our future ability to dose locally metabolites at the scale of the milieu surrounding a cell as well as cellular micro-compartmentalization. This, together with our ability to measure enzymatic activities and at the same scale will certainly make our task of making sense of metabolism an easier one. Our computing ability to integrate all those parameters will also facilitate the large-scale understanding of deciphering how access and competition for nutrients shape immunity and to what extent this can be used as new therapeutic handles.

AUTHOR CONTRIBUTIONS

AG and SI outlined the manuscript. AG, MIS, JM and SI wrote the manuscript. AG generated the figures and tables. RRG, LYC and SI edited the manuscript. All authors approved the final submission of the manuscript.

CONFLICTS OF INTEREST

The authors have no disclosure and conflict of interest to declare.

FUNDING

AG is supported by the French government, through the UCAJedi Investments in the Future projects managed by the National Research Agency (ANR) with the reference number ANR-15-IDEX-01. RRG is supported by Centre National de la Recherche Scientifique (CNRS). LYC is supported by grants from the European Research Council (ERC) consolidator program (ERC2016COG724838). SI is supported by Institut National de la Sante et de la Recherche Medicale (INSERM) and Agence Nationale de la Recherche (ANR-17-CE14-0017-01 and ANR-19-ECVD-0005-01).

REFERENCES

1. Libby P, Lichtman AH, Hansson GK. Immune effector mechanisms implicated in atherosclerosis: from mice to humans. *Immunity*. 2013;38(6):1092-104.
2. Kobiyama K, Ley K. Atherosclerosis. *Circ Res*. 2018;123(10):1118-20.
3. Fredrickson DS, Lees RS. A System for Phenotyping Hyperlipoproteinemia. *Circulation*. 1965;31:321-7.
4. Dawber TR, Moore FE, Mann GV. Coronary heart disease in the Framingham study. *Am J Public Health Nations Health*. 1957;47(4 Pt 2):4-24.
5. Moore KJ, Tabas I. Macrophages in the pathogenesis of atherosclerosis. *Cell*. 2011;145(3):341-55.
6. Otsuka F, Joner M, Prati F, Virmani R, Narula J. Clinical classification of plaque morphology in coronary disease. *Nat Rev Cardiol*. 2014;11(7):379-89.
7. Tabas I. Heart disease: Death-defying plaque cells. *Nature*. 2016;536(7614):32-3.
8. Davies MJ, Richardson PD, Woolf N, Katz DR, Mann J. Risk of thrombosis in human atherosclerotic plaques: role of extracellular lipid, macrophage, and smooth muscle cell content. *Br Heart J*. 1993;69(5):377-81.
9. Virmani R, Kolodgie FD, Burke AP, Farb A, Schwartz SM. Lessons from sudden coronary death: a comprehensive morphological classification scheme for atherosclerotic lesions. *Arterioscler Thromb Vasc Biol*. 2000;20(5):1262-75.
10. Guillems M, Ginhoux F, Jakubzick C, Naik SH, Onai N, Schraml BU, et al. Dendritic cells, monocytes and macrophages: a unified nomenclature based on ontology. *Nat Rev Immunol*. 2014;14(8):571-8.
11. Gautier EL, Shay T, Miller J, Greter M, Jakubzick C, Ivanov S, et al. Gene-expression profiles and transcriptional regulatory pathways that underlie the identity and diversity of mouse tissue macrophages. *Nat Immunol*. 2012;13(11):1118-28.
12. Tabas I, Bornfeldt KE. Intracellular and Intercellular Aspects of Macrophage Immunometabolism in Atherosclerosis. *Circ Res*. 2020;126(9):1209-27.
13. Nishizawa T, Kanter JE, Kramer F, Barnhart S, Shen X, Vivekanandan-Giri A, et al. Testing the role of myeloid cell glucose flux in inflammation and atherosclerosis. *Cell Rep*. 2014;7(2):356-65.
14. Shirai T, Nazarewicz RR, Wallis BB, Yanes RE, Watanabe R, Hilhorst M, et al. The glycolytic enzyme PKM2 bridges metabolic and inflammatory dysfunction in coronary artery disease. *J Exp Med*. 2016;213(3):337-54.

15. Tomas L, Edsfeldt A, Mollet IG, Perisic Matic L, Prehn C, Adamski J, et al. Altered metabolism distinguishes high-risk from stable carotid atherosclerotic plaques. *Eur Heart J*. 2018;39(24):2301-10.
16. Jonasson L, Holm J, Skalli O, Bondjers G, Hansson GK. Regional accumulations of T cells, macrophages, and smooth muscle cells in the human atherosclerotic plaque. *Arteriosclerosis*. 1986;6(2):131-8.
17. Koltsova EK, Garcia Z, Chodaczek G, Landau M, McArdle S, Scott SR, et al. Dynamic T cell-APC interactions sustain chronic inflammation in atherosclerosis. *J Clin Invest*. 2012;122(9):3114-26.
18. Lin JD, Nishi H, Poles J, Niu X, McCauley C, Rahman K, et al. Single-cell analysis of fate-mapped macrophages reveals heterogeneity, including stem-like properties, during atherosclerosis progression and regression. *JCI Insight*. 2019;4(4):e124574.
19. Williams JW, Winkels H, Durant CP, Zaitsev K, Ghosheh Y, Ley K. Single Cell RNA Sequencing in Atherosclerosis Research. *Circ Res*. 2020;126(9):1112-26.
20. Fernandez DM, Rahman AH, Fernandez NF, Chudnovskiy A, Amir ED, Amadori L, et al. Single-cell immune landscape of human atherosclerotic plaques. *Nat Med*. 2019;25(10):1576-88.
21. Cochain C, Vafadarnejad E, Arampatzi P, Pelisek J, Winkels H, Ley K, et al. Single-Cell RNA-Seq Reveals the Transcriptional Landscape and Heterogeneity of Aortic Macrophages in Murine Atherosclerosis. *Circ Res*. 2018;122(12):1661-74.
22. Winkels H, Ehinger E, Vassallo M, Buscher K, Dinh HQ, Kobiyama K, et al. Atlas of the Immune Cell Repertoire in Mouse Atherosclerosis Defined by Single-Cell RNA-Sequencing and Mass Cytometry. *Circ Res*. 2018;122(12):1675-88.
23. Kim K, Shim D, Lee JS, Zaitsev K, Williams JW, Kim KW, et al. Transcriptome Analysis Reveals Nonfoamy Rather Than Foamy Plaque Macrophages Are Proinflammatory in Atherosclerotic Murine Models. *Circ Res*. 2018;123(10):1127-42.
24. Cole JE, Park I, Ahern DJ, Kassiteridi C, Danso Abeam D, Goddard ME, et al. Immune cell census in murine atherosclerosis: cytometry by time of flight illuminates vascular myeloid cell diversity. *Cardiovasc Res*. 2018;114(10):1360-71.
25. Kalluri AS, Vellarikkal SK, Edelman ER, Nguyen L, Subramanian A, Ellinor PT, et al. Single-Cell Analysis of the Normal Mouse Aorta Reveals Functionally Distinct Endothelial Cell Populations. *Circulation*. 2019;140(2):147-63.
26. Zerneck A, Winkels H, Cochain C, Williams JW, Wolf D, Soehnlein O, et al. Meta-Analysis of Leukocyte Diversity in Atherosclerotic Mouse Aortas. *Circ Res*. 2020;127(3):402-26.
27. Wolf AA, Yanez A, Barman PK, Goodridge HS. The Ontogeny of Monocyte Subsets. *Front Immunol*. 2019;10:1642.
28. Jakubzick CV, Randolph GJ, Henson PM. Monocyte differentiation and antigen-presenting functions. *Nat Rev Immunol*. 2017;17(6):349-62.
29. Dai XM, Ryan GR, Hapel AJ, Dominguez MG, Russell RG, Kapp S, et al. Targeted disruption of the mouse colony-stimulating factor 1 receptor gene results in

- osteopetrosis, mononuclear phagocyte deficiency, increased primitive progenitor cell frequencies, and reproductive defects. *Blood*. 2002;99(1):111-20.
30. Williams M, Thierry GR, Bonnardel J, Bajenoff M. Establishment and Maintenance of the Macrophage Niche. *Immunity*. 2020;52(3):434-51.
 31. Friedman GD, Klatsky AL, Siegelau AB. The leukocyte count as a predictor of myocardial infarction. *N Engl J Med*. 1974;290(23):1275-8.
 32. Barron HV, Cannon CP, Murphy SA, Braunwald E, Gibson CM. Association between white blood cell count, epicardial blood flow, myocardial perfusion, and clinical outcomes in the setting of acute myocardial infarction: a thrombolysis in myocardial infarction 10 substudy. *Circulation*. 2000;102(19):2329-34.
 33. Cannon CP, McCabe CH, Wilcox RG, Bentley JH, Braunwald E. Association of white blood cell count with increased mortality in acute myocardial infarction and unstable angina pectoris. OPUS-TIMI 16 Investigators. *Am J Cardiol*. 2001;87(5):636-9, A10.
 34. Averill LE, Meagher RC, Gerrity RG. Enhanced monocyte progenitor cell proliferation in bone marrow of hyperlipemic swine. *Am J Pathol*. 1989;135(2):369-77.
 35. Feldman DL, Mogelesky TC, Liptak BF, Gerrity RG. Leukocytosis in rabbits with diet-induced atherosclerosis. *Arterioscler Thromb*. 1991;11(4):985-94.
 36. Lessner SM, Prado HL, Waller EK, Galis ZS. Atherosclerotic lesions grow through recruitment and proliferation of circulating monocytes in a murine model. *Am J Pathol*. 2002;160(6):2145-55.
 37. Geissmann F, Jung S, Littman DR. Blood monocytes consist of two principal subsets with distinct migratory properties. *Immunity*. 2003;19(1):71-82.
 38. Sunderkotter C, Nikolic T, Dillon MJ, Van Rooijen N, Stehling M, Drevets DA, et al. Subpopulations of mouse blood monocytes differ in maturation stage and inflammatory response. *J Immunol*. 2004;172(7):4410-7.
 39. Chong SZ, Evrard M, Devi S, Chen J, Lim JY, See P, et al. CXCR4 identifies transitional bone marrow premonocytes that replenish the mature monocyte pool for peripheral responses. *J Exp Med*. 2016;213(11):2293-314.
 40. Hanna RN, Carlin LM, Hubbeling HG, Nackiewicz D, Green AM, Punt JA, et al. The transcription factor NR4A1 (Nur77) controls bone marrow differentiation and the survival of Ly6C⁺ monocytes. *Nat Immunol*. 2011;12(8):778-85.
 41. Auffray C, Fogg D, Garfa M, Elain G, Join-Lambert O, Kayal S, et al. Monitoring of blood vessels and tissues by a population of monocytes with patrolling behavior. *Science*. 2007;317(5838):666-70.
 42. Carlin LM, Stamatiades EG, Auffray C, Hanna RN, Glover L, Vizcay-Barrena G, et al. Nr4a1-dependent Ly6C^{low} monocytes monitor endothelial cells and orchestrate their disposal. *Cell*. 2013;153(2):362-75.
 43. Weber C, Belge KU, von Hundelshausen P, Draude G, Steppich B, Mack M, et al. Differential chemokine receptor expression and function in human monocyte subpopulations. *J Leukoc Biol*. 2000;67(5):699-704.
 44. Palframan RT, Jung S, Cheng G, Weninger W, Luo Y, Dorf M, et al. Inflammatory chemokine transport and presentation in HEV: a remote

- control mechanism for monocyte recruitment to lymph nodes in inflamed tissues. *J Exp Med*. 2001;194(9):1361-73.
45. Dyer DP, Medina-Ruiz L, Bartolini R, Schuette F, Hughes CE, Pallas K, et al. Chemokine Receptor Redundancy and Specificity Are Context Dependent. *Immunity*. 2019;50(2):378-89.e5.
 46. Swirski FK, Libby P, Aikawa E, Alcaide P, Luscinskas FW, Weissleder R, et al. Ly-6Chi monocytes dominate hypercholesterolemia-associated monocytosis and give rise to macrophages in atheromata. *J Clin Invest*. 2007;117(1):195-205.
 47. Tacke F, Alvarez D, Kaplan TJ, Jakubzick C, Spanbroek R, Llodra J, et al. Monocyte subsets differentially employ CCR2, CCR5, and CX3CR1 to accumulate within atherosclerotic plaques. *J Clin Invest*. 2007;117(1):185-94.
 48. Imhof BA, Aurrand-Lions M. Adhesion mechanisms regulating the migration of monocytes. *Nat Rev Immunol*. 2004;4(6):432-44.
 49. Ley K, Laudanna C, Cybulsky MI, Nourshargh S. Getting to the site of inflammation: the leukocyte adhesion cascade updated. *Nat Rev Immunol*. 2007;7(9):678-89.
 50. Verweij SL, Duivenvoorden R, Stiekema LCA, Nurmohamed NS, van der Valk FM, Versloot M, et al. CCR2 expression on circulating monocytes is associated with arterial wall inflammation assessed by 18F-FDG PET/CT in patients at risk for cardiovascular disease. *Cardiovasc Res*. 2018;114(3):468-75.
 51. Yoshida H, Hayashi S, Kunisada T, Ogawa M, Nishikawa S, Okamura H, et al. The murine mutation osteopetrosis is in the coding region of the macrophage colony stimulating factor gene. *Nature*. 1990;345(6274):442-4.
 52. Qiao JH, Tripathi J, Mishra NK, Cai Y, Tripathi S, Wang XP, et al. Role of macrophage colony-stimulating factor in atherosclerosis: studies of osteopetrotic mice. *Am J Pathol*. 1997;150(5):1687-99.
 53. Smith JD, Trogan E, Ginsberg M, Grigaux C, Tian J, Miyata M. Decreased atherosclerosis in mice deficient in both macrophage colony-stimulating factor (op) and apolipoprotein E. *Proc Natl Acad Sci U S A*. 1995;92(18):8264-8.
 54. Rajavashisth T, Qiao JH, Tripathi S, Tripathi J, Mishra N, Hua M, et al. Heterozygous osteopetrotic (op) mutation reduces atherosclerosis in LDL receptor-deficient mice. *J Clin Invest*. 1998;101(12):2702-10.
 55. Boring L, Gosling J, Cleary M, Charo IF. Decreased lesion formation in CCR2^{-/-} mice reveals a role for chemokines in the initiation of atherosclerosis. *Nature*. 1998;394(6696):894-7.
 56. Gu L, Okada Y, Clinton SK, Gerard C, Sukhova GK, Libby P, et al. Absence of monocyte chemoattractant protein-1 reduces atherosclerosis in low density lipoprotein receptor-deficient mice. *Mol Cell*. 1998;2(2):275-81.
 57. Ingersoll MA, Spanbroek R, Lottaz C, Gautier EL, Frankenberger M, Hoffmann R, et al. Comparison of gene expression profiles between human and mouse monocyte subsets. *Blood*. 2010;115(3):e10-9.
 58. Ait-Oufella H, Taleb S, Mallat Z, Tedgui A. Recent advances on the role of cytokines in atherosclerosis. *Arterioscler Thromb Vasc Biol*. 2011;31(5):969-79.

59. Galea J, Armstrong J, Gadsdon P, Holden H, Francis SE, Holt CM. Interleukin-1 beta in coronary arteries of patients with ischemic heart disease. *Arterioscler Thromb Vasc Biol.* 1996;16(8):1000-6.
60. Kirii H, Niwa T, Yamada Y, Wada H, Saito K, Iwakura Y, et al. Lack of interleukin-1beta decreases the severity of atherosclerosis in ApoE-deficient mice. *Arterioscler Thromb Vasc Biol.* 2003;23(4):656-60.
61. Isoda K, Sawada S, Ishigami N, Matsuki T, Miyazaki K, Kusuhara M, et al. Lack of interleukin-1 receptor antagonist modulates plaque composition in apolipoprotein E-deficient mice. *Arterioscler Thromb Vasc Biol.* 2004;24(6):1068-73.
62. Gomez D, Baylis RA, Durgin BG, Newman AAC, Alencar GF, Mahan S, et al. Interleukin-1beta has atheroprotective effects in advanced atherosclerotic lesions of mice. *Nat Med.* 2018;24(9):1418-29.
63. Ridker PM, MacFadyen JG, Everett BM, Libby P, Thuren T, Glynn RJ, et al. Relationship of C-reactive protein reduction to cardiovascular event reduction following treatment with canakinumab: a secondary analysis from the CANTOS randomised controlled trial. *Lancet.* 2018;391(10118):319-28.
64. Ridker PM, Everett BM, Thuren T, MacFadyen JG, Chang WH, Ballantyne C, et al. Antiinflammatory Therapy with Canakinumab for Atherosclerotic Disease. *N Engl J Med.* 2017;377(12):1119-31.
65. Doran AC, Yurdagul A Jr, Tabas I. Efferocytosis in health and disease. *Nat Rev Immunol.* 2020;20(4):254-67.
66. Bianconi E, Piovesan A, Facchin F, Beraudi A, Casadei R, Frabetti F, et al. An estimation of the number of cells in the human body. *Ann Hum Biol.* 2013;40(6):463-71.
67. Wolf Y, Boura-Halfon S, Cortese N, Haimon Z, Sar Shalom H, Kuperman Y, et al. Brown-adipose-tissue macrophages control tissue innervation and homeostatic energy expenditure. *Nat Immunol.* 2017;18(6):665-74.
68. Kohyama M, Ise W, Edelson BT, Wilker PR, Hildner K, Mejia C, et al. Role for Spi-C in the development of red pulp macrophages and splenic iron homeostasis. *Nature.* 2009;457(7227):318-21.
69. Schulz C, Gomez Perdiguero E, Chorro L, Szabo-Rogers H, Cagnard N, Kierdorf K, et al. A lineage of myeloid cells independent of Myb and hematopoietic stem cells. *Science.* 2012;336(6077):86-90.
70. Gomez Perdiguero E, Klapproth K, Schulz C, Busch K, Azzoni E, Crozet L, et al. Tissue-resident macrophages originate from yolk-sac-derived erythro-myeloid progenitors. *Nature.* 2015;518(7540):547-51.
71. Guilliams M, De Kleer I, Henri S, Post S, Vanhoutte L, De Prijck S, et al. Alveolar macrophages develop from fetal monocytes that differentiate into long-lived cells in the first week of life via GM-CSF. *J Exp Med.* 2013;210(10):1977-92.
72. Bain CC, Mowat AM. Macrophages in intestinal homeostasis and inflammation. *Immunol Rev.* 2014;260(1):102-17.
73. Epelman S, Lavine KJ, Beaudin AE, Sojka DK, Carrero JA, Calderon B, et al. Embryonic and adult-derived resident cardiac macrophages are maintained through distinct mechanisms at steady state and during inflammation. *Immunity.* 2014;40(1):91-104.

74. Silva HM, Bafica A, Rodrigues-Luiz GF, Chi J, Santos PDA, Reis BS, et al. Vasculature-associated fat macrophages readily adapt to inflammatory and metabolic challenges. *J Exp Med*. 2019;216(4):786-806.
75. Wang Y, Szretter KJ, Vermi W, Gilfillan S, Rossini C, Cella M, et al. IL-34 is a tissue-restricted ligand of CSF1R required for the development of Langerhans cells and microglia. *Nat Immunol*. 2012;13(8):753-60.
76. Ivanov S, Gallerand A, Gros M, Stunault MI, Merlin J, Vaillant N, et al. Mesothelial cell CSF1 sustains peritoneal macrophage proliferation. *Eur J Immunol*. 2019;49(11):2012-8.
77. Chakarov S, Lim HY, Tan L, Lim SY, See P, Lum J, et al. Two distinct interstitial macrophage populations coexist across tissues in specific subtissular niches. *Science*. 2019;363(6432):eaau0964.
78. Cochain C, Saliba AE, Zerneck A. Letter by Cochain et al Regarding Article, "Transcriptome Analysis Reveals Nonfoamy Rather Than Foamy Plaque Macrophages Are Proinflammatory in Atherosclerotic Murine Models". *Circ Res*. 2018;123(11):e48-9.
79. Kim K, Choi JH. Response by Kim and Choi to Letter Regarding Article, "Transcriptome Analysis Reveals Nonfoamy Rather Than Foamy Plaque Macrophages Are Proinflammatory in Atherosclerotic Murine Models". *Circ Res*. 2018;123(11):e50.
80. Satpathy AT, Kc W, Albring JC, Edelson BT, Kretzer NM, Bhattacharya D, et al. Zbtb46 expression distinguishes classical dendritic cells and their committed progenitors from other immune lineages. *J Exp Med*. 2012;209(6):1135-52.
81. Meredith MM, Liu K, Darrasse-Jeze G, Kamphorst AO, Schreiber HA, Guermonprez P, et al. Expression of the zinc finger transcription factor zDC (Zbtb46, Btbd4) defines the classical dendritic cell lineage. *J Exp Med*. 2012;209(6):1153-65.
82. Murphy TL, Grajales-Reyes GE, Wu X, Tussiwand R, Briseno CG, Iwata A, et al. Transcriptional Control of Dendritic Cell Development. *Annu Rev Immunol*. 2016;34:93-119.
83. Doring Y, Zerneck A. Plasmacytoid dendritic cells in atherosclerosis. *Front Physiol*. 2012;3:230.
84. Jensen J, Vazquez-Torres A, Balish E. Poly(I:C)-induced interferons enhance susceptibility of SCID mice to systemic candidiasis. *Infect Immun*. 1992;60(11):4549-57.
85. Thacker SG, Zhao W, Smith CK, Luo W, Wang H, Vivekanandan-Giri A, et al. Type I interferons modulate vascular function, repair, thrombosis, and plaque progression in murine models of lupus and atherosclerosis. *Arthritis Rheum*. 2012;64(9):2975-85.
86. Ait-Oufella H, Sage AP, Mallat Z, Tedgui A. Adaptive (T and B cells) immunity and control by dendritic cells in atherosclerosis. *Circ Res*. 2014;114(10):1640-60.
87. Weber C, Meiler S, Doring Y, Koch M, Drechsler M, Megens RT, et al. CCL17-expressing dendritic cells drive atherosclerosis by restraining regulatory T cell homeostasis in mice. *J Clin Invest*. 2011;121(7):2898-910.
88. Kimura T, Kobiyama K, Winkels H, Tse K, Miller J, Vassallo M, et al. Regulatory CD4(+) T Cells Recognize Major Histocompatibility Complex Class II Molecule-

- Restricted Peptide Epitopes of Apolipoprotein B. *Circulation*. 2018;138(11):1130-43.
89. Kimura T, Tse K, McArdle S, Gerhardt T, Miller J, Mikulski Z, et al. Atheroprotective vaccination with MHC-II-restricted ApoB peptides induces peritoneal IL-10-producing CD4 T cells. *Am J Physiol Heart Circ Physiol*. 2017;312(4):H781-90.
 90. Tse K, Gonen A, Sidney J, Ouyang H, Witztum JL, Sette A, et al. Atheroprotective Vaccination with MHC-II Restricted Peptides from ApoB-100. *Front Immunol*. 2013;4:493.
 91. Lin Z, Qian S, Gong Y, Ren J, Zhao L, Wang D, et al. Deep sequencing of the T cell receptor beta repertoire reveals signature patterns and clonal drift in atherosclerotic plaques and patients. *Oncotarget*. 2017;8(59):99312-22.
 92. Paulsson G, Zhou X, Tornquist E, Hansson GK. Oligoclonal T cell expansions in atherosclerotic lesions of apolipoprotein E-deficient mice. *Arterioscler Thromb Vasc Biol*. 2000;20(1):10-7.
 93. Buono C, Pang H, Uchida Y, Libby P, Sharpe AH, Lichtman AH. B7-1/B7-2 costimulation regulates plaque antigen-specific T-cell responses and atherogenesis in low-density lipoprotein receptor-deficient mice. *Circulation*. 2004;109(16):2009-15.
 94. Haddad Y, Lahoute C, Clement M, Laurans L, Metghalchi S, Zeboudj L, et al. The Dendritic Cell Receptor DNGR-1 Promotes the Development of Atherosclerosis in Mice. *Circ Res*. 2017;121(3):234-43.
 95. Nathan C. Neutrophils and immunity: challenges and opportunities. *Nat Rev Immunol*. 2006;6(3):173-82.
 96. Doring Y, Drechsler M, Wantha S, Kemmerich K, Lievens D, Vijayan S, et al. Lack of neutrophil-derived CRAMP reduces atherosclerosis in mice. *Circ Res*. 2012;110(8):1052-6.
 97. Zerneck A, Bot I, Djalali-Talab Y, Shagdarsuren E, Bidzhekov K, Meiler S, et al. Protective role of CXC receptor 4/CXC ligand 12 unveils the importance of neutrophils in atherosclerosis. *Circ Res*. 2008;102(2):209-17.
 98. Naruko T, Ueda M, Haze K, van der Wal AC, van der Loos CM, Itoh A, et al. Neutrophil infiltration of culprit lesions in acute coronary syndromes. *Circulation*. 2002;106(23):2894-900.
 99. Rotzius P, Thams S, Soehnlein O, Kenne E, Tseng CN, Bjorkstrom NK, et al. Distinct infiltration of neutrophils in lesion shoulders in ApoE^{-/-} mice. *Am J Pathol*. 2010;177(1):493-500.
 100. Yang, Han Z, Oppenheim JJ. Alarmins and immunity. *Immunol Rev*. 2017;280(1):41-56.
 101. Pruenster M, Kurz AR, Chung KJ, Cao-Ehlker X, Bieber S, Nussbaum CF, et al. Extracellular MRP8/14 is a regulator of beta2 integrin-dependent neutrophil slow rolling and adhesion. *Nat Commun*. 2015;6:6915.
 102. Chen Q, Jin Y, Zhang K, Li H, Chen W, Meng G, et al. Alarmin HNP-1 promotes pyroptosis and IL-1beta release through different roles of NLRP3 inflammasome via P2X7 in LPS-primed macrophages. *Innate Immun*. 2014;20(3):290-300.

103. Willingham SB, Allen IC, Bergstralh DT, Brickey WJ, Huang MT, Taxman DJ, et al. NLRP3 (NALP3, Cryopyrin) facilitates in vivo caspase-1 activation, necrosis, and HMGB1 release via inflammasome-dependent and -independent pathways. *J Immunol.* 2009;183(3):2008-15.
104. Kahlenberg JM, Carmona-Rivera C, Smith CK, Kaplan MJ. Neutrophil extracellular trap-associated protein activation of the NLRP3 inflammasome is enhanced in lupus macrophages. *J Immunol.* 2013;190(3):1217-26.
105. Soehnlein O, Zernecke A, Eriksson EE, Rothfuchs AG, Pham CT, Herwald H, et al. Neutrophil secretion products pave the way for inflammatory monocytes. *Blood.* 2008;112(4):1461-71.
106. Qi H, Yang S, Zhang L. Neutrophil Extracellular Traps and Endothelial Dysfunction in Atherosclerosis and Thrombosis. *Front Immunol.* 2017;8:928.
107. Schuster S, Hurrell B, Tacchini-Cottier F. Crosstalk between neutrophils and dendritic cells: a context-dependent process. *J Leukoc Biol.* 2013;94(4):671-5.
108. Narula J, Kolodgie FD, Virmani R. Apoptosis and cardiomyopathy. *Curr Opin Cardiol.* 2000;15(3):183-8.
109. Denny MF, Yalavarthi S, Zhao W, Thacker SG, Anderson M, Sandy AR, et al. A distinct subset of proinflammatory neutrophils isolated from patients with systemic lupus erythematosus induces vascular damage and synthesizes type I IFNs. *J Immunol.* 2010;184(6):3284-97.
110. Chavez-Sanchez L, Espinosa-Luna JE, Chavez-Rueda K, Legorreta-Haquet MV, Montoya-Diaz E, Blanco-Favela F. Innate immune system cells in atherosclerosis. *Arch Med Res.* 2014;45(1):1-14.
111. van Leeuwen M, Gijbels MJ, Duijvestijn A, Smook M, van de Gaar MJ, Heeringa P, et al. Accumulation of myeloperoxidase-positive neutrophils in atherosclerotic lesions in LDLR^{-/-} mice. *Arterioscler Thromb Vasc Biol.* 2008;28(1):84-9.
112. Aratani Y. Myeloperoxidase: Its role for host defense, inflammation, and neutrophil function. *Arch Biochem Biophys.* 2018;640:47-52.
113. Podrez EA, Schmitt D, Hoff HF, Hazen SL. Myeloperoxidase-generated reactive nitrogen species convert LDL into an atherogenic form in vitro. *J Clin Invest.* 1999;103(11):1547-60.
114. Khan MA, Palaniyar N. Transcriptional firing helps to drive NETosis. *Sci Rep.* 2017;7:41749.
115. Doring Y, Libby P, Soehnlein O. Neutrophil Extracellular Traps Participate in Cardiovascular Diseases: Recent Experimental and Clinical Insights. *Circ Res.* 2020;126(9):1228-41.
116. Sriranjana RS, Tarkin JM, Evans NR, Le EPV, Chowdhury MM, Rudd JHF. Atherosclerosis imaging using PET: Insights and applications. *Br J Pharmacol.* 2019. doi: 10.1111/bph.14868
117. Yamashita A, Zhao Y, Matsuura Y, Yamasaki K, Moriguchi-Goto S, Sugita C, et al. Increased metabolite levels of glycolysis and pentose phosphate pathway in rabbit atherosclerotic arteries and hypoxic macrophage. *PLoS One.* 2014;9(1):e86426.

118. Yvan-Charvet L, Pagler T, Gautier EL, Avagyan S, Siry RL, Han S, et al. ATP-binding cassette transporters and HDL suppress hematopoietic stem cell proliferation. *Science*. 2010;328(5986):1689-93.
119. Murphy AJ, Akhtari M, Tolani S, Pagler T, Bijl N, Kuo CL, et al. ApoE regulates hematopoietic stem cell proliferation, monocytosis, and monocyte accumulation in atherosclerotic lesions in mice. *J Clin Invest*. 2011;121(10):4138-49.
120. Wang M, Subramanian M, Abramowicz S, Murphy AJ, Gonen A, Witztum J, et al. Interleukin-3/granulocyte macrophage colony-stimulating factor receptor promotes stem cell expansion, monocytosis, and atheroma macrophage burden in mice with hematopoietic ApoE deficiency. *Arterioscler Thromb Vasc Biol*. 2014;34(5):976-84.
121. Morgan PK, Fang L, Lancaster GI, Murphy AJ. Hematopoiesis is regulated by cholesterol efflux pathways and lipid rafts: connections with cardiovascular diseases. *J Lipid Res*. 2020;61(5):667-75.
122. Hermetet F, Buffiere A, Aznague A, Pais de Barros JP, Bastie JN, Delva L, et al. High-fat diet disturbs lipid raft/TGF-beta signaling-mediated maintenance of hematopoietic stem cells in mouse bone marrow. *Nat Commun*. 2019;10(1):523.
123. Babaev VR, Runner RP, Fan D, Ding L, Zhang Y, Tao H, et al. Macrophage Mal1 deficiency suppresses atherosclerosis in low-density lipoprotein receptor-null mice by activating peroxisome proliferator-activated receptor-gamma-regulated genes. *Arterioscler Thromb Vasc Biol*. 2011;31(6):1283-90.
124. Takahashi M, Yagy H, Tazoe F, Nagashima S, Ohshiro T, Okada K, et al. Macrophage lipoprotein lipase modulates the development of atherosclerosis but not adiposity. *J Lipid Res*. 2013;54(4):1124-34.
125. Chang CL, Garcia-Arcos I, Nyren R, Olivecrona G, Kim JY, Hu Y, et al. Lipoprotein Lipase Deficiency Impairs Bone Marrow Myelopoiesis and Reduces Circulating Monocyte Levels. *Arterioscler Thromb Vasc Biol*. 2018;38(3):509-19.
126. Jordan S, Tung N, Casanova-Acebes M, Chang C, Cantoni C, Zhang D, et al. Dietary Intake Regulates the Circulating Inflammatory Monocyte Pool. *Cell*. 2019;178(5):1102-14.e17.
127. Fowler S, Shio H, Haley NJ. Characterization of lipid-laden aortic cells from cholesterol-fed rabbits. IV. Investigation of macrophage-like properties of aortic cell populations. *Lab Invest*. 1979;41(4):372-8.
128. Brown MS, Goldstein JL. Lipoprotein metabolism in the macrophage: implications for cholesterol deposition in atherosclerosis. *Annu Rev Biochem*. 1983;52:223-61.
129. Brown MS, Goldstein JL. A receptor-mediated pathway for cholesterol homeostasis. *Science*. 1986;232(4746):34-47.
130. Suzuki H, Kurihara Y, Takeya M, Kamada N, Kataoka M, Jishage K, et al. A role for macrophage scavenger receptors in atherosclerosis and susceptibility to infection. *Nature*. 1997;386(6622):292-6.
131. Kunjathoor VV, Febbraio M, Podrez EA, Moore KJ, Andersson L, Koehn S, et al. Scavenger receptors class A-I/II and CD36 are the principal receptors

- responsible for the uptake of modified low density lipoprotein leading to lipid loading in macrophages. *J Biol Chem.* 2002;277(51):49982-8.
132. Yvan-Charvet L, Ranalletta M, Wang N, Han S, Terasaka N, Li R, et al. Combined deficiency of ABCA1 and ABCG1 promotes foam cell accumulation and accelerates atherosclerosis in mice. *J Clin Invest.* 2007;117(12):3900-8.
 133. Accad M, Smith SJ, Newland DL, Sanan DA, King LE Jr, Linton MF, et al. Massive xanthomatosis and altered composition of atherosclerotic lesions in hyperlipidemic mice lacking acyl CoA:cholesterol acyltransferase 1. *J Clin Invest.* 2000;105(6):711-9.
 134. Duewell P, Kono H, Rayner KJ, Sirois CM, Vladimer G, Bauernfeind FG, et al. NLRP3 inflammasomes are required for atherogenesis and activated by cholesterol crystals. *Nature.* 2010;464(7293):1357-61.
 135. Schuster GU, Parini P, Wang L, Alberti S, Steffensen KR, Hansson GK, et al. Accumulation of foam cells in liver X receptor-deficient mice. *Circulation.* 2002;106(9):1147-53.
 136. Larrede S, Quinn CM, Jessup W, Frisdal E, Olivier M, Hsieh V, et al. Stimulation of cholesterol efflux by LXR agonists in cholesterol-loaded human macrophages is ABCA1-dependent but ABCG1-independent. *Arterioscler Thromb Vasc Biol.* 2009;29(11):1930-6.
 137. Calkin AC, Tontonoz P. Liver \times receptor signaling pathways and atherosclerosis. *Arterioscler Thromb Vasc Biol.* 2010;30(8):1513-8.
 138. Bischoff ED, Daige CL, Petrowski M, Dedman H, Pattison J, Juliano J, et al. Non-redundant roles for LXRA α and LXRB β in atherosclerosis susceptibility in low density lipoprotein receptor knockout mice. *J Lipid Res.* 2010;51(5):900-6.
 139. Westerterp M, Murphy AJ, Wang M, Pagler TA, Vengrenyuk Y, Kappus MS, et al. Deficiency of ATP-binding cassette transporters A1 and G1 in macrophages increases inflammation and accelerates atherosclerosis in mice. *Circ Res.* 2013;112(11):1456-65.
 140. Chinetti-Gbaguidi G, Baron M, Bouhrel MA, Vanhoutte J, Copin C, Sebti Y, et al. Human atherosclerotic plaque alternative macrophages display low cholesterol handling but high phagocytosis because of distinct activities of the PPAR γ and LXRA α pathways. *Circ Res.* 2011;108(8):985-95.
 141. Vats D, Mukundan L, Odegaard JI, Zhang L, Smith KL, Morel CR, et al. Oxidative metabolism and PGC-1 β attenuate macrophage-mediated inflammation. *Cell Metab.* 2006;4(1):13-24.
 142. Chinetti G, Lestavel S, Bocher V, Remaley AT, Neve B, Torra IP, et al. PPAR- α and PPAR- γ activators induce cholesterol removal from human macrophage foam cells through stimulation of the ABCA1 pathway. *Nat Med.* 2001;7(1):53-8.
 143. Chawla A, Boisvert WA, Lee CH, Laffitte BA, Barak Y, Joseph SB, et al. A PPAR γ -LXR-ABCA1 pathway in macrophages is involved in cholesterol efflux and atherogenesis. *Mol Cell.* 2001;7(1):161-71.
 144. Li AC, Binder CJ, Gutierrez A, Brown KK, Plotkin CR, Pattison JW, et al. Differential inhibition of macrophage foam-cell formation and atherosclerosis in mice by PPAR α , β / δ , and γ . *J Clin Invest.* 2004;114(11):1564-76.

145. Babaev VR, Ishiguro H, Ding L, Yancey PG, Dove DE, Kovacs WJ, et al. Macrophage expression of peroxisome proliferator-activated receptor- α reduces atherosclerosis in low-density lipoprotein receptor-deficient mice. *Circulation*. 2007;116(12):1404-12.
146. Rigamonti E, Chinetti-Gbaguidi G, Staels B. Regulation of macrophage functions by PPAR- α , PPAR- γ , and LXRs in mice and men. *Arterioscler Thromb Vasc Biol*. 2008;28(6):1050-9.
147. Dubois V, Eeckhoutte J, Lefebvre P, Staels B. Distinct but complementary contributions of PPAR isotypes to energy homeostasis. *J Clin Invest*. 2017;127(4):1202-14.
148. Viaud M, Ivanov S, Vujic N, Duta-Mare M, Aira LE, Barouillet T, et al. Lysosomal Cholesterol Hydrolysis Couples Efferocytosis to Anti-Inflammatory Oxysterol Production. *Circ Res*. 2018;122(10):1369-84.
149. Wild PS, Zeller T, Schillert A, Szymczak S, Sinning CR, Deiseroth A, et al. A genome-wide association study identifies LIPA as a susceptibility gene for coronary artery disease. *Circ Cardiovasc Genet*. 2011;4(4):403-12.
150. Evans TD, Zhang X, Clark RE, Alisio A, Song E, Zhang H, et al. Functional Characterization of LIPA (Lysosomal Acid Lipase) Variants Associated With Coronary Artery Disease. *Arterioscler Thromb Vasc Biol*. 2019;39(12):2480-91.
151. Horkko S, Bird DA, Miller E, Itabe H, Leitinger N, Subbanagounder G, et al. Monoclonal autoantibodies specific for oxidized phospholipids or oxidized phospholipid-protein adducts inhibit macrophage uptake of oxidized low-density lipoproteins. *J Clin Invest*. 1999;103(1):117-28.
152. Tsimikas S, Miyanohara A, Hartvigsen K, Merki E, Shaw PX, Chou MY, et al. Human oxidation-specific antibodies reduce foam cell formation and atherosclerosis progression. *J Am Coll Cardiol*. 2011;58(16):1715-27.
153. Que X, Hung MY, Yeang C, Gonen A, Prohaska TA, Sun X, et al. Oxidized phospholipids are proinflammatory and proatherogenic in hypercholesterolaemic mice. *Nature*. 2018;558(7709):301-6.
154. Palinski W, Tangirala RK, Miller E, Young SG, Witztum JL. Increased autoantibody titers against epitopes of oxidized LDL in LDL receptor-deficient mice with increased atherosclerosis. *Arterioscler Thromb Vasc Biol*. 1995;15(10):1569-76.
155. Harmon EY, Fronhofer V, 3rd, Keller RS, Feustel PJ, Zhu X, Xu H, et al. Anti-inflammatory immune skewing is atheroprotective: *Apoe*^{-/-}*FcgammaRIIb*^{-/-} mice develop fibrous carotid plaques. *J Am Heart Assoc*. 2014;3(6):e001232.
156. Pagano S, Magenta A, D'Agostino M, Martino F, Barilla F, Satta N, et al. Anti-ApoA-1 IgGs in Familial Hypercholesterolemia Display Paradoxical Associations with Lipid Profile and Promote Foam Cell Formation. *J Clin Med*. 2019;8(12):2035.
157. van den Berg VJ, Vroegindewey MM, Kardys I, Boersma E, Haskard D, Hartley A, et al. Anti-Oxidized LDL Antibodies and Coronary Artery Disease: A Systematic Review. *Antioxidants (Basel)*. 2019;8(10):484.
158. van Dierendonck X, de la Rosa Rodriguez MA, Georgiadi A, Mattijssen F, Dijk W, van Weeghel M, et al. HILPDA Uncouples Lipid Droplet Accumulation in

- Adipose Tissue Macrophages from Inflammation and Metabolic Dysregulation. *Cell Rep.* 2020;30(6):1811-22.e6.
159. Maier A, Wu H, Cordasic N, Oefner P, Dietel B, Thiele C, et al. Hypoxia-inducible protein 2 Hig2/Hilpda mediates neutral lipid accumulation in macrophages and contributes to atherosclerosis in apolipoprotein E-deficient mice. *FASEB J.* 2017;31(11):4971-84.
 160. Gomez I, Foudi N, Longrois D, Norel X. The role of prostaglandin E2 in human vascular inflammation. *Prostaglandins Leukot Essent Fatty Acids.* 2013;89(2-3):55-63.
 161. Spann NJ, Garmire LX, McDonald JG, Myers DS, Milne SB, Shibata N, et al. Regulated accumulation of desmosterol integrates macrophage lipid metabolism and inflammatory responses. *Cell.* 2012;151(1):138-52.
 162. Huang SC, Everts B, Ivanova Y, O'Sullivan D, Nascimento M, Smith AM, et al. Cell-intrinsic lysosomal lipolysis is essential for alternative activation of macrophages. *Nat Immunol.* 2014;15(9):846-55.
 163. Divakaruni AS, Hsieh WY, Minarrieta L, Duong TN, Kim KKO, Desousa BR, et al. Etomoxir Inhibits Macrophage Polarization by Disrupting CoA Homeostasis. *Cell Metab.* 2018;28(3):490-503.e7.
 164. Mogilenko DA, Haas JT, L'Homme L, Fleury S, Quemener S, Levavasseur M, et al. Metabolic and Innate Immune Cues Merge into a Specific Inflammatory Response via the UPR. *Cell.* 2019;177(5):1201-16.e19.
 165. Nomura M, Liu J, Rovira, II, Gonzalez-Hurtado E, Lee J, Wolfgang MJ, et al. Fatty acid oxidation in macrophage polarization. *Nat Immunol.* 2016;17(3):216-7.
 166. Marcovecchio PM, Thomas GD, Mikulski Z, Ehinger E, Mueller KAL, Blatchley A, et al. Scavenger Receptor CD36 Directs Nonclassical Monocyte Patrolling Along the Endothelium During Early Atherogenesis. *Arterioscler Thromb Vasc Biol.* 2017;37(11):2043-52.
 167. Febbraio M, Podrez EA, Smith JD, Hajjar DP, Hazen SL, Hoff HF, et al. Targeted disruption of the class B scavenger receptor CD36 protects against atherosclerotic lesion development in mice. *J Clin Invest.* 2000;105(8):1049-56.
 168. Seimon TA, Nadolski MJ, Liao X, Magallon J, Nguyen M, Feric NT, et al. Atherogenic lipids and lipoproteins trigger CD36-TLR2-dependent apoptosis in macrophages undergoing endoplasmic reticulum stress. *Cell Metab.* 2010;12(5):467-82.
 169. Kuchibhotla S, Vanegas D, Kennedy DJ, Guy E, Nimako G, Morton RE, et al. Absence of CD36 protects against atherosclerosis in ApoE knock-out mice with no additional protection provided by absence of scavenger receptor A I/II. *Cardiovasc Res.* 2008;78(1):185-96.
 170. Sheedy FJ, Grebe A, Rayner KJ, Kalantari P, Ramkhelawon B, Carpenter SB, et al. CD36 coordinates NLRP3 inflammasome activation by facilitating intracellular nucleation of soluble ligands into particulate ligands in sterile inflammation. *Nat Immunol.* 2013;14(8):812-20.
 171. Park YM, Febbraio M, Silverstein RL. CD36 modulates migration of mouse and human macrophages in response to oxidized LDL and may contribute to macrophage trapping in the arterial intima. *J Clin Invest.* 2009;119(1):136-45.

172. Gautier EL, Huby T, Saint-Charles F, Ouzilleau B, Pirault J, Deswaerte V, et al. Conventional dendritic cells at the crossroads between immunity and cholesterol homeostasis in atherosclerosis. *Circulation*. 2009;119(17):2367-75.
173. Birnberg T, Bar-On L, Sapoznikov A, Caton ML, Cervantes-Barragan L, Makia D, et al. Lack of conventional dendritic cells is compatible with normal development and T cell homeostasis, but causes myeloid proliferative syndrome. *Immunity*. 2008;29(6):986-97.
174. Paulson KE, Zhu SN, Chen M, Nurmohamed S, Jongstra-Bilen J, Cybulsky MI. Resident intimal dendritic cells accumulate lipid and contribute to the initiation of atherosclerosis. *Circ Res*. 2010;106(2):383-90.
175. Yun TJ, Lee JS, Machmach K, Shim D, Choi J, Wi YJ, et al. Indoleamine 2,3-Dioxygenase-Expressing Aortic Plasmacytoid Dendritic Cells Protect against Atherosclerosis by Induction of Regulatory T Cells. *Cell Metab*. 2016;23(5):852-66.
176. Macritchie N, Grassia G, Sabir SR, Maddaluno M, Welsh P, Sattar N, et al. Plasmacytoid dendritic cells play a key role in promoting atherosclerosis in apolipoprotein E-deficient mice. *Arterioscler Thromb Vasc Biol*. 2012;32(11):2569-79.
177. Doring Y, Manthey HD, Drechsler M, Lievens D, Megens RT, Soehnlein O, et al. Auto-antigenic protein-DNA complexes stimulate plasmacytoid dendritic cells to promote atherosclerosis. *Circulation*. 2012;125(13):1673-83.
178. Chen HJ, Tas SW, de Winther MPJ. Type-I interferons in atherosclerosis. *J Exp Med*. 2020;217(1):e20190459.
179. Daissormont IT, Christ A, Temmerman L, Sampedro Millares S, Seijkens T, Manca M, et al. Plasmacytoid dendritic cells protect against atherosclerosis by tuning T-cell proliferation and activity. *Circ Res*. 2011;109(12):1387-95.
180. Oh H, Mohler ER, 3rd, Tian A, Baumgart T, Diamond SL. Membrane cholesterol is a biomechanical regulator of neutrophil adhesion. *Arterioscler Thromb Vasc Biol*. 2009;29(9):1290-7.
181. Westerterp M, Fotakis P, Ouimet M, Bochem AE, Zhang H, Molusky MM, et al. Cholesterol Efflux Pathways Suppress Inflammasome Activation, NETosis, and Atherogenesis. *Circulation*. 2018;138(9):898-912.
182. Yvan-Charvet L, Ng LG. Granulopoiesis and Neutrophil Homeostasis: A Metabolic, Daily Balancing Act. *Trends Immunol*. 2019;40(7):598-612.
183. Yvan-Charvet L, Welch C, Pagler TA, Ranalletta M, Lamkanfi M, Han S, et al. Increased inflammatory gene expression in ABC transporter-deficient macrophages: free cholesterol accumulation, increased signaling via toll-like receptors, and neutrophil infiltration of atherosclerotic lesions. *Circulation*. 2008;118(18):1837-47.
184. Guasti L, Dentali F, Castiglioni L, Maroni L, Marino F, Squizzato A, et al. Neutrophils and clinical outcomes in patients with acute coronary syndromes and/or cardiac revascularisation. A systematic review on more than 34,000 subjects. *Thromb Haemost*. 2011;106(4):591-9.
185. Milligan G, Alvarez-Curto E, Hudson BD, Prihandoko R, Tobin AB. FFA4/GPR120: Pharmacology and Therapeutic Opportunities. *Trends Pharmacol Sci*. 2017;38(9):809-21.

186. Williams JW, Martel C, Potteaux S, Esaulova E, Ingersoll MA, Elvington A, et al. Limited Macrophage Positional Dynamics in Progressing or Regressing Murine Atherosclerotic Plaques-Brief Report. *Arterioscler Thromb Vasc Biol.* 2018;38(8):1702-10.
187. Ross S, Gerstein HC, Eikelboom J, Anand SS, Yusuf S, Pare G. Mendelian randomization analysis supports the causal role of dysglycaemia and diabetes in the risk of coronary artery disease. *Eur Heart J.* 2015;36(23):1454-62.
188. Ahmad OS, Morris JA, Mujammami M, Forgetta V, Leong A, Li R, et al. A Mendelian randomization study of the effect of type-2 diabetes on coronary heart disease. *Nat Commun.* 2015;6:7060.
189. Emami H, Singh P, MacNabb M, Vucic E, Lavender Z, Rudd JH, et al. Splenic metabolic activity predicts risk of future cardiovascular events: demonstration of a cardiosplenic axis in humans. *JACC Cardiovasc Imaging.* 2015;8(2):121-30.
190. Oburoglu L, Tardito S, Fritz V, de Barros SC, Merida P, Craveiro M, et al. Glucose and glutamine metabolism regulate human hematopoietic stem cell lineage specification. *Cell Stem Cell.* 2014;15(2):169-84.
191. Sarrazy V, Viaud M, Westerterp M, Ivanov S, Giorgetti-Peraldi S, Guinamard R, et al. Disruption of Glut1 in Hematopoietic Stem Cells Prevents Myelopoiesis and Enhanced Glucose Flux in Atheromatous Plaques of ApoE(-/-) Mice. *Circ Res.* 2016;118(7):1062-77.
192. Nagareddy PR, Murphy AJ, Stirzaker RA, Hu Y, Yu S, Miller RG, et al. Hyperglycemia promotes myelopoiesis and impairs the resolution of atherosclerosis. *Cell Metab.* 2013;17(5):695-708.
193. van der Valk FM, Kuijk C, Verweij SL, Stiekema LCA, Kaiser Y, Zeerleder S, et al. Increased haematopoietic activity in patients with atherosclerosis. *Eur Heart J.* 2017;38(6):425-32.
194. Freemerman AJ, Zhao L, Pingili AK, Teng B, Cozzo AJ, Fuller AM, et al. Myeloid Slc2a1-Deficient Murine Model Revealed Macrophage Activation and Metabolic Phenotype Are Fueled by GLUT1. *J Immunol.* 2019;202(4):1265-86.
195. Morioka S, Perry JSA, Raymond MH, Medina CB, Zhu Y, Zhao L, et al. Efferocytosis induces a novel SLC program to promote glucose uptake and lactate release. *Nature.* 2018;563(7733):714-8.
196. Fukuzumi M, Shinomiya H, Shimizu Y, Ohishi K, Utsumi S. Endotoxin-induced enhancement of glucose influx into murine peritoneal macrophages via GLUT1. *Infect Immun.* 1996;64(1):108-12.
197. Huang SC, Smith AM, Everts B, Colonna M, Pearce EL, Schilling JD, et al. Metabolic Reprogramming Mediated by the mTORC2-IRF4 Signaling Axis Is Essential for Macrophage Alternative Activation. *Immunity.* 2016;45(4):817-30.
198. Covarrubias AJ, Aksoylar HI, Yu J, Snyder NW, Worth AJ, Iyer SS, et al. Akt-mTORC1 signaling regulates Acly to integrate metabolic input to control of macrophage activation. *Elife.* 2016;5:e11612.
199. Namgaladze D, Zukunft S, Schnutgen F, Kurrle N, Fleming I, Fuhrmann D, et al. Polarization of Human Macrophages by Interleukin-4 Does Not Require ATP-Citrate Lyase. *Front Immunol.* 2018;9:2858.

200. Folco EJ, Sheikine Y, Rocha VZ, Christen T, Shvartz E, Sukhova GK, et al. Hypoxia but not inflammation augments glucose uptake in human macrophages: Implications for imaging atherosclerosis with ¹⁸fluorine-labeled 2-deoxy-D-glucose positron emission tomography. *J Am Coll Cardiol*. 2011;58(6):603-14.
201. Sluimer JC, Gasc JM, van Wanroij JL, Kisters N, Groeneweg M, Sollewijn Gelpke MD, et al. Hypoxia, hypoxia-inducible transcription factor, and macrophages in human atherosclerotic plaques are correlated with intraplaque angiogenesis. *J Am Coll Cardiol*. 2008;51(13):1258-65.
202. Bjornheden T, Levin M, Evaldsson M, Wiklund O. Evidence of hypoxic areas within the arterial wall in vivo. *Arterioscler Thromb Vasc Biol*. 1999;19(4):870-6.
203. Vink A, Schoneveld AH, Lamers D, Houben AJ, van der Groep P, van Diest PJ, et al. HIF-1 alpha expression is associated with an atheromatous inflammatory plaque phenotype and upregulated in activated macrophages. *Atherosclerosis*. 2007;195(2):e69-75.
204. Parathath S, Mick SL, Feig JE, Joaquin V, Grauer L, Habel DM, et al. Hypoxia is present in murine atherosclerotic plaques and has multiple adverse effects on macrophage lipid metabolism. *Circ Res*. 2011;109(10):1141-52.
205. Chaudhari SM, Sluimer JC, Koch M, Theelen TL, Manthey HD, Busch M, et al. Deficiency of HIF1alpha in Antigen-Presenting Cells Aggravates Atherosclerosis and Type 1 T-Helper Cell Responses in Mice. *Arterioscler Thromb Vasc Biol*. 2015;35(11):2316-25.
206. Aarup A, Pedersen TX, Junker N, Christoffersen C, Bartels ED, Madsen M, et al. Hypoxia-Inducible Factor-1alpha Expression in Macrophages Promotes Development of Atherosclerosis. *Arterioscler Thromb Vasc Biol*. 2016;36(9):1782-90.
207. Haschemi A, Kosma P, Gille L, Evans CR, Burant CF, Starkl P, et al. The sedoheptulose kinase CARKL directs macrophage polarization through control of glucose metabolism. *Cell Metab*. 2012;15(6):813-26.
208. Robbins CS, Hilgendorf I, Weber GF, Theurl I, Iwamoto Y, Figueiredo JL, et al. Local proliferation dominates lesional macrophage accumulation in atherosclerosis. *Nat Med*. 2013;19(9):1166-72.
209. Van den Bossche J, Baardman J, Otto NA, van der Velden S, Neele AE, van den Berg SM, et al. Mitochondrial Dysfunction Prevents Repolarization of Inflammatory Macrophages. *Cell Rep*. 2016;17(3):684-96.
210. Krawczyk CM, Holowka T, Sun J, Blagih J, Amiel E, DeBerardinis RJ, et al. Toll-like receptor-induced changes in glycolytic metabolism regulate dendritic cell activation. *Blood*. 2010;115(23):4742-9.
211. Everts B, Amiel E, van der Windt GJ, Freitas TC, Chott R, Yarasheski KE, et al. Commitment to glycolysis sustains survival of NO-producing inflammatory dendritic cells. *Blood*. 2012;120(7):1422-31.
212. Amiel E, Everts B, Fritz D, Beauchamp S, Ge B, Pearce EL, et al. Mechanistic target of rapamycin inhibition extends cellular lifespan in dendritic cells by preserving mitochondrial function. *J Immunol*. 2014;193(6):2821-30.
213. Thwe PM, Pelgrom LR, Cooper R, Beauchamp S, Reisz JA, D'Alessandro A, et al. Cell-Intrinsic Glycogen Metabolism Supports Early Glycolytic

- Reprogramming Required for Dendritic Cell Immune Responses. *Cell Metab.* 2017;26(3):558-67.e5.
214. Lu H, Yao K, Huang D, Sun A, Zou Y, Qian J, et al. High glucose induces upregulation of scavenger receptors and promotes maturation of dendritic cells. *Cardiovasc Diabetol.* 2013;12:80.
215. Borregaard N, Herlin T. Energy metabolism of human neutrophils during phagocytosis. *J Clin Invest.* 1982;70(3):550-7.
216. Riffelmacher T, Clarke A, Richter FC, Stranks A, Pandey S, Danielli S, et al. Autophagy-Dependent Generation of Free Fatty Acids Is Critical for Normal Neutrophil Differentiation. *Immunity.* 2017;47(3):466-80.e5.
217. Rodriguez-Espinosa O, Rojas-Espinosa O, Moreno-Altamirano MM, Lopez-Villegas EO, Sanchez-Garcia FJ. Metabolic requirements for neutrophil extracellular traps formation. *Immunology.* 2015;145(2):213-24.
218. Jha AK, Huang SC, Sergushichev A, Lampropoulou V, Ivanova Y, Loginicheva E, et al. Network integration of parallel metabolic and transcriptional data reveals metabolic modules that regulate macrophage polarization. *Immunity.* 2015;42(3):419-30.
219. Liu PS, Wang H, Li X, Chao T, Teav T, Christen S, et al. alpha-ketoglutarate orchestrates macrophage activation through metabolic and epigenetic reprogramming. *Nat Immunol.* 2017;18(9):985-94.
220. Tavakoli S, Downs K, Short JD, Nguyen HN, Lai Y, Jerabek PA, et al. Characterization of Macrophage Polarization States Using Combined Measurement of 2-Deoxyglucose and Glutamine Accumulation: Implications for Imaging of Atherosclerosis. *Arterioscler Thromb Vasc Biol.* 2017;37(10):1840-8.
221. Sonoki T, Nagasaki A, Gotoh T, Takiguchi M, Takeya M, Matsuzaki H, et al. Coinduction of nitric-oxide synthase and arginase I in cultured rat peritoneal macrophages and rat tissues in vivo by lipopolysaccharide. *J Biol Chem.* 1997;272(6):3689-93.
222. Ren B, Van Kampen E, Van Berkel TJ, Cruickshank SM, Van Eck M. Hematopoietic arginase 1 deficiency results in decreased leukocytosis and increased foam cell formation but does not affect atherosclerosis. *Atherosclerosis.* 2017;256:35-46.
223. Kierszenbaum F, Wirth JJ, McCann PP, Sjoerdsma A. Impairment of macrophage function by inhibitors of ornithine decarboxylase activity. *Infect Immun.* 1987;55(10):2461-4.
224. Tarasenko TN, Singh LN, Chatterji-Len M, Zerfas PM, Cusmano-Ozog K, McGuire PJ. Kupffer cells modulate hepatic fatty acid oxidation during infection with PR8 influenza. *Biochim Biophys Acta.* 2015;1852(11):2391-401.
225. Yurdagul A, Jr., Subramanian M, Wang X, Crown SB, Ilkayeva OR, Darville L, et al. Macrophage Metabolism of Apoptotic Cell-Derived Arginine Promotes Continual Efferocytosis and Resolution of Injury. *Cell Metab.* 2020;31(3):518-33.e10.
226. Ponnuswamy P, Ostermeier E, Schrottler A, Chen J, Huang PL, Ertl G, et al. Oxidative stress and compartment of gene expression determine

- proatherosclerotic effects of inducible nitric oxide synthase. *Am J Pathol.* 2009;174(6):2400-10.
227. Everts B, Amiel E, Huang SC, Smith AM, Chang CH, Lam WY, et al. TLR-driven early glycolytic reprogramming via the kinases TBK1-IKK ϵ supports the anabolic demands of dendritic cell activation. *Nat Immunol.* 2014;15(4):323-32.
228. Guak H, Al Habyan S, Ma EH, Aldossary H, Al-Masri M, Won SY, et al. Glycolytic metabolism is essential for CCR7 oligomerization and dendritic cell migration. *Nat Commun.* 2018;9(1):2463.
229. Liu J, Zhang X, Chen K, Cheng Y, Liu S, Xia M, et al. CCR7 Chemokine Receptor-Inducible Inc-Dpf3 Restrains Dendritic Cell Migration by Inhibiting HIF-1 α -Mediated Glycolysis. *Immunity.* 2019;50(3):600-15.e15.
230. Luchtefeld M, Grothusen C, Gagalick A, Jagavelu K, Schuett H, Tietge UJ, et al. Chemokine receptor 7 knockout attenuates atherosclerotic plaque development. *Circulation.* 2010;122(16):1621-8.
231. Potteaux S, Gautier EL, Hutchison SB, van Rooijen N, Rader DJ, Thomas MJ, et al. Suppressed monocyte recruitment drives macrophage removal from atherosclerotic plaques of Apo $e^{-/-}$ mice during disease regression. *J Clin Invest.* 2011;121(5):2025-36.
232. Wan W, Lionakis MS, Liu Q, Roffe E, Murphy PM. Genetic deletion of chemokine receptor Ccr7 exacerbates atherogenesis in ApoE-deficient mice. *Cardiovasc Res.* 2013;97(3):580-8.
233. Miller A, Nagy C, Knapp B, Laengle J, Ponweiser E, Groeger M, et al. Exploring Metabolic Configurations of Single Cells within Complex Tissue Microenvironments. *Cell Metab.* 2017;26(5):788-800.e6.

How to cite this article:

Gallerand A, Stunault MI, Merlin J, Guinamard RR, Yvan-Charvet L, Ivanov S. Myeloid Cell Diversity and Impact of Metabolic Cues during Atherosclerosis. *Immunometabolism.* 2020;2(4):e200028.
<https://doi.org/10.20900/immunometab20200028>

Lymphatic and Blood Network Analysis During Obesity

Rafael S Czepielewski^{*1}, Alexandre Gallerand^{*2,3}, Jérôme Gilleron^{2,4}, Narges Khedher^{2,3}, Gwendalyn J. Randolph¹, Stoyan Ivanov^{2,3}

¹ Department of Pathology and Immunology, Washington University School of Medicine ² Université Côte d'Azur ³ Mediterranean Center of Molecular Medicine C3M, Team 13, Institut National de la Santé et de la Recherche Médicale (Inserm) UMR1065 ⁴ Mediterranean Center of Molecular Medicine C3M, Team 7, Institut National de la Santé et de la Recherche Médicale (Inserm) UMR1065

* These authors contributed equally

Corresponding Author

Stoyan Ivanov

stoyan.ivanov@univ-cotedazur.fr

Citation

Czepielewski, R.S., Gallerand, A., Gilleron, J., Khedher, N., Randolph, G.J., Ivanov, S. Lymphatic and Blood Network Analysis During Obesity. *J. Vis. Exp.* (165), e61814, doi:10.3791/61814 (2020).

Date Published

November 19, 2020

DOI

10.3791/61814

URL

jove.com/video/61814

Abstract

Lymphatic collecting vessels and lymph nodes are inevitably embedded in adipose tissue. The physiological significance of this observation remains still not elucidated. However, obesity is characterized by impaired lymphatic function and increased vessel permeability. Inversely, lymphatic dysfunction induces obesity in mice, suggesting a significant interplay between lymphatic vessels and the adipose tissue. Therefore, understanding factors leading to lymphatic dysfunction might open new therapeutic windows to prevent obesity and associated comorbidities. The first step in this process requires a precise and detailed visualization of the lymphatic network in healthy and inflamed adipose tissue. Here, we describe a rapid, inexpensive, and efficient method that allows to label and analyze lymphatic and blood vessels. This approach takes advantage of the skin-draining brachial lymph node localization within the subcutaneous adipose tissue. The lymphatic arborization of this tissue can be revealed by injecting fluorochrome-conjugated lectins subcutaneously. Moreover, the in vivo labeling approach provides a way to evaluate lymphatic vessel density and functions. Coupled to blood vessel, adipocyte and immune cell staining, the protocol allows for high-resolution mapping of the subcutaneous adipose tissue by 3D imaging.

Introduction

The lymphatic circulatory system plays a crucial role in the maintenance of tissue homeostasis and the induction of efficient immune responses. Lymphatic vessels run parallel to blood vessels and carry interstitial fluid, metabolites, and immune cells to the local draining lymph node (LN) and finally towards the venous circulation¹. Dysfunctional lymphatic drainage has been observed during infection,

inflammation and metabolic diseases^{2,3,4,5}. The lymphatic vasculature is composed of small size vessels named lymphatic capillaries. Lymphatic capillaries are formed by a single layer of thin lymphatic endothelial cells (LECs) characterized by open junctions (“button-like” junctions) facilitating interstitial fluid, metabolites, and immune cells, mainly dendritic cells (DCs) and T cells, entry into the

lymphatic capillary lumen⁵. Lymphatic capillaries merge into larger vessels named lymphatic collecting vessels. Lymphatic collectors are characterized by a layer of LECs surrounded by a muscle layer providing autonomous contractile tonus and maintaining fluid flow⁵. Moreover, collecting vessels possess valves assuring a unidirectional lymph flow.

The LECs of collectors and capillaries express a specific set of markers that distinguish them from blood endothelial cells (BECs). Among those factors, Prox1 is a transcription factor guiding LECs generation and is highly expressed in LECs while absent in BECs. The critical involvement of Prox1 in LECs biology was illustrated by the generation and analysis of Prox1-deficient mice⁶. Prox1 heterozygous mice have a defective lymphatic vasculature development characterized by reduced lymphatic vessel density and increased vascular permeability⁶. LECs highly express VEGFR3, Podoplanin and CCL21⁵. Those markers are not found on BECs and allow to separately analyze the network of lymphatic and blood vessels. Lyve1 is selectively expressed by lymphatic capillaries while absent on collecting vessels⁵.

Three types of adipose tissue have been described based on their mitochondrial content and subsequent color. Mitochondria-rich thermogenic brown adipose tissue plays a key role during cold exposure and is located in the interscapular region in mice^{7,8}. White and beige adipocytes have lower mitochondrial density and are mainly involved in energy storing in the form of lipid droplets. White and beige adipocytes are located in visceral and subcutaneous depots⁹.

Clinical observations established a link between obesity and lymphatic dysfunction¹⁰. Obesity induces morphological changes of adipose tissue lymphatic vasculature and leads to an impaired lymph transport¹¹. Data obtained in pre-clinical models revealed that High Fat Diet (HFD) induces

a lymphatic remodeling and obese mice have smaller lymph nodes and fewer number of lymphatic vessels¹². Nevertheless, the precise molecular mechanisms governing this phenotype remain to be elucidated. LECs involvement during obesity is further supported by observations in genetic models with impaired lymphatic vessel development. As discussed earlier, Prox1 heterozygous mice (Prox1^{+/-}) present an ill-functioning lymphatic system, and coincidentally develop excessive visceral adipose tissue accumulation in comparison to Prox1 sufficient animals⁶. Interestingly, this adipose tissue phenotype is rescued by restoration of lymphatic function¹³. Together, these results have brought to light strong inter-connections between lymphatic vessels and the adipose tissue, which need further investigation.

In the context of inflammation, a hallmark of obesity, the altered expression of LEC and BEC markers compromises the analysis of these cells via classical antibody staining^{14,15}. Genetic models to label specifically LECs and BECs have been developed and allow to palliate this problem^{16,17,18,19}. However, the usage of genetic reporter lines requires multiple steps of breeding and considerably increases the length and cost of a project. Thus, we propose to use fluorochrome-conjugated lectin injections to investigate blood and lymphatic circulatory systems in the subcutaneous adipose tissue, a simple and relatively non-expensive approach. Lectin conjugated to various fluorochromes are commercially available and can be injected intravenously to label blood vessels, or subcutaneously to label the skin-draining lymphatic vessels embedded in the subcutaneous adipose tissue. This approach relies on the use of separate fluorochrome-lectin conjugates for each injection and allows the distinct labeling of each vasculature. This method is also compatible with the use of genetic models to label the lymphatic or blood vasculature network. Importantly, it

provides multiple readouts to analyze the overall health status of the subcutaneous adipose tissue and the blood and lymphatics vasculatures perfusing it. This procedure could be easily applied to analyze the lymphatic and blood vasculature networks during acute and chronic skin diseases including psoriasis and infections.

Protocol

All animal experimentation was performed in accordance with local ethical committees.

NOTE: Prox1-cre-ERT2 (Prox1tm3^(cre/ERT2)Gco/J, Jax #022075) and Rosa26-LSL-tdTomato (B6.Cg-Gt(ROSA)26Sortm9(CAG-tdTomato)Hze/J, Ai9, Jax #007914) were obtained from The Jackson Laboratory and crossed to obtain the inducible lymphatic reporter mouse line Prox1-cre-ERT2::tdTomato. Mice were backcrossed to C57BL/6 background for 10 generations. Six-week-old Prox1-cre-ERT2::tdTomato male mice received tamoxifen diet for 3 weeks. Tamoxifen diet from Envigo Teklad (diet no. TD.130857; 500 mg/kg) was used. Experiments were performed in 12-14-week-old mice. This protocol is applicable to mice of any age, sex or strain.

1. Material preparation

1. Sterilize scissors, forceps and dissecting pins using 70% ethanol.
2. Prepare two 1 mL syringes with 25 to 27 gauge needles. For subcutaneous injection we recommend using a micro-syringe to inject 10 μ L in the upper footpad.
3. In a plastic 1.5 mL tube, prepare 200 μ L of DyLight 488-conjugated lectin diluted in sterile PBS at a final concentration of 100 μ g/mL.

4. In another plastic, 1.5 mL tube prepare 100 μ L of DyLight 649-conjugated lectin diluted in sterile PBS at a final concentration of 100 μ g/mL.
5. Prepare a 6-well plate containing PBS and keep it on ice.
6. Prepare a solution of 4% paraformaldehyde and 30% sucrose.

2. Labeling of subcutaneous adipose tissue blood and lymphatic vessels.

1. Anesthetize the mouse by inhalation of 5% isoflurane. Assess anesthesia depth by firmly pinching the animal's paw to ensure that the animal is not harmed during the procedure. Anesthesia should be maintained until the end of the lectin injection steps or until euthanasia.
2. Inject 100 μ L of DyLight 488-conjugated lectin intravenously in the tail vein to label the blood vasculature. Wait 15 minutes before proceeding to tissue harvesting.
3. Using a different syringe, inject 10 μ L of DyLight 649-conjugated lectin subcutaneously on the upper footpad of the animal to label the draining lymphatic vessels. Wait 15 minutes before proceeding to tissue harvesting.
4. Euthanize the mouse by cervical dislocation or exposure to CO₂ 15 minutes post-injection.

3. Harvesting of subcutaneous adipose tissue

1. Lay the mouse on its back on a dissection board.
2. Sterilize the fur of the mouse using 70% ethanol.
3. Lift the skin of the flank using forceps and make a transversal incision to expose the brachial fat pad.
4. Gently pull on the skin to dissociate it from the brachial adipose tissue depot, thus revealing the entire

subcutaneous brachial adipose tissue containing the lymph node and the lymphatic collector vessel.

- Using forceps and scissors, gently remove subcutaneous fat depots and transfer them to a dish containing cold PBS. For best results, we recommend removing the fat depots as one single piece.
- From here on out, protect the tissue from light.

4. Tissue fixation

- Submerge the harvested tissue in a solution containing 4% paraformaldehyde and 30% sucrose.
- Incubate the tissue in this solution at least overnight before preparing it for imaging.

5. Staining and imaging

- For optimal results, perform tissue clearing and 3D confocal acquisition as described by Gilleron and colleagues²⁰. We recommend using a light sheet microscope for analysis of large tissues. Additional staining can be performed during the clearing process.
- To achieve best tissue mapping, use of the following antibodies:

For adipocytes: Perilipin

For macrophages: CD68 and CD11b staining.

For dendritic cells: MHC II and CD11b.

For B cells: B220 (CD45R) staining.

For T cells: CD3 staining.

NOTE: This method is compatible with the use of genetic models to label immune cells.

- For the analysis of the lymphatic collector vessel by intravital 2-photon microscopy, inject the lectin subcutaneously in the lower footpad and visualizing the popliteal lymphatic collecting vessel.

Representative Results

To perform topological analysis of brachial adipose tissue blood and lymphatic vessel networks, we subcutaneously injected Alexa Fluor 649-conjugated lectin, and intravenously injected Alexa Fluor 488-conjugated lectin. The brachial adipose tissue was carefully excised, fixed, submitted to clearing protocol, and analyzed by whole-mount staining. A schematic representation of the procedure is included in **Figure 1A**. Blood vessels are labeled in green and lymphatics are in red. The brachial adipose tissue contains a single lymphatic collector vessel that enters the brachial lymph node. We previously published the results obtained via this method¹⁶. Furthermore, we obtained similar data using genetic lymphatic labeling ($\text{Prox1}^{\text{creERT2}} \times \text{TdTomato}^{\text{fl/fl}}$ mice)¹⁶ (**Figure 1B**). The blood vasculature was efficiently labelled (in blue) following i.v. lectin injection. Of interest, subcutaneous lectin injection labelled the lymphatic collector vessel (in red) (**Figure 1B**). To ensure that lymphatic and blood vessels were labelled specifically, we took advantage of $\text{Prox1}^{\text{creERT2}} \times \text{TdTomato}^{\text{fl/fl}}$ mice. Subcutaneous lectin administration specifically labelled only the lymphatic vessels, as illustrated by the co-localization with the Prox1-reporter (**Figure 1B**). We also detected a second lymphatic collector vessel that stained positive for Prox1 but not for lectin injected subcutaneously (**Figure 1B**). This might be the efferent collector vessel leaving the brachial lymph node. The absence of lectin staining could be explained by: 1) a kinetic issue, assuming that 15 minutes are not sufficient for the lectin to exit from the draining lymph node; 2) insufficient amount of lectin injected, providing only a labelling in the first afferent collector and the brachial lymph node. Those points require further investigation and might be used to optimize the current protocol described in this manuscript. MHC II

staining (in green) revealed the presence of many antigen-presenting cells, likely dendritic cells, in the subcutaneous brachial adipose tissue (**Figure 1C**). The same observation was made in Prox1-reporter mice crossed to CD11c^{YFP}-reporter mice (**Figure 1D**).

To further confirm that the lectin labeling method specifically stains lymphatic vessels, we performed podoplanin staining

in the brachial adipose tissue extracted from CD11c-YFP reporter mice. Podoplanin staining efficiently labels lymphatic endothelial cells. Again, we obtained similar results to our lectin-injection method (**Figure 1E**). Thus, we believe that the protocol is well-suited for the analysis of lymphatic and blood vessels structure in healthy and inflamed adipose tissue. This procedure is highly and easily reproducible.

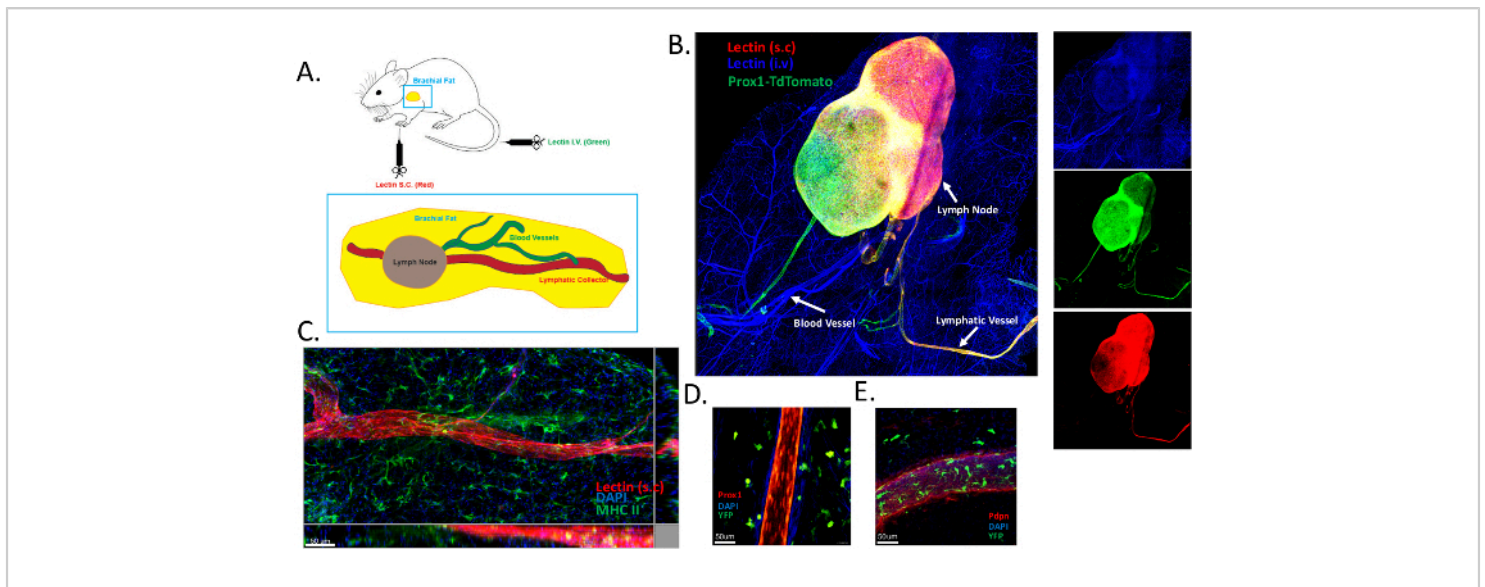


Figure 1: Labeling of blood and lymphatic vasculatures in the subcutaneous adipose tissue. (A) Schematic representation of brachial subcutaneous adipose tissue containing the brachial lymph node. DyLight 649–conjugated lectin (red) was injected subcutaneously (s.c) to visualize the draining lymphatic vasculature, and DyLight 488–conjugated lectin was administered intravenously (i.v) in order to map the blood vasculature. **(B)** Representative image illustrating blood (in blue) and lymphatic (red and green) labelling using the protocol described in panel **A**. Prox1-TdTomato (in green) mice were used in this experiment to ensure that lectins separately bound to blood and lymphatic endothelial cells. **(C)** Identification of the lymphatic collecting vessel in brachial subcutaneous adipose tissue using lectin administration. Antigen-presenting cells were labeled using MHC-II staining (green). **(D,E)** Identification of lymphatic vessels in the brachial subcutaneous adipose tissue of CD11c^{YFP} reporter mice crossed to Prox1^{Cre} x TdTomato^{fl/fl} mice (D) or stained for podoplanin (Pdnp) (E). [Please click here to view a larger version of this figure.](#)

Discussion

This approach provides efficient and robust labeling of the blood and lymphatic vasculatures of the subcutaneous

adipose tissue. The separate analysis of blood and lymphatic endothelial networks might unravel pathological mechanisms affecting one or both of the circulatory systems during obesity

or other pathological conditions. This protocol aims to analyze the architecture of the vascular systems, their interaction with stromal and immune cells, and their functionality during health and disease.

The method is facilitated by the presence of the brachial skin-draining lymph node, which is embedded in subcutaneous adipose tissue. As shown in **Figure 1**, the method provides similar results to genetic reporter labeling or antibody staining, while also being exempt of the caveats we discussed earlier. It not only provides a practical way of separately labeling blood and lymphatic vasculatures, but also provides multiple readouts on the functionality of the latter and on the overall health of the tissue. Notably, the appearance of the dye in the interstitial tissue space could indicate an increased vascular permeability. Moreover, the presence of the dye in the draining lymph node may be analyzed in a time-course fashion as a relative measure of the lymph flow rate.

Another parameter to take into account is the association of leukocytes with blood and lymphatic vessels. Immune cells, and particularly macrophages, dendritic cells and B cells, are known to play a key role in obesity²¹. Notably, we previously reported on the role played by dendritic cells in the control of lymphatic permeability¹⁶. We therefore highly suggest coupling labeling of blood and lymphatic vasculatures with labeling of subcutaneous adipose tissue immune cells to determine their localization relative to both vasculatures. Cell-type specific labeling can be achieved by traditional antibody staining or by the use of reporter mice (e.g., CD11c^{YFP}, CX3CR1^{GFP}, Zbtb46^{GFP}, LysM^{Cre} x tdTomato^{fl/fl}) in which case the fluorochromes used for lectin labeling must be adapted. Changes in adipocyte number or morphology can be appreciated using perilipin staining, which also provides a great way of mapping the tissue structure.

Lastly, although the methodology is described here to fit a 3D confocal imaging approach, we have previously adapted this protocol for intravital imaging¹⁶. This alternative approach has the benefit of providing additional information on immune cell motility within and around lymphatic collecting vessels, as well as vessel contractility. We therefore suggest lectin labeling of blood and lymphatic vasculatures as a versatile approach to study adipose tissue biology in health and disease.

Disclosures

The authors have no disclosure and conflict of interest to declare.

Acknowledgments

SI is supported by Institut National de la Sante et de la Recherche Medicale (INSERM) and Agence Nationale de la Recherche (ANR-17-CE14-0017-01 and ANR-19-ECVD-0005-01). AG is supported by the French government, through the UCAJedi Investments in the Future projects managed by the National Research Agency (ANR) with the reference number ANR-15-IDEX-01. RSC is supported by FA-2020-01-IBD-1 from the Lawrence C. Pakula, MD IBD Education & Innovation Fund”.

References

- Baluk, P. et al. Functionally specialized junctions between endothelial cells of lymphatic vessels. *Journal of Experimental Medicine*. **204** (10), 2349-2362 (2007).
- Fonseca, D. M. et al. Microbiota-Dependent Sequelae of Acute Infection Compromise Tissue-Specific Immunity. *Cell*. **163** (2), 354-366 (2015).
- Thomas, S. N. et al. Impaired humoral immunity and tolerance in K14-VEGFR-3-Ig mice that lack dermal

- lymphatic drainage. *The Journal of Immunology*. **189** (5), 2181-2190 (2012).
4. Kuan, E. L. et al. Collecting lymphatic vessel permeability facilitates adipose tissue inflammation and distribution of antigen to lymph node-homing adipose tissue dendritic cells. *The Journal of Immunology*. **194** (11), 5200-5210 (2015).
 5. Randolph, G. J., Ivanov, S., Zinselmeyer, B. H., Scallan, J. P. The Lymphatic System: Integral Roles in Immunity. *Annual Review of Immunology*. **35** 31-52 (2017).
 6. Harvey, N. L. et al. Lymphatic vascular defects promoted by Prox1 haploinsufficiency cause adult-onset obesity. *Nature Genetics*. **37** (10), 1072-1081 (2005).
 7. Kajimura, S., Spiegelman, B. M., Seale, P. Brown and Beige Fat: Physiological Roles beyond Heat Generation. *Cell Metabolism*. **22** (4), 546-559 (2015).
 8. Wu, J., Cohen, P., Spiegelman, B. M. Adaptive thermogenesis in adipocytes: is beige the new brown? *Genes and Development*. **27** (3), 234-250 (2013).
 9. Cinti, S. The adipose organ. *Prostaglandins, Leukotrienes & Essential Fatty Acids*. **73** (1), 9-15 (2005).
 10. Kataru, R. P. et al. Regulation of Lymphatic Function in Obesity. *Frontiers in Physiology*. **11** 459 (2020).
 11. Escobedo, N., Oliver, G. The Lymphatic Vasculature: Its Role in Adipose Metabolism and Obesity. *Cell Metabolism*. **26** (4), 598-609 (2017).
 12. Weitman, E. S. et al. Obesity impairs lymphatic fluid transport and dendritic cell migration to lymph nodes. *PLoS One*. **8** (8), e70703 (2013).
 13. Escobedo, N. et al. Restoration of lymphatic function rescues obesity in Prox1-haploinsufficient mice. *JCI Insight*. **1** (2) (2016).
 14. Commerford, C. D. et al. Mechanisms of Tumor-Induced Lymphovascular Niche Formation in Draining Lymph Nodes. *Cell Reports*. **25** (13), 3554-3563 e3554 (2018).
 15. Gregory, J. L. et al. Infection Programs Sustained Lymphoid Stromal Cell Responses and Shapes Lymph Node Remodeling upon Secondary Challenge. *Cell Reports*. **18** (2), 406-418 (2017).
 16. Ivanov, S. et al. CCR7 and IRF4-dependent dendritic cells regulate lymphatic collecting vessel permeability. *Journal of Clinical Investigation*. **126** (4), 1581-1591 (2016).
 17. Zhong, W. et al. Prox1-GFP/Flt1-DsRed transgenic mice: an animal model for simultaneous live imaging of angiogenesis and lymphangiogenesis. *Angiogenesis*. **20** (4), 581-598 (2017).
 18. Choi, I. et al. Visualization of lymphatic vessels by Prox1-promoter directed GFP reporter in a bacterial artificial chromosome-based transgenic mouse. *Blood*. **117** (1), 362-365 (2011).
 19. Pham, T. H. et al. Lymphatic endothelial cell sphingosine kinase activity is required for lymphocyte egress and lymphatic patterning. *Journal of Experimental Medicine*. **207** (1), 17-27 (2010).
 20. Gilleron, J. et al. Exploring Adipose Tissue Structure by Methylsalicylate Clearing and 3D Imaging. *Journal of Visualized Experiments*. (162) (2020).
 21. Ivanov, S., Merlin, J., Lee, M. K. S., Murphy, A. J., Guinamard, R. R. Biology and function of adipose tissue macrophages, dendritic cells and B cells. *Atherosclerosis*. **271** 102-110 (2018).



Escherichia coli Rho GTPase-activating toxin CNF1 mediates NLRP3 inflammasome activation via p21-activated kinases-1/2 during bacteraemia in mice

Océane Dufies¹, Anne Doye¹, Johan Courjon^{1,2}, Cédric Torre¹, Gregory Michel¹, Celine Loubatier¹, Arnaud Jacquet¹, Paul Chaintreuil¹, Alissa Major¹, Rodolphe R. Guinamard¹, Alexandre Gallerand¹, Pedro H. V. Saavedra³, Els Verhoeyen^{1,4}, Amaury Rey^{1,4}, Sandrine Marchetti¹, Raymond Ruimy^{1,2}, Dorota Czerucka^{5,6}, Mohamed Lamkanfi³, Bénédicte F. Py⁴, Patrick Munro¹, Orane Visvikis¹ and Laurent Boyer^{1,6} ✉

Inflammasomes are signalling platforms that are assembled in response to infection or sterile inflammation by cytosolic pattern recognition receptors. The consequent inflammasome-triggered caspase-1 activation is critical for the host defence against pathogens. During infection, NLRP3, which is a pattern recognition receptor that is also known as cryopyrin, triggers the assembly of the inflammasome-activating caspase-1 through the recruitment of ASC and Nek7. The activation of the NLRP3 inflammasome is tightly controlled both transcriptionally and post-translationally. Despite the importance of the NLRP3 inflammasome regulation in autoinflammatory and infectious diseases, little is known about the mechanism controlling the activation of NLRP3 and the upstream signalling that regulates the NLRP3 inflammasome assembly. We have previously shown that the Rho-GTPase-activating toxin from *Escherichia coli* cytotoxic necrotizing factor-1 (CNF1) activates caspase-1, but the upstream mechanism is unclear. Here, we provide evidence of the role of the NLRP3 inflammasome in sensing the activity of bacterial toxins and virulence factors that activate host Rho GTPases. We demonstrate that this activation relies on the monitoring of the toxin's activity on the Rho GTPase Rac2. We also show that the NLRP3 inflammasome is activated by a signalling cascade that involves the p21-activated kinases 1 and 2 (Pak1/2) and the Pak1-mediated phosphorylation of Thr 659 of NLRP3, which is necessary for the NLRP3-Nek7 interaction, inflammasome activation and IL-1 β cytokine maturation. Furthermore, inhibition of the Pak-NLRP3 axis decreases the bacterial clearance of CNF1-expressing UTI89 *E. coli* during bacteraemia in mice. Taken together, our results establish that Pak1 and Pak2 are critical regulators of the NLRP3 inflammasome and reveal the role of the Pak-NLRP3 signalling axis in vivo during bacteraemia in mice.

Uropathogenic *E. coli* is the leading causative agent of bacteraemia¹. It is therefore fundamental to decipher the mechanisms that determine the fate of this pathogen in the blood. The innate immune sensing of *E. coli* is mediated by pattern recognition receptors (PRRs), mainly by Toll-like receptor-4 (TLR4), which detects bacterial lipopolysaccharides (LPS). LPS are the principal component of the external membrane of both pathogenic and non-pathogenic *E. coli* and, therefore, pattern-triggered immunity does not seem to be sufficient to gauge the pathogenic potential of microorganisms. As TLR4 is activated by both live and dead bacteria, pattern-triggered immunity is certainly important for monitoring the quantity of bacteria, but is not sufficient to determine their quality². One strategy to determine microbial pathogenicity is the detection of virulence factor activities that are specific to pathogens³. Virulence factors of uropathogenic *E. coli* include CNF1, which is a Rho-GTPase-targeting toxin. The CNF1 toxin bears enzymatic activity that is responsible for the post-translational deamidation

of a specific glutamine residue on a subset of Rho GTPases, namely Rac, Cdc42 and RhoA^{4–6}. This modification destroys the intrinsic and GTPase-activating-protein- (GAP)-regulated ability of these Rho GTPases to hydrolyse GTP, conferring dominant positive mutant characteristics to Rho proteins^{4–6}. This modification increases GTP-bound activated Rho proteins and the activation of their downstream signalling pathways⁶. By modulating the host cytoskeleton, these virulence factors confer to bacteria invasion properties and the ability to modulate inflammatory responses^{7–10}. Among the virulence factors, there are more than 30 that target Rho GTPases. They are either activators or inhibitors of Rho GTPases, both of which activate caspase-1 (refs. ^{11,12}).

Inflammasomes are signalling platforms that are assembled by cytosolic PRRs that activate caspase-1. NLRP3 oligomerizes on infection or cellular damage, and recruits ASC, Nek7 and caspase-1 to form the NLRP3 inflammasome. This assembly results in ASC speck formation, cleavage of pro-caspase-1 into active caspase-1 and

¹Université Côte d'Azur, Inserm, C3M, Nice, France. ²Université Côte d'Azur, CHU Nice, Nice, France. ³Department of Internal Medicine and Pediatrics, Ghent University, Ghent, Belgium. ⁴CIRI, Centre International de Recherche en Infectiologie, Université de Lyon, Inserm U1111, Université Claude Bernard Lyon 1, CNRS UMR5308, ENS de Lyon, Lyon, France. ⁵Centre Scientifique de Monaco, Monaco, Monaco. ⁶LIA ROPSE, Laboratoire International Associé Université Côte d'Azur, Centre Scientifique de Monaco, Nice, France. ✉e-mail: laurent.boyer@univ-cotedazur.fr

the maturation of pro-IL-1 β into IL-1 β . The NLRP3 inflammasome assembly is controlled by both the priming by TLR ligands and activation signals. Furthermore, the NLRP3 inflammasome assembly is regulated by phosphorylation and ubiquitination events^{13,14}. Despite a variety of identified NLRP3 activators, the upstream signalling pathways that control NLRP3 post-translational modifications and activation mechanisms remain unclear¹⁴. Interestingly, toxins that inactivate Rho GTPases activate the Pyrin inflammasome through the modification of its phosphorylation status by the PKN1/2 kinases. The Pyrin inflammasome has been shown to detect toxins that inhibit Rho GTPases, but information about the sensing of toxins that activate Rho GTPases through inflammasomes is lacking^{15,16}. In this Article, we used the CNF1 toxin as a model of the Rho-GTPase-activating virulence factor to demonstrate the role of the Pak–NLRP3 axis in sensing CNF1 activity and controlling the clearance of bacteria during bacteraemia.

Results

CNF1-triggered immunity requires NLRP3. We set up an assay to monitor the CNF1-triggered activation of caspase-1 using a FAM-YVAD-FMK (FAM-FLICA) probe. Primary bone-marrow-derived macrophages (BMDMs) isolated from BALB/c mice were treated with CNF1 and analysed using confocal microscopy. Cells with dots of FAM-FLICA staining corresponding to ASC specks were counted (Extended Data Fig. 1a). This unbiased screen revealed that NLRP3 is the major NLR involved in CNF1-triggered caspase-1 activation (Fig. 1a). The role of NLRP3 in this pathway was confirmed in BMDMs isolated from C57BL/6J mice bearing ASC–citricine knockin using flow cytometry (Extended Data Fig. 1b,c). In this assay, we quantified the percentage of cells with ASC specks as previously described^{17,18}. These data revealed the conserved role of NLRP3 in the response to CNF1 in macrophages isolated from both BALB/c and C57BL/6J background.

Next, we investigated the role of NLRP3 in CNF1-triggered immunity. Co-treatment of BMDMs isolated from wild-type (WT) mice with the CNF1 toxin together with the NLRP3 inhibitor MCC950 was sufficient to block caspase-1 activity, demonstrating that the CNF1 toxin is an NLRP3 activator (Fig. 1b,c). Importantly, the number of FAM-FLICA⁺ cells was substantially reduced in BMDMs that were treated with catalytically inactive mutant CNF1^{C86S}. This result provided evidence that CNF1 toxin activity is monitored by NLRP3, rather than the pattern of the toxin³. Furthermore, CNF1-triggered maturation and secretion of IL-1 β and activation of caspase-1 was impaired in NLRP3-knockout BMDMs (Fig. 1d and Supplementary Fig. 1). By contrast, CNF1 treatment did not affect the secretion of IL-6 or TNF- α , two cytokines that are not regulated by inflammasomes (Fig. 1d and Supplementary Fig. 1). Activation of the NLRP3 inflammasome is often associated with pyroptosis¹⁹. To investigate whether CNF1 triggered pyroptosis, we measured propidium iodide incorporation (Extended Data Fig. 2a), lactate dehydrogenase (LDH) release (Extended Data Fig. 2b) and gasdermin D (GSDMD) cleavage (Extended Data Fig. 2c). In contrast to nigericin, we did not observe any of these pyroptosis markers after CNF1 treatment and we observed a similar level of CNF1-triggered caspase-1 activation and IL-1 β maturation/secretion in WT and GSDMD-knockout macrophages (Extended Data Fig. 2d,e). We subsequently tested the role of the NLRP3 inflammasome regulator Nek7 in CNF1-triggered immunity. Transfection of *Nlrp3* or *Nek7* short interfering RNA (siRNA) in BMDMs inhibited CNF1-triggered IL-1 β maturation (Extended Data Fig. 3a,b). K⁺ efflux is an upstream event for NLRP3 inflammasome activation and Nek7 requires K⁺ efflux for NLRP3 inflammasome assembly^{14,20}. We observed that KCl treatment was sufficient to inhibit CNF1-triggered caspase-1 cleavage (Extended Data Fig. 3c). Importantly, we confirmed that the KCl treatment did not inhibit CNF1 toxin activity towards Rho GTPase activation using a glutathione S-transferase (GST)–Pak–Rac-binding domain

(RBD) pull-down assay (Extended Data Fig. 3d). We next investigated whether other toxins that target Rho GTPases have the ability to activate the NLRP3 inflammasome. Dermonecrotic toxin (DNT) from *Bordetella* has transglutaminase activity towards Rho GTPases that enables the constitutive activation of Rho GTPases^{6,10}. We observed that purified recombinant DNT triggered the activation of caspase-1 in WT macrophages, but not in NLRP3-knockout macrophages (Extended Data Fig. 4a). We next tested whether the NLRP3 activation was triggered specifically by virulence factors activating Rho GTPases using NLRP3 inflammasome reconstitution in HEK293T cells²¹. Cells were transfected with plasmids encoding the DNT toxin or the injected bacterial virulence factors YopE from *Yersinia* containing a GAP domain that enables inactivation of the Rho GTPases⁶. We observed NLRP3-dependent IL-1 β maturation when cells were transfected with the Rho-GTPase-activating toxin DNT, but not when cells were transfected with the Rho GTPase inhibitor YopE (Extended Data Fig. 4b). The expression of the virulence factor SopE from *Salmonella* containing a guanine nucleotide exchange factor (GEF) domain activating Rac and Cdc42 (refs. 6,22) or the expression of the GEF domain of the Dbl exchange factor (Dbl^{495–826})²³ were sufficient to trigger NLRP3-dependent IL-1 β maturation (Extended Data Fig. 4b,c). Taken together, we showed that the activation of Rho GTPases by toxins and virulence factors triggered the activation of the NLRP3 inflammasome and that Rac has a major role in this pathway.

Activation of the NLRP3 inflammasome by CNF1 relies on Rac2 and the Pak serine–threonine kinases. Although the CNF1 toxin is a Rho GTPases activator and Rac2 is a haematopoietic-specific Rho GTPase that is involved in the innate immune response to the CNF1 toxin²⁴, the contribution of Rac1 and Rac2 in this process is still unknown. To investigate the role of Rac in the CNF1-triggered NLRP3 inflammasome activation, we knocked down *Rac1* and/or *Rac2* using siRNA in BMDMs. Interestingly, *Rac1* knockdown resulted in an increase in the level of CNF1-triggered IL-1 β maturation whereas *Rac2* knockdown was sufficient to block it (Fig. 2a). We tested whether activated GTP-bound Rac2 levels would increase when *Rac1* was targeted by siRNA. The GST–Pak–RBD pull-down analysis showed an increase in activated Rac2 when *Rac1* was knocked-down using siRNA (Fig. 2b). These data demonstrate the critical role of Rac2 in CNF1-triggered IL-1 β maturation (Fig. 2a,b). To determine the molecular mechanism of the caspase-1 activation, we used a system of NLRP3 inflammasome reconstitution in HEK293T cells. This analysis showed that CNF1 is sufficient for the NLRP3 inflammasome activation-triggered caspase-1 cleavage and that the co-treatment of CNF1 with MCC950 inhibited this caspase-1 activation (Fig. 2c). The transfection of Rac2 GTPase or activated mutant forms of Rac2 (including Q61E mimicking the CNF1 modification or Q61L and G12V) were sufficient to activate caspase-1, in contrast to the inactive mutant Rac2^{T17N} (Fig. 2d). Interestingly, the strength of caspase-1 activation observed using the activated forms of Rac2 GTPase was correlated with the amount of Rho GTPases that were bound to GST–Pak–RBD (Fig. 2e). These data indicate that NLRP3 senses the activation level of the Rho GTPase Rac2 proportionally to the strength of activation rather than by detecting the structural modification made by the toxin as it would be predicted for a classical PRR.

The correlation between caspase-1 activation and the amount of Rac2 bound to GST–Pak–RBD suggested a potential role of Pak kinases in CNF1-triggered NLRP3 inflammasome activation. We therefore knocked-down Pak1 and/or Pak2 in BMDMs by transfecting siRNA (Pak3 is predominantly expressed in the brain^{25,26}). We observed a major decrease in caspase-1 cleavage in cells treated with *Pak1* siRNA but a moderate impact when using siRNA targeting *Pak2*, indicating that Pak1 has a main role (Fig. 3a). However, we could not exclude the possibility that the total inhibition of

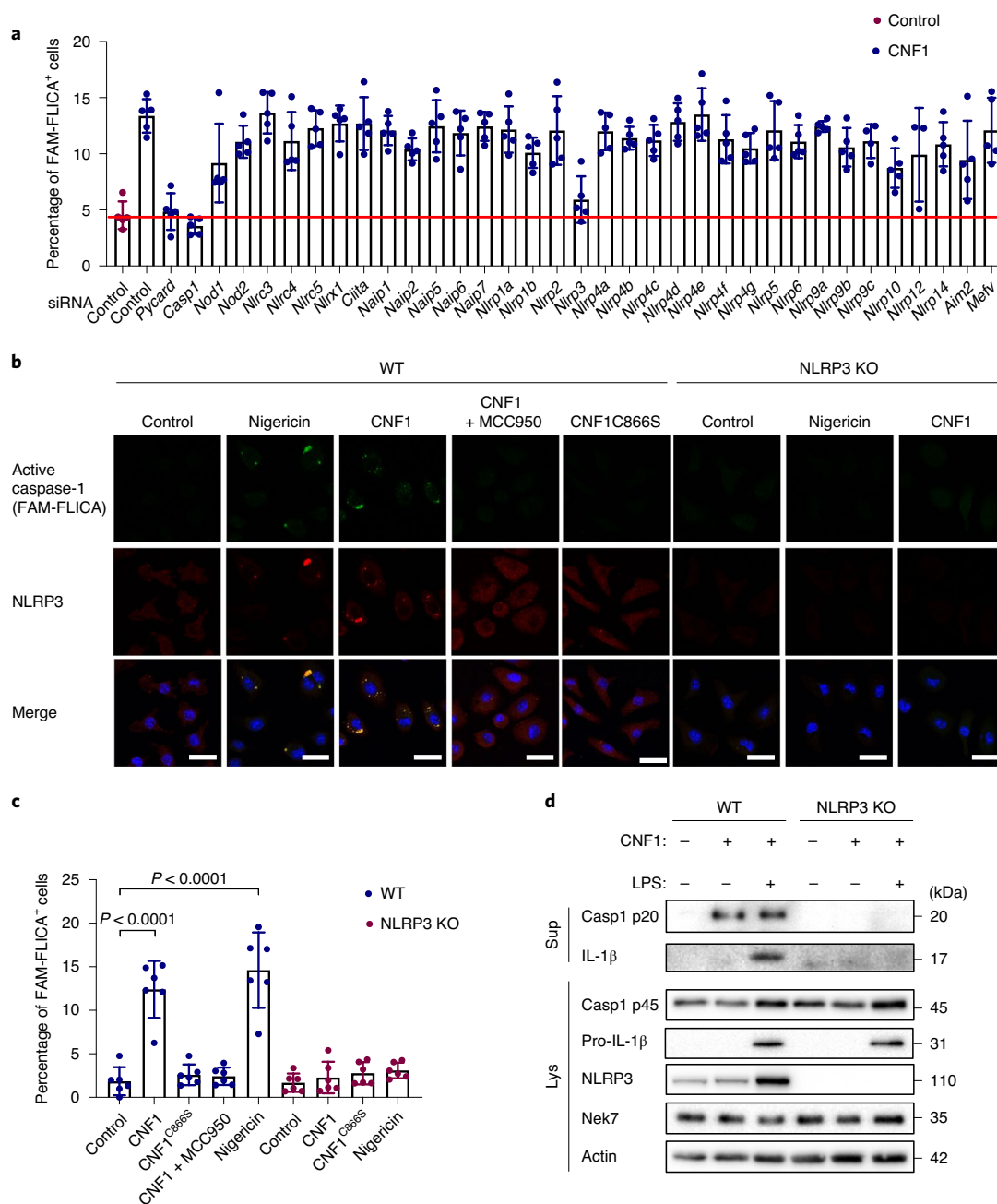


Fig. 1 | CNF1-triggered caspase-1 activation and IL-1 β maturation requires NLRP3. **a**, BMDMs isolated from BALB/c mice were transfected with the indicated siRNA for 72 h before treatment for 6 h with CNF1 (500 ng ml⁻¹). Active caspase-1 was detected using the FAM-FLICA probe. Cells harbouring FAM-FLICA dots were counted as positive using Fiji. The red horizontal line indicates the mean percentage of FAM-FLICA⁺ cells in the untreated control. Each dot represents 200 cells. $n = 1,800$ cells. Data are mean \pm s.e.m. **b, c**, BMDMs extracted from WT or NLRP3-knockout C57BL/6J mice were or were not pretreated for 45 min with MCC950 (1 μ M) before treatment for 6 h with CNF1 (500 ng ml⁻¹), or the CNF1 catalytic inactive mutant CNF1^{C866S} (500 ng ml⁻¹) or nigericin (5 μ M). **b**, Cells were analysed using immunofluorescence and confocal imaging. Active caspase-1 (FAM-FLICA) is shown in green, NLRP3 in red and nuclei in blue. Scale bars, 20 μ m. **c**, Quantification of FAM-FLICA⁺ cells in WT (blue) or NLRP3-knockout BMDMs (red). Each dot represents 100 cells. $n = 600$ cells. Data are mean \pm s.e.m. Statistical analyses were performed using two-tailed unpaired Student's *t*-tests. **d**, WT or NLRP3-knockout BMDMs were treated with CNF1 (500 ng ml⁻¹) and/or LPS (100 ng ml⁻¹) for 8 h before the supernatants (Sup) and cell lysates (Lys) were collected and analysed using immunoblotting. Experiments were repeated at least three times, and representative data are shown.

caspase-1 cleavage observed with the *Pak1* siRNA treatment might be due to a limit in the detection level of cleaved caspase-1, or to *Pak1* siRNA that may affect *Pak2*, suggesting that there is a partial *Pak1/2* redundancy. The treatment with *Pak1* inhibitors (IPA-3 or FRAX597) was sufficient to block the CNF1-triggered IL-1 β maturation that was observed in macrophages treated with LPS,

and was also sufficient to block caspase-1 activation (Fig. 3b,c). The inhibition of the caspase-1 cleavage after IPA-3 treatment was similarly observed in macrophages treated with DNT (Extended Data Fig. 4d). Interestingly, IPA-3 was shown to inhibit the binding of activated forms of Rac and Cdc42 to *Pak1*, thereby inhibiting the autophosphorylation of Thr423, whereas the FRAX597

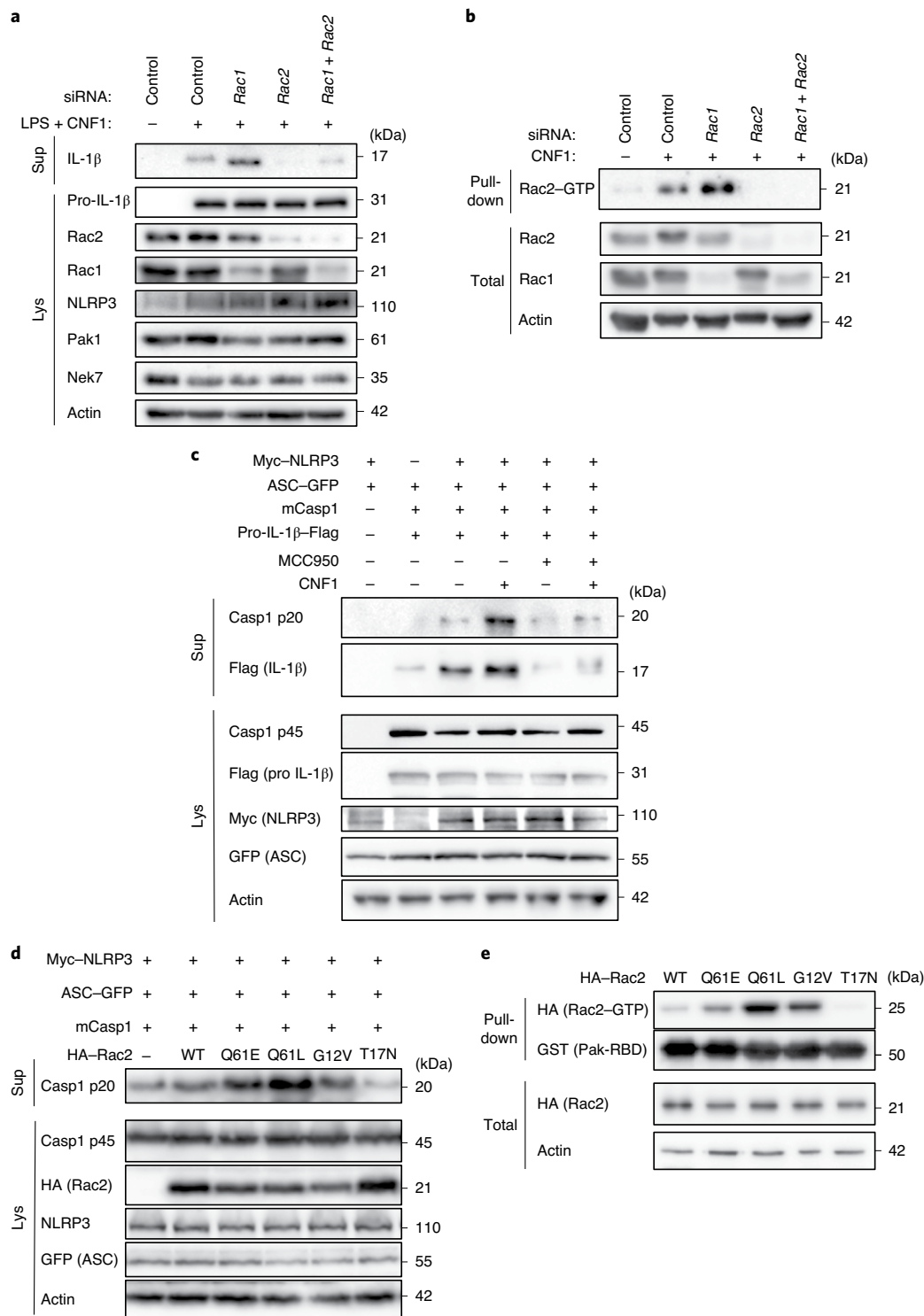


Fig. 2 | Rac2 activation triggers NLRP3 inflammasome activation. **a**, BMDMs extracted from BALB/c mice were transfected with siRNA targeting the indicated isoform of Rac GTPase for 72 h and treated with CNF1 (500 ng ml⁻¹) and LPS (100 ng ml⁻¹) for 8 h. Supernatants and cell lysates were analysed using immunoblotting. **b**, Immortalized BMDMs (iBMDMs) were transfected with the indicated siRNA for 72 h before being treated or not treated with CNF1 (500 ng ml⁻¹) for 6 h before analysis using a GST-Pak-RBD pull-down assay. The Rac2 associated with the GST-Pak-RBD beads is indicated as Rac2-GTP. **c,d**, HEK293T cells were transfected for 16 h with plasmids encoding NLRP3 inflammasome components: Myc-NLRP3, green fluorescent protein (GFP)-tagged ASC, mouse caspase-1 (mCasp1) and pro-IL-1 β -Flag as indicated, before analysing caspase-1 cleavage or pro-IL-1 β maturation using immunoblotting. **c**, Cells were pretreated or not with 1 μ M MCC950 for 45 min before treatment for 6 h with CNF1 (500 ng ml⁻¹). **d**, Cells were transfected with the following haemagglutinin (HA)-tagged mutants of Rac2: the constitutively active mutant mimicking CNF1-induced deamidation Rac2^{Q61E} (Q61E), the constitutively active mutants Rac2^{Q61L} (Q61L) or Rac2^{G12V} (G12V), or the dominant negative mutant Rac2^{T17N} (T17N). Supernatants and cell lysates were analysed using immunoblotting. **e**, HEK293T cells were transfected for 16 h with HA-tagged active mutants Rac2^{Q61E}, Rac2^{Q61L} or Rac2^{G12V}, or the dominant negative mutant Rac2^{T17N} before analysis using a GST-Pak-RBD pull-down assay. HA-Rac2 associated with the GST-Pak-RBD beads is indicated as Rac2-GTP. Experiments were repeated at least three times, and representative data are shown.

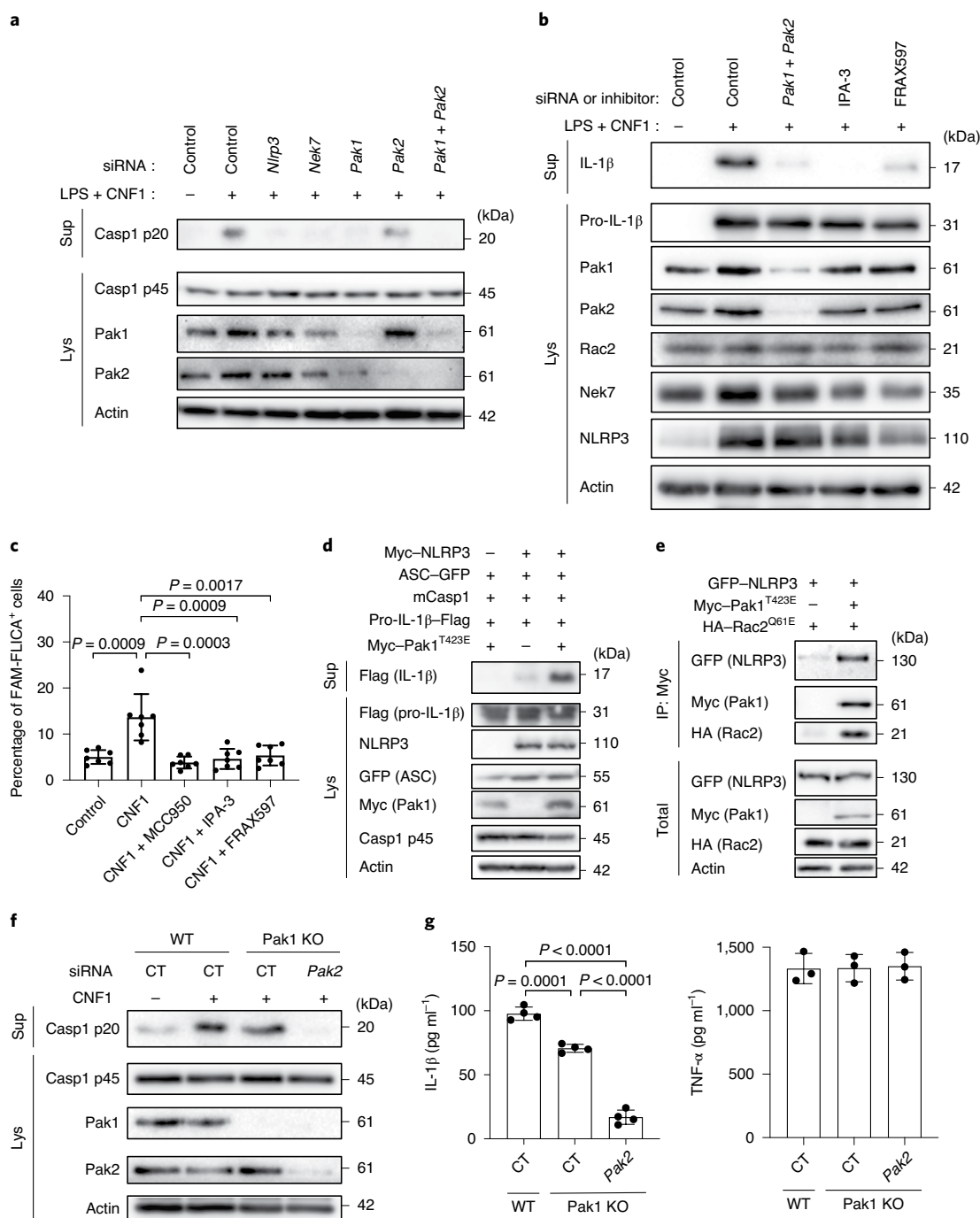


Fig. 3 | Rac2-NLRP3 signalling is dependent on Pak1 kinase. **a**, BMDMs isolated from BALB/c mice were transfected for 72 h with siRNA targeting *Nlrp3*, *Nek7*, *Pak1* or *Pak2* as indicated; non-targeting siRNA was used as a control. Cells were treated with CNF1 (500 ng ml⁻¹) and LPS (100 ng ml⁻¹) for 8 h, as indicated. Supernatants and cell lysates were analysed using immunoblotting. **b**, BMDMs isolated from BALB/c mice were transfected with *Pak1*- and *Pak2*-targeting siRNA or with non-targeting siRNA for 72 h, and treated with 5 μM IPA-3, 1 μM FRAX597 or vehicle for 45 min before treatment with CNF1 (500 ng ml⁻¹) and LPS (100 ng ml⁻¹) for 8 h. Supernatants and cell lysates were analysed using immunoblotting. **c**, BMDMs isolated from BALB/c mice were treated with vehicle (control), or treated either with 1 μM MCC950, 5 μM IPA-3 or 1 μM FRAX597 for 45 min before treatment with CNF1 (500 ng ml⁻¹) for 6 h. Active caspase-1 was stained with FAM-FLICA, analysed using microscopy and FAM-FLICA⁺ cells were counted. Each dot represents 100 cells. *n* = 800 cells. Data are mean ± s.e.m. Statistical analyses were performed using two-tailed unpaired Student's *t*-tests. **d**, HEK293T cells were transfected as indicated with plasmids encoding components of the NLRP3 inflammasome (Myc-NLRP3, ASC-GFP, mouse caspase-1) and pro-IL-1β-Flag together with Myc-Pak1^{T423E}, and pro-IL-1β-Flag cleavage was analysed using immunoblotting. **e**, HEK293T cells were transfected with plasmids encoding GFP-NLRP3, Myc-Pak1^{T423E} and HA-Rac2^{Q61E}. Cell lysates were processed for anti-Myc immunoprecipitation (IP). **f**, BMDMs isolated from WT or Pak1-knockout C57BL/6J mice were transfected 72 h with non-targeting or *Pak2*-targeting siRNA before treatment with CNF1 (500 ng ml⁻¹) for 8 h. Supernatants and cell lysates were analysed using immunoblotting. CT, control. **g**, BMDMs isolated from WT or Pak1-knockout C57BL/6J mice were transfected for 72 h with non-targeting or *Pak2*-targeting siRNA before treatment with CNF1 (500 ng ml⁻¹) and LPS (100 ng ml⁻¹) for 8 h. Supernatants were analysed using enzyme-linked immunosorbent assay (ELISA) for IL-1β (*n* = 4 biologically independent samples) and TNF-α (*n* = 3 biologically independent samples). Data are mean ± s.e.m. Statistical analyses were performed using two-tailed unpaired Student's *t*-tests. Experiments were repeated at least three times, and representative data are shown.

is an ATP-competitive inhibitor²⁷. In the inflammasome reconstitution system in HEK293T, we expressed the activated form of Pak1 (T423E) together with caspase-1, ASC and pro-IL-1 β , and we observed no IL-1 β maturation. By contrast, when NLRP3 was transfected together with ASC and caspase-1, the expression of the activated form of Pak1 was sufficient to trigger maturation of IL-1 β (Fig. 3d). Furthermore, phosphorylated forms of Pak colocalized in dot-like structures with NLRP3 and active caspase-1 (Supplementary Fig. 2). We next investigated whether Rac2, Pak1 and NLRP3 proteins formed a complex. We found NLRP3 interacting with activated Rac2 when activated Pak1 was expressed (Fig. 3e). We next investigated whether Pak1 was involved in the nigericin-triggered activation of the NLRP3 inflammasome and observed that IPA-3 treatment was sufficient to inhibit both caspase-1 cleavage and the release of LDH (Extended Data Fig. 5a,b). Furthermore, siRNA targeting of *Pak1* was found to decrease nigericin-triggered caspase-1 maturation (Extended Data Fig. 5c).

To genetically prove the involvement of Pak1 in NLRP3 inflammasome activation, we used Pak1-knockout mice. We observed a reduction in caspase-1 cleavage triggered by CNF1 in Pak1-knockout macrophages and a reduction in IL-1 β secretion (Fig. 3f,g). By contrast, the secretion of TNF- α was unaffected (Fig. 3g). Both caspase-1 cleavage and IL-1 β secretion triggered by CNF1 were substantially reduced when the Pak1-knockout macrophages were treated with the *Pak2* siRNA, suggesting that there is a partial compensation in Pak1-knockout macrophages (Fig. 3f,g).

Pak1 phosphorylates NLRP3 and triggers inflammasome activation. To further investigate whether NLRP3 is a substrate for the Pak1 serine–threonine kinase, we set-up an in vitro kinase assay. When both Pak1 and NLRP3 proteins were incubated with ATP- γ -³²P, we observed a band at the size of NLRP3, indicating that NLRP3 is directly phosphorylated by Pak1 in vitro (Fig. 4a). The in vitro kinase assay was then used to identify the phosphorylated sites of NLRP3 by analysing the band corresponding to NLRP3 using mass spectrometry. The analysis revealed that Pak1 phosphorylates NLRP3 at three independent positions that correspond to Ser 163, Ser 198 and Thr 659 in the human NLRP3 (Extended Data Fig. 6a,c and Supplementary Table 1). Interestingly, the Ser 163 and Ser 198 residues were previously reported to be phosphorylated, and Ser 198 was reported to be important for NLRP3 priming²⁸. NLRP3 Thr 659 was not reported to be phosphorylated and, interestingly, the identified peptide appears to be conserved between humans and mice (Extended Data Fig. 6d). Reinforcing the potential conservation of the Pak–NLRP3 axis, CNF1-triggered caspase-1 activation was observed in primary human macrophages and was inhibited by treatment with NLRP3 inhibitor or Pak1 inhibitor (Extended Data Fig. 7a,b). In the inflammasome reconstitution system, we next expressed the activated Pak1^{T423E} and compared the effect of the expression of NLRP3 WT with the triple-mutant NLRP3^{S163A S198A T659A} or single mutants NLRP3^{S163A}, NLRP3^{S198A} and

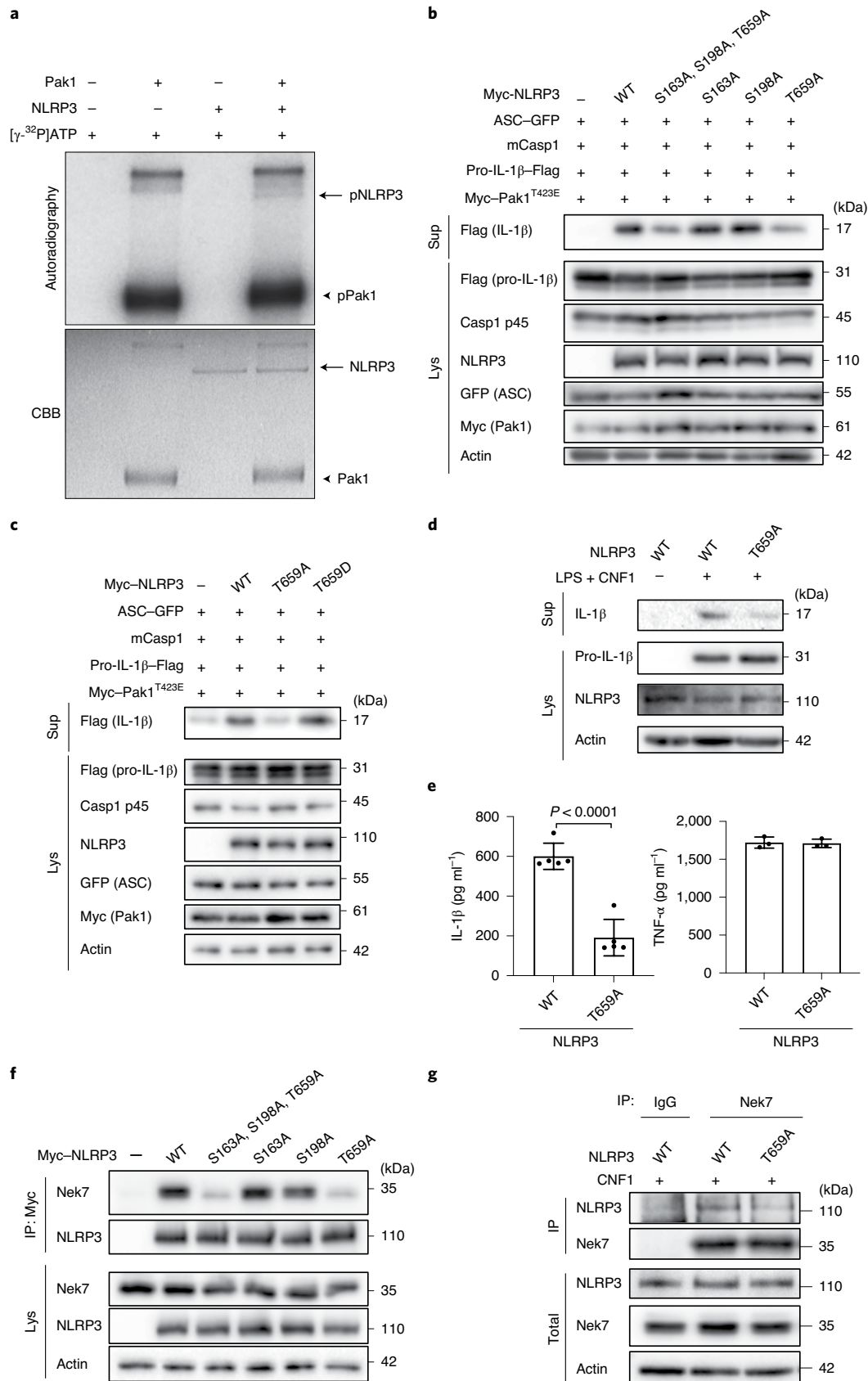
NLRP3^{T659A} in which the phosphorylated residues were replaced with alanine residues, which are not sensitive to phosphorylation. The results show that the triple-mutant NLRP3^{S163A S198A T659A} and the single mutant NLRP3^{T659A} is impaired in IL-1 β maturation triggered by the activated Pak1^{T423E}, indicating that the NLRP3 Thr 659 residue has an important role in Pak1-triggered NLRP3 inflammasome activation (Fig. 4b). Furthermore, we generated a T659D phosphomimetic NLRP3 mutant and observed that, compared with NLRP3^{T659A}, the NLRP3^{T659D} mutant had an increased ability to trigger pro-IL-1 β maturation (Fig. 4c). Importantly, similar results were obtained when the Rho-GTPase-activating virulence factor SopE was transfected to activate the pathway, highlighting the involvement of this NLRP3 post-translational regulation for the sensing of other virulence factors activating Rho GTPases (Extended Data Fig. 8a). We next stably reconstituted immortalized macrophages knocked-out for NLRP3 with plasmids encoding either NLRP3 or NLRP3^{T659A}. Confirming our results, we observed impaired CNF1-triggered IL-1 β maturation/secretion in macrophages expressing NLRP3^{T659A} compared with macrophages expressing WT NLRP3 (Fig. 4d,e). By contrast, TNF- α was similarly secreted by macrophages expressing either NLRP3 or NLRP3^{T659A} (Fig. 4e). After treatment with the DNT toxin, we also observed an impairment in CNF1-triggered IL-1 β maturation in macrophages expressing the NLRP3^{T659A} mutant compared with macrophages expressing WT NLRP3 (Extended Data Fig. 8b). Reinforcing the importance of this NLRP3 phosphorylation site in the inflammasome activation process, nigericin-triggered IL-1 β maturation and secretion were reduced in macrophages expressing the NLRP3^{T659A} compared with the macrophages expressing NLRP3, whereas TNF- α secretion was unaffected (Extended Data Fig. 9). Taken together, these results show that phosphorylation of NLRP3 at Thr 659 has a functional role, and that Pak1 is a regulator of the NLRP3 inflammasome. Structural analysis of the NLRP3–Nek7 interaction revealed a putative interaction domain at the level of the Thr 659 of NLRP3 (ref. ²⁹). Using co-immunoprecipitation experiments, we tested whether the NLRP3^{S163A S198A T659A} triple mutant or NLRP3^{S163A}, NLRP3^{S198A} and NLRP3^{T659A} single mutants affected the interaction with endogenous Nek7. The interaction between NLRP3 and Nek7 was impaired in the NLRP3^{S163A S198A T659A} triple mutant and in the NLRP3^{T659A} mutant, indicating that Thr 659 is a critical site for NLRP3–Nek7 interaction and suggesting that the phosphorylation of NLRP3 at Thr 659 is important for the NLRP3–Nek7 interaction (Fig. 4f). This observation was confirmed using anti-Nek7 immunoprecipitation in macrophages in which we found a decrease in NLRP3^{T659A} binding to Nek7 compared with WT NLRP3 (Fig. 4g).

Clearance of CNF1-expressing *E. coli* during bacteraemia requires the Pak–NLRP3 signalling axis. We next addressed the relevance of the CNF1-triggered Pak–NLRP3 signalling axis during infection. We observed an increase in caspase-1 maturation when macrophages were infected with CNF1-expressing *E. coli* compared

Fig. 4 | Pak1 phosphorylates NLRP3 to promote inflammasome activation. **a**, In vitro [γ -³²P]ATP kinase assay using human recombinant NLRP3 (arrows) and human recombinant Pak1 (arrowheads) analysed using autoradiography and Coomassie brilliant blue (CBB) staining. **b**, HEK293T cells were transfected with plasmids encoding components of the NLRP3 inflammasome (ASC–GFP, mouse caspase-1), pro-IL-1 β –Flag, Myc–Pak1^{T423E}, with Myc–NLRP3, Myc–NLRP3^{S163A}, Myc–NLRP3^{S198A}, Myc–NLRP3^{T659A} or Myc–NLRP3^{S163A S198A T659A}, and IL-1 β maturation was analysed using immunoblotting. **c**, HEK293T cells were transfected with plasmids encoding components of the NLRP3 inflammasome (ASC–GFP, mouse caspase-1) and Myc–Pak1^{T423E}, with Myc–NLRP3, Myc–NLRP3^{T659A} or Myc–NLRP3^{T659D}, and IL-1 β maturation was analysed using immunoblotting. **d,e**, NLRP3-knockout iBMDMs that were reconstituted with either NLRP3 or NLRP3^{T659A} were treated with vehicle or LPS (100 ng ml⁻¹) and CNF1 (500 ng ml⁻¹) for 8 h. **d**, Supernatants and cell lysates were analysed using immunoblotting. **e**, Supernatants were analysed using ELISA for IL-1 β ($n = 4$ biologically independent samples) and TNF- α ($n = 3$ biologically independent samples). Data are mean \pm s.e.m. Statistical analyses were performed using two-tailed unpaired Student's *t*-tests. **f**, HEK293T cells were transfected with plasmids encoding Myc–NLRP3, Myc–NLRP3^{S163A}, Myc–NLRP3^{S198A}, Myc–NLRP3^{T659A} or Myc–NLRP3^{S163A S198A T659A}. Cell lysates were processed for anti-Myc immunoprecipitation and endogenous Nek7 was revealed using anti-Nek7 antibodies. **g**, NLRP3-knockout iBMDMs that were reconstituted with either NLRP3 or NLRP3^{T659A} were treated with CNF1 (500 ng ml⁻¹) for 6 h. Cell lysates were analysed using immunoprecipitation with anti-Nek7 antibodies or isotopic IgG. Experiments were repeated at least three times, and representative data are shown.

with the isogenic *E. coli* CNF1-knockout strain, and treatment with NLRP3 or Pak1 inhibitors decreased the caspase-1 cleavage triggered by the *E. coli* expressing CNF1 (Fig. 5a). Furthermore, IL-1 β secretion triggered by the CNF1-expressing *E. coli* was reduced when

bacteria were added to NLRP3-knockout macrophages (Fig. 5b). Furthermore, the secretion of IL-1 β triggered by CNF1-expressing *E. coli* in macrophages complemented with the NLRP3^{T659A} mutant was decreased compared with control macrophages expressing



NLRP3 (Fig. 5c). TNF- α secretion measured during infection with CNF1-expressing *E. coli* was not affected in macrophages that were isolated from NLRP3-knockout mice or macrophages expressing the NLRP3^{T659A} mutant (Fig. 5b,c). We previously demonstrated that the CNF1 toxin expressed by *E. coli* triggered both an immune response in vivo and bacterial clearance during bacteraemia¹¹. To investigate the role of Pak1 during CNF1-expressing *E. coli* bacteraemia, we used the Pak1 inhibitor AZ13711265, which blocks CNF1-triggered IL-1 β maturation (Supplementary Fig. 3) and is associated with good in vivo pharmacokinetic properties²⁷. We monitored the bacterial burden during bacteraemia in control mice or mice injected with AZ13711265. Mice bacteraemia was measured for each mouse at 4 h, 24 h and 48 h after infection (Fig. 5d). The bacterial clearance of CNF1-expressing *E. coli* was observed; no bacteria were detectable at 48 h in all of the control animals (Fig. 5d). We measured a statistically significant higher bacterial load at 48 h and 77% of the animals were found to be positive for bacteraemia in the mice that were injected with the Pak1 inhibitor, indicating that in vivo the inhibition of Pak1 is sufficient to inhibit the CNF1-expressing *E. coli* clearance (Fig. 5d). We next used an NLRP3 inhibitor, MCC950, which has been shown to be efficient in vivo³⁰. We monitored bacteraemia in mice injected with MCC950 compared with the controls. The bacterial clearance of CNF1-expressing *E. coli* in mice injected with the NLRP3 inhibitor was significantly higher at 48 h, and 70% of the animals were found to be positive for bacteraemia (Fig. 5d). Consistent with our model, we observed no significant effect of both AZ13711265 and MCC950 towards the bacterial clearance when we infected mice with the isogenic *E. coli* CNF1-knockout strain (Extended Data Fig. 10a). To genetically prove this point, we infected WT mice, NLRP3-knockout mice or Pak1-knockout mice, and compared the CNF1-expressing *E. coli* burden. Consistent with the results obtained with the NLRP3 and Pak1 inhibitors, we did not detect any bacteria in the blood of infected WT mice at 48 h, whereas we measured a mean of 1.5×10^4 and 2.5×10^2 bacteria per mouse in the blood of NLRP3-knockout and Pak1-knockout mice, respectively (Fig. 5e,f). The smaller effect observed in Pak1-knockout mice compared with NLRP3-knockout mice could be explained by the redundancy observed between Pak1 and Pak2 at the cellular level. The difference in the clearance of CNF1-expressing *E. coli* measured at 48 h between WT and NLRP3-knockout mice was still observable at later time points and was not observed when mice were infected with the isogenic *E. coli* CNF1-knockout strain, indicating the specificity of the CNF1 response towards the NLRP3 pathway in vivo (Extended Data Fig. 10b,c). Furthermore, we measured a similar trend in the clearance of the CNF1-expressing *E. coli* strain in WT and GSDMD-knockout mice (Extended Data Fig. 10d). We next monitored the bacterial burden in mice that were infected with CNF1-expressing *E. coli* and treated with AZ13711265, MCC950 or both. We observed no differences in the bacterial clearance between the three groups (Fig. 5d). NLRP3-knockout mice that were injected with vehicle or with AZ13711265 demonstrated no differences in bacterial clearance, suggesting that Pak1 and NLRP3 act within the

same signalling pathway during bacteraemia (Fig. 5g). Together, these results unravel the critical role of Pak1 and NLRP3 in the clearance of CNF1-expressing bacteria and their importance in the innate immune response during bacteraemia.

Discussion

Our results shed light on a regulatory mechanism for NLRP3 after the activation of Rac2 by the bacterial toxin CNF1. The level of NLRP3 inflammasome activation is correlated with the strength of the interaction between activated Rac2 and Pak1-RBD, indicating that the innate immune system can adapt its response to the level of Rac2 activity. This seems to be an elegant strategy to deliver a commensurate response to the level of CNF1 toxin activity. Notably, the phosphorylated peptide containing Thr 659 of human NLRP3 isolated by mass spectrometry is highly conserved between species, and the Pak–NLRP3 axis is conserved in human macrophages and is involved in the nigericin-triggered NLRP3 inflammasome activation. Complementary studies will be necessary to determine the precise molecular mechanism in other species or in other contexts as well as to determine whether the phosphorylation of NLRP3 at Thr 659 is a consensus site used by other kinases. Nevertheless, our results show that phosphorylation of NLRP3 at Thr 659 is important for NLRP3 inflammasome activation and suggest that it is implicated in NLRP3-related inflammatory disorders or susceptibility to infection.

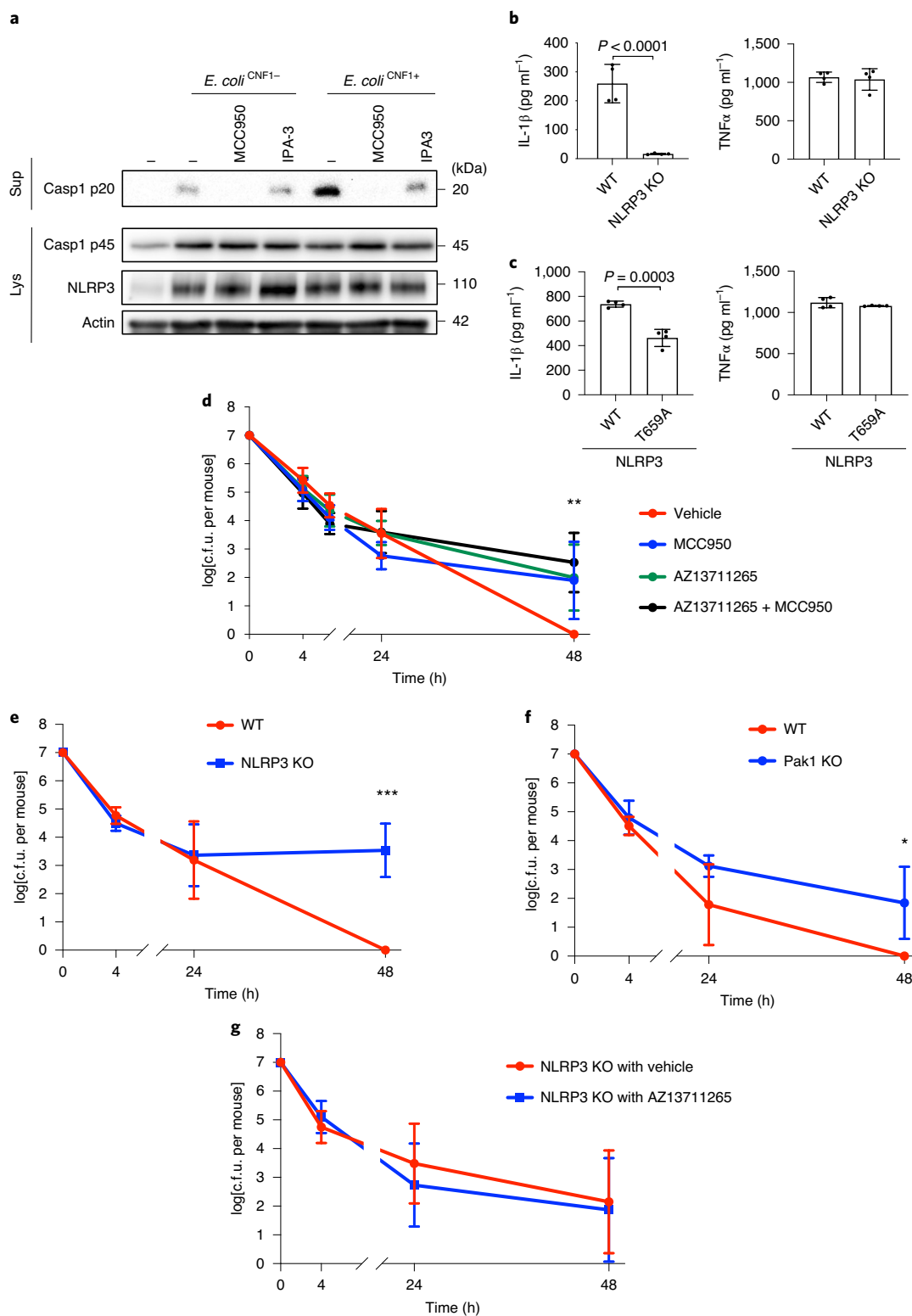
Our results suggest that there is redundancy between Pak1 and Pak2, as shown by a partial compensation by Pak2 in Pak1-knockout macrophages and mice. Further studies are required to clarify the importance of each of the group-1 Pak proteins in the activation of the NLRP3 inflammasome. Unfortunately, the Pak2-knockout mutations in mice are embryonically lethal (at embryonic day 8.0) and these studies would require the generation of conditional transgenic mice³¹.

We unravelled a CNF1-triggered secretion of IL-1 β that is not linked to an increase in cell death and is independent of GSDMD. Studies of NLRP3 inflammasome canonical triggers have demonstrated different IL-1 β secretion scenarios. In the conventional scenario, caspase-1 cleaves the inflammasome-related cytokines and GSDMD to generate active N-GSDMD^{32,33}. N-GSDMD relocates in the plasma membrane to form pores, enabling IL-1 β secretion^{32,33}. GSDMD pores are associated with pyroptosis in the case of classical inflammasome activation or are controlled during inflammasome hyperactivation, leading to secretion without pyroptosis^{34–36}. The CNF1-triggered IL-1 β secretion seems to fall into another category, independent of both GSDMD cleavage and cell death, that may share similarities with the unconventional IL-1 β secretion³⁷. This unconventional secretion relies on the affinity of IL-1 β to the plasma membrane ruffles that are characteristic of the CNF1-triggered Rac GTPase activation. The mechanism explaining how CNF1 triggered caspase-1 activation without GSDMD cleavage remains to be elucidated and may be unique to toxins activating Rho GTPases. One hypothesis is that the activation of Rac2, in parallel to the

Fig. 5 | Pak1 and NLRP3 control the burden of CNF1-expressing *E. coli* during bacteraemia. **a**, BMDMs isolated from C57BL/6 mice were pretreated for 45 min with 1 μ M MCC950 or 5 μ M IPA-3 and were infected or not (multiplicity of infection (m.o.i.) = 5) with either *E. coli*^{CNF1+} or isogenic CNF1-deleted mutant *E. coli*^{CNF1-}. Supernatants and cell lysates were analysed using immunoblotting. **b,c**, BMDMs isolated from C57BL/6 or C57BL/6 NLRP3-knockout mice (**b**) or iBMDMs expressing NLRP3 or NLRP3^{T659A} (**c**) were infected (m.o.i. = 5) with *E. coli*^{CNF1+}. The supernatants were analysed using ELISA. $n = 4$ biologically independent samples per group. Data are mean \pm s.e.m. Statistical analyses were performed using two-tailed unpaired Student's *t*-tests. **d–g**, Mice were intravenously infected with 10^7 colony-forming units (c.f.u.) of *E. coli*^{CNF1+}, before collecting peripheral blood at 4 h, 24 h and 48 h for the measurement of bacteraemia. **d**, C57BL/6J mice were injected intraperitoneally with vehicle, or with 50 mg kg⁻¹ MCC950 ($n = 10$ mice), 10 mg kg⁻¹ AZ13711265 ($n = 10$ mice) or both once a day ($n = 9$ mice). $^{**}P < 0.01$ (each individual inhibitor-treated group compared with the group injected with vehicle). **e**, WT ($n = 7$ mice) or NLRP3-knockout C57BL/6J mice ($n = 6$ mice) were analysed. $^{***}P < 0.001$. **f**, WT ($n = 4$ mice) or Pak1-knockout C57BL/6J mice were analysed ($n = 4$ mice). $^{*}P < 0.05$. **g**, NLRP3-knockout C57BL/6J mice were injected intraperitoneally with 10 mg kg⁻¹ AZ13711265 ($n = 7$ mice) or vehicle ($n = 9$ mice) once each day. Experiments were repeated at least two times, and representative data are shown. Data are the geometric mean \pm 95% confidence interval. Statistical analyses were performed using two-tailed nonparametric Mann-Whitney *U*-tests. $^{*}P < 0.05$, $^{**}P < 0.01$, $^{***}P < 0.001$.

Pak1–NLRP3 pathway activation, inhibits the cleavage of GSDMD. Similar to *Toxoplasma gondii*, the NF- κ B activation triggered by Rac2 might be another mechanism explaining the IL-1 β secretion independent of cell death and GSDMD³⁸. Rac2 signalling may also regulate a potassium channel explaining the inhibition by KCl of the CNF1-triggered IL-1 β secretion. Favouring this hypothesis, Rac GTPases have been found to modulate Kir2.1, a Kir-family potassium channel³⁹.

Our study shows that NLRP3 is a major sensor of toxins that activate Rho GTPases, whereas previous research has shown the sensing of Rho-GTPase-inactivating toxins by Pyrin¹². These studies highlight that the mammalian innate immune system has evolved strategies that share similarities with the effector-triggered immunity to detect abnormal activation of Rho GTPases^{3,40,41}. Interestingly, both inactivation of RhoA and activation of Rac2 by bacterial toxins are monitored by Pyrin and NLRP3, respectively. More precisely,



here we show that Rac GTPases that activate bacterial factors are sensed by NLRP3 independently of the type of modification made. Similarly, bacterial factors that inactivate RhoA activate Pyrin independently of the type of modifications^{12,42,43}. These results suggest that the host guarding of Rho GTPase signalling integrity relies on two sensors that monitor the abnormal Rho GTPase cycling rather than toxin-triggered post-translational modifications of host proteins or virulence factor enzymatic activities. Interestingly, both Pyrin and NLRP3 require regulation by the serine–threonine kinases PKN1/2 and Pak1/2, respectively. The fact that two different inflammasomes have been evolutionarily selected to detect bacterial toxins that modify Rho GTPases highlights the importance of Rho GTPases in innate immunity.

Further studies are necessary to determine the *in vivo* conservation of the Pak–NLRP3 axis and whether the sensing of other Rho–GTPase-activating virulence factors by the NLRP3 inflammasome impacts the bacterial burden during infection. Similarly, we expect that further studies will determine the importance of other inflammasomes in detecting bacterial virulence factors that are endowed with enzymatic activities.

Our results reveal the importance of Pak1 and NLRP3 in controlling the bacterial burden during bacteraemia in mice. Even though further studies will be required to determine the role of the Pak–NLRP3 signalling axis in patients with bacteraemia, our results showing an increase in bacterial burden in MCC950-treated mice suggest that caution will be necessary for the use of NLRP3 inhibitors in the clinical setting. This is consistent with clinical data showing that there is an increased risk of infections associated with IL-1 signalling inhibition^{44,45}. One option would be to consider combining inflammasome inhibitors with antibiotherapies or with an enhanced surveillance for a potential for bacteraemia risk.

Methods

Ethics statement. This study was carried out in strict accordance with the guidelines of the Council of the European Union (Directive 86/609/EEC) regarding the protection of animals used for experimental and other scientific purposes. The protocol was approved by the Institutional Animal Care and Use Committee on the Ethics of Animal Experiments of Nice, France (APAFIS#18322-20181218099427035 v2 and APAFIS#24906-2020031614223228 v2).

Bacterial strains and toxins. The *E. coli* UTI89 clinical isolate was originally obtained from a patient with cystitis⁴⁶ and the isogenic UTI89 CNF1⁺ (*E. coli*^{CNF1+}) or UTI89 CNF1⁻ (*E. coli*^{CNF1-}) streptomycin-resistant strain generation and culture conditions were previously described⁴¹. For the infections, a 1/100 dilution of an overnight culture was inoculated and grown up to an optical density at 600 nm of 1.2 using a Luria–Bertani (LB) medium supplemented with streptomycin (200 µg ml⁻¹). Bacteria were collected by centrifugation and washed twice in PBS before dilution in PBS to obtain the desired bacterial concentrations for the mouse infection experiments. Recombinant WT CNF1 and its catalytically inactive form (CNF1^{C865S}) were produced and purified as previously reported^{47,48}. The recombinant DNT toxin was purified from pQEDNTwt using the same protocol⁴⁹. The recombinant proteins were passed through a polymyxin B column (Affinity Detoxi-Gel, Pierce). The removal of endotoxin was verified using a colorimetric limulus amoebocyte lysate (LAL) assay (LAL QCL-1000, Cambrex). Each stock of the CNF1 preparation (2 mg ml⁻¹) was shown to contain less than 0.5 endotoxin units per ml. Plasmid expressing the virulence factor pCMV-SopE-HA was previously reported²² and SopE expression was stabilized by adding MG132 (10 µM) to the cells to block its proteasomal degradation as previously described⁵⁰. Plasmids expressing the PRK5-Myc-DNT were obtained by PCR amplification of pQEDNTwt, and pCMV-HA-YopE was obtained by PCR amplification and subcloning from pACY184-YopE-GSK (gift from I. Brodsky). All of the plasmids were verified by sequencing (Eurofins).

Cell culture, transfection and inhibitors. HEK293T cells were obtained from ATCC (CRL-3216) and maintained according to the ATCC instructions. BMDMs were extracted from the femurs of BALB/c, C57BL/6J, C57BL/6J knockout or C57BL/6J knockout mice (aged 6–10 weeks) as indicated in the legends and were cultured in RPMI GlutaMax medium (Life Technologies) supplemented with 100 ng ml⁻¹ M-CSF (premium grade, Miltenyi Biotec), 10% heat-inactivated FBS (Biowest) and 50 µg ml⁻¹ gentamycin (Life Technologies) at 37 °C in an atmosphere containing 5% CO₂. The cells were seeded at a concentration of 10⁶ cells per well in a six-well plate. After 6 d of differentiation, BMDMs were used for

experiments. HEK293T cells were transfected with plasmids using Lipofectamine 2000 (Life Technologies) according to the manufacturer's instructions. siRNAs were transfected in BMDMs for 72 h using Lipofectamine RNAiMAX Reagent (Thermo Fisher Scientific) according to the manufacturer's instructions. Cells were transfected as indicated in the figure legends with siRNAs (Dharmacon) targeting *Nlrp3* (L-053455-00), *Rac1* (L-041170-00), *Rac2* (L-041171-01), *Nek7* (J-063266-09), *Pak1* (L-048101-00), *Pak2* (L-040615-00) or non-targeting control siRNA (D-001810-10). For the siRNA screen, the BMDMs were transfected with siRNA (Dharmacon) targeting *Nod1* (L-055182-00), *Nod2* (L-052735-00), *Nlr3* (L-052823-01), *Nlr4* (L-055000-00), *Nlr5* (L-067620-01), *Nlr1* (L-057712-01), *Ciita* (L-043166-02), *Naip1* (L-047682-00), *Naip2* (L-044151-01), *Naip5* (L-044142-01), *Naip6* (L-044145-01), *Naip7* (L-065757-00), *Nlrp1a* (L-066229-00), *Nlrp1b* (L-161107-01), *Nlrp2* (L-053528-01), *Nlrp3* (L-053455-01), *Nlrp4a* (L-052395-01), *Nlrp4b* (L-058181-01), *Nlrp4c* (L-049416-01), *Nlrp4d* (L-067051-01), *Nlrp4e* (L-068064-01), *Nlrp4f* (L-052668-01), *Nlrp4g* (L-066364-01), *Nlrp5* (L-045315-01), *Nlrp6* (L-066157-01), *Nlrp9a* (L-058269-01), *Nlrp9b* (L-066417-01), *Nlrp9c* (L-057344-01), *Nlrp10* (L-056559-01), *Nlrp12* (L-060234-01), *Nlrp14* (L-066093-01), *Pycard* (L-051439-01), *Mefv* (L-048693-01) and *Aim2* (L-044968-01). BMDMs were pretreated with the following inhibitors for 45 min: 1 µM CP-456773 or MCC950 (Sigma-Aldrich), 5 µM IPA-3 (Tocris), 1 µM FRAX597 (Tocris) or the indicated concentration of AZ13711265 (AGV Discovery) in 2% FBS containing RPMI followed by the addition of CNF1 500 ng ml⁻¹ and/or ultrapure LPS 100 ng ml⁻¹ (Invivogen) as indicated in the figure legends. Cells treated with nigericin 5 µM (Invivogen) or ATP 5 mM (Invivogen) for 30 min were used as positive control for NLRP3 inflammasome activation. For K⁺-efflux-preventing experiments, BMDMs were treated with 10 mM, 20 mM or 40 mM KCl. Primary macrophages were infected with *E. coli*^{CNF1+} or the isogenic *E. coli*^{CNF1-} (m.o.i. = 5) for 16 h. Immortalized NLRP3-knockout BMDMs were stably complemented with pINDUCER21 plasmids encoding human NLRP3 WT or NLRP3^{T659A} under a doxycycline-inducible promoter as previously described⁵¹. NLRP3 expression was induced by adding 2 µg ml⁻¹ doxycycline for 16 h (Takara Bio). All of the cell lines were authenticated using PCR assays with species-specific primers. Mycoplasma testing was negative.

Mouse model of infection. Female C57BL/6J mice (aged 7 weeks; Charles River Laboratory) were injected intraperitoneally with MCC950 (Sigma-Aldrich) at 50 mg kg⁻¹ every 24 h or AZ13711265 (AGV Discovery) at 10 mg kg⁻¹ every 24 h or both. NLRP3-knockout mice were provided by V. Petrilli and were described previously⁵². The Pak1-knockout, GSDMD-knockout and ASC–citricine-knockin mice used in this study were reported previously^{17,32,53}. Female NLRP3-knockout or Pak1-knockout and female congenic WT C57BL/6J littermate mice were injected intravenously with 10⁷ colony-forming units of *E. coli* and the determination of bacteraemia was monitored as previously described⁴¹. Mice were housed with their littermates and kept under a regular 12 h–12 h light–dark cycle at room temperature (20–25 °C) and a relative humidity of 50–70%. Food and water were available *ad libitum*. Experiments were performed under pathogen-free conditions with randomly chosen animals (same sex, matched by age and body weight). Investigators were blinded for *in vivo* experiments. Sample size was determined on the basis of our previous research⁴¹ and using G*Power software.

Reconstituted NLRP3 inflammasome in HEK293T cells. HEK293T cells were transfected with plasmids encoding the NLRP3 inflammasome components as previously described^{41,28}. HEK293T cells were transfected with plasmids encoding Myc–NLRP3 or NLRP3 mutants, ASC–GFP, mpro-caspase1 and pro-IL-1β–Flag. Where indicated in the legend, cells were cotransfected with HA–Rac2, the constitutively active mutant of Rac2 mimicking CNF1-induced deamidation Rac2^{Q61E}, Rac2^{Q61L}, Rac2^{G12V} or Rac2^{T17N}, a dominant negative mutant of Rac2 for 16 h. The monitoring of caspase-1 or IL-1β cleavage was performed using supernatant immunoblotting.

Immunoprecipitation. HEK293T cells were transfected with plasmids encoding Myc–NLRP3, Myc–NLRP3^{S163A/S198A/T659A}, Myc–NLRP3^{S163A} and Myc–NLRP3^{T659A}, GFP–NLRP3, Myc–Pak1^{T423E} and HA–Rac2^{Q61E}, or NLRP3 expression was induced by adding 2 µg ml⁻¹ doxycycline for 16 h to iBMDMs stably expressing NLRP3 or NLRP3^{T659A}. Cells were lysed and processed for immunoprecipitation using 2 µg of anti-Myc or 3 µg of anti-Nek7 antibodies according to previously described conditions⁵⁴. The expression of NLRP3 and endogenous levels of Nek7 were monitored in the cell lysate as well as in the immunoprecipitated fraction.

LDH release. The supernatant of stimulated macrophages was collected and centrifuged at 300g for 5 min to remove cellular debris. LDH measurement was performed using the LDH Cytotoxicity Assay Kit (Thermo Fisher Scientific) according to the manufacturer's instructions, in samples diluted 1:5 in PBS. Data were plotted as the percentage of LDH release considering a Triton X-100 treated well as 100%.

Cell permeabilization kinetics. BMDMs were plated and stimulated in a 96-well plate in medium containing propidium iodide (0.1 µg ml⁻¹) and data were acquired with a ×10 objective using the InCyte Zoom system v.6.2.9200.0

(Essen BioScience) under a CO₂- and temperature-controlled environment. Each condition was run in quadruplicate. The number of fluorescent objects was counted using Incucyte Zoom (Essen BioScience).

In vitro kinase assay. Recombinant purified Pak1 (500 ng) was incubated with 1 µg of recombinant human NLRP3 protein (Abcam, ab165022), and with 50 µM ATP and 4 µCi of [³²P]ATP in kinase buffer (50 mM HEPES pH 7.3, 50 mM NaCl, 0.05% Triton X-100, 10 mM β-glycerophosphate, 5 mM NaF, 10 mM MgCl₂ and 0.2 mM MnCl₂) at 30°C for 30 min in a final volume of 39 µl. The reaction was stopped by adding 15 µl of LDS (Thermo Fisher Scientific) and 6 µl of dithiothreitol 500 mM. Samples were analysed by electrophoresis using Bolt 4–12% Bis-Tris Plus gels (Thermo Fisher Scientific) followed by Coomassie blue staining and autoradiography.

Immunofluorescence staining, antibodies and ELISA assays. Caspase-1 activation was detected using the fluorescent probe FAM-FLICA (ImmunoChemistry Technologies) after 6 h of treatment, according to the manufacturer's instructions. After labelling, cells were fixed in 4% paraformaldehyde for 15 min, PFA was neutralized with 50 mM NH₄Cl for 15 min, cells were permeabilized with 0.5% Triton X-100 for 5 min and blocked with 2% TBS-BSA. Cells were incubated with mouse anti-NLRP3 (clone Cryo-2, Adipogen) and/or rabbit anti-ASC (AG-25B-0006, Adipogen) or rabbit anti-phosphorylated-Pak (ab40795, Abcam) antibodies for 1 h followed by incubation with the secondary antibodies TexasRed anti-mouse IgG (TI-2000, Vector Laboratories) or Cy5 anti-mouse IgG (715-175-151, Jackson ImmunoResearch) and/or TexasRed anti-rabbit IgG (711-075-152, Jackson ImmunoResearch) and/or phalloidin Alexa Fluor 647 (ab176759, Abcam) and Hoechst 33342 (H1399, Thermo Fisher Scientific) for 30 min. Cells were imaged using a Nikon A1R confocal microscope. The following antibodies were used in this study: rabbit anti-IL-1β (GTX74034, Genetex), mouse anti-caspase-1 (clone Casper-1, Adipogen), mouse anti-Rac (clone 102/Rac1, BD Biosciences), goat anti-Rac2 (ab2244, Abcam), mouse anti-NLRP3 (clone Cryo-2, Adipogen), rabbit anti-Nek7 (ab133514, Abcam), rabbit anti-Pak1 (2602, CST), rabbit anti-Pak2 (2608, CST), rabbit monoclonal anti-GSDMD (ab209845), mouse anti-β-actin (AC-74, Sigma-Aldrich), mouse anti-Myc (9E10, Roche), mouse anti-HA (16B12, Covance), mouse anti-Flag (clone M2, Sigma-Aldrich), mouse anti-GFP (clone 7.1, 13.1, Roche). Cytokine secretion was determined by ELISA using the mouse Quantikine ELISA kits for mouse IL-6, IL-18, TNF-α and IL-1β (R&D Systems) according to the manufacturer's instructions.

Flow cytometry analysis. BMDMs isolated from C57BL/6J mice constitutively expressing ASC–citrine fusion protein (R26-CAG-ASC–citrine) were treated with LPS (100 ng ml⁻¹) for 16 h before 6 h of treatment with vehicle or CNF1 (500 ng ml⁻¹) or 30 min with nigericin (5 µM). Cells were collected and analysed by flow cytometry using a BD FACSCanto II cytometer (BD Biosciences). Cytometry data were analysed using FlowJo v.10.6.2. Doublets were excluded using a side scatter (SSC)-A (area) and SSC-H (height) plot; cells with a high expression of ASC–citrine were gated and then analysed for ASC–citrine signal area (ASC–citrine-A) and ASC–citrine signal height (ASC–citrine-H). Cells with ASC specks were defined with a higher ASC-H:ASC-A ratio.

Statistical analyses. Statistical analyses were performed using GraphPad Prism v.8.2.1. Comparisons of the bacterial load of mice were performed using nonparametric Mann–Whitney *U*-tests. Statistical analyses of FAM-FLICA⁺ cells, cytokine secretion and LDH release were performed using unpaired two-tailed Student's *t*-tests.

Reporting Summary. Further information on research design is available in the Nature Research Reporting Summary linked to this article.

Data availability

All data supporting the findings of this study are available within the Article and its Supplementary Information or from the corresponding author on reasonable request. Source data are provided with this paper.

Received: 21 August 2019; Accepted: 13 November 2020;

Published online: 11 January 2021

References

- Martin, G. S., Mannino, D. M., Eaton, S. & Moss, M. The epidemiology of sepsis in the United States from 1979 through 2000. *N. Engl. J. Med.* **348**, 1546–1554 (2003).
- Vance, R. E., Isberg, R. R. & Portnoy, D. A. Patterns of pathogenesis: discrimination of pathogenic and nonpathogenic microbes by the innate immune system. *Cell Host Microbe* **6**, 10–21 (2009).
- Stuart, L. M., Paquette, N. & Boyer, L. Effector-triggered versus pattern-triggered immunity: how animals sense pathogens. *Nat. Rev. Immunol.* **13**, 199–206 (2013).
- Flatau, G. et al. Toxin-induced activation of the G protein p21 Rho by deamidation of glutamine. *Nature* **387**, 729–733 (1997).
- Schmidt, G. et al. Gln63 of Rho is deamidated by *Escherichia coli* cytotoxic necrotizing factor-1. *Nature* **387**, 725–729 (1997).
- Aktories, K. & Barbieri, J. Bacterial cytotoxins: targeting eukaryotic switches. *Nat. Rev. Microbiol.* **3**, 397–410 (2005).
- Galán, J. E. Common themes in the design and function of bacterial effectors. *Cell Host Microbe* **5**, 571–579 (2009).
- Bruno, V. M. et al. *Salmonella* Typhimurium type III secretion effectors stimulate innate immune responses in cultured epithelial cells. *PLoS Pathog.* **5**, e1000538 (2009).
- Munro, P. et al. Activation and proteasomal degradation of Rho GTPases by cytotoxic necrotizing factor-1 elicit a controlled inflammatory response. *J. Biol. Chem.* **279**, 35849–35857 (2004).
- Boquet, P. & Lemichez, E. Bacterial virulence factors targeting Rho GTPases: parasitism or symbiosis? *Trends Cell Biol.* **13**, 238–246 (2003).
- Diabate, M. et al. *Escherichia coli* α-hemolysin counteracts the anti-virulence innate immune response triggered by the Rho GTPase activating toxin CNF1 during bacteremia. *PLoS Pathog.* **11**, e1004732 (2015).
- Xu, H. et al. Innate immune sensing of bacterial modifications of Rho GTPases by the pyrin inflammasome. *Nature* **513**, 237–241 (2014).
- Gros Lambert, M. & Py, B. F. Spotlight on the NLRP3 inflammasome pathway. *J. Inflamm. Res.* **11**, 359–374 (2018).
- Yang, Y., Wang, H., Kouadir, M., Song, H. & Shi, F. Recent advances in the mechanisms of NLRP3 inflammasome activation and its inhibitors. *Cell Death Dis.* **10**, 128 (2019).
- Gao, W., Yang, J., Liu, W., Wang, Y. & Shao, F. Site-specific phosphorylation and microtubule dynamics control pyrin inflammasome activation. *Proc. Natl Acad. Sci. USA* **113**, E4857–E4866 (2016).
- Park, Y. H., Wood, G., Kastner, D. L. & Chae, J. J. Pyrin inflammasome activation and RhoA signaling in the autoinflammatory diseases FMF and HIDS. *Nat. Immunol.* **17**, 914–921 (2016).
- Zheng, T. C. et al. A fluorescent reporter mouse for inflammasome assembly demonstrates an important role for cell-bound and free ASC specks during in vivo infection. *Cell Rep.* **16**, 571–582 (2016).
- Sester, D. P. et al. Assessment of inflammasome formation by flow cytometry. *Curr. Protoc. Immunol.* **114**, 14.40.1–14.40.29 (2016).
- Lamkanfi, M. & Dixit, V. M. In retrospect: the inflammasome turns 15. *Nature* **548**, 534–535 (2017).
- He, Y., Hara, H. & Núñez, G. Mechanism and regulation of NLRP3 inflammasome activation. *Trends Biochem. Sci.* **41**, 1012–1021 (2016).
- Shi, H., Murray, A. & Beutler, B. Reconstruction of the mouse inflammasome system in HEK293T cells. *Bio. Protoc.* **6**, e1986 (2016).
- Keestra, A. M. et al. Manipulation of small Rho GTPases is a pathogen-induced process detected by NOD1. *Nature* **496**, 233–237 (2013).
- Doye, A. et al. CNF1 exploits the ubiquitin-proteasome machinery to restrict Rho GTPase activation for bacterial host cell invasion. *Cell* **111**, 553–564 (2002).
- Boyer, L. et al. Pathogen-derived effectors trigger protective immunity via activation of the Rac2 enzyme and the IMD or Rip kinase signaling pathway. *Immunity* **35**, 536–549 (2011).
- Manser, E., Leung, T., Salihuddin, H., Zhao, Z. S. & Lim, L. A brain serine/threonine protein kinase activated by Cdc42 and Rac1. *Nature* **367**, 40–46 (1994).
- Wells, C. M. & Jones, G. E. The emerging importance of group II PAKs. *Biochem. J.* **425**, 465–473 (2010).
- Semenova, G. & Chernoff, J. Targeting PAK1. *Biochem. Soc. Trans.* **45**, 79–88 (2017).
- Song, N. et al. NLRP3 phosphorylation is an essential priming event for inflammasome activation. *Mol. Cell* **68**, 185–197 (2017).
- Sharif, H. et al. Structural mechanism for NEK7-licensed activation of NLRP3 inflammasome. *Nature* **570**, 338–343 (2019).
- Coll, R. C. et al. A small-molecule inhibitor of the NLRP3 inflammasome for the treatment of inflammatory diseases. *Nat. Med.* **21**, 248–255 (2015).
- Kelly, M. L. & Chernoff, J. Mouse models of PAK function. *Cell Logist.* **2**, 84–88 (2012).
- Shi, J. et al. Cleavage of GSDMD by inflammatory caspases determines pyroptotic cell death. *Nature* **526**, 660–665 (2015).
- He, W. T. et al. Gasdermin D is an executor of pyroptosis and required for interleukin-1β secretion. *Cell Res.* **25**, 1285–1298 (2015).
- Broz, P., Pelegrín, P. & Shao, F. The gasdermins, a protein family executing cell death and inflammation. *Nat. Rev. Immunol.* **20**, 143–157 (2020).
- Rühl, S. et al. ESCRT-dependent membrane repair negatively regulates pyroptosis downstream of GSDMD activation. *Science* **362**, 956–960 (2018).
- Evavold, C. L. et al. The pore-forming protein gasdermin D regulates interleukin-1 secretion from living macrophages. *Immunity* **48**, 35–44 (2018).
- Monteleone, M. et al. Interleukin-1β maturation triggers its relocation to the plasma membrane for gasdermin-D-dependent and -independent secretion. *Cell Rep.* **24**, 1425–1433 (2018).

38. Pandori, W. J. et al. *Toxoplasma gondii* activates a Syk-CARD9-NF- κ B signaling axis and gasdermin D-independent release of IL-1 β during infection of primary human monocytes. *PLoS Pathog.* **15**, e1007923 (2019).
39. Muessel, M. J., Harry, G. J., Armstrong, D. L. & Storey, N. M. SDF-1 α and LPA modulate microglia potassium channels through rho GTPases to regulate cell morphology. *Glia* **61**, 1620–1628 (2013).
40. Jones, J. D. & Dangl, J. L. The plant immune system. *Nature* **444**, 323–329 (2006).
41. Lopes Fischer, N., Naseer, N., Shin, S. & Brodsky, I. E. Effector-triggered immunity and pathogen sensing in metazoans. *Nat. Microbiol.* **5**, 14–26 (2020).
42. Aubert, D. F. et al. A *Burkholderia* type VI effector deamidates Rho GTPases to activate the pyrin inflammasome and trigger inflammation. *Cell Host Microbe* **19**, 664–674 (2016).
43. Medici, N. P., Rashid, M. & Bliska, J. B. Characterization of pyrin dephosphorylation and inflammasome activation in macrophages as triggered by the yersinia effectors YopE and YopT. *Infect. Immun.* **87**, e00822-18 (2019).
44. Cabral, V. P., Andrade, C. A., Passos, S. R., Martins, M. F. & Hökerberg, Y. H. Severe infection in patients with rheumatoid arthritis taking anakinra, rituximab, or abatacept: a systematic review of observational studies. *Rev. Bras. Reumatol. Engl. Ed.* **56**, 543–550 (2016).
45. Ridker, P. M. et al. Antiinflammatory therapy with canakinumab for atherosclerotic disease. *N. Engl. J. Med.* **377**, 1119–1131 (2017).
46. Mulvey, M. A., Schilling, J. D. & Hultgren, S. J. Establishment of a persistent *Escherichia coli* reservoir during the acute phase of a bladder infection. *Infect. Immun.* **69**, 4572–4579 (2001).
47. Buetow, L., Flatau, G., Chiu, K., Boquet, P. & Ghosh, P. Structure of the Rho-activating domain of *Escherichia coli* cytotoxic necrotizing factor 1. *Nat. Struct. Biol.* **8**, 584–588 (2001).
48. Doye, A., Boyer, L., Mettouchi, A. & Lemichez, E. Ubiquitin-mediated proteasomal degradation of Rho proteins by the CNF1 toxin. *Methods Enzymol.* **406**, 447–456 (2006).
49. Matsuzawa, T., Kashimoto, T., Katahira, J. & Horiguchi, Y. Identification of a receptor-binding domain of *Bordetella* dermonecrotic toxin. *Infect. Immun.* **70**, 3427–3432 (2002).
50. Kubori, T. & Galán, J. E. Temporal regulation of salmonella virulence effector function by proteasome-dependent protein degradation. *Cell* **115**, 333–342 (2003).
51. Lagrange, B. et al. Human caspase-4 detects tetra-acylated LPS and cytosolic *Francisella* and functions differently from murine caspase-11. *Nat. Commun.* **9**, 242 (2018).
52. Martinon, F., Pétrilli, V., Mayor, A., Tardivel, A. & Tschopp, J. Gout-associated uric acid crystals activate the NALP3 inflammasome. *Nature* **440**, 237–241 (2006).
53. McDaniel, A. S. et al. *Pak1* regulates multiple c-Kit mediated Ras-MAPK gain-in-function phenotypes in *Nf1*^{+/-} mast cells. *Blood* **112**, 4646–4654 (2008).
54. Stutz, A. et al. NLRP3 inflammasome assembly is regulated by phosphorylation of the pyrin domain. *J. Exp. Med.* **214**, 1725–1736 (2017).

Acknowledgements

We thank P. Auberger, A. Baumler, I. Brodsky, J. Chernoff, D. Golenbock, T. Henry, M. Keestra-Gounder, E. Lemichez, E. Manser, E. Meunier, V. Petrilli, D. Pisani, J.-E. Ricci, G. Robert, P.-M. Roger, L. Stuart, P. Vandenabeele, S. Ivanov and L. Yvan-Charvet for sharing materials or discussions; A.-S. Dufour, E. Garcia, M. Irdelle and J. Murdaca for technical assistance; members of the Innate Sensors Community (InnaSCO) for sharing tools; A. Cuttriss and staff at the Office of International Scientific Visibility of Université Côte d'Azur for professional language editing; staff at the Etablissement Français du Sang of Marseille for providing human blood from human healthy donors; and staff at the C3M facilities (animal, genomic, cytometry and imaging) and the Harvard Taplin mass spectrometry core. The mouse strain used for this research project, B6.129S2-Pak1tm1Cher/Mmnc (RRID, MMRRRC_031838-UNC) was obtained from the Mutant Mouse Resource and Research Center (MMRRC) at University of North Carolina at Chapel Hill, an NIH-funded strain repository, and was donated to the MMRRRC by J. Chernoff, Fox Chase Cancer Center. This work was supported by grants from the ANR (ANR-17-CE15-0001), Investments for the Future programs LABEX SIGNALIFE ANR-11-LABX-0028-01, IDEX UCA^{EDU} ANR-15-IDEX-01, ARC (RAC15014AAA), Université Côte d'Azur, Infectiopole sud and REDPIT. B.F.P. is supported by ERC (ERC-2013-CoG_616986). A.M. is supported by a fellowship from FRM; C.T. by a fellowship from Ville de Nice; and O.D. by a fellowship from INSERM and Université Côte d'Azur.

Author contributions

O.D. and A.D. designed, performed and analysed most of the experiments with input from C.T., C.L., A.J., A.G., A.M., P.C., A.R. and S.M.; J.C. and R.R. provided advice on the mice infection model. E.V., R.R.G., D.C., B.F.P., A.R., P.H.V.S. and M.L. provided tools and advice on NLRP3 inflammasome regulation. P.M. generated NLRP3 mutants and, with G.M. and O.D., performed and analysed most of the in vivo experiments. O.V. performed virulence factor and toxin subcloning, protein purifications, the in vitro kinase assay and analysed the mass spectrometry results. L.B. conceived the project, designed experiments and wrote the manuscript.

Competing interests

The authors declare no competing interests.

Additional information

Extended data is available for this paper at <https://doi.org/10.1038/s41564-020-00832-5>.

Supplementary information is available for this paper at <https://doi.org/10.1038/s41564-020-00832-5>.

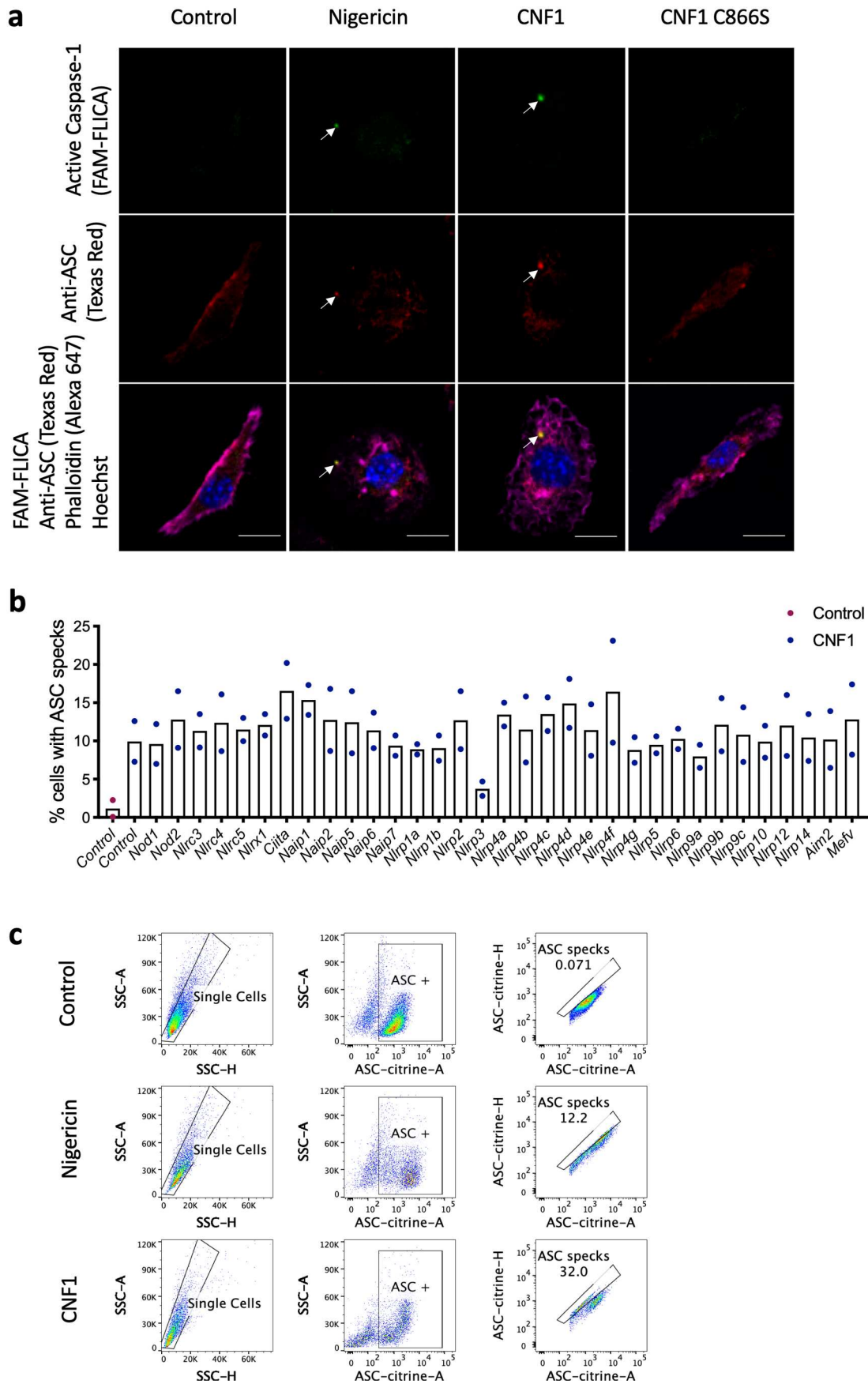
Correspondence and requests for materials should be addressed to L.B.

Peer review information *Nature Microbiology* thanks Igor Brodsky, Gad Frankel and the other, anonymous, reviewer(s) for their contribution to the peer review of this work.

Reprints and permissions information is available at www.nature.com/reprints.

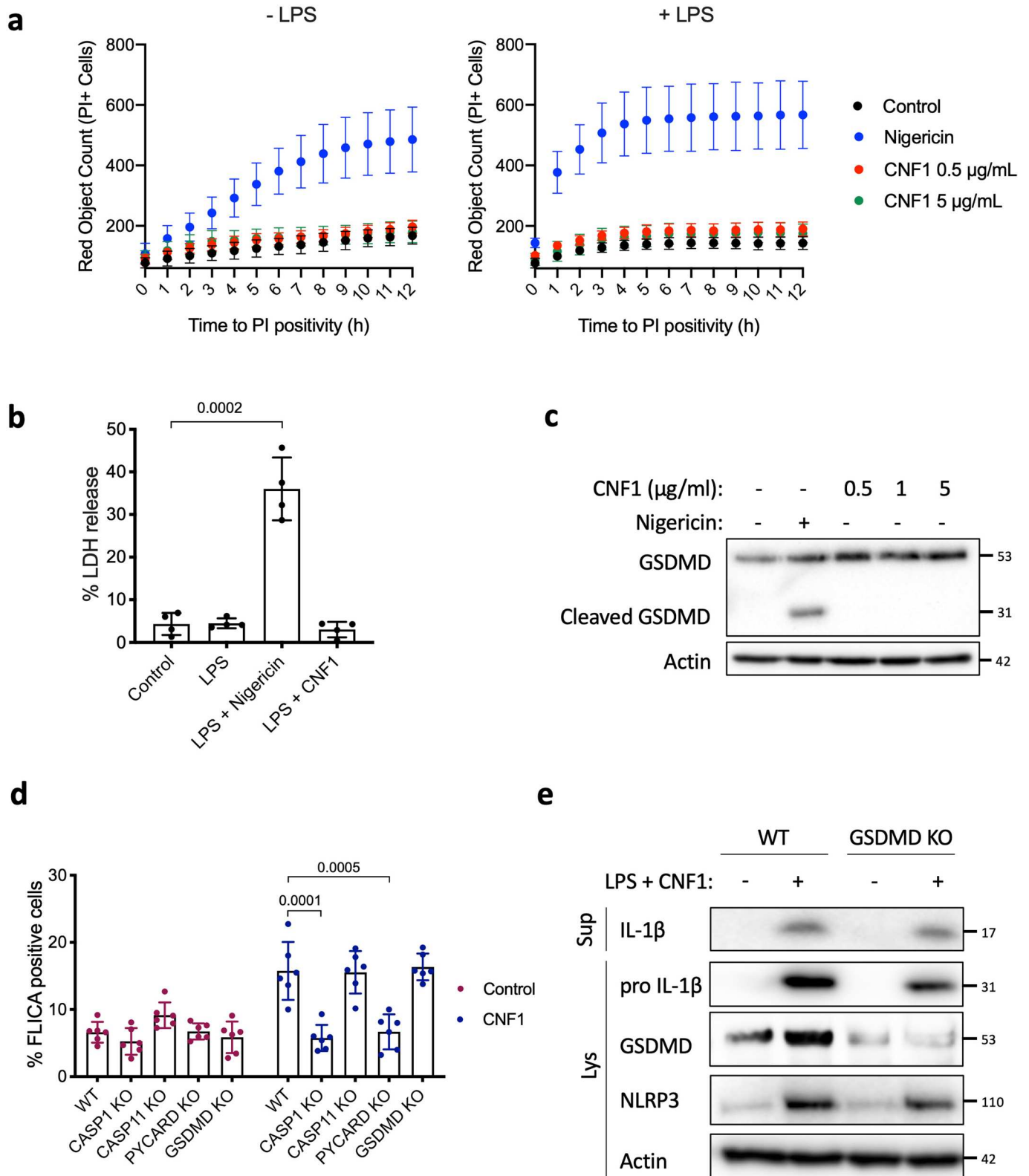
Publisher's note Springer Nature remains neutral with regard to jurisdictional claims in published maps and institutional affiliations.

© The Author(s), under exclusive licence to Springer Nature Limited 2021



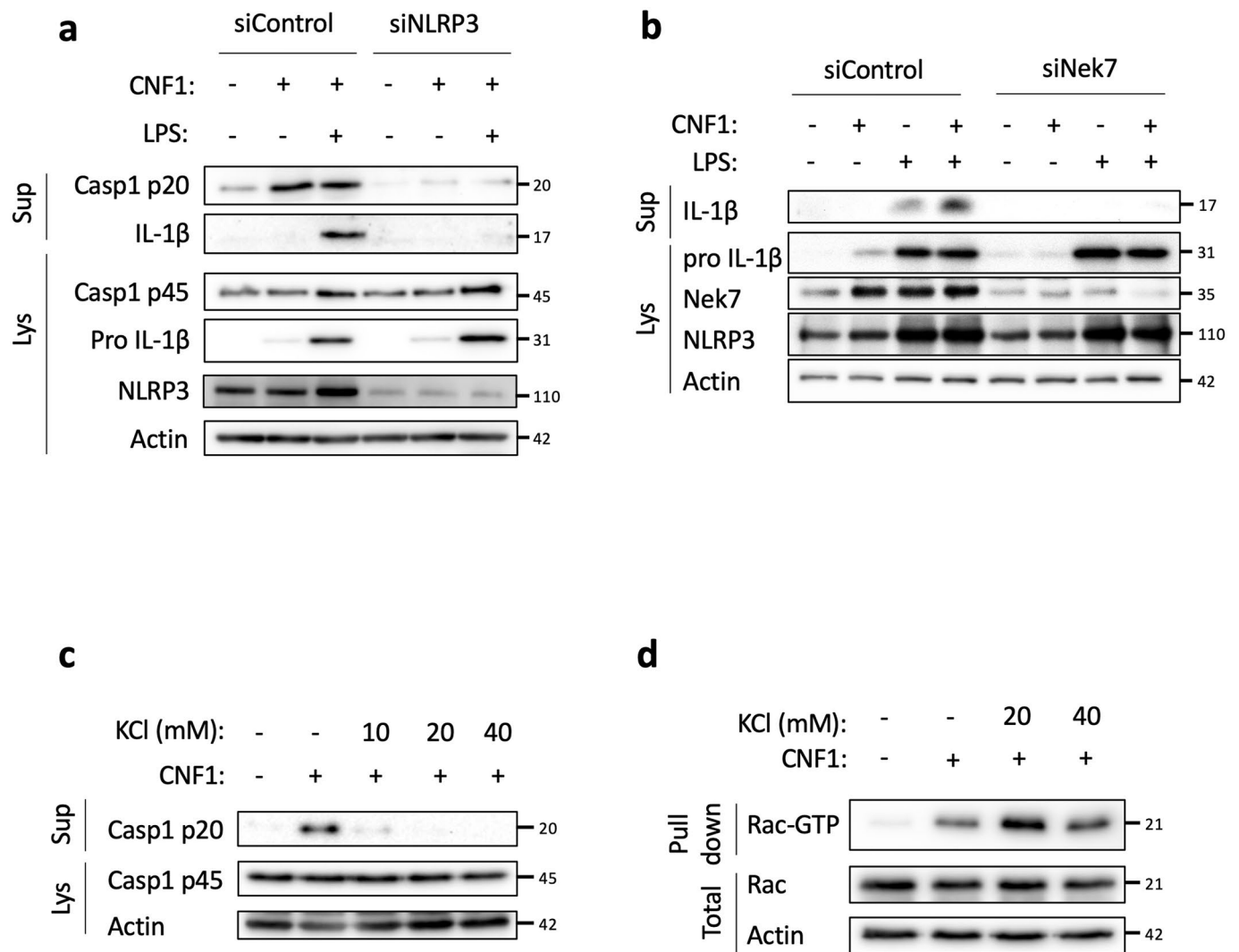
Extended Data Fig. 1 | See next page for caption.

Extended Data Fig. 1 | CNF1 triggers Caspase-1 activation and ASC specks formation. **a**, BMDMs isolated from BALB/c mice were either treated with vehicle (control) or CNF1 (500 ng ml⁻¹), inactive catalytic mutant CNF1 C866S (500 ng/mL) for 6 h, or Nigericin (5 μM) for 30 min. Active Caspase-1 was revealed with FAM-FLICA (green), ASC was stained using an anti-ASC antibody (Texas Red), nuclei and actin filament were stained with Hoechst and phalloidin-Alexa 647 respectively. Cells were analyzed by confocal microscopy. Arrows indicates FAM-FLICA dots that colocalize with the ASC staining. Scale bar: 10 μm. **b**, BMDM isolated from C57BL/6 J mice constitutively expressing ASC-citrine fusion protein (R26-CAG-ASC-citrine) were transfected with the indicated siRNA for 72 h prior to 6 h of CNF1 treatment (500 ng/mL) or treated with vehicle (control). Percent of cells with ASC specks. Data are expressed as the mean ± SEM. Each dot represents 10⁵ cells (n = 2 biologically independent samples). **c**, BMDM isolated from C57BL/6 J mice constitutively expressing ASC-citrine fusion protein (R26-CAG-ASC-citrine) were treated 6 h with CNF1 (500 ng/mL) or Nigericin (5 μM) for 30 min or vehicle (control). Cells were analyzed for ASC speck formation by flow cytometry as indicated, doublets were excluded using SSC-A and SSC-H plot, cells with a high expression of ASC-citrine were gated and then analyzed for ASC-citrine area (ASC-citrine-A) and ASC-citrine height (ASC-citrine-H). Cells with ASC specks are defined with a higher ASC-H:ASC-A ratio. Experiments were repeated at least three times, and representative data are shown.

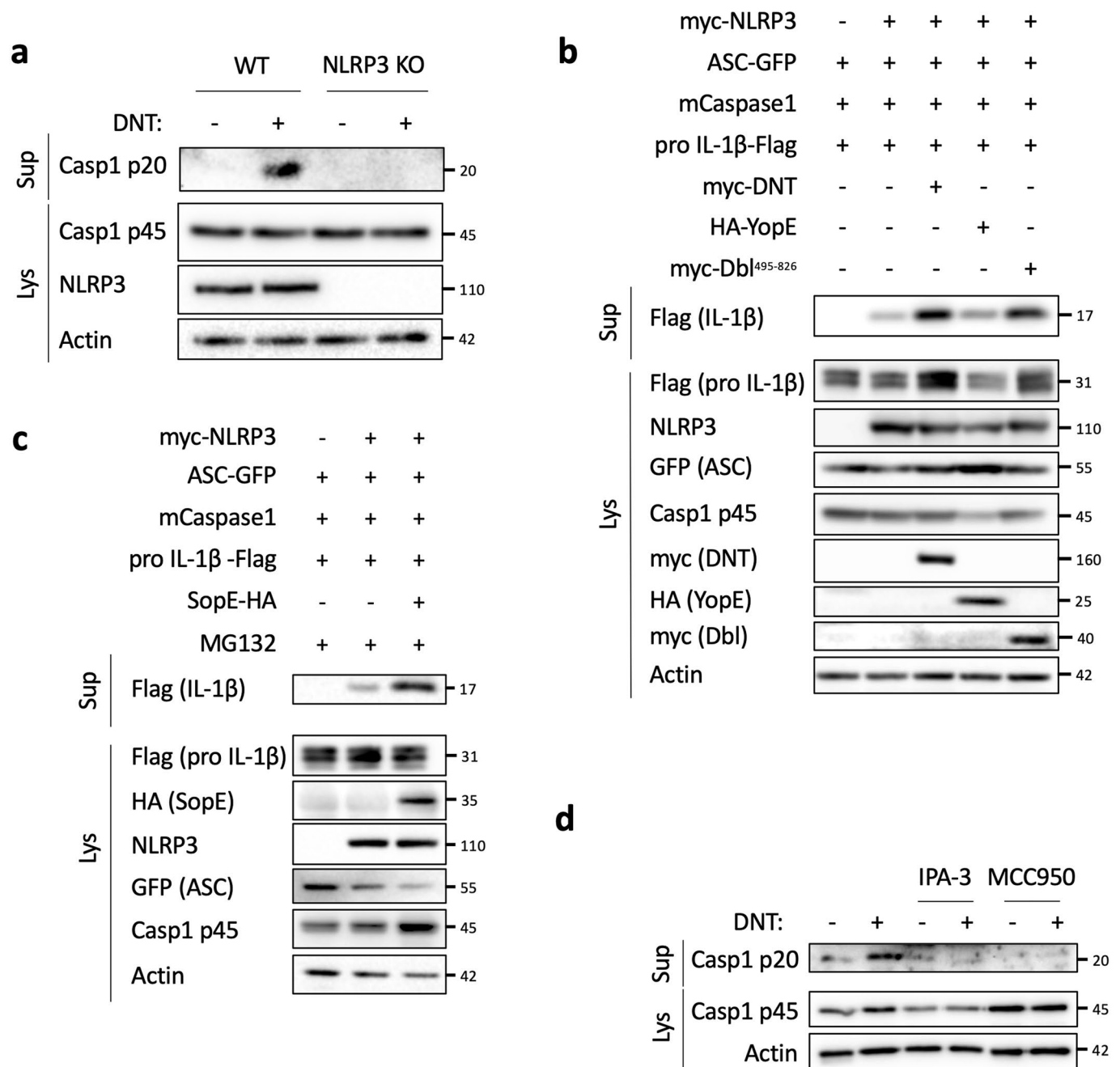


Extended Data Fig. 2 | See next page for caption.

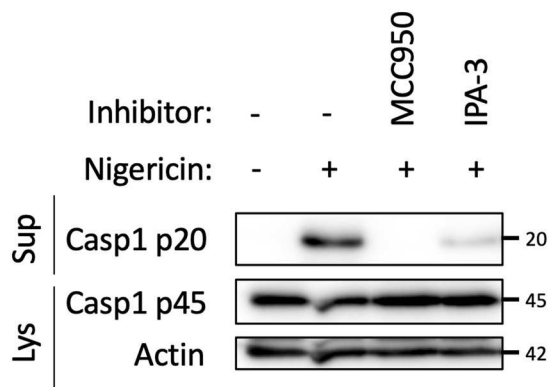
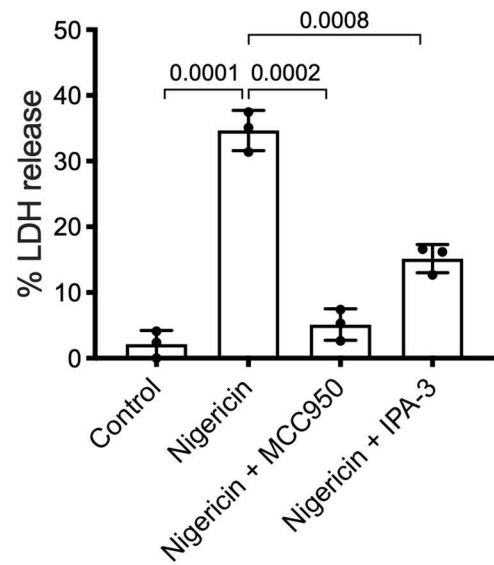
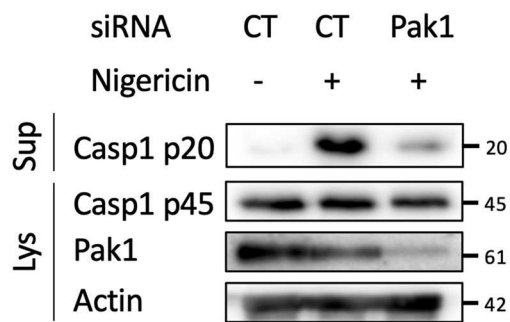
Extended Data Fig. 2 | NLRP3 inflammasome activation by CNF1 does not induce pyroptosis. **a**, BMDMs isolated from C57BL/6 J mice were treated with vehicle (control), Nigericin (5 μ M) or CNF1 (500 ng/mL or 5 μ g/mL) with or without LPS (100 ng/mL). Propidium iodide (PI) uptake was monitored over time (red object count) by real time imaging. Data are expressed as mean \pm SD. 10^4 cells were analyzed for each replicate (n = 4 independent wells). **b**, BMDMs isolated from C57BL/6 J mice were treated with vehicle (control, n = 6 independent experiments), LPS (100 ng/mL, n = 4 independent experiments), LPS and CNF1 (500 ng/mL, n = 6 independent experiments) or LPS and Nigericin (5 μ M, n = 4 independent experiments), and LDH release was assessed. Data are expressed as the mean \pm SEM. Statistical analyses were performed using a two-tailed nonparametric Mann Whitney test. **c**, BMDMs isolated from C57BL/6 J mice were treated either with Nigericin (5 μ M) for 30 min or CNF1 (0.5, 1 or 5 μ g/mL) for 8 h and GSDMD cleavage in cell lysates is shown. **d**, BMDMs isolated from C57BL/6 J wild-type or CASP1, CASP11, PYCARD (coding for ASC) or GSDMD knock-out mice were untreated or treated with CNF1 (500 ng/mL) for 6 h and were analyzed for Caspase-1 activation using the FAM-FLICA probe. Data are expressed as the mean \pm SEM. Statistical analyses were performed using a two-tailed unpaired Student's t-test. Each dot represents 100 cells (n = 700 cells). **e**, BMDMs isolated from wild-type or GSDMD knock-out mice were treated with CNF1 (500 ng/mL) and LPS (100 ng/mL) for 8 h as indicated. Supernatants and cell lysates were analyzed by immunoblot. The numbers on the side of the immunoblots indicate molecular weight (kDa). Experiments were repeated at least three times, and representative data are shown.



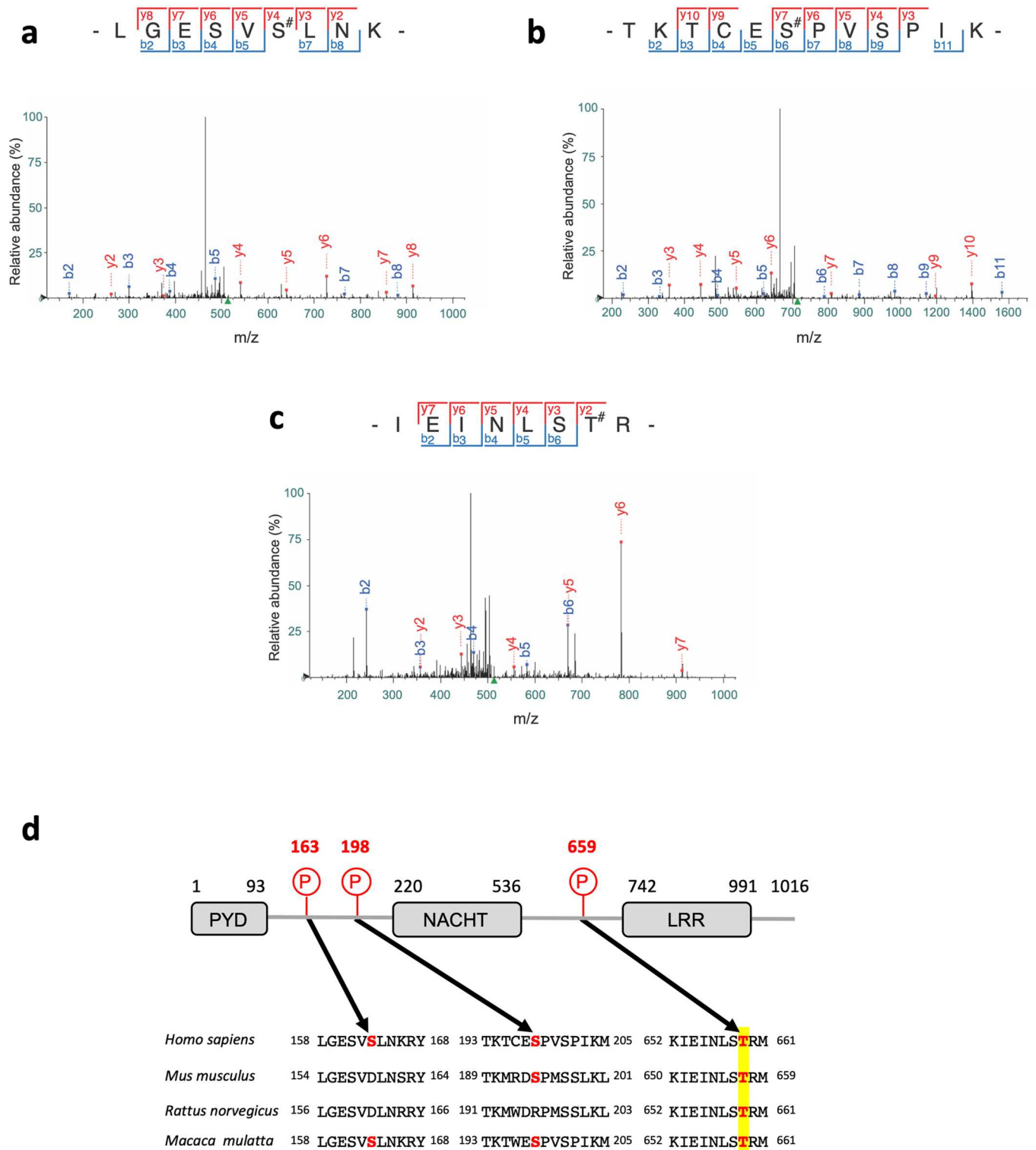
Extended Data Fig. 3 | CNF1-triggered inflammasome activation depends on NLRP3, Nek7 and K⁺ efflux. **a,b**, BMDMs isolated from C57BL/6J mice were transfected with siRNA-targeting NLRP3 (**a**), siRNA-targeting Nek7 (**b**), or control non-targeting siRNA for 72 h before treatment with CNF1 (500 ng/mL) and/or LPS (100 ng/mL) for 8 h. Supernatants and cell lysates were analyzed by immunoblot. **c,d**, BMDMs isolated from C57BL/6J mice (**c**) or iBMDMs (**d**) were treated with the indicated KCl concentration and CNF1 (500 ng/mL) for 8 h. **c**, Supernatants and cell lysates were analyzed by immunoblot, or (**d**) cell lysates were analyzed using a GST-Pak-RBD pull-down assay. The Rac associated with the GST-Pak-RBD beads is indicated as Rac-GTP. The numbers on the side of the immunoblots indicate molecular weight (kDa). Experiments were repeated at least three times, and representative data are shown.



Extended Data Fig. 4 | Toxins mediated Rho GTPases activation but not inhibition trigger the NLRP3 inflammasome. a, BMDMs isolated from wild-type or NLRP3 knock out C57BL/6J mice were treated with DNT (1 μ g/mL) for 8 h. Supernatants and cell lysates were analyzed by immunoblot. **b-c**, HEK293T cells were transfected as indicated with plasmids encoding NLRP3 inflammasome components (myc-NLRP3, ASC-GFP, mCaspase-1) and pro-IL-1 β -Flag together with **(b)** myc-DNT, HA-YopE or myc-DbI⁴⁹⁵⁻⁸²⁶ or **(c)** transfected with SopE-HA and treated with MG132 to block SopE degradation (10 μ M). Supernatants and cell lysates were analyzed by immunoblot. **d**, BMDMs isolated from C57BL/6J mice were treated with IPA-3 (5 μ M) or MCC950 (1 μ M) for 45 min prior to 8 h of DNT treatment (1 μ g/mL). Supernatants and cell lysates were analyzed by immunoblot. The numbers on the side of the immunoblots indicate molecular weight (kDa). Experiments were repeated at least three times, and representative data are shown.

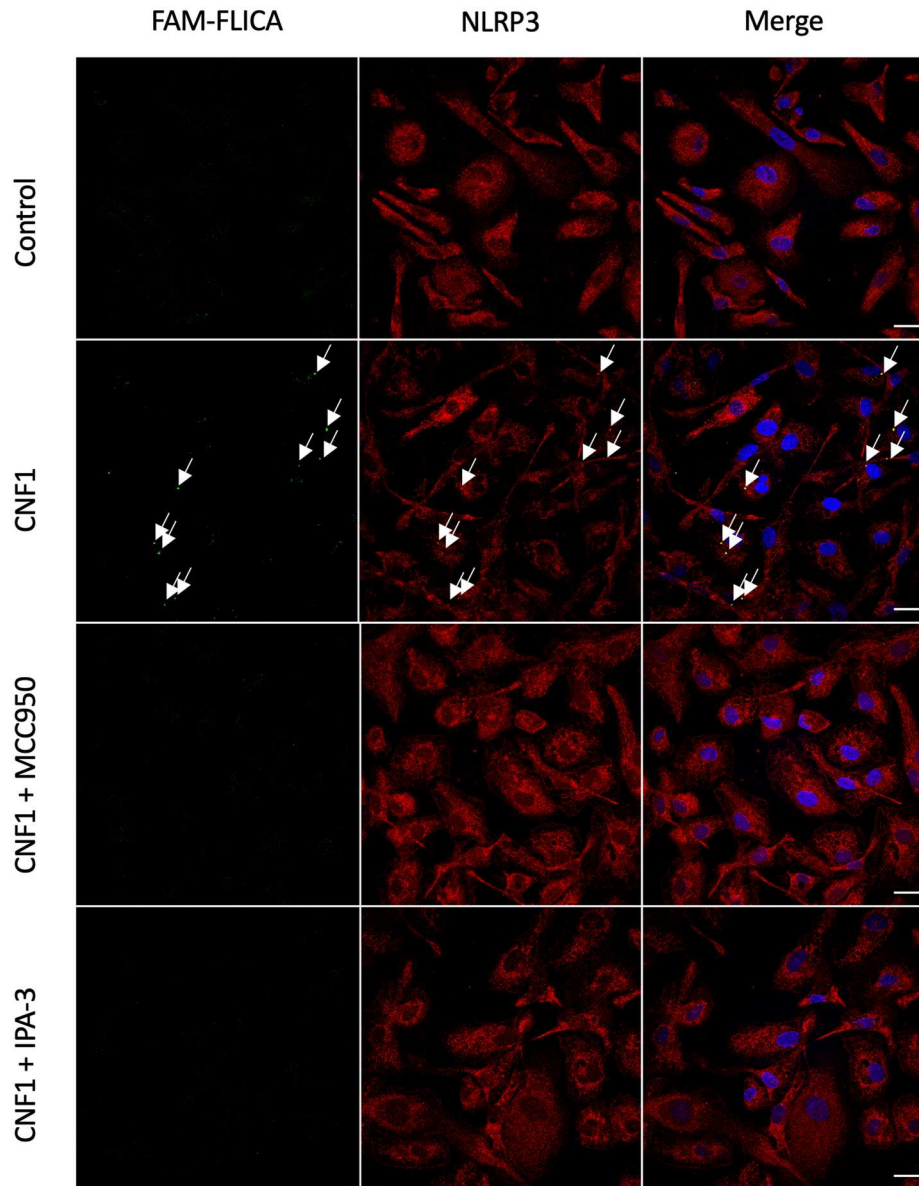
a**b****c**

Extended Data Fig. 5 | Inhibition of Pak1 diminishes NLRP3 activation by Nigericin. a,b, BMDMs isolated from C57BL/6 J mice were treated with MCC950 (1 μ M) or IPA-3 (5 μ M) for 45 min prior to Nigericin (5 μ M) treatment for 30 min. Supernatants and cell lysates were analyzed by (a) immunoblot and (b) supernatants were analyzed for LDH release (n = 3 biologically independent experiments). Statistical analyses were performed using a two-tailed nonparametric Mann Whitney test. n = 3 biologically independent samples were analyzed. **c,** BMDMs isolated from C57BL/6 J mice were treated for 72 h with non-targeting (CT) or Pak1-targeting siRNA before treatment with Nigericin (5 μ M) for 30 min. Supernatants and cell lysates were analyzed by immunoblot. The numbers on the side of the immunoblots indicate molecular weight (kDa). Experiments were repeated at least three times, and representative data are shown. Data are expressed as the mean \pm SEM.

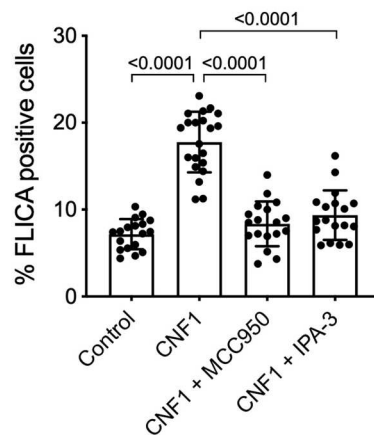


Extended Data Fig. 6 | Mass spectrometry analysis of Pak1 triggered NLRP3 phosphorylation. **a-c**, Fragmentation spectra of human NLRP3 peptides showing phosphorylation of Ser-163, Ser-198 and Thr-659. **d**, Representation of NLRP3 domain structure and sequence alignment of NLRP3 ortholog peptides surrounding phosphorylated residues identified by mass spectrometry. The phosphorylated residues are in bold red.

a

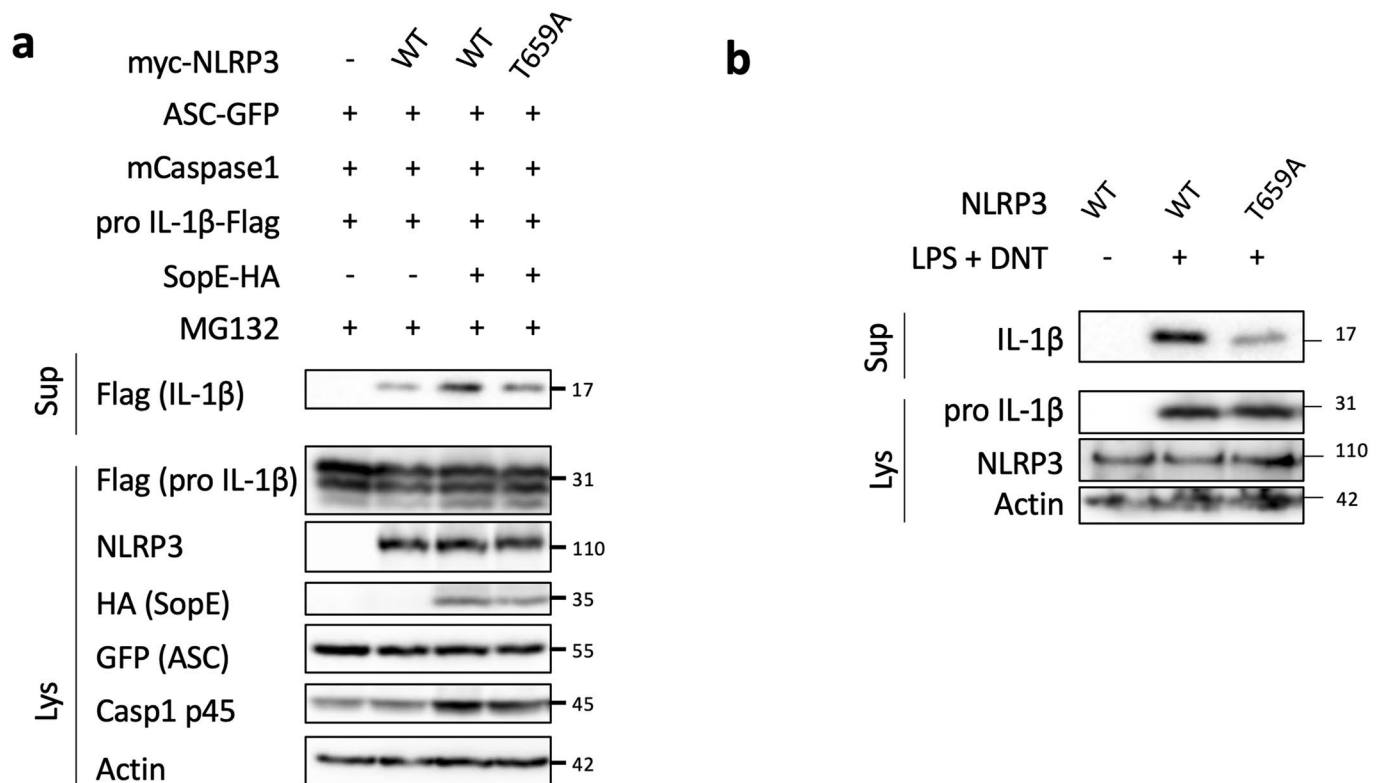


b



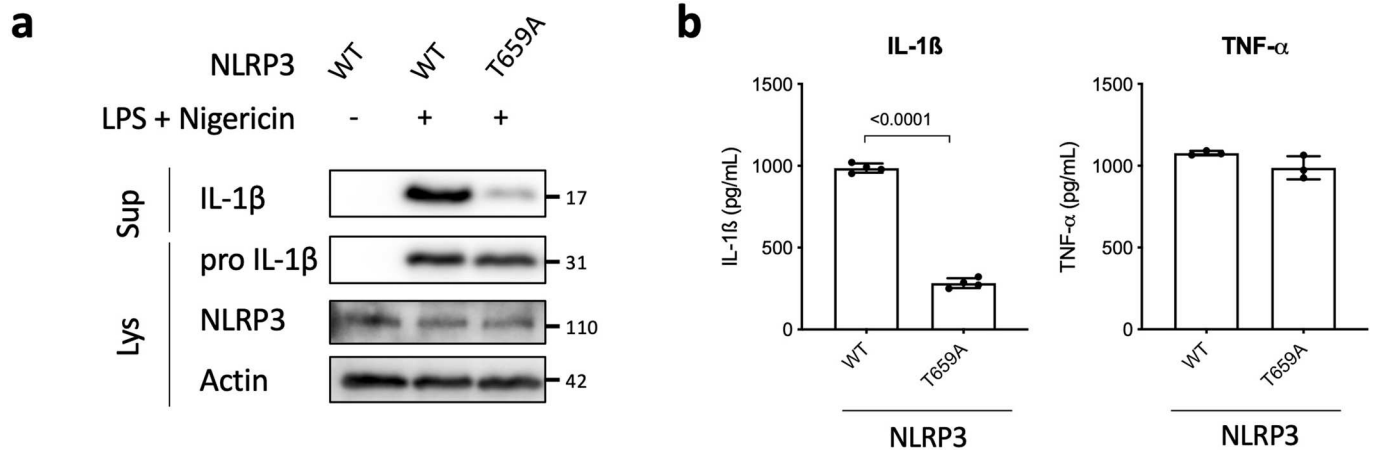
Extended Data Fig. 7 | See next page for caption.

Extended Data Fig. 7 | Conservation of the Pak-NLRP3 axis in Human monocyte-derived macrophages. a-b, Human monocyte-derived macrophages (hMDMs) were pretreated with vehicle, MCC950 (1 μ M) or IPA-3 (5 μ M) for 45 min before CNF1 (500 ng/mL) treatment for 6 h. Active Caspase-1 was stained with FAM-FLICA (green), NLRP3 (red) and nuclei (blue) were stained for immunofluorescence and confocal microscopy imaging. Arrows indicates FAM-FLICA dots that colocalize with NLRP3. Scale bar: 20 μ m. **b,** quantification of FAM-FLICA positive cells. Data are expressed as the mean \pm SEM. Statistical analyses were performed using a two-tailed unpaired Student's t-test. Each dot represents 100 cells (n = 1800 cells). Experiments were repeated at least three times, and representative data are shown.

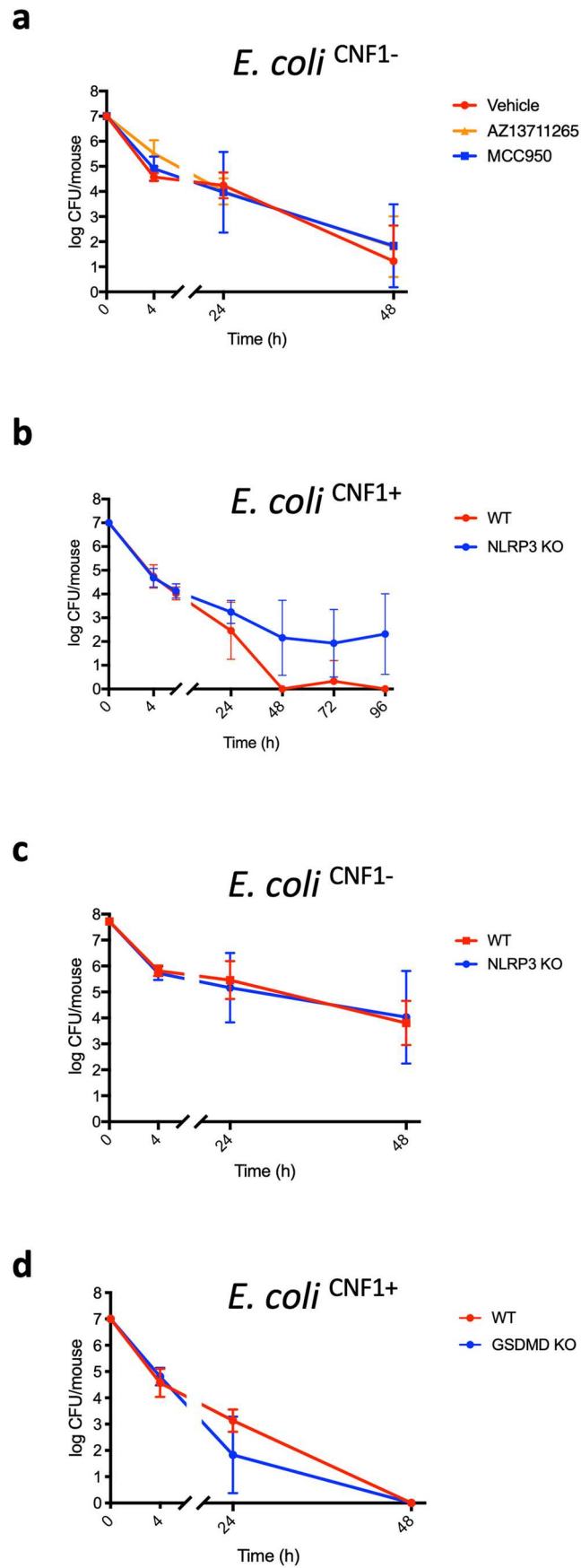


Extended Data Fig. 8 | The NLRP3 T659A mutant inhibit the IL-1 β maturation triggered by SopE and DNT. **a**, HEK293T cells were transfected with plasmids encoding NLRP3 inflammasome components (ASC-GFP, mCaspase-1) and pro-IL-1 β -Flag and either myc-NLRP3 (WT) or myc-NLRP3 T659A together with SopE-HA and treated with MG132 (10 μ M) to block SopE degradation. Supernatants and cell lysates were analyzed by immunoblot.

b, NLRP3 knock-out iBMDMs reconstituted either with NLRP3 or NLRP3 T659A were treated with vehicle or LPS (100 ng/mL) and DNT (1 μ g/mL) for 8 h. The numbers on the side of the immunoblots indicate molecular weight (kDa). Experiments were repeated at least three times, and representative data are shown.



Extended Data Fig. 9 | Macrophages expressing the NLRP3 T659A mutant have an impaired Nigericin- triggered IL-1 β maturation. a-b, iBMDMs stably expressing either NLRP3 or NLRP3 T659A were treated with Nigericin (5 μ M) for 30 min. Supernatants and cell lysates were analyzed by immunoblot and by ELISA for IL-1 β ($n = 4$ biologically independent samples) and TNF- α ($n = 3$ biologically independent samples). Data are expressed as the mean \pm SEM. Statistical analyses were performed using a two-tailed unpaired Student's t-test. The numbers on the side of the immunoblots indicate molecular weight (kDa). Experiments were repeated at least three times, and representative data are shown.




Extended Data Fig. 10 | See next page for caption.

Extended Data Fig. 10 | *E. coli*^{CNF1-} clearing is not affected by Pak1 or NLRP3 inhibition and *E. coli*^{CNF1+} clearing does not rely on GSDMD. a-d, Wild-type or knock-out mice were infected intravenously with isogenic CNF1-deleted *E. coli* (*E. coli*^{CNF1-}) or CNF1 expressing *E. coli* (*E. coli*^{CNF1+}). **a**, Wild-type mice were injected intraperitoneally with 10 mg/kg AZ13711265 or 50 mg/kg MCC950 or vehicle once a day and were infected intravenously with isogenic CNF1-deleted *E. coli* (*E. coli*^{CNF1-}) prior to the collection of peripheral blood at 4 h, 24 h and 48 h for measurement of bacteraemia (n = 5 mice per group). **b**, Wild-type or NLRP3 knock-out C57BL/6 J mice were infected intravenously with CNF1 expressing *E. coli* (*E. coli*^{CNF1+}) prior to the collection of peripheral blood at 4 h, 24 h, 48 h, 72 h and 96 h for measurement of bacteraemia (n = 6 per group). **c**, Wild-type (n = 6 mice) or NLRP3 knock-out C57BL/6 J mice (n = 4 mice) were infected intravenously with isogenic CNF1-deleted *E. coli* (*E. coli*^{CNF1-}) prior to the collection of peripheral blood at 4 h, 24 h and 48 h for measurement of bacteraemia (n = 6 per group). **d**, Wild-type (n = 6 mice) or GSDMD knock-out C57BL/6 J mice (n = 6 mice) were infected intravenously with *E. coli*^{CNF1+} prior to the collection of peripheral blood at 4 h, 24 h and 48 h for measurement of bacteraemia. Experiments were repeated two times and representative data are shown. Data are expressed as the geometric mean \pm 95 CI.



Influenza Virus Infection Impairs the Gut's Barrier Properties and Favors Secondary Enteric Bacterial Infection through Reduced Production of Short-Chain Fatty Acids

Valentin Sencio,^{a,b,c,d,e} Alexandre Gallerand,^f Marina Gomes Machado,^{a,b,c,d,e,g} Lucie Deruyter,^{a,b,c,d,e} Séverine Heumel,^{a,b,c,d,e} Daphnée Soulard,^{a,b,c,d,e} Johanna Barthelemy,^{a,b,c,d,e} Céline Cuinat,^h Angelica T. Vieira,^f Adeline Barthelemy,^{a,b,c,d,e} Luciana P. Tavares,^f Rodolphe Guinamard,^g Stoyan Ivanov,^g Corinne Grangette,^{a,b,c,d,e} Mauro M. Teixeira,^f Benoit Foligné,ⁱ Isabelle Wolowczuk,^{a,b,c,d,e} Ronan Le Goffic,^j Muriel Thomas,^h  François Trottein^{a,b,c,d,e}

^aUniversité Lille, US 41, UMS 2014, PLBS, U1019, UMR 9017, CIL, Centre d'Infection et d'Immunité de Lille, Lille, France

^bCentre National de la Recherche Scientifique, UMR 9017, Lille, France

^cInstitut National de la Santé et de la Recherche Médicale, U1019, Lille, France

^dCentre Hospitalier Universitaire de Lille, Lille, France

^eInstitut Pasteur de Lille, Lille, France

^fCentre Méditerranéen de Médecine Moléculaire (C3M), Institut National de la Santé et de la Recherche Médicale U1065, Université Côte d'Azur, Nice, France

^gInstituto de Ciências Biológicas, Universidade Federal de Minas Gerais, Belo Horizonte, Brazil

^hMicalis Institute, Institut National de Recherche pour l'Agriculture, l'Alimentation et l'Environnement UMR1319, AgroParisTech, Université Paris-Saclay, Jouy-en-Josas, France

ⁱUniversité Lille, INSERM, CHU Lille, U995, Lille Inflammation Research International Center (LIRIC), Lille, France

^jUniversité Paris-Saclay, Institut National de Recherche pour l'Agriculture, l'Alimentation et l'Environnement UR892, UVSQ, VIM, Jouy-en-Josas, France

ABSTRACT Along with respiratory tract disease *per se*, viral respiratory infections can also cause extrapulmonary complications with a potentially critical impact on health. In the present study, we used an experimental model of influenza A virus (IAV) infection to investigate the nature and outcome of the associated gut disorders. In IAV-infected mice, the signs of intestinal injury and inflammation, altered gene expression, and compromised intestinal barrier functions peaked on day 7 postinfection. As a likely result of bacterial component translocation, gene expression of inflammatory markers was upregulated in the liver. These changes occurred concomitantly with an alteration of the composition of the gut microbiota and with a decreased production of the fermentative, gut microbiota-derived products short-chain fatty acids (SCFAs). Gut inflammation and barrier dysfunction during influenza were not attributed to reduced food consumption, which caused in part gut dysbiosis. Treatment of IAV-infected mice with SCFAs was associated with an enhancement of intestinal barrier properties, as assessed by a reduction in the translocation of dextran and a decrease in inflammatory gene expression in the liver. Lastly, SCFA supplementation during influenza tended to reduce the translocation of the enteric pathogen *Salmonella enterica* serovar Typhimurium and to enhance the survival of doubly infected animals. Collectively, influenza virus infection can remotely impair the gut's barrier properties and trigger secondary enteric infections. The latter phenomenon can be partially countered by SCFA supplementation.

KEYWORDS bacterial translocation, gut microbial dysbiosis, short-chain fatty acids, enteric infection, influenza

Even though vaccines and antiviral drugs are available, influenza still constitutes a serious health problem and a key economic issue. Although influenza virus infection generally causes mild-to-moderate disease, it can sometimes, depending on the strain's virulence and the host's health status, trigger severe disease. Seasonal influenza leads to

Citation Sencio V, Gallerand A, Gomes Machado M, Deruyter L, Heumel S, Soulard D, Barthelemy J, Cuinat C, Vieira AT, Barthelemy A, Tavares LP, Guinamard R, Ivanov S, Grangette C, Teixeira MM, Foligné B, Wolowczuk I, Le Goffic R, Thomas M, Trottein F. 2021. Influenza virus infection impairs the gut's barrier properties and favors secondary enteric bacterial infection through reduced production of short-chain fatty acids. *Infect Immun* 89:e00734-20. <https://doi.org/10.1128/IAI.00734-20>.

Editor Andreas J. Bäumlér, University of California, Davis

Copyright © 2021 American Society for Microbiology. All Rights Reserved.

Address correspondence to François Trottein, francois.trottein@pasteur-lille.fr.

Received 21 November 2020

Returned for modification 29 December 2020

Accepted 22 March 2021

Accepted manuscript posted online 5 April 2021

Published 16 August 2021

~300,000 deaths a year worldwide (1). Most of these influenza-related deaths are due to acute respiratory distress symptoms, compromised pulmonary functions, multiorgan dysfunction, and secondary bacterial infections (2, 3). Along with lung disease *per se*, influenza is frequently associated with extrapulmonary complications, including intestinal disorders (4). Indeed, the results of preclinical and clinical studies indicate that influenza can lead to nausea, vomiting, and/or diarrhea (4–8). The causes, nature, and consequences of these associated intestinal disorders have yet to be fully characterized.

We and others have shown that influenza alters the composition and function of the gut microbiota (6–10). The consequences of this dysbiosis on the disease's outcome remain to be fully defined (11). Wang and colleagues (6) were the first to report a link between gut dysbiosis and intestinal inflammation. An impact of gut dysbiosis on secondary bacterial infection in the intestine has also been suggested (7, 8). Lastly, our recent findings indicate that by reducing the production of short-chain fatty acids (SCFAs; the main metabolites of the gut microbiota), influenza favors secondary bacterial infection of the lungs (10). With regard to the role of SCFAs in gut homeostasis (12–17), we hypothesize herein that the influenza virus infection's impairment of SCFA production weakens the gut's barrier function and thus favors secondary enteric infections.

Short-chain fatty acids represent the end products of dietary fiber fermentation (for reviews, see references 18 and 19). The SCFAs supply energy to colonocytes and are critical for intestinal homeostasis, gut functions, and gut metabolism. Although the SCFAs' role in the control of gut inflammation appears to be a function of the disease state, these compounds tend to reinforce the gut barrier, a critical property for controlling the dissemination of gut commensals, opportunistic pathogens, and microbial components. Moreover, SCFAs display antimicrobial activity by favoring the synthesis of antimicrobial components (including antimicrobial peptides) in the intestine (17–20). In the present study, we sought to specify the nature of gut disorders (including disruption of barrier functions) during an experimental influenza A virus (IAV) infection. We found that (i) decreased SCFA production is important for these effects and (ii) SCFA supplementation during IAV infection partially protects animals from secondary infection with the enteric pathogen *Salmonella enterica* serovar Typhimurium. Taken as a whole, our data emphasize that viral respiratory infections can remotely impact gut homeostasis and intestinal barrier functions and thereby favor secondary bacterial infections. Reduced production of gut microbiota-derived fermentative products (SCFAs) might have a critical role in these alterations.

RESULTS

Influenza virus infection is associated with intestinal inflammation and disorders. Influenza virus infection can be accompanied by intestinal symptoms, leading to intestinal inflammation and immune injury (5, 6). We first characterized the nature of these intestinal disorders in a mouse model of sublethal influenza virus infection (see Fig. S1A in the supplemental material). In line with a previous study (6), no IAV genomic RNA was detected in the intestine over the course of the infection (Fig. S1B). Relative to that in mock-infected mice, significant but transient colon shortening (a marker of inflammation) was observed at 7 days postinfection (dpi) in IAV-infected animals (Fig. 1A). The use of NF- κ B-luciferase reporter mice also indicated an increase in intestinal NF- κ B activity, a marker of stress and inflammation, at 7 dpi (Fig. 1B and Fig. S1C). The expression of NF- κ B was most obvious in the cecum and colon but was also observed in the small intestine (Fig. 1B and Fig. S1D). In contrast (but in line with other published studies [7, 9]), the intestine had a normal histological appearance at 7 dpi, with no difference (i.e., no remodeling) in crypt depth in the colon and the crypt/villus length in the duodenum (Fig. 1C and Fig. S1E). Influenza virus infection was also associated with a low blood concentration of citrulline (a marker of the functional enterocyte mass and metabolic activity [21]) at 7 dpi (Fig. 1D). Overall, a sublethal influenza virus infection was associated with colon shortening, NF- κ B activation, and a relative decrease in intestinal metabolic function but not major structural remodeling of the epithelium.

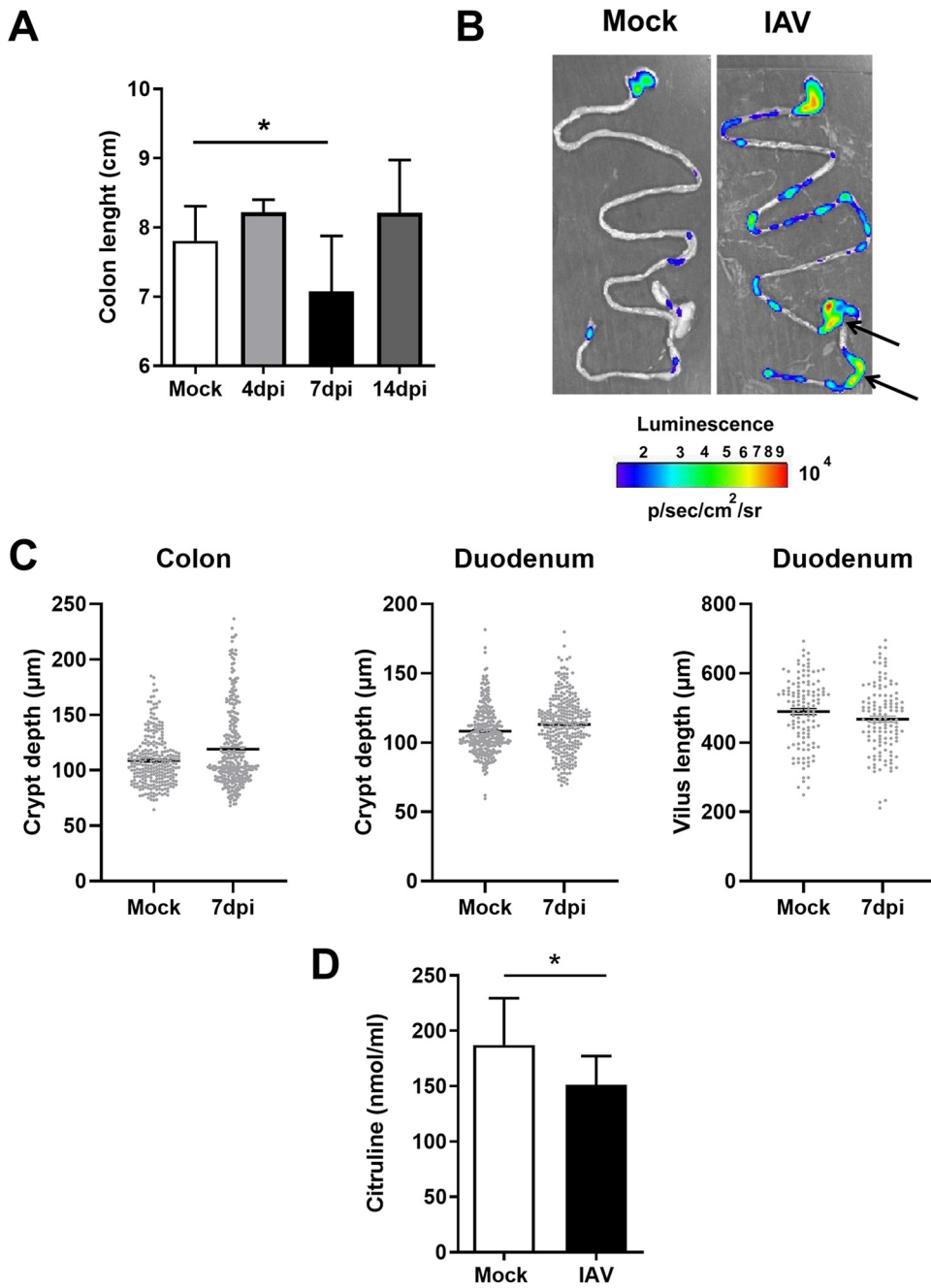


FIG 1 Intestinal inflammation and disorders during IAV infection. Mice were infected or not (mock) with IAV (H3N2). (A) The colon length was measured at 4, 7, and 14 dpi ($n=6$ to 13). For the mock control, colons were collected at day 7. (B) *Ex vivo* bioluminescence imaging was performed on guts collected from naive and IAV-infected (7 dpi) NF- κ B-luciferase transgenic mice. Arrows indicate higher NK- κ B expression. The scale indicates the average radiance. One representative image of at least 10 mice is shown. (C) Histological analysis of intestinal (colon and duodenum) sections in mock-treated mice and IAV-infected mice (7 dpi). Crypt depths and villus lengths were determined after hematoxylin and eosin coloration ($n=9$ to 10/group). (D) Citrulline concentrations in the blood collected from mock-treated mice and IAV-infected mice (7 dpi) ($n=14$). Results represent two pooled experiments. Significant differences were determined using the Mann-Whitney U test (C and D) and the Kruskal-Wallis ANOVA test (A). (*, $P < 0.05$).

Influenza leads to alterations in intestinal gene expression and impairment of the gut barrier. We next analyzed gene expression in the colons of the IAV-infected mice. The expression of a large number of genes (1,433 genes with a fold change of >2 ; adjusted P value, <0.05) was modulated at 7 dpi (Fig. S2A). An ontological analysis highlighted the upregulation of several families of genes with immune and

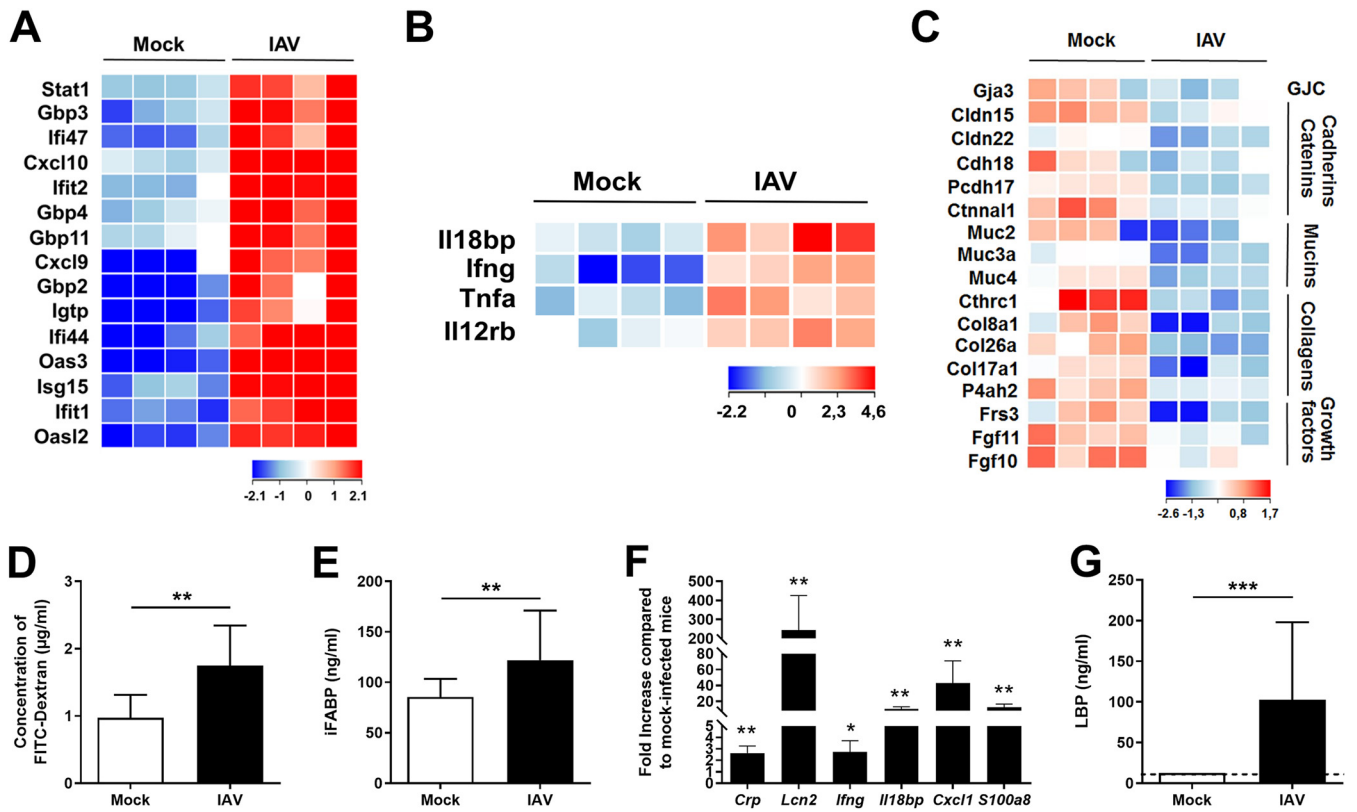


FIG 2 Altered colonic gene expression and increased gut permeability during IAV infection. (A to C) Transcriptomic analysis of colon samples from mock-treated and IAV-infected mice (7 dpi). Shown are heat maps representing ISGs (A), NF-κB-dependent inflammatory genes (B), and transcriptional expression of components involved in barrier functions and epithelial integrity (GJC, gap junction components) (C) ($n=4$ /group). (D) Fluorescence intensity quantified in the blood of mice 4 h after FITC-dextran oral administration ($n=8$). (E) Intestinal fatty acid-binding protein (iFABP) concentration in the blood ($n=21$ to 28). (F) Analysis of gene expression in liver by RT-qPCR ($n=5$). (G) LPS-binding protein (LBP) concentration in the blood ($n=11$ to 15). (D to G) Results are from two to three pooled experiments (7 dpi). Significant differences were determined using the Mann-Whitney U test (D, E, and G) and the Kruskal-Wallis ANOVA test (F) (*, $P < 0.05$; **, $P < 0.01$; ***, $P < 0.001$).

inflammatory functions (Fig. S2B). Large numbers of interferon-stimulated genes (ISGs) and, to a lesser extent, NF-κB-dependent inflammatory genes were upregulated during influenza (Fig. 2A and B). A reverse transcription-quantitative PCR (RT-qPCR) analysis confirmed the transient alteration in gene expression in the colon (Fig. S2C). Many of the downregulated genes had cell functions (e.g., transport) and metabolic functions (e.g., O-linked glycosylation) (Fig. S2D). IAV infection was also associated with the altered expression of genes involved in mucin type O glycan biosynthesis (Fig. S2E). Transcripts of genes involved in barrier functions were also downregulated, albeit more moderately; these included the gap junction component *Gja3*, cadherin/catenin family members, collagens, and fibroblast growth factors (Fig. 2C and Fig. S2C).

The barrier function is one of the gut's most important features. Under normal conditions, an intact gut barrier prevents the excessive spreading of microbial components into the blood and peripheral tissues. Disease conditions can disrupt the barrier function and thus lead to bacterial translocation, systemic inflammation, and septic shock. IAV's impact on the gut's barrier property has not been characterized in detail and so warranted investigation. To this end, we orally administered fluorescein isothiocyanate (FITC)-dextran to IAV-infected mice and then assayed its concentration in plasma. Relative to the translocation of FITC-dextran from the gut lumen to the plasma in the control, enhanced translocation was observed at 7 dpi in infected mice (Fig. 2D). Accordingly, the blood concentration of intestinal fatty acid-binding protein (a systemic marker associated with altered intestinal permeability) was significantly elevated at 7 dpi (Fig. 2E). Disturbances in the intestinal barrier can result in the increased portal influx of bacteria or their products into the liver, where they can cause inflammation

and acute injury. A quantitative RT-PCR analysis highlighted the upregulated expression of inflammatory genes in the liver, including acute-phase proteins (i.e., C-reactive protein, lipocalin-2), cytokines, chemokines, and antimicrobial peptides (Fig. 2F and data not shown). Lastly, the serum concentration of lipopolysaccharide (LPS)-binding protein (which is produced primarily as an acute-phase protein in the liver) was elevated at 7 dpi (Fig. 2G). Overall, influenza virus infection strongly modified gene expression in the gut and altered the intestinal epithelium's barrier properties.

A restricted food intake mimicking influenza disease does not recapitulate intestinal inflammation and barrier dysfunction. We and others have shown that reduced food intake and associated weight loss due to acute viral respiratory infection trigger an alteration of the composition of the gut microbiota (10, 22). As dysbiotic microbiotas can lead to gut inflammation and altered barrier properties, we investigated whether rapid reduction of food consumption, as observed during IAV infection, may lead to intestinal inflammation and gut disorders. To this end, we designed a pair-feeding experiment exactly as described previously (10). Pair-fed mice were sacrificed when weight loss attained 15% of the initial weight. As depicted in Fig. 3A, the colon length of pair-fed mice was significantly reduced, as is the case during an IAV infection. However, the intestinal barrier, as measured by FITC-dextran, intestinal fatty acid-binding protein, and LPS-binding protein in blood, was unchanged (Fig. 3B). Transcriptomic analysis of colons collected from pair-fed mice and IAV-infected mice revealed a global resemblance, as assessed by gene set enrichment analysis (GSEA) (Fig. 3C). However, among the major differences between the two signatures was the absence of ISG expression in pair-fed mice (Fig. S3A). Expression of genes belonging to the NF- κ B pathway was also specifically altered in IAV-infected mice. In line with Fig. 3B, the expression of transcripts of genes involved in barrier functions were not decreased in the colons of pair-fed mice, unlike with IAV-infected mice (Fig. S3B). An ontological analysis highlighted the upregulation of several families of genes involved in metabolism, signaling, and transport in the colons of pair-fed mice (Fig. 3D). In particular, pathways involved in lipid (fatty acid) metabolism and the transport of small molecules were induced in pair-fed mice and IAV-infected mice (Fig. 3E). Families of genes found to be downregulated in pair-fed mice and in part in IAV-infected mice included genes involved in cell cycle and mitosis (Fig. 3F and Fig. S3C). Collectively, inappetence and rapid weight loss do not appear to play major roles in gut inflammation and an altered intestinal barrier during influenza virus infection.

SCFA supplementation partially reverses intestinal barrier disruption. We have previously reported that influenza virus infection leads to gut dysbiosis and strongly reduces the production of the fermentative products SCFAs (10). In the IAV-infected mouse model studied here, we confirmed that cecal concentrations of acetate (the most abundant SCFA), propionate, and butyrate were abnormally low at 7 dpi (Fig. 4A). Although SCFAs are important for intestinal homeostasis and function, their role in gut inflammation is more context dependent (12, 15–17). We hypothesized that the drop in SCFA production during influenza virus infection might influence intestinal disorders. To this end, the mice's drinking water was supplemented with acetate, propionate, and butyrate starting 2 days after IAV infection. Treatment with SCFAs moderately but significantly rescued the decrease in colon length in these animals and thus indicated that the inflammation was less intense (Fig. 4B). The translocation of FITC-dextran from the gut lumen to the plasma was reduced in SCFA-treated animals relative to that in controls (Fig. 4C). This finding indicates that SCFA treatment partially restored the intestine's physical barrier. We then looked at whether the restoration of barrier function translated into less inflammation in the liver. As shown in Fig. 4D, the expression of inflammatory genes in the liver was significantly lower in mice fed SCFA-supplemented drinking water than in nonsupplemented mice. SCFA treatment may indirectly exert these effects by modulating the composition of the gut microbiota. To investigate this possibility, the feces from SCFA-treated and untreated mice, previously infected or not infected with IAV, were collected, and 16S rRNA sequencing was performed. An analysis of the beta diversity by principal-coordinate analysis (PCoA) clearly

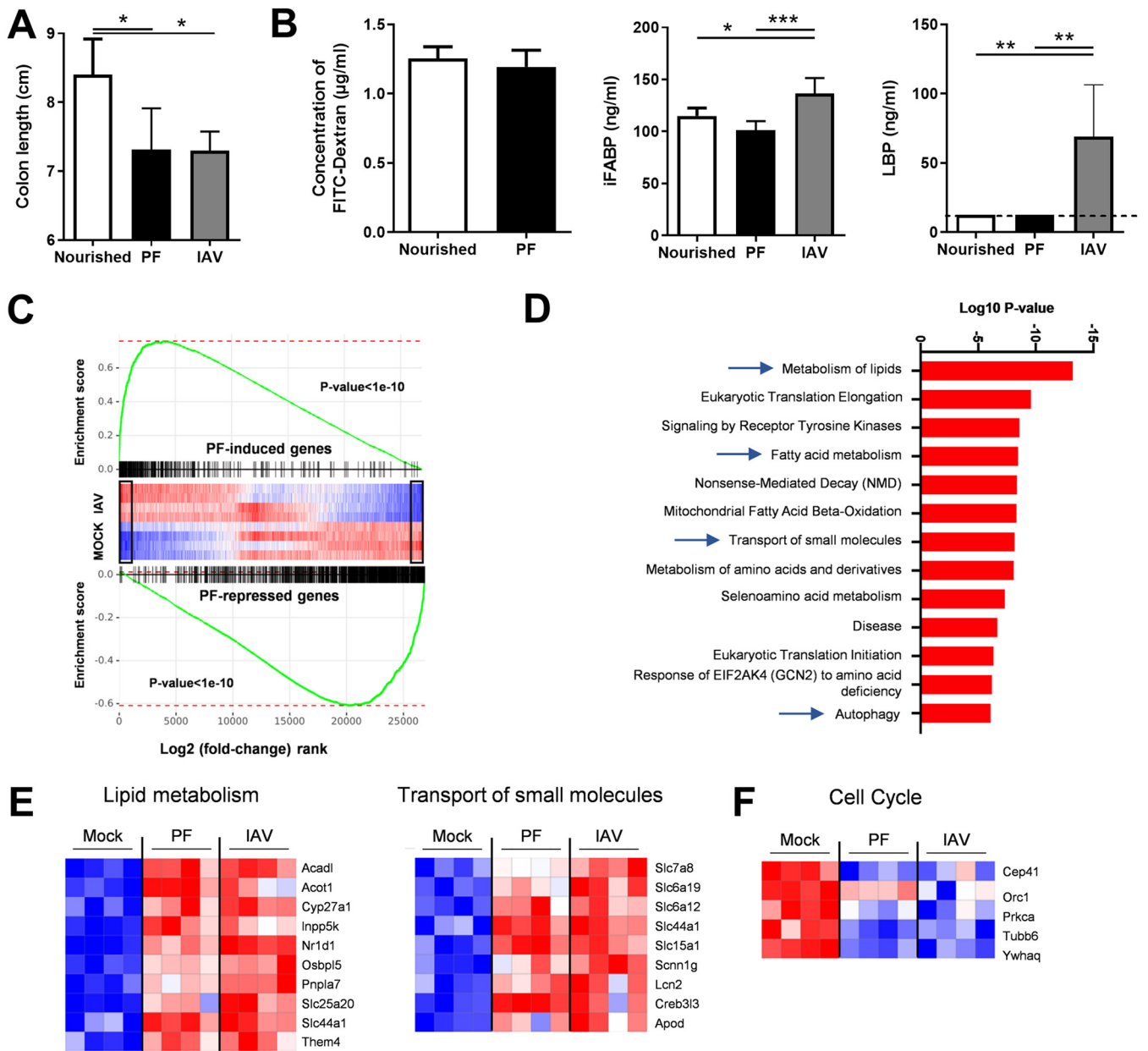


FIG 3 Analysis of gut disorders in pair-fed mice. The food access was restricted in order to mimic the weight loss of IAV-infected mice (7 dpi, ~15% of body mass). (A) The colon lengths of pair-fed mice and normally nourished mice were measured. (B) FITC-dextran, intestinal fatty acid-binding protein (iFABP), and LPS-binding protein (LBP) concentrations in the blood. (C and D) Analysis of gene expression in the colons of pair-fed mice and IAV-infected mice. (E) GSEA plot showing enrichment of pair-feeding (PF)-induced (top) and pair-feeding-repressed (bottom) genes in mock-treated and IAV-infected mice. Black rectangles indicate statistically significant differences in the mock-versus-IAV comparison. Global IAV and pair-feeding signatures appear statistically correlated. (F) Gene set enrichment analysis was run on pair-feeding (PF)-induced genes in a comparison with those in the mock condition (fold change, >2; adjusted *P* value < 0.05) using the Reactome database. (E, left) Heatmap showing significantly modulated genes (fold change, >2; adjusted *P* value < 0.05) related to lipid metabolism from the Reactome database’s “Metabolism of lipids,” “Fatty acid metabolism,” and “Mitochondrial Fatty Acid Beta-Oxidation” pathways. (E, right) Heatmap representing the expression of genes from the Reactome database’s “Transport of small molecules” pathway. (F) Heatmap representing the expression of genes from the Reactome database’s “Cell Cycle” pathway. (A and B) Significant differences were determined using the Kruskal-Wallis ANOVA test and the Mann-Whitney *U* test (FITC dextran) (*n* = 6 to 12) (*, *P* < 0.05; **, *P* < 0.01; ***, *P* < 0.001).

showed that, whatever the condition (mock or IAV infection), the bacterial populations from SCFA-treated mice and untreated mice did not differ (Fig. 4E). On the other hand, in line with the results in references 7, 8, and 10 and relative to mock-infected animals, PCoA clearly indicated an intergroup difference in the fecal microbiota at 7 dpi. A taxonomic analysis did not reveal any major changes at the phylum and lower taxonomic levels between SCFA-treated and untreated mice (Fig. S4A and S4B and data not shown). This indicates that SCFA treatment does not reverse intestinal barrier

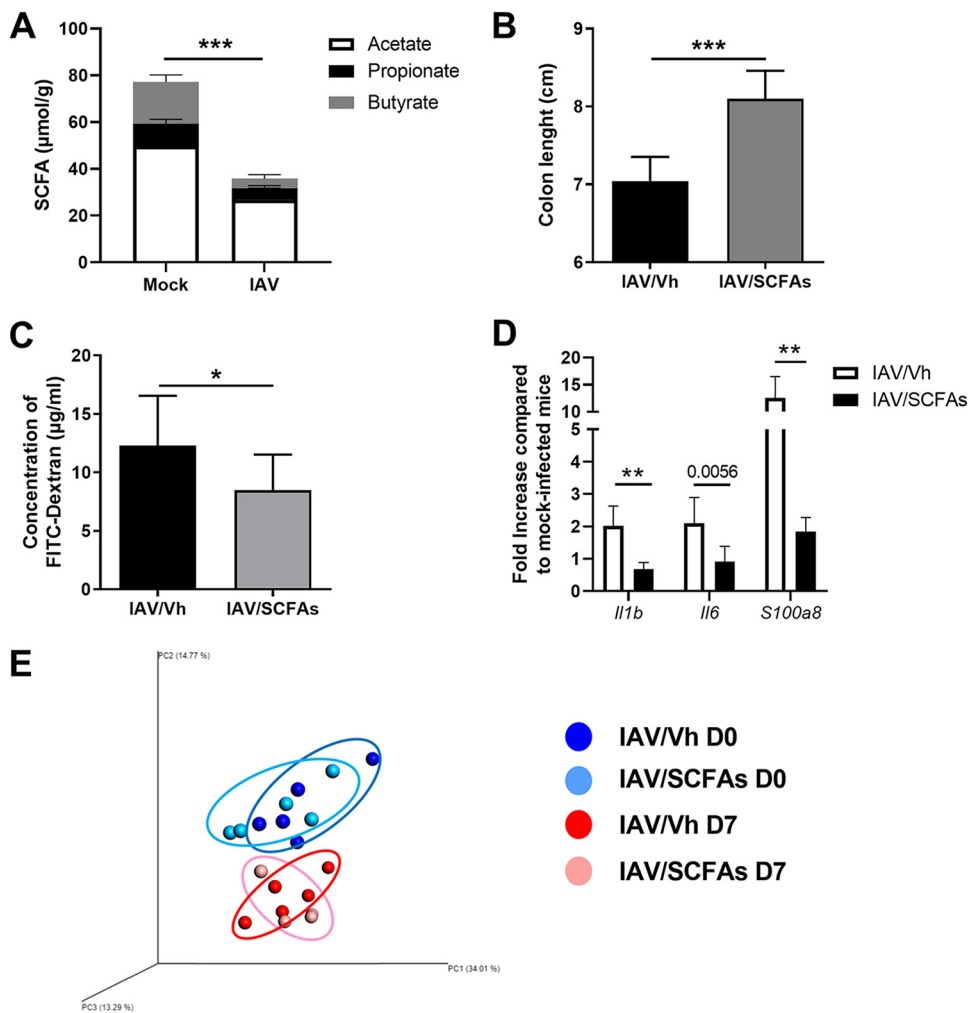


FIG 4 Effect of SCFA supplementation during IAV infection on gut disorders. (A) Cecal concentrations of total and individual SCFAs in mock-treated and IAV-infected mice (7 dpi) ($n=7$, one experiment out of at least six performed). (B to D) Mice were infected with IAV. Two days after infection, mice were treated with acetate, propionate, and butyrate (150 mM, 50 mM, 20 mM, respectively, in drinking water) or with vehicle (Vh). (B) The colon length was measured at 7 dpi ($n=6$ to 9; one representative experiment out of two). (C) Fluorescence intensity quantified in the blood of mice 4 h after FITC-dextran oral administration ($n=14$; two pooled experiments). (D) Gene expression in total liver was analyzed by RT-qPCR ($n=6$; one representative experiment out of two). (E) Analysis of the gut microbiota's composition was performed on feces collected from uninfected mice treated (bright blue) or not (dark blue) with SCFAs for 5 days and from mice infected 7 days earlier with IAV and treated (pink) or not (red) with SCFAs at 2 dpi ($n=4$ to 5). Bacterial communities were clustered using PCoA of weighted UniFrac distance matrices (beta diversity). The first three principal coordinates (PC1, PC2, and PC3) are plotted for each sample, and the percentage variation in the plotted principal coordinates is indicated on the axes. Each spot represents one sample, and each group of mice is denoted by a different color. The distance between dots represents the extent of compositional difference. D0 and D7, days 0 and 7. Significant differences were determined using the Mann-Whitney U test (A to C) and the Kruskal-Wallis ANOVA test (D) (*, $P < 0.05$; **, $P < 0.01$, ***, $P < 0.001$).

disruption by modulating the composition of the gut microbiota. Taken as a whole, the reduced production of SCFAs by the gut microbiota influences barrier leakage during influenza virus infection.

SCFA supplementation during influenza attenuates bacterial enteric infections.

Recent research indicates that gut alterations during an influenza virus infection may favor the local colonization and systemic dissemination of the foodborne pathogen *Salmonella enterica* serovar Typhimurium (7, 8). The underlying mechanism has yet to be defined. We postulated that the influenza-associated drop in intestinal SCFA production and epithelial permeability are causally related to these secondary enteric infections. To test this hypothesis, we developed a model of secondary enteric

bacterial infection (Fig. S5A). Mice previously infected with IAV were orally exposed to *S. Typhimurium*. Unlike in other studies (7, 8), we deliberately did not treat the mice with antibiotics prior to *S. Typhimurium* infection. After preliminary dose-response experiments, a sublethal dose was inoculated into IAV-infected mice by gavage (7 dpi). We measured weight loss and the mortality index in doubly infected mice. In contrast to naive mice infected with *S. Typhimurium* or IAV alone, IAV-infected mice lost weight 6 to 7 days after *S. Typhimurium* infection (Fig. 5A and Fig. S5B). Lastly, IAV-infected mice succumbed to secondary enteric infection, while mice infected with *S. Typhimurium* or IAV alone did not (Fig. 5B). Of note, in contrast to IAV-infected mice and the control mice, pair-fed mice were not susceptible to secondary *Salmonella* infection (Fig. S5C).

To investigate whether the local drop in SCFA levels during IAV infection was involved in secondary *S. Typhimurium* infection, the mice's drinking water was supplemented with SCFAs from day 2 after influenza virus infection onwards (Fig. S5A). In oral infection models in mice, *S. Typhimurium* colonizes sites in the distal intestine, such as the cecum, before spreading to systemic tissues and shedding via the feces into the environment (23). SCFA treatment failed to lower the bacterial load in the cecum, indicating that SCFAs did not have a local impact on bacterial growth (Fig. 5C). Supplementation of SCFAs also failed to reduce the number of *Salmonella* organisms in the feces (not shown). This suggested that SCFA supplementation has no role in the local control of *Salmonella* infection. In line with this, SCFA supplementation failed to enhance the intestinal transcription of factors known to participate in the host defense against *Salmonella* (7), including cytokines and antimicrobial peptides (Fig. S5D). In contrast, SCFA supplementation reduced the translocation of bacteria, as revealed by the lower bacterial count in the liver (Fig. 5D). Lastly, the body weight loss due to secondary enteric infection and the mortality rate were lower in SCFA-supplemented mice, although the difference from controls was not statistically significant (Fig. 5E and F). We conclude that SCFA treatment during the course of influenza tended to reduce secondary enteric infection and mitigate the latter's systemic consequences.

DISCUSSION

Our data support the hypothesis that viral respiratory infection can remotely trigger intestinal disorders (namely, mild inflammation and altered barrier functions) and thus have a major impact on secondary enteric infections. Furthermore, our data show that SCFA supplementation during an influenza virus infection ameliorated gut disorders and reduced secondary *Salmonella* infection. Given that gut dysfunction has been described in many critical illnesses, these relationships might have clinical relevance.

Several studies have highlighted the impact of influenza virus infection on gut homeostasis, with dysbiosis and inflammation (6–10, 22). In line with other researchers (7, 9), we did not observe major intestinal architecture remodeling at 7 dpi (i.e., when gut disorders peak). However, a shorter colon and altered intestinal metabolic functions (as revealed by systemic citrulline levels) indicated the presence of intestinal dysfunction in our mouse model. Furthermore, the present study is the first to have shown that influenza virus infection is associated with disruption of the intestine's barrier functions. In line with the results of Deriu and colleagues (7), our overall transcript analysis indicated that the expression of a large panel of inflammatory (NF- κ B-dependent) genes and immune genes (in particular, ISGs) was modulated in the intestine during an IAV infection. ISG expression probably reflects the increased systemic interferon levels during infection, since a quantitative PCR did not detect any genomic IAV RNA in the intestine (6, 10). Although speculative at this stage, a change in the enteric virome during influenza (exposure to virus-associated signals) might also influence local ISG expression (24). Influenza virus infection is also associated with a low expression of genes involved in the maintenance of barrier functions and with elevated paracellular permeability, as assessed by enhanced passage of FITC-dextran into the blood. This alteration in barrier function was combined with enhanced inflammatory gene

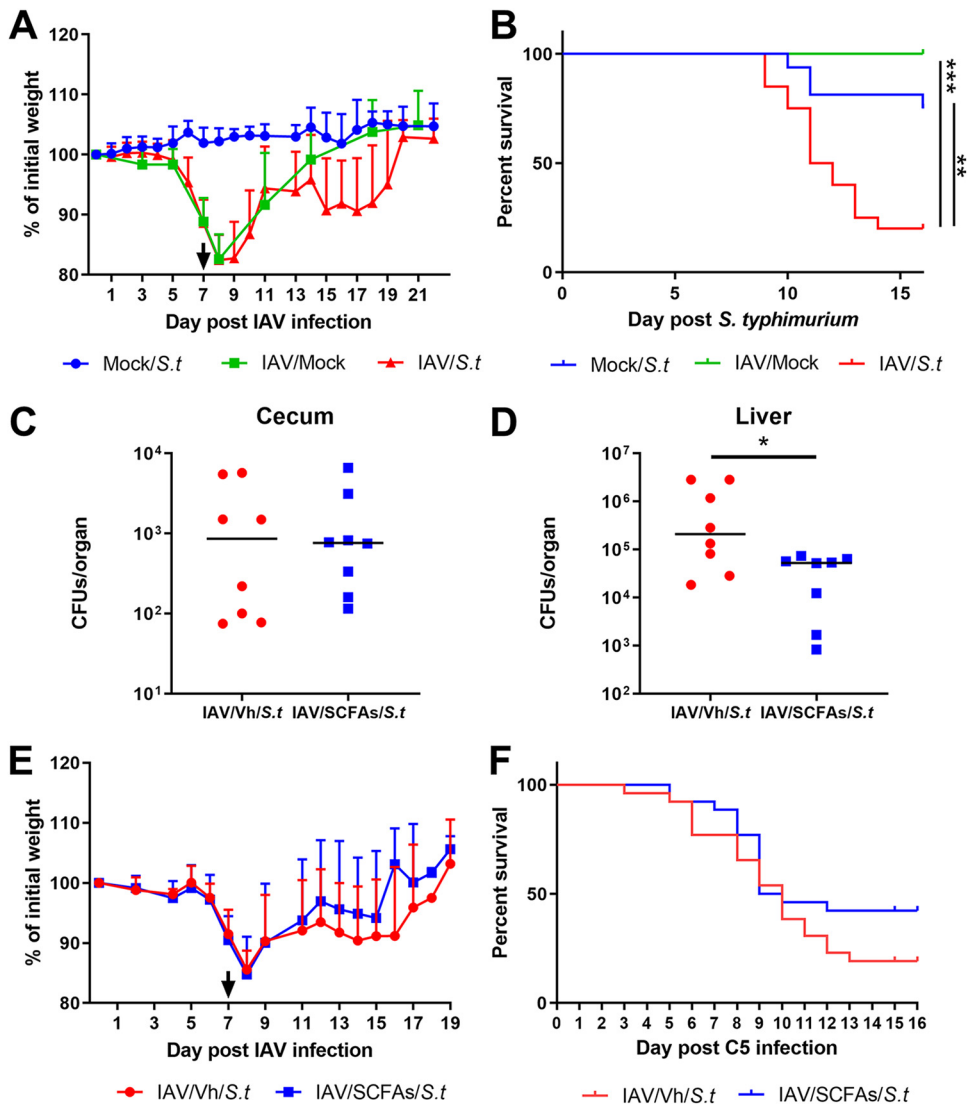


FIG 5 Effect of SCFA supplementation during IAV infection on secondary *Salmonella* Typhimurium (*S.t*) infection. (A and B) Mice were infected or not (mock) with IAV (H3N2). At 7 dpi, mice were (super)infected or not with *S. Typhimurium*. (A) Body weight evolution (percentages of initial body weights). (B) The survival of singly infected and doubly infected animals was monitored. (A and B) Results from two pooled experiments are shown ($n=16$). (C to E) The same operation was repeated for IAV-infected mice treated or not with acetate, propionate, and butyrate (150 mM, 50 mM, and 20 mM, respectively, in drinking water) at 2 dpi. (C and D) The numbers of bacteria in the cecum (C) and liver (D) were determined 7 days after the bacterial challenge ($n=8$; a representative experiment out of two). The body weight (E) and survival rate (F) of superinfected animals were monitored ($n=24$; results from three pooled experiments are shown). (C and D) Significant differences were determined using the Mann-Whitney *U* test. (B, F) Rates of mouse survival were compared using Kaplan-Meier analysis and the log rank test (*, $P < 0.05$).

expression in the liver, perhaps as a result of the portal translocation of bacterial components from the gut. Pair-feeding experiments indicated that reduced food consumption during influenza is not involved in gut inflammation and barrier disruption (and secondary *Salmonella* infection). There are probably many causes of intestinal barrier leakage. One can reasonably hypothesize that microbiota dysbiosis, altered microbiota-host interactions, and inflammation during influenza are causally linked to the alterations in barrier properties (25, 26). Hence, the loss of beneficial members of the microbial community (*Lachnospiraceae* and *Lactobacillus*), the overgrowth of pathosymbionts (*Alphaproteobacteria*, *Gammaproteobacteria*, and the *Escherichia* genus) and/or a shift in metabolism (such as altered fermentation) may accentuate the gut's leakiness (10). Enhanced production of toxic metabolites may also be involved in barrier

disruption. For instance, the excessive production of phenolic and sulfur-containing compounds by dysbiotic microbiota can alter tight junctions between cells and disrupt barrier functions (27, 28). Counts of mucin-degrading bacteria like *Ruminococcus* increase during influenza (10). These bacteria erode the colonic mucosa and favor interactions between luminal bacteria and the intestinal epithelium, which in turn may lead to inflammation and the impairment of barrier function (29).

The question of the impact of gut dysbiosis and intestinal disorders on influenza outcomes then arises. Increased leakiness of the gut barrier and dissemination of commensal bacteria and/or their components might lead to extraintestinal complications, such as acute liver injury, acute respiratory distress syndrome, bacterial respiratory tract coinfections, and systemic symptoms (e.g., a cytokine storm, circulatory collapse, sepsis, and multiorgan dysfunction) (11). These complications are observed in critically ill patients and constitute key causes of mortality (30–32). However, the extent to which gut perturbations cause extraintestinal disorders remains to be determined. Gut barrier dysfunction is a well-known feature of aging and chronic metabolic diseases, like obesity (25, 33–36). It would be interesting to look at whether these alterations amplify secondary extraintestinal complications in obese and older individuals, who are particularly at risk of developing critical illnesses during influenza (31). The dissemination of microbial components through the gut wall might affect not only inflammation and organ functions but also host metabolism (such as glucose homeostasis) and other outcomes (37–39). Our present data highlighted the altered expression of many inflammatory genes and metabolic genes (data not shown) in the liver. We also recently showed that the homeostasis of adipose tissue is dramatically altered during experimental influenza, with inflammation and metabolic perturbations (40). The impact of compromised gut barrier function on hepatic and adipose inflammation and metabolism warrants investigation.

Influenza virus infection is associated with a drop in the production of SCFAs; this phenomenon is due, at least in part, to reduced food (fiber) consumption by the diseased host (10). This drop may limit the energy supply to colonocytes, accentuate mucosal inflammation, and alter the intestine's barrier functions. SCFAs are currently considered to be a promising adjunct treatment for active inflammatory bowel disease and diversion colitis (for a review, see reference 20). Various approaches (including enemas of butyrate and mixtures of acetate, propionate, and butyrate) have given differing clinical outcomes (41–43). In the present study, we observed a beneficial effect of SCFA supplementation on gut barrier functions, as measured by greater gut permeability and diminished inflammatory gene expression in the liver. This effect was not associated with major changes in the composition of the gut microbiota. In contrast, we did not find a marked effect on local inflammatory gene expression (data not shown), even though SCFA supplementation rescued the colon shortening typically observed in a setting of inflammation. This is in line with suggestions that the SCFAs' functional activities depend on the disease context and severity. Recent research indicates that gut disorders during influenza virus infection may favor the local colonization and systemic dissemination of the intestinal pathogenic bacterium *Salmonella* (7, 8), a leading cause of acute gastroenteritis and inflammatory diarrhea. Our data confirm these findings, although the underlying mechanism has yet to be defined. However, we postulated that the influenza-associated drop in intestinal SCFA production might cause, at least in part, secondary enteric infections. Acetate can protect against *E. coli* (13), while propionate and butyrate can protect against *S. Typhimurium* (44) and *Citrobacter rodentium* (45, 46). In these settings, SCFAs inhibited pathogen growth directly or (through host signaling) indirectly, leading to the production of cytokines and antimicrobial compounds (13, 45, 47, 48) and to increased bactericidal activity by macrophages (46). SCFAs can also prevent the abnormal expansion of antibiotic-resistant strains of *Enterobacteriaceae*, in part by increasing intracellular acidification (49). SCFAs (including propionate) have also been shown to regulate (favor) the growth and virulence of enteric pathogens, such as enterohemorrhagic and adherent-

invasive *E. coli* (50, 51). In our experimental model, mice fed SCFAs before an *S. Typhimurium* infection did not show a lower degree of local bacterial colonization, indicating a lack of a direct effect on bacterial growth. In contrast, SCFA supplementation limited systemic bacterial dissemination, probably by reinforcing intestinal barrier properties, as our data show. Interestingly, SCFA supplementation tended to lower the degree of morbidity (i.e., improved weight loss recovery) and to increase the survival rate of doubly infected animals. Mechanisms through which SCFAs reduced *Salmonella* dissemination in our setting are still elusive. They might include a direct role in virulence factors involved in bacterial invasion and translocation (52) and/or an indirect role in host signaling pathways. Among them, activation of the G protein-coupled receptors free fatty acid receptor 3 and/or 2 (receptors for acetate and/or propionate) and/or inhibition of histone deacetylase (butyrate and, to a lower extent, propionate) are probable. Together with the fact that acetate protected against postinfluenza pneumococcal infection in the lungs (10), our finding highlights the potential benefit of using SCFAs to lower secondary influenza outcomes. In this context, the restoration of mucosa homeostasis might be achieved by stimulating SCFA production via prebiotics (e.g., high-fiber diets) or probiotics (i.e., SCFA producers themselves). The clinical efficacy of this adjunct treatment remains to be determined.

MATERIALS AND METHODS

Mice and ethics statement. Specific-pathogen-free C57BL/6J mice (7 weeks old, male) were purchased from Janvier (Le Genest-St-Isle, France). Mice were maintained in a biosafety level 2 facility in the Animal Resource Center at the Lille Pasteur Institute for at least 2 weeks prior to usage to allow appropriate acclimation. Unless specified, mice were fed a standard rodent chow (SAFE A04; SAFE, Augy, France) and had access to water *ad libitum*. This diet contains ~11.8% fiber, including ~10% water-insoluble fiber (3.6% cellulose) and 1.8% water-soluble fiber. All experiments complied with current national and institutional regulations and ethical guidelines (Institut Pasteur de Lille/B59-350009). The protocols were approved by the institutional ethical committee (Comité d'Éthique en Experimentation Animale [CEEAA] 75), Nord Pas-de-Calais. All experiments were approved by the Education, Research and Innovation Ministry, France, under registration number APAFIS 13743-201802221144403. Transgenic mice expressing the firefly luciferase gene under the control of a nuclear factor κ B (NF- κ B) promoter (NF- κ B-luciferase reporter) have been previously described (53). NF- κ B-luciferase transgenic BALB/c mice express the luciferase gene driven by two NF- κ B sites from the κ light chain enhancer in front of a minimal *fos* promoter. They were obtained by backcrossing NF- κ B-luciferase transgenic B10.A mice (a kind gift of Richard Flavell, Howard Hughes Medical Institute) with BALB/c mice to ensure the production of transgenic mice with white fur to avoid absorption of the light by the dark skin and fur of the B10.A mice.

Viruses and bacteria. The mouse-adapted H3N2 IAV strain Scotland/20/1974 and the *Salmonella enterica* serovar Typhimurium strain C5 are described in references 54 and 55, respectively.

Infections and assessment of bacterial loads. For infection with IAV alone, mice were anesthetized by intramuscular injection of 1.25 mg of ketamine plus 0.25 mg of xylazine in 100 μ l of phosphate-buffered saline (PBS) and then intranasally (i.n.) infected with 50 μ l of PBS containing (or not, in a mock sample) 30 PFU of IAV (54, 56). For infection with *S. Typhimurium* alone, gradual doses were used (oral gavage, 200 μ l). For secondary infection, IAV-infected mice were intragastrically challenged at 7 dpi with *S. Typhimurium* (1×10^4 CFU, 200 μ l). This dose is sufficient to allow bacterial outgrowth, dissemination, and death in mice previously infected with IAV. In doubly infected mice, bacteria in the cecum and liver were counted 7 days after the bacterial challenge by plating serial 10-fold dilutions of cecum or liver homogenates onto Hektoen agar plates. The plates were incubated at 37°C with 5% CO₂ overnight, and viable bacteria were counted 24 h later. Survival and body weight were monitored daily after IAV infection, and mice were euthanized when they lost in excess of 20% of their initial body weight.

Measurement of NF- κ B activity. Bioluminescence measurements of the NF- κ B-luciferase transgenic mice were measured using the IVIS 200 imaging system (PerkinElmer, Waltham, MA). Mice were anaesthetized, and luminescence was measured 7 days after IAV infection as described previously (53). Briefly, after anesthesia, luciferin was i.n. instilled (0.75 mg \cdot kg of body weight⁻¹). Living Image software (version 4.0; PerkinElmer) was used to measure the luciferase activities. Bioluminescence images were acquired for 1 min with the f-stop equal to 1 and binning equal to 8. A digital false-color photon emission image of the mouse was generated, and photons were counted within the whole-body area. Photon emission was measured as radiance, which corresponds to the sum of the photons per second from each pixel inside the region of interest (ROI) per number of pixels (photons per second per square centimeter per steradian).

Transcriptomic analysis. Colon transcriptional profiling was performed using Agilent's SurePrint G3 mouse GE 8 \times 60K kit (G4852A). Minimum information about the microarray experiment (MIAME) was deposited in ArrayExpress at EMBL (<http://www.ebi.ac.uk/microarray-as/ae>; accession numbers E-MTAB-6707 [IAV] and E-MTAB-10036 [pair-feeding]). Arrays were hybridized according to the manufacturer's instructions and as previously described (57). Differentially expressed genes were identified using a moderated *t* test. A Benjamini-Hochberg false-discovery rate (FDR) was then used as a multiple-testing correction method, and a corrected *P* value cutoff of 5% was applied. A fold change cutoff of >2 was

TABLE 1 Oligonucleotides used in this study

Oligonucleotide	Sequence
<i>Gapdh</i>	Forward, 5'-GCAAAGTGGAGATTGTTGCCA-3' Reverse, 5'-GCCTTGACTGTGCCGTTGA-3'
<i>lav m1</i>	Forward, 5'-AAGAACAATCCTGTCACCTCTGA-3' Reverse, 5'-CAAAGCGTCTACGCTGCAGTCC-3'
<i>Crp</i>	Forward, 5'-GTGCGCAGCTTCAGTGTCTTC-3' Reverse, 5'-AGCACCACCCACTCCAAAAGCA-3'
<i>Lcn2</i>	Forward, 5'-GCCCAGGACTCAACTCAGAATT-3' Reverse, 5'-GCTCATAGATGGTGTGTACATCG-3'
<i>lfng</i>	Forward, 5'-CAACAGCAAGGCGAAAAAG-3' Reverse, 5'-GTGGACCACTCGGATGAGCT-3'
<i>Il18bp</i>	Forward, 5'-ACTGAGCCCCACCTACGAA-3' Reverse, 5'-GGAGCTGTCTTCAACCCATCC-3'
<i>Cxcl1</i>	Forward, 5'-GCGCCTATCGCCAATGAGC-3' Reverse, 5'-GCAAGCCTCGGACCATTTC-3'
<i>S100a8</i>	Forward, 5'-CACCATGCCCTTACAAGAATG-3' Reverse, 5'-CACCATCGCAAGGAACTCC-3'
<i>Cxcl10</i>	Forward, 5'-ACCCAAGTGTGCCGTCAT-3' Reverse, 5'-CATTCTCACTGGCCCGTCAT-3'
<i>Ifi44</i>	Forward, 5'-GGCCATGAGAAGCTCGTTTGACA-3' Reverse, 5'-ACTTCTGCACACTGCCTTGTA-3'
<i>Gbp4</i>	Forward, 5'-CACAAATGCTCCCATTTGTC-3' Reverse, 5'-GGACCATCCAACAATAGCCACT-3'
<i>Foxj1</i>	Forward, 5'-CCCCAAGTCACTCTGTGG-3' Reverse, 5'-AGGACAGTTGTGGCCGAT-3'
<i>Muc2</i>	Forward, 5'-TGCTGACGAGTGGTTGGTGA-3' Reverse, 5'-TTAAGCGAAAGCCCTGGTGT-3'
<i>Il1b</i>	Forward, 5'-TCGTGCTGTCGACCCATA-3' Reverse, 5'-GTCGTTGCTTGGTTCTCCTTGT-3'
<i>Il6</i>	Forward, 5'-CAACCACGGCCTTCCCTACT-3' Reverse, 5'-CCACGATTTCCAGAGAACATG-3'
<i>S100a9</i>	Forward, 5'-GACACCCTGACACCCTGA-3' Reverse, 5'-GCCATCAGCATCATACTCCTC-3'

then added to select the differentially expressed genes between the mock and infected conditions. For functional analysis, data files were uploaded into the Ingenuity Pathways Analysis (IPA) software (Ingenuity Systems, Redwood City, CA). Pathway enrichment analysis was performed using the GSEA software (<https://www.gsea-msigdb.org/gsea/index.jsp>).

Measurement of SCFA concentrations and treatment with SCFAs. Concentrations of SCFAs in the cecal content were determined after extraction with diethyl ether using GC-2014 gas chromatography with a model AOC-20i auto-injector (Shimadzu, Hertogenbosch, The Netherlands) as described previously (58). Results are expressed as micromoles per gram of cecal content. To assess the effects of SCFAs on intestinal permeability and defense against secondary enteric bacterial infection, mice infected with IAV were treated (drinking water) with a combination of acetate, propionate, and butyrate (200 mM, 50 mM, and 5 mM, respectively) after 2 days of IAV infection. Treatment was continued after secondary bacterial infection until animal sacrifice.

Assessment of gene expression and quantification of viral loads by quantitative RT-PCR. Total RNA from colon tissues was extracted with the NucleoSpin RNA kit (Macherey-Nagel, Hoerd, Germany). RNA was reverse transcribed with the high-capacity cDNA Archive kit (Life Technologies, USA). The resulting cDNA was amplified using SYBR green-based real-time PCR and the QuantStudio 12K Flex real-time PCR systems (Applied Biosystems, USA) according to the manufacturer's protocol. Relative quantification was performed using the gene coding for glyceraldehyde 3-phosphate dehydrogenase (*Gapdh*). Specific primers were designed using Primer Express software (Applied Biosystems, Villebon sur Yvette, France). Relative mRNA levels ($2^{-\Delta C_t}$, where C_t is the cycle threshold) were determined by comparing (a) the PCR C_t for the gene of interest and the housekeeping gene *Gapdh* (ΔC_t) and (b) ΔC_t values for treated and control groups (ΔC_t). Data are expressed as a fold change over the mean gene expression level in mock-treated mice. Quantification of viral RNA was performed as described in reference 10. Viral load is expressed as viral RNA normalized to the *Gapdh* expression level. Data were normalized to expression of the *Gapdh* gene and were expressed as C_t s. The sequences of the oligonucleotides used in this study are shown in Table 1.

Measurement of intestinal permeability. To measure the perturbation of intestinal permeability following influenza virus infection or pair-feeding, fluorescein isothiocyanate (FITC)-dextran (dextran size, 4,000 kDa) dissolved in sterile saline was administered by oral gavage (200 μ l, 60 mg/ml). After 4 h,

mock-infected, IAV-infected mice and pair-fed mice were euthanized and their blood was collected by cardiac puncture. FITC-dextran in plasma was quantified using a Tecan (Männedorf, Switzerland) plate reader (excitation, 485 nm; emission, 528 nm). Serum citrulline, intestinal fatty acid-binding protein, and lipopolysaccharide (LPS)-binding protein were quantified by enzyme-linked immunosorbent assay (ELISA) (MyBioSource, CA).

Histological examination of gut sections. Histological examination of the duodenum and proximal colon was performed on 4- μ m-thick sections stained with hematoxylin, eosin, and saffron. Thirty crypts per mouse were analyzed to determine the average crypt depth and villus length. Slides were scanned using Panoramic Scan (3DHistech), and CaseViewer software (3DHistech) was used to measure crypt depth and villus length.

Sample collection, genomic DNA extraction and sequencing, and gut microbiota analysis. To study the potential impact of SCFA treatment on the gut microbiota's composition, feces were collected from uninfected mice treated or not treated with SCFAs for 5 days and from mice infected 7 days earlier with IAV and treated or not with SCFAs at 2 days postinfection. Extraction of microbial DNA and determination of microbial diversity and composition by 16S rRNA gene pyrosequencing (V3 and V4 hypervariable regions) were determined exactly as described previously (10). Taxonomic and diversity analyses were performed with the Metabiote Online v2.0 pipeline (GenoScreen, Lille, France), which is partially based on the software QIIME v1.9.1. Beta diversity (between samples) was used to examine changes in microbial community structure between mouse fecal group samples. Principal-component analyses (PCoA) of the Bray-Curtis distance index were performed to assess beta diversity. Differences in the relative abundances of individual taxa, between mouse cecal group samples, were assessed for significance using the Mann-Whitney *U* test, controlling for the false-discovery rate implemented within the software package QIIME.

Pair-feeding experiments. To provide the pair-fed group with only as much food daily as is consumed by IAV-infected mice, intake was restricted during the last 3 days by 15% (day 4), 35% (day 5), and 85% (day 6) of mice (sacrifice at day 7) (10). Mice were anesthetized at day 0. Food was supplied twice a day to pair-fed animals, and water was available at all times. The *ad libitum* (normally nourished) group mice were allowed unrestricted access to food and water. At the sacrifice, pair-fed mice lost ~15% of their body mass.

Statistical analysis. Results are expressed as means \pm standard deviations (SD) unless otherwise stated. All statistical analysis was performed using GraphPad Prism v6 software. A Mann-Whitney *U* test was used to compare two groups unless otherwise stated. Comparisons of more than two groups with each other were analyzed with the one-way analysis of variance (ANOVA) Kruskal-Wallis test (nonparametric), followed by Dunn's posttest. The rates of survival of mice were compared using Kaplan-Meier analysis and the log rank test (*, $P < 0.05$; **, $P < 0.01$; ***, $P < 0.001$).

Data availability. MIAME was deposited in ArrayExpress at EMBL under accession numbers [E-MTAB-6707](#) (IAV) and [E-MTAB-10036](#) (pair-feeding). For the gut microbiota analysis, raw sequence data are accessible in the National Center for Biotechnology Information (project number [PRJNA675027](#)), biosample accession numbers [SAMN16686871](#) to [SAMN16686906](#).

SUPPLEMENTAL MATERIAL

Supplemental material is available online only.

SUPPLEMENTAL FILE 1, PDF file, 1.2 MB.

ACKNOWLEDGMENTS

We acknowledge Richard Flavell (Howard Hughes Medical Institute, Princeton University, Princeton, NJ) for the gift of the NF- κ B-luciferase transgenic B10.A mice and Hugues Lelouard (CIML, Marseille, France) for scientific discussions. We thank the animal facility (PLETHA) of the Pasteur Institute, Lille, France, for animal maintenance and the PICT platform (INRAE, Jouy-en-Josas, France) for microarray technical assistance.

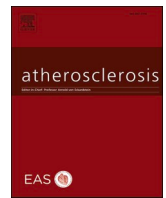
This work was supported in part by the INSERM, CNRS, University of Lille, Pasteur Institute of Lille, Région des Hauts-de-France (FLUMICROBIOTE), and the Agence Nationale de la Recherche (AAP Générique 2017, ANR-17-CE15-0020-01, ACROBAT) (F.T.). V.S., M.G.M., and A.B. received salary support (Ph.D. fellowship) from Lille University and from the Fondation pour la Recherche Médicale (V.S.).

REFERENCES

- Coates BM, Staricha KL, Wiese KM, Ridge KM. 2015. Influenza A virus infection, innate immunity, and childhood. *JAMA Pediatr* 169:956–963. <https://doi.org/10.1001/jamapediatrics.2015.1387>.
- Rynda-Apple A, Robinson KM, Alcorn JF. 2015. Influenza and bacterial superinfection: illuminating the immunologic mechanisms of disease. *Infect Immun* 83:3764–3770. <https://doi.org/10.1128/IAI.00298-15>.
- McCullers JA. 2014. The co-pathogenesis of influenza viruses with bacteria in the lung. *Nat Rev Microbiol* 12:252–262. <https://doi.org/10.1038/nrmicro3231>.
- Sellers SA, Hagan RS, Hayden FG, Fischer WA. 2017. The hidden burden of influenza: a review of the extra-pulmonary complications of influenza infection. *Influenza Other Respir Viruses* 11:372–393. <https://doi.org/10.1111/irv.12470>.

5. Dilantika C, Sedyaningsih ER, Kasper MR, Agtini M, Listiyaningsih E, Uyeki TM, Burgess TH, Blair PJ, Putnam SD. 2010. Influenza virus infection among pediatric patients reporting diarrhea and influenza-like illness. *BMC Infect Dis* 10:3–7. <https://doi.org/10.1186/1471-2334-10-3>.
6. Wang J, Li F, Wei H, Lian Z-X, Sun R, Tian Z. 2014. Respiratory influenza virus infection induces intestinal immune injury via microbiota-mediated Th17 cell-dependent inflammation. *J Exp Med* 211:2397–2410. <https://doi.org/10.1084/jem.20140625>.
7. Deriu E, Boxx GM, He X, Pan C, Benavidez SD, Cen L, Rozengurt N, Shi W, Cheng G. 2016. Influenza virus affects intestinal microbiota and secondary Salmonella infection in the gut through type I interferons. *PLoS Pathog* 12:e1005572. <https://doi.org/10.1371/journal.ppat.1005572>.
8. Yildiz S, Mazel-Sanchez B, Kandasamy M, Manicassamy B, Schmolke M. 2018. Influenza A virus infection impacts systemic microbiota dynamics and causes quantitative enteric dysbiosis. *Microbiome* 6:9. <https://doi.org/10.1186/s40168-017-0386-z>.
9. Groves HT, Cuthbertson L, James P, Moffatt MF, Cox MJ, Tregoning JS. 2018. Respiratory disease following viral lung infection alters the murine gut microbiota. *Front Immunol* 9:182. <https://doi.org/10.3389/fimmu.2018.00182>.
10. Sencio V, Barthelemy A, Tavares LP, Machado MG, Soulard D, Cuiat C, Queiroz-Junior CM, Noordine M-L, Salomé-Desnoullez S, Deryuter L, Foligné B, Wahl C, Frisch B, Vieira AT, Paget C, Milligan G, Ulven T, Wolowczuk I, Faveeuw C, Le Goffic R, Thomas M, Ferreira S, Teixeira MM, Trottein F. 2020. Gut dysbiosis during influenza contributes to pulmonary pneumococcal superinfection through altered short-chain fatty acid production. *Cell Rep* 30:2934–2947.e6. <https://doi.org/10.1016/j.celrep.2020.02.013>.
11. Sencio V, Machado MG, Trottein F. 2021. The lung-gut axis during viral respiratory infections: the impact of gut dysbiosis on secondary disease outcomes. *Mucosal Immunol* 14:296–304. <https://doi.org/10.1038/s41385-020-00361-8>.
12. Maslowski KM, Vieira AT, Ng A, Kranich J, Sierro F, Yu D, Schilter HC, Rolph MS, Mackay F, Artis D, Xavier RJ, Teixeira MM, Mackay CR. 2009. Regulation of inflammatory responses by gut microbiota and chemoattractant receptor GPR43. *Nature* 461:1282–1286. <https://doi.org/10.1038/nature08530>.
13. Fukuda S, Toh H, Hase K, Oshima K, Nakanishi Y, Yoshimura K, Tobe T, Clarke JM, Topping DL, Suzuki T, Taylor TD, Itoh K, Kikuchi J, Morita H, Hattori M, Ohno H. 2011. Bifidobacteria can protect from enteropathogenic infection through production of acetate. *Nature* 469:543–547. <https://doi.org/10.1038/nature09646>.
14. Singh N, Gurav A, Sivaprakasam S, Brady E, Padia R, Shi H, Thangaraju M, Prasad PD, Manicassamy S, Munn DH, Lee JR, Offermanns S, Ganapathy V. 2014. Activation of the receptor (Gpr109a) for niacin and the commensal metabolite butyrate suppresses colonic inflammation and carcinogenesis. *Immunity* 40:128–139. <https://doi.org/10.1016/j.immuni.2013.12.007>.
15. Macia L, Tan J, Vieira AT, Leach K, Stanley D, Luong S, Maruya M, Ian McKenzie C, Hijikata A, Wong C, Binge L, Thorburn AN, Chevalier N, Ang C, Marino E, Robert R, Offermanns S, Teixeira MM, Moore RJ, Flavell RA, Fagarasan S, Mackay CR. 2015. Metabolite-sensing receptors GPR43 and GPR109A facilitate dietary fibre-induced gut homeostasis through regulation of the inflammasome. *Nat Commun* 6:6734–6748. <https://doi.org/10.1038/ncomms7734>.
16. Koh A, De Vadder F, Kovatcheva-Datchary P, Bäckhed F. 2016. From dietary fiber to host physiology: short-chain fatty acids as key bacterial metabolites. *Cell* 165:1332–1345. <https://doi.org/10.1016/j.cell.2016.05.041>.
17. Milligan G, Shimpukade B, Ulven T, Hudson BD. 2017. Complex pharmacology of free fatty acid receptors. *Chem Rev* 117:67–110. <https://doi.org/10.1021/acs.chemrev.6b00056>.
18. Thorburn AN, Macia L, Mackay CR. 2014. Diet, metabolites, and “western-lifestyle” inflammatory diseases. *Immunity* 40:833–842. <https://doi.org/10.1016/j.immuni.2014.05.014>.
19. Sun M, Wu W, Liu Z, Cong Y. 2017. Microbiota metabolite short chain fatty acids, GPCR, and inflammatory bowel diseases. *J Gastroenterol* 52:1–8. <https://doi.org/10.1007/s00535-016-1242-9>.
20. Parada Venegas D, De la Fuente MK, Landskron G, González MJ, Quera R, Dijkstra G, Harmsen HJM, Faber KN, Hermoso MA. 2019. Short chain fatty acids (SCFAs)-mediated gut epithelial and immune regulation and its relevance for inflammatory bowel diseases. *Front Immunol* 10:277. <https://doi.org/10.3389/fimmu.2019.00277>.
21. Jianfeng G, Weiming Z, Ning L, Fangnan L, Li T, Nan L, Jieshou L. 2005. Serum citrulline is a simple quantitative marker for small intestinal enterocytes mass and absorption function in short bowel patients. *J Surg Res* 127:177–182. <https://doi.org/10.1016/j.jss.2005.04.004>.
22. Groves HT, Higham SL, Moffatt MF, Cox MJ, Tregoning JS. 2020. Respiratory viral infection alters the gut microbiota by inducing inappetence. *mBio* 11:e03236-19. <https://doi.org/10.1128/mBio.03236-19>.
23. Lam LH, Monack DM. 2014. Intraspecies competition for niches in the distal gut dictate transmission during persistent Salmonella infection. *PLoS Pathog* 10:e1004527. <https://doi.org/10.1371/journal.ppat.1004527>.
24. Norman JM, Handley SA, Baldrige MT, Droit L, Liu CY, Keller BC, Kambal A, Monaco CL, Zhao G, Fleshner P, Stappenbeck TS, McGovern DPB, Keshavarzian A, Mutlu EA, Sauk J, Gevers D, Xavier RJ, Wang D, Parkes M, Virgin HW. 2015. Disease-specific alterations in the enteric virome in inflammatory bowel disease. *Cell* 160:447–460. <https://doi.org/10.1016/j.cell.2015.01.002>.
25. Thevaranjan N, Puchta A, Schulz C, Naidoo A, Szamosi JC, Verschoor CP, Loukov D, Schenck LP, Jury J, Foley KP, Schertzer JD, Larché MJ, Davidson DJ, Verdú EF, Surette MG, Bowdish DME. 2017. Age-associated microbial dysbiosis promotes intestinal permeability, systemic inflammation, and macrophage dysfunction. *Cell Host Microbe* 21:455–466.e4. <https://doi.org/10.1016/j.chom.2017.03.002>.
26. Turner JR. 2009. Intestinal mucosal barrier function in health and disease. *Nat Rev Immunol* 9:799–809. <https://doi.org/10.1038/nri2653>.
27. Hughes R, Kurth MJ, McGilligan V, McGlynn H, Rowland I. 2008. Effect of colonic bacterial metabolites on Caco-2 cell paracellular permeability in vitro. *Nutr Cancer* 60:259–266. <https://doi.org/10.1080/0163580701649644>.
28. McCall IC, Betanzos A, Weber DA, Nava P, Miller GW, Parkos CA. 2009. Effects of phenol on barrier function of a human intestinal epithelial cell line correlate with altered tight junction protein localization. *Toxicol Appl Pharmacol* 241:61–70. <https://doi.org/10.1016/j.taap.2009.08.002>.
29. Derrien M, Belzer C, de Vos WM. 2017. Akkermansia muciniphila and its role in regulating host functions. *Microb Pathog* 106:171–181. <https://doi.org/10.1016/j.micpath.2016.02.005>.
30. Florescu DF, Kalil AC. 2014. The complex link between influenza and severe sepsis. *Virulence* 5:137–142. <https://doi.org/10.4161/viru.27103>.
31. Kalil AC, Thomas PG. 2019. Influenza virus-related critical illness: pathophysiology and epidemiology. *Crit Care* 23:258–264. <https://doi.org/10.1186/s13054-019-2539-x>.
32. Cheng VCC, To KKW, Tse H, Hung IFN, Yuen K-Y. 2012. Two years after pandemic influenza A/2009/H1N1: what have we learned? *Clin Microbiol Rev* 25:223–263. <https://doi.org/10.1128/CMR.05012-11>.
33. Bischoff SC, Barbara G, Buurman W, Ockhuizen T, Schulzke J-D, Serino M, Tilg H, Watson A, Wells JM. 2014. Intestinal permeability—a new target for disease prevention and therapy. *BMC Gastroenterol* 14:189. <https://doi.org/10.1186/s12876-014-0189-7>.
34. Cani PD, Amar J, Iglesias MA, Poggi M, Knauf C, Bastelica D, Neyrinck AM, Fava F, Tuohy KM, Chabo C, Waget A, Delmée E, Cousin B, Sulpire T, Chamontin B, Ferrières J, Tanti J-F, Gibson GR, Casteilla L, Delzenne NM, Alessi MC, Burcelin R. 2007. Metabolic endotoxemia initiates obesity and insulin resistance. *Diabetes* 56:1761–1772. <https://doi.org/10.2337/db06-1491>.
35. Scott KA, Ida M, Peterson VL, Prenderville JA, Moloney GM, Izumo T, Murphy K, Murphy A, Ross RP, Stanton C, Dinan TG, Cryan JF. 2017. Revisiting Metchnikoff: age-related alterations in microbiota-gut-brain axis in the mouse. *Brain Behav Immun* 65:20–32. <https://doi.org/10.1016/j.bbi.2017.02.004>.
36. Boutagy NE, McMillan RP, Frisard MI, Hulver MW. 2016. Metabolic endotoxemia with obesity: is it real and is it relevant? *Biochimie* 124:11–20. <https://doi.org/10.1016/j.biochi.2015.06.020>.
37. Amar J, Chabo C, Waget A, Klopp P, Vachoux C, Bermúdez-Humarán LG, Smirnova N, Bergé M, Sulpire T, Lahtinen S, Ouwehand A, Langella P, Rautonen N, Sansonetti PJ, Burcelin R. 2011. Intestinal mucosal adherence and translocation of commensal bacteria at the early onset of type 2 diabetes: molecular mechanisms and probiotic treatment. *EMBO Mol Med* 3:559–572. <https://doi.org/10.1002/emmm.201100159>.
38. Lelouvier B, Servant F, Païssé S, Brunet A-C, Benyahya S, Serino M, Valle C, Ortiz MR, Puig J, Courtney M, Federici M, Fernández-Real J-M, Burcelin R, Amar J. 2016. Changes in blood microbiota profiles associated with liver fibrosis in obese patients: a pilot analysis. *Hepatology* 64:2015–2027. <https://doi.org/10.1002/hep.28829>.
39. Alvarez-Silva C, Schierwagen R, Pohlmann A, Magdaleno F, Uschner FE, Ryan P, Vehreschild MJGT, Claria J, Latz E, Lelouvier B, Arumugam M, Trebicka J. 2019. Compartmentalization of immune response and microbial translocation in decompensated cirrhosis. *Front Immunol* 10:69. <https://doi.org/10.3389/fimmu.2019.00699>.
40. Ayari A, Rosa-Calatrava M, Lancel S, Barthelemy J, Pizzorno A, Mayeuf-Louchart A, Baron M, Hot D, Deruyter L, Soulard D, Julien T, Faveeuw C, Molendi-Coste O, Dombrowicz D, Sedano L, Sencio V, Le Goffic R,

- Trottein F, Wolowczuk I. 2020. Influenza infection rewires energy metabolism and induces browning features in adipose cells and tissues. *Commun Biol* 3:237. <https://doi.org/10.1038/s42003-020-0965-6>.
41. Hamer HM, Jonkers D, Venema K, Vanhoutvin S, Troost FJ, Brummer R-J. 2008. Review article: the role of butyrate on colonic function. *Aliment Pharmacol Ther* 27:104–119. <https://doi.org/10.1111/j.1365-2036.2007.03562.x>.
 42. Gill PA, van Zelm MC, Muir JG, Gibson PR. 2018. Review article: short chain fatty acids as potential therapeutic agents in human gastrointestinal and inflammatory disorders. *Aliment Pharmacol Ther* 48:15–34. <https://doi.org/10.1111/apt.14689>.
 43. Tominaga K, Kamimura K, Takahashi K, Yokoyama J, Yamagiwa S, Terai S. 2018. Diversion colitis and pouchitis: a mini-review. *World J Gastroenterol* 24:1734–1747. <https://doi.org/10.3748/wjg.v24.i16.1734>.
 44. Jacobson A, Lam L, Rajendram M, Tamburini F, Honeycutt J, Pham T, Van Treuren W, Pruss K, Stabler SR, Lugo K, Bouley DM, Vilches-Moure JG, Smith M, Sonnenburg JL, Bhatt AS, Huang KC, Monack D. 2018. A gut commensal-produced metabolite mediates colonization resistance to *Salmonella* infection. *Cell Host Microbe* 24:296–307.e7. <https://doi.org/10.1016/j.chom.2018.07.002>.
 45. Jimenez JA, Uwiera TC, Abbott DW, Uwiera RRE, Inglis GD. 2017. Butyrate supplementation at high concentrations alters enteric bacterial communities and reduces intestinal inflammation in mice infected with *Citrobacter rodentium*. *mSphere* 2:e00243-17. <https://doi.org/10.1128/mSphere.00243-17>.
 46. Schulthess J, Pandey S, Capitani M, Rue-Albrecht KC, Arnold I, Franchini F, Chomka A, Ilott NE, Johnston DGW, Pires E, McCullagh J, Sansom SN, Arancibia-Carcamo CV, Uhlig HH, Powrie F. 2019. The short chain fatty acid butyrate imprints an antimicrobial program in macrophages. *Immunity* 50:432–445.e7. <https://doi.org/10.1016/j.immuni.2018.12.018>.
 47. Sarker P, Ahmed S, Tiash S, Rekha RS, Stromberg R, Andersson J, Bergman P, Gudmundsson GH, Agerberth B, Raqib R. 2011. Phenylbutyrate counteracts *Shigella* mediated downregulation of cathelicidin in rabbit lung and intestinal epithelia: a potential therapeutic strategy. *PLoS One* 6:e20637. <https://doi.org/10.1371/journal.pone.0020637>.
 48. Jellbauer S, Perez Lopez A, Behnsen J, Gao N, Nguyen T, Murphy C, Edwards RA, Raffatellu M. 2016. Beneficial effects of sodium phenylbutyrate administration during infection with *Salmonella enterica* serovar Typhimurium. *Infect Immun* 84:2639–2652. <https://doi.org/10.1128/IAI.00132-16>.
 49. Sorbara MT, Dubin K, Littmann ER, Moody TU, Fontana E, Seok R, Leiner IM, Taur Y, Peled JU, van den Brink MRM, Litvak Y, Bäuml AJ, Chaudard J-L, Pickard AJ, Cross JR, Pamer EG. 2019. Inhibiting antibiotic-resistant Enterobacteriaceae by microbiota-mediated intracellular acidification. *J Exp Med* 216:84–98. <https://doi.org/10.1084/jem.20181639>.
 50. Ormsby MJ, Johnson SA, Carpena N, Meikle LM, Goldstone RJ, McIntosh A, Wessel HM, Hulme HE, McConnachie CC, Connolly JPR, Roe AJ, Hasson C, Boyd J, Fitzgerald E, Gerasimidis K, Morrison D, Hold GL, Hansen R, Walker D, Smith DGE, Wall DM. 2020. Propionic acid promotes the virulent phenotype of Crohn's disease-associated adherent-invasive *Escherichia coli*. *Cell Rep* 30:2297–2305.e5. <https://doi.org/10.1016/j.celrep.2020.01.078>.
 51. Pobeguts OV, Ladygina VG, Evsyutina DV, Ereemeev AV, Zubov AI, Matyushkina DS, Scherbakov PL, Rakitina DV, Fisunov GY. 2020. Propionate induces virulent properties of Crohn's disease-associated *Escherichia coli*. *Front Microbiol* 11:1460. <https://doi.org/10.3389/fmicb.2020.01460>.
 52. Lawhon SD, Maurer R, Suyemoto M, Altier C. 2002. Intestinal short-chain fatty acids alter *Salmonella typhimurium* invasion gene expression and virulence through BarA/SirA: short-chain fatty acids and *Salmonella* invasion. *Mol Microbiol* 46:1451–1464. <https://doi.org/10.1046/j.1365-2958.2002.03268.x>.
 53. Vidy A, Maisonnasse P, Da Costa B, Delmas B, Chevalier C, Le Goffic R. 2016. The influenza virus protein PB1-F2 increases viral pathogenesis through neutrophil recruitment and NK cells inhibition. *PLoS One* 11:e0165361. <https://doi.org/10.1371/journal.pone.0165361>.
 54. Barthelemy A, Sencio V, Soulard D, Deruyter L, Faveeuw C, Le Goffic R, Trottein F. 2018. Interleukin-22 immunotherapy during severe influenza enhances lung tissue integrity and reduces secondary bacterial systemic invasion. *Infect Immun* 86:e00706-17. <https://doi.org/10.1128/IAI.00706-17>.
 55. Zoumpopoulou G, Foliage B, Christodoulou K, Grangette C, Pot B, Tsakalidou E. 2008. *Lactobacillus fermentum* ACA-DC 179 displays probiotic potential in vitro and protects against trinitrobenzene sulfonic acid (TNBS)-induced colitis and *Salmonella* infection in murine models. *Int J Food Microbiol* 121:18–26. <https://doi.org/10.1016/j.ijfoodmicro.2007.10.013>.
 56. Barthelemy A, Ivanov S, Fontaine J, Soulard D, Bouabe H, Paget C, Faveeuw C, Trottein F. 2017. Influenza A virus-induced release of interleukin-10 inhibits the anti-microbial activities of invariant natural killer T cells during invasive pneumococcal superinfection. *Mucosal Immunol* 10:460–469. <https://doi.org/10.1038/mi.2016.49>.
 57. Le Goffic R, Leymarie O, Chevalier C, Rebours E, Da Costa B, Vidic J, Descamps D, Sallenave J-M, Rauch M, Samson M, Delmas B. 2011. Transcriptomic analysis of host immune and cell death responses associated with the influenza A virus PB1-F2 protein. *PLoS Pathog* 7:e1002202. <https://doi.org/10.1371/journal.ppat.1002202>.
 58. De Weirdt R, Possemiers S, Vermeulen G, Moerdijk-Poortvliet TCW, Boschker HTS, Verstraete W, Van de Wiele T. 2010. Human faecal microbiota display variable patterns of glycerol metabolism. *FEMS Microbiol Ecol* 74:601–611. <https://doi.org/10.1111/j.1574-6941.2010.00974.x>.



Macrophage metabolic regulation in atherosclerotic plaque

Bastien Dolfi ^{a,1}, Alexandre Gallerand ^{a,1}, Arvand Haschemi ^b, Rodolphe R. Guinamard ^c, Stoyan Ivanov ^{a,*}

^a Université Côte D'Azur, INSERM, C3M, Nice, France

^b Department of Laboratory Medicine, Medical University of Vienna, 1090, Vienna, Austria

^c Université Côte D'Azur, Laboratoire de PhysioMédecine Moléculaire, CNRS, Nice, France

ARTICLE INFO

Keywords:

Monocyte
Macrophage
Foamy cells
Immunometabolism
Glucose
Atherosclerosis

ABSTRACT

Metabolism plays a key role in controlling immune cell functions. In this review, we will discuss the diversity of plaque resident myeloid cells and will focus on their metabolic demands that could reflect on their particular intraplaque localization. Defining the metabolic configuration of plaque resident myeloid cells according to their topologic distribution could provide answers to key questions regarding their functions and contribution to disease development.

1. Introduction

Atherosclerosis is a chronic inflammatory disease characterized by the accumulation of lipids and immune cells in the intima of blood vessels. Atherosclerosis is the underlying cause of cardiovascular events such as myocardial infarctions and strokes, that together are responsible for 17.9 million deaths per year worldwide (World Health Organization). Atherosclerotic plaque progression is favored in conditions of hypercholesterolemia and dyslipidemia. Its development initiates when intima-resident macrophages uptake excess lipids and form foam cells [1]. Subsequent plaque progression is dependent on a constant influx of monocytes from the blood circulation that fuels plaque macrophage accumulation [1]. In the last two decades, advances in the field of atherosclerosis have identified myelopoiesis, plaque macrophage proliferation and efferocytosis as key elements defining both atherosclerosis development and regression. More recently, it became clear that these parameters are influenced by immune cell metabolism. The atherosclerotic lesion forms a complex micro-environment defined, at least in part, by its developmental pattern. Newly recruited monocytes are highly motile cells, located close to the lumen. On the other hand, macrophages are sessile and situated deeper within the plaque [2], where specific nutrients could hypothetically be scarce, and where necrotic cores develop. Metabolite availability therefore appears as an additional potential regulator of plaque myeloid cell metabolism and

functions, depending on the cell's intra-plaque localization. Here, we discuss the metabolic regulation of macrophage functions and inflammatory properties within the plaque.

1.1. Immune cell diversity in atherosclerotic plaque

Pioneering studies performed in pre-clinical models and human subjects detected the presence of immune cells in atherosclerotic lesions. Multiple immune cells including T cells, both CD4⁺ and CD8⁺, B cells, macrophages, monocytes and dendritic cells (DC) were present in plaques [3–7]. These early reports used immunostaining and microscopy to determine the cellular composition of the plaque. The main limitation of this technology is the limited number of markers that could be simultaneously used to accurately define the precise nature of plaque-residing cells. More recently, flow cytometry analysis, providing the possibility to greatly extend the number of membrane markers simultaneously investigated, demonstrated that plaque cellular composition was more complex than initially described. The presence of tertiary lymphoid organs, structures enriched in T cells that develop in the vessel adventitia adjacent to plaques [8], could also contribute to plaque immune cell contamination in flow cytometry analyses. Indeed, this approach does not provide insights about the precise intra-plaque localization of the diverse immune cells. Intra-tissue localization is important since it could have an impact on oxygen and metabolites supply and therefore on

* Corresponding author.

E-mail address: Stoyan.ivanov@unice.fr (S. Ivanov).

¹ These authors contributed equally to this work.

immune cell metabolism and activation state within the plaque.

Single-cell RNA sequencing (scRNA seq) analyses further enriched our knowledge about the phenotypic diversity of mouse and human plaque-residing immune cells [1,9–13]. These studies revealed that plaque cellular composition was impressively complex and contained many diverse myeloid and lymphoid cells. Macrophages were the most abundant cells in the plaque. Several distinct macrophage and monocyte subsets were identified in the plaque of atherogenic (*LdlR*^{-/-} and *ApoE*^{-/-}) mice and patients. Initially described as a key feature of advanced lesions, foamy macrophages, a population of lipid-laden cells, were attributed a pro-inflammatory role mediated by the release of cytokines and chemokines [14,15]. This dogma was challenged when scRNA seq analysis demonstrated that monocytes and inflammatory macrophages, rather than foamy cells, were enriched in mRNA encoding for pro-inflammatory mediators including *il1β*, *il12*, *tnfα*, *ccl2* and *cxcl2* [10].

Two main mechanisms account for lesion growth depending on the plaque stage development. Early lesions are mainly sustained through monocyte recruitment from the blood circulation and their local retention [16–18]. In contrast, in advanced plaques, *in situ* macrophage proliferation favors plaque progression [19]. Whether these two processes require a specific metabolic rewiring and rely on different metabolic pathways remains to be established. Macrophage intraplaque proliferation correlates with plasma lipoprotein levels [20]. Lowering plasma lipid levels and genetic ablation of lipoprotein uptake receptors in macrophages (*Msr1* and *CD36*) decreased plaque macrophage proliferation rate [20]. However, the underlying molecular and metabolic mechanisms remain unknown. A recent study using multi-isotope imaging mass spectrometry found that plaque proliferating cells used preferentially glucose in comparison to neighboring non-proliferating cells [21]. Surprisingly, foamy cells were highly glucose consuming and this was correlated with increased proliferation [21]. This observation is rather surprising because foamy cells are characterized by massive lipid accumulation, and they highly express genes associated with lipid metabolism. Whether glucose or lipids serve as the main energy source for foamy cells remains to be defined. To better apprehend the metabolic configuration of plaque resident myeloid cells and foamy cells in particular, this set of data could be complemented using a new flow cytometry-based strategy named SCENITH that has recently been described [22]. This approach provides insights into cellular metabolic status with a single-cell resolution, allowing the comparison of multiple cell types contained in a given sample. Although this method requires relatively low numbers of cells, the analysis of quiescent or over-stressed aortic cells after tissue digestion could be challenging.

1.2. Heterogeneity and metabolic control of macrophages and monocytes during atherosclerosis

Metabolism emerged as a central regulator of macrophage and monocyte functions. Indeed, metabolic adaptations modulate key macrophage functions including cytokine production, efferocytosis and phagocytosis (for review [23–25]). *In vitro* studies, using either interleukine-4 (IL-4) or lipopolysaccharide (LPS)/interferon (IFN) γ stimulation led to mimicry of particular macrophage activation states (M1 and M2). These simple models were broadly used to define macrophage metabolic adaptation to external stimuli. Anti-inflammatory (M2-like) macrophages exhibit a mitochondrial oxidative metabolism while pro-inflammatory (M1-like) macrophages are characterized by a glycolytic metabolism. More than just another polarization marker, metabolic rewiring is a key player in those differentiations, and interfering with glucose flux or mitochondrial fitness prohibits M1 and M2 polarization respectively. Nevertheless, while such *in vitro* polarization models have fruitfully brought forward the importance of metabolism in immune cell decision processes, their translation to cell decisions inside complex environmental conditions is not straightforward.

In atheromatous plaque, recently generated scRNA-seq datasets [9, 10] highlighted the co-existence of several distinct populations of pro-inflammatory and anti-inflammatory macrophages and the expression of canonical M1 or M2 macrophages was shared by one or the other population (Fig. 1). Canonical M2 markers (*mrc1*, *clec10a*, *mgl2*) prevailed in plaque resident macrophages in comparison to M1 (*cd11c*, *il1β*, *ccl2*) markers (Fig. 1). Surprisingly, M2-like macrophages, supposed to have an anti-inflammatory function, displayed a pro-inflammatory transcriptomic signature. These cells highly expressed the mRNAs encoding for pro-inflammatory cytokines (*il1β*, *tnfα*) and chemokines (*ccl2*, *cxcl2* and *cxcl1*). The clinical significance of inflammation, and namely IL-1 β , during cardiovascular diseases was perfectly illustrated by the CANTOS trial [26]. The abundance of M2-like macrophages in plaque is surprising because local presence of IL-4 and IL-13 is limited. IL-13 levels in plaques are below the detection limit, while IL-4 concentration is also low [27]. Similarly, the impact of IFN γ on plaque macrophage phenotype appears minimal, as myeloid-specific IFN γ receptor deficiency did not alter atherosclerosis development in *LdlR*^{-/-} mice [28]. Attempts have been made to explore metabolite impact on macrophage activation *in vitro*. Kratz and colleagues reported that macrophages stimulated with a combination of insulin, glucose and palmitate show an activated phenotype with traits of both M1 and M2 polarization [29]. These cells were named “metabolically activated macrophages” and showed enhanced expression of the inflammatory cytokines TNF α , IL-1 β and IL-6. On the other hand, M2 markers were globally unaffected while M2-associated lipid metabolism-related genes were induced in metabolically activated macrophages [29].

Thus, one might consider that locally available metabolites, in combination with metabolic reprogramming induced by M1/M2-polarizing cytokines, could contribute to a specific and spatially defined metabolism and activation state of macrophages during plaque initiation and progression.

1.3. Metabolites and associated pathways mediating macrophage activation

1.3.1. Glucose and cellular carbohydrate metabolism

Glucose metabolism plays a central role in macrophage functional adaptation. Pioneering work revealed M1- and M2-like macrophage specific glucose fluxes into the two major pathways of cellular carbohydrate metabolism, namely glycolysis and the pentose phosphate pathway (PPP) [30]. Glucose utilization by glycolysis generates energy in form of ATP and crucial intermediates, which can act as substrates for other metabolic pathways. This includes pyruvate, which can be further converted to lactate or Acetyl-CoA, two major metabolites important for macrophage metabolic adaptations. Another example is glycolysis-derived serine generation to sustain cellular one-carbon metabolism, which is regulating epigenetic reprogramming during macrophage activation [31]. Glucose utilization by the PPP is crucial for generating the required redox power by the formation of NADPH, in order to sustain macrophage functions such as ROS handling and anti-oxidative protection by the generation of reduced glutathione. NADPH is also a critical co-factor for lipid metabolism and other metabolic branches as it acts similar to ATP as a universal energy carrier, which is used by many different enzymes throughout the metabolic networks of cells. Also, redox-sensitive protein signaling during macrophage activation is dependent on PPP activity. Another hallmark of the PPP is to provide pentose molecules, which can serve as precursors for nucleotide metabolism or become reconverted to glycolytic intermediates in the non-oxidative branch of the PPP. We recently comprehensively discussed the function and distribution of key enzymes involved in those two pathways to atherosclerosis development [32]. One critical factor for this metabolic system in macrophages, and in immune cells in general, is glucose uptake mediated by the membrane transporter *Glut1* (*slc2a1*) and subsequent phosphorylation by carbohydrate kinases (Fig. 2). Even though macrophages have been suggested

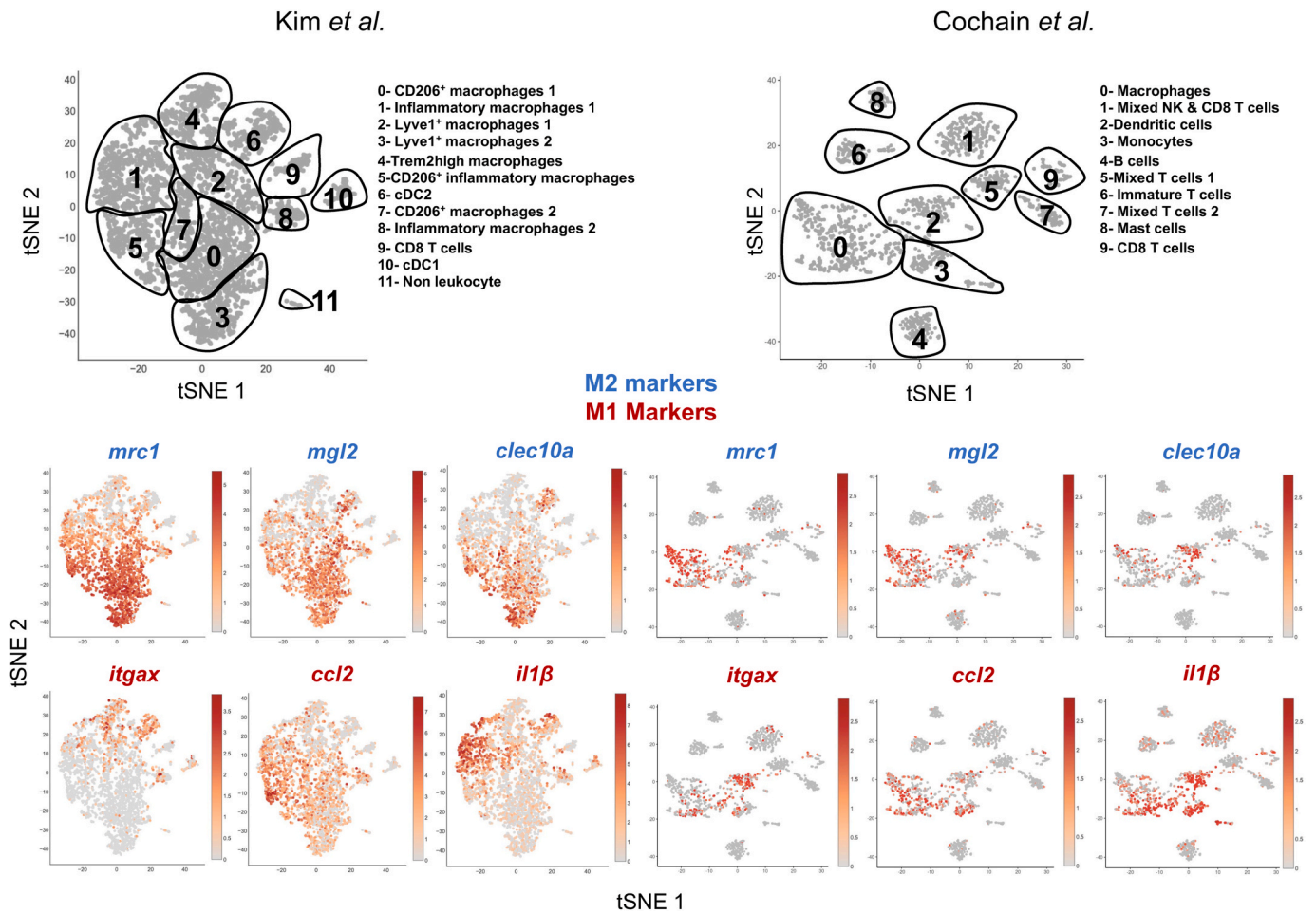


Fig. 1. Single-cell analysis of plaque immune cell activation markers. Single-Cell RNA-Seq of aortic CD45+ cells from *Ldlr*^{-/-} mice fed a HFD for (left) 11 weeks or (right) 12 weeks. Data from (left) Kim et al. (GSM3215435) and (right) Cochain et al. (GSE97310) were analyzed using the Single-Cell Explorer software (Artyomov lab). Expression of M1 and M2 markers in both datasets is shown in tSne plots. Markers used in Kim et al.: CD206+ Macrophages: *Fcgr1*, *Itgam*, *Mafb*, *Mrc1*. Inflammatory macrophages: *Fcgr1*, *Itgam*, *Mafb*, *Nlrp3*, *Il1b*, *Nfkbia*. Lyve1+ macrophages: *Fcgr1*, *Itgam*, *Mafb*, *Lyve1*. TREM2high macrophages: *Fcgr1*, *Itgam*, *Mafb*, *Trem2*, *Abcg1*, *Lpl*, *Lipa*. CD206+ Inflammatory macrophages: *Fcgr1*, *Itgam*, *Mafb*, *Mrc1*, *Nlrp3*, *Il1b* (low), *Nfkbia*, *Tnf*. CD8 T cells: *Lck*, *Cd3*, *Cd8*. cDC2: *Zbtb46*, *Itgax*, *Flt3*, *Itgam* (+), *Itgae* (-). cDC1: *Zbtb46*, *Itgax*, *Flt3*, *Itgam* (-), *Itgae*, *Irfl8*. Non leukocyte: *Ptprc* (-). Markers used in Cochain et al.: Macrophages (mixed subsets): *Itgam*, *Fcgr1*, *MerTK*. Mixed NK and CD8 T cells: *Cd3*, *Cd8*, *Klrb1c*, *Ncr1*, *Gzmb*. Dendritic cells (mixed subsets): *Itgax*, *Ciita*, *Zbtb46*. Monocytes: *Itgam*, *Fcgr1*, *Ly6c*, *Ccr2*. B cells: *Ciita*, *CD19*, *CD79a/b*. Mixed T cells: *Lck*, *CD3*, *CD4*, *CD8*, *Rag1*. Immature T cells: *Lck* (-), *CD3*(+), *Rag1* (-), *CD4* (-), *CD8* (-). Mast cells: *Furin*, *Il1rl1*. CD8 T cells: *Lck*, *CD3*, *CD8*.

to express several Glut-family members, the functional significance of Glut1-mediated glucose uptake was illustrated by the selective Glut1 ablation leading to compromised glucose entry [33]. Under inflammatory conditions, more particularly in a context of atherosclerosis, macrophages display increased glucose metabolism and Glut1 expression [34,35]. Macrophage-specific Glut1-deficiency greatly affected glycolysis and the PPP, resulting in decreased metabolite content [33]. Interestingly, Glut1-deficiency also led to an increase in the level of some of the metabolites in the aforementioned pathways, including 2- and 3-phosphoglycerate, when compared to control cells [33]. This observation suggests that compensatory pathways were able to restore, at least partially, the absence of glucose entry in macrophages and generate metabolic blocks in glycolysis and the PPP independently of extracellular glucose. However, Glut1-macrophage deletion translated into defective efferocytosis and increased plaque necrotic core area [33, 36]. Whether myeloid-cell specific Glut1 deletion also affects monocyte plaque recruitment and local proliferation, on top of efferocytosis, remains to be documented. It is currently unknown if CCR2 expression, the key chemokine receptor allowing for monocyte recruitment into the growing plaque, is modulated by glucose metabolism. This information will provide a better understating on how Glut1-mediated glucose flux

contributes or prevents disease progression. Glucose metabolism was further demonstrated to increase bone marrow hematopoiesis and monocyte generation, thus leading to augmented blood monocyte counts [37–39]. Monocytosis, high circulating monocyte numbers, is an independent risk factor during atherosclerosis development and managing normal blood monocyte levels is a therapeutic avenue. However, interfering with cellular glucose metabolism of macrophages may also adversely alter efferocytosis efficiency and necrotic core development.

Another key aspect of glucose utilization for macrophage functions is the balance of glycolysis and the PPP, which appears to adapt in the course of immune activation to sustain specific metabolic demands of the cells in a timely manner [40]. These two pathways are highly interconnected by sharing crucial intermediates and their interfaces appear as highly regulated in macrophages. M1 activated macrophages specifically express isoform 3 of 6-phosphofructo-2-kinase B (PFKFB3) resulting in increased glycolytic flux [41]. Deficiency of PFKFB3 reduces glycolysis and shifts glucose utilization towards the PPP. Regulations of enzyme activities forming the oxidative branch of the PPP are critical for inflammatory activation of macrophages, as independently shown for G6PD or for PDG during hypercholesterolemia [42]. Glyceraldehyde-3-phosphate (G3P) is a key intermediate of glucose

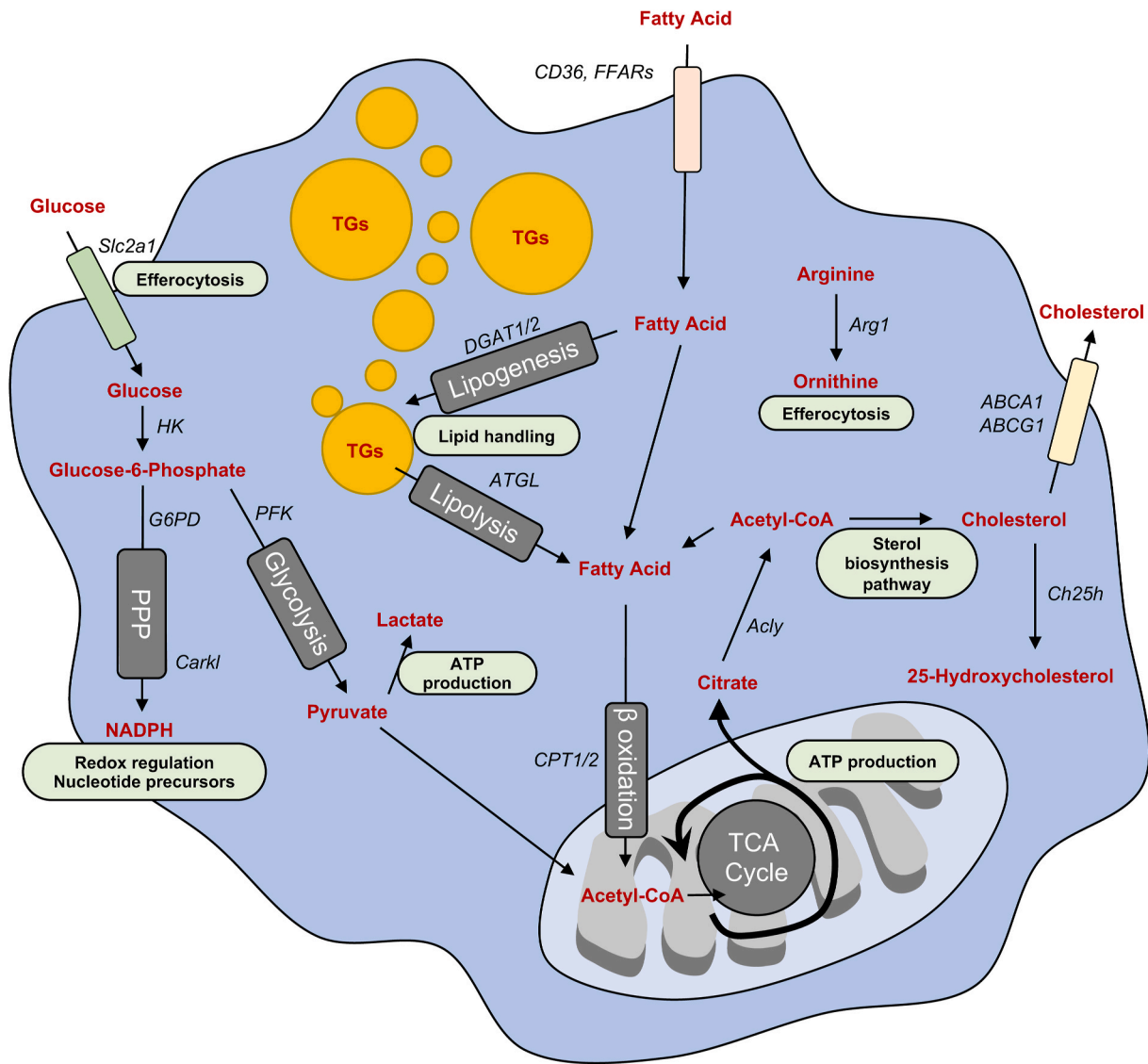


Fig. 2. Schematic representation of macrophage metabolic pathways discussed in the manuscript.

metabolism and is formed in glycolysis and the non-oxidative PPP. Both pathways seem to share this molecule to allow reflux and cycling of carbohydrates within these pathways. This mechanism allows cells to selectively set metabolism to respective needs, which may differ between macrophages or monocytes undergoing oxidative bursts, proliferation or even both at the same time. In M1-like activated macrophages expression of *Carkl* (now known as *Shpk*), a heptose-specific kinase of the PPP forming sedoheptulose-7-P (S7P), is reprimanded [30]. *CARKL*-derived S7P acts as co-substrate to incorporate glycolytic-derived G3P into the PPP and its bioavailability appears rate-limiting for this process. *Carkl* regulation shapes macrophage activation-specific effector functions and sets cellular redox-states [30]. An independent study reported increased S7P levels as metabolic feature of efferocytotic macrophages [43]. Taken together these observations suggest that fine-tuning of glucose flux into glycolysis and the PPP is a tightly regulated process and linked to specific macrophage phenotypes. Thus, considering approaches to modulate glucose intracellular utilization in macrophages could provide an efficient way to influence macrophage inflammatory status and the subsequent cytokine release. High Fat Diet (HFD) feeding deflected glucose flux into the PPP in macrophages, and this might be part of the metabolic reprogramming in plaque [42]. To validate whether this process occurs *in vivo* during

plaque development will require further investigation.

Whether monocytes, pro-inflammatory macrophages and foamy cells within the atherosclerotic plaque rely on specific and exclusive glucose-dependent pathways remains to be established. It will be of importance to determine whether metabolic rewiring of macrophage glucose metabolism occurs at a specific stage of disease progression, in a specific localization, and in a specific cell type. The emergence of new single-cell technologies providing the unique opportunity to define the metabolic configuration of cells in their native environment and locally available metabolites, could offer solutions to solve the aforementioned questions [44].

1.4. Lipids, lipogenesis, lipolysis and lipid oxidation

Recent reports showed that pathways involved in lipid synthesis are modulated in classically activated macrophages. For instance, LPS-stimulated macrophages display an increased phosphorylation of ATP citrate lyase (*Acly*), the enzyme that converts TCA-derived citrate into acetyl-CoA and oxaloacetate (Fig. 2) [45]. Acetyl-CoA can in turn favor cholesterol and lipid biosynthesis. *Acly*-deficient macrophages showed increased expression of genes involved in fatty acid and cholesterol biosynthesis. However, this did not translate into intracellular lipid

accumulation, suggesting that Acly-dependent lipid synthesis is not involved in lipid droplet formation [45]. Acly-deficient macrophages showed an increased inflammatory response to LPS and impaired alternative polarization in response to IL-4. Surprisingly, transplantation of *Lyz2^{cre}* x *Acly^{fl/fl}* bone marrow into *Ldlr^{-/-}* mice did not affect plaque size, but rather promoted a more stable, collagenous phenotype [45]. Another recent report demonstrated that *in vitro* macrophage stimulation with LPS and IFN γ favors lipid droplet formation [46]. Triglyceride (TG) generation in macrophages relies on two key enzymes that catalyze the addition of a fatty acyl chain to diacylglycerol. These two enzymes are named acyl-CoA diacylglycerol acyltransferases 1 and 2 (DGAT1 and DGAT2) (Fig. 2). LPS and IFN γ treatment increased the expression of DGAT1 and 2 in macrophages and this was paralleled by increased intracellular lipid content [46]. In agreement with a role for these enzymes as drivers of lipid droplet formation, the genetic and pharmacological DGAT inhibition decreased macrophage lipid content [46]. This is consistent with the observation that plaque lipid-laden cells express CD11c. Nevertheless, this inhibition led to decreased production of pro-inflammatory cytokines (IL-1 β and IL-6). Thus, one could speculate that the generation of foamy cells in the plaque is a biphasic process where the early accumulation of TGs is associated with a pro-inflammatory program which is later replaced by anti-inflammatory signature in “terminally-differentiated” foamy cells. Such mechanism could resemble CD8⁺ T cells exhaustion, a process where cells lose effector ability including cytokine secretion, during persistent high antigen stimulation. Interestingly, the observed metabolic dysfunction precedes the development of exhaustion itself and does not simply reflect secondary changes in metabolism. Exhaustion is suggestive of glucose deprivation, with suppression of both glycolysis and OXPHOS and altered levels of the glycolytic metabolite phosphoenolpyruvate in exhausted cells that contribute to effector dysfunction [47]. It will be interesting to follow metabolic perturbations in lipid-accumulating macrophages over time to investigate whether similar mechanisms are at play.

Several studies demonstrated that alternatively activated (M2) macrophages exhibit a preference towards fatty acid oxidation metabolism [48]. Nevertheless, the causal link between lipid oxidation and alternative activation was challenged by a recent study using Cpt2-deficient macrophages [49]. Cpt2 is a mitochondrial enzyme involved in fatty acid mitochondrial metabolism. Cpt2-deficient macrophages have compromised fatty acid oxidation, but their IL-4 response is intact [49]. Early reports suggested that Cpt1 pharmacological inhibition with Etomoxir, using a high inhibitor concentration, prevents alternative macrophage activation [48,50]. However, lowering Etomoxir concentration demonstrated no effect on the expression of canonical M2 markers upon IL-4 stimulation while preserving Cpt1 inhibition [51–53]. The use of genetic models allowing for macrophage-selective Cpt1 and Cpt2 ablation (*Lyz2^{cre}* x *Cpt1^{fl/fl}* and *Lyz2^{cre}* x *Cpt2^{fl/fl}* mice) revealed that high Etomoxir concentration decrease macrophage M2-polarization independently from long chain fatty acid mitochondrial entry and oxidation [51]. Thus, how precisely fatty acids modulate macrophage activation state is still to be elucidated. Whether Cpt1 and Cpt2 play a role in plaque macrophage and blood monocyte metabolism and activation is yet to be established. Modulating macrophage lipid metabolism could have an impact on plaque myeloid cell content and therefore on its stability. A recent study, using a Bodipy staining, allowed to separately analyze plaque foamy macrophages [10]. The authors were able to define a clear transcriptomic signature associated with foamy cells. Those cells were enriched for genes encoding for proteins involved in lipid metabolism including *Lipa*, *Fabp4*, *Fabp5*, *CD36* and *Abca1* among others [10]. The relative contributions of these genes to atherosclerosis development were investigated in previous studies [54–60], but how precisely they affect foamy macrophages formation remains to be defined. Bodipy staining revealed that foamy cells were present in plaques after 4 weeks of Western Diet in both *Ldlr^{-/-}* and *ApoE^{-/-}* mice [10]. What precisely leads to foamy cells

formation and expansion remains to be determined. Surprisingly, non-foamy macrophages displayed a pro-inflammatory phenotype in comparison to foamy cells [10]. Thus, one might expect that newly recruited plaque monocytes and monocyte-derived macrophages adopt a pro-inflammatory phenotype and that they contribute to inflammation amplification by secreting inflammatory cytokines and chemokines. A recent study investigating monocyte and macrophage dynamics in plaque development, demonstrated that monocytes progress in deeper plaque layers during atherosclerosis progression [2]. Over a long period of time, these cells can uptake locally available lipids and might become foamy cells. During this process their inflammatory phenotype progressively diminishes. The critical checkpoints leading to foamy macrophages establishment are yet to be validated.

1.5. Prostaglandin and sterol metabolism

In addition to cytokines like IL-4 or IL-13, metabolites also have been shown to induce alternative activation. This is the case of inflammation-resolving lipid mediators such as prostaglandin E2 (PGE2). PGE2 independently induced a fraction of the IL-4 induced transcripts in macrophages, and broadly modified the effects of IL-4. This subtle PGE2 effect was recently demonstrated to play a crucial role in macrophage alternative polarization. This reprogramming was associated with a profound effect on alternatively activated macrophage phenotype [61]. On its own, PGE2 treatment enhanced the expression of canonical M2 markers (CD301, Arg1). The precise function of CD301 (encoded by *clec10a*) during atherosclerosis development remains to be established and recent data suggested that CD301 could be involved in macrophage fusion and the formation of multinucleated cells [62]. Arginase 1 (Arg1) converts arginine to ornithine. A recent study investigated the role of hematopoietic cell Arg1 (*Tie2^{cre}* x *Arg1^{flox/flox}*) during atherosclerosis progression [62]. *Tie2^{cre}* x *Arg1^{flox/flox}* mice had similar plaque size in comparison to control animals. However, *Arg1*-deletion in macrophages favored foamy cell generation [62]. Additionally, arginine promotes continual efferocytosis and this mechanism is crucial to eliminate apoptotic cells from the plaque [63]. PGE2 further potentiated the expression of these markers in the presence of IL-4, but also dampened the IL-4-driven activation of mitochondrial metabolism, without affecting lactate production [61]. These results suggest that surface markers alone cannot predict the cellular metabolic state. PGE2 treatment also inhibited macrophage proliferation, one of the mechanisms leading to plaque development [61]. Production of PGE2 was shown to occur in LPS-treated BMDMs [64], and plaque macrophages selectively express its receptor EP4. In plaque, PGE2 is mainly synthesized by endothelial and smooth muscle cells [65]. Whether locally produced PGE2 plays a role in macrophage metabolic reprogramming during atherosclerosis remains to be defined.

Further distancing from the classical/non classical bipolar activation state is the case of the integrin CD11c in atherosclerotic plaques. CD11c expression appears higher in the population of Trem2^{hi} foamy cells (Fig. 1). This observation is puzzling because plaque foamy cells have an anti-inflammatory phenotype, the contrary of *in vitro* induced classically activated macrophages that display high CD11c expression. A previous study demonstrated that foamy cells are characterized by an anti-inflammatory gene signature [66]. Using peritoneal foamy cells, the authors demonstrated that these cells have decreased mRNA expression of *il1 β* , *cxcl9* and *cxcl10* [66]. The anti-inflammatory effects were mediated by desmosterol accumulation. Indeed, desmosterol was the most abundant sterol detected in foamy peritoneal macrophages [66]. The accumulation of lanosterol, the first sterol in the cholesterol biosynthetic pathway, also triggers anti-inflammatory response in macrophages [67]. Whether the aforementioned mechanisms contribute to the formation of anti-inflammatory foamy cells in plaque remains to be demonstrated. 25-hydroxycholesterol also plays an anti-inflammatory role as demonstrated using genetic ablation of Ch25h, the enzyme converting cholesterol to 25-hydroxycholesterol

(Fig. 2) [68]. 25-hydroxycholesterol addition to peritoneal macrophages isolated from Ch25h-deficient mice decreased their production of pro-inflammatory cytokines (IL-6, IL-1 β , TNF α) while promoting anti-inflammatory cytokine generation (IL-10). Ch25h^{-/-}ApoE^{-/-} mice developed increased atherosclerotic lesions compared to Ch25h^{+/+}ApoE^{-/-} control animals, further validating the anti-atherogenic role of 25-hydroxycholesterol [68]. In peritoneal and bone marrow-derived macrophages, TLR activation induced Ch25h mRNA expression and subsequent 25-hydroxycholesterol synthesis [69–71]. The transcription factor ATF3 was demonstrated to regulate Ch25h expression in macrophages [72]. Of interest, ATF3^{-/-}ApoE^{-/-} mice developed increased plaque lesions and accumulated 25-hydroxycholesterol in the aorta in comparison to control animals [72]. Interferons (IFN), and in particular type I interferons (IFN α and IFN β), are involved in macrophage 25-hydroxycholesterol production [71].

1.6. Intra-plaque localization drives immune cells metabolic configuration?

The precise localization of macrophage subsets in nascent and advanced lesions remains to be fully defined. A diversity in macrophage plaque subsets was also documented in humans [73]. It was documented that plaque shoulders contain mainly a population of pro-inflammatory M1-like macrophages [74]. These regions are typically prone to rupture. Additionally, the presence of CD68⁺MR⁻ (mannose receptor), M1-like macrophages, was also detected mainly in lipid-rich areas of human carotid lesions [75]. The presence of M2-like macrophages in human carotid plaques, co-expressing CD68 and MR, was initially reported in 2007 [76]. Adventitial macrophages displayed a prominent M2-like phenotype [74]. A comparative analysis of macrophage content and diversity in progressive disease stages revealed that both M1- and M2-like macrophages accumulate in plaque during atherosclerosis progression [74]. A comparison of macrophage content and activation state in asymptomatic and symptomatic carotid plaques revealed that CD11c-expressing M1-like macrophages were enriched in symptomatic tissues [77]. Inversely, CD163⁺ M2-like macrophages were more frequent in asymptomatic plaques [77]. Indeed, M1 polarization was associated with instable plaques [78]. Most of the current studies were performed on carotid samples. Comparative analysis of macrophage content and phenotype among vessels isolated from different parts of the body is limited. Plaques in femoral arteries contained a greater proportion of M2-like macrophages when compared to plaques in carotids [79]. M1-like cells were more abundant in carotid plaques in comparison to femoral lesions [79]. The metabolic configuration of these plaque resident macrophage populations is yet to be defined. To determine plaque macrophage subsets metabolism using standard technologies like the Seahorse Analyzer, one would first need to digest the tissue and sort these cells for further analysis. This experiment requires large number of cells and seems challenging to perform due to the low relative frequency and increasing diversity of macrophages residing in advanced plaques notwithstanding that incubating tissue-derived cells with culture media and inhibitors will most likely perturb their metabolic profile beforehand. Alternative strategies to assess metabolic states of cells have now been described that could cope with these limitations [44]. Recently, mass cytometry (CyTOF) and scRNAseq analysis of human atherosclerotic plaques confirmed the presence of M1- and M2-like macrophages [80]. These state-of-the-art technologies further identified the co-existence of multiple macrophage subsets in the plaque [80,81]. Importantly, the relative abundance of these macrophage subsets differed in symptomatic and asymptomatic plaques [80]. The tissue distribution, metabolic profile and contribution to disease progression of the different macrophage subpopulations remains to be established. A metabolic imaging approach based on enzyme histochemistry was developed to assess metabolic configuration of single cells within their specific tissue microenvironments by profiling multiple key enzyme activities of cellular metabolism [82].

Defining the metabolic configuration of nascent and advanced plaques could help to understand whether a specific macrophage activation status could be linked or due to a particular plaque localization and metabolite access. One could expect that deeper plaque zones might have limited access to bloodborne nutrients. Therefore, cells residing in deeper plaque layers would need to rewire their metabolic configuration to adapt to their local microenvironment and ensure their survival or proliferation. For instance, it has been shown that deeper plaque regions, enriched in macrophage content, are characterized by a hypoxia and this leads to Hif1a stabilization in macrophages and the activation of hypoxia response element (HRE) [83]. Hif1a stabilization leads to glycolysis induction in macrophages through the increase of the expression of Glut-1, VEGF secretion and a well-defined metabolic configuration [83]. Low oxygen concentration in deep layer of the plaque stabilizes the transcription factor HIF-1 which promote a glycolytic metabolism and therefore favor macrophage efferocytosis. This observation suggests that glucose promotes efficient apoptotic cells removal from the plaque and that lowering systemic glucose level might dampen macrophage efferocytosis [33,36]. VEGF production leads to the generation of blood vessels locally. This neovascularization would likely play a role in providing local metabolites. The presence of Hif1 protein was identified in atherosclerotic plaque [84]. Hypoxia triggered cholesterol synthesis and blunted cholesterol efflux leading to its accumulation in macrophages [84]. One could expect that hypoxia might trigger foamy cell formation in the plaque and modulate their inflammatory phenotype. Thus, having more information about the metabolic milieu in different areas of the plaque could allow us to consider different strategy to modify local immune cell metabolism and prevent plaque destabilization in these hypoxic areas (Fig. 2).

2. Conclusions

Understanding the metabolic reprogramming of immune cells in nascent and advanced plaque might help to better apprehend the mechanisms leading to plaque progression. We are still in early stages and the information of the local metabolite distribution in plaques is still incomplete. Glucose, fatty acid and amino acid metabolism have been shown to modulate immune cell functions and disease development. However, how precisely these pathways are interconnected and how they influence the recruitment, survival and function of the multiple immune cell populations residing in plaque needs to be established. Combining the cartography of immune cell metabolite content, together with single-cell enzyme activity profiling *in situ* and *ex-vivo* metabolic profiling using SCENITH would offer some powerful new tools to investigate the regulation of immune cell metabolism within the plaque. Recently, single-cell metabolic regulome profiling (scMEP) was published and this technology offers the opportunity to associate a particular metabolic configuration with a cell type [85]. A better knowledge of the metabolic regulation of monocytes and macrophages will most certainly pave the way to new and more subtle treatments for cardiometabolic diseases.

Financial support

Stoyan Ivanov is supported by Institut National de la Sante et de la Recherche Medicale (INSERM) and Agence Nationale de la Recherche (ANR-17-CE14-0017-01 and ANR-19-ECVD-0005-01). Alexandre Gallerand is supported by the French government, through the UCAJedi Investments in the Future projects managed by the National Research Agency (ANR) (ANR-15-IDEX-01).

Declaration of competing interest

The authors declare that they have no known competing financial interests or personal relationships that could have appeared to influence the work reported in this paper.

References

- [1] J.W. Williams, K. Zaitsev, K.W. Kim, et al., Limited proliferation capacity of aortic intima resident macrophages requires monocyte recruitment for atherosclerotic plaque progression, *Nat. Immunol.* 21 (2020) 1194–1204.
- [2] J.W. Williams, C. Martel, S. Potteaux, et al., Limited macrophage positional dynamics in progressing or regressing murine atherosclerotic plaques—brief report, *Arterioscler. Thromb. Vasc. Biol.* 38 (2018) 1702–1710.
- [3] X. Zhou, G.K. Hansson, Detection of B cells and proinflammatory cytokines in atherosclerotic plaques of hypercholesterolaemic apolipoprotein E knockout mice, *Scand. J. Immunol.* 50 (1999) 25–30.
- [4] L. Jonasson, J. Holm, O. Skalli, et al., Regional accumulations of T cells, macrophages, and smooth muscle cells in the human atherosclerotic plaque, *Arteriosclerosis* 6 (1986) 131–138.
- [5] R.G. Gerrity, H.K. Naito, M. Richardson, et al., Dietary induced atherogenesis in swine. Morphology of the intima in prelesion stages, *Am. J. Pathol.* 95 (1979) 775–792.
- [6] I. Joris, T. Zand, J.J. Nunnari, et al., Studies on the pathogenesis of atherosclerosis. I. Adhesion and emigration of mononuclear cells in the aorta of hypercholesterolemic rats, *Am. J. Pathol.* 113 (1983) 341–358.
- [7] C.W. Adams, O.B. Bayliss, Detection of macrophages in atherosclerotic lesions with cytochrome oxidase, *Br. J. Exp. Pathol.* 57 (1976) 30–36.
- [8] D. Hu, S.K. Mohanta, C. Yin, et al., Artery tertiary lymphoid organs control aorta immunity and protect against atherosclerosis via vascular smooth muscle cell lymphotoxin beta receptors, *Immunity* 42 (2015) 1100–1115.
- [9] C. Cochain, E. Vafadarnejad, P. Arampatz, et al., Single-cell RNA-seq reveals the transcriptional landscape and heterogeneity of aortic macrophages in murine atherosclerosis, *Circ. Res.* 122 (2018) 1661–1674.
- [10] K. Kim, D. Shim, J.S. Lee, et al., Transcriptome analysis reveals nonfoamy rather than foamy plaque macrophages are proinflammatory in atherosclerotic murine models, *Circ. Res.* 123 (2018) 1127–1142.
- [11] A. Zernecke, H. Winkels, C. Cochain, et al., Meta-analysis of leukocyte diversity in atherosclerotic mouse aortas, *Circ. Res.* 127 (2020) 402–426.
- [12] J.D. Lin, H. Nishi, J. Poles, et al., Single-cell Analysis of Fate-Mapped Macrophages Reveals Heterogeneity, Including Stem-like Properties, during Atherosclerosis Progression and Regression, 4, *JCI Insight*, 2019.
- [13] H. Winkels, E. Ehinger, M. Vassallo, et al., Atlas of the immune cell repertoire in mouse atherosclerosis defined by single-cell RNA-sequencing and mass cytometry, *Circ. Res.* 122 (2018) 1675–1688.
- [14] G.K. Hansson, A. Hermansson, The immune system in atherosclerosis, *Nat. Immunol.* 12 (2011) 204–212.
- [15] K.J. Moore, I. Tabas, Macrophages in the pathogenesis of atherosclerosis, *Cell* 145 (2011) 341–355.
- [16] F.K. Swirski, M.J. Pittet, M.F. Kircher, et al., Monocyte accumulation in mouse atherosclerosis is progressive and proportional to extent of disease, *Proc. Natl. Acad. Sci. U. S. A.* 103 (2006) 10340–10345.
- [17] F.K. Swirski, P. Libby, E. Aikawa, et al., Ly-6Chi monocytes dominate hypercholesterolemia-associated monocytes and give rise to macrophages in atheromata, *J. Clin. Invest.* 117 (2007) 195–205.
- [18] F. Tacke, D. Alvarez, T.J. Kaplan, et al., Monocyte subsets differentially employ CCR2, CCR5, and CX3CR1 to accumulate within atherosclerotic plaques, *J. Clin. Invest.* 117 (2007) 185–194.
- [19] C.S. Robbins, I. Hilgendorf, G.F. Weber, et al., Local proliferation dominates lesional macrophage accumulation in atherosclerosis, *Nat. Med.* 19 (2013) 1166–1172.
- [20] C. Hardtner, J. Kornemann, K. Krebs, et al., Inhibition of macrophage proliferation dominates plaque regression in response to cholesterol lowering, *Basic Res. Cardiol.* 115 (2020) 78.
- [21] C. Guillemier, S.P. Doherty, A.G. Whitney, et al., Imaging Mass Spectrometry Reveals Heterogeneity of Proliferation and Metabolism in Atherosclerosis, 4, *JCI Insight*, 2019.
- [22] R.J. Arguello, A.J. Combes, R. Char, et al., SCENITH: a flow cytometry-based method to functionally profile energy metabolism with single-cell resolution, *Cell Metabol.* 32 (2020) 1063–1075 e1067.
- [23] I. Tabas, K.E. Bornfeldt, Intracellular and intercellular aspects of macrophage immunometabolism in atherosclerosis, *Circ. Res.* 126 (2020) 1209–1227.
- [24] L.A. O'Neill, E.J. Pearce, Immunometabolism governs dendritic cell and macrophage function, *J. Exp. Med.* 213 (2016) 15–23.
- [25] L.A. O'Neill, R.J. Kishton, J. Rathmell, A guide to immunometabolism for immunologists, *Nat. Rev. Immunol.* 16 (2016) 553–565.
- [26] P.M. Ridker, B.M. Everett, T. Thuren, et al., Antiinflammatory therapy with canakinumab for atherosclerotic disease, *N. Engl. J. Med.* 377 (2017) 1119–1131.
- [27] A. Weinstock, K. Rahman, O. Yaacov, et al., Wnt signaling enhances macrophage responses to IL-4 and promotes resolution of atherosclerosis, *Elife* (2021) 10.
- [28] M.C. Boshuizen, A.E. Neele, M.J. Gijbels, et al., Myeloid interferon-gamma receptor deficiency does not affect atherosclerosis in LDLR(-/-) mice, *Atherosclerosis* 246 (2016) 325–333.
- [29] M. Kratz, B.R. Coats, K.B. Hiser, et al., Metabolic dysfunction drives a mechanistically distinct proinflammatory phenotype in adipose tissue macrophages, *Cell Metabol.* 20 (2014) 614–625.
- [30] A. Haschemi, P. Kosma, L. Gille, et al., The sedoheptulose kinase CARKL directs macrophage polarization through control of glucose metabolism, *Cell Metabol.* 15 (2012) 813–826.
- [31] W. Yu, Z. Wang, K. Zhang, et al., One-carbon metabolism supports S-adenosylmethionine and histone methylation to drive inflammatory macrophages, *Mol. Cell.* 75 (2019) 1147–1160 e1145.
- [32] A. Gallerand, M.I. Stunault, J. Merlin, et al., Myeloid cell diversity and impact of metabolic cues during atherosclerosis, *Immunometabolism* 2 (2020), e200028.
- [33] A.J. Freermerman, L. Zhao, A.K. Pingili, et al., Myeloid slc2a1-deficient murine model revealed macrophage activation and metabolic phenotype Are fueled by GLUT1, *J. Immunol.* 202 (2019) 1265–1286.
- [34] T. Nishizawa, J.E. Kanter, F. Kramer, et al., Testing the role of myeloid cell glucose flux in inflammation and atherosclerosis, *Cell Rep.* 7 (2014) 356–365.
- [35] M. Fukuzumi, H. Shinomiya, Y. Shimizu, et al., Endotoxin-induced enhancement of glucose influx into murine peritoneal macrophages via GLUT1, *Infect. Immun.* 64 (1996) 108–112.
- [36] S. Morioka, J.S.A. Perry, M.H. Raymond, et al., Efferocytosis induces a novel SLC program to promote glucose uptake and lactate release, *Nature* 563 (2018) 714–718.
- [37] L. Oburoglu, S. Tardito, V. Fritz, et al., Glucose and glutamine metabolism regulate human hematopoietic stem cell lineage specification, *Cell Stem Cell* 15 (2014) 169–184.
- [38] V. Sarrazy, M. Viaud, M. Westertep, et al., Disruption of Glut1 in hematopoietic stem cells prevents myelopoiesis and enhanced glucose flux in atheromatous plaques of ApoE(-/-) mice, *Circ. Res.* 118 (2016) 1062–1077.
- [39] P.R. Nagareddy, A.J. Murphy, R.A. Stirzaker, et al., Hyperglycemia promotes myelopoiesis and impairs the resolution of atherosclerosis, *Cell Metabol.* 17 (2013) 695–708.
- [40] C. Nagy, A. Haschemi, Time and demand are two critical dimensions of immunometabolism: the process of macrophage activation and the pentose phosphate pathway, *Front. Immunol.* 6 (2015) 164.
- [41] E.M. Palsson-McDermott, A.M. Curtis, G. Goel, et al., Pyruvate kinase M2 regulates Hif-1alpha activity and IL-1beta induction and is a critical determinant of the warburg effect in LPS-activated macrophages, *Cell Metabol.* 21 (2015) 65–80.
- [42] J. Baardman, S.G.S. Verberk, K.H.M. Prange, et al., A defective pentose phosphate pathway reduces inflammatory macrophage responses during hypercholesterolemia, *Cell Rep.* 25 (2018) 2044–2052 e2045.
- [43] S. Zhang, S. Weinberg, M. DeBerge, et al., Efferocytosis fuels requirements of fatty acid oxidation and the electron transport chain to polarize macrophages for tissue repair, *Cell Metabol.* 29 (2019) 443–456 e445.
- [44] M.N. Artyomov, Van den Bossche, J, Immunometabolism in the Single-Cell Era, *Cell Metab* 32 (2020) 710–725.
- [45] J. Baardman, S.G.S. Verberk, S. van der Velden, et al., Macrophage ATP citrate lyase deficiency stabilizes atherosclerotic plaques, *Nat. Commun.* 11 (2020) 6296.
- [46] A. Castoldi, L.B. Monteiro, N. van Teijlingen Bakker, et al., Triacylglycerol synthesis enhances macrophage inflammatory function, *Nat. Commun.* 11 (2020) 4107.
- [47] E.F. McKinney, K.G.C. Smith, Metabolic exhaustion in infection, cancer and autoimmunity, *Nat. Immunol.* 19 (2018) 213–221.
- [48] S.C. Huang, B. Everts, Y. Ivanova, et al., Cell-intrinsic lysosomal lipolysis is essential for alternative activation of macrophages, *Nat. Immunol.* 15 (2014) 846–855.
- [49] M. Nomura, J. Liu, Rovira II, et al., Fatty acid oxidation in macrophage polarization, *Nat. Immunol.* 17 (2016) 216–217.
- [50] A.J. Covarrubias, H.I. Aksoylar, J. Yu, et al., Akt-mTORC1 signaling regulates Acly to integrate metabolic input to control of macrophage activation, *Elife* 5 (2016).
- [51] A.S. Divakaruni, W.Y. Hsieh, L. Minarrieta, et al., Etomoxir inhibits macrophage polarization by disrupting CoA homeostasis, *Cell Metabol.* 28 (2018) 490–503 e497.
- [52] J. Van den Bossche, J. Baardman, N.A. Otto, et al., Mitochondrial dysfunction prevents repolarization of inflammatory macrophages, *Cell Rep.* 17 (2016) 684–696.
- [53] Z. Tan, N. Xie, H. Cui, et al., Pyruvate dehydrogenase kinase 1 participates in macrophage polarization via regulating glucose metabolism, *J. Immunol.* 194 (2015) 6082–6089.
- [54] V.R. Babaei, R.P. Runner, D. Fan, et al., Macrophage Mal1 deficiency suppresses atherosclerosis in low-density lipoprotein receptor-null mice by activating peroxisome proliferator-activated receptor-gamma-regulated genes, *Arterioscler. Thromb. Vasc. Biol.* 31 (2011) 1283–1290.
- [55] A.J. Murphy, M. Akhtari, S. Tolani, et al., ApoE regulates hematopoietic stem cell proliferation, monocytes, and monocyte accumulation in atherosclerotic lesions in mice, *J. Clin. Invest.* 121 (2011) 4138–4149.
- [56] L. Yvan-Charvet, T. Pagler, E.L. Gautier, et al., ATP-binding cassette transporters and HDL suppress hematopoietic stem cell proliferation, *Science* 328 (2010) 1689–1693.
- [57] M. Viaud, S. Ivanov, N. Vujic, et al., Lysosomal cholesterol hydrolysis couples efferocytosis to anti-inflammatory oxysterol production, *Circ. Res.* 122 (2018) 1369–1384.
- [58] M. Febbraio, E.A. Podrez, J.D. Smith, et al., Targeted disruption of the class B scavenger receptor CD36 protects against atherosclerotic lesion development in mice, *J. Clin. Invest.* 105 (2000) 1049–1056.
- [59] T.A. Seimon, M.J. Nadolski, X. Liao, et al., Atherogenic lipids and lipoproteins trigger CD36-TLR2-dependent apoptosis in macrophages undergoing endoplasmic reticulum stress, *Cell Metabol.* 12 (2010) 467–482.
- [60] S. Kuchibhotla, D. Vanegas, D.J. Kennedy, et al., Absence of CD36 protects against atherosclerosis in ApoE knock-out mice with no additional protection provided by absence of scavenger receptor A I/II, *Cardiovasc. Res.* 78 (2008) 185–196.
- [61] D.E. Sanin, M. Matsushita, R.I. Klein Geltink, et al., Mitochondrial membrane potential regulates nuclear gene expression in macrophages exposed to prostaglandin E2, *Immunity* 49 (2018) 1021–1033 e1026.

- [62] B. Ren, E. Van Kampen, T.J. Van Berkel, et al., Hematopoietic arginase 1 deficiency results in decreased leukocytosis and increased foam cell formation but does not affect atherosclerosis, *Atherosclerosis* 256 (2017) 35–46.
- [63] A. Yurdagul Jr., M. Subramanian, X. Wang, et al., Macrophage metabolism of apoptotic cell-derived arginine promotes continual efferocytosis and resolution of injury, *Cell Metabol.* 31 (2020) 518–533 e510.
- [64] T. Tang, T.E. Scambler, T. Smallie, et al., Macrophage responses to lipopolysaccharide are modulated by a feedback loop involving prostaglandin E2, dual specificity phosphatase 1 and tristetraprolin, *Sci. Rep.* 7 (2017) 4350.
- [65] I. Gomez, N. Foudi, D. Longrois, et al., The role of prostaglandin E2 in human vascular inflammation, *Prostaglandins Leukot. Essent. Fatty Acids* 89 (2013) 55–63.
- [66] N.J. Spann, L.X. Garmire, J.G. McDonald, et al., Regulated accumulation of desmosterol integrates macrophage lipid metabolism and inflammatory responses, *Cell* 151 (2012) 138–152.
- [67] E. Araldi, M. Fernandez-Fuertes, A. Canfran-Duque, et al., Lanosterol modulates TLR4-mediated innate immune responses in macrophages, *Cell Rep.* 19 (2017) 2743–2755.
- [68] Z. Li, M. Martin, J. Zhang, et al., Kruppel-like factor 4 regulation of cholesterol-25-hydroxylase and liver X receptor mitigates atherosclerosis susceptibility, *Circulation* 136 (2017) 1315–1330.
- [69] D.R. Bauman, A.D. Bitmansour, J.G. McDonald, et al., 25-Hydroxycholesterol secreted by macrophages in response to Toll-like receptor activation suppresses immunoglobulin A production, *Proc. Natl. Acad. Sci. U. S. A.* 106 (2009) 16764–16769.
- [70] U. Diczfalussy, K.E. Olofsson, A.M. Carlsson, et al., Marked upregulation of cholesterol 25-hydroxylase expression by lipopolysaccharide, *J. Lipid Res.* 50 (2009) 2258–2264.
- [71] K. Park, A.L. Scott, Cholesterol 25-hydroxylase production by dendritic cells and macrophages is regulated by type I interferons, *J. Leukoc. Biol.* 88 (2010) 1081–1087.
- [72] E.S. Gold, S.A. Ramsey, M.J. Sartain, et al., ATF3 protects against atherosclerosis by suppressing 25-hydroxycholesterol-induced lipid body formation, *J. Exp. Med.* 209 (2012) 807–817.
- [73] S. Colin, G. Chinetti-Gbaguidi, B. Staels, Macrophage phenotypes in atherosclerosis, *Immunol. Rev.* 262 (2014) 153–166.
- [74] J.L. Stoger, M.J. Gijbels, S. van der Velden, et al., Distribution of macrophage polarization markers in human atherosclerosis, *Atherosclerosis* 225 (2012) 461–468.
- [75] G. Chinetti-Gbaguidi, M. Baron, M.A. Bouhlel, et al., Human atherosclerotic plaque alternative macrophages display low cholesterol handling but high phagocytosis because of distinct activities of the PPARgamma and LXRalpha pathways, *Circ. Res.* 108 (2011) 985–995.
- [76] M.A. Bouhlel, B. Derudas, E. Rigamonti, et al., PPARgamma activation primes human monocytes into alternative M2 macrophages with anti-inflammatory properties, *Cell Metabol.* 6 (2007) 137–143.
- [77] K.Y. Cho, H. Miyoshi, S. Kuroda, et al., The phenotype of infiltrating macrophages influences arteriosclerotic plaque vulnerability in the carotid artery, *J. Stroke Cerebrovasc. Dis.* 22 (2013) 910–918.
- [78] C.W. Lee, I. Hwang, C.S. Park, et al., Macrophage heterogeneity of culprit coronary plaques in patients with acute myocardial infarction or stable angina, *Am. J. Clin. Pathol.* 139 (2013) 317–322.
- [79] S. Shaikh, J. Brittenden, R. Lahiri, et al., Macrophage subtypes in symptomatic carotid artery and femoral artery plaques, *Eur. J. Vasc. Endovasc. Surg.* 44 (2012) 491–497.
- [80] D.M. Fernandez, A.H. Rahman, N.F. Fernandez, et al., Single-cell immune landscape of human atherosclerotic plaques, *Nat. Med.* 25 (2019) 1576–1588.
- [81] M.A.C. Depuydt, K.H.M. Prange, L. Slenders, et al., Microanatomy of the human atherosclerotic plaque by single-cell transcriptomics, *Circ. Res.* 127 (2020) 1437–1455.
- [82] A. Miller, C. Nagy, B. Knapp, et al., Exploring metabolic configurations of single cells within complex tissue microenvironments, *Cell Metabol.* 26 (2017) 788–800 e786.
- [83] J.C. Sluimer, J.M. Gasc, J.L. van Wanroij, et al., Hypoxia, hypoxia-inducible transcription factor, and macrophages in human atherosclerotic plaques are correlated with intraplaque angiogenesis, *J. Am. Coll. Cardiol.* 51 (2008) 1258–1265.
- [84] S. Parathath, S.L. Mick, J.E. Feig, et al., Hypoxia is present in murine atherosclerotic plaques and has multiple adverse effects on macrophage lipid metabolism, *Circ. Res.* 109 (2011) 1141–1152.
- [85] F.J. Hartmann, D. Mrdjen, E. McCaffrey, et al., Single-cell metabolic profiling of human cytotoxic T cells, *Nat. Biotechnol.* 39 (2021) 186–197.